# Theory and Numerics of Open System Continuum Thermodynamics – Spatial and Material Settings –

dem Fachbereich Maschinenbau und Verfahrenstechnik
der Technischen Universität Kaiserslautern
zur Erlangung der venia legendi für das Fach

**Mechanik**

vorgelegte Habilitationsschrift

von
Dr.–Ing. Ellen Kuhl
aus Hannover

Gutachter:

Prof. Dr.–Ing. P. Steinmann
Prof. Dr. G. A. Holzapfel
Prof. Dr.–Ing. C. Miehe

Tag der Einreichung: 30. Juli 2003
Vollzug des Habilitationsverfahrens: 25. Februar 2004

Another value in science is the fun called intellectual enjoyment which some people get from reading and learning and thinking about it, and which others get from working in it. This is an important point, one which is not considered enough by those who tell us it is our social responsibility to reflect on the impact of science on society.

Richard P. Feynman,
The Meaning of it All, 1963

# Abstract

The present treatise aims at deriving a general framework for the thermodynamics of open systems typically encountered in chemo– or biomechanical applications. Due to the fact that an open system is allowed to constantly gain or lose mass, the classical conservation law of mass has to be recast into a balance equation balancing the rate of change of the current mass with a possible in- or outflux of matter and an additional volume source term. The influence of the generalized mass balance on the balance of momentum, kinetic energy, total energy and entropy is highlighted. Thereby, special focus is dedicated to the strict distinction between a volume specific and a mass specific format of the balance equations which is of no particular relevance in classical thermodynamics of closed systems.
The change in density furnishes a typical example of the local rearrangement of material inhomogeneities which can be characterized most elegantly in the material setting. The set of balance equations for open systems will thus be derived for both, the spatial and the material motion problem. Thereby, we focus on the one hand on highlighting the remarkable duality between both approaches. On the other hand, special emphasis is placed on deriving appropriate relations between the spatial and the material motion quantities.
The second part of this work suggests different numerical solution strategies based on the finite element technique. Three different problem classes, i.e. adiabatic closed systems, closed systems and open systems are elaborated. Each of them can be cast into a two–field finite element formulation whereby either the material motion map, the temperature or the density is introduced as a second continuous field next to the classical spatial motion map. Alternatively, this second field can be introduced discontinuously on the integration point level. While for the former approach, the discrete balance equations are solved simultaneously on the global level, the latter strategy is typically related to a staggered solution with the second field treated as internal variable. The resulting algorithms of the alternative solution techniques are compared in terms of stability, uniqueness, efficiency and robustness.
Finally, a number of numerical examples is given to illustrate the features of the proposed approach. Applications range from mesh optimization to thermo-, chemo- and biomechanical problems, whereby the latter is maybe the most attractive one. Numerical solutions are presented not only for the classical spatial motion problem but also for the material motion problem.

# Zusammenfassung

Ziel der vorliegenden Arbeit ist die Bereitstellung eines allgemeinen Rahmens zur Beschreibung der Thermodynamik offener Systeme, wie sie üblicherweise in der Chemo- oder Biomechanik Anwendung finden. Um einer permanent stattfindenden Massenänderung Rechnung zu tragen, muss die klassische Massenbilanz für offene Systeme um zusätzliche Zu- oder Abflussterme sowie um Volumenquellterme erweitert werden. Diese generalisierte Massenbilanz beeinflusst konsequenterweise alle höheren Bilanzgleichungen, die entsprechend zu modifiziert sind. Eine Besonderheit dieser Arbeit liegt in der strikten Unterscheidung zwischen der sogenannten volumenspezifischen und der massenspezifischen Formulierung der Bilanzgleichungen. Im Gegensatz zu klassischen geschlossenen Systemen ist diese Unterscheidung bei offenen Systemen von besonderer Bedeutung.
Dichteänderungen sind ein typisches Beispiel für die lokale Reorganisation materieller Inhomogenitäten, die sich ausgesprochen elegant in der materiellen Darstellung charakterisieren lässt. Aus diesem Grund wird der Satz der Bilanzgleichungen nicht allein in der allgemein gebräuchlichen räumlichen Form, sondern auch in der materiellen Darstellung hergeleitet. Ein besonderer Schwerpunkt liegt hierbei in der Herausarbeitung der Dualität beider Darstellungen. Darüberhinaus werden Transformationsbeziehungen zwischen räumlichen und materiellen Grössen bereitgestellt.
Der zweite Teil dieser Arbeit ist der numerischen Umsetzung im Rahmen der Finite Element Methode gewidmet. Dabei werden exemplarisch drei unterschiedliche Problemklassen näher analysiert, adiabate geschlossene Systeme, geschlossene Systeme und offene Systeme. Diese lassen sich jeweils in eine Zweifeldformulierung überführen, wobei entweder die materielle Deformationsabbildung, die Temperatur oder die Dichte als kontinuierliches zweites Feld neben der räumlichen Deformationsabbildung berücksichtigt wird. Alternativ kann dieses zweite Feld auch diskontinuierlich auf Integrationspunktebene eingeführt werden. Während die diskreten Bilanzgleichungen im ersten Fall simultan auf globaler Ebene gelöst werden, führt die zweite Strategie auf eine gestaffelte Lösung mit dem zweiten Feld als interne Variable. Die resultierende Algorithmen der alternativen Lösungsverfahren werden im Hinblick auf Stabilität, Eindeutigkeit, Effizienz und Robustheit miteinander verglichen.
Schliesslich werden die Eigenschaften der entwickelten Algorithmen anhand zahlreicher numerischer Beispiele veranschaulicht. Die Anwendungen reichen hierbei von der Optimierung der Finiten Element Vernetzung bis hin zu thermo-, chemo- und biomechanischen Problemstellungen. Numerische Lösungen werden nicht nur für das klassische räumliche Problem, sondern auch für das materielle Problem bereit gestellt und diskutiert.

# Preface

The research presented in this thesis was carried out at the Chair of Applied Mechanics at the Technical University of Kaiserslautern. Part of the work was financed through the DFG habilitation grant KU 1313/3-1 the support of which is gratefully acknowledged.
I would like to thank Professor Paul Steinmann for creating the most stimulating and inspiring working environment i have ever experienced. Those who have had the chance to work with him should know this exceptional synthesis of serious tensor crunching and non-serious joking which, to me, was a source of creativity and motivation that made me enjoy my work over the past ten years. Thanks!
Moreover, I would like to thank Professor Gerhard Holzapfel and Professor Christian Miehe for accepting to be correferees of this thesis. Stimulating discussions with both of them at various occasions had a great impact on the present work. Special thanks go to Professor René de Borst who supported my post doc stay at the TU Delft. He encouraged me to work in a completely different field and always gave me the feeling of having a second home in the Netherlands.
Finally, I would like to thank all the people who have contributed to this research, in one way or the other, and made these last four years an unforgettable period of my life: Tadesse fish-in-the-dam Abdi, Harm what-do-you-mean-by-low-humor-threshold Askes, Swantje addicted-to-nederlandse-dropjes Bargmann, Franz Josef hilfe-herr-barth-nichts-geht-mehr Barth, Peter master-of-fem Betsch, Alberto that-don't-impress-me-much Bordallo, Alexandru call-me-al Constantiniu, Ralf schmeiss-das-aus-dem-fenster Denzer, Aitor què-pasa Elizondo, Inna gehaktballen-voor-het-ontbijt Gitman, Jürgen le-dictionnaire-courant Glaser, Michael was-ist-schlimmer-als-verlieren Gross, Oliver muss-ich-jetzt-beisitzer-machen Häsner, Grieta wir-grillen-heute-bei-dir Himpel, Steve what's-a-rieman-solver Hulshoff, Nina kind-im-hort Kirchner, Bernd isst-du-das-nicht Kleuter, Natalia mit-vergnügen-quälen Kondratieva, Detlef lord-of-the-board Kuhl, Sigrid piesporter-glüh-wein Leyendecker, Tina always-on-the-run Liebe, Erik Jan that's-very-simple Lingen, Kurt happy-birthday Maute, Andreas one-more-fish Menzel, Julia singulär-diskontinuierlich-nachtblind Mergheim, Christian het-groene-boek Michler, Wolf Christian welt-rettungs-zentrale Müller, Jerzy do-it-yourself Pamin, Areti cocktails-haben-eine-jahrtausende-alte-tradition-in-griechenland Papastavrou, Gunnar hauptsache's-das's-klebt Possart, Joris wo-ist-der-bahnhof Remmers, Gerald immer-noch-kein-park-ticket Scheday, Rolf customer-oriented-twenty-four-seven Schneider, Angelo italian-habilitation-is-better-than-german-habilitation Simone, Bert look-me-in-the-ice Sluys, Holger das-muss-man-immer-machen Steeb, Martijn sunglasses-collector Stroeven, Garth zack-zack Wells, Christopher kauft-ihr-schon-mal-den-salat Wissmann and, of course, my family, my mother and my sisters Anke and Katja.

Kaiserslautern, February 2004 Ellen Kuhl

# Contents

# 1 Introduction

Why do we need to get involved in a field of knowledge which, within the last hundred years, has exhibited the largest number of schizophrenics and megalomaniacs, imbalanced scientists, paranoiacs, egocentrists, and probably insomniacs and sleepwalkers?

Gérard A. Maugin,
The Thermomechanics of Nonlinear
Irreversible Behaviors, 1999

## 1.1 State of the art review

Although classical thermodynamics can with no doubt be characterized as one of the outstanding achievements of the scientific mind there is hardly any field in research that has been discussed more controversially than thermodynamics. When referring to classical thermodynamics, we typically think of closed thermodynamic systems for which the amount of matter within a fixed material domain is assumed to be constant throughout the entire thermodynamical process. Conceptually speaking, classical thermodynamics deals with closed systems which are allowed to exchange mechanical work and heat with their surroundings while the exchange of matter with the environment is a priori excluded. For most traditional applications, the conservation of mass, which is in fact nothing but a mere definition, yields sufficiently accurate results. Nevertheless, within the last decades, the field of application of thermodynamics, supplemented by appropriate computational solution techniques, has been growing tremendously. Biomechanical and chemomechanical problems furnish typical examples of recent fields of interest. As opposed to the traditional applications, both, biomechanics and chemomechanics, typically fall within the category of open system thermodynamics allowing for the in– or outflux of matter as well as for the local creation of mass. Consequently, the traditional balance of mass has to be enhanced by additional open system contributions. It is quite obvious, that the exchange of matter with the environment not only affects the balance of mass itself since the newly generated or inflowing mass typically carries a specific amount of momentum, energy and entropy. Thus, all the other balance equations have to be reconsidered as well in the view of open system thermodynamics. Surprisingly, more than forty years ago, the subject of open systems was addressed in nearly every textbook of thermodynamics, whereas one can hardly find any remark on open systems in the modern literature on thermodynamic nowadays.

One of the most challenging applications of open system thermodynamics is certainly the field of biomechanics, a well–recognized, fast–growing but not yet clearly defined subject that is unquestionably an interdisciplinary science par excellence. In contrast to traditional engineering materials, living organisms show the remarkable ability to adapt not only their geometry, but also their internal architecture and their material properties to environmental changes. Biomechanics thus provides a number of new and fascinating areas of application such as the internal and external remodeling of hard tissues, healing of fracture in bones, growth of tumors, wound healing of the epidermis, regeneration of microdamaged muscles, the functional adaption of bones as well as of arteries and general repair processes of the cardiovascular system to name but a few. Since hard tissues typically undergo small deformations and behave nearly elastic in the range of interest, the first rigorous mathematical models for biological tissues that were introduced in the mid 70s were restricted to the functional adaption of hard tissues such as bones. It was only in the mid 90s, that geometrically exact models for soft tissues were derived which also addressed the aspect of pre–stress. Ever since then, more sophisticated models have been developed to capture the effects of anisotropy, viscosity, damage or plasticity. In some cases, it even became necessary, to include the viscous pore fluid into the characterization and to change the underlying theory from open system thermodynamics to the theory of porous media. Despite of all these tremendous developments, biomechanics today is still in its infancy and it would certainly be too ambitious to claim, that our biomechanical models should explain every single detail of the individual medical processes. Rather, the goal is to develop models which capture the essence of mechanical and biological interactions allowing their outcome to be more fully understood. Computational simulations should provide further insight into complex biomechanical phenomena and capture basic dependencies and trends. In this respect, the whole field of tissue engineering which aims at creating living artificial tissue substitutes with human cells can certainly be identified as one of the most promising applications of biomechanics in the future. Another equally interesting field of future application is the area of patient specific medical care. In modern biomechanics research, a strong trend from diagnostic empirical evidence based medicine towards predictive medicine with the help of reliable computational simulations can be observed. Based on the development of modern computer technologies in combination with diagnostic imaging, we might one day be able to simulate each patient's problems individually and provide patient specific medical treatment.

The equations characterizing biomechanical phenomena are typically too complex to be solved analytically. The finite element method which has been introduced in the late 50s by aerospace engineers provides a powerful numerical tool which is able to capture not only complex geometries but also nonlinear phenomena and multiple interacting fields in a straightforward way. The first application of the finite element method to biomechanical problems dates back to the beginning of the 80s and was again dominated by hard tissue mechanics. The first models basically made use of the classical displacement solution of commercial finite element codes. Starting with an initially homogeneous density distribution, changes in the density field were typically calculated within the post–processing step. Next, the material input data for each element was

modified manually in response to the new density distribution and a new calculation loop was carried out. Needless to say, that after a few iteration loops, these first algorithms typically suffered from the loss of stability and uniqueness. Nevertheless, their results were in surprisingly good agreement with observed experimental findings and they gave way for more enhanced algorithmic realizations.
Since the mid 90s, finite element research has been dominated by multifield physics which essentially required increasingly sophisticated mathematical techniques. Conceptually speaking, the interacting fields can either be determined in a monolithic or in a partitioned way, whereby the latter approach can either be related to a partitioned staggered or to a partitioned sequential solution. The additional field quantities can either be introduced locally on the integration point level, an approach which is commonly followed in computational inelasticity, or globally on the node point level, a strategy which becomes mandatory if higher order spatial gradients of the additional field are present in the governing equations. Typical examples of the latter are non–adiabatic thermoelasticity, gradient plasticity or gradient damage, or, in the case of biomechanics, open systems which are characterized through a mass flux proportional to the density gradient. In contrast to the first finite element models of the late 60s which were restricted to linear elasticity in combination with linear kinematics, modern finite element technologies typically apply nonlinear constitutive relations and geometrically nonlinear kinematics. The resulting nonlinear system of equations is typically solved within an incremental iterative Newton–Raphson solution procedure which essentially relies on the consistent linearization of the governing equations. Nowadays, the solution of multifield problems within the finite element framework can be classified as modern standard as documented by a number of recent textbooks on nonlinear multifield finite element technologies.
The basic task in biomechanics is to determine the reaction of a biological structure in response to prescribed mechanical forces. In the context of classical mechanics, the notion of forces is typically associated with spatial forces in the sense of Newton which can be considered as the driving force for positional changes relative to the ambient space. In complete duality, we could introduce material forces in the sense of Eshelby which are nothing but the driving forces for positional changes relative to the ambient material. The mechanics on the material manifold which date back to the early work of Eshelby in the mid 50s provide an elegant tool to describe the local rearrangement of material inhomogeneities. In the context of linear elastic fracture mechanics, material forces can be understood as a vector–valued generalization of the classical J–integral. A promising state–of–the–art application of material forces is provided by open system thermodynamics. In particular in the context of biomechanics, material forces can be utilized to characterize the local reorganization of matter. As such, they sense geometric imperfections such as local wounds or cracks and indicate the tendency towards the apposition of new biomaterial to close geometric defects in the context of soft tissue mechanics. In the context of hard tissue mechanics, they can be applied as indicators for external and internal remodeling. As a particularly appealing side aspect, the algorithmic determination of the material forces is straightforward and extremely cheap from a computational point of view. The material force method, which has been introduced successfully into modern finite element technologies within the last three years,

essentially makes use of the fact, that the solution to the spatial motion problem has been determined beforehand. Then, the calculation of the discrete material node point forces represents nothing but a post–processing step which makes use of existing finite element structures and requires no computationally expensive inversion of huge system matrices.
Next to the material force method, another branch of application of the material motion problem has proven extremely promising in modern finite element technologies. Discrete material forces can be utilized as driving forces for mesh optimization in the context of Arbitrary Lagrangian Eulerian finite element formulations. While continuous material forces typically indicate the existence of inhomogeneities of the continuum problem, discrete material forces can be interpreted as an indicator for discrete inhomogeneities. In the context of the finite element framework, the nodes of the underlying finite element discretization typically represent a discrete source of inhomogeneity. Consequently, a non–vanishing discrete material force residual indicates that the finite element nodes are not placed in the optimal position, i.e. the underlying discretization is not yet optimal. An additional release of energy takes place when finite element nodes are moved in the direction opposite to the resulting discrete material node point forces. The discrete numerical solution of the equilibrium of spatial and material forces, which basically follows from the minimization of the ALE Dirichlet principle, defines the optimal spatial and the material configuration in the sense of energy minimization. Being derived from a consistent variational framework, the resulting set of equations is inherently symmetric unlike classical ALE formulations.

## 1.2 Structure of the present work

The present monograph is basically divided in two parts. In the first part consisting of chapters 2–4, we will introduce the basic continuous equations that constitute the general theoretical framework of open system thermodynamics. We thus begin by defining the relevant kinematic quantities for both, the spatial and the material motion problem in chapter 2. In anticipation of further elaborations, we will not only introduce the classical material and spatial configuration but also a third arbitrary reference configuration. Appropriate kinematic relations will be defined between these three configurations. Next, the balance equations for open systems are introduced in chapter 3. Thereby, we shall derive every balance equation except for the balance of mass in a volume specific and in a mass specific format. This strict distinction which is of no particular interest in closed system thermodynamics will prove essential when discussing appropriate constitutive assumptions. It will turn out, that the mass specific format of the balance equations for open systems is formally identical to the familiar format known from closed system thermodynamics. The set of governing equations is finally closed by the constitutive equations set up in chapter 4. It will be demonstrated that the evaluation of the dissipation inequality provides additional restrictions for the constitutive equations for the momentum flux and the heat flux. The choice of the mass flux and source, however, is only restricted implicitly through the extra entropy flux and source. The appropriate specification of the constitutive equations is then ex-

emplified for the adiabatic closed system case of hyperelasticity, for the closed system case of thermohyperelasticity and finally for the open system case.
In the second part of this work, namely in chapters 5–7, we focus on the numerical evaluation of the derived set of equations. To this end, we specify three classes of model problems, adiabatic closed, closed and open systems. Each of these problem classes naturally lends itself into a two–field formulation in terms of the spatial deformation map and a second field. In all three cases, the individual coupled problems are solved simultaneously within a monolithic incremental iterative Newton–Raphson solution procedure. Within the algorithmic evaluation, particular focus will be dedicated to the physical interpretation of the discrete material node point forces resulting from the discretized material motion problem.
Chapter 5 deals with classical adiabatic closed systems for which the material deformation map will be introduced as second vector–valued field in addition to the spatial deformation map. For the considered hyperelastic case, the governing equations, i.e. the spatial and the material version of the balance of linear momentum, can alternatively be derived within a consistent variational framework based on the ALE Dirichlet principle. Its minimization defines both, the balance of spatial forces in the sense of Newton and the balance of material forces in the sense of Eshelby. The corresponding finite element formulation is parameterized in terms of the material and the spatial reference mapping. Its numerical solution renders the optimal spatial and the optimal material configuration in the sense of energy minimization whereby the latter characterizes the optimal mesh. A number of selected examples will demonstrate the potential of the variational ALE strategy in the context of mesh optimization.
While chapter 5 focuses on adiabatic closed systems, non–adiabatic closed systems will be elaborated in chapter 6. We thus introduce the temperature field as second scalar–valued field next to the vector–valued spatial motion field. Chapter 6 highlights the finite element discretization and the monolithic solution of the coupled problem which is basically characterized through the spatial versions of the balance of momentum and energy. To this end, we suggest an incremental iterative Newton–Raphson solution strategy supplemented by the consistent linearization of the governing equations. In the context of closed systems, the material motion problem will be elaborated with the help of the material force method. Thereby, discrete material node point forces are calculated in a post–processing step, once the converged solution to the spatial motion problem has been determined. Several examples will be given to illustrate the physical meaning of the individual contributions to the material node point forces, which, in the context of closed systems, consist not only of an internal but also of a volume dependent contribution.
Finally, we shall address the algorithmic realization of open system thermodynamics in chapter 7. Similar to the previous chapter, we introduce a second scalar–valued quantity namely the material density next to the spatial deformation map. The computational solution of the coupled problem which is essentially defined through the spatial version of the balance of mass and momentum is carried out in complete analogy to the previous chapter. We thus introduce the density and the spatial deformation map as nodal unknowns on the global level. In addition to this node point based approach, we suggest an alternative discretization strategy in the form of an integration

point based approach. Thereby, the density is introduced as internal variable on the integration point level and solved for in a local Newton iteration which is embedded in the global Newton–Raphson solution for the spatial deformation map. Both strategies, the node point based and the integration point based approach will be compared in terms of stability, uniqueness and efficiency with the help of characteristic model problems. For the node point based approach, discrete material node point forces will again be calculated in an additional post–processing step. Moreover, we shall demonstrate the influence of the mass flux, which enables the simulation of the classical size effect within the node point based approach. The potential of the derived algorithmic setup will be elaborated with the help of representative examples taken from the biomechanical literature. In particular, we shall simulate the functional adaption of hard tissues such as growth of bones as well as healing phenomena of soft tissues such as wound healing of skin.

Throughout the entire thesis, we shall apply a three–step strategy. First, the well–known equations of the classical spatial motion problem are discussed. Next, guided by arguments of duality, we shall formally introduce the material motion equations in complete analogy to the corresponding spatial motion versions. In a third step, appropriate transformations between both settings are set up helping to identify the introduced material motion quantities in terms of their spatial motion counterparts.

# 2 Kinematics

Two monks were arguing about the temple flag waving in the wind. One said, 'The flag moves.' The other said, 'The wind moves.' They argued back and forth but could not agree. The sixth ancestor said, 'Gentlemen! It is not the wind that moves; It is not the flag that moves; It is your mind that moves.' The two monks were struck with awe.

Koan 29,
The Mumon Koan, 13th century

In the present chapter, we shall briefly summarize the fundamental relations of the underlying geometrically exact kinematic framework. For further details, we advise the early monographs by Murnaghan [164], Eringen [58, 59], Malvern [147], Chadwick [28] and Marsden & Hughes [148] or the recent enlighting overviews by Bonet & Wood [16], Ogden [172], Podio–Guidugli [175], Holzapfel [93] and Haupt [91]. Our particular kinematic description is essentially characterized through the introduction of an independent fixed reference domain $\mathcal{B}_\square$ next to the classical spatial and material domain $\mathcal{B}_t$ and $\mathcal{B}_0$. For different options of setting up appropriate kinematic relations between these three domains, we refer to the classical literature on Arbitrary Lagrangian Eulerian techniques, e.g. to the early work of Hughes et al. [103], Liu & Gvildys [145], Donéa et. al [48, 49, 51], Huerta & Liu [101] or the excellent recent textbooks by Belytschko et al. [14] and Donéa & Huerta [52]. To clarify the following discussions, we shall strictly distinguish between the terminology of parametrization, reference, description and motion as suggested by Steinmann [198–200], see also Kuhl et al. [125, 127, 132, 135].

**Definition 2.1 (Parametrization)** *Any quantity expressed in terms of the referential coordinate $\boldsymbol{\xi}$ as $\{\bullet\}(\boldsymbol{\xi}, t)$ will be referred to as referential parametrization of $\{\bullet\}$. The spatial parametrization $\{\bullet\}(\boldsymbol{x}, t)$ is formulated in terms of the spatial coordinate $\boldsymbol{x}$, while quantities formulated in terms of the material coordinate $\boldsymbol{X}$ as $\{\bullet\}(\boldsymbol{X}, t)$ will be referred to as material parametrization.*

**Definition 2.2 (Reference)** *Irrespective of the parametrization, we will distinguish between the referential, the spatial and the material reference of a volume specific scalar– or tensor–valued quantity denoted as $\{\bullet\}_\square$, $\{\bullet\}_t$ or $\{\bullet\}_0$, respectively. Thereby, the former relates to the referential domain $\mathcal{B}_\square$, the second relates to the spatial domain $\mathcal{B}_t$ and the third represents a quantity in the material domain $\mathcal{B}_0$.*

**Definition 2.3 (Description)** *Moreover, for tensor–valued quantities, we shall distinguish between the referential, the spatial, the material and the two–point description. While tensorial*

*quantities in the referential description are elements of the tangent or cotangent space to $\mathcal{B}_\square$, tensorial quantities in the spatial or in the material description are elements of the tangent or cotangent space to $\mathcal{B}_t$ or $\mathcal{B}_0$, respectively. Tensorial quantities in the two–point description are thus elements of any mixed pair of tangent or cotangent spaces to $\mathcal{B}_\square$, $\mathcal{B}_t$ or $\mathcal{B}_0$.*

**Definition 2.4 (Motion)** *Finally, we shall strictly distinguish between the spatial and the material motion problem. Thereby, the classical spatial motion problem, which is sometimes introduced as 'direct motion problem' is based on the idea of following physical particles from a fixed material position $\boldsymbol{X}$ through the ambient space. It is thus closely related to a Lagrangian viewpoint. In contrast to this, within the material motion or 'inverse motion problem', physical particles are followed through the ambient material at fixed spatial position $\boldsymbol{x}$. The observer thus takes the Eulerian viewpoint.*

With these introductory definitions at hand, we can now formulate the kinematics of the spatial and the material motion problem. First, we introduce the spatial and the material motion map and their gradients in section 2.1. We then turn to the evaluation of corresponding time rates in section 2.2. Last, aspects of variation and linearization will be discussed in section 2.3. In all sections, we begin by formally introducing the spatial and the material motion problem in complete analogy to one another. Only then, comparative relations between the individual quantities will be set up.

## 2.1 Motion

### 2.1.1 Spatial motion problem

In the spatial motion problem, the placement $\boldsymbol{x}$ of a physical particle in the spatial configuration $\mathcal{B}_t$ is described by the nonlinear spatial deformation map $\boldsymbol{\varphi}$ in terms of the placement $\boldsymbol{X}$ in the material configuration $\mathcal{B}_0$, compare figure 2.1.

$$\boldsymbol{x} = \boldsymbol{\varphi}\,(\,\boldsymbol{X}, t\,) = \bar{\boldsymbol{\varphi}}\,(\,\boldsymbol{\xi}, t\,) \circ \tilde{\boldsymbol{\varphi}}\,(\,\boldsymbol{X}, t\,) \;:\quad \mathcal{B}_0 \to \mathcal{B}_t \tag{2.1.1}$$

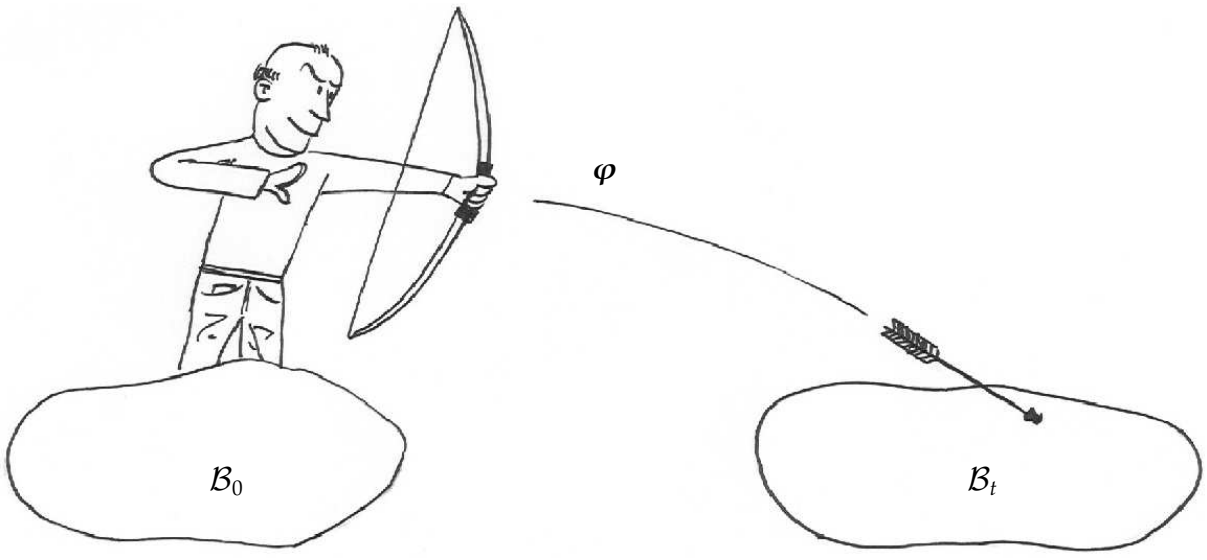


**Figure 2.1:** Spatial motion problem

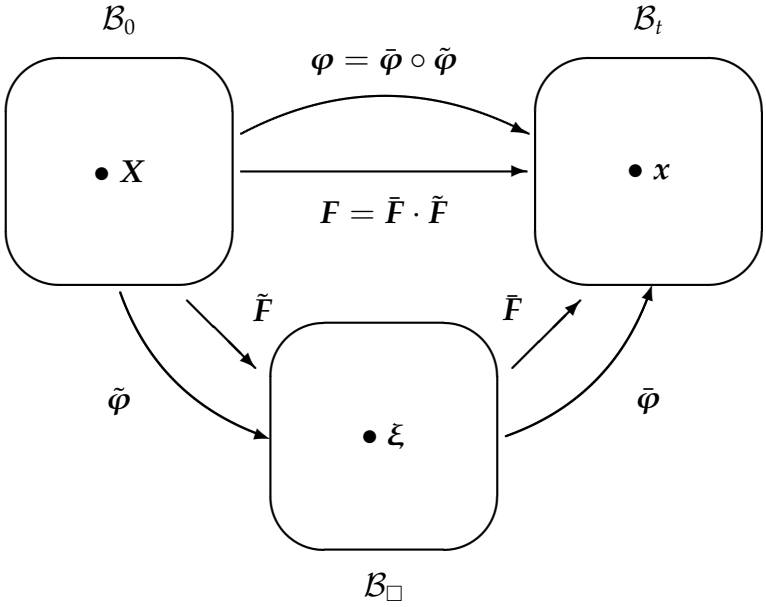


**Figure 2.2:** Spatial motion problem – Kinematics

Alternatively, the spatial motion map $\boldsymbol{\varphi}$ can be interpreted as a composition of the referential maps $\bar{\boldsymbol{\varphi}}$ and $\tilde{\boldsymbol{\varphi}}$, as indicated in figure 2.2. Thereby, the latter maps placements $\boldsymbol{X}$ from the material configuration $\mathcal{B}_0$ to the referential configuration $\mathcal{B}_\square$, while the former maps placements $\boldsymbol{\xi}$ from the referential configuration $\mathcal{B}_\square$ to the spatial configuration $\mathcal{B}_t$.

$$\begin{aligned} \boldsymbol{\xi} &= \tilde{\boldsymbol{\varphi}}\,(\,\boldsymbol{X}, t\,): \qquad \mathcal{B}_0 \rightarrow \mathcal{B}_\square \\ \boldsymbol{x} &= \bar{\boldsymbol{\varphi}}\,(\,\boldsymbol{\xi}, t\,): \qquad \mathcal{B}_\square \rightarrow \mathcal{B}_t \end{aligned} \tag{2.1.2}$$

The spatial motion deformation gradient $\boldsymbol{F}$, i.e. the linear tangent map from the material tangent space $T\mathcal{B}_0$ to the spatial tangent space $T\mathcal{B}_t$, is given as

$$\boldsymbol{F} = \nabla_{\boldsymbol{X}} \boldsymbol{\varphi}\,(\boldsymbol{X}, t) = \bar{\boldsymbol{F}} \cdot \tilde{\boldsymbol{F}}: \quad T\mathcal{B}_0 \rightarrow T\mathcal{B}_t \qquad J = \det \boldsymbol{F} = \bar{J}\,\tilde{J} > 0 \tag{2.1.3}$$

with $J$ denoting the related Jacobian. As illustrated in figure 2.2, the spatial motion deformation gradient can alternatively be characterized through the multiplicative decomposition in terms of the referential gradients $\bar{\boldsymbol{F}}$ and $\tilde{\boldsymbol{F}}$ which can be expressed in the following form.

$$\begin{aligned} \tilde{\boldsymbol{F}} &= \nabla_{\boldsymbol{X}}\, \bar{\boldsymbol{\varphi}}\,(\,\boldsymbol{X}\,, t\,): \qquad T\mathcal{B}_0 \rightarrow T\mathcal{B}_\square \qquad \tilde{J} = \det \tilde{\boldsymbol{F}} > 0 \\ \bar{\boldsymbol{F}} &= \nabla_{\boldsymbol{\xi}}\, \bar{\boldsymbol{\varphi}}\,(\,\boldsymbol{\xi}\,, t\,): \qquad T\mathcal{B}_\square \rightarrow T\mathcal{B}_t \qquad \bar{J} = \det \bar{\boldsymbol{F}} > 0 \end{aligned} \tag{2.1.4}$$

The right and left spatial motion Cauchy–Green strain tensors $\boldsymbol{C}$ and $\boldsymbol{b}$

$$\boldsymbol{C} = \boldsymbol{F}^t \cdot \boldsymbol{g} \cdot \boldsymbol{F} \qquad \boldsymbol{b} = \boldsymbol{F} \cdot \boldsymbol{G} \cdot \boldsymbol{F}^t \tag{2.1.5}$$

can be introduced as typical strain measures of the material motion problem. While the former can be interpreted as the the spatial motion pull back of the covariant spatial metric $\boldsymbol{g}$, the latter can be generated by the push forward of the material metric $\boldsymbol{G}$.

### 2.1.2 Material motion problem

In complete analogy to the spatial motion map $\boldsymbol{\varphi}$, we can introduce a material motion map $\boldsymbol{\Phi}$ defining mappings of the placements $\boldsymbol{X}$ of physical particles in the material configuration $\mathcal{B}_0$ in terms of the related placements $\boldsymbol{x}$ in the spatial configuration $\mathcal{B}_t$,

$$\boldsymbol{X} = \boldsymbol{\Phi}\,(\,\boldsymbol{x}, t\,) = \tilde{\boldsymbol{\Phi}}\,(\,\boldsymbol{\xi}, t\,) \circ \bar{\boldsymbol{\Phi}}\,(\,\boldsymbol{x}, t\,) \;:\quad \mathcal{B}_t \to \mathcal{B}_0 \tag{2.1.6}$$

compare figure 2.3. As illustrated in figure 2.4, the material deformation map can be introduced as a composition of the referential mappings $\tilde{\boldsymbol{\Phi}}$ and $\bar{\boldsymbol{\Phi}}$. Herein, $\bar{\boldsymbol{\Phi}}$ charac-

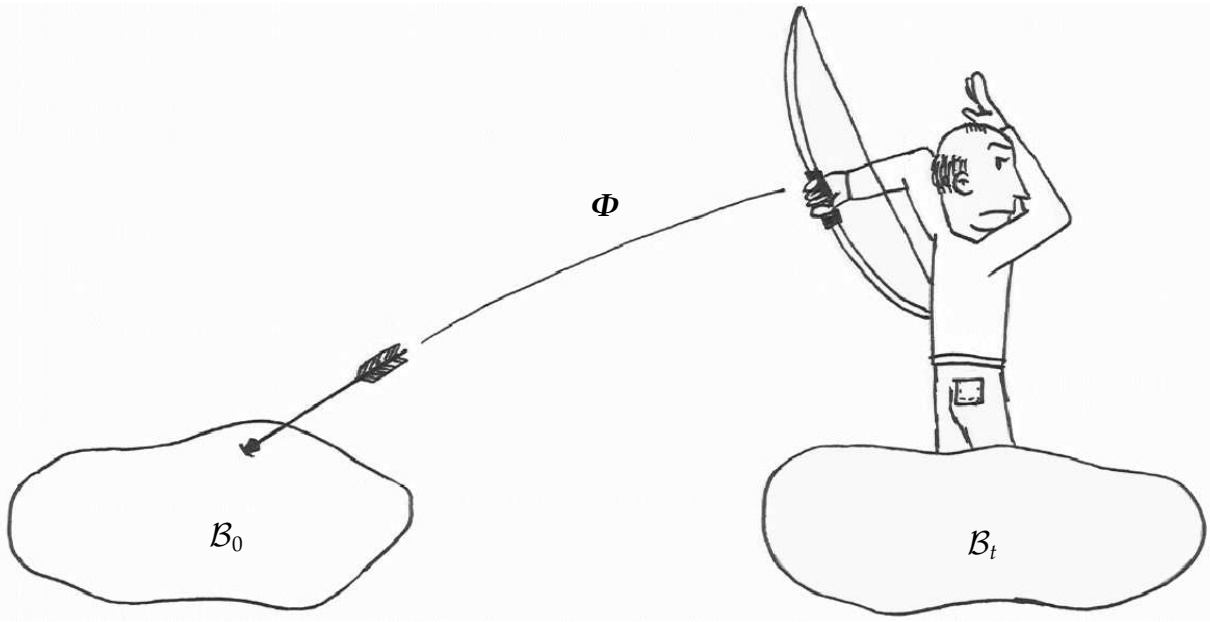


**Figure 2.3:** Material motion problem

terizes the mapping of placements $\boldsymbol{x}$ from the spatial to the referential domain whereas $\tilde{\boldsymbol{\Phi}}$ denotes the mapping of placements $\boldsymbol{\xi}$ from the referential to the material domain.

$$\begin{aligned} \boldsymbol{\xi} &= \bar{\boldsymbol{\Phi}}\,(\,\boldsymbol{x}, t\,) : \qquad \mathcal{B}_t \to \mathcal{B}_\square \\ \boldsymbol{X} &= \tilde{\boldsymbol{\Phi}}\,(\,\boldsymbol{\xi}, t\,) : \qquad \mathcal{B}_\square \to \mathcal{B}_0 \end{aligned} \tag{2.1.7}$$

The related linear tangent map from the spatial tangent space $T\mathcal{B}_t$ to the material tangent space $T\mathcal{B}_0$ is defined through the material motion deformation gradient $\boldsymbol{f}$ and its Jacobian $j$,

$$\boldsymbol{f} = \nabla_{\boldsymbol{x}} \boldsymbol{\Phi}\,(\boldsymbol{x}, t) = \tilde{\boldsymbol{f}} \cdot \bar{\boldsymbol{f}} : \quad T\mathcal{B}_t \to T\mathcal{B}_0 \qquad j = \det \boldsymbol{f} = \tilde{j}\,\bar{j} > 0 \tag{2.1.8}$$

whereby $\boldsymbol{f}$ can be decomposed multiplicatively in terms of the referential gradients $\tilde{\boldsymbol{f}}$ and $\bar{\boldsymbol{f}}$.

$$\begin{aligned} \bar{\boldsymbol{f}} &= \nabla_{\boldsymbol{x}}\, \bar{\boldsymbol{\Phi}}\,(\,\boldsymbol{x}\,, t\,) : \qquad T\mathcal{B}_t \to T\mathcal{B}_\square \qquad \bar{j} = \det \bar{\boldsymbol{f}} > 0 \\ \tilde{\boldsymbol{f}} &= \nabla_{\boldsymbol{\xi}}\, \bar{\boldsymbol{\Phi}}\,(\,\boldsymbol{\xi}\,, t\,) : \qquad T\mathcal{B}_\square \to T\mathcal{B}_0 \qquad \tilde{j} = \det \tilde{\boldsymbol{f}} > 0 \end{aligned} \tag{2.1.9}$$

The material motion pull back of the covariant material metric $\boldsymbol{G}$ and the push forward of the spatial metric $\boldsymbol{g}$ introduce the right and left material motion Cauchy–Green strain tensors $\boldsymbol{c}$ and $\boldsymbol{B}$.

$$\boldsymbol{c} = \boldsymbol{f}^t \cdot \boldsymbol{G} \cdot \boldsymbol{f} \qquad \boldsymbol{B} = \boldsymbol{f} \cdot \boldsymbol{g} \cdot \boldsymbol{f}^t \tag{2.1.10}$$

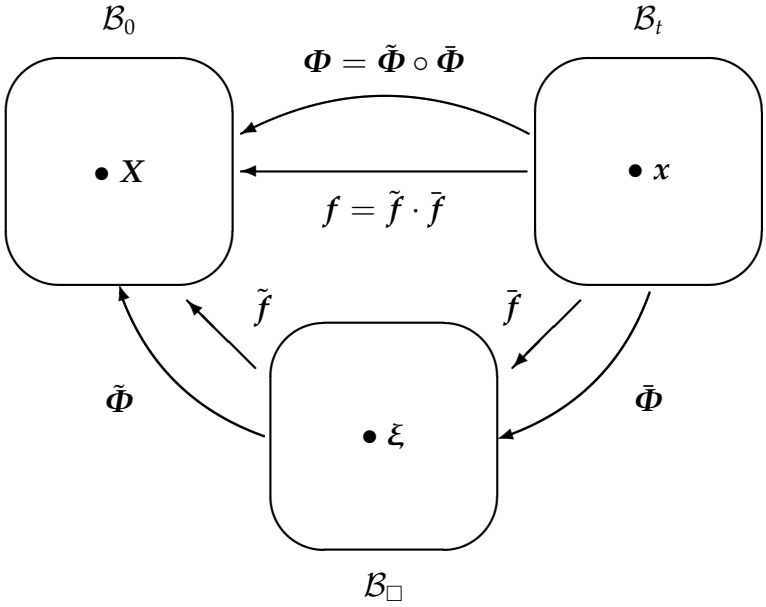


**Figure 2.4:** Material motion problem – Kinematics

**Remark 2.1.1 (Spatial vs. material motion problem)** *The spatial and the material motion problem are related through the identity maps in $\mathcal{B}_0$ and $\mathcal{B}_t$*

$$\boldsymbol{id}_{\mathcal{B}_0} = \boldsymbol{\Phi} \circ \boldsymbol{\varphi}(\boldsymbol{X}, t) = \boldsymbol{\Phi}\,(\,\boldsymbol{\varphi}(\boldsymbol{X}, t), t\,) \qquad \boldsymbol{id}_{\mathcal{B}_t} = \boldsymbol{\varphi} \circ \boldsymbol{\Phi}(\boldsymbol{x}, t) = \boldsymbol{\varphi}\,(\,\boldsymbol{\Phi}(\boldsymbol{x}, t), t\,) \tag{2.1.11}$$

*with $\circ$ denoting the composition of mappings. Consequently, the spatial and the material deformation gradient are simply related by their inverses.*

$$\boldsymbol{F}^{-1} = \boldsymbol{f} \circ \boldsymbol{\varphi}(\boldsymbol{X}, t) = \boldsymbol{f}\,(\,\boldsymbol{\varphi}(\boldsymbol{X}, t), t\,) \qquad \boldsymbol{f}^{-1} = \boldsymbol{F} \circ \boldsymbol{\Phi}(\boldsymbol{x}, t) = \boldsymbol{F}\,(\,\boldsymbol{\Phi}(\boldsymbol{x}, t), t\,) \tag{2.1.12}$$

*Likewise, the spatial Cauchy–Green strain tensors $\boldsymbol{C}$ and $\boldsymbol{b}$ are related to their material motion counterparts $\boldsymbol{B}$ and $\boldsymbol{c}$ via their inverses.*

$$\boldsymbol{C}^{-1} = \boldsymbol{B} \qquad \boldsymbol{b}^{-1} = \boldsymbol{c} \tag{2.1.13}$$

**Remark 2.1.2 (Piola transforms)** *In the following, we will distinguish between scalar-valued or tensorial volume specific quantities with material reference $\{\bullet\}_0$ and spatial reference $\{\bullet\}_t$ whereby the integration of a quantity with material reference over the material domain $\mathcal{B}_0$ yields the identical result as the integration of a quantity with spatial reference over the spatial domain $\mathcal{B}_t$.*

$$\int_{\mathcal{B}_0} \{\bullet\}_0 \,\mathrm{d}V_0 = \int_{\mathcal{B}_t} \{\bullet\}_t \,\mathrm{d}V_t \tag{2.1.14}$$

*The above equation introduces the well-known transformation formulae.*

$$\{\bullet\}_t = j\,\{\bullet\}_0 = \tilde{j}\,\bar{j}\,\{\bullet\}_0 \qquad \{\bullet\}_0 = J\,\{\bullet\}_t = \bar{J}\,\tilde{J}\,\{\bullet\}_t \tag{2.1.15}$$

*Moreover, the equivalence of a vector- or tensor-valued surface contribution* $\{\,\square\,\}$ *on the boundary of the material domain* $\partial\mathcal{B}_0$ *and the corresponding contribution* $\{\,\lozenge\,\}$ *on the spatial boundary* $\partial\mathcal{B}_t$ *as*

$$\int_{\partial\mathcal{B}_0} \{\,\square\,\} \cdot \mathrm{d}\boldsymbol{A}_0 = \int_{\partial\mathcal{B}_t} \{\,\lozenge\,\} \cdot \mathrm{d}\boldsymbol{A}_t \tag{2.1.16}$$

*can be transformed into the following relation*

$$\int_{\mathcal{B}_0} \mathrm{Div}\,\{\,\square\,\}\,\mathrm{d}V_0 = \int_{\mathcal{B}_t} \mathrm{div}\,\{\,\lozenge\,\}\,\mathrm{d}V_t \tag{2.1.17}$$

*through the application of Gauss' theorem. Clearly, the material and spatial flux terms* $\{\,\square\,\}$ *and* $\{\,\lozenge\,\}$ *are related through the well–known Nanson's formula.*

$$\{\lozenge\} = j\,\{\square\} \cdot \boldsymbol{F}^t = \tilde{j}\,\bar{j}\,\{\square\} \cdot \tilde{\bar{\boldsymbol{F}}}^t \cdot \bar{\boldsymbol{F}}^t \qquad \{\square\} = J\,\{\lozenge\} \cdot \boldsymbol{f}^t = \bar{J}\,\tilde{J}\,\{\lozenge\} \cdot \bar{\tilde{\boldsymbol{f}}}^t \cdot \tilde{\boldsymbol{f}}^t \tag{2.1.18}$$

**Remark 2.1.3 (Lagrangian vs. Eulerian viewpoint)** *The classical Lagrangian and Eulerian viewpoint can be derived as special cases of the above formulation with keeping either* $\tilde{\boldsymbol{\Phi}}$ *or* $\bar{\boldsymbol{\varphi}}$ *fixed such that either* $\boldsymbol{\varphi} \equiv \bar{\boldsymbol{\varphi}}$ *or* $\boldsymbol{\Phi} \equiv \tilde{\boldsymbol{\Phi}}$*. In the first case corresponding to the Lagrangian viewpoint, the referential configuration* $\mathcal{B}_\square$ *coincides with the material configuration* $\mathcal{B}_0$ *while in the second case corresponding to the Eulerian viewpoint, the referential configuration* $\mathcal{B}_\square$ *coincides with the spatial configuration* $\mathcal{B}_t$*.*

## 2.2 Time rates

### 2.2.1 Spatial motion problem

In what follows, the material time derivative of an arbitrary quantity $\{\bullet\}$ at fixed material placement $\boldsymbol{X}$ will be denoted as $\mathrm{D}_t$.

$$\mathrm{D}_t\{\bullet\} = \partial_t\{\bullet\}|_{\boldsymbol{X}\,\text{fixed}} \tag{2.2.1}$$

A well-known representative is the material time derivative of the spatial motion map $\boldsymbol{\varphi}$ which introduces the spatial velocity $\boldsymbol{v}$.

$$\boldsymbol{v} = \mathrm{D}_t\boldsymbol{\varphi}\,(\boldsymbol{X}, t) \tag{2.2.2}$$

Recall, that its material gradient is equal to the material time derivative of the spatial deformation gradient $\mathrm{D}_t\boldsymbol{F}$ while its spatial gradient will be denoted as $\boldsymbol{l}$ in the sequel.

$$\mathrm{D}_t\boldsymbol{F} = \nabla_X \boldsymbol{v} \qquad \boldsymbol{l} = \nabla_x \boldsymbol{v} \tag{2.2.3}$$

With these definitions at hand, e.g. the material time derivative of the spatial motion Jacobian $J$ can be expressed through the well–known Euler identity $\mathrm{D}_t J = J\,\mathrm{div}\,\boldsymbol{v}$ with $\mathrm{div}\,\boldsymbol{v} = \boldsymbol{F}^{-t} : \mathrm{D}_t\boldsymbol{F}$ denoting the spatial divergence of the spatial velocity $\boldsymbol{v}$. In the transient context, the subscript $D$ will be assigned to the material and spatial flux terms as $\{\,\square\,\}_D$ and $\{\,\lozenge\,\}_D$ indicating that the corresponding flux refers to the material time derivative $\mathrm{D}_t$ of the related balanced quantity.

### 2.2.2 Material motion problem

With the definition of the spatial time derivative $\mathrm{d}_t$ of a quantity $\{\bullet\}$ at fixed spatial placements $\boldsymbol{x}$

$$\mathrm{d}_t\{\bullet\} = \partial_t\{\bullet\}|_{\boldsymbol{x}\,\text{fixed}} \tag{2.2.4}$$

the material velocity $\boldsymbol{V}$ can be defined as spatial time derivative of the material motion map $\boldsymbol{\Phi}$.

$$\boldsymbol{V} = \mathrm{d}_t\boldsymbol{\Phi}\,(\boldsymbol{x}, t) \tag{2.2.5}$$

Its spatial gradient is equal to the spatial time derivative of the material motion deformation gradient $\boldsymbol{f}$ while the material gradient of the material velocity will be denoted as $\boldsymbol{L}$.

$$\mathrm{d}_t\boldsymbol{f} = \nabla_x\boldsymbol{V} \qquad \boldsymbol{L} = \nabla_X\boldsymbol{V} \tag{2.2.6}$$

Consequently, the spatial time derivative of the material motion Jacobian $j$ can be expressed as $\mathrm{d}_t j = j\,\mathrm{Div}\,\boldsymbol{V}$ whereby $\mathrm{Div}\,\boldsymbol{V} = \boldsymbol{f}^{-t} : \mathrm{d}_t\boldsymbol{f}$ denotes the material divergence of the material velocity $\boldsymbol{V}$. In what follows, we shall assign the subscript $d$ to any material or spatial flux term $\{\,\square\,\}_d$ or $\{\,\lozenge\,\}_d$ to indicate that it refers to the spatial time derivative $\mathrm{d}_t$.

**Remark 2.2.1 (Spatial vs. material motion problem)** *Note, that the total differentials of the spatial and material identity map*

$$\begin{aligned}
\mathrm{d}\boldsymbol{X} &= \mathrm{d}_t\boldsymbol{\Phi}\,\mathrm{d}t + \nabla_x\boldsymbol{\Phi}\cdot\mathrm{d}\boldsymbol{x} = \mathrm{d}_t\boldsymbol{\Phi}\,\mathrm{d}t + \nabla_x\boldsymbol{\Phi}\cdot[\mathrm{D}_t\boldsymbol{\varphi}\mathrm{d}t + \nabla_X\boldsymbol{\varphi}\cdot\mathrm{d}\boldsymbol{X}] = \boldsymbol{V}\,\mathrm{d}t + \boldsymbol{f}\cdot[\boldsymbol{v}\mathrm{d}t + \boldsymbol{F}\cdot\mathrm{d}\boldsymbol{X}] \\
\mathrm{d}\boldsymbol{x} &= \mathrm{D}_t\boldsymbol{\varphi}\,\mathrm{d}t + \nabla_X\boldsymbol{\varphi}\cdot\mathrm{d}\boldsymbol{X} = \mathrm{D}_t\boldsymbol{\varphi}\,\mathrm{d}t + \nabla_X\boldsymbol{\varphi}\cdot[\,\mathrm{d}_t\boldsymbol{\Phi}\mathrm{d}t + \nabla_x\boldsymbol{\Phi}\cdot\mathrm{d}\boldsymbol{x}\,] = \boldsymbol{v}\,\mathrm{d}t + \boldsymbol{F}\cdot[\boldsymbol{V}\mathrm{d}t + \boldsymbol{f}\cdot\mathrm{d}\boldsymbol{x}]
\end{aligned} \tag{2.2.7}$$

*yield the following fundamental relations between the spatial and the material velocity $\boldsymbol{v}$ and $\boldsymbol{V}$,*

$$\boldsymbol{V} = -\boldsymbol{f}\cdot\boldsymbol{v} \qquad \boldsymbol{v} = -\boldsymbol{F}\cdot\boldsymbol{V} \tag{2.2.8}$$

*which will essentially be needed later on to set up relations between the spatial and the material momentum density.*

**Remark 2.2.2 (Euler theorem)** *The celebrated Euler theorem relates the material and the spatial time derivative $\mathrm{D}_t$ and $\mathrm{d}_t$ of a scalar– or vector–valued function $\{\bullet\}$ through the individual convective terms $\nabla_x\{\bullet\}\cdot\boldsymbol{v}$ and $\nabla_X\{\bullet\}\cdot\boldsymbol{V}$.*

---

$$\mathrm{D}_t\{\bullet\} = \mathrm{d}_t\{\bullet\} + \nabla_x\{\bullet\}\cdot\boldsymbol{v} \qquad \mathrm{d}_t\{\bullet\} = \mathrm{D}_t\{\bullet\} + \nabla_X\{\bullet\}\cdot\boldsymbol{V} \tag{2.2.9}$$

---

*The first equation corresponds to the classical Euler theorem of the spatial motion problem, while the second equation represents its material motion counterpart.*

**Remark 2.2.3 (Reynold's transport theorem)** *From the above equations, we obtain the differential form of the spatial and material motion version of Reynold's transport theorem.*

$$j\,\mathrm{D}_t\{\bullet\}_0 = \mathrm{d}_t\{\bullet\}_t + \mathrm{div}\,(\,\{\bullet\}_t \otimes \boldsymbol{v}\,) \qquad J\,\mathrm{d}_t\{\bullet\}_t = \mathrm{D}_t\{\bullet\}_0 + \mathrm{Div}\,(\,\{\bullet\}_0 \otimes \boldsymbol{V}\,) \tag{2.2.10}$$

*The global form of the spatial motion version of Reynold's transport theorem (2.2.10)$_1$, which originally goes back to Kelvin in 1869, states that the rate of change of the quantity $\{\bullet\}_0$ over a material volume $\mathcal{B}_0$ equals the rate of change of the quantity over a spatial volume $\mathcal{B}_t$ plus the flux through the boundary surface $\partial\mathcal{B}_t$. Later on, we will further invoke the following relations between the derivative of a scalar–valued function $\{\bullet\}_0$ or $\{\bullet\}_t$ with respect to the spatial and material motion deformation gradient*

$$\mathrm{D}_{\boldsymbol{F}}\{\bullet\}_0 = \{\bullet\}_0 \boldsymbol{f}^t - J\boldsymbol{f}^t \cdot \mathrm{d}_f\{\bullet\}_t \cdot \boldsymbol{f}^t \qquad \mathrm{d}_f\{\bullet\}_t = \{\bullet\}_t \boldsymbol{F}^t - j\boldsymbol{F}^t \cdot \mathrm{D}_{\boldsymbol{F}}\{\bullet\}_0 \cdot \boldsymbol{F}^t \tag{2.2.11}$$

*which have been given earlier by Steinmann [198].*

## 2.3 Variation and linearization

The variation $\delta$ and the linearization $\Delta$ of any function $\{\bullet\}$ at fixed referential coordinate $\xi$ denoted as

$$\begin{aligned} \delta\{\bullet\} &= \delta\{\bullet\}|_{\xi\,\text{fixed}} \\ \Delta\{\bullet\} &= \Delta\{\bullet\}|_{\xi\,\text{fixed}} \end{aligned} \tag{2.3.1}$$

will be referred to as total variation and total linearization in the sequel. The essential idea is now, to express this total variation or linearization in terms of the variation or linearization with respect to the spatial coordinates $\boldsymbol{x}$ at fixed material coordinates $\boldsymbol{X}$ denoted as $\delta_{\boldsymbol{x}}\{\bullet\}$ or $\Delta_{\boldsymbol{x}}\{\bullet\}$, respectively, plus a contribution with respect to the material coordinates $\boldsymbol{X}$ at fixed spatial coordinates $\boldsymbol{x}$ denoted as $\delta_{\boldsymbol{X}}\{\bullet\}$ or $\Delta_{\boldsymbol{X}}\{\bullet\}$.

$$\begin{aligned} \delta\{\bullet\} &= \delta_{\boldsymbol{x}}\{\bullet\} + \delta_{\boldsymbol{X}}\{\bullet\} \\ \Delta\{\bullet\} &= \Delta_{\boldsymbol{x}}\{\bullet\} + \Delta_{\boldsymbol{X}}\{\bullet\} \end{aligned} \tag{2.3.2}$$

The individual contributions $\delta_{\boldsymbol{x}}\{\bullet\}$, $\Delta_{\boldsymbol{x}}\{\bullet\}$, $\delta_{\boldsymbol{X}}\{\bullet\}$ and $\Delta_{\boldsymbol{X}}\{\bullet\}$ will be specified in the following subsections.

### 2.3.1 Spatial motion problem

In chapter 5, we will particularly need to evaluate the variation $\delta$ and the linearization $\Delta$ of a function $\{\bullet\}$ with respect to the spatial coordinates $\boldsymbol{x}$ at fixed material coordinates $\boldsymbol{X}$. This variation and linearization will be denoted as follows.

$$\begin{aligned} \delta_{\boldsymbol{x}}\{\bullet\} &= \delta\{\bullet\}|_{\boldsymbol{X}\,\text{fixed}} \\ \Delta_{\boldsymbol{x}}\{\bullet\} &= \Delta\{\bullet\}|_{\boldsymbol{X}\,\text{fixed}} \end{aligned} \tag{2.3.3}$$

Consequently, the variation and linearization of the spatial motion deformation map $\boldsymbol{\varphi}$ and its gradient $\boldsymbol{F}$ can be expressed exclusively in terms of the referential map $\bar{\boldsymbol{\varphi}}$ and its gradient.

$$\begin{aligned} \delta_x \boldsymbol{\varphi} &= \delta\, \bar{\boldsymbol{\varphi}} \qquad & \delta_x \boldsymbol{F} &= \nabla_X \delta\, \bar{\boldsymbol{\varphi}} \\ \Delta_x \boldsymbol{\varphi} &= \Delta \bar{\boldsymbol{\varphi}} \qquad & \Delta_x \boldsymbol{F} &= \nabla_X \Delta \bar{\boldsymbol{\varphi}} \end{aligned} \tag{2.3.4}$$

In chapter 5, we will make use of the following fundamental expressions,

$$\begin{aligned} \delta_x \{\bullet\}_0 (\boldsymbol{F}, \boldsymbol{\varphi}; \boldsymbol{X}) &= \mathrm{D}_F \{\bullet\}_0 : \nabla_X \delta\, \bar{\boldsymbol{\varphi}} + \partial_x \{\bullet\}_0 \cdot \delta\, \bar{\boldsymbol{\varphi}} \\ \Delta_x \{\bullet\}_0 (\boldsymbol{F}, \boldsymbol{\varphi}; \boldsymbol{X}) &= \mathrm{D}_F \{\bullet\}_0 : \nabla_X \Delta \bar{\boldsymbol{\varphi}} + \partial_x \{\bullet\}_0 \cdot \Delta \bar{\boldsymbol{\varphi}} \end{aligned} \tag{2.3.5}$$

which relate the linearization and variation of a scalar–valued function $\{\bullet\}_0$ with a possible dependence on the deformation gradient $\boldsymbol{F}$, the deformation map $\boldsymbol{\varphi}$ and the material position $\boldsymbol{X}$ to its derivative with respect to the deformation gradient $\mathrm{D}_F \{\bullet\}_0$ and its explicit derivative with respect to the spatial coordinate $\partial_x \{\bullet\}_0$.

### 2.3.2 Material motion problem

Analogously, the variation $\delta$ and the linearization $\Delta$ of any function $\{\bullet\}$ with respect to the material coordinates $\boldsymbol{X}$ at fixed spatial coordinates $\boldsymbol{x}$ denoted as

$$\begin{aligned} \delta_X \{\bullet\} &= \delta \{\bullet\}|_{x\,\text{fixed}} \\ \Delta_X \{\bullet\} &= \Delta \{\bullet\}|_{x\,\text{fixed}} \end{aligned} \tag{2.3.6}$$

define the variation and linearization of the material motion deformation map and its gradient in the following form.

$$\begin{aligned} \delta_X \boldsymbol{\Phi} &= \delta\, \tilde{\boldsymbol{\Phi}} \qquad & \delta_X \boldsymbol{f} &= \nabla_x \delta\, \tilde{\boldsymbol{\Phi}} \\ \Delta_X \boldsymbol{\Phi} &= \Delta \tilde{\boldsymbol{\Phi}} \qquad & \Delta_X \boldsymbol{f} &= \nabla_x \Delta \tilde{\boldsymbol{\Phi}} \end{aligned} \tag{2.3.7}$$

Note, that they can be expressed exclusively in terms of the referential mapping $\tilde{\boldsymbol{\Phi}}$ and its gradient. Moreover, for the formulation to be derived in chapter 5, we will essentially need the following relations

$$\begin{aligned} \delta_X \{\bullet\}_t (\boldsymbol{f}, \boldsymbol{\Phi}; \boldsymbol{x}) &= \mathrm{d}_f \{\bullet\}_t : \nabla_x \delta\, \tilde{\boldsymbol{\Phi}} + \partial_X \{\bullet\}_t \cdot \delta\, \tilde{\boldsymbol{\Phi}} \\ \Delta_X \{\bullet\}_t (\boldsymbol{f}, \boldsymbol{\Phi}; \boldsymbol{x}) &= \mathrm{d}_f \{\bullet\}_t : \nabla_x \Delta \tilde{\boldsymbol{\Phi}} + \partial_X \{\bullet\}_t \cdot \Delta \tilde{\boldsymbol{\Phi}} \end{aligned} \tag{2.3.8}$$

between the variation and the linearization of a scalar–valued function $\{\bullet\}_t$ as a function of $\boldsymbol{f}$, $\boldsymbol{\Phi}$ and $\boldsymbol{x}$, the related derivative with respect to the material motion deformation gradient $\mathrm{d}_f \{\bullet\}_t$ and the explicit derivative with respect to the material coordinate $\partial_X \{\bullet\}_t$.

# 3 Balance equations

Wir glauben nicht a priori an ein Erhaltungsgesetz, sondern wir wissen a priori die Möglichkeit einer logischen Form.

Ludwig Wittgenstein,
Tractatus logico–philosophicus, §6.33, 1921

## 3.1 Introduction

It is a well–established fact, that in classical non–relativistic continuum mechanics, each part of a body can be assigned a specific mass which never changes no matter how the body is moved, accelerated or deformed. Although valid for most practical applications, the statement of the 'conservation of mass' is nothing but a mere definition. Yet, there exist particular problem classes for which the conservation of mass is no longer appropriate. Typical examples can be found in biomechanical or chemomechanical applications. In both cases, the apparent changes in mass result from confining attention to only a part of the overall matter present. Thus one might argue, that these problems can be overcome naturally by using the 'theory of mixtures', as proposed by Truesdell & Toupin [210] §155 or Bowen [17]. Therein, the loss or gain of mass of one constituent is compensated by the others while the mass of the overall mixture itself remains constant.
Nevertheless, it is possible to think of classes of problems for which it might seem more reasonable to restrict focus to one single constituent which is allowed to exchange mass, momentum, energy and entropy with its environment, i.e. the outside world. This approach typically falls within the category of 'thermodynamics of open systems'. Such systems can be understood as being enclosed by a permeable, deformable and diathermal membrane. Along these lines, four different types of thermodynamic systems can be distinguished, isolated, adiabatic closed, closed and open ones. Their classification is typically characterized through their ability to interact with their surroundings or rather the outside world. In analogy to Maugin [151] §2.1, de Groot [79] §10, Kirkwood & Oppenheim [120] §1.1, de Groot & Mazur [80], Katchalsky & Curran [116] §1.1, Haase [84] §1.1, Kestin [117, 118], §1.4 and Hutter [111] §6.1.2 we apply the following definitions.

**Definition 3.1 (Isolated system)** *A thermodynamic system which is not allowed to have any interaction at all with its surroundings is said to be an isolated system. Isolated systems are enclosed by an impermeable, rigid, adiabatic membrane.*

**Definition 3.2 (Adiabatic closed system)** *A thermodynamic system which is allowed to exchange exclusively mechanical work with its environment is an adiabatic closed system. It can be interpreted to be enclosed by an impermeable, deformable, adiabatic membrane. Its thermodynamic state is characterized by the deformation $\boldsymbol{\varphi}$ or $\boldsymbol{\Phi}$ alone.*

**Definition 3.3 (Closed system)** *A thermodynamic system of constant mass which is allowed to exchange mechanical work and heat with its surrounding is called a closed system. Closed systems are enclosed by an impermeable, deformable, diathermal membrane. Their thermodynamic state is characterized through the deformation $\boldsymbol{\varphi}$ or $\boldsymbol{\Phi}$ and through the temperature $\theta$.*

**Definition 3.4 (Open system)** *A thermodynamic system which is allowed to exchange mass, mechanical work and heat with its surroundings is said to be an open system. An open system is enclosed by a permeable, deformable and diathermal membrane. Its thermodynamic state is thus essentially characterized through the density $\rho$, the deformation $\boldsymbol{\varphi}$ or alternatively $\boldsymbol{\Phi}$ and through the temperature $\theta$.*

A classical example of an open system that can be found in nearly every textbook of mechanics is furnished by the motion of a burning body typically encountered in rocket propulsion, see e.g. Sommerfeld [194] §4, Truesdell & Toupin [210] §155, Müller [162] §1.4.6 or Haupt [91] §3.5. The introductory monograph by Roberts [181] §2 provides a number of additional illustrative examples of systems with non–constant mass. In chemomechanical applications, e.g. in chemically reacting concrete, the dissolution of portlandite or ettringite and progressive decalcification of calcium silicate hydrates represent typical examples of changes in mass of the cementitious skeleton, see e.g. Coussy [35], Ulm & Coussy [211], Stark & Wicht [195], Kuhl, Bangert & Meschke [124] or Kuhl & Steinmann [134]. Moisture transport, e.g. in the context of calcium leaching, is a classical example of a mass flux, as illustrated by Ulm et al. [212], Torrenti et al. [208] or Carmeliet [23]. For chemical reactions in general, we refer to the standard textbook by Atkins [10] while the early works of Kirkwood & Oppenheim [120], Katchalsky & Curran [116] and Guggenheim [81] provide excellent introductions to chemical thermodynamics. The functional adaption of bones to changes in the mechanical loading situation represents another well–known example of open systems in biomechanics of hard tissues, see e.g. Cowin & Hegedus [41], Taber [204] or Carter & Beaupré [24]. In soft tissue biomechanics, proliferation, hyperplasia, hypertrophy and atrophy can be considered as typical examples of mass sources on the microlevel, while the migration of cells might cause an additional mass flux, as illustrated in the classical overview monographs by Taber [204], Humphrey [108] and Humphrey & Rajagopal [109].
The first continuum model for open systems in the context of biomechanics has been presented by Cowin & Hegedus [41], Hegedus & Cowin [92] and Cowin & Nachlinger [43] under the name of 'theory of adaptive elasticity'. Nowadays, most of the biomechanical models and the related numerical simulations are based on this theory for which the set of common balance equations has been enhanced by additional volume sources, see e.g. Beaupré et al. [12], Weinans et al. [214], Harrigan & Hamilton [86], [87]. Only recently, Epstein & Maugin [57] have proposed the 'theory of volumetric growth' for which the exchange with the environment is not a priori restricted

to source terms by allowing for additional fluxes of mass, momentum, energy and entropy through the domain boundary, see also Kuhl & Steinmann [131, 132]. Its numerical realization within the context of the finite element method has been illustrated recently by Kuhl et al. [129, 133, 135].
Typically, the process or growth encountered in open systems will be accompanied by the development of inhomogeneities responsible for residual stresses in the body. The interpretation of growth as 'local rearrangement of material inhomogeneities' suggests the formulation of the governing equations in the material setting as proposed by Epstein & Maugin [57]. The appealing advantage of the material motion point of view is that local inhomogeneities such as abrupt changes in density are reflected elegantly by the governing equations which result from a complete projection of the standard balance equations onto the material manifold. The material motion point of view originally dates back to the early works of Eshelby [60] on defect mechanics. It was elaborated in detail by Chadwick [27], Eshelby [62] and Rogula [184] and has attracted an increasing attention only recently as documented by the trendsetting textbooks by Maugin [149], Gurtin [83], Kienzler & Herrmann [119] and also by Silhavý [191] or by the recent publications by Epstein & Maugin [56], Maugin & Trimarco [152], Maugin [150], Gurtin [82]. Thereby, the remarkable duality between the spatial or 'direct motion problem' and the material or 'inverse motion problem' as pointed out originally by Shield [189] is of particular importance. The works of our own group along these lines are documented in Kuhl & Steinmann [130, 132, 135], see also Steinmann [197–200] to which we refer for further motivation of the material motion point of view in the context of fracture and defect mechanics.
This chapter aims at deriving a general framework for the balance equations of open systems highlighting the striking duality between the spatial and the material motion point of view. Thereby, we shall consider the most general formulation by allowing for mass exchanges not only through the supply of mass within the domain itself but also through the in– or outflux of mass through the domain boundary. The influence of a non–constant mass on all the other balance equations will be discussed for both, the spatial and the material motion framework. Thereby, particular emphasis is dedicated to the strict distinction between the 'volume specific' and the 'mass specific' format according to the following definitions.

**Definition 3.5 (Volume specific)** *Any volume specific quantity, such as the volume specific momentum density, the kinetic or internal energy density, the total energy density, the entropy or the free energy density, depends on the volume of the subsystem under consideration. Volume specific quantities are thus essentially defined by the corresponding reference, i.e. the referential reference denoted as* $\{\bullet\}_\square$*, the spatial reference* $\{\bullet\}_t$ *or the material reference* $\{\bullet\}_0$*. Volume specific quantities can be classified as homogeneous functions of the first order in the density. The volume specific format of the balance equations defines relations between volume specific quantities.*

**Definition 3.6 (Mass specific)** *Mass specific quantities such as the mass specific momentum density, the kinetic or internal energy density, the total energy density, the entropy or the free energy density do not depend on the volume of the considered subsystem. As such, they are independent from the density. Mass specific quantities can be related to their volume specific*

*counterparts upon division by the density as* $\{\bullet\} = \{\bullet\}_\square/\rho_\square = \{\bullet\}_t/\rho_t = \{\bullet\}_0/\rho_0$. *The mass specific format of the balance equations defines relations between mass specific quantities.*

Unlike in classical mechanics of closed systems, the balance equations for the mechanics of open systems differ considerably in the volume specific and the mass specific context. In contrast to former models and in our opinion as a benefit, the mass specific format introduced herein is free from explicit open system contributions. In our formulation, all mass specific balance equations thus take the standard format typically encountered in classical closed system thermodynamics.
To illustrate the nature of the mechanics of open systems, we begin by reviewing the classical example of rocket propulsion in section 3.2. Based on the relevant kinematics of continuum mechanics as introduced in chapter 2, we then discuss the balance of mass for open systems in section 3.3. The notions of 'volume specific' and 'mass specific' format will be defined in section 3.4 for a generic prototype balance law. Having introduced the balance of momentum in the spatial and the material motion context in section 3.5, we can derive the balance of kinetic energy as a useful byproduct. The balance of energy and entropy will be highlighted in sections 3.6 and 3.7. The latter naturally lends itself to the formulation of the dissipation inequality which will be shown to place further restrictions on the constitutive response functions in the chapter 4.

## 3.2 Motivation

To illustrate the nature of open systems and the corresponding mechanics, we consider the classical example of the loss of mass through combustion and ejection during rocket propulsion, as illustrated e.g. by Sommerfeld [194] §4, Truesdell & Toupin [210] §155, Müller [162] §1.4.6 or Haupt [91] §3.5. Thereby, the rocket head, the subsystem of the rocket hull plus the amount of fuel present, can be understood as an open system constantly losing mass due to the process of combustion and ejection. Consequently, the balance of mass of the rocket head balances the time rate of change of the rocket head mass $\mathfrak{m}$ with the rate of mass ejection $\mathfrak{R}$, compare figure 3.1.

$$\mathrm{D}_t\, \mathfrak{m} = \mathfrak{R} \tag{3.2.1}$$

The case of combustion and ejection is characterized through negative growth $\mathfrak{R} \leq 0$ since the mass of the rocket head decreases with time. The related balance of momentum states that the time rate of change of the rocket head momentum $\mathfrak{p}$ is equal to the total force $\mathfrak{f}$ acting on it.

$$\mathrm{D}_t\, \mathfrak{p} = \mathfrak{f} \qquad \mathfrak{f} = \mathfrak{f}^{\text{closed}} + \mathfrak{f}^{\text{open}} \qquad \mathfrak{f}^{\text{open}} = \bar{\mathfrak{f}}^{\text{open}} + \mathfrak{v}\, \mathfrak{R} \tag{3.2.2}$$

Thereby, the total force can be interpreted as the sum of the closed system contribution $\mathfrak{f}^{\text{closed}}$ and the open system contribution $\mathfrak{f}^{\text{open}}$. The latter can be understood as the sum of a reduced open system term $\bar{\mathfrak{f}}^{\text{open}}$ and explicit effects due to the added or in this case removed amount of mass $\mathfrak{v}\, \mathfrak{R}$. Note that this version of the balance of momentum will be referred to as 'volume specific' version in the sequel. The momentum $\mathfrak{p}$ of the rocket head is defined as the rocket head velocity $\mathfrak{v}$ weighted by its actual mass $\mathfrak{m}$.

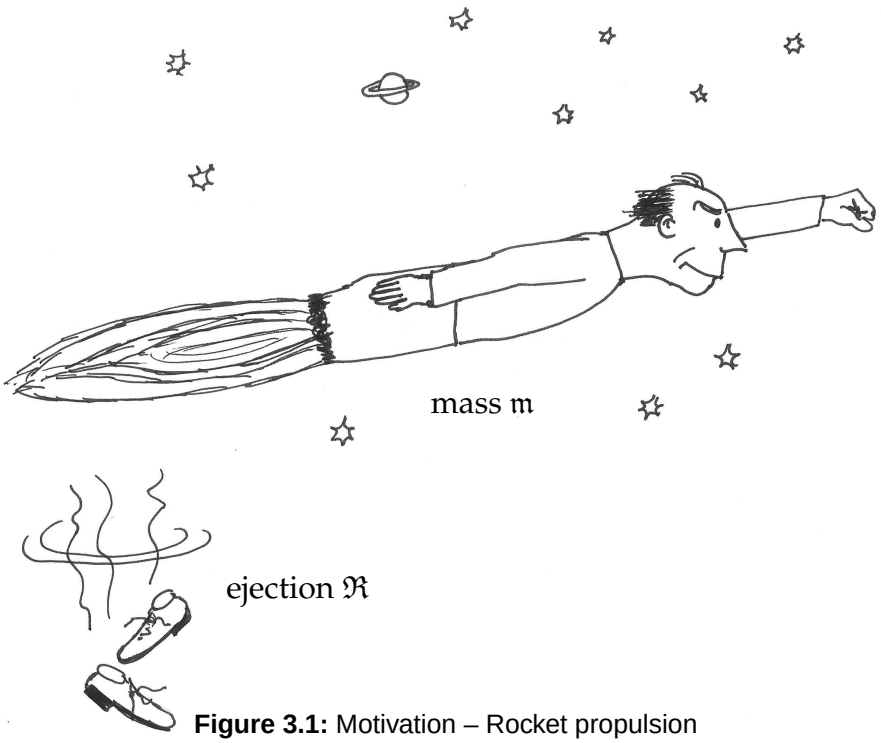


**Figure 3.1:** Motivation – Rocket propulsion

Consequently, the material time derivative of the momentum $\mathfrak{p}$ can be evaluated with the help of the chain rule.

$$\mathfrak{p} = \mathfrak{m}\,\mathfrak{v} \qquad D_t\,\mathfrak{p} = \mathfrak{m}\,D_t\mathfrak{v} + \mathfrak{v}\,D_t\mathfrak{m} = \mathfrak{m}\,D_t\mathfrak{v} + \mathfrak{v}\,\mathfrak{R} \tag{3.2.3}$$

A reduced form of the balance of momentum follows from subtracting the balance of mass (3.2.1) weighted by the rocket head velocity $\mathfrak{v}$ from the volume specific balance of momentum (3.2.2).

$$\mathfrak{m}\,D_t\mathfrak{v} = \bar{\mathfrak{f}} \qquad \bar{\mathfrak{f}} = \mathfrak{f}^{\text{closed}} + \bar{\mathfrak{f}}^{\text{open}} = \mathfrak{f} - \mathfrak{v}\,\mathfrak{R} \tag{3.2.4}$$

The above equation, which we will refer to as 'mass specific' version of the balance of momentum, defines the reduced force $\bar{\mathfrak{f}}$, the overall force responsible for changes in the rocket velocity, as the sum of the closed system contributions, i.e. the mechanical forces $\mathfrak{f}^{\text{closed}}$, and a reduced open system forces term $\bar{\mathfrak{f}}^{\text{open}}$, the so–called propulsive force. However, of course, the standard balance equations hold for the overall closed system composed of the rocket head and the exhausted mass. The balance of momentum of this overall system requires that the sum of the rate of change of rocket head momentum $D_t\mathfrak{p}$ minus the rate of change of the momentum of the ejected mass $\bar{\mathfrak{v}}\,\mathfrak{R}$ be in equilibrium with closed system force term $\mathfrak{f}^{\text{closed}}$,

$$D_t\mathfrak{p} - \bar{\mathfrak{v}}\,\mathfrak{R} = \mathfrak{f}^{\text{closed}} \tag{3.2.5}$$

whereby $\bar{\mathfrak{v}}$ denotes the total velocity of the ejected mass, see e.g. Goldstein [75] §1.6. From the above equations, the reduced open system force term $\bar{\mathfrak{f}}^{\text{open}}$, which is responsible for the rocket thrust, can be identified as the force caused by the difference of the velocity of the ejection $\bar{\mathfrak{v}}$ with respect to the rocket head velocity $\mathfrak{v}$.

$$\mathfrak{f}^{\text{open}} = \bar{\mathfrak{v}}\,\mathfrak{R} \qquad \bar{\mathfrak{f}}^{\text{open}} = [\,\bar{\mathfrak{v}} - \mathfrak{v}\,]\,\mathfrak{R} \tag{3.2.6}$$

Note that in the literature, the propulsive term $[\,\bar{\mathfrak{v}} - \mathfrak{v}\,]\,\mathfrak{R}$ is sometimes also referred to as 'irreversible' contribution while the extra force $\mathfrak{v}\,\mathfrak{R}$ generated by the ejection leaving the system at the same velocity as the remaining rocket head is then denoted as 'reversible' contribution. In what follows, we will generalize the above considerations to the continuum mechanics of open systems.

## 3.3 Balance of mass

While in classical mechanics of closed systems, the amount of matter contained in a body $\mathcal{B}_0$ generally does not change, the mass of a body can no longer be considered a conservation property within the thermodynamics of open systems. Accordingly, the balance of mass plays a key role within the present theory. It can be used to transform the volume specific version of any other balance law to its mass specific counterpart. In abstract terms, the local balance of mass states that the appropriate rate of change

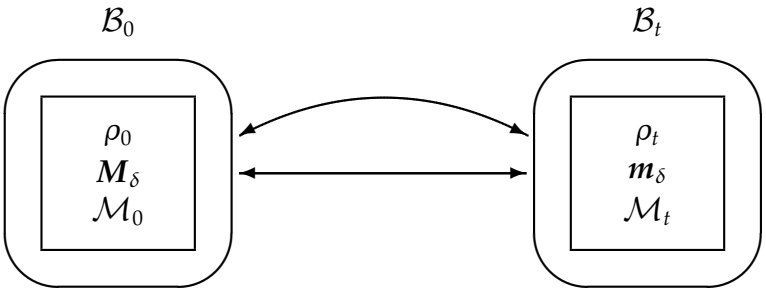


**Figure 3.2:** Balance of mass – Densities, mass fluxes and mass sources

of the density $\rho_\tau$ with $\tau = 0, t$ is equal to the sum of the divergence of the related mass flux $\boldsymbol{M}_\delta$ or $\boldsymbol{m}_\delta$ with $\delta = D, d$ and the mass source $\mathcal{M}_\tau$, see figure 3.2. It should be emphasized that most theories for open systems except for the one developed by Epstein & Maugin [57] a priori exclude the influx of mass as $\boldsymbol{M}_D = \boldsymbol{0}$ and $\boldsymbol{m}_D = \boldsymbol{0}$. Although according to the 'equivalence of surface and volume sources' as stated by Truesdell & Toupin [210] §157, it is in principle possible to express any influx $\boldsymbol{M}_\delta$ or $\boldsymbol{m}_\delta$ through an equivalent source term of the form $\operatorname{Div} \boldsymbol{M}_\delta$ or $\operatorname{div} \boldsymbol{m}_\delta$, we shall allow for independent flux terms to keep the underlying theory as general as possible for the time being. Thus, the balance of mass with material reference and material parametrization takes the following form.

$$\mathrm{D}_t\, \rho_0 = \operatorname{Div} \boldsymbol{M}_D + \mathcal{M}_0 \tag{3.3.1}$$

With the standard Piola transforms

$$\rho_0 = J\, \rho_t \qquad \mathcal{M}_0 = J\, \mathcal{M}_t \qquad \boldsymbol{M}_D = J\, \boldsymbol{m}_D \cdot \boldsymbol{F}^{-t} \tag{3.3.2}$$

the push forward of the different terms in equation (3.3.1) yields the balance of mass with spatial reference and material parametrization.

$$j\, \mathrm{D}_t\, \rho_0 = \operatorname{div} \boldsymbol{m}_D + \mathcal{M}_t \tag{3.3.3}$$

Note that in classical continuum mechanics, equation $(3.3.2)_1$ is usually referred to as 'equation of material continuity'. The application of Reynold's transport theorem $(2.2.10)_1$

$$j\,\mathrm{D}_t\,\rho_0 = \mathrm{d}_t\,\rho_t + \mathrm{div}\,(\,\rho_t\,\boldsymbol{v}\,) \qquad \text{and} \qquad \boldsymbol{m}_d = \boldsymbol{m}_D - \rho_t\,\boldsymbol{v} \tag{3.3.4}$$

introduce the spatial parametrization of the balance of mass.

$$\mathrm{d}_t\,\rho_t = \mathrm{div}\,\boldsymbol{m}_d + \mathcal{M}_t \tag{3.3.5}$$

Equation $(3.3.4)_1$ which has been introduced as 'spatial continuity equation' by Euler as early as 1757, represents one of the basic equations in classical fluid mechanics. The above statement with spatial reference and spatial parametrization can easily be transformed into the local balance of mass with material reference and spatial parametrization by applying the related Piola transforms

$$\rho_t = j\,\rho_0 \qquad \mathcal{M}_t = j\,\mathcal{M}_0 \qquad \boldsymbol{m}_d = j\,\boldsymbol{M}_d\cdot\boldsymbol{f}^{-t} \tag{3.3.6}$$

together with the classical pull back formalism.

$$J\,\mathrm{d}_t\,\rho_t = \mathrm{Div}\,\boldsymbol{M}_d + \mathcal{M}_0 \tag{3.3.7}$$

The application of Reynold's transport theorem $(2.2.10)_2$ with

$$J\,\mathrm{d}_t\,\rho_t = \mathrm{D}_t\rho_0 + \mathrm{Div}\,(\,\rho_t\,\boldsymbol{V}\,) \qquad \text{and} \qquad \boldsymbol{M}_D = \boldsymbol{M}_d - \rho_0\,\boldsymbol{V} \tag{3.3.8}$$

can be used to finally retransform equation (3.3.7) into the original version (3.3.1). In summary, four different versions of the balance of mass can be distinguished.

---

$$\begin{array}{lll}
\text{mr mp} & \mathrm{D}_t\,\rho_0 = \mathrm{Div}\,\boldsymbol{M}_D + \mathcal{M}_0 \\
\text{sr mp} & j\,\mathrm{D}_t\,\rho_0 = \mathrm{div}\,\boldsymbol{m}_D + \mathcal{M}_t \\
\text{mr sp} & J\,\mathrm{d}_t\,\rho_t = \mathrm{Div}\,\boldsymbol{M}_d + \mathcal{M}_0 \\
\text{sr sp} & \mathrm{d}_t\,\rho_t = \mathrm{div}\,\boldsymbol{m}_d + \mathcal{M}_t
\end{array} \tag{3.3.9}$$

---

Thereby, the mass fluxes $\boldsymbol{M}_\delta$ and $\boldsymbol{m}_\delta$ can be understood as the sum of a 'convective contribution' $\bar{\boldsymbol{M}}_\delta$ and $\bar{\boldsymbol{m}}_\delta$ and the open system contribution through the influx of mass $\boldsymbol{R}$ or $\boldsymbol{r} = j\,\boldsymbol{R}\cdot\boldsymbol{f}^{-t}$,

$$\begin{array}{lll}
\boldsymbol{M}_D = \bar{\boldsymbol{M}}_D + \boldsymbol{R} & \bar{\boldsymbol{M}}_D = & \boldsymbol{0} \\
\boldsymbol{m}_D = \bar{\boldsymbol{m}}_D + \boldsymbol{r} & \bar{\boldsymbol{m}}_D = & \boldsymbol{0} \\
\boldsymbol{M}_d = \bar{\boldsymbol{M}}_d + \boldsymbol{R} & \bar{\boldsymbol{M}}_d = + & \rho_0\,\boldsymbol{V} \\
\boldsymbol{m}_d = \bar{\boldsymbol{m}}_d + \boldsymbol{r} & \bar{\boldsymbol{m}}_d = - & \rho_t\,\boldsymbol{v}
\end{array} \tag{3.3.10}$$

while the corresponding extra mass sources $\mathcal{M}_\tau$ are formally given as follows.

$$\begin{array}{lll}
\mathcal{M}_0 = \bar{\mathcal{M}}_0 + \mathcal{R}_0 & \bar{\mathcal{M}}_0 = & 0 \\
\mathcal{M}_t = \bar{\mathcal{M}}_t + \mathcal{R}_t & \bar{\mathcal{M}}_t = & 0
\end{array} \tag{3.3.11}$$

For further elaborations, it proves convenient to independently introduce the abbreviations $\mathsf{m}_\tau$ and $\mathsf{M}_\tau$ solely taking into account the effects of convection of mass as present in classical continuum mechanics of closed systems.

$$\begin{aligned}
\mathsf{m}_0 &= \mathrm{Div}\ \bar{\boldsymbol{M}}_D + \bar{\mathcal{M}}_0 = 0 \\
\mathsf{m}_\mathsf{t} &= \mathrm{div}\ \bar{\boldsymbol{m}}_D + \bar{\mathcal{M}}_t = 0 \\
\mathsf{M}_0 &= \mathrm{Div}\ \bar{\boldsymbol{M}}_d + \bar{\mathcal{M}}_0 = +\ \mathrm{Div}\ (\ \rho_0 \boldsymbol{V}\ ) \\
\mathsf{M}_\mathsf{t} &= \mathrm{div}\ \bar{\boldsymbol{m}}_d + \bar{\mathcal{M}}_t = -\ \mathrm{div}\ (\ \rho_t \boldsymbol{v}\ )
\end{aligned} \tag{3.3.12}$$

In the following, the convective terms $\mathsf{m}_\tau$ and $\mathsf{M}_\tau$, which vanish for the spatial motion problem but are non–zero in the material motion case, will prove instrumental to highlight the dualities between the spatial and the material motion problem. In particular, we will make use of the definition of $\mathsf{M}_0$ as $\mathsf{M}_0 = \nabla_X \rho_0 \cdot \boldsymbol{V} + \rho_0 \boldsymbol{f}^{-t} : \mathrm{d}_t \boldsymbol{f}$. With the help of equations (3.3.12), the four fundamental versions of the balance of mass (3.3.9) can be reformulated in the following form, which is particularly tailored to our needs since closed and open system contributions are clearly separated.

$$\begin{aligned}
\text{mr mp} \quad & \mathrm{D}_t\ \rho_0 = \mathrm{Div}\ \boldsymbol{R} + \mathcal{R}_0 + \mathsf{m}_0 \\
\text{sr mp} \quad & j\ \mathrm{D}_t\ \rho_0 = \mathrm{div}\ \boldsymbol{r} + \mathcal{R}_t + \mathsf{m}_\mathsf{t} \\
\text{mr sp} \quad & J\ \mathrm{d}_t\ \rho_t = \mathrm{Div}\ \boldsymbol{R} + \mathcal{R}_0 + \mathsf{M}_0 \\
\text{sr sp} \quad & \mathrm{d}_t\ \rho_t = \mathrm{div}\ \boldsymbol{r} + \mathcal{R}_t + \mathsf{M}_\mathsf{t}
\end{aligned} \tag{3.3.13}$$

**Remark 3.3.1 (Reynold's transport theorem)** *Note that by making use of the balance of mass, the volume specific forms of Reynold's transport theorem (2.2.10) can be transformed into corresponding mass specific formulations.*

$$\begin{aligned}
\rho_t\ \mathrm{D}_t\ \{\bullet\} &= \rho_t\ \mathrm{d}_t\ \{\bullet\} + \mathrm{div}\ (\ \rho_t\ \{\bullet\} \otimes \boldsymbol{v}\ ) + [\ \mathsf{M}_\mathsf{t} - \mathsf{m}_\mathsf{t}\ ]\ \{\bullet\} \\
\rho_0\ \mathrm{d}_t\ \{\bullet\} &= \rho_0\ \mathrm{D}_t\ \{\bullet\} + \mathrm{Div}\ (\ \rho_0\ \{\bullet\} \otimes \boldsymbol{V}\ ) + [\ \mathsf{m}_0 - \mathsf{M}_0\ ]\ \{\bullet\}
\end{aligned} \tag{3.3.14}$$

*Herein, $\{\bullet\}$ denotes the mass specific density of a scalar– or vector–valued quantity which is related to its volume specific counterpart as $\{\bullet\}_\tau = \rho_\tau\{\bullet\}$. While the volume specific version of Reynold's transport theorem (2.2.10) will later on be applied to relate the spatial and material motion quantities in the volume specific format, the mass specific version of the transport theorem (3.3.14) will serve to relate the corresponding mass specific quantities.*

## 3.4 Generic balance law

In what follows, we will illustrate how the different versions of a balance law can be derived from one another. For the sake of transparency, we will restrict ourselves to

the discussion of the local or differential forms of the master balance law

$$\begin{aligned} \mathrm{D}_t \{\bullet\}_0 &= \mathrm{Div}\ \{\,\square\,\}_D + \{\circ\}_0 \\ \mathrm{d}_t \{\bullet\}_t &= \mathrm{div}\ \ \{\,\lozenge\,\}_d + \{\circ\}_t \end{aligned} \tag{3.4.1}$$

which can of course be derived from the related global or integral form

$$\begin{aligned} \mathrm{D}_t \int_{\mathcal{B}_0} \{\bullet\}_0 \,\mathrm{d}V_0 &= \int_{\partial\mathcal{B}_0} \{\,\square\,\}_D \cdot \mathrm{d}\boldsymbol{A}_0 + \int_{\mathcal{B}_0} \{\circ\}_0 \,\mathrm{d}V_0 \\ \mathrm{d}_t \int_{\mathcal{B}_t} \{\bullet\}_t \,\mathrm{d}V_t &= \int_{\partial\mathcal{B}_t} \{\,\lozenge\,\}_d \cdot \mathrm{d}\boldsymbol{A}_t + \int_{\mathcal{B}_t} \{\circ\}_t \,\mathrm{d}V_t \end{aligned} \tag{3.4.2}$$

if sufficient smoothness criteria are fulfilled by the related fields of the balance quantity $\{\bullet\}_\tau$ itself, the related fluxes $\{\,\square\,\}_\delta$ and $\{\,\lozenge\,\}_\delta$ and the related source terms $\{\circ\}_\tau$. Recall that in classical closed system continuum mechanics, it is not necessary to distinguish between volume and mass specific representations of the balance equations. In this context, in a material parametrization with material reference, which is commonly referred to as Lagrangian formulation, not only the mass flux and source but also the convective terms vanish. Consequently, the rate of change of any volume specific quantity $\mathrm{D}_t \{\bullet\}_0 = \mathrm{D}_t ( \rho_0 \{\bullet\} )$ is equivalent to the rate of change of $\{\bullet\}$ weighted by the material density $\rho_0$ as $\mathrm{D}_t \{\bullet\}_0 = \rho_0 \mathrm{D}_t\{\bullet\}$ since $\{\bullet\} \mathrm{D}_t \rho_0 = 0$. Within the thermodynamics of open systems, however, the volume and the mass specific version of the balance laws differ considerably since $\mathrm{D}_t \rho_0 \neq 0$. In the following, we will derive a prototype set of balance equations in the volume and in the mass specific format. Particular interest will be dedicated to the fact, that the mass specific version of a balance law takes the standard format known from classical continuum mechanics, merely enhanced by the effects of convection of mass.

### 3.4.1 Volume specific version

In the volume specific version of a balance law, the quantity to be balanced $\{\bullet\}_\tau$ can either be given in a material or spatial reference as $\{\bullet\}_0 = \rho_0 \{\bullet\}$ or $\{\bullet\}_t = \rho_t \{\bullet\}$. It

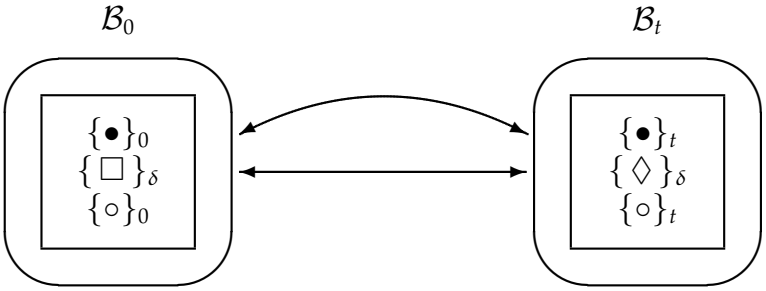


**Figure 3.3:** Generic balance law – Balance quantities, fluxes and sources

is balanced with the sum of the divergence of the corresponding fluxes $\{\,\square\,\}_\delta$, $\{\,\lozenge\,\}_\delta$ and the volume sources $\{\circ\}_\tau$, see figure 3.3. In analogy to the balance of mass, we start with the formulation with material reference and material parametrization.

$$\mathrm{D}_t\{\bullet\}_0 = \mathrm{Div}\,\{\,\square\,\}_D + \{\circ\}_0 \tag{3.4.3}$$

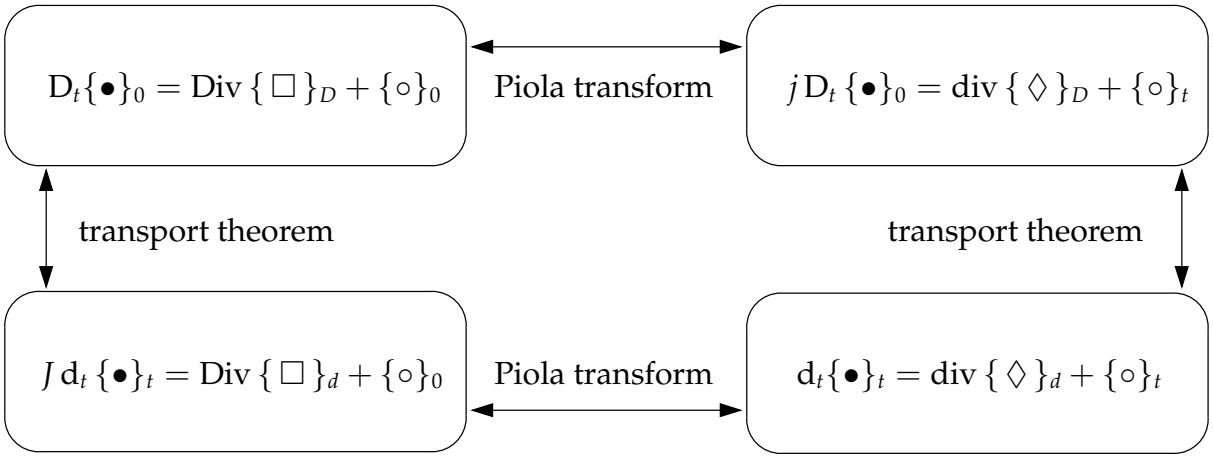


**Figure 3.4:** Transformation scheme for balance equations

Its individual terms can be pushed forward by making use of the related Piola transforms

$$\{\bullet\}_0 = J\,\{\bullet\}_t \qquad \{\circ\}_0 = J\,\{\circ\}_t \qquad \{\,\square\,\}_D = J\{\,\lozenge\,\}_D \cdot \boldsymbol{F}^{-t} \tag{3.4.4}$$

to render the formulation with spatial reference and material parametrization.

$$j\,\mathrm{D}_t\,\{\bullet\}_0 = \mathrm{div}\,\{\,\lozenge\,\}_D + \{\circ\}_t \tag{3.4.5}$$

The application of Reynold's transport theorem $(2.2.10)_1$ with

$$j\,\mathrm{D}_t\{\bullet\}_0 = \mathrm{d}_t\{\bullet\}_t + \mathrm{div}\,(\,\{\bullet\}_t \otimes \boldsymbol{v}\,) \qquad \text{and} \qquad \{\,\lozenge\,\}_d = \{\,\lozenge\,\}_D - \{\bullet\}_t \otimes \boldsymbol{v} \tag{3.4.6}$$

yield the corresponding version with spatial reference and spatial parametrization.

$$\mathrm{d}_t\{\bullet\}_t = \mathrm{div}\,\{\,\lozenge\,\}_d + \{\circ\}_t \tag{3.4.7}$$

The related Piola transforms

$$\{\bullet\}_t = j\,\{\bullet\}_0 \qquad \{\circ\}_t = j\,\{\circ\}_0 \qquad \{\,\lozenge\,\}_d = j\{\,\square\,\}_d \cdot \boldsymbol{f}^{-t} \tag{3.4.8}$$

together with the classical pull back formalism then yield the general form of a balance law with material reference and spatial parametrization.

$$J\,\mathrm{d}_t\,\{\bullet\}_t = \mathrm{Div}\,\{\,\square\,\}_d + \{\circ\}_0 \tag{3.4.9}$$

The original equation (3.4.3) can eventually be rederived by applying the appropriate version of Reynold's transport theorem $(2.2.10)_2$

$$J\,\mathrm{d}_t\,\{\bullet\}_t = \mathrm{D}_t\{\bullet\}_0 + \mathrm{Div}\,(\,\{\bullet\}_0 \otimes \boldsymbol{V}\,) \qquad \text{and} \qquad \{\,\square\,\}_D = \{\,\square\,\}_d - \{\bullet\}_0 \otimes \boldsymbol{V}. \tag{3.4.10}$$

The closed loop of transformations inherit to any balance equation is illustrated in figure 3.4. In summary, each balance equation can be expressed in four different ways.

$$
\begin{aligned}
\text{mr mp} \quad & \mathrm{D}_t\ \{\bullet\}_0 = \mathrm{Div}\ \{\square\}_D + \{\circ\}_0 \\
\text{sr mp} \quad & j\ \mathrm{D}_t\ \{\bullet\}_0 = \mathrm{div}\ \{\lozenge\}_D + \{\circ\}_t \\
\text{mr sp} \quad & J\ \mathrm{d}_t\ \{\bullet\}_t = \mathrm{Div}\ \{\square\}_d + \{\circ\}_0 \\
\text{sr sp} \quad & \mathrm{d}_t\ \{\bullet\}_t = \mathrm{div}\ \{\lozenge\}_d + \{\circ\}_t
\end{aligned}
\tag{3.4.11}
$$

Therein, the flux terms $\{\square\}_\delta$ and $\{\lozenge\}_\delta$ with either $\delta = D$ for the spatial motion problem or $\delta = d$ for the material motion problem are related to the corresponding Neumann boundary conditions in terms of the standard closed system surface contributions $\blacksquare^{\text{closed}}$ and $\blacklozenge^{\text{closed}}$ and the open system supplements $\blacksquare^{\text{open}}$ and $\blacklozenge^{\text{open}}$.

$$
\begin{aligned}
\{\square\}_\delta \cdot \boldsymbol{N} &= \blacksquare^{\text{closed}} + \blacksquare^{\text{open}} & \blacksquare^{\text{open}} &= \bar{\blacksquare}^{\text{open}} + [\,\{\bullet\} \otimes \boldsymbol{R}\,] \cdot \boldsymbol{N} \\
\{\lozenge\}_\delta \cdot \boldsymbol{n} &= \blacklozenge^{\text{closed}} + \blacklozenge^{\text{open}} & \blacklozenge^{\text{open}} &= \bar{\blacklozenge}^{\text{open}} + [\,\{\bullet\} \otimes \boldsymbol{r}\,] \cdot \boldsymbol{n}
\end{aligned}
\tag{3.4.12}
$$

Moreover, the source terms are composed of the standard closed and the additional open system contributions.

$$
\begin{aligned}
\{\circ\}_0 &= \{\circ\}_0^{\text{closed}} + \{\circ\}_0^{\text{open}} & \{\circ\}_0^{\text{open}} &= \{\bar{\circ}\}_0^{\text{open}} + \{\bullet\}\,\mathcal{R}_0 - \nabla_X\,\{\bullet\} \cdot \boldsymbol{R} \\
\{\circ\}_t &= \{\circ\}_t^{\text{closed}} + \{\circ\}_t^{\text{open}} & \{\circ\}_t^{\text{open}} &= \{\bar{\circ}\}_t^{\text{open}} + \{\bullet\}\,\mathcal{R}_t - \nabla_x\,\{\bullet\} \cdot \boldsymbol{r}
\end{aligned}
\tag{3.4.13}
$$

### 3.4.2 Mass specific version

Each balance law can be transformed into a mass specific version balancing the rate of change of the mass specific quantity $\{\bullet\} = \{\bullet\}_\tau \,/\, \rho_\tau$ with the corresponding reduced fluxes $\{\bar{\square}\}_\delta$ and $\{\bar{\lozenge}\}_\delta$ and the reduced source terms $\{\,\bar{\circ}\,\}_\tau$, whereby $\tau = 0, t$ and $\delta = d, D$. The mass specific version can be derived by subtracting $\{\bullet\}$ times the balance of mass (3.3.13) from the corresponding volume specific version of the balance law (3.4.11). Consequently, we obtain the following remarkably simple generic forms of the mass specific balance laws,

$$
\begin{aligned}
\text{mr mp} \quad & \rho_0\ \mathrm{D}_t\ \{\bullet\} = \mathrm{Div}\ \{\bar{\square}\}_D + \{\bar{\circ}\}_0 - \mathsf{m}_0\ \{\bullet\} \\
\text{sr mp} \quad & \rho_t\ \mathrm{D}_t\ \{\bullet\} = \mathrm{div}\ \{\bar{\lozenge}\}_D + \{\bar{\circ}\}_t - \mathsf{m}_t\ \{\bullet\} \\
\text{mr sp} \quad & \rho_0\ \mathrm{d}_t\ \{\bullet\} = \mathrm{Div}\ \{\bar{\square}\}_d + \{\bar{\circ}\}_0 - \mathsf{M}_0\ \{\bullet\} \\
\text{sr sp} \quad & \rho_t\ \mathrm{d}_t\ \{\bullet\} = \mathrm{div}\ \{\bar{\lozenge}\}_d + \{\bar{\circ}\}_t - \mathsf{M}_t\ \{\bullet\}
\end{aligned}
\tag{3.4.14}
$$

whereby the reduced flux terms $\{\bar{\square}\}_\delta$ and $\{\bar{\lozenge}\}_\delta$ are related to their overall counterparts as $\{\bar{\square}\}_\delta = \{\square\}_\delta - \{\bullet\} \otimes \boldsymbol{R}$ and $\{\bar{\lozenge}\}_\delta = \{\lozenge\}_\delta - \{\bullet\} \otimes \boldsymbol{r}$. Again, the reduced fluxes are related to the corresponding Neumann boundary conditions in terms of the

standard closed system contributions $\blacksquare^{\text{closed}}$ and $\blacklozenge^{\text{closed}}$ and the reduced open system supplements $\bar{\blacksquare}^{\text{open}}$ and $\bar{\blacklozenge}^{\text{open}}$.

$$\begin{aligned} \{\bar{\square}\}_\delta \cdot \boldsymbol{N} &= \blacksquare^{\text{closed}} + \bar{\blacksquare}^{\text{open}} \\ \{\bar{\lozenge}\}_\delta \cdot \boldsymbol{n} &= \blacklozenge^{\text{closed}} + \bar{\blacklozenge}^{\text{open}} \end{aligned} \tag{3.4.15}$$

For the spatial motion problem, these Neumann boundary conditions are given for the fluxes denoted by $\delta = D$ while for the material motion problem, we can formally introduce Neumann type of boundary conditions for the fluxes $\delta = d$. In a similar way, the reduced source terms of the mass specific balance equations are composed of closed and reduced open system contributions.

$$\begin{aligned} \{\bar{\circ}\}_0 &= \{\circ\}_0^{\text{closed}} + \{\bar{\circ}\}_0^{\text{open}} \\ \{\bar{\circ}\}_t &= \{\circ\}_t^{\text{closed}} + \{\bar{\circ}\}_t^{\text{open}} \end{aligned} \tag{3.4.16}$$

It is important to note, that the mass specific format is free from all the explicit extra terms caused by the changes in mass. The influence of the open system manifests itself only implicitly through the prescribed boundary terms $\bar{\blacksquare}^{\text{open}}$ and $\bar{\blacklozenge}^{\text{open}}$ and the prescribed volume sources $\{\bar{\circ}\}_\tau^{\text{open}}$. The convective influence introduced through the $\mathsf{m}_\tau$ and $\mathsf{M}_\tau$ terms, however, is also present in the closed system case.

**Remark 3.4.1 (Theory of open systems vs. theory of volumetric growth)** *It is worth noting, that in the theory of volumetric growth derived earlier by Epstein & Maugin [57], the source terms in equation (3.4.11) are introduced in the following form.*

$$\begin{aligned} \{\circ\}_0 &= \{\circ\}_0^{\text{closed}} + \{\circ\}_0^{\text{open}} & \{\circ\}_0^{\text{open}} &= \{\hat{\circ}\}_0^{\text{open}} + \{\bullet\}\,\mathcal{R}_0 \\ \{\circ\}_t &= \{\circ\}_t^{\text{closed}} + \{\circ\}_t^{\text{open}} & \{\circ\}_t^{\text{open}} &= \{\hat{\circ}\}_t^{\text{open}} + \{\bullet\}\,\mathcal{R}_t \end{aligned}$$

*Consequently, the gradient terms $-\nabla_X\{\bullet\} \cdot \boldsymbol{R}$ and $-\nabla_x\{\bullet\} \cdot \boldsymbol{r}$ that are part of the volume specific definition (3.4.13) in our formulation appear with a positive sign in the definition of the reduced source terms of Epstein & Maugin [57] pertaining to equation (3.4.14).*

$$\begin{aligned} \{\bar{\circ}\}_0 &= \{\circ\}_0^{\text{closed}} + \{\hat{\circ}\}_0^{\text{open}} + \nabla_X\,\{\bullet\} \cdot \boldsymbol{R} \\ \{\bar{\circ}\}_t &= \{\circ\}_t^{\text{closed}} + \{\hat{\circ}\}_t^{\text{open}} + \nabla_x\,\{\bullet\} \cdot \boldsymbol{r} \end{aligned}$$

*The different introduction of these source terms is visible in every balance equation and finally results in a significantly different dissipation inequality. The line of thought followed within this contribution is believed to be more convenient especially when pointing out the duality between the spatial and the material motion problem. However, both formulations can be understood as a natural extension of the classical formulation of growth, the theory of adaptive elasticity by Cowin & Hegedus [41] which does not include any flux of mass since $\boldsymbol{R} = \boldsymbol{0}$ and $\boldsymbol{r} = \boldsymbol{0}$.*

## 3.5 Balance of momentum

Keeping in mind the derivation of the generic balance laws of the previous section, we now elaborate their specification to yield the balance of linear momentum. Unlike

the balance of mass, the balance of momentum takes different forms in the spatial and the material motion context due to the vector–valued nature of the balanced quantity. Consequently, we will discuss the spatial and the material motion problem in separate subsections. The balance of kinetic energy can be interpreted as a particular weighted form of the balance of momentum, i.e. weighted by the appropriate velocity field $\boldsymbol{v}$ or $\boldsymbol{V}$ modified by a weighted version of the balance of mass in case of open systems. Thus, the balance of kinetic energy does not constitute an independent balance law. Yet, it proves significant to discuss it in detail since it will help to introduce work conjugate pairs of stress and strain. Moreover, the balance of kinetic energy will be used to identify the external and internal mechanical power which are essential for our further thermodynamical considerations.

### 3.5.1 Volume specific version

#### 3.5.1.1 Spatial motion problem

The balance of momentum, which can be understood as the continuum version of Newton's axiom for a system of discrete particles, balances the rate of change of the spatial momentum density $\boldsymbol{p}_\tau$ with the spatial or rather physical forces generated by a change of the actual spatial placement of physical particles. These forces can essentially be divided into two types, namely the contact or surface forces represented by the momentum fluxes $\boldsymbol{\Pi}^t_\delta$ and $\boldsymbol{\sigma}^t_\delta$ and the at–a–distance forces, i.e. the momentum sources $\boldsymbol{b}_\tau$. The volume specific momentum density $\boldsymbol{p}_\tau$ of the spatial motion problem is canonically defined as spatial covector given through the partial derivative of the volume specific kinetic energy density $K_\tau$

$$K_\tau = \frac{1}{2}\,\rho_\tau\,\boldsymbol{v}\cdot\boldsymbol{g}\cdot\boldsymbol{v} \tag{3.5.1}$$

with respect to the spatial velocity $\boldsymbol{v}$.

$$\boldsymbol{p}_\tau = \partial_v K_\tau = \rho_\tau\,\boldsymbol{g}\cdot\boldsymbol{v} \tag{3.5.2}$$

The volume specific balance of momentum with material reference and material parametrization can then be expressed as

$$\mathrm{D}_t\,\boldsymbol{p}_0 = \mathrm{Div}\,\boldsymbol{\Pi}^t_D + \boldsymbol{b}_0 \tag{3.5.3}$$

whereby $\boldsymbol{\Pi}^t_D$ is referred to as the classical two–field first Piola–Kirchhoff stress tensor in standard continuum mechanics. With the help of the well–known Piola transforms

$$\boldsymbol{p}_0 = J\,\boldsymbol{p}_t \qquad \boldsymbol{b}_0 = J\,\boldsymbol{b}_t \qquad \boldsymbol{\Pi}^t_D = J\,\boldsymbol{\sigma}^t_D\cdot\boldsymbol{F}^{-t} \tag{3.5.4}$$

the individual terms of equation (3.5.3) can be pushed forward to the spatial configuration.

$$j\,\mathrm{D}_t\,\boldsymbol{p}_0 = \mathrm{div}\,\boldsymbol{\sigma}^t_D + \boldsymbol{b}_t \tag{3.5.5}$$

Note that the corresponding momentum flux $\boldsymbol{\sigma}_D^t$ is commonly denoted as Cauchy stress tensor in standard continuum mechanics. The application of Reynold's transport theorem $(2.2.10)_1$

$$j\,\mathrm{D}_t\,\boldsymbol{p}_0 = \mathrm{d}_t\boldsymbol{p}_t + \mathrm{div}\,(\,\boldsymbol{p}_t \otimes \boldsymbol{v}\,) \qquad \text{and} \qquad \boldsymbol{\sigma}_d^t = \boldsymbol{\sigma}_D^t - \boldsymbol{p}_t \otimes \boldsymbol{v} \tag{3.5.6}$$

yield the balance of momentum with spatial reference and spatial parametrization.

$$\mathrm{d}_t\,\boldsymbol{p}_t = \mathrm{div}\,\boldsymbol{\sigma}_d^t + \boldsymbol{b}_t \tag{3.5.7}$$

The definition of the stress tensor $\boldsymbol{\sigma}_d^t$ reflects the convective nature of the above equation in terms of the 'transport of linear momentum' $\boldsymbol{p}_t \otimes \boldsymbol{v}$. The individual terms of equation (3.5.7), which is typically applied in classical fluid mechanics, can be pulled back to the material configuration with the help of the related Piola transforms

$$\boldsymbol{p}_t = j\,\boldsymbol{p}_0 \qquad \boldsymbol{b}_t = j\,\boldsymbol{b}_0 \qquad \boldsymbol{\sigma}_d^t = j\,\boldsymbol{\Pi}_d^t \cdot \boldsymbol{f}^{-t} \tag{3.5.8}$$

thus leading to the following expression.

$$J\,\mathrm{d}_t\,\boldsymbol{p}_t = \mathrm{Div}\,\boldsymbol{\Pi}_d^t + \boldsymbol{b}_0 \tag{3.5.9}$$

Finally, the starting point version of the balance of momentum (3.5.3) can be recovered though the application of Reynold's transport theorem $(2.2.10)_2$

$$J\,\mathrm{d}_t\,\boldsymbol{p}_t = \mathrm{D}_t\,\boldsymbol{p}_0 + \mathrm{Div}\,(\,\boldsymbol{p}_0 \otimes \boldsymbol{V}\,) \qquad \text{and} \qquad \boldsymbol{\Pi}_D^t = \boldsymbol{\Pi}_d^t - \boldsymbol{p}_0 \otimes \boldsymbol{V}. \tag{3.5.10}$$

In summary, four different versions of the volume specific balance of momentum can be distinguished for the spatial motion problem.

$$\begin{aligned}
&\text{mr mp} \quad \mathrm{D}_t\,\boldsymbol{p}_0 = \mathrm{Div}\;\boldsymbol{\Pi}_D^t + \boldsymbol{b}_0\\
&\text{sr mp} \quad j\,\mathrm{D}_t\,\boldsymbol{p}_0 = \mathrm{div}\;\boldsymbol{\sigma}_D^t + \boldsymbol{b}_t\\
&\text{mr sp} \quad J\,\mathrm{d}_t\,\boldsymbol{p}_t = \mathrm{Div}\;\boldsymbol{\Pi}_d^t + \boldsymbol{b}_0\\
&\text{sr sp} \quad \mathrm{d}_t\,\boldsymbol{p}_t = \mathrm{div}\;\boldsymbol{\sigma}_d^t + \boldsymbol{b}_t
\end{aligned} \tag{3.5.11}$$

On the Neumann boundary, the normal projection of the momentum fluxes $\boldsymbol{\Pi}_D^t$ and $\boldsymbol{\sigma}_D^t$ is required to be in equilibrium with the corresponding closed and the open system spatial stress vector contributions $\boldsymbol{t}_\tau^{\text{closed}}$ and $\boldsymbol{t}_\tau^{\text{open}}$.

$$\begin{aligned}
\boldsymbol{\Pi}_D^t \cdot \boldsymbol{N} &= \boldsymbol{t}_0^{\text{closed}} + \boldsymbol{t}_0^{\text{open}} \qquad & \boldsymbol{t}_0^{\text{open}} &= \bar{\boldsymbol{t}}_0^{\text{open}} + [\;\boldsymbol{p} \otimes \boldsymbol{R}\;] \cdot \boldsymbol{N}\\
\boldsymbol{\sigma}_D^t \cdot \boldsymbol{n} &= \boldsymbol{t}_t^{\text{closed}} + \boldsymbol{t}_t^{\text{open}} \qquad & \boldsymbol{t}_t^{\text{open}} &= \bar{\boldsymbol{t}}_t^{\text{open}} + [\;\boldsymbol{p} \otimes \boldsymbol{r}\;] \cdot \boldsymbol{n}
\end{aligned} \tag{3.5.12}$$

Correspondingly, the momentum sources $\boldsymbol{b}_\tau$ can be understood as the sum of the closed and the open system volume force contributions $\boldsymbol{b}_\tau^{\text{closed}}$ and $\boldsymbol{b}_\tau^{\text{open}}$.

$$\begin{aligned}
\boldsymbol{b}_0 &= \boldsymbol{b}_0^{\text{closed}} + \boldsymbol{b}_0^{\text{open}} \qquad & \boldsymbol{b}_0^{\text{open}} &= \bar{\boldsymbol{b}}_0^{\text{open}} + \boldsymbol{p}\,\mathcal{R}_0 - \nabla_X\,\boldsymbol{p} \cdot \boldsymbol{R}\\
\boldsymbol{b}_t &= \boldsymbol{b}_t^{\text{closed}} + \boldsymbol{b}_t^{\text{open}} \qquad & \boldsymbol{b}_t^{\text{open}} &= \bar{\boldsymbol{b}}_t^{\text{open}} + \boldsymbol{p}\,\mathcal{R}_t - \nabla_x\,\boldsymbol{p} \cdot \boldsymbol{r}
\end{aligned} \tag{3.5.13}$$

The material time derivative of the volume specific kinetic energy density $K_0 = 1/2\,\rho_0\,\boldsymbol{v}\cdot\boldsymbol{g}\cdot\boldsymbol{v}$ as introduced in equation (3.5.1) can be expressed as follows,

$$\mathrm{D}_t K_0 = \boldsymbol{v}\cdot[\,\mathrm{D}_t\,\boldsymbol{p}_0 - \partial_{\boldsymbol{\varphi}} K_0\,] - \mathrm{D}_{\boldsymbol{F}} K_0 : \mathrm{D}_t\,\boldsymbol{F} - K\,[\,\mathrm{D}_t\,\rho_0 - \mathsf{m}_0\,] \tag{3.5.14}$$

whereby the second, the third and the fifth term vanish identically for the spatial motion problem as $\partial_{\boldsymbol{\varphi}} K_0 = \boldsymbol{0}$, $\mathrm{D}_{\boldsymbol{F}} K_0 = \boldsymbol{0}$ and $\mathsf{m}_0 = 0$. With the projection of the volume specific balance of momentum (3.5.3) with the spatial velocity $\boldsymbol{v}$

$$\boldsymbol{v}\cdot\mathrm{D}_t\,\boldsymbol{p}_0 = \mathrm{Div}\,(\boldsymbol{v}\cdot\boldsymbol{\Pi}^t_D) + \boldsymbol{v}\cdot[\,\boldsymbol{b}^{\mathrm{ext}}_0 + \boldsymbol{b}^{\mathrm{int}}_0 + \partial_{\boldsymbol{\varphi}} K_0\,] - [\,\boldsymbol{\Pi}^t - \mathrm{D}_{\boldsymbol{F}} K_0\,] : \mathrm{D}_t\boldsymbol{F} \tag{3.5.15}$$

and the balance of mass $(3.3.13)_1$ weighted by the mass specific kinetic energy density $K$

$$K\,\mathrm{D}_t\,\rho_0 = \mathrm{Div}\,(\,K\boldsymbol{R}\,) + K\,\mathcal{R}_0 - \nabla_X K\cdot\boldsymbol{R} + \mathsf{m}_0\,K \tag{3.5.16}$$

equation (3.5.14) can be rewritten in explicit form.

$$\mathrm{D}_t K_0 = \mathrm{Div}\,(\,\boldsymbol{v}\cdot\boldsymbol{\Pi}^t_D - K\,\boldsymbol{R}\,) + \boldsymbol{v}\cdot\boldsymbol{b}^{\mathrm{ext}}_0 - K\,\mathcal{R}_0 + \nabla_X K\cdot\boldsymbol{R} - \boldsymbol{\Pi}^t : \mathrm{D}_t\boldsymbol{F} + \boldsymbol{v}\cdot\boldsymbol{b}^{\mathrm{int}}_0 \tag{3.5.17}$$

In what follows, it will prove convenient to reformulate the above equation in terms of the reduced momentum flux $\bar{\boldsymbol{\Pi}}^t_D$ and the reduced momentum source $\bar{\boldsymbol{b}}^{\mathrm{ext}}_0$ which can be related to their overall counterparts $\boldsymbol{\Pi}^t_D$ and $\boldsymbol{b}^{\mathrm{ext}}_0$ through the following identities.

$$\begin{array}{lcll}
\mathrm{Div}\,(\,\boldsymbol{v}\cdot\boldsymbol{\Pi}^t_D\,) & = & \mathrm{Div}\,(\,\boldsymbol{v}\cdot\bar{\boldsymbol{\Pi}}^t_D\,) & + \quad \mathrm{Div}\,(\,2\,K\;\;\boldsymbol{R}\,) \\
\boldsymbol{v}\cdot\boldsymbol{b}^{\mathrm{ext}}_0 & = & \boldsymbol{v}\cdot\bar{\boldsymbol{b}}^{\mathrm{ext}}_0 & + \quad 2\,K\,\mathcal{R}_0 - \boldsymbol{v}\cdot\nabla_X\boldsymbol{p}\cdot\boldsymbol{R} \\
\boldsymbol{\Pi}^t : \mathrm{D}_t\boldsymbol{F} & = & \bar{\boldsymbol{\Pi}}^t : \mathrm{D}_t\boldsymbol{F} & + \quad \boldsymbol{p}\cdot\nabla_X\boldsymbol{v}\cdot\boldsymbol{R}
\end{array} \tag{3.5.18}$$

With the help of the above equations and the identity $\boldsymbol{v}\cdot\nabla_X\boldsymbol{p} + \boldsymbol{p}\cdot\nabla_X\boldsymbol{v} = 2\,\nabla_X K$ following from $\boldsymbol{v}\cdot\boldsymbol{p} = 2\,K$, equation (3.5.17) can be reformulated in the following way.

$$\mathrm{D}_t K_0 = \mathrm{Div}\,(\,\boldsymbol{v}\cdot\bar{\boldsymbol{\Pi}}^t_D + K\,\boldsymbol{R}\,) + \boldsymbol{v}\cdot\bar{\boldsymbol{b}}^{\mathrm{ext}}_0 + K\,\mathcal{R}_0 - \nabla_X K\cdot\boldsymbol{R} - \bar{\boldsymbol{\Pi}}^t : \mathrm{D}_t\boldsymbol{F} + \boldsymbol{v}\cdot\bar{\boldsymbol{b}}^{\mathrm{int}}_0 \tag{3.5.19}$$

As stated already by Stokes as early as 1857, the rate of increase of the kinetic energy is equal to the input of external mechanical power minus the internal mechanical power. In the spatial motion context the latter is nothing but the stress power. The righthand side of the above equation thus motivates the identification of the volume specific external and internal mechanical power $\mathsf{p}^{\mathrm{ext}}_0$ and $\mathsf{p}^{\mathrm{int}}_0$,

$$\begin{array}{lcl}
\mathsf{p}^{\mathrm{ext}}_0 & := & \mathrm{Div}\,(\,\boldsymbol{v}\cdot\bar{\boldsymbol{\Pi}}^t_D + K\,\boldsymbol{R}\,) + \boldsymbol{v}\cdot\bar{\boldsymbol{b}}^{\mathrm{ext}}_0 + K\,\mathcal{R}_0 - \nabla_X K\cdot\boldsymbol{R} \\
\mathsf{p}^{\mathrm{int}}_0 & := & \bar{\boldsymbol{\Pi}}^t : \mathrm{D}_t\boldsymbol{F} - \boldsymbol{v}\cdot\bar{\boldsymbol{b}}^{\mathrm{int}}_0
\end{array} \tag{3.5.20}$$

whereby $\mathsf{p}^{\mathrm{ext}}_0$ characterizes the total rate of working of mechanical actions on the body. This rate of working consists of the flux contribution $\boldsymbol{v}\cdot\bar{\boldsymbol{\Pi}}^t_D + K\,\boldsymbol{R}$ and the source term $\boldsymbol{v}\cdot\bar{\boldsymbol{b}}^{\mathrm{ext}}_0 + K\,\mathcal{R}_0 - \nabla_X K\cdot\boldsymbol{R}$. The internal mechanical power $\mathsf{p}^{\mathrm{int}}_0$ includes the production term for the kinetic energy as $\bar{\boldsymbol{\Pi}}^t : \mathrm{D}_t\boldsymbol{F} - \boldsymbol{v}\cdot\bar{\boldsymbol{b}}^{\mathrm{int}}_0$. The definition of the latter suggests the interpretation of the reduced momentum flux $\bar{\boldsymbol{\Pi}}^t$ and the material time derivative of the spatial motion deformation gradient $\mathrm{D}_t\boldsymbol{F}$ as work conjugate pairs. To highlight

the duality with the material motion problem, the internal force contribution $\boldsymbol{v} \cdot \bar{\boldsymbol{b}}_0^{\text{int}}$ has been included in the definition of the internal mechanical power $\mathsf{p}_0^{\text{int}}$ although this term vanishes identically in the spatial motion case as $\bar{\boldsymbol{b}}_0^{\text{int}} = \boldsymbol{0}$. With the above abbreviations at hand, the balance of kinetic energy can be rewritten in the following form,

$$\begin{array}{rr} \text{mr mp} & \mathrm{D}_t\, K_0 = \mathsf{p}_0^{ext} - \mathsf{p}_0^{int} \\ \text{sr mp} & j\, \mathrm{D}_t\, K_0 = \mathsf{p}_\mathsf{t}^{ext} - \mathsf{p}_\mathsf{t}^{int} \\ \text{mr sp} & J\, \mathrm{d}_t\, K_t = \mathsf{p}_0^{ext} - \mathsf{p}_0^{int} + \mathrm{Div}\, (\, K_0\, \boldsymbol{V}\,) \\ \text{sr sp} & \mathrm{d}_t\, K_t = \mathsf{p}_\mathsf{t}^{ext} - \mathsf{p}_\mathsf{t}^{int} - \mathrm{div}\, (\, K_t\, \boldsymbol{v}\,) \end{array} \tag{3.5.21}$$

which has been denoted as the local form the 'theorem of energy', by Maugin [149]. With the related Piola transforms $K_0 = J\, K_t$, $\mathsf{p}_0^{\text{ext}} = J\, \mathsf{p}_\mathsf{t}^{\text{ext}}$ and $\mathsf{p}_0^{\text{int}} = J\, \mathsf{p}_\mathsf{t}^{\text{int}}$ and the volume specific version of Reynold's transport theorem (2.2.10), we easily obtain the alternative versions $(3.5.21)_2$ to $(3.5.21)_4$ of the volume specific kinetic energy balance of the spatial motion problem.

### 3.5.1.2 Material motion problem

Conceptually speaking, the balance of momentum of the material motion problem follows from a complete projection of the classical version of the standard momentum balance (3.5.11) onto the material manifold. For the particular case of a thermohyperelastic material, this projection is illustrated in detail in chapter 4.2. For the time being, we will introduce the balance of momentum of the material motion problem in a more abstract way. For that purpose, we make use of the definition of the volume specific material motion momentum density based on the related volume specific kinetic energy density $K_\tau$.

$$K_\tau = \frac{1}{2}\, \rho_\tau\, \boldsymbol{V} \cdot \boldsymbol{C} \cdot \boldsymbol{V} \tag{3.5.22}$$

Consequently, the rate of change of the volume specific material momentum density $\boldsymbol{P}_\tau$,

$$\boldsymbol{P}_\tau = \partial_{\boldsymbol{V}} K_\tau = \rho_\tau\, \boldsymbol{C} \cdot \boldsymbol{V} \tag{3.5.23}$$

which is typically referred to as 'pseudomomentum' by Maugin [149] is balanced with the momentum fluxes $\boldsymbol{\pi}_\delta^t$ and $\boldsymbol{\Sigma}_\delta^t$ and the momentum sources $\boldsymbol{B}_\tau$. The balance of momentum of the material motion problem with spatial reference and spatial parametrization can thus be postulated as

$$\mathrm{d}_t\, \boldsymbol{P}_t = \mathrm{div}\, \boldsymbol{\pi}_d^t + \boldsymbol{B}_t \tag{3.5.24}$$

whereby the related Piola transforms

$$\boldsymbol{P}_t = j\, \boldsymbol{P}_0 \qquad \boldsymbol{B}_t = j\, \boldsymbol{B}_0 \qquad \boldsymbol{\pi}_d^t = j\, \boldsymbol{\Sigma}_d^t \cdot \boldsymbol{f}^{-t} \tag{3.5.25}$$

and a pull back to the material configuration yield the following expression.

$$J\,\mathrm{d}_t \boldsymbol{P}_t = \mathrm{Div}\,\boldsymbol{\Sigma}^t_d + \boldsymbol{B}_0 \tag{3.5.26}$$

In the honor of Eshelby who originally introduced the material momentum flux $\boldsymbol{\Sigma}^t$ as the 'energy momentum tensor', $\boldsymbol{\Sigma}^t_\delta$ is nowadays often referred to as the dynamic generalization of the classical Eshelby stress tensor in the related literature. The application of Reynold's transport theorem $(2.2.10)_2$

$$J\,\mathrm{d}_t\,\boldsymbol{P}_t = \mathrm{D}_t\boldsymbol{P}_0 + \mathrm{Div}\,(\,\boldsymbol{P}_0 \otimes \boldsymbol{V}\,) \qquad \text{and} \qquad \boldsymbol{\Sigma}^t_D = \boldsymbol{\Sigma}^t_d - \boldsymbol{P}_0 \otimes \boldsymbol{V} \tag{3.5.27}$$

lead to the formulation with material reference and material parametrization.

$$\mathrm{D}_t\boldsymbol{P}_0 = \mathrm{Div}\,\boldsymbol{\Sigma}^t_D + \boldsymbol{B}_0 \tag{3.5.28}$$

The individual terms of the latter can again be transformed by the related Piola transforms

$$\boldsymbol{P}_0 = J\,\boldsymbol{P}_t \qquad \boldsymbol{B}_0 = J\,\boldsymbol{B}_t \qquad \boldsymbol{\Sigma}^t_D = J\,\boldsymbol{\pi}^t_D \cdot \boldsymbol{F}^{-t} \tag{3.5.29}$$

and pushed forward to the spatial configuration.

$$j\,\mathrm{D}_t\,\boldsymbol{P}_0 = \mathrm{div}\,\boldsymbol{\pi}^t_D + \boldsymbol{B}_t \tag{3.5.30}$$

Again, the application of Reynold's transport theorem $(2.2.10)_1$

$$j\,\mathrm{D}_t\,\boldsymbol{P}_0 = \mathrm{d}_t\boldsymbol{P}_t + \mathrm{div}\,(\,\boldsymbol{P}_t \otimes \boldsymbol{v}\,) \qquad \text{and} \qquad \boldsymbol{\pi}^t_d = \boldsymbol{\pi}^t_D - \boldsymbol{P}_t \otimes \boldsymbol{v} \tag{3.5.31}$$

can be used to gain back the original formulation (3.5.24). The four different versions of the volume specific balance of momentum of the material motion problem are summarized in the following.

$$\begin{aligned}
&\text{mr mp} && \mathrm{D}_t\,\boldsymbol{P}_0 = \mathrm{Div}\;\boldsymbol{\Sigma}^t_D + \boldsymbol{B}_0\\
&\text{sr mp} && j\,\mathrm{D}_t\,\boldsymbol{P}_0 = \mathrm{div}\;\boldsymbol{\pi}^t_D + \boldsymbol{B}_t\\
&\text{mr sp} && J\,\mathrm{d}_t\,\boldsymbol{P}_t = \mathrm{Div}\;\boldsymbol{\Sigma}^t_d + \boldsymbol{B}_0\\
&\text{sr sp} && \mathrm{d}_t\,\boldsymbol{P}_t = \mathrm{div}\;\boldsymbol{\pi}^t_d + \boldsymbol{B}_t
\end{aligned} \tag{3.5.32}$$

To illustrate the duality with the spatial motion problem, we can formally introduce the following Neumann type boundary conditions relating the momentum fluxes $\boldsymbol{\pi}^t_d$ and $\boldsymbol{\Sigma}^t_d$ to the sum of the closed and the open system material stress vector contributions $\boldsymbol{T}^{\text{closed}}_\tau$ and $\boldsymbol{T}^{\text{open}}_\tau$.

$$\begin{aligned}
\boldsymbol{\pi}^t_d \cdot \boldsymbol{n} &= \boldsymbol{T}^{\text{closed}}_t + \boldsymbol{T}^{\text{open}}_t \qquad & \boldsymbol{T}^{\text{open}}_t &= \bar{\boldsymbol{T}}^{\text{open}}_t + [\;\boldsymbol{P} \otimes \boldsymbol{r}\;] \cdot \boldsymbol{n}\\
\boldsymbol{\Sigma}^t_d \cdot \boldsymbol{N} &= \boldsymbol{T}^{\text{closed}}_0 + \boldsymbol{T}^{\text{open}}_0 \qquad & \boldsymbol{T}^{\text{open}}_0 &= \bar{\boldsymbol{T}}^{\text{open}}_0 + [\;\boldsymbol{P} \otimes \boldsymbol{R}\;] \cdot \boldsymbol{N}
\end{aligned} \tag{3.5.33}$$

Moreover, the volume specific momentum sources $\boldsymbol{B}_\tau$ can be expressed as the sum of the closed and the open system material force contributions $\boldsymbol{B}_\tau^{\text{closed}}$ and $\boldsymbol{B}_\tau^{\text{open}}$.

$$\begin{aligned} \boldsymbol{B}_t &= \boldsymbol{B}_t^{\text{closed}} + \boldsymbol{B}_t^{\text{open}} \qquad & \boldsymbol{B}_t^{\text{open}} &= \bar{\boldsymbol{B}}_t^{\text{open}} + \boldsymbol{P}\,\mathcal{R}_t - \nabla_x\,\boldsymbol{P}\cdot\boldsymbol{r} \\ \boldsymbol{B}_0 &= \boldsymbol{B}_0^{\text{closed}} + \boldsymbol{B}_0^{\text{open}} \qquad & \boldsymbol{B}_0^{\text{open}} &= \bar{\boldsymbol{B}}_0^{\text{open}} + \boldsymbol{P}\,\mathcal{R}_0 - \nabla_X\,\boldsymbol{P}\cdot\boldsymbol{R} \end{aligned} \tag{3.5.34}$$

In complete analogy to the spatial motion problem, the spatial time derivative of the volume specific kinetic energy density $K_t = 1/2\,\rho_t\,\boldsymbol{V}\cdot\boldsymbol{C}\cdot\boldsymbol{V}$ is given in the following form.

$$\mathrm{d}_t K_t = \boldsymbol{V}\cdot[\,\mathrm{d}_t\boldsymbol{P}_t - \partial_{\boldsymbol{\Phi}}K_t\,] - \mathrm{d}_f K_t : \mathrm{d}_t\boldsymbol{f} - K\,[\,\mathrm{d}_t\rho_t - \mathsf{M}_\mathsf{t}\,] \tag{3.5.35}$$

Note, however, that in contrast to the spatial motion problem, the terms $\partial_{\boldsymbol{\Phi}}K_t$, $\mathrm{d}_f K_t$ and $\mathsf{M}_\mathsf{t}$ do not vanish for the material motion problem. With the projection of the volume specific balance of momentum (3.5.24) with the material velocity $\boldsymbol{V}$

$$\boldsymbol{V}\cdot\mathrm{d}_t\boldsymbol{P}_t = \operatorname{div}(\boldsymbol{V}\cdot\boldsymbol{\pi}_d^t) + \boldsymbol{V}\cdot[\boldsymbol{B}_t^{\text{ext}} + \boldsymbol{B}_t^{\text{int}} + \partial_{\boldsymbol{\Phi}}K_t] - [\boldsymbol{\pi}^t - \mathrm{d}_f K_t] : \mathrm{d}_t\boldsymbol{f} \tag{3.5.36}$$

and the balance of mass (3.3.13.4) weighted by the mass specific kinetic energy density $K$

$$K\,\mathrm{d}_t\,\rho_t = \operatorname{div}(\,K\boldsymbol{r}\,) + K\,\mathcal{R}_t - \nabla_x K\cdot\boldsymbol{r} + \mathsf{M}_\mathsf{t}\,K \tag{3.5.37}$$

the above stated balance of kinetic energy can be reformulated in the following explicit form.

$$\mathrm{d}_t K_t = \operatorname{div}(\,\boldsymbol{V}\cdot\boldsymbol{\pi}_d^t - K\boldsymbol{r}\,) + \boldsymbol{V}\cdot\boldsymbol{B}_t^{\text{ext}} - K\mathcal{R}_t + \nabla_x K\cdot\boldsymbol{r} - \boldsymbol{\pi}^t : \mathrm{d}_t\boldsymbol{f} + \boldsymbol{V}\cdot\boldsymbol{B}_t^{\text{int}} \tag{3.5.38}$$

Similar to the spatial motion problem, we will now reformulate the above equation by making use of the fundamental relations between the reduced and non–reduced flux and source terms

$$\begin{aligned} \operatorname{div}(\,\boldsymbol{V}\cdot\boldsymbol{\pi}_d^t\,) &= \operatorname{div}(\,\boldsymbol{V}\cdot\bar{\boldsymbol{\pi}}_d^t\,) + \operatorname{Div}(\,2\,K\boldsymbol{r}\,) \\ \boldsymbol{V}\cdot\boldsymbol{B}_t^{\text{ext}} &= \boldsymbol{V}\cdot\bar{\boldsymbol{B}}_t^{\text{ext}} + 2\,K\,\mathcal{R}_t - \boldsymbol{V}\cdot\nabla_x\boldsymbol{P}\cdot\boldsymbol{r} \\ \boldsymbol{\pi}^t : \mathrm{d}_t\boldsymbol{f} &= \bar{\boldsymbol{\pi}}^t : \mathrm{d}_t\boldsymbol{f} + \boldsymbol{P}\cdot\nabla_x\boldsymbol{V}\cdot\boldsymbol{r} \end{aligned} \tag{3.5.39}$$

which render the following expression.

$$\mathrm{d}_t K_t = \operatorname{div}(\,\boldsymbol{V}\cdot\bar{\boldsymbol{\pi}}_d^t + K\boldsymbol{r}\,) + \boldsymbol{V}\cdot\bar{\boldsymbol{B}}_t^{\text{ext}} + K\mathcal{R}_t - \nabla_x K\cdot\boldsymbol{r} - \bar{\boldsymbol{\pi}}^t : \mathrm{d}_t\boldsymbol{f} + \boldsymbol{V}\cdot\bar{\boldsymbol{B}}_t^{\text{int}} \tag{3.5.40}$$

Notice the remarkable duality of the above expression with its spatial motion counterpart (3.5.19). This beautiful analogy is only possible due to our specific choice of volume sources. The identification of the material motion external and internal mechanical power $\mathsf{P}_\mathsf{t}^{\text{ext}}$ and $\mathsf{P}_\mathsf{t}^{\text{int}}$

$$\begin{aligned} \mathsf{P}_\mathsf{t}^{\text{ext}} &:= \operatorname{div}(\boldsymbol{V}\cdot\bar{\boldsymbol{\pi}}_d^t + K\boldsymbol{r}) + \boldsymbol{V}\cdot\bar{\boldsymbol{B}}_t^{\text{ext}} + K\,\mathcal{R}_t - \nabla_x K\cdot\boldsymbol{r} \\ \mathsf{P}_\mathsf{t}^{\text{int}} &:= \bar{\boldsymbol{\pi}}^t : \mathrm{d}_t\boldsymbol{f} - \boldsymbol{V}\cdot\bar{\boldsymbol{B}}_t^{\text{int}} \end{aligned} \tag{3.5.41}$$

allows for the following shorthanded notation of equation (3.5.40).

$$
\begin{aligned}
\text{mr mp} \qquad & \mathrm{D}_t\, K_0 = \mathsf{P}_0^{\text{ext}} - \mathsf{P}_{\text{t}}^{\text{int}} - \mathrm{Div}\ (\ K_0\, \boldsymbol{V}\ ) \\
\text{sr mp} \qquad & j\, \mathrm{D}_t\, K_0 = \mathsf{P}_{\text{t}}^{\text{ext}} - \mathsf{P}_{\text{t}}^{\text{int}} + \mathrm{div}\ (\ K_t\, \boldsymbol{v}\ ) \\
\text{mr sp} \qquad & J\ \mathrm{d}_t\ K_t = \mathsf{P}_0^{\text{ext}} - \mathsf{P}_0^{\text{int}} \\
\text{sr sp} \qquad & \mathrm{d}_t\ K_t = \mathsf{P}_{\text{t}}^{\text{ext}} - \mathsf{P}_{\text{t}}^{\text{int}}
\end{aligned}
\tag{3.5.42}
$$

Similar to the spatial motion problem, the definition of the material motion internal power $\mathsf{P}_{\text{t}}^{\text{int}}$ motivates the definition of the reduced momentum flux $\bar{\boldsymbol{\pi}}^t$ and the spatial time derivative of the material motion deformation gradient $\mathrm{d}_t\, \boldsymbol{f}$ as work conjugate pairs. The appropriate Piola transforms $K_t = j\, K_0$, $\mathsf{P}_{\text{t}}^{\text{ext}} = j\, \mathsf{P}_0^{\text{ext}}$ and $\mathsf{P}_{\text{t}}^{\text{int}} = j\, \mathsf{P}_0^{\text{int}}$ and the application of the volume specific version of Reynold's transport theorem (2.2.10) could be used to derive the alternative formulations $(3.5.42)_2$ to $(3.5.42)_4$.

**Remark 3.5.1 (Spatial vs. material motion problem)** *In order to distinguish the balance of momentum of the spatial and the material motion problem, the former has been introduced as the 'balance of physical momentum' while the latter is referred to as the 'balance of pseudomomentum' by Maugin [149]. The balance of momentum of the material motion problem (3.5.32) can be interpreted as the projection of the corresponding spatial motion balance equations (3.5.11) onto the material manifold $\mathcal{B}_0$. In this respect, the spatial and the material momentum densities are clearly related via the spatial and the material deformation gradient $\boldsymbol{F}$ and $\boldsymbol{f}$.*

$$
\begin{aligned}
\boldsymbol{p}_0 &= -\,\boldsymbol{f}^t \cdot \boldsymbol{P}_0 \qquad & \boldsymbol{P}_0 &= -\,\boldsymbol{F}^t \cdot \boldsymbol{p}_0 \\
\boldsymbol{p}_t &= -\,\boldsymbol{f}^t \cdot \boldsymbol{P}_t \qquad & \boldsymbol{P}_t &= -\,\boldsymbol{F}^t \cdot \boldsymbol{p}_t
\end{aligned}
\tag{3.5.43}
$$

*At this point, it proves convenient to additively decompose the dynamical stress measures $\boldsymbol{\Pi}_D^t$ $\boldsymbol{\sigma}_D^t$, $\boldsymbol{\pi}_d^t$ and $\boldsymbol{\Sigma}_d^t$ into the static stress measures $\boldsymbol{\Pi}^t$, $\boldsymbol{\sigma}^t$, $\boldsymbol{\pi}^t$ and $\boldsymbol{\Sigma}^t$ and the additional contributions stemming from the volume specific kinetic energy density $K_\tau$, see Steinmann [200].*

$$
\begin{aligned}
\boldsymbol{\Pi}_D^t &= \boldsymbol{\Pi}^t - \mathrm{D}_{\boldsymbol{F}} K_0 \qquad & \boldsymbol{\Sigma}_d^t &= \boldsymbol{\Sigma}^t - K_0 \boldsymbol{I} + \boldsymbol{F}^t \cdot \mathrm{d}_{\boldsymbol{F}} K_0 \\
\boldsymbol{\sigma}_D^t &= \boldsymbol{\sigma}^t - K_t \boldsymbol{I} + \boldsymbol{f}^t \cdot \mathrm{D}_f K_t \qquad & \boldsymbol{\pi}_d^t &= \boldsymbol{\pi}^t - \mathrm{d}_f K_t
\end{aligned}
\tag{3.5.44}
$$

*With the help of the partial derivative of the kinetic energy with respect to the deformation gradients,*

$$
\begin{aligned}
\mathrm{D}_{\boldsymbol{F}} K_0 &= \boldsymbol{0} \qquad & \boldsymbol{F}^t \cdot \mathrm{d}_{\boldsymbol{F}} K_0 &= \boldsymbol{P}_0 \otimes \boldsymbol{V} \\
\boldsymbol{f}^t \cdot \mathrm{D}_f K_t &= K_t\, \boldsymbol{I} \qquad & \mathrm{d}_f K_t &= K_t \boldsymbol{F}^t + \boldsymbol{P}_t \otimes \boldsymbol{v}
\end{aligned}
\tag{3.5.45}
$$

*we conclude that the dynamic stress measures of the spatial motion problem $\boldsymbol{\Pi}_D^t = \boldsymbol{\Pi}^t$ and $\boldsymbol{\sigma}_D^t = \boldsymbol{\sigma}^t$ remain unaffected by these additional contributions. In a similar manner, the associated volume forces $\boldsymbol{b}_\tau$ and $\boldsymbol{B}_\tau$ can be introduced as the sum of an external and an internal static*

*contribution and an additional dynamic term whereby the latter can be expressed in terms of the explicit derivative $\partial_{\boldsymbol{\varphi}}$ and $\partial_{\boldsymbol{\Phi}}$ of the volume specific kinetic energy density $K_\tau$.*

$$\begin{aligned} \boldsymbol{b}_0 &= \boldsymbol{b}_0^{\text{ext}} + \boldsymbol{b}_0^{\text{int}} + \partial_{\boldsymbol{\varphi}}\, K_0 \qquad & \boldsymbol{B}_0 &= \boldsymbol{B}_0^{\text{ext}} + \boldsymbol{B}_0^{\text{int}} + \partial_{\boldsymbol{\Phi}}\, K_0 \\ \boldsymbol{b}_t &= \boldsymbol{b}_t^{\text{ext}} + \boldsymbol{b}_t^{\text{int}} + \partial_{\boldsymbol{\varphi}}\, K_t \qquad & \boldsymbol{B}_t &= \boldsymbol{B}_t^{\text{ext}} + \boldsymbol{B}_t^{\text{int}} + \partial_{\boldsymbol{\Phi}}\, K_t \end{aligned} \tag{3.5.46}$$

*While the standard forces $\boldsymbol{b}_\tau$ perform work over positional changes relative to the ambient space, the configurational forces $\boldsymbol{B}_\tau$ perform work over positional changes relative to the ambient material. The latter have originally been introduced by Eshelby [60] as forces acting on defects. As a matter of fact, the internal forces, which are sometimes also interpreted as a measure of inhomogeneity in the material motion context, vanish identically for the spatial motion problem as $\boldsymbol{b}_\tau^{\text{int}} = \boldsymbol{0}$. Likewise, the dynamic contributions can only be found in the material motion context since $\partial_{\boldsymbol{\varphi}} K_\tau = \boldsymbol{0}$ whereas $\partial_{\boldsymbol{\Phi}} K_\tau = \partial_{\boldsymbol{\Phi}} \rho_\tau\, K$. Note that in the above decomposition, the external forces $\boldsymbol{b}_\tau^{\text{ext}}$ and $\boldsymbol{B}_\tau^{\text{ext}}$ are composed of a closed and an open system contribution while the internal forces $\boldsymbol{b}_\tau^{\text{int}}$ and $\boldsymbol{B}_\tau^{\text{int}}$ can be understood as a natural outcome of the particular underlying constitutive assumption. Moreover, a comparison of the balance of kinetic energy of the spatial and the material motion problem (3.5.21) and (3.5.42) based on the volume specific version of Reynold's transport theorem (2.2.10) reveals the following identities.*

$$\begin{aligned} \mathsf{p}_0^{\text{ext}} - \mathsf{p}_0^{\text{int}} &= \mathsf{P}_0^{\text{ext}} - \mathsf{P}_0^{\text{int}} - \text{Div}\ (\ K_0\ \boldsymbol{V}\ ) \\ \mathsf{P}_{\text{t}}^{\text{ext}} - \mathsf{P}_{\text{t}}^{\text{int}} &= \mathsf{p}_{\text{t}}^{\text{ext}} - \mathsf{p}_{\text{t}}^{\text{int}} - \text{div}\ (\ K_t\ \boldsymbol{v}\ ) \end{aligned} \tag{3.5.47}$$

**Remark 3.5.2 (Alternative derivation of balance of momentum)** *It shall be emphasized, that the balance of momentum of the spatial motion problem which is often introduced as the 'physical force balance' can be interpreted as a natural consequence of the invariance of the working under changes in spatial observer, see e.g. Gurtin [83] §4b. The balance of momentum of the material motion problem can be understood as the 'balance of configurational forces' . In complete analogy to the spatial motion problem, it follows from invariance requirements posed on the working under changes in material observer, see Gurtin [83] §5c.*

### 3.5.2 Mass specific version

#### 3.5.2.1 Spatial motion problem

The mass specific version of the balance of momentum is based on the mass specific kinetic energy density

$$K = \frac{1}{2}\, \boldsymbol{v} \cdot \mathbf{g} \cdot \boldsymbol{v} \tag{3.5.48}$$

defining the quantity to be balanced as its partial derivative with respect to the spatial velocity $\boldsymbol{v}$.

$$\boldsymbol{p} = \partial_v K = \boldsymbol{g} \cdot\, \boldsymbol{v} \tag{3.5.49}$$

The rate of change of the mass specific spatial motion momentum density $\boldsymbol{p}$, i.e. the covariant spatial velocity, is balanced with the reduced momentum fluxes $\bar{\boldsymbol{\Pi}}^t_\delta$ and $\bar{\boldsymbol{\sigma}}^t_\delta$,

the reduced momentum sources $\bar{\boldsymbol{b}}_\tau$ and the convective contribution in terms of $\mathsf{m}_\tau$ and $\mathsf{M}_\tau$, whereby $\mathsf{m}_\tau$ vanishes identically as $\mathsf{m}_\tau = 0$. By subtracting the balance of mass (3.3.13) weighted by the momentum density $\boldsymbol{p}$ from the volume specific momentum balance (3.5.11), we can derive four different statements of the mass specific momentum balance.

$$
\begin{aligned}
&\text{mr mp} && \rho_0\ \mathrm{D}_t\ \boldsymbol{p} = \mathrm{Div}\ \bar{\boldsymbol{\Pi}}^t_D + \bar{\boldsymbol{b}}_0 - \mathsf{m}_0\ \boldsymbol{p}\\
&\text{sr mp} && \rho_t\ \mathrm{D}_t\ \boldsymbol{p} = \mathrm{div}\ \bar{\boldsymbol{\sigma}}^t_D + \bar{\boldsymbol{b}}_t - \mathsf{m}_\mathsf{t}\ \boldsymbol{p}\\
&\text{mr sp} && \rho_0\ \mathrm{d}_t\ \boldsymbol{p} = \mathrm{Div}\ \bar{\boldsymbol{\Pi}}^t_d + \bar{\boldsymbol{b}}_0 - \mathsf{M}_0\ \boldsymbol{p}\\
&\text{sr sp} && \rho_t\ \mathrm{d}_t\ \boldsymbol{p} = \mathrm{div}\ \bar{\boldsymbol{\sigma}}^t_d + \bar{\boldsymbol{b}}_t - \mathsf{M}_\mathsf{t}\ \boldsymbol{p}
\end{aligned}
\tag{3.5.50}
$$

Note that the reduced momentum fluxes $\bar{\boldsymbol{\Pi}}^t_\delta$ and $\bar{\boldsymbol{\sigma}}^t_\delta$ which are related to the overall momentum fluxes $\boldsymbol{\Pi}^t_\delta$ and $\boldsymbol{\sigma}^t_\delta$ through $\bar{\boldsymbol{\Pi}}^t_\delta = \boldsymbol{\Pi}^t_\delta - \boldsymbol{p} \otimes \boldsymbol{R}$ and $\bar{\boldsymbol{\sigma}}^t_\delta = \boldsymbol{\sigma}^t_\delta - \boldsymbol{p} \otimes \boldsymbol{r}$ are determined by the closed and open system spatial stress vector contributions $\boldsymbol{t}^{\text{closed}}_\tau$ and $\bar{\boldsymbol{t}}^{\text{open}}_\tau$ on the Neumann boundary,

$$
\begin{aligned}
\bar{\boldsymbol{\Pi}}^t_D \cdot \boldsymbol{N} &= \boldsymbol{t}^{\text{closed}}_0 + \bar{\boldsymbol{t}}^{\text{open}}_0\\
\bar{\boldsymbol{\sigma}}^t_D \cdot \boldsymbol{n} &= \boldsymbol{t}^{\text{closed}}_t + \bar{\boldsymbol{t}}^{\text{open}}_t
\end{aligned}
\tag{3.5.51}
$$

while the reduced spatial momentum sources $\bar{\boldsymbol{b}}_\tau$ are given as the sum of the classical closed system volume force contributions $\boldsymbol{b}^{\text{closed}}_\tau$ and the reduced open system contributions $\bar{\boldsymbol{b}}^{\text{open}}_\tau$,

$$
\begin{aligned}
\bar{\boldsymbol{b}}_0 &= \boldsymbol{b}^{\text{closed}}_0 + \bar{\boldsymbol{b}}^{\text{open}}_0\\
\bar{\boldsymbol{b}}_t &= \boldsymbol{b}^{\text{closed}}_t + \bar{\boldsymbol{b}}^{\text{open}}_t
\end{aligned}
\tag{3.5.52}
$$

whereby $\boldsymbol{b}^{\text{closed}}_\tau$ contributes to the external, the internal and the kinetic contributions $\boldsymbol{b}^{\text{ext}}_\tau$, $\boldsymbol{b}^{\text{int}}_\tau$ and $\partial_{\boldsymbol{\varphi}} K_\tau$ while $\bar{\boldsymbol{b}}^{\text{open}}_\tau$ contributes exclusively to the external sources $\boldsymbol{b}^{\text{ext}}_\tau$. To investigate the mass specific version of the balance of kinetic energy, we need to evaluate the material time derivative of the mass specific kinetic energy density $K = 1/2\, \boldsymbol{v} \cdot \boldsymbol{g} \cdot \boldsymbol{v}$ which can easily be derived by subtracting the weighted balance of mass (3.5.16) from the material time derivative of the volume specific kinetic energy density $K_0$ given in equation (3.5.19) as

$$
\rho_0\, \mathrm{D}_t\, K = \mathrm{D}_t\, K_0 - K\, \mathrm{D}_t\, \rho_0 \tag{3.5.53}
$$

and thus

$$
\rho_0\, \mathrm{D}_t\, K = \mathrm{Div}\,(\boldsymbol{v} \cdot \bar{\boldsymbol{\Pi}}^t_D) + \boldsymbol{v} \cdot \bar{\boldsymbol{b}}^{\text{ext}}_0 - \mathsf{m}_0\, K - \bar{\boldsymbol{\Pi}}^t : \mathrm{D}_t \boldsymbol{F} + \boldsymbol{v} \cdot \bar{\boldsymbol{b}}^{\text{int}}_0. \tag{3.5.54}
$$

Consequently, we can identify the mass specific external and internal mechanical power $\bar{\mathsf{p}}^{\text{ext}}_0$ and $\bar{\mathsf{p}}^{\text{int}}_0$,

$$
\begin{aligned}
\bar{\mathsf{p}}^{\text{ext}}_0 &:= \mathsf{p}^{\text{ext}}_0 - K\, \mathrm{D}_t \rho_0 + \mathsf{m}_0\, K = \mathrm{Div}\,(\,\boldsymbol{v} \cdot \bar{\boldsymbol{\Pi}}^t_D\,) + \boldsymbol{v} \cdot \bar{\boldsymbol{b}}^{\text{ext}}_0\\
\bar{\mathsf{p}}^{\text{int}}_0 &:= \mathsf{p}^{\text{int}}_0 \qquad\qquad\qquad\qquad = \bar{\boldsymbol{\Pi}}^t : \mathrm{D}_t \boldsymbol{F} - \boldsymbol{v} \cdot \bar{\boldsymbol{b}}^{\text{int}}_0
\end{aligned}
\tag{3.5.55}
$$

keeping in mind that the internal force term $\bar{\boldsymbol{b}}_0^{\text{int}} = \boldsymbol{0}$ vanishes identically for the spatial motion case and has only been included to stress the duality with the definition based on the material motion problem. With the above definitions at hand, the mass specific balance of kinetic energy can be expressed in the following form.

$$
\begin{aligned}
\text{mr mp} \qquad & \rho_0 \, \mathrm{D}_t \, K = \bar{\mathsf{p}}_0^{\text{ext}} - \bar{\mathsf{p}}_0^{\text{int}} - \mathsf{m}_0 \, K \\
\text{sr mp} \qquad & \rho_t \, \mathrm{D}_t \, K = \bar{\mathsf{p}}_{\mathsf{t}}^{\text{ext}} - \bar{\mathsf{p}}_{\mathsf{t}}^{\text{int}} - \mathsf{m}_{\mathsf{t}} \, K \\
\text{mr sp} \qquad & \rho_0 \, \mathrm{d}_t \, K = \bar{\mathsf{p}}_0^{\text{ext}} - \bar{\mathsf{p}}_0^{\text{int}} - \mathsf{m}_0 \, K + \rho_0 \, \boldsymbol{V} \cdot \nabla_X \, K \\
\text{sr sp} \qquad & \rho_t \, \mathrm{d}_t \, K = \bar{\mathsf{p}}_{\mathsf{t}}^{\text{ext}} - \bar{\mathsf{p}}_{\mathsf{t}}^{\text{int}} - \mathsf{m}_{\mathsf{t}} \, K - \rho_t \, \boldsymbol{v} \cdot \nabla_x \, K
\end{aligned}
\tag{3.5.56}
$$

It is worth noting, that the difference of the mass and volume specific formulation manifests itself only in the definition of the external mechanical power while the mass specific internal power is identical to its volume specific counterpart as $\bar{\mathsf{p}}_0^{\text{int}} = \mathsf{p}_0^{\text{int}}$. To derive the alternative formulations of equation $(3.5.56)_1$ we have to make use of the related Piola transforms with $\bar{\mathsf{p}}_0^{\text{ext}} = J \, \bar{\mathsf{p}}_{\mathsf{t}}^{\text{ext}}$ and $\bar{\mathsf{p}}_0^{\text{int}} = J \, \bar{\mathsf{p}}_{\mathsf{t}}^{\text{int}}$ and the Euler theorem (2.2.9).

### 3.5.2.2 Material motion problem

In a similar way, the mass specific balance of momentum of the material motion problem is based on the material version of the mass specific kinetic energy density

$$
K = \frac{1}{2} \, \boldsymbol{V} \cdot \boldsymbol{\mathsf{C}} \cdot \boldsymbol{V}
\tag{3.5.57}
$$

defining the mass specific material momentum density.

$$
\boldsymbol{P} = \partial_{\boldsymbol{V}} K = \boldsymbol{C} \cdot \boldsymbol{V}
\tag{3.5.58}
$$

Its rate of change is balanced with the reduced momentum fluxes $\bar{\boldsymbol{\pi}}_{\delta}^{t}$ and $\bar{\boldsymbol{\Sigma}}_{\delta}^{t}$, the reduced momentum sources $\bar{\boldsymbol{B}}_{\tau}$ and the additional $\mathsf{M}_{\tau}$–term taking into account the convective contributions. Again, four different versions can be derived as the difference of the volume specific balance of momentum (3.5.32) and the balance of mass (3.3.13) weighted by the mass specific material momentum density $\boldsymbol{P}$, i.e. the covariant material velocity with the appropriate metric $\boldsymbol{C}$.

$$
\begin{aligned}
\text{mr mp} \qquad & \rho_0 \, \mathrm{D}_t \, \boldsymbol{P} = \mathrm{Div} \; \bar{\boldsymbol{\Sigma}}_{D}^{t} + \bar{\boldsymbol{B}}_0 - \mathsf{m}_0 \, \boldsymbol{P} \\
\text{sr mp} \qquad & \rho_t \, \mathrm{D}_t \, \boldsymbol{P} = \mathrm{div} \; \bar{\boldsymbol{\pi}}_{D}^{t} + \bar{\boldsymbol{B}}_t - \mathsf{m}_{\mathsf{t}} \, \boldsymbol{P} \\
\text{mr sp} \qquad & \rho_0 \, \mathrm{d}_t \, \boldsymbol{P} = \mathrm{Div} \; \bar{\boldsymbol{\Sigma}}_{d}^{t} + \bar{\boldsymbol{B}}_0 - \mathsf{M}_0 \, \boldsymbol{P} \\
\text{sr sp} \qquad & \rho_t \, \mathrm{d}_t \, \boldsymbol{P} = \mathrm{div} \; \bar{\boldsymbol{\pi}}_{d}^{t} + \bar{\boldsymbol{B}}_t - \mathsf{M}_{\mathsf{t}} \, \boldsymbol{P}
\end{aligned}
\tag{3.5.59}
$$

Thereby, the corresponding reduced momentum fluxes $\bar{\boldsymbol{\pi}}_{\delta}^{t}$ and $\bar{\boldsymbol{\Sigma}}_{\delta}^{t}$ which are related to the overall momentum fluxes $\boldsymbol{\pi}_{\delta}^{t}$ and $\boldsymbol{\Sigma}_{\delta}^{t}$ as $\bar{\boldsymbol{\pi}}_{\delta}^{t} = \boldsymbol{\pi}_{\delta}^{t} - \boldsymbol{P} \otimes \boldsymbol{r}$ and $\bar{\boldsymbol{\Sigma}}_{\delta}^{t} = \boldsymbol{\Sigma}_{\delta}^{t} - \boldsymbol{P} \otimes \boldsymbol{R}$

are formally determined by the corresponding material stress vectors $\boldsymbol{T}_t^{\text{closed}}$ and $\bar{\boldsymbol{T}}_t^{\text{open}}$ through the Neumann boundary conditions.

$$\begin{aligned} \bar{\boldsymbol{\pi}}_d^t \cdot \boldsymbol{n} &= \boldsymbol{T}_t^{\text{closed}} + \bar{\boldsymbol{T}}_t^{\text{open}} \\ \bar{\boldsymbol{\Sigma}}_d^t \cdot \boldsymbol{N} &= \boldsymbol{T}_0^{\text{closed}} + \bar{\boldsymbol{T}}_0^{\text{open}} \end{aligned} \tag{3.5.60}$$

Moreover, the reduced material volume forces $\bar{\boldsymbol{B}}_\tau$ are given as the sum of the standard closed system material volume forces $\boldsymbol{B}_\tau^{\text{closed}}$ and the reduced open system contribution $\bar{\boldsymbol{B}}_\tau^{\text{open}}$.

$$\begin{aligned} \bar{\boldsymbol{B}}_t &= \boldsymbol{B}_t^{\text{closed}} + \bar{\boldsymbol{B}}_t^{\text{open}} \\ \bar{\boldsymbol{B}}_0 &= \boldsymbol{B}_0^{\text{closed}} + \bar{\boldsymbol{B}}_0^{\text{open}} \end{aligned} \tag{3.5.61}$$

Again, the closed system part $\boldsymbol{B}_\tau^{\text{closed}}$ contributes to the external, the internal and the kinetic contributions $\boldsymbol{B}_\tau^{\text{ext}}$, $\boldsymbol{B}_\tau^{\text{int}}$ and $\partial_{\boldsymbol{\Phi}} K_\tau$ while the open system term $\bar{\boldsymbol{B}}_\tau^{\text{open}}$ only contributes to the external sources $\boldsymbol{B}_\tau^{\text{ext}}$. In analogy to the spatial motion problem, the spatial time derivative of the mass specific kinetic energy density $K = 1/2\, \boldsymbol{V} \cdot \boldsymbol{C} \cdot \boldsymbol{V}$ is given as the difference of the volume specific version (3.5.40) and the corresponding weighted balance of mass (3.5.37).

$$\rho_t \, \mathrm{d}_t \, K = \mathrm{d}_t \, K_t - K \, \mathrm{d}_t \rho_t \tag{3.5.62}$$

Consequently, the explicit form

$$\rho_t \, \mathrm{d}_t K = \operatorname{div} (\boldsymbol{V} \cdot \bar{\boldsymbol{\pi}}_d^t) + \boldsymbol{V} \cdot \bar{\boldsymbol{B}}_t^{\text{ext}} - \mathsf{M}_\mathsf{t} \, K - \bar{\boldsymbol{\pi}}^t : \mathrm{d}_t \boldsymbol{f} + \boldsymbol{V} \cdot \bar{\boldsymbol{B}}_t^{\text{int}} \tag{3.5.63}$$

defines the mass specific external and internal power $\bar{\mathsf{P}}_\mathsf{t}^{\text{ext}}$ and $\bar{\mathsf{P}}_\mathsf{t}^{\text{int}}$ as

$$\begin{aligned} \bar{\mathsf{P}}_\mathsf{t}^{\text{ext}} &:= \mathsf{P}_\mathsf{t}^{\text{ext}} - K \, \mathrm{d}_t \rho_t + \mathsf{M}_\mathsf{t} \, K = \operatorname{div} (\boldsymbol{V} \cdot \bar{\boldsymbol{\pi}}_d^t) + \boldsymbol{V} \cdot \bar{\boldsymbol{B}}_t^{\text{ext}} \\ \bar{\mathsf{P}}_\mathsf{t}^{\text{int}} &:= \mathsf{P}_\mathsf{t}^{\text{int}} \qquad\qquad\qquad\qquad = \bar{\boldsymbol{\pi}}^t : \mathrm{d}_t \boldsymbol{f} - \boldsymbol{V} \cdot \bar{\boldsymbol{B}}_t^{\text{int}} \end{aligned} \tag{3.5.64}$$

whereby again, the mass specific internal power is defined to be identical to its volume specific counterpart as $\bar{\mathsf{P}}_\mathsf{t}^{\text{int}} = \mathsf{P}_\mathsf{t}^{\text{int}}$. The mass specific balance of kinetic energy of the material motion problem could alternatively be reformulated with the related Piola transforms $\bar{\mathsf{P}}_\mathsf{t}^{\text{ext}} = j \, \bar{\mathsf{P}}_0^{\text{ext}}$ and $\bar{\mathsf{P}}_\mathsf{t}^{\text{int}} = j \, \bar{\mathsf{P}}_0^{\text{int}}$ and the corresponding versions of the Euler theorem (2.2.9).

---

$$\begin{aligned} \text{mr mp} \quad & \rho_0 \, \mathrm{D}_t \, K = \bar{\mathsf{P}}_0^{\text{ext}} - \bar{\mathsf{P}}_0^{\text{int}} - \mathsf{M}_0 \, K - \rho_0 \, \boldsymbol{V} \cdot \nabla_X K \\ \text{sr mp} \quad & \rho_t \, \mathrm{D}_t \, K = \bar{\mathsf{P}}_\mathsf{t}^{\text{ext}} - \bar{\mathsf{P}}_\mathsf{t}^{\text{int}} - \mathsf{M}_\mathsf{t} \, K + \rho_t \, \boldsymbol{v} \cdot \nabla_x K \\ \text{mr sp} \quad & \rho_0 \, \mathrm{d}_t \, K = \bar{\mathsf{P}}_0^{\text{ext}} - \bar{\mathsf{P}}_0^{\text{int}} - \mathsf{M}_0 \, K \\ \text{sr sp} \quad & \rho_t \, \mathrm{d}_t \, K = \bar{\mathsf{P}}_\mathsf{t}^{\text{ext}} - \bar{\mathsf{P}}_\mathsf{t}^{\text{int}} - \mathsf{M}_\mathsf{t} \, K \end{aligned} \tag{3.5.65}$$

---

**Remark 3.5.3 (Spatial vs. material motion problem)** *Similar to the kinematic relation (2.2.8) between the contravariant velocities $\boldsymbol{v}$ and $\boldsymbol{V}$, the covariant mass specific spatial and material momentum densities $\boldsymbol{p}$ and $\boldsymbol{P}$ are related via the corresponding deformation gradients.*

$$\boldsymbol{p} = -\boldsymbol{f}^t \cdot \boldsymbol{P} \qquad \boldsymbol{P} = -\boldsymbol{F}^t \cdot \boldsymbol{p} \tag{3.5.66}$$

*Moreover, the additive decomposition of the dynamic momentum fluxes introduced for the volume specific case can be transferred to the mass specific context.*

$$\begin{aligned} \bar{\boldsymbol{\Pi}}^t_D &= \bar{\boldsymbol{\Pi}}^t - \mathrm{D}_{\boldsymbol{F}} K_0 & \bar{\boldsymbol{\Sigma}}^t_d &= \bar{\boldsymbol{\Sigma}}^t - K_0 \boldsymbol{I} + \boldsymbol{F}^t \cdot \mathrm{d}_{\boldsymbol{F}} K_0 \\ \bar{\boldsymbol{\sigma}}^t_D &= \bar{\boldsymbol{\sigma}}^t - K_t \boldsymbol{I} + \boldsymbol{f}^t \cdot \mathrm{D}_f K_t & \bar{\boldsymbol{\pi}}^t_d &= \bar{\boldsymbol{\pi}}^t - \mathrm{d}_f K_t. \end{aligned} \tag{3.5.67}$$

*Correspondingly, the additive decomposition of the volume forces $\boldsymbol{b}_\tau$ and $\boldsymbol{B}_\tau$ is likewise valid for the reduced volume forces $\bar{\boldsymbol{b}}_\tau$ and $\bar{\boldsymbol{B}}_\tau$.*

$$\begin{aligned} \bar{\boldsymbol{b}}_0 &= \bar{\boldsymbol{b}}^{\mathrm{ext}}_0 + \bar{\boldsymbol{b}}^{\mathrm{int}}_0 + \partial_{\boldsymbol{\varphi}} K_0 & \bar{\boldsymbol{B}}_0 &= \bar{\boldsymbol{B}}^{\mathrm{ext}}_0 + \bar{\boldsymbol{B}}^{\mathrm{int}}_0 + \partial_{\boldsymbol{\Phi}} K_0 \\ \bar{\boldsymbol{b}}_t &= \bar{\boldsymbol{b}}^{\mathrm{ext}}_t + \bar{\boldsymbol{b}}^{\mathrm{int}}_t + \partial_{\boldsymbol{\varphi}} K_t & \bar{\boldsymbol{B}}_t &= \bar{\boldsymbol{B}}^{\mathrm{ext}}_t + \bar{\boldsymbol{B}}^{\mathrm{int}}_t + \partial_{\boldsymbol{\Phi}} K_t \end{aligned} \tag{3.5.68}$$

*Finally, a comparison of the mass specific balance of kinetic energy of the spatial and the material motion problem (3.5.56) and (3.5.65) based on the mass specific version of Reynold's transport theorem (3.3.14) reveals the following identities.*

$$\begin{aligned} \bar{\mathsf{p}}^{\mathrm{ext}}_0 - \bar{\mathsf{p}}^{\mathrm{int}}_0 &= \bar{\mathsf{P}}^{\mathrm{ext}}_0 - \bar{\mathsf{P}}^{\mathrm{int}}_0 - \mathrm{Div}\ (\ K_0\ \boldsymbol{V}\ ) \\ \bar{\mathsf{P}}^{\mathrm{ext}}_{\mathrm{t}} - \bar{\mathsf{P}}^{\mathrm{int}}_{\mathrm{t}} &= \bar{\mathsf{p}}^{\mathrm{ext}}_{\mathrm{t}} - \bar{\mathsf{p}}^{\mathrm{int}}_{\mathrm{t}} - \mathrm{div}\ (\ K_t\ \boldsymbol{v}\ ) \end{aligned} \tag{3.5.69}$$

*Remarkably, the difference of the spatial and the material motion quantities,* $\mathrm{Div}\,(\,K_0\,\boldsymbol{V}\,)$ *or* $\mathrm{div}\,(\,K_t\,\boldsymbol{v}\,)$*, respectively, is identical for the volume specific and the mass specific formulation, compare (3.5.47).*

## 3.6 Balance of energy

The balance of total energy as a representation of the first law of thermodynamics balances the rate of change of the volume specific total energy density $E_\tau = \rho_\tau\, E$ as the sum of the kinetic and internal energy density $E_\tau = K_\tau + I_\tau$ with the external power. In classical continuum mechanics of closed systems, this external power is composed of a purely mechanical contribution $\mathsf{p}^{\mathrm{ext}}_\tau$ or $\mathsf{P}^{\mathrm{ext}}_\tau$ and a non–mechanical thermal contribution $\mathsf{q}^{\mathrm{ext}}_\tau$ or $\mathsf{Q}^{\mathrm{ext}}_\tau$. Therefore, the balance of energy is sometimes referred to as 'principle of interconvertibility of heat and mechanical work', a notion which goes back to Carnot 1832. However, when dealing with open systems, we have to generalize the definition of the non–mechanical external power by including an additional external open system contribution in the definition of $\mathsf{q}^{\mathrm{ext}}_\tau$ and $\mathsf{Q}^{\mathrm{ext}}_\tau$.

### 3.6.1 Volume specific version

#### 3.6.1.1 Spatial motion problem

For the spatial motion problem, the rate of change of the volume specific total energy density $E_0 = \rho_0 E$ can be expressed in the following form.

$$\mathrm{D}_t E_0 = \mathrm{Div}\,(\, \boldsymbol{v} \cdot \bar{\boldsymbol{\Pi}}^t_D - \bar{\boldsymbol{Q}}_D + E\,\boldsymbol{R}\,) + \boldsymbol{v} \cdot \bar{\boldsymbol{b}}^{\mathrm{ext}}_0 + \bar{\mathcal{Q}}_0 + E\,\mathcal{R}_0 - \nabla_X E \cdot \boldsymbol{R} \tag{3.6.1}$$

Thereby, in addition to the purely mechanical external power $\mathsf{p}^{\mathrm{ext}}_0$ already defined in equation (3.5.20), we have included the non–mechanical external power $\mathsf{q}^{\mathrm{ext}}_0$ accounting for the classical thermal effects of the closed system and the additional open system effects as an additional non–mechanical supply of energy.

$$\mathsf{q}^{\mathrm{ext}}_0 := \mathrm{Div}\,(-\boldsymbol{Q}_D) + \mathcal{Q}_0 \tag{3.6.2}$$

Similar to the mechanical power, the non–mechanical power consists of a flux and a source contribution, denoted by $\boldsymbol{Q}_D$ and $\mathcal{Q}_0$, respectively. The former is composed of the reduced outward non–mechanical energy flux $\bar{\boldsymbol{Q}}_D$ modified by the explicit extra energy flux due to the open system $I\,\boldsymbol{R}$, while the latter is the sum of the reduced non–mechanical energy source $\bar{\mathcal{Q}}_0$ enhanced by the explicit effects of the open system $I\,\mathcal{R}_0$ and $\nabla_X I \cdot \boldsymbol{R}$.

$$\begin{aligned}
\mathsf{p}^{\mathrm{ext}}_0 &:= \mathrm{Div}\ (\ \boldsymbol{v} \cdot \bar{\boldsymbol{\Pi}}^t_D + K\,\boldsymbol{R}\ ) + \boldsymbol{v} \cdot \bar{\boldsymbol{b}}^{\mathrm{ext}}_0 + K\,\mathcal{R}_0 - \nabla_X K \cdot \boldsymbol{R} \\
\mathsf{q}^{\mathrm{ext}}_0 &:= \mathrm{Div}\ (\ -\bar{\boldsymbol{Q}}_D\ +\ I\ \boldsymbol{R}\ ) +\quad \bar{\mathcal{Q}}_0\quad +\ I\ \mathcal{R}_0 - \nabla_X I \cdot \boldsymbol{R}
\end{aligned} \tag{3.6.3}$$

With the help of the above definitions, equation (3.6.1) can be reformulated in the following concise form, which for the classical closed system case dates back to the early works of Duhem [53].

$$\begin{aligned}
\text{mr mp} \qquad & \mathrm{D}_t\, E_0 = \mathsf{p}^{ext}_0 + \mathsf{q}^{ext}_0 \\
\text{sr mp} \qquad & j\,\mathrm{D}_t\, E_0 = \mathsf{p}^{ext}_{\mathsf{t}} + \mathsf{q}^{ext}_{\mathsf{t}} \\
\text{mr sp} \qquad & J\ \mathrm{d}_t\ E_t = \mathsf{p}^{ext}_0 + \mathsf{q}^{ext}_0 + \mathrm{Div}\ (\ E_0\ \boldsymbol{V}\ ) \\
\text{sr sp} \qquad & \mathrm{d}_t\ E_t = \mathsf{p}^{ext}_{\mathsf{t}} + \mathsf{q}^{ext}_{\mathsf{t}} - \mathrm{div}\ (\ E_t\ \boldsymbol{v}\ )
\end{aligned} \tag{3.6.4}$$

The appropriate Piola transforms $E_0 = J\,E_t$, $\mathsf{p}^{\mathrm{ext}}_0 = J\,\mathsf{p}^{\mathrm{ext}}_{\mathsf{t}}$, $\mathsf{q}^{\mathrm{ext}}_0 = J\,\mathsf{q}^{\mathrm{ext}}_{\mathsf{t}}$, $\boldsymbol{Q}_D = J\,\boldsymbol{q}_D \cdot \boldsymbol{F}^{-t}$ and $\bar{\boldsymbol{Q}}_D = J\,\bar{\boldsymbol{q}}_D \cdot \boldsymbol{F}^{-t}$ can be used together with the application of the volume specific transport theorem to derive the alternative formulations of equation $(3.6.4)_1$. On the Neumann boundary, the non–mechanical energy fluxes of Piola–Kirchhoff and Cauchy type $\boldsymbol{Q}_D$ and $\boldsymbol{q}_D$ are given in terms of the normal projection of the classical heat flux related to the closed system $q^{\mathrm{closed}}_\tau$ and the additional open system contribution $q^{\mathrm{open}}_\tau$.

$$\begin{aligned}
\boldsymbol{Q}_D \cdot \boldsymbol{N} &= q^{\mathrm{closed}}_0 + q^{\mathrm{open}}_0 \qquad & q^{\mathrm{open}}_0 &= \bar{q}^{\mathrm{open}}_0 - I\,\boldsymbol{R} \cdot \boldsymbol{N} \\
\boldsymbol{q}_D \cdot \boldsymbol{n} &= q^{\mathrm{closed}}_t + q^{\mathrm{open}}_t \qquad & q^{\mathrm{open}}_t &= \bar{q}^{\mathrm{open}}_t - I\ \boldsymbol{r} \cdot \boldsymbol{n}
\end{aligned} \tag{3.6.5}$$

Moreover, the non–mechanical energy sources $\mathcal{Q}_\tau$ can be understood as the sum of the classical heat source of the closed system $\mathcal{Q}_\tau^{\text{closed}}$ and an additional non–mechanical energy source taking into account the nature of the open system $\mathcal{Q}_\tau^{\text{open}}$.

$$\begin{aligned} \mathcal{Q}_0 &= \mathcal{Q}_0^{\text{closed}} + \mathcal{Q}_0^{\text{open}} \qquad & \mathcal{Q}_0^{\text{open}} &= \bar{\mathcal{Q}}_0^{\text{open}} + I\,\mathcal{R}_0 - \nabla_X I \cdot \boldsymbol{R} \\ \mathcal{Q}_t &= \mathcal{Q}_t^{\text{closed}} + \mathcal{Q}_t^{\text{open}} \qquad & \mathcal{Q}_t^{\text{open}} &= \bar{\mathcal{Q}}_t^{\text{open}} + I\,\mathcal{R}_t - \nabla_x I \cdot \boldsymbol{r} \end{aligned} \tag{3.6.6}$$

By subtracting the balance of kinetic energy (3.5.21) from the total energy balance (3.6.4), we obtain the balance equation of the internal energy density $I_0 = E_0 - K_0$,

$$\begin{aligned} \text{mr mp} \qquad & \mathrm{D}_t\, I_0 = \mathsf{p}_0^{int} + \mathsf{q}_0^{ext} \\ \text{sr mp} \qquad & j\,\mathrm{D}_t\, I_0 = \mathsf{p}_\mathsf{t}^{int} + \mathsf{q}_\mathsf{t}^{ext} \\ \text{mr sp} \qquad & J\,\mathrm{d}_t\, I_t = \mathsf{p}_0^{int} + \mathsf{q}_0^{ext} + \mathrm{Div}\,(\, I_0\, \boldsymbol{V}\,) \\ \text{sr sp} \qquad & \mathrm{d}_t\, I_t = \mathsf{p}_\mathsf{t}^{int} + \mathsf{q}_\mathsf{t}^{ext} - \mathrm{div}\,(\, I_t\, \boldsymbol{v}\,) \end{aligned} \tag{3.6.7}$$

which will be useful for our further thermodynamical considerations.

### 3.6.1.2 Material motion problem

The balance of the volume specific total energy density $E_t = \rho_t\, E$ of the material motion problem can formally be stated as follows.

$$\mathrm{d}_t\, E_t = \mathrm{div}\,(\, \boldsymbol{V} \cdot \bar{\boldsymbol{\pi}}_d^t - \bar{\boldsymbol{q}}_d + E\,\boldsymbol{r}\,) + \boldsymbol{V} \cdot \bar{\boldsymbol{B}}_t^{\text{ext}} + \bar{\mathcal{Q}}_t + E\,\mathcal{R}_t - \nabla_x E \cdot \boldsymbol{r}. \tag{3.6.8}$$

It balances the spatial rate of change of the total energy density $E_t = K_t + I_t$ with the material external mechanical power $\mathsf{P}_\mathsf{t}^{\text{ext}}$ and the external non–mechanical power $\mathsf{Q}_\mathsf{t}^{\text{ext}}$, whereby the latter consists of the material motion flux of non–mechanical energy $\boldsymbol{q}_d$ and the related material motion source $\mathcal{Q}_t$.

$$\mathsf{Q}_\mathsf{t}^{\text{ext}} := \mathrm{div}\,(-\boldsymbol{q}_d) + \mathcal{Q}_t \tag{3.6.9}$$

As for the spatial motion problem, the contributions $\boldsymbol{q}_d$ and $\mathcal{Q}_t$ can be expressed explicitly in terms of their reduced counterparts $\bar{\boldsymbol{q}}_d$ and $\bar{\mathcal{Q}}_t$ and the additional open system extra terms $I\,\boldsymbol{r}$, $I\,\mathcal{R}_t$ and $\nabla_x I \cdot \boldsymbol{r}$.

$$\begin{aligned} \mathsf{P}_\mathsf{t}^{\text{ext}} &:= \mathrm{div}\;\,(\, \boldsymbol{V} \cdot \bar{\boldsymbol{\pi}}_d^t + K\,\boldsymbol{r}\,) + \boldsymbol{V} \cdot \bar{\boldsymbol{B}}_t^{\text{ext}} + K\,\mathcal{R}_t - \nabla_x K \cdot \boldsymbol{r} \\ \mathsf{Q}_\mathsf{t}^{\text{ext}} &:= \mathrm{Div}\;(\;\; -\bar{\boldsymbol{q}}_d \;\; + I\,\boldsymbol{r}\,) + \quad \bar{\mathcal{Q}}_t \quad + I\,\mathcal{R}_t - \nabla_x I \cdot \boldsymbol{r} \end{aligned} \tag{3.6.10}$$

Equation (3.6.8) can thus be rewritten as follows.

$$\begin{aligned} \text{mr mp} \qquad & \mathrm{D}_t\, E_0 = \mathsf{P}_0^{ext} + \mathsf{Q}_0^{ext} - \mathrm{Div}\,(\, E_0\, \boldsymbol{V}\,) \\ \text{sr mp} \qquad & j\,\mathrm{D}_t\, E_0 = \mathsf{P}_\mathsf{t}^{ext} + \mathsf{Q}_\mathsf{t}^{ext} + \mathrm{div}\,(\, E_t\, \boldsymbol{v}\,) \\ \text{mr sp} \qquad & J\,\mathrm{d}_t\, E_t = \mathsf{P}_0^{ext} + \mathsf{Q}_0^{ext} \\ \text{sr sp} \qquad & \mathrm{d}_t\, E_t = \mathsf{P}_\mathsf{t}^{ext} + \mathsf{Q}_\mathsf{t}^{ext} \end{aligned} \tag{3.6.11}$$

The four alternative formulations could be derived through the application of the related Piola transforms $E_t = j\,E_0$, $\mathsf{P}_\mathsf{t}^{\text{ext}} = j\,\mathsf{P}_0^{\text{ext}}$, $\mathsf{Q}_\mathsf{t}^{\text{ext}} = j\,\mathsf{Q}_0^{\text{ext}}$, $\boldsymbol{q}_d = j\,\boldsymbol{Q}_d \cdot \boldsymbol{f}^{-t}$ and $\bar{\boldsymbol{q}}_d = j\,\bar{\boldsymbol{Q}}_d \cdot \boldsymbol{f}^{-t}$ in combination with the volume specific transport theorem (2.2.10). In complete analogy to the spatial motion problem, we can formally introduce boundary conditions for the non–mechanical energy flux $\boldsymbol{q}_d$ and $\boldsymbol{Q}_d$

$$\begin{aligned} \boldsymbol{q}_d \cdot \boldsymbol{n} &= Q_t^{\text{closed}} + Q_t^{\text{open}} \qquad & Q_t^{\text{open}} &= \bar{Q}_t^{\text{open}} - I\ \boldsymbol{r} \cdot \boldsymbol{n} \\ \boldsymbol{Q}_d \cdot \boldsymbol{N} &= Q_0^{\text{closed}} + Q_0^{\text{open}} \qquad & Q_0^{\text{open}} &= \bar{Q}_0^{\text{open}} - I\ \boldsymbol{R} \cdot \boldsymbol{N} \end{aligned} \tag{3.6.12}$$

and define the non–mechanical heat sources $\mathcal{Q}_\tau$ in analogy to the spatial motion case.

$$\begin{aligned} \mathcal{Q}_t &= \mathcal{Q}_t^{\text{closed}} + \mathcal{Q}_t^{\text{open}} \qquad & \mathcal{Q}_t^{\text{open}} &= \bar{\mathcal{Q}}_t^{\text{open}} + I\ \mathcal{R}_t - \nabla_x\ I \cdot \boldsymbol{r} \\ \mathcal{Q}_0 &= \mathcal{Q}_0^{\text{closed}} + \mathcal{Q}_0^{\text{open}} \qquad & \mathcal{Q}_0^{\text{open}} &= \bar{\mathcal{Q}}_0^{\text{open}} + I\ \mathcal{R}_0 - \nabla_X\ I \cdot \boldsymbol{R} \end{aligned} \tag{3.6.13}$$

Again, a reduction to the useful balance of internal energy density $I_t = E_t - K_t$ can be derived by subtracting the balance of kinetic energy (3.5.42) from the balance of total energy (3.6.11).

---

$$\begin{aligned} \text{mr mp} \qquad & \mathrm{D}_t\ I_0 = \mathsf{P}_0^{int} + \mathsf{Q}_0^{ext} - \mathrm{Div}\ (\ I_0\ \boldsymbol{V}\ ) \\ \text{sr mp} \qquad & j\ \mathrm{D}_t\ I_0 = \mathsf{P}_\mathsf{t}^{int} + \mathsf{Q}_\mathsf{t}^{ext} + \mathrm{div}\ (\ I_t\ \boldsymbol{v}\ ) \\ \text{mr sp} \qquad & J\ \mathrm{d}_t\ I_t = \mathsf{P}_0^{int} + \mathsf{Q}_0^{ext} \\ \text{sr sp} \qquad & \mathrm{d}_t\ I_t = \mathsf{P}_\mathsf{t}^{int} + \mathsf{Q}_\mathsf{t}^{ext} \end{aligned} \tag{3.6.14}$$

---

**Remark 3.6.1 (Spatial vs. material motion problem)** *A comparison of the balance of total energy of the spatial and the material motion problem (3.6.4) and (3.6.11) together with the volume specific version of Reynold's transport theorem (2.2.10) reveals the following relations.*

$$\begin{aligned} \mathsf{p}_0^{\text{ext}} + \mathsf{q}_0^{\text{ext}} &= \mathsf{P}_0^{\text{ext}} + \mathsf{Q}_0^{\text{ext}} - \mathrm{Div}\ (\ E_0\ \boldsymbol{V}\ ) \\ \mathsf{P}_\mathsf{t}^{\text{ext}} + \mathsf{Q}_\mathsf{t}^{\text{ext}} &= \mathsf{p}_\mathsf{t}^{\text{ext}} + \mathsf{q}_\mathsf{t}^{\text{ext}} - \mathrm{div}\ (\ E_t\ \boldsymbol{v}\ ) \end{aligned} \tag{3.6.15}$$

*Furthermore, we can state the following identities,*

$$\begin{aligned} \mathsf{p}_0^{\text{int}} + \mathsf{q}_0^{\text{ext}} &= \mathsf{P}_0^{\text{int}} + \mathsf{Q}_0^{\text{ext}} - \mathrm{Div}\ (\ I_0\ \boldsymbol{V}\ ) \\ \mathsf{P}_\mathsf{t}^{\text{int}} + \mathsf{Q}_\mathsf{t}^{\text{ext}} &= \mathsf{p}_\mathsf{t}^{\text{int}} + \mathsf{q}_\mathsf{t}^{\text{ext}} - \mathrm{div}\ (\ I_t\ \boldsymbol{v}\ ) \end{aligned} \tag{3.6.16}$$

*which follow from a comparison of the different versions of the volume specific balance of internal energy. Note in anticipation of the relations to be set up in section 3.6.2, that their closer evaluation yields the same results as the evaluation of the corresponding mass specific equations which will be elaborated later on.*

### 3.6.2 Mass specific version

#### 3.6.2.1 Spatial motion problem

The mass specific counterpart of the equations derived above balances the mass specific energy density $E = E_0 \,/\, \rho_0$ with the mass specific external mechanical power $\bar{\mathsf{p}}_0^{\text{ext}}$ introduced in (3.5.55) and the mass specific non–mechanical power $\bar{\mathsf{q}}_0^{\text{ext}}$.

$$\bar{\mathsf{q}}_0^{\text{ext}} := \mathsf{q}_0^{\text{ext}} - I\,\mathrm{D}_t\rho_0 + \mathsf{m}_0\, I = -\mathrm{Div}\,\bar{\boldsymbol{Q}}_D + \bar{\mathcal{Q}}_0 \tag{3.6.17}$$

The corresponding balance equation follows from subtracting the corresponding balance of mass $(3.3.13)_1$ weighted by the total energy $E$ from the volume specific energy balance $(3.6.4)_1$. Alternative formulations can be derived by applying the corresponding Piola transforms with $\bar{\mathsf{p}}_0^{\text{ext}} = J\,\bar{\mathsf{p}}_{\mathsf{t}}^{\text{ext}}$ and $\bar{\mathsf{q}}_0^{\text{ext}} = J\,\bar{\mathsf{q}}_{\mathsf{t}}^{\text{ext}}$ and the Euler theorem (2.2.9).

$$\begin{aligned}
\text{mr mp} \qquad & \rho_0\,\mathrm{D}_t\,E = \bar{\mathsf{p}}_0^{ext} + \bar{\mathsf{q}}_0^{ext} - \mathsf{m}_0\,E \\
\text{sr mp} \qquad & \rho_t\,\mathrm{D}_t\,E = \bar{\mathsf{p}}_{\mathsf{t}}^{ext} + \bar{\mathsf{q}}_{\mathsf{t}}^{ext} - \mathsf{m}_{\mathsf{t}}\,E \\
\text{mr sp} \qquad & \rho_0\,\mathrm{d}_t\,E = \bar{\mathsf{p}}_0^{ext} + \bar{\mathsf{q}}_0^{ext} - \mathsf{m}_0\,E + \rho_0\,\boldsymbol{V}\cdot\nabla_X\,E \\
\text{sr sp} \qquad & \rho_t\,\mathrm{d}_t\,E = \bar{\mathsf{p}}_{\mathsf{t}}^{ext} + \bar{\mathsf{q}}_{\mathsf{t}}^{ext} - \mathsf{m}_{\mathsf{t}}\,E - \rho_t\,\boldsymbol{v}\cdot\nabla_x\,E
\end{aligned} \tag{3.6.18}$$

Again, we can relate the reduced energy fluxes $\bar{\boldsymbol{Q}}_D$ and $\bar{\boldsymbol{q}}_D$ defined through $\bar{\boldsymbol{Q}}_D = \boldsymbol{Q}_D - I\,\boldsymbol{R}$ and $\bar{\boldsymbol{q}}_D = \boldsymbol{q}_D - I\,\boldsymbol{r}$ to the classical heat flux $q_\tau^{\text{closed}}$ and the energy flux caused by additional effects of the open system $\bar{q}_\tau^{\text{open}}$.

$$\begin{aligned}
\bar{\boldsymbol{Q}}_D\cdot\boldsymbol{N} &= q_0^{\text{closed}} + \bar{q}_0^{\text{open}} \\
\bar{\boldsymbol{q}}_D\cdot\boldsymbol{n} &= q_t^{\text{closed}} + \bar{q}_t^{\text{open}}
\end{aligned} \tag{3.6.19}$$

Moreover, the reduced non–mechanical energy sources $\bar{\mathcal{Q}}_\tau$ are given as the sum of the classical heat source of the closed system $\mathcal{Q}_\tau^{\text{closed}}$ and the additional open system contribution to the energy $\bar{\mathcal{Q}}_\tau^{\text{open}}$.

$$\begin{aligned}
\bar{\mathcal{Q}}_0 &= \mathcal{Q}_0^{\text{closed}} + \bar{\mathcal{Q}}_0^{\text{open}} \\
\bar{\mathcal{Q}}_t &= \mathcal{Q}_t^{\text{closed}} + \bar{\mathcal{Q}}_t^{\text{open}}
\end{aligned} \tag{3.6.20}$$

A reduction to the balance of internal energy $I = E - K$ follows from by subtracting the balance of kinetic energy (3.5.56) from the balance of total energy (3.6.18).

$$\begin{aligned}
\text{mr mp} \qquad & \rho_0\,\mathrm{D}_t\,I = \bar{\mathsf{p}}_0^{int} + \bar{\mathsf{q}}_0^{ext} - \mathsf{m}_0\,I \\
\text{sr mp} \qquad & \rho_t\,\mathrm{D}_t\,I = \bar{\mathsf{p}}_{\mathsf{t}}^{int} + \bar{\mathsf{q}}_{\mathsf{t}}^{ext} - \mathsf{m}_{\mathsf{t}}\,I \\
\text{mr sp} \qquad & \rho_0\,\mathrm{d}_t\,I = \bar{\mathsf{p}}_0^{int} + \bar{\mathsf{q}}_0^{ext} - \mathsf{m}_0\,I + \rho_0\,\boldsymbol{V}\cdot\nabla_X\,I \\
\text{sr sp} \qquad & \rho_t\,\mathrm{d}_t\,I = \bar{\mathsf{p}}_{\mathsf{t}}^{int} + \bar{\mathsf{q}}_{\mathsf{t}}^{ext} - \mathsf{m}_{\mathsf{t}}\,I - \rho_t\,\boldsymbol{v}\cdot\nabla_x\,I
\end{aligned} \tag{3.6.21}$$

Recall that the convective mass contribution $\mathsf{m}_0 = 0$ vanishes identically for the spatial motion case. The mass specific balance equations of total and internal energy are thus free from all the explicit extra terms caused by the changes in mass. Remarkably, they take a similar structure as the standard balance equations for classical closed systems.

#### 3.6.2.2 Material motion problem

The mass specific balance of energy of the material motion problem balances the rate of change of the mass specific energy $E = E_t \,/\, \rho_t$ with the corresponding mechanical external power $\bar{\mathsf{P}}_{\mathsf{t}}^{\text{ext}}$ and the non–mechanical external power $\bar{\mathsf{Q}}_{\mathsf{t}}^{\text{ext}}$.

$$\bar{\mathsf{Q}}_{\mathsf{t}}^{\text{ext}} := \mathsf{Q}_{\mathsf{t}}^{\text{ext}} - I\,\mathrm{d}_t\rho_t + \mathsf{M}_{\mathsf{t}}\,I = -\mathrm{div}\,\bar{\boldsymbol{q}}_d + \bar{\mathcal{Q}}_t. \tag{3.6.22}$$

In short form, the mass specific balance of energy with spatial reference and spatial parametrization can be expressed as

$$\begin{aligned}
\text{mr mp} \qquad & \rho_0\,\mathrm{D}_t\,E = \bar{\mathsf{P}}_0^{ext} + \bar{\mathsf{Q}}_0^{ext} - \mathsf{M}_0\,E - \rho_0\,\boldsymbol{V}\cdot\nabla_X\,E \\
\text{sr mp} \qquad & \rho_t\,\mathrm{D}_t\,E = \bar{\mathsf{P}}_{\mathsf{t}}^{ext} + \bar{\mathsf{Q}}_{\mathsf{t}}^{ext} - \mathsf{M}_{\mathsf{t}}\,E + \rho_t\,\boldsymbol{v}\cdot\nabla_x\,E \\
\text{mr sp} \qquad & \rho_0\,\mathrm{d}_t\,E = \bar{\mathsf{P}}_0^{ext} + \bar{\mathsf{Q}}_0^{ext} - \mathsf{M}_0\,E \\
\text{sr sp} \qquad & \rho_t\,\mathrm{d}_t\,E = \bar{\mathsf{P}}_{\mathsf{t}}^{ext} + \bar{\mathsf{Q}}_{\mathsf{t}}^{ext} - \mathsf{M}_{\mathsf{t}}\,E
\end{aligned} \tag{3.6.23}$$

whereby the alternative formulations can be derived through the corresponding Piola transforms with $\bar{\mathsf{P}}_{\mathsf{t}}^{\text{ext}} = j\,\bar{\mathsf{P}}_0^{\text{ext}}$ and $\bar{\mathsf{Q}}_{\mathsf{t}}^{\text{ext}} = j\,\bar{\mathsf{Q}}_0^{\text{ext}}$ in combination with the Euler theorem (2.2.9). Again, to illustrate the duality with the classical spatial motion problem, Neumann boundary conditions can formally be introduced for the reduced non–mechanical energy fluxes $\bar{\boldsymbol{q}}_d$ and $\bar{\boldsymbol{Q}}_d$ defined through $\bar{\boldsymbol{q}}_d = \boldsymbol{q}_d - I\,\boldsymbol{r}$ and $\bar{\boldsymbol{Q}}_d = \boldsymbol{Q}_d - I\,\boldsymbol{R}$ in the following way,

$$\begin{aligned}
\bar{\boldsymbol{q}}_d \cdot \boldsymbol{n} &= \mathcal{Q}_t^{\text{closed}} + \bar{\mathcal{Q}}_t^{\text{open}} \\
\bar{\boldsymbol{Q}}_d \cdot \boldsymbol{N} &= \mathcal{Q}_0^{\text{closed}} + \bar{\mathcal{Q}}_0^{\text{open}}
\end{aligned} \tag{3.6.24}$$

while the reduced non–mechanical energy sources are given as follows.

$$\begin{aligned}
\bar{\mathcal{Q}}_t &= \mathcal{Q}_t^{\text{closed}} + \bar{\mathcal{Q}}_t^{\text{open}} \\
\bar{\mathcal{Q}}_0 &= \mathcal{Q}_0^{\text{closed}} + \bar{\mathcal{Q}}_0^{\text{open}}
\end{aligned} \tag{3.6.25}$$

Finally, by subtracting the balance of kinetic energy (3.5.65) from the balance of total energy (3.6.23) the mass specific balance of internal energy $I = E - K$ can be derived.

$$\begin{aligned}
\text{mr mp} \qquad & \rho_0\,\mathrm{D}_t\,I = \bar{\mathsf{P}}_0^{int} + \bar{\mathsf{Q}}_0^{ext} - \mathsf{M}_0\,I - \rho_0\,\boldsymbol{V}\cdot\nabla_X\,I \\
\text{sr mp} \qquad & \rho_t\,\mathrm{D}_t\,I = \bar{\mathsf{P}}_{\mathsf{t}}^{int} + \bar{\mathsf{Q}}_{\mathsf{t}}^{ext} - \mathsf{M}_{\mathsf{t}}\,I + \rho_t\,\boldsymbol{v}\cdot\nabla_x\,I \\
\text{mr sp} \qquad & \rho_0\,\mathrm{d}_t\,I = \bar{\mathsf{P}}_0^{int} + \bar{\mathsf{Q}}_0^{ext} - \mathsf{M}_0\,I \\
\text{sr sp} \qquad & \rho_t\,\mathrm{d}_t\,I = \bar{\mathsf{P}}_{\mathsf{t}}^{int} + \bar{\mathsf{Q}}_{\mathsf{t}}^{ext} - \mathsf{M}_{\mathsf{t}}\,I
\end{aligned} \tag{3.6.26}$$

**Remark 3.6.2 (Spatial vs. material motion problem)** *By comparing the spatial motion balance equations (3.6.18) and (3.6.21) with their material motion counterparts (3.6.23) and (3.6.26), we easily obtain the identities*

$$\begin{aligned} \bar{\mathsf{p}}_0^{\text{ext}} + \bar{\mathsf{q}}_0^{\text{ext}} &= \bar{\mathsf{P}}_0^{\text{ext}} + \bar{\mathsf{Q}}_0^{\text{ext}} - \text{Div}\ (\ E_0\ \boldsymbol{V}\ ) \\ \bar{\mathsf{P}}_t^{\text{ext}} + \bar{\mathsf{Q}}_t^{\text{ext}} &= \bar{\mathsf{p}}_t^{\text{ext}} + \bar{\mathsf{q}}_t^{\text{ext}} - \text{div}\ (\ E_t\ \boldsymbol{v}\ ) \end{aligned} \tag{3.6.27}$$

*and*

$$\begin{aligned} \bar{\mathsf{p}}_0^{\text{int}} + \bar{\mathsf{q}}_0^{\text{ext}} &= \bar{\mathsf{P}}_0^{\text{int}} + \bar{\mathsf{Q}}_0^{\text{ext}} - \text{Div}\ (\ I_0\ \boldsymbol{V}\ ) \\ \bar{\mathsf{P}}_t^{\text{int}} + \bar{\mathsf{Q}}_t^{\text{ext}} &= \bar{\mathsf{p}}_t^{\text{int}} + \bar{\mathsf{q}}_t^{\text{ext}} - \text{div}\ (\ I_t\ \boldsymbol{v}\ ) \end{aligned} \tag{3.6.28}$$

*by making use of the mass specific version of Reynold's transport theorem (3.3.14). Remarkably, the differences of the spatial and the material motion quantities* $\text{Div}\ (\ E_0\ \boldsymbol{V}\ )$ *or* $\text{div}\ (\ E_t\ \boldsymbol{v}\ )$ *as well as* $\text{Div}\ (\ I_0\ \boldsymbol{V}\ )$ *or* $\text{div}\ (\ I_t\ \boldsymbol{v}\ )$ *are identical to the volume specific case. According to Gurtin [83], we now introduce the scalar fields* $C_0$ *and* $C_t$ *which are related through the corresponding Jacobians.*

$$C_t = j\ C_0 \qquad C_0 = J\ C_t \tag{3.6.29}$$

*For the time being, the fields* $C_\tau$ *which can be interpreted as configurational energy change are introduced by mere definition while in the following chapter they will be determined explicitly by exploiting the balance of entropy. With the help of the fields* $C_\tau$*, we can set up the following relations between the spatial and material reduced non–mechanical energy fluxes.*

$$\bar{\boldsymbol{q}}_D = \bar{\boldsymbol{q}}_d - C_t\ \boldsymbol{v} \qquad \bar{\boldsymbol{Q}}_d = \bar{\boldsymbol{Q}}_D - C_0\ \boldsymbol{V} \tag{3.6.30}$$

*Remarkably, in the above equation, the energy fluxes* $\bar{\boldsymbol{q}}_\delta$ *and* $\bar{\boldsymbol{Q}}_\delta$ *are related via the configurational energy change* $-C_\tau$ *while the mass fluxes* $\bar{\boldsymbol{m}}_D = \bar{\boldsymbol{m}}_d + \rho_t\,\boldsymbol{v}$ *and* $\bar{\boldsymbol{M}}_d = \bar{\boldsymbol{M}}_D + \rho_0\,\boldsymbol{V}$ *introduced in equation (3.3.10) are related in an identical format via the density* $\rho_\tau$*. With the help of the configurational energy change and the definitions of the external power, the comparisons (3.6.27) can be restated as follows.*

$$\begin{aligned} \text{Div}\ (\ \boldsymbol{v}\cdot\bar{\boldsymbol{\Pi}}_D\ ) + \boldsymbol{v}\cdot\bar{\boldsymbol{b}}_0^{\text{ext}} &= \text{Div}\ (\ \boldsymbol{V}\cdot\bar{\boldsymbol{\Sigma}}_d + [\ C_0 - E_0\ ]\ \boldsymbol{V}\ ) + \boldsymbol{V}\cdot\bar{\boldsymbol{B}}_0^{\text{ext}} \\ \text{div}\ (\ \boldsymbol{V}\cdot\ \bar{\boldsymbol{\pi}}_d\ ) + \boldsymbol{V}\cdot\bar{\boldsymbol{B}}_t^{\text{ext}} &= \text{div}\ (\ \boldsymbol{v}\cdot\bar{\boldsymbol{\sigma}}_D + [\ C_t - E_t\ ]\ \boldsymbol{v}\ ) + \boldsymbol{v}\cdot\bar{\boldsymbol{b}}_t^{\text{ext}} \end{aligned} \tag{3.6.31}$$

*A comparison of the flux terms reveals the following identities in terms of the spatial and the material motion reduced dynamic momentum fluxes* $\bar{\boldsymbol{\Pi}}_D$*,* $\bar{\boldsymbol{\sigma}}_D$*,* $\bar{\boldsymbol{\pi}}_d$ *and* $\bar{\boldsymbol{\Sigma}}_d$*.*

$$\begin{aligned} \boldsymbol{v}\cdot\bar{\boldsymbol{\sigma}}_D^t &= \boldsymbol{v}\cdot[\,[\,E_t - C_t\,]\,\boldsymbol{I} - \boldsymbol{f}^t\cdot\ \bar{\boldsymbol{\pi}}_d^t\ ] \\ \boldsymbol{V}\cdot\bar{\boldsymbol{\Sigma}}_d^t &= \boldsymbol{V}\cdot[\,[\,E_0 - C_0\,]\,\boldsymbol{I} - \boldsymbol{F}^t\cdot\bar{\boldsymbol{\Pi}}_D^t\,] \end{aligned} \tag{3.6.32}$$

*These can be further simplified by making use of the definition of the dynamic momentum fluxes (3.5.44) as* $\bar{\boldsymbol{\pi}}_d = \bar{\boldsymbol{\pi}} - K_t\boldsymbol{F}^t - \boldsymbol{P}_t\otimes\boldsymbol{v}$ *and* $\bar{\boldsymbol{\Sigma}}_d = \bar{\boldsymbol{\Sigma}} - K_0\boldsymbol{I} + \boldsymbol{P}_0\otimes\boldsymbol{V}$ *and the identities* $\bar{\boldsymbol{\sigma}}_D = \bar{\boldsymbol{\sigma}}$ *and* $\bar{\boldsymbol{\Pi}}_D = \bar{\boldsymbol{\Pi}}$*. Consequently, equations (3.6.32) can be rewritten as follows.*

$$\begin{aligned} \boldsymbol{v}\cdot\bar{\boldsymbol{\sigma}}^t &= \boldsymbol{v}\cdot[\,[\,E_t - C_t + K_t\,]\,\boldsymbol{I} - \boldsymbol{f}^t\cdot\bar{\boldsymbol{\pi}}^t - \boldsymbol{p}_t\otimes\boldsymbol{v}\,] \\ \boldsymbol{V}\cdot\bar{\boldsymbol{\Sigma}}^t &= \boldsymbol{V}\cdot[\,[\,E_0 - C_0 + K_0\,]\,\boldsymbol{I} - \boldsymbol{F}^t\cdot\bar{\boldsymbol{\Pi}}^t - \boldsymbol{P}_0\otimes\boldsymbol{V}\,] \end{aligned} \tag{3.6.33}$$

*Taking into account the fact that $E_\tau = K_\tau + I_\tau$ along with the orthogonality conditions*

$$\begin{aligned} \boldsymbol{v} \cdot [\, 2\, K_t\, \boldsymbol{I} - \boldsymbol{p}_t \otimes \boldsymbol{v}\, ] &= 0 \\ \boldsymbol{V} \cdot [\, 2\, K_0\, \boldsymbol{I} - \boldsymbol{P}_0 \otimes \boldsymbol{V}\, ] &= 0 \end{aligned} \tag{3.6.34}$$

*as emphasized by Steinmann [198], we end up with the following tentative relations between the spatial and the material motion reduced static momentum fluxes $\bar{\boldsymbol{\Pi}}$, $\bar{\boldsymbol{\sigma}}$, $\bar{\boldsymbol{\pi}}$ and $\bar{\boldsymbol{\Sigma}}$.*

$$\begin{aligned} \bar{\boldsymbol{\sigma}}^t &= [\, I_t - C_t\, ]\, \boldsymbol{I} - \boldsymbol{f}^t \cdot \bar{\boldsymbol{\pi}}^t \\ \bar{\boldsymbol{\Sigma}}^t &= [\, I_0 - C_0\, ]\, \boldsymbol{I} - \boldsymbol{F}^t \cdot \bar{\boldsymbol{\Pi}}^t \end{aligned} \tag{3.6.35}$$

*A comparison of the related source terms yields the transformation formulae between the spatial and the material motion reduced external forces,*

$$\begin{aligned} \bar{\boldsymbol{b}}_t^{\text{ext}} &= -\, \boldsymbol{f}^t \cdot \bar{\boldsymbol{B}}_t^{\text{ext}} \\ \bar{\boldsymbol{B}}_0^{\text{ext}} &= -\, \boldsymbol{F}^t \cdot \bar{\boldsymbol{b}}_0^{\text{ext}} \end{aligned} \tag{3.6.36}$$

*see also Steinmann [200].*

## 3.7 Balance of entropy

The first law of thermodynamics in the form of the balance of energy expresses the interconvertibility of heat and work. However, the balance of energy itself does not place any restrictions on the direction of the thermodynamical process. The second law of thermodynamics, the balance of entropy, postulates the existence of an absolute temperature and of a specific entropy as a state function. Through the internal production of the latter, which is required to either vanish for reversible processes or to be strictly positive for irreversible processes, a direction is imposed on the thermodynamical process.

### 3.7.1 Volume specific version

#### 3.7.1.1 Spatial motion problem

The balance of entropy balances the volume specific entropy density $S_0 = \rho_0\, S$ with the external entropy input $\mathsf{h}_0^{\text{ext}}$ and the internal entropy production $\mathsf{h}_0^{\text{int}}$. Thereby, the former consists of the entropy flux $\boldsymbol{H}_D$ across the material surface $\partial\mathcal{B}_0$ and the entropy source $\mathcal{H}_0$ in the material domain $\mathcal{B}_0$.

$$\mathsf{h}_0^{\text{ext}} := \text{Div}\,(-\boldsymbol{H}_D) + \mathcal{H}_0 \tag{3.7.1}$$

Recall that we are dealing with open systems for which a fixed material volume $\mathcal{B}_0$ is allowed to constantly gain or lose mass. Open systems naturally exhibit an additional entropy flux and entropy source caused by the added mass as pointed out earlier in the famous monograph by Schrödinger [186] §6

'A living organism can only keep alive by continually drawing from its environment negative entropy. It feeds upon negative entropy to compensate the entropy increase it produces by living.'

as well as by Malvern [147] §5.6 or only recently by Epstein & Maugin [57]. As one consequence, the external entropy flux $\boldsymbol{H}_D$ is introduced as the sum of the reduced external entropy flux $\bar{\boldsymbol{H}}_D$ enhanced by the explicit open system contribution $S\,\boldsymbol{R}$. Accordingly, the external entropy source $\mathcal{H}_0$ consists of the reduced entropy source $\bar{\mathcal{H}}_0$ modified by additional terms $S\,\mathcal{R}_0$ and $-\nabla_X S \cdot \boldsymbol{R}$ accounting for the explicit open system contributions to the entropy supply.

$$\begin{aligned} \mathsf{h}_0^{\text{ext}} &:= \operatorname{Div}\left(-\bar{\boldsymbol{H}}_D + S\,\boldsymbol{R}\right) + \bar{\mathcal{H}}_0 + S\,\mathcal{R}_0 - \nabla_X S \cdot \boldsymbol{R} \\ \mathsf{h}_0^{\text{int}} &\geq 0 \end{aligned} \tag{3.7.2}$$

Just like in classical thermodynamics, the internal entropy production $\mathsf{h}_0^{\text{int}}$ is required to be point–wise non–negative. This condition naturally induces a direction to the thermodynamic process. Consequently, the local version of the balance of entropy of the material motion problem with material reference and material parametrization can be stated in the following form.

---

$$\begin{aligned} \text{mr mp} \qquad & \mathrm{D}_t\, S_0 = \mathsf{h}_0^{ext} + \mathsf{h}_0^{int} \\ \text{sr mp} \qquad & j\,\mathrm{D}_t\, S_0 = \mathsf{h}_t^{ext} + \mathsf{h}_t^{int} \\ \text{mr sp} \qquad & J\,\mathrm{d}_t\, S_t = \mathsf{h}_0^{ext} + \mathsf{h}_0^{int} + \operatorname{Div}\,(\,S_0\,\boldsymbol{V}\,) \\ \text{sr sp} \qquad & \mathrm{d}_t\, S_t = \mathsf{h}_t^{ext} + \mathsf{h}_t^{int} - \operatorname{div}\,(\,S_t\,\boldsymbol{v}\,) \end{aligned} \tag{3.7.3}$$

---

Again, we can derive alternative formats of the above statement by applying the related Piola transforms $S_0 = J\ S_t$, $\mathsf{h}_0^{\text{ext}} = J\,\mathsf{h}_t^{\text{ext}}$, $\mathsf{h}_0^{\text{int}} = J\,\mathsf{h}_t^{\text{int}}$, $\boldsymbol{H}_D = J\,\boldsymbol{h}_D \cdot \boldsymbol{F}^{-t}$ and $\bar{\boldsymbol{H}}_D = J\,\bar{\boldsymbol{h}}_D \cdot \boldsymbol{F}^{-t}$ in combination with the volume specific version of Reynold's transport theorem. By making use of the requirement that the internal entropy production be non–negative as $\mathsf{h}_0^{\text{int}} \geq 0$, the equation $(3.7.3)_1$ can be recast into the inequality $\mathrm{D}_t S_0 - \mathsf{h}_0^{\text{ext}} \geq 0$ which is referred to as 'postulate of irreversibility' in classical thermodynamics, see Truesdell & Toupin [210] §258. Next, we will introduce Neumann boundary conditions for the spatial motion Kirchhoff and Cauchy type entropy flux $\boldsymbol{H}_D$ and $\boldsymbol{h}_D$ in terms of the classical closed system entropy flux contribution $h_\tau^{\text{closed}}$ and the additional open system contribution $h_\tau^{\text{open}}$.

$$\begin{aligned} \boldsymbol{H}_D \cdot \boldsymbol{N} &= h_0^{\text{closed}} + h_0^{\text{open}} \qquad & h_0^{\text{open}} &= \bar{h}_0^{\text{open}} - S\,\boldsymbol{R} \cdot \boldsymbol{N} \\ \boldsymbol{h}_D \cdot \boldsymbol{n} &= h_t^{\text{closed}} + h_t^{\text{open}} \qquad & h_t^{\text{open}} &= \bar{h}_t^{\text{open}} - S\ \boldsymbol{r} \cdot \boldsymbol{n} \end{aligned} \tag{3.7.4}$$

Accordingly, the entropy sources $\mathcal{H}_\tau$ are introduced as the sum of the classical entropy source of the closed system $\mathcal{H}_\tau^{\text{closed}}$ and the additional entropy source accounting for the nature of the open system $\mathcal{H}_\tau^{\text{open}}$.

$$\begin{aligned} \mathcal{H}_0 &= \mathcal{H}_0^{\text{closed}} + \mathcal{H}_0^{\text{open}} \qquad & \mathcal{H}_0^{\text{open}} &= \bar{\mathcal{H}}_0^{\text{open}} + S\,\mathcal{R}_0 - \nabla_X\, S \cdot \boldsymbol{R} \\ \mathcal{H}_t &= \mathcal{H}_t^{\text{closed}} + \mathcal{H}_t^{\text{open}} \qquad & \mathcal{H}_t^{\text{open}} &= \bar{\mathcal{H}}_t^{\text{open}} + S\,\mathcal{R}_t - \nabla_x\, S \cdot \boldsymbol{r} \end{aligned} \tag{3.7.5}$$

### 3.7.1.2 Material motion problem

In complete analogy to the spatial motion problem, we can formally introduce the balance of entropy for the material motion problem balancing the rate of change of the volume specific entropy density $S_t = \rho_t \; S$ with the external entropy input $\mathsf{H}_t^{\text{ext}}$ and the internal entropy production $\mathsf{H}_t^{\text{int}}$. The former can be introduced as the sum of the material motion entropy flux $\boldsymbol{h}_d$ and the material motion entropy source $\mathcal{H}_t$.

$$\mathsf{H}_t^{\text{ext}} := \text{div}\,(-\boldsymbol{h}_d) + \mathcal{H}_t \tag{3.7.6}$$

Again, the contributions $\boldsymbol{h}_d$ and $\mathcal{H}_t$ will be expressed in terms of their reduced counterparts $\bar{\boldsymbol{h}}_d$ and $\bar{\mathcal{H}}_t$ and the explicit open system extra terms $S\,\boldsymbol{r}$, $S\,\mathcal{R}_t$ and $\nabla_x S \cdot \boldsymbol{r}$,

$$\begin{aligned} \mathsf{H}_t^{\text{ext}} &:= \text{div}\,(-\bar{\boldsymbol{h}}_d + S\,\boldsymbol{r}) + \bar{\mathcal{H}}_t + S\,\mathcal{R}_t - \nabla_x S \cdot \boldsymbol{r} \\ \mathsf{H}_t^{\text{int}} &\geq 0 \end{aligned} \tag{3.7.7}$$

giving rise to the material motion entropy balance of the following form.

---

$$\begin{aligned} &\text{mr mp} && \text{D}_t\, S_0 = \mathsf{H}_0^{ext} + \mathsf{H}_0^{int} - \text{Div}\ (\ S_0\ \boldsymbol{V}\ ) \\ &\text{sr mp} && j\,\text{D}_t\, S_0 = \mathsf{H}_t^{ext} + \mathsf{H}_t^{int} + \text{div}\ (\ S_t\ \boldsymbol{v}\ ) \\ &\text{mr sp} && J\ \text{d}_t\ S_t = \mathsf{H}_0^{ext} + \mathsf{H}_0^{int} \\ &\text{sr sp} && \text{d}_t\ S_t = \mathsf{H}_t^{ext} + \mathsf{H}_t^{int} \end{aligned} \tag{3.7.8}$$

---

The related transport theorem and the corresponding Piola transforms with $S_t = j\,S_0$, $\mathsf{H}_t^{\text{ext}} = j\,\mathsf{H}_0^{\text{ext}}$, $\mathsf{H}_t^{\text{int}} = j\,\mathsf{H}_0^{\text{int}}$, $\boldsymbol{h}_d = j\,\boldsymbol{H}_d \cdot \boldsymbol{f}^{-t}$ and $\bar{\boldsymbol{h}}_d = j\,\bar{\boldsymbol{H}}_d \cdot \boldsymbol{f}^{-t}$ can be used to derive the alternative formats of the statement $(3.7.8)_1$. Again, we can formally introduce Neumann boundary conditions for the material motion entropy fluxes $\boldsymbol{h}_d$ and $\boldsymbol{H}_d$

$$\begin{aligned} \boldsymbol{h}_d \cdot \boldsymbol{n} &= H_t^{\text{closed}} + H_t^{\text{open}} \qquad & H_t^{\text{open}} &= \bar{H}_t^{\text{open}} - S\ \boldsymbol{r} \cdot \boldsymbol{n} \\ \boldsymbol{H}_d \cdot \boldsymbol{N} &= H_0^{\text{closed}} + H_0^{\text{open}} \qquad & H_0^{\text{open}} &= \bar{H}_0^{\text{open}} - S\,\boldsymbol{R} \cdot \boldsymbol{N} \end{aligned} \tag{3.7.9}$$

and define the material motion entropy sources $\mathcal{H}_\tau$ in complete analogy to the spatial motion case.

$$\begin{aligned} \mathcal{H}_t &= \mathcal{H}_t^{\text{closed}} + \mathcal{H}_t^{\text{open}} \qquad & \mathcal{H}_t^{\text{open}} &= \bar{\mathcal{H}}_t^{\text{open}} + S\ \mathcal{R}_t - \nabla_x\ S \cdot \boldsymbol{r} \\ \mathcal{H}_0 &= \mathcal{H}_0^{\text{closed}} + \mathcal{H}_0^{\text{open}} \qquad & \mathcal{H}_0^{\text{open}} &= \bar{\mathcal{H}}_0^{\text{open}} + S\,\mathcal{R}_0 - \nabla_X\ S \cdot \boldsymbol{R} \end{aligned} \tag{3.7.10}$$

**Remark 3.7.1 (Spatial vs. material motion problem)** *A comparison of the rate of change of the entropy density based on the spatial and the material motion problem (3.7.3) and (3.7.8) with the help of the volume specific version of Reynold's transport theorem (2.2.10) reveals the following identities.*

$$\begin{aligned} \mathsf{h}_0^{\text{ext}} + \mathsf{h}_0^{\text{int}} &= \mathsf{H}_0^{\text{ext}} + \mathsf{H}_0^{\text{int}} - \text{Div}\ (\ S_0\ \boldsymbol{V}\ ) \\ \mathsf{H}_t^{\text{ext}} + \mathsf{H}_t^{\text{int}} &= \mathsf{h}_t^{\text{ext}} + \mathsf{h}_t^{\text{int}} - \text{div}\ (\ S_t\ \boldsymbol{v}\ ) \end{aligned} \tag{3.7.11}$$

*In addition, we will make use of the natural but crucial assumption that the internal entropy production is independent of the particular type of motion problem considered by postulating that*

$$\mathsf{h}_0^{\text{int}} = \mathsf{H}_0^{\text{int}} \qquad \mathsf{H}_t^{\text{int}} = \mathsf{h}_t^{\text{int}} \tag{3.7.12}$$

*see e.g. Steinmann [200]. It will turn out in the sequel, that this assertion essentially determines the connection between the constitutive relations of the spatial and the material motion problem.*

**Remark 3.7.2 (Alternative derivation of balance of entropy)** *Alternatively, the balance of entropy can be derived from the energy balance rather than being introduced as a mere definition. This approach has been suggested by Green & Naghdi [77,78] who interprete the balance of entropy as a natural consequence of the invariance of working under changes of a thermal motion observer. A similar approach has been followed for the material motion problem only recently by Kalpakides & Dascalu [115].*

### 3.7.2 Mass specific version

#### 3.7.2.1 Spatial motion problem

The mass specific counterpart of the above equations states, that the rate of change of the mass specific entropy $S = S_0 \,/\, \rho_0$ be in equilibrium with the mass specific external entropy input $\bar{\mathsf{h}}_0^{\text{ext}}$ and the mass specific internal entropy production $\bar{\mathsf{h}}_0^{\text{int}}$ which are introduced in the following way.

$$\begin{array}{lcll} \bar{\mathsf{h}}_0^{\text{ext}} & := & \mathsf{h}_0^{\text{ext}} - S\,\mathrm{D}_t\rho_0 + \mathsf{m}_0\,S & = \quad -\mathrm{Div}\,\bar{\boldsymbol{H}}_D + \bar{\mathcal{H}}_0 \\ \bar{\mathsf{h}}_0^{\text{int}} & := & \mathsf{h}_0^{\text{int}} & \geq \quad 0 \end{array} \tag{3.7.13}$$

The resulting mass specific balance of entropy which can be derived by subtracting $S$ times the balance of mass (3.3.13) from the volume specific balance of entropy (3.7.3) can be recast into the related alternative forms by applying the Piola transforms $\bar{\mathsf{h}}_0^{\text{ext}} = J\,\bar{\mathsf{h}}_{\mathsf{t}}^{\text{ext}}$ and $\bar{\mathsf{h}}_0^{\text{int}} = J\,\bar{\mathsf{h}}_{\mathsf{t}}^{\text{int}}$ and the Euler theorem (2.2.9).

$$\begin{array}{ll} \text{mr mp} & \rho_0\,\mathrm{D}_t\,S = \bar{\mathsf{h}}_0^{ext} + \bar{\mathsf{h}}_0^{int} - \mathsf{m}_0\,S \\ \text{sr mp} & \rho_t\,\mathrm{D}_t\,S = \bar{\mathsf{h}}_{\mathsf{t}}^{ext} + \bar{\mathsf{h}}_{\mathsf{t}}^{int} - \mathsf{m}_{\mathsf{t}}\,S \\ \text{mr sp} & \rho_0\,\mathrm{d}_t\,S = \bar{\mathsf{h}}_0^{ext} + \bar{\mathsf{h}}_0^{int} - \mathsf{m}_0\,S + \rho_0\,\boldsymbol{V}\cdot\nabla_X\,S \\ \text{sr sp} & \rho_t\,\mathrm{d}_t\,S = \bar{\mathsf{h}}_{\mathsf{t}}^{ext} + \bar{\mathsf{h}}_{\mathsf{t}}^{int} - \mathsf{m}_{\mathsf{t}}\,S - \rho_t\,\boldsymbol{v}\cdot\nabla_x\,S \end{array} \tag{3.7.14}$$

Moreover, we can relate the reduced entropy fluxes $\bar{\boldsymbol{H}}_D$ and $\bar{\boldsymbol{h}}_D$ defined through $\bar{\boldsymbol{H}}_D = \boldsymbol{H}_D - S\,\boldsymbol{R}$ and $\bar{\boldsymbol{h}}_D = \boldsymbol{h}_D - S\,\boldsymbol{r}$ to the classical entropy flux of the closed system $h_\tau^{\text{closed}}$ and the entropy flux caused by additional effects of the open system $\bar{h}_\tau^{\text{open}}$.

$$\begin{aligned} \bar{\boldsymbol{H}}_D\cdot\boldsymbol{N} &= h_0^{\text{closed}} + \bar{h}_0^{\text{open}} \\ \bar{\boldsymbol{h}}_D\cdot\boldsymbol{n} &= h_t^{\text{closed}} + \bar{h}_t^{\text{open}} \end{aligned} \tag{3.7.15}$$

Accordingly, the reduced entropy sources $\bar{\mathcal{H}}_0 = \mathcal{H}_0 - S\,\mathcal{R}_0 + \nabla_X S \cdot \boldsymbol{R}$ and $\bar{\mathcal{H}}_t = \mathcal{H}_t - S\,\mathcal{R}_t + \nabla_x S \cdot \boldsymbol{r}$ are given as the sum of the classical closed system entropy source $\mathcal{H}_\tau^{\text{closed}}$ and the additional open system contribution to the entropy source $\bar{\mathcal{H}}_\tau^{\text{open}}$.

$$\begin{aligned} \bar{\mathcal{H}}_0 &= \mathcal{H}_0^{\text{closed}} + \bar{\mathcal{H}}_0^{\text{open}} \\ \bar{\mathcal{H}}_t &= \mathcal{H}_t^{\text{closed}} + \bar{\mathcal{H}}_t^{\text{open}} \end{aligned} \tag{3.7.16}$$

#### 3.7.2.2 Material motion problem

For the material motion problem, the rate of change of the mass specific entropy $S = S_t \,/\, \rho_t$ is balanced with the mass specific material motion external entropy input $\bar{\mathsf{H}}_{\mathsf{t}}^{\text{ext}}$ and the internal entropy production $\bar{\mathsf{H}}_{\mathsf{t}}^{\text{int}}$.

$$\begin{aligned} \bar{\mathsf{H}}_{\mathsf{t}}^{\text{ext}} &:= \mathsf{H}_{\mathsf{t}}^{\text{ext}} - S\,\mathrm{d}_t \rho_t + \mathsf{M}_{\mathsf{t}}\, S &&= -\operatorname{div} \bar{\boldsymbol{h}}_d + \bar{\mathcal{H}}_t \\ \bar{\mathsf{H}}_{\mathsf{t}}^{\text{int}} &:= \mathsf{H}_{\mathsf{t}}^{\text{int}} &&\geq 0 \end{aligned} \tag{3.7.17}$$

The mass specific entropy balance of the material motion problem can then be derived by subtracting $S$ times the balance of mass (3.3.13) from the volume specific balance of entropy (3.7.8).

---

$$\begin{aligned} &\text{mr mp} && \rho_0\, \mathrm{D}_t\, S = \bar{\mathsf{H}}_0^{ext} + \bar{\mathsf{H}}_0^{int} - \mathsf{M}_0\, S - \rho_0\, \boldsymbol{V} \cdot \nabla_X\, S \\ &\text{sr mp} && \rho_t\, \mathrm{D}_t\, S = \bar{\mathsf{H}}_{\mathsf{t}}^{ext} + \bar{\mathsf{H}}_{\mathsf{t}}^{ext} - \mathsf{M}_{\mathsf{t}}\, S + \rho_t\, \boldsymbol{v} \cdot \nabla_x\, S \\ &\text{mr sp} && \rho_0\, \mathrm{d}_t\, S = \bar{\mathsf{H}}_0^{ext} + \bar{\mathsf{H}}_0^{int} - \mathsf{M}_0\, S \\ &\text{sr sp} && \rho_t\, \mathrm{d}_t\, S = \bar{\mathsf{H}}_{\mathsf{t}}^{ext} + \bar{\mathsf{H}}_{\mathsf{t}}^{int} - \mathsf{M}_{\mathsf{t}}\, S \end{aligned} \tag{3.7.18}$$

---

Again, we could derive the alternative versions of the equation $(3.7.18)_1$ through the corresponding Piola transforms $\bar{\mathsf{H}}_{\mathsf{t}}^{\text{ext}} = j\,\bar{\mathsf{H}}_0^{\text{ext}}$ and $\bar{\mathsf{H}}_{\mathsf{t}}^{\text{int}} = j\,\bar{\mathsf{H}}_0^{\text{int}}$ and the Euler theorem (2.2.9). In complete analogy to the spatial motion problem, the reduced entropy fluxes $\bar{\boldsymbol{h}}_d = \boldsymbol{h}_d - S\,\boldsymbol{r}$ and $\bar{\boldsymbol{H}}_d = \boldsymbol{H}_d - S\,\boldsymbol{R}$ can be defined through the corresponding Neumann boundary conditions as

$$\begin{aligned} \bar{\boldsymbol{h}}_d \cdot \boldsymbol{n} &= H_t^{\text{closed}} + \bar{H}_t^{\text{open}} \\ \bar{\boldsymbol{H}}_d \cdot \boldsymbol{N} &= H_0^{\text{closed}} + \bar{H}_0^{\text{open}} \end{aligned} \tag{3.7.19}$$

while the reduced entropy sources are given as follows.

$$\begin{aligned} \bar{\mathcal{H}}_t &= \mathcal{H}_t^{\text{closed}} + \bar{\mathcal{H}}_t^{\text{open}} \\ \bar{\mathcal{H}}_0 &= \mathcal{H}_0^{\text{closed}} + \bar{\mathcal{H}}_0^{\text{open}} \end{aligned} \tag{3.7.20}$$

**Remark 3.7.3 (Spatial vs. material motion problem)** *By comparing the spatial and the material motion entropy balance (3.7.14) and (3.7.18) in their mass specific format with the*

*help of the mass specific version of Reynold's transport theorem (3.3.14), we find the following identities which again take a remarkably similar structure as for the volume specific case compare (3.7.11).*

$$\begin{aligned} \bar{\mathsf{h}}_0^{\text{ext}} + \bar{\mathsf{h}}_0^{\text{int}} &= \bar{\mathsf{H}}_0^{\text{ext}} + \bar{\mathsf{H}}_0^{\text{int}} - \text{Div } ( S_0 \boldsymbol{V} ) \\ \bar{\mathsf{H}}_{\mathsf{t}}^{\text{ext}} + \bar{\mathsf{H}}_{\mathsf{t}}^{\text{int}} &= \bar{\mathsf{h}}_{\mathsf{t}}^{\text{ext}} + \bar{\mathsf{h}}_{\mathsf{t}}^{\text{int}} - \text{div } ( S_t \boldsymbol{v} ) \end{aligned} \tag{3.7.21}$$

*With the help of the definitions of the external entropy input of the spatial and the material motion problem* $\mathsf{h}_0^{\text{ext}}$ *in (3.7.2) and* $\mathsf{H}_0^{\text{ext}}$ *in (3.7.7) and the essential assertion that* $\mathsf{h}_0^{\text{int}} = \mathsf{H}_0^{\text{int}}$ *and* $\mathsf{H}_t^{\text{int}} = \mathsf{h}_t^{\text{int}}$ *stated in equation (3.7.12), the above identities yield the fundamental relations between the spatial and the material entropy fluxes.*

$$\bar{\boldsymbol{h}}_D = \bar{\boldsymbol{h}}_d - S_t \boldsymbol{v} \qquad \bar{\boldsymbol{H}}_d = \bar{\boldsymbol{H}}_D - S_0 \boldsymbol{V} \tag{3.7.22}$$

**Remark 3.7.4 (Theory of open systems vs. theory of mixtures)** *At first sight, the theory of open systems might seem to be closely related to the theory of mixtures, as illustrated e.g. by Truesdell & Toupin [210] Bowen [17], Ehlers [54], Wilmanski98 [219], de Boer [15], Kühn & Hauger [136] or Diebels [47]. Indeed, up to the second law of thermodynamics, the balance equations for one single constituent of a mixture are formally almost identical to the balance equations for open systems. Severe differences between the theory of open systems and the theory of mixtures will be introduced upon the formulation of the dissipation inequality which will be carried out in the following chapter.*

In what follows, we shall formulate the dissipation inequality for open systems thermodynamics. Its appropriate evaluation will define basic rules to set up the constitutive equations for the mass fluxes $\boldsymbol{R}$ and $\boldsymbol{r}$, the mass sources $\mathcal{R}_0$ and $\mathcal{R}_t$, the reduced momentum fluxes $\bar{\boldsymbol{\Pi}}^t$ and $\bar{\boldsymbol{\pi}}^t$, the internal forces $\bar{\boldsymbol{b}}_0^{\text{int}}$ and $\bar{\boldsymbol{B}}_t^{\text{int}}$, the entropy $S$ and the heat fluxes $\boldsymbol{Q}$ and $\boldsymbol{q}$.

# 4 Constitutive equations

In some of his more exaltered moments the physicist ascribes to the first and second law of thermodynamics the most far–reaching generality he has ever achieved in formulating laws of nature, while on other grayer mornings he depreciates the insight attainable by thermodynamic analysis, extols the superior virtues of statistical mechanics and kinetic theory, and may even go so far as to maintain that the existence of phenomena like Brownian fluctuations is positively inconsistent with the through of thermodynamics.

P. W. Bridgman,
The nature of thermodynamics, 1941

## 4.1 Dissipation inequality

In the present chapter, we shall illustrate the derivation of thermodynamically consistent constitutive equations for adiabatic closed, for closed and for open systems. To this end, the dissipation inequality will be evaluated individually for the spatial and the material motion problem in sections 4.1.1 and 4.1.2. Next, we present a generic framework for the constitutive equations for both, the spatial and the material motion setting in sections 4.2.1 and 4.2.2. We then specify sets of constitutive equations for adiabatic closed systems in section 4.3, for closed systems in section 4.4 and finally for open systems in section 4.5.

### 4.1.1 Spatial motion problem

We begin with the evaluation of the mass specific balance of entropy

$$\rho_0 \, \mathrm{D}_t S = \bar{\mathsf{h}}_0^{\mathrm{ext}} + \bar{\mathsf{h}}_0^{\mathrm{int}} - \mathsf{m}_0 \, S \tag{4.1.1}$$

as introduced in equation $(3.7.14)_1$ of the previous chapter. For further elaborations, it proves convenient to set up constitutive relations between the reduced entropy flux $\bar{\boldsymbol{H}}_D$ and the reduced non–mechanical energy flux $\bar{\boldsymbol{Q}}_D$ as well as between the reduced entropy source $\bar{\mathcal{H}}_0$ and the reduced non–mechanical energy source $\bar{\mathcal{Q}}_0$ in terms of the absolute temperature $\theta$.

$$\bar{\boldsymbol{H}}_D = \frac{1}{\theta} \, \bar{\boldsymbol{Q}}_D + \boldsymbol{S} \qquad \bar{\mathcal{H}}_0 = \frac{1}{\theta} \, \bar{\mathcal{Q}}_0 + \mathcal{S}_0 \tag{4.1.2}$$

Thereby, the above equations, which are a mere constitutive assumption at this point, can be understood as a generalization of the ideas of Cowin & Hegedus [41]. They have suggested to include the extra entropy source $\mathcal{S}_0$ accounting for changes in entropy caused by changes in mass that are not considered implicitly through the changes in energy $\bar{\mathcal{Q}}_0$. To keep the underlying theory as general as possible, we suggest to additionally include an extra entropy flux $\boldsymbol{S}$ accounting for the in– or outflux of entropy that is not implicitly included in the reduced energy flux term $\bar{\boldsymbol{Q}}_D$, see also Maugin [151] §3.3 and §4.7. Both, the additional entropy flux and source $\boldsymbol{S}$ and $\mathcal{S}_0$, which we shall summarize in the term $\mathsf{s}_0 = -\mathrm{Div}\,\boldsymbol{S} + \mathcal{S}_0$ in the sequel, can be understood as an explicit representation of the exchange of entropy with the outside world. We now turn to the evaluation of the above stated second law of thermodynamics by recasting it into an appropriate form of the dissipation inequality, a statement that places further restrictions on the form of the constitutive response functions. For this purpose, we shall introduce the dissipation rate $\bar{\mathsf{d}}_0$ as the internal entropy production $\bar{\mathsf{h}}_0^{\mathrm{int}}$ weighted by the absolute temperature $\theta$.

$$\bar{\mathsf{d}}_0 := \theta\, \bar{\mathsf{h}}_0^{\mathrm{int}} \geq 0 \tag{4.1.3}$$

With the help of the following transformations based on the combination of equations (4.1.1) and (4.1.3)

$$\begin{aligned}
\bar{\mathsf{d}}_0 &= \mathsf{m}_0\, \theta\, S + \theta\, \rho_0\, \mathrm{D}_t\, S - \theta \bar{\mathsf{h}}_0^{\mathrm{ext}} \\
&= \mathsf{m}_0\, \theta\, S + \theta\, \rho_0\, \mathrm{D}_t\, S - \bar{\mathsf{q}}_0^{\mathrm{ext}} - \mathsf{s}_0\, \theta - \bar{\boldsymbol{Q}}_D \cdot \nabla_X \ln \theta \\
&= \mathsf{m}_0\, \theta\, S + \rho_0\, \mathrm{D}_t\, [\, \theta\, S\,] - \rho_0\, S\, \mathrm{D}_t\, \theta + \bar{\mathsf{p}}_0^{\mathrm{int}} - \mathsf{m}_0\, I - \rho_0\, \mathrm{D}_t\, I - \mathsf{s}_0\, \theta - \bar{\boldsymbol{Q}}_D \cdot \nabla_X \ln \theta
\end{aligned} \tag{4.1.4}$$

and by making use of equations (4.1.2), the dissipation rate can be reformulated yielding the spatial motion version of the Clausius–Duhem inequality in an internal energy based fashion.

$$\bar{\mathsf{d}}_0 = \bar{\mathsf{p}}_0^{\mathrm{int}} - \rho_0\, \mathrm{D}_t\, [\, I - \theta\, S\,] - \mathsf{m}_0\, [\, I - \theta\, S\,] - \rho_0\, S\, \mathrm{D}_t\, \theta - \mathsf{s}_0\, \theta - \bar{\boldsymbol{Q}}_D \cdot \nabla_X \ln \theta \geq 0 \tag{4.1.5}$$

By making use of the appropriate Legendre–Fenchel transform introducing the Helmholtz free energy $\psi = I - \theta\, S$, we finally end up with classical free energy based version of the Clausius–Duhem inequality.

$$\bar{\mathsf{d}}_0 = \bar{\boldsymbol{\Pi}}^t : \mathrm{D}_t \boldsymbol{F} - \boldsymbol{v} \cdot \bar{\boldsymbol{b}}_0^{\mathrm{int}} - \rho_0\, \mathrm{D}_t\, \psi - \mathsf{m}_0\, \psi - \rho_0\, S\, \mathrm{D}_t\, \theta - \mathsf{s}_0\, \theta - \bar{\boldsymbol{Q}}_D \cdot \nabla_X \ln \theta \geq 0 \tag{4.1.6}$$

This formulation is particularly useful when the temperature $\theta$ rather than the entropy $S$ is used as independent variable. Recall that for reasons of notational comparability we have included the internal force contribution $\boldsymbol{v} \cdot \bar{\boldsymbol{b}}_0^{\mathrm{int}} = 0$ and the term reflecting the convective effects of growth $\mathsf{m}_0\, \psi = 0$ keeping in mind that both vanish identically for the spatial motion problem. In classical thermodynamics, the Clausius–Duhem inequality (4.1.6) is typically decomposed into a local and a conductive contribution $\bar{\mathsf{d}}_0^{\mathrm{loc}}$ and $\bar{\mathsf{d}}_0^{\mathrm{con}}$ as $\bar{\mathsf{d}}_0 = \bar{\mathsf{d}}_0^{\mathrm{loc}} + \bar{\mathsf{d}}_0^{\mathrm{con}}$, whereby the conductive part $\bar{\mathsf{d}}_0^{\mathrm{con}} \geq 0$ represents the

classical Fourier inequality while the remaining local term $\bar{\mathsf{d}}_0^{\text{loc}} \geq 0$ is typically referred to as Clausius–Planck inequality.

$$\begin{array}{rcccl} \bar{\mathsf{d}}_0^{\text{loc}} & = & \bar{\boldsymbol{\Pi}}^t : \mathrm{D}_t \boldsymbol{F} - \boldsymbol{v} \cdot \bar{\boldsymbol{b}}_0^{\text{int}} - \rho_0 \mathrm{D}_t \psi - \mathsf{m}_0 \psi - \rho_0 S\, \mathrm{D}_t \theta - \mathsf{s}_0 \theta & \geq & 0 \\ \bar{\mathsf{d}}_0^{\text{con}} & = & -\bar{\boldsymbol{Q}}_D \cdot \nabla_X \ln \theta & \geq & 0 \end{array} \tag{4.1.7}$$

Both are required to hold separately as a sufficient condition for $\bar{\mathsf{d}}_0 \geq 0$.

### 4.1.2 Material motion problem

The analogous evaluation of the the mass specific version of the balance of entropy of the material motion problem is essentially based on equation $(3.7.18)_4$ introduced in the previous chapter.

$$\rho_t \, \mathrm{d}_t S = \bar{\mathsf{H}}_{\mathsf{t}}^{\text{ext}} + \bar{\mathsf{H}}_{\mathsf{t}}^{\text{int}} - \mathsf{M}_{\mathsf{t}} \, S \tag{4.1.8}$$

Subsequently, we shall assume that the reduced material entropy flux $\bar{\boldsymbol{h}}_d$ and the reduced entropy source $\bar{\mathcal{H}}_t$ can be related constitutively to the corresponding energy flux $\bar{\boldsymbol{q}}_d$ and source $\bar{\mathcal{Q}}_t$ through the absolute temperature $\theta$. Generalizing the ideas of Cowin & Hegedus [41], we shall again include the entropy in– or outflux $\boldsymbol{s}$ and the corresponding entropy source $\mathcal{S}_t$ accounting for the explicit entropy exchange with the outside world.

$$\bar{\boldsymbol{h}}_d = \frac{1}{\theta} \, \bar{\boldsymbol{q}}_d + \boldsymbol{s} \qquad \bar{\mathcal{H}}_t = \frac{1}{\theta} \, \bar{\mathcal{Q}}_t + \mathcal{S}_t \tag{4.1.9}$$

This extra external entropy input will be summarized in the term $\mathsf{S}_{\mathsf{t}} = -\mathrm{div}\, \boldsymbol{s} + \mathcal{S}_t$. Next, we can again reinterpret the balance of entropy (4.1.8) by introducing the non–negative dissipation rate $\bar{\mathsf{D}}_{\mathsf{t}}$.

$$\bar{\mathsf{D}}_{\mathsf{t}} := \theta \, \bar{\mathsf{H}}_{\mathsf{t}}^{\text{int}} \geq 0 \tag{4.1.10}$$

By making use of equations (4.1.9), we can transform the dissipation rate

$$\begin{aligned} \bar{\mathsf{D}}_{\mathsf{t}} &= \mathsf{M}_{\mathsf{t}} \, \theta \, S + \theta \, \rho_t \, \mathrm{d}_t \, S - \theta \bar{\mathsf{H}}_{\mathsf{t}}^{\text{ext}} \\ &= \mathsf{M}_{\mathsf{t}} \, \theta \, S + \theta \, \rho_t \, \mathrm{d}_t \, S - \bar{\mathsf{Q}}_{\mathsf{t}}^{\text{ext}} - \mathsf{S}_{\mathsf{t}} \, \theta - \bar{\boldsymbol{q}}_d \cdot \nabla_x \ln \theta \\ &= \mathsf{M}_{\mathsf{t}} \, \theta \, S + \rho_t \, \mathrm{d}_t \, [\, \theta \, S \,] - \rho_t \, S \, \mathrm{d}_t \, \theta + \bar{\mathsf{P}}_{\mathsf{t}}^{\text{int}} - \mathsf{M}_{\mathsf{t}} \, I - \rho_t \, \mathrm{d}_t \, I - \mathsf{S}_{\mathsf{t}} \, \theta - \bar{\boldsymbol{q}}_d \cdot \nabla_x \ln \theta \end{aligned} \tag{4.1.11}$$

into the internal energy based version of the Clausius–Duhem inequality.

$$\bar{\mathsf{D}}_{\mathsf{t}} = \bar{\mathsf{P}}_{\mathsf{t}}^{\text{int}} - \rho_t \, \mathrm{d}_t \, [\, I - \theta \, S \,] - \mathsf{M}_{\mathsf{t}} \, [\, I - \theta \, S \,] - \rho_t \, S \, \mathrm{d}_t \, \theta - \mathsf{S}_{\mathsf{t}} \, \theta - \bar{\boldsymbol{q}}_d \cdot \nabla_x \ln \theta \geq 0 \tag{4.1.12}$$

Finally, the introduction of the corresponding Legendre–Fenchel transform $\psi = I - \theta \, S$ renders the more familiar free energy based version of the Clausius–Duhem inequality,

$$\bar{\mathsf{D}}_{\mathsf{t}} = \bar{\boldsymbol{\pi}}^t : \mathrm{d}_t \boldsymbol{f} - \boldsymbol{V} \cdot \bar{\boldsymbol{B}}_t^{\text{int}} - \rho_t \, \mathrm{d}_t \, \psi - \mathsf{M}_{\mathsf{t}} \, \psi - \rho_t \, S \, \mathrm{d}_t \, \theta - \mathsf{S}_{\mathsf{t}} \, \theta - \bar{\boldsymbol{q}}_d \cdot \nabla_x \ln \theta \geq 0 \tag{4.1.13}$$

which can again be additively decomposed into a local and a conductive contribution $\bar{\mathsf{D}}_{\mathsf{t}}^{\mathrm{loc}}$ and $\bar{\mathsf{D}}_{\mathsf{t}}^{\mathrm{con}}$ as $\bar{\mathsf{D}}_{\mathsf{t}} = \bar{\mathsf{D}}_{\mathsf{t}}^{\mathrm{loc}} + \bar{\mathsf{D}}_{\mathsf{t}}^{\mathrm{con}}$.

$$\begin{aligned} \bar{\mathsf{D}}_{\mathsf{t}}^{\mathrm{loc}} &= \bar{\boldsymbol{\pi}}^{t} : \mathrm{d}_t \boldsymbol{f} - \boldsymbol{V} \cdot \bar{\boldsymbol{B}}_t^{\mathrm{int}} - \rho_t \, \mathrm{d}_t \, \psi - \mathsf{M}_{\mathsf{t}} \, \psi - \rho_t \, S \, \mathrm{d}_t \, \theta - \mathsf{S}_{\mathsf{t}} \, \theta \\ \bar{\mathsf{D}}_{\mathsf{t}}^{\mathrm{con}} &= - \bar{\boldsymbol{q}}_d \cdot \nabla_x \ln \theta \end{aligned} \tag{4.1.14}$$

However, neither the material motion counterpart of the Fourier inequality $\bar{\mathsf{D}}_{\mathsf{t}}^{\mathrm{con}}$, nor of the material motion Clausius–Planck inequality $\bar{\mathsf{D}}_{\mathsf{t}}^{\mathrm{loc}}$ can be required to become non–negative independently, but rather $\bar{\mathsf{D}}_{\mathsf{t}} = \bar{\mathsf{D}}_{\mathsf{t}}^{\mathrm{loc}} + \bar{\mathsf{D}}_{\mathsf{t}}^{\mathrm{con}} \geq 0$.

**Remark 4.1.1 (Spatial vs. material motion problem)** *In the balance of entropy, the influence of the outside world is reflected through the extra entropy fluxes $\boldsymbol{S}$ and $\boldsymbol{s}$ and the extra entropy sources $\mathcal{S}_0$ and $\mathcal{S}_t$ for the spatial and the material motion problem, respectively. While the extra entropy fluxes are related through the appropriate Piola transforms,*

$$\boldsymbol{s} = j \, \boldsymbol{S} \cdot \boldsymbol{f}^{-t} \qquad \boldsymbol{S} = J \, \boldsymbol{s} \cdot \boldsymbol{F}^{-t} \tag{4.1.15}$$

*the transformations between the extra entropy sources*

$$\mathcal{S}_t = j \, \mathcal{S}_0 \qquad \mathcal{S}_0 = J \, \mathcal{S}_t \tag{4.1.16}$$

*and the spatial and material motion extra external entropy input $\mathsf{s}_0$ and $\mathsf{S}_{\mathsf{t}}$*

$$\mathsf{S}_{\mathsf{t}} = \mathsf{s}_{\mathsf{t}} = j \, \mathsf{s}_0 \qquad \mathsf{s}_0 = \mathsf{S}_0 = J \, \mathsf{S}_{\mathsf{t}} \tag{4.1.17}$$

*are given in terms of the corresponding Jacobians. Recall the relation between the spatial and material non–mechanical energy fluxes introduced in (3.6.30) as $\bar{\boldsymbol{q}}_D = \bar{\boldsymbol{q}}_d - C_t \; \boldsymbol{v}$ and $\bar{\boldsymbol{Q}}_d = \bar{\boldsymbol{Q}}_D - C_0 \; \boldsymbol{V}$ as well as the relations between the spatial and material entropy fluxes introduced in (3.7.22) as $\bar{\boldsymbol{h}}_D = \bar{\boldsymbol{h}}_d - S_t \; \boldsymbol{v}$ and $\bar{\boldsymbol{H}}_d = \bar{\boldsymbol{H}}_D - S_0 \; \boldsymbol{V}$. With the help equations (4.1.2) and (4.1.9) relating the corresponding energy and entropy fluxes through the temperature as $\bar{\boldsymbol{H}}_\delta = \bar{\boldsymbol{Q}}_\delta \, / \, \theta + \boldsymbol{S}$ and $\bar{\boldsymbol{h}}_\delta = \bar{\boldsymbol{q}}_\delta \, / \, \theta + \boldsymbol{s}$ and the relations between the extra entropy fluxes $\boldsymbol{S}$ and $\boldsymbol{s}$ as stated in equation (4.1.15), we can easily identify the configurational energy increase $C_\tau$ as the entropy density $S_\tau$ weighted by the absolute temperature $\theta$.*

$$C_t = \theta \, S_t \qquad C_0 = \theta \, S_0 \tag{4.1.18}$$

*This interpretation enables us to formulate the following relations between the external entropy input, the external non–mechanical energy, the external mechanical energy and the internal mechanical energy of the spatial and the material motion problem.*

$$\begin{aligned} \bar{\mathsf{H}}_0^{\mathrm{ext}} &= \bar{\mathsf{h}}_0^{\mathrm{ext}} + \mathrm{Div} \, ( \quad S_0 \quad \boldsymbol{V} \, ) & \bar{\mathsf{h}}_{\mathsf{t}}^{\mathrm{ext}} &= \bar{\mathsf{H}}_{\mathsf{t}}^{\mathrm{ext}} + \mathrm{div} \, ( \quad S_t \quad \boldsymbol{v} \, ) \\ \bar{\mathsf{Q}}_0^{\mathrm{ext}} &= \bar{\mathsf{q}}_0^{\mathrm{ext}} + \mathrm{Div} \, ( \quad \theta \, S_0 \quad \boldsymbol{V} \, ) & \bar{\mathsf{q}}_{\mathsf{t}}^{\mathrm{ext}} &= \bar{\mathsf{Q}}_{\mathsf{t}}^{\mathrm{ext}} + \mathrm{div} \, ( \quad \theta \, S_t \quad \boldsymbol{v} \, ) \\ \bar{\mathsf{P}}_0^{\mathrm{ext}} &= \bar{\mathsf{p}}_0^{\mathrm{ext}} + \mathrm{Div} \, ( \, [ \, K_0 + \psi_0 \, ] \, \boldsymbol{V} \, ) & \bar{\mathsf{p}}_{\mathsf{t}}^{\mathrm{ext}} &= \bar{\mathsf{P}}_{\mathsf{t}}^{\mathrm{ext}} + \mathrm{div} \, ( \, [ \, K_t + \psi_t \, ] \, \boldsymbol{v} \, ) \\ \bar{\mathsf{P}}_0^{\mathrm{int}} &= \bar{\mathsf{p}}_0^{\mathrm{int}} + \mathrm{Div} \, ( \quad \psi_0 \quad \boldsymbol{V} \, ) & \bar{\mathsf{p}}_{\mathsf{t}}^{\mathrm{int}} &= \bar{\mathsf{P}}_{\mathsf{t}}^{\mathrm{int}} + \mathrm{div} \, ( \quad \psi_t \quad \boldsymbol{v} \, ) \end{aligned} \tag{4.1.19}$$

*Moreover, with the relation between the non–mechanical energy fluxes (3.6.30) and the interpretation of the configurational energy increase (4.1.18), we can easily relate the spatial and the material motion version of the conductive dissipation* $\bar{\mathsf{D}}_0^{\mathrm{con}}$ *and* $\bar{\mathsf{d}}_{\mathsf{t}}^{\mathrm{con}}$ *and set up an equivalent relation between the local dissipation terms* $\bar{\mathsf{D}}_0^{\mathrm{loc}}$ *and* $\bar{\mathsf{d}}_{\mathsf{t}}^{\mathrm{loc}}$.

$$\begin{aligned} j\,\bar{\mathsf{D}}_0^{\mathrm{con}} &= \bar{\mathsf{d}}_{\mathsf{t}}^{\mathrm{con}} + S_t\,\nabla_x\theta\cdot\boldsymbol{v} \qquad & j\,\bar{\mathsf{D}}_0^{\mathrm{loc}} &= \bar{\mathsf{d}}_{\mathsf{t}}^{\mathrm{loc}} - S_t\,\nabla_x\theta\cdot\boldsymbol{v} \\ J\,\bar{\mathsf{d}}_{\mathsf{t}}^{\mathrm{con}} &= \bar{\mathsf{D}}_0^{\mathrm{con}} + S_0\,\nabla_X\theta\cdot\boldsymbol{V} \qquad & J\,\bar{\mathsf{d}}_{\mathsf{t}}^{\mathrm{loc}} &= \bar{\mathsf{D}}_0^{\mathrm{loc}} - S_0\,\nabla_X\theta\cdot\boldsymbol{V} \end{aligned} \tag{4.1.20}$$

**Remark 4.1.2 (Extra entropy flux and source)** *Note that at this stage, the identification of the reduced entropy fluxes and sources in terms of the reduced non–mechanical energy fluxes and sources, the absolute temperature and the additional extra terms* $\bar{\boldsymbol{H}}_\delta = \bar{\boldsymbol{Q}}_\delta / \theta + \boldsymbol{S}$, $\bar{\boldsymbol{h}}_\delta = \bar{\boldsymbol{q}}_\delta / \theta + \boldsymbol{s}$ *and* $\bar{\mathcal{H}}_\tau = \bar{\mathcal{Q}}_\tau / \theta + \mathcal{S}_\tau$ *as introduced in equations (4.1.2) and (4.1.9) is a mere constitutive assumption. Nevertheless, for particular constitutive model problems, the postulated relations can be verified through the evaluation of the dissipation inequality according to Liu [142,143] and Müller [161]. In the simplest case, equations (4.1.2) and (4.1.9) are justified with* $\boldsymbol{S} = \boldsymbol{0}$, $\boldsymbol{s} = \boldsymbol{0}$ *and* $\mathcal{S}_\tau = 0$. *However, assuming this result from the outset might be too restrictive for complex constitutive models when diffusive processes other than heat phenomena are included, see Epstein & Maugin [57]. In these cases, it will become necessary to introduce* $\boldsymbol{S}$, $\boldsymbol{s}$ *and* $\mathcal{S}_\tau$ *such, that they at least compensate the possible amount of 'negative entropy' generated by a possible mass flux* $\boldsymbol{R}$ *or* $\boldsymbol{r}$ *and a mass source* $\mathcal{R}_\tau$.

**Remark 4.1.3 (Theory of open systems vs. theory of volumetric growth)** *It is important to note, that the terms* $\boldsymbol{S}$ *and* $\mathcal{S}_0$ *or* $\boldsymbol{s}$ *and* $\mathcal{S}_t$ *introduced in equations (4.1.2) and (4.1.9), respectively, are not included in the theory of volumetric growth by Epstein & Maugin [57], who relate the reduced entropy flux and source to the reduced non–mechanical energy flux and source as*

$$\bar{\boldsymbol{H}}_D = \bar{\boldsymbol{Q}}_D / \theta \qquad \bar{\mathcal{H}}_0 = \hat{\mathcal{Q}}_0 / \theta \tag{4.1.21}$$

*whereby* $\hat{\mathcal{Q}}_0 = \mathcal{Q}_0 - S\,\mathcal{R}$.

**Remark 4.1.4 (Theory of open systems vs. theory of mixtures)** *Note that up to the formulation of the dissipation inequality, the fundamental equations for the open system are formally identical to those of one single constituent within the theory of mixtures. However, in the theory of mixtures, the dissipation inequality is usually stated for the mixture as a whole rather than for each individual constituent. The latter approach, which is indeed a sufficient condition, is thus felt to be too restrictive in most practical applications, see e.g. Bowen [17]. Nevertheless, here, we shall focus on the open system itself rather than aiming at characterizing the other constituents representing the outside world, since in our case, the constituents are not superposed at each spatial point as in the theory of mixtures but are rather spatially separated. In this context, recall the example of rocket propulsion due to combustion which would typically never be modeled within the mixture theory. In the present case, the influence of the outside world is represented through the extra terms* $\mathsf{s}_0$ *and* $\mathsf{S}_{\mathsf{t}}$ *in the spatial and the material motion dissipation inequality (4.1.7) and (4.1.14).*

## 4.2 Generic constitutive equations

We are now in the position to exploit the second law of thermodynamics in the form of the Clausius–Duhem inequality for thermohyperelastic open systems whereby we will essentially follow the approach suggested by Coleman & Noll [32]. The straightforward evaluation of the local part of the dissipation inequalities in the form of the Clausius–Planck inequalities $(4.1.7)_1$ and $(4.1.14)_1$ will result in the definitions of the reduced momentum fluxes $\bar{\boldsymbol{\Pi}}^t$ and $\bar{\boldsymbol{\pi}}^t$ and the mass specific entropy density $S$. Their conductive supplements $(4.1.7)_2$ and $(4.1.14)_2$, the Fourier inequalities, suggest the definition of the reduced non–mechanical energy fluxes $\bar{\boldsymbol{Q}}$ and $\bar{\boldsymbol{q}}$ along the lines of the classical linear theory of heat conduction introduced by Fourier in 1822. Finally, the mass fluxes $\boldsymbol{R}$ and $\boldsymbol{r}$ will be introduced constitutively in the context of classical linear mass diffusion according to Fick's law. Herein, we will thus restrict ourselves to a locally reversible model problem for which all the dissipation is caused exclusively by mass, heat and entropy exchanges with the outside world.

### 4.2.1 Spatial motion problem

For the spatial motion problem, we shall assume, that the volume specific free energy density $\psi_0$ is a linear function of the material density $\rho_0$ and can thus be multiplicatively decomposed in the following way.

$$\psi_0 = \rho_0 \, \psi \tag{4.2.1}$$

Within the thermodynamics of open systems, the material density $\rho_0$ is allowed to vary in space and time. It is thus introduced as a function of the material placement $\boldsymbol{X}$ and the time $t$. Moreover, the mass specific free energy density $\psi$ can be expressed in terms of the material density $\rho_0$, the material motion deformation gradient $\boldsymbol{F}$ and the absolute temperature $\theta$ with a possible explicit dependence on the material placement $\boldsymbol{X}$.

$$\rho_0 = \rho_0(\, \boldsymbol{X}, t \,) \qquad \psi = \psi \,(\, \rho_0, \boldsymbol{F}, \theta; \boldsymbol{X} \,) \tag{4.2.2}$$

Consequently, the material time derivative of the free energy density can be expressed in the following form.

$$\mathrm{D}_t \psi = \mathrm{D}_{\rho_0} \psi \, \mathrm{D}_t \rho_0 + \mathrm{D}_{\boldsymbol{F}} \psi : \mathrm{D}_t \boldsymbol{F} + \mathrm{D}_\theta \psi \, \mathrm{D}_t \theta \tag{4.2.3}$$

The evaluation of the Clausius–Planck inequality $(4.1.7)_1$

$$\begin{aligned} \bar{\mathsf{d}}_0^{\mathrm{loc}} &= [\, \bar{\boldsymbol{\Pi}}^t - \rho_0 \, \mathrm{D}_{\boldsymbol{F}} \psi \,] : \mathrm{D}_t \boldsymbol{F} - \bar{\boldsymbol{b}}_0^{\mathrm{int}} \cdot \boldsymbol{v} \\ &- \mathsf{m}_0 \, \psi - [\, \rho_0 S + \rho_0 \, \mathrm{D}_\theta \psi \,] \, \mathrm{D}_t \, \theta - \rho_0 \mathrm{D}_{\rho_0} \psi \, \mathrm{D}_t \rho_0 - \mathsf{s}_0 \, \theta \geq 0 \end{aligned} \tag{4.2.4}$$

with $\mathsf{m}_0 = 0$ defines the spatial motion momentum flux, i.e. the reduced first Piola–Kirchhoff stress tensor $\bar{\boldsymbol{\Pi}}^t$ and the mass specific entropy $S$

$$\bar{\boldsymbol{\Pi}}^t = \rho_0 \, \mathrm{D}_{\boldsymbol{F}} \psi \qquad S = -\mathrm{D}_\theta \psi \qquad \bar{\boldsymbol{b}}_0^{\mathrm{int}} = \boldsymbol{0} \tag{4.2.5}$$

as thermodynamically conjugate variables to the spatial motion deformation gradient $\boldsymbol{F}$ and the absolute temperature $\theta$. Furthermore, we conclude, that the internal forces $\bar{\boldsymbol{b}}_0^{\text{int}}$ of the spatial motion problem vanish identically. Moreover, we are left with the remaining inequality,

$$\bar{\mathsf{d}}_0^{\text{loc}} = -\rho_0 \, \mathrm{D}_{\rho_0}\psi \, [\, \mathrm{Div}\, \boldsymbol{R} + \mathcal{R}_0 \,] + \theta \, [\, \mathrm{Div}\, \boldsymbol{S} - \mathcal{S}_0 \,] \geq 0 \tag{4.2.6}$$

which places additional restrictions on the constitutive assumptions for the extra external entropy flux $\boldsymbol{S}$ and the extra external entropy source $\mathcal{S}_0$ to ensure that the overall dissipation does not become negative. In addition, the classical Fourier inequality

$$\bar{\mathsf{d}}_0^{\text{con}} = -\bar{\boldsymbol{Q}}_D \cdot \nabla_X \theta \geq 0 \tag{4.2.7}$$

restricts the definition of the non–mechanical energy flux vector $\bar{\boldsymbol{Q}}_D$.

**Remark 4.2.1 (Closed systems)** *For the classical case of adiabatic closed systems, the volume specific free energy density $\psi_0$ can again be multiplicatively decomposed,*

$$\psi_0 = \rho_0 \, \psi \tag{4.2.8}$$

*whereby the material density $\rho_0$ is now no longer allowed to vary in time. The mass specific free energy density $\psi$ can then be expressed in terms of the material motion deformation gradient $\boldsymbol{F}$ and the absolute temperature $\theta$ with a possible explicit dependence on the material placement $\boldsymbol{X}$.*

$$\rho_0 = \rho_0(\, \boldsymbol{X} \,) \qquad \psi = \psi \,(\, \boldsymbol{F}, \theta; \boldsymbol{X} \,) \tag{4.2.9}$$

*With the help of the material time derivative of the free energy,*

$$\mathrm{D}_t \psi_0 = \mathrm{D}_{\boldsymbol{F}} \psi_0 : \mathrm{D}_t \boldsymbol{F} + \mathrm{D}_\theta \psi_0 \, \mathrm{D}_t \theta \tag{4.2.10}$$

*the classical Clausius–Planck inequality for closed systems takes the following familiar format.*

$$\mathsf{d}_0^{\text{loc}} = [\, \boldsymbol{\Pi}^t - \mathrm{D}_{\boldsymbol{F}} \psi_0 \,] : \mathrm{D}_t \boldsymbol{F} - \boldsymbol{b}_0^{\text{int}} \cdot \boldsymbol{v} - [\, S_0 + \mathrm{D}_\theta \psi_0 \,] \, \mathrm{D}_t \theta \geq 0 \tag{4.2.11}$$

*It defines the classical first Piola–Kirchhoff stress $\boldsymbol{\Pi}^t = \bar{\boldsymbol{\Pi}}^t$ and the specific entropy density $S_0$ as thermodynamically conjugate quantities to the spatial motion deformation gradient $\boldsymbol{F}$ and the absolute temperature $\theta$.*

---

$$\boldsymbol{\Pi}^t = \mathrm{D}_{\boldsymbol{F}} \psi_0 \qquad S_0 = -\mathrm{D}_\theta \psi_0 \qquad \boldsymbol{b}_0^{\text{int}} = \boldsymbol{0} \tag{4.2.12}$$

---

*Moreover, we are left with the classical Fourier inequality for adiabatic closed systems,*

$$\mathsf{d}_0^{\text{con}} = -\boldsymbol{Q}_D \cdot \nabla_X \theta \geq 0 \tag{4.2.13}$$

*which places additional restrictions on the choice of the heat flux vector $\boldsymbol{Q}_D = \bar{\boldsymbol{Q}}_D$.*

### 4.2.2 Material motion problem

In a similar way, the volume specific free energy density $\psi_t$ of the material motion problem can be assumed to be representable by the mass specific free energy $\psi$ weighted by the spatial density $\rho_t$.

$$\psi_t = \rho_t \, \psi \tag{4.2.14}$$

Within the material motion context, the spatial density $\rho_t$ is a function of the material motion deformation gradient $\boldsymbol{f}$, the material placement $\boldsymbol{\Phi}$ and the time $t$. The mass specific free energy $\psi$ consequently depends on the material density $\rho_0$, the material motion deformation gradient $\boldsymbol{f}$, the absolute temperature $\theta$ and the material placement $\boldsymbol{\Phi} = \boldsymbol{\Phi}(\boldsymbol{x})$, representing a field in the spatial parametrization.

$$\rho_t = \rho_t( \, \boldsymbol{f}, \boldsymbol{\Phi}; t \, ) \qquad \psi = \psi \, ( \, \rho_0, \boldsymbol{f}, \theta, \boldsymbol{\Phi} \, ) \tag{4.2.15}$$

The spatial time derivative of the free energy $\psi$ thus takes the following form.

$$\mathrm{d}_t \psi = \mathrm{d}_{\rho_0} \psi \, \mathrm{d}_t \rho_0 + \mathrm{d}_f \psi : \mathrm{d}_t \boldsymbol{f} + \mathrm{d}_\theta \psi \, \mathrm{d}_t \theta + \partial_{\boldsymbol{\Phi}} \psi \cdot \mathrm{d}_t \boldsymbol{\Phi} \tag{4.2.16}$$

Recall that $\mathrm{d}_t \boldsymbol{\Phi} = \boldsymbol{V}$ by definition. The evaluation of the dissipation inequality of the material motion problem expressed by equation (4.1.20) as $\bar{\mathsf{d}}_{\mathsf{t}}^{\mathrm{loc}} = \bar{\mathsf{D}}_{\mathsf{t}}^{\mathrm{loc}} - S_t \, \nabla_X \theta \cdot \boldsymbol{V}$

$$\begin{aligned} \bar{\mathsf{d}}_{\mathsf{t}}^{\mathrm{loc}} &= [ \, \bar{\boldsymbol{\pi}}^t - \rho_t \, \mathrm{d}_f \psi \, ] : \mathrm{d}_t \boldsymbol{f} - [ \, \bar{\boldsymbol{B}}_t^{\mathrm{int}} - \rho_t S \, \nabla_X \theta + \rho_t \, \mathrm{d}_{\rho_0} \psi \, \nabla_X \rho_0 + \rho_t \partial_{\boldsymbol{\Phi}} \psi \, ] \cdot \boldsymbol{V} \\ &- \mathsf{M}_{\mathsf{t}} \, \psi - [ \, \rho_t \, S + \rho_t \, \mathrm{d}_\theta \psi \, ] \, \mathrm{d}_t \, \theta - \rho_t \, \mathrm{d}_{\rho_0} \psi \, \mathrm{D}_t \, \rho_0 - \mathsf{S}_{\mathsf{t}} \, \theta \end{aligned} \tag{4.2.17}$$

with $\mathsf{M}_{\mathsf{t}} \, \psi = \psi \, \partial_{\boldsymbol{\Phi}} \rho_t \cdot \boldsymbol{V} + \psi \, \mathrm{d}_f \, \rho_t : \mathrm{d}_t \, \boldsymbol{f}$ renders the definition of the reduced momentum flux $\bar{\boldsymbol{\pi}}^t$, the mass specific entropy $S$ and the reduced internal forces $\bar{\boldsymbol{B}}_t^{\mathrm{int}}$ of the material motion problem,

$$\begin{aligned} \bar{\boldsymbol{\pi}}^t &= \rho_t \, \mathrm{d}_f \psi + \psi \, \mathrm{d}_f \, \rho_t \qquad\qquad S = -\mathrm{d}_\theta \psi \\ \bar{\boldsymbol{B}}_t^{\mathrm{int}} &= \rho_t \, S \, \nabla_X \theta - \rho_t \, \partial_{\boldsymbol{\Phi}} \psi - \rho_t \, \mathrm{d}_{\rho_0} \psi \, \nabla_X \rho_0 - \psi \, \partial_{\boldsymbol{\Phi}} \rho_t \end{aligned} \tag{4.2.18}$$

whereby the latter apparently do not vanish identically for the material motion case. Again, the remaining contribution $-\rho_t \, \mathrm{d}_{\rho_0} \psi \; J \, [ \, \mathrm{div} \, \boldsymbol{r} + \mathcal{R}_t \, ] + \theta \, [ \, \mathrm{div} \, \boldsymbol{s} - \mathcal{S}_t \, ]$ can be used to define constitutive assumptions for the extra external entropy flux and source $\boldsymbol{s}$ and $\mathcal{S}_t$.

**Remark 4.2.2 (Closed systems)** *Similar to the open system case, the volume specific free energy density $\psi_t$ can be represented by the mass specific free energy $\psi$ weighted by the spatial density $\rho_t$.*

$$\psi_t = \rho_t \, \psi \tag{4.2.19}$$

*However, for the case of adiabatic closed systems, the spatial density $\rho_t$ is a function of the material motion deformation gradient $\boldsymbol{f}$ and the material placement $\boldsymbol{\Phi}$ alone. In this case, the*

*free energy $\psi$ depends exclusively on the material motion deformation gradient $\boldsymbol{f}$, the absolute temperature $\theta$ and the material placement $\boldsymbol{\Phi} = \boldsymbol{\Phi}(\boldsymbol{x})$.*

$$\rho_t = \rho_t(\, \boldsymbol{f}, \boldsymbol{\Phi}\,) \qquad \psi = \psi\,(\, \boldsymbol{f}, \theta, \boldsymbol{\Phi}\,) \tag{4.2.20}$$

*The spatial time derivative of the free energy $\psi_t$ can thus be expressed as follows.*

$$\mathrm{d}_t \psi_t = \mathrm{d}_f \psi_t : \mathrm{d}_t \boldsymbol{f} + \mathrm{d}_\theta \psi_t \, \mathrm{d}_t \theta + \partial_{\boldsymbol{\Phi}} \psi_t \cdot \mathrm{d}_t \boldsymbol{\Phi} \tag{4.2.21}$$

*The evaluation of the dissipation inequality for adiabatic closed systems*

$$\bar{\mathrm{d}}_{\mathrm{t}}^{\mathrm{loc}} = [\, \boldsymbol{\pi}^t - \mathrm{d}_f \psi_t \,] : \mathrm{d}_t \boldsymbol{f} - [\, \boldsymbol{B}_t^{\mathrm{int}} - S_t \, \nabla_X \theta + \partial_{\boldsymbol{\Phi}} \psi_t \,] \cdot \boldsymbol{V} - [\, S_t + \mathrm{d}_\theta \psi_t \,] \, \mathrm{d}_t \, \theta \tag{4.2.22}$$

*finally renders the definition of the material motion momentum flux $\boldsymbol{\pi}^t = \bar{\boldsymbol{\pi}}^t$, the specific entropy density $S_t$ and the internal forces $\boldsymbol{B}_t^{\mathrm{int}} = \bar{\boldsymbol{B}}_t^{\mathrm{int}}$ of the material motion problem.*

---

$$\boldsymbol{\pi}^t = \mathrm{d}_f \, \psi_t \qquad S_t = -\mathrm{d}_\theta \, \psi_t \qquad \boldsymbol{B}_t^{\mathrm{int}} = S_t \, \nabla_X \theta - \partial_{\boldsymbol{\Phi}} \psi_t \tag{4.2.23}$$

---

**Remark 4.2.3 (Spatial vs. material quantities)** *The relations between the balance of momentum of the spatial motion problem and the material motion problem have already been sketched in section 3.5. They are characterized by the complete pull back of the balance of physical momentum onto the material manifold. For a specific choice of constitutive relations, e.g. the presented thermohyperelastic material, the transitions between the spatial and the material motion problem can be further specified, compare e.g. Maugin [149], Steinmann [200] or Kuhl & Steinmann [132]. Equation (3.5.3), the spatial motion momentum balance with material reference and material parametrization*

$$\mathrm{D}_t \, \boldsymbol{p}_0 = \mathrm{Div}\,(\, \bar{\boldsymbol{\Pi}}_D^t + \boldsymbol{p} \otimes \boldsymbol{R}\,) + \bar{\boldsymbol{b}}_0 + \mathcal{R}_0 \, \boldsymbol{p} - \nabla_X \boldsymbol{p} \cdot \boldsymbol{R} \tag{4.2.24}$$

*serves as starting point for this derivation. Thereby, we have made use of the definitions $\boldsymbol{\Pi}_D^t = \bar{\boldsymbol{\Pi}}_D^t + \boldsymbol{p} \otimes \boldsymbol{R}$ and $\boldsymbol{b}_0 = \bar{\boldsymbol{b}}_0 + \mathcal{R}_0 \, \boldsymbol{p} - \nabla_X \boldsymbol{p} \cdot \boldsymbol{R}$. The pull back of the momentum rate term, the momentum flux term and the momentum source term yields the following results.*

$$\begin{aligned}
-j \, \boldsymbol{F}^t \cdot \mathrm{D}_t \, \boldsymbol{p}_0 \quad &= \quad \mathrm{d}_t \, [\, -j \, \boldsymbol{F}^t \cdot \boldsymbol{p}_0 \,] + \mathrm{div}\,(\, \rho_t \, \mathrm{d}_f K\,) - \rho_t \, \partial_{\boldsymbol{\Phi}} K \\
-j \, \boldsymbol{F}^t \cdot \mathrm{Div}\, \boldsymbol{\Pi}_D^t \quad &= \quad \mathrm{div}\,(\, -j \, \boldsymbol{F}^t \cdot \bar{\boldsymbol{\Pi}}_D^t \cdot \boldsymbol{F}^t + \boldsymbol{P} \otimes \boldsymbol{r}\,) + j \, \bar{\boldsymbol{\Pi}}^t : \nabla_X \boldsymbol{F} + j \, [\, \boldsymbol{p} \otimes \boldsymbol{R}\,] : \nabla_X \boldsymbol{F} \\
-j \, \boldsymbol{F}^t \cdot \boldsymbol{b}_0 \quad &= \quad -j \, \boldsymbol{F}^t \cdot \bar{\boldsymbol{b}}_0 + \mathcal{R}_t \, \boldsymbol{P} - \nabla_x \boldsymbol{P} \cdot \boldsymbol{r} - j \, [\, \boldsymbol{p} \otimes \boldsymbol{R}\,] : \nabla_X \boldsymbol{F}
\end{aligned} \tag{4.2.25}$$

*Herein, we have applied the transport theorem (2.2.10) and the appropriate Piola transforms. Furthermore, the definition of the dynamic momentum flux $\bar{\boldsymbol{\Pi}}_D^t = \bar{\boldsymbol{\Pi}}^t$ and the kinematic compatibility condition $\nabla_X \boldsymbol{F}^t : \bar{\boldsymbol{\Pi}}^t = \bar{\boldsymbol{\Pi}}^t : \nabla_X \boldsymbol{F}$ have been included. Next, we shall assume the*

*existence of a potential $\psi_0 = \rho_0 \psi$ according to the thermohyperelastic model problem advocated in the present chapter. Consequently, the second term of the pull back of the divergence of the momentum flux can be further specified.*

$$j\,\bar{\boldsymbol{\Pi}}^t : \nabla_X \boldsymbol{F} = \operatorname{div}(\,\rho_t\,\psi \boldsymbol{F}^t\,) - \rho_t\,\mathrm{d}_{\rho_0}\psi\,\nabla_X\rho_0 + \rho_t\,S\,\nabla_X\theta - \rho_t\,\partial_{\boldsymbol{\Phi}}\psi \tag{4.2.26}$$

*By introducing the material motion momentum density $\boldsymbol{P}_t$, the material motion momentum flux $\bar{\boldsymbol{\pi}}^t_d$ and the material motion source $\bar{\boldsymbol{B}}_t$ as*

$$\begin{aligned}
\boldsymbol{P}_t &= -j\,\boldsymbol{F}^t \cdot \boldsymbol{p}_0 \\
\bar{\boldsymbol{\pi}}^t_d &= -j\,\boldsymbol{F}^t \cdot \bar{\boldsymbol{\Pi}}^t_D \cdot \boldsymbol{F}^t + \rho_t \psi\,\boldsymbol{F}^t - \rho_t\,\mathrm{d}_f K \\
\bar{\boldsymbol{B}}_t &= -j\,\boldsymbol{F}^t \cdot \bar{\boldsymbol{b}}_0 - \rho_t\,\mathrm{d}_{\rho_0}\psi\,\nabla_X\rho_0 + \rho_t\,S\,\nabla_X\theta + \rho_t\,\partial_{\boldsymbol{\Phi}}[\,K - \psi\,]
\end{aligned} \tag{4.2.27}$$

*we end up with the balance of momentum of the material motion problem with spatial reference and spatial parametrization (3.5.24),*

$$\mathrm{d}_t\,\boldsymbol{P}_t = \operatorname{div}(\,\bar{\boldsymbol{\pi}}^t_d + \boldsymbol{P} \otimes \boldsymbol{r}\,) + \bar{\boldsymbol{B}}_t + \mathcal{R}_t\,\boldsymbol{P} - \nabla_x \boldsymbol{P} \cdot \boldsymbol{r} \tag{4.2.28}$$

*whereby we have made use of the definitions $\boldsymbol{\pi}^t_d = \bar{\boldsymbol{\pi}}^t_d + \boldsymbol{P} \otimes \boldsymbol{r}$ and $\boldsymbol{B}_t = \bar{\boldsymbol{B}}_t + \mathcal{R}_t\,\boldsymbol{P} - \nabla_x \boldsymbol{P} \cdot \boldsymbol{r}$. Again, due to the specific choice of the source terms, we can observe the remarkable duality of equations (4.2.24) and (4.2.28).*

## 4.3 Adiabatic closed systems

By making use of the general constitutive relations derived in the previous section, we will now specify the constitutive equations for the model problem of a classical compressible Neo–Hooke material characterizing a hyperelastic response of isothermal closed systems.

### 4.3.1 Spatial motion problem

For the isothermal hyperelastic case to be considered in the sequel, the internal potential energy $W_0$ corresponds to the Helmholtz free energy $\psi_0$, such that $W_0 = \psi_0$. For the spatial motion problem, this free energy density $\psi_0(\boldsymbol{F})$ is a function of the deformation gradient $\boldsymbol{F}$ in the classical compressible Neo–Hookean case.

$$\psi_0 = \frac{1}{2}\lambda_0 \ln^2(J) + \frac{1}{2}\mu_0\,[\,\boldsymbol{F} : \boldsymbol{F}^t - n^{\dim} - 2\,\ln(J)\,] \tag{4.3.1}$$

It can essentially be expressed in terms of the spatial motion deformation gradient $\boldsymbol{F}$, its Jacobian $J$ and the corresponding Lamé constants $\lambda_0$ and $\mu_0$, whereby $n^{\dim}$ denotes the number of spatial dimensions. The internal potential energy basically defines the spatial motion momentum fluxes, i.e. the first Piola–Kirchhoff stress tensor $\boldsymbol{\Pi}^t = \mathrm{D}_{\boldsymbol{F}} W_0 = \mathrm{D}_{\boldsymbol{F}} \psi_0$ and the Cauchy stress tensor $\boldsymbol{\sigma}^t = j\,\boldsymbol{\Pi}^t \cdot \boldsymbol{F}^t$ which take the following explicit expressions.

$$\begin{aligned}
\boldsymbol{\Pi}^t &= [\ \lambda_0\ \ln(J)\ -\ \mu_0\ ]\ \boldsymbol{f}^t\ +\ \mu_0\ \boldsymbol{F} \\
\boldsymbol{\sigma}^t &= [\ \lambda_t\ \ln(J)\ -\ \mu_t\ ]\ \boldsymbol{I}\ \ +\ \mu_t\ \boldsymbol{b}
\end{aligned} \tag{4.3.2}$$

Next, we can introduce the following abbreviations

$$\begin{aligned} \mathbf{A} &= \mathrm{D}^2_{\boldsymbol{FF}}\,\psi_0 = \mathrm{D}_{\boldsymbol{F}}\boldsymbol{\Pi}^t & \mathbf{c} &= [\,\boldsymbol{I}\;\overline{\otimes}\,\boldsymbol{F}\,] : \mathbf{A} : [\,\boldsymbol{I}\,\overline{\otimes}\,\boldsymbol{F}^t\,] \\ \mathrm{d}_f\boldsymbol{\sigma}^t &= \boldsymbol{I}\otimes\boldsymbol{\pi}^t - \boldsymbol{I}\underline{\otimes}\boldsymbol{\pi} - \mathbf{g} & \mathbf{g} &= [\,\boldsymbol{f}^t\,\overline{\otimes}\,\boldsymbol{I}\,] : \mathbf{a} : [\,\boldsymbol{I}\,\overline{\otimes}\;\boldsymbol{I}\,] \end{aligned} \tag{4.3.3}$$

for the fourth order tangent operators that will essentially be needed for the linearization to be carried out in section 5.6. Note that the component representation of the non–standard dyadic products $\overline{\otimes}$ and $\underline{\otimes}$ defined in the above equations can be expressed componentwise as $\{\bullet\overline{\otimes}\circ\}_{ijkl} = \{\bullet\}_{ik}\otimes\{\circ\}_{jl}$ and $\{\bullet\underline{\otimes}\circ\}_{ijkl} = \{\bullet\}_{il}\otimes\{\circ\}_{jk}$. The fourth order operator $\mathbf{g}$ is defined in terms of the material motion tangent operator $\mathbf{a}$ to be introduced in the next section. For the classical compressible Neo–Hooke material, the individual tangent operators $\mathbf{A}$, $\mathbf{c}$ and $\mathbf{g}$ take the following format,

$$\begin{aligned} \mathbf{A} &= \lambda_0\,\boldsymbol{f}^t\otimes\boldsymbol{f}^t + \mu_0\;\boldsymbol{I}\;\overline{\otimes}\;\boldsymbol{I} + [\,\mu_0 - \lambda_0\ln(J)\,]\;\boldsymbol{f}^t\,\underline{\otimes}\,\boldsymbol{f} \\ \mathbf{c} &= \lambda_0\;\boldsymbol{I}\otimes\boldsymbol{I} + \mu_0\;\boldsymbol{I}\;\overline{\otimes}\,\boldsymbol{b} + [\,\mu_0 - \lambda_0\ln(J)\,]\;\boldsymbol{I}\,\underline{\otimes}\,\boldsymbol{I} \\ \mathbf{G} &= \lambda_0\;\boldsymbol{I}\otimes\boldsymbol{f}^t + \mu_0\,\boldsymbol{F}^t\,\overline{\otimes}\,\boldsymbol{I} + [\,\mu_0 - \lambda_0\ln(J)\,]\;\boldsymbol{I}\,\underline{\otimes}\,\boldsymbol{f} \end{aligned} \tag{4.3.4}$$

whereby, in particular, $\mathbf{A} = \mathrm{D}^2_{\boldsymbol{FF}}W_0 = \mathrm{D}^2_{\boldsymbol{FF}}\psi_0$ denotes the well–known classical tangent operator of the spatial motion problem.

### 4.3.2 Material motion problem

The internal potential energy $W_t$ of the material motion problem, which corresponds to the Helmholtz free energy $\psi_t$ as $W_t = \psi_t$ for the isothermal hyperelastic case,

$$\psi_t = \frac{1}{2}\lambda_t\ln^2\left(\frac{1}{j}\right) + \frac{1}{2}\mu_t\,[\,\boldsymbol{f}^{-1} : \boldsymbol{f}^{-t} - n^{\dim} - 2\,\ln\left(\frac{1}{j}\right)\,] \tag{4.3.5}$$

is typically parameterized in terms of the material motion deformation gradient $\boldsymbol{f}$ as $\psi_t(\boldsymbol{f})$, whereby $j$ denotes the corresponding Jacobian and $\lambda_t$ and $\mu_t$ are the related Lamé constants. The material motion momentum fluxes $\boldsymbol{\pi}^t = \mathrm{d}_f W_t = \mathrm{d}_f\psi_t$ and $\boldsymbol{\Sigma}^t = J\,\boldsymbol{\pi}^t\cdot\boldsymbol{f}^t$ thus take the following format.

$$\begin{aligned} \boldsymbol{\pi}^t &= [\;\psi_t \;-\; \lambda_t\;\ln(J) \;+\; \mu_t\;]\;\boldsymbol{F}^t \;-\; \mu_t\;\boldsymbol{C}\cdot\boldsymbol{F}^t \\ \boldsymbol{\Sigma}^t &= [\;\psi_0 \;-\; \lambda_0\;\ln(J) \;+\; \mu_0\;]\;\boldsymbol{I} \;-\; \mu_0\;\boldsymbol{C} \end{aligned} \tag{4.3.6}$$

Finally, we can specify the fourth order tangent operators $\mathbf{a}$, $\mathbf{C}$ and $\mathbf{g}$

$$\begin{aligned} \mathbf{a} &= \mathrm{d}^2_{ff}\,\psi_t = \mathrm{d}_f\boldsymbol{\pi}^t & \mathbf{C} &= [\,\boldsymbol{I}\;\overline{\otimes}\,\boldsymbol{f}\,] : \mathbf{a} : [\,\boldsymbol{I}\,\overline{\otimes}\,\boldsymbol{f}^t\,] \\ \mathrm{D}_{\boldsymbol{F}}\boldsymbol{\Sigma}^t &= \boldsymbol{I}\otimes\boldsymbol{\Pi}^t - \boldsymbol{I}\underline{\otimes}\boldsymbol{\Pi} - \mathbf{G} & \mathbf{G} &= [\,\boldsymbol{F}^t\,\overline{\otimes}\,\boldsymbol{I}\,] : \mathbf{A} : [\,\boldsymbol{I}\,\overline{\otimes}\;\boldsymbol{I}\,] \end{aligned} \tag{4.3.7}$$

whereby the fourth order operator $\mathbf{G}$ is defined in terms of the spatial motion tangent operator $\mathbf{A}$ which was introduced in equation (4.3.3) of the previous section. For the particular case of a classical compressible Neo–Hooke material, the individual tangent

operators **a**, **C** and **G** can be expressed as

$$\begin{aligned}
\mathbf{a} &= [\,\psi_t - 2\,\lambda_t \ln(J) + 2\,\mu_t + \lambda_t\,]\,\boldsymbol{F}^t \otimes \boldsymbol{F}^t - [\,\psi_t - \lambda_t \ln(J) + \mu_t\,]\,\boldsymbol{F}^t \underline{\otimes} \boldsymbol{F} \\
&- \mu_t\,[\,\boldsymbol{C}\cdot\boldsymbol{F}^t \underline{\otimes} \boldsymbol{F} + \boldsymbol{F}^t \underline{\otimes} \boldsymbol{F}\cdot\boldsymbol{C} - \boldsymbol{C}\cdot\boldsymbol{F}^t \otimes \boldsymbol{F}^t - \boldsymbol{F}^t \otimes \boldsymbol{C}\cdot\boldsymbol{F}^t + \boldsymbol{C}\overline{\otimes}\boldsymbol{b}\,] \\
\mathbf{C} &= [\,\psi_t - 2\,\lambda_t \ln(J) + 2\,\mu_t + \lambda_t\,]\,\boldsymbol{I} \otimes \boldsymbol{I} - [\,\psi_t - \lambda_t \ln(J) + \mu_t\,]\,\boldsymbol{I} \underline{\otimes} \boldsymbol{I} \\
&- \mu_t\,[\,\boldsymbol{C} \underline{\otimes} \boldsymbol{I} + \boldsymbol{I} \underline{\otimes} \boldsymbol{C} - \boldsymbol{C} \otimes \boldsymbol{I} - \boldsymbol{I} \otimes \boldsymbol{C} + \boldsymbol{C}\overline{\otimes}\boldsymbol{I}\,] \\
\mathbf{g} &= [\,\psi_t - 2\,\lambda_t \ln(J) + 2\,\mu_t + \lambda_t\,]\,\boldsymbol{I} \otimes \boldsymbol{F}^t - [\,\psi_t - \lambda_t \ln(J) + \mu_t\,]\,\boldsymbol{I} \underline{\otimes} \boldsymbol{F} \\
&- \mu_t\,[\,\boldsymbol{b} \underline{\otimes} \boldsymbol{F} + \boldsymbol{I} \underline{\otimes} \boldsymbol{b}\cdot\boldsymbol{F} - \boldsymbol{b} \otimes \boldsymbol{F}^t - \boldsymbol{I} \otimes \boldsymbol{F}^t\cdot\boldsymbol{b} + \boldsymbol{F}\overline{\otimes}\boldsymbol{b}\,]
\end{aligned} \tag{4.3.8}$$

with $\mathbf{a} = \mathrm{d}^2_{ff} W_t = \mathrm{d}^2_{ff} \psi_t$ denoting the tangent operator of the material motion problem.

**Remark 4.3.1 (Spatial vs. material quantities)** *The corresponding internal potential energies $W_0$ and $W_t$, the free energy densities $\psi_0$ and $\psi_t$ and the Lamé constants $\lambda_0$ and $\lambda_t$ as well as $\mu_0$ and $\mu_t$*

$$W_t = j\,W_0 \qquad \psi_t = j\,\psi_0 \qquad \lambda_t = j\,\lambda_0 \qquad \mu_t = j\,\mu_0 \tag{4.3.9}$$

*are related according to the above–stated transformation formulae.*

## 4.4 Closed systems

Next, we turn to the specification of the general constitutive equations of section 4.2 for the thermohyperelastic case. To this end, we introduce the following Helmholtz free energy for thermohyperelastic materials,

$$\begin{aligned}
\psi_0 &= \frac{1}{2}\,\lambda_0\,\ln^2(J) + \frac{1}{2}\,\mu_0\,[\,\boldsymbol{F}:\boldsymbol{F}^t - n^{\dim} - 2\,\ln(J)\,] \\
&- 3\,\alpha\,\kappa_0\,[\,\theta - \theta_0^*\,]\,\frac{\ln(J)}{J} + c_0\,[\,\theta - \theta_0^* - \theta\ln\left(\frac{\theta}{\theta_0^*}\right)\,] - S_0^*\,[\,\theta - \theta_0^*\,]
\end{aligned} \tag{4.4.1}$$

whereby the first two terms represent the classical free energy function of Neo–Hooke type $\psi_0^{\mathrm{neo}}$ characterized through the two Lamé constants $\lambda_0$ and $\mu_0$ according to equation (4.3.1). The third term introduces a thermomechanical coupling in terms of the thermal expansion coefficient $\alpha$ weighting the product of the bulk modulus $\kappa_0$ and the difference between the current temperature $\theta$ and the reference temperature $\theta_0^*$. The fourth term finally accounts for the purely thermal behavior in terms of the specific heat capacity $c_0$ while the last term introduces the material specific absolute entropy $S_0^*$. According to the general constitutive equation (4.2.5), the momentum flux in the form of the first Piola–Kirchhoff stress can be derived as thermodynamically conjugate variable to the spatial motion deformation gradient as $\boldsymbol{\Pi}^t = \mathrm{D}_{\boldsymbol{F}}\psi_0$.

$$\boldsymbol{\Pi}^t = [\lambda_0 \ln(J) - \mu_0]\boldsymbol{F}^{-t} + \mu_0\boldsymbol{F} - \frac{3\,\alpha\,\kappa_0}{J}[\theta - \theta_0^*][1 - \ln(J)]\boldsymbol{F}^{-t} \tag{4.4.2}$$

Again, the first two terms reflect the purely mechanical response corresponding to the classical first Piola–Kirchhoff stress of Neo–Hooke type $\boldsymbol{\Pi}^{\mathrm{neo}t}$ as introduced in equation $(4.3.2)_1$ while the third term accounts for thermally induced stresses. For further

elaborations, it proves convenient to introduce the thermomechanical coupling term $\mathcal{Q}_0^{\text{mech}} = \theta\, \mathrm{D}_\theta \boldsymbol{\Pi}^t : \mathrm{D}_t \boldsymbol{F}$ accounting for the so–called Gough–Joule effect. With the first Piola–Kirchhoff stress tensor given in equation (4.4.2), this thermomechanical coupling term takes the following explicit representation,

$$\mathcal{Q}_0^{\text{mech}} = -\theta\, \frac{3\,\alpha\,\kappa_0}{J}\,[1 - \ln(J)]\,\operatorname{div} \boldsymbol{v} \tag{4.4.3}$$

whereby we have essentially made use of the fact that $\boldsymbol{F}^{-t} : \mathrm{D}_t \boldsymbol{F} = \operatorname{div} \boldsymbol{v}$. Moreover, the evaluation of the Fourier inequality $(4.1.7)_2$ as $\bar{\mathrm{d}}_0^{\text{con}} = -\boldsymbol{Q} \cdot \nabla_X \ln\theta \geq 0$ suggests the definition of the heat flux $\boldsymbol{q}$ or $\boldsymbol{Q}$ according to Fourier's law as

$$\boldsymbol{q} = -K_0\, \boldsymbol{b} \cdot \nabla_x \theta \qquad \boldsymbol{Q} = -k_t\, \boldsymbol{B} \cdot \nabla_X \theta \tag{4.4.4}$$

with $K_0$ and $k_t$ denoting the materially or spatially isotropic heat conduction coefficient, respectively. In order to a priori guarantee the satisfaction of the Fourier inequality $(4.1.7)_2$, the conductivity is required to be non–negative, $K_0 \geq 0$ and $k_t \geq 0$. With the above definitions at hand, the derivatives of the momentum flux $\boldsymbol{\Pi}^t$, the resulting thermomechanical coupling term $\mathcal{Q}_0^{\text{mech}}$ and the mechanically isotropic heat flux $\boldsymbol{Q} = -K_0\, \boldsymbol{G} \cdot \nabla_X \theta$ according to equation $(4.4.4)_1$ with respect to the deformation gradient $\boldsymbol{F}$, the temperature $\theta$ and the temperature gradient $\nabla_X \theta$ which will essentially be needed to compute the global tangential stiffness matrix defined in equation (6.6.3) can be expressed as follows.

$$\begin{aligned}
\mathrm{D}_{\boldsymbol{F}} \quad \boldsymbol{\Pi}^t \quad &= \quad \mu_0\, \boldsymbol{I} \,\overline{\otimes}\, \boldsymbol{I} + \lambda_0 \boldsymbol{F}^{-t} \otimes \boldsymbol{F}^{-t} - [\lambda_0 \ln(J) - \mu_0]\, \boldsymbol{F}^{-t} \underline{\otimes} \boldsymbol{F}^{-1} \\
\mathrm{D}_\theta \quad \boldsymbol{\Pi}^t \quad &= \quad -\frac{3\,\alpha\,\kappa}{J}\,[1 - \ln(J)]\boldsymbol{F}^{-t} \\
\mathrm{D}_{\boldsymbol{F}} \quad \mathcal{Q}_0^{\text{mech}} \quad &= \quad \theta \frac{3\,\alpha\,\kappa}{J^2}\,[\,[3 - 2\ln(J)]\operatorname{div} \boldsymbol{v} - [1 - \ln(J)]\,\mathrm{D}_J(\mathrm{D}_t J)\,]\, J\, \boldsymbol{F}^{-t} \\
\mathrm{D}_\theta \quad \mathcal{Q}_0^{\text{mech}} \quad &= \quad -\frac{3\,\alpha\,\kappa}{J}\,[1 - \ln(J)]\operatorname{div} \boldsymbol{v} \\
\mathrm{D}_{\nabla_X \theta} \boldsymbol{Q} \quad &= \quad -K_0\, \boldsymbol{G}
\end{aligned} \tag{4.4.5}$$

Again, the component representation of the non–standard dyadic products $\overline{\otimes}$ and $\underline{\otimes}$ reads $\{\bullet \overline{\otimes} \circ\}_{ijkl} = \{\bullet\}_{ik} \otimes \{\circ\}_{jl}$ and $\{\bullet \underline{\otimes} \circ\}_{ijkl} = \{\bullet\}_{il} \otimes \{\circ\}_{jk}$. Recall that with the temporal discretization based on the traditional Euler backward method which will be suggested in chapter 6.5, the temperature dependent term $\mathrm{D}_J(\mathrm{D}_t J)$ of equation $(4.4.5)_3$ typically simplifies to $\mathrm{D}_J(\mathrm{D}_t J) = 1/\Delta t$.

**Remark 4.4.1 (Materially vs. spatially isotropic heat flux)** *Observe that in the present contribution, we assume the heat flux to be isotropic in the reference configuration as* $\boldsymbol{Q} = -K_0\, \boldsymbol{G} \cdot \nabla_X \theta$ *or alternatively* $\boldsymbol{q} = -j\, K_0\, \boldsymbol{b} \cdot \nabla_x \theta$. *In the related literature, however, we typically find a spatially isotropic rather than a materially isotropic behavior as* $\boldsymbol{q} = -k_t\, \boldsymbol{g} \cdot \nabla_x \theta$ *which corresponds to an anisotropic behavior in the reference configuration in the context of finite thermoelasticity as* $\boldsymbol{Q} = -J\, k_t\, \boldsymbol{B} \cdot \nabla_X \theta$, *see e.g. Miehe [155,156], Reese & Wriggers [179] or Simo [192].*

**Remark 4.4.2 (Absolute entropy)** *Note that the last term of equation (4.4.1) in terms of the absolute entropy $S_0^*$ is typically not accounted for in classical thermohyperelastic constitutive equations. However, the inclusion of this term will prove essential when calculating the discrete material volume forces in chapter 6, see also Kuhl et al. [127].*

## 4.5 Open systems

Let us finally discuss the specification of appropriate constitutive equations for hyperelasticity of open systems. Thereby, in the first part, we shall particularly focus on biomaterials such as hard or soft tissues in section 4.5.1. In the second part, in section 4.5.2, we then suggest a constitutive formulation for chemomechanical damage. For the sake of transparency, we shall restrict ourselves to the isothermal case for both problem classes.

### 4.5.1 Biomechanics

A typical choice for the free energy function $\psi = \psi_0 / \rho_0$ for cellular materials like open–pored biological tissues is based on the classical Neo–Hooke type Helmholtz free energy function $\psi^{\text{neo}}$ according to equation (4.3.1) weighted by the actual relative density $[\,\rho_0/\rho_0^*\,]^n$, see e.g. Carter & Hayes [25] or Gibson & Ashby [73,74].

$$\psi = \left[\frac{\rho_0}{\rho_0^*}\right]^n \psi^{\text{neo}} \qquad \psi^{\text{neo}} = \frac{1}{\rho_0}\left[\frac{1}{2}\lambda_0\,\ln^2(J) + \frac{1}{2}\mu_0\,[\,\boldsymbol{F}:\boldsymbol{F}^t - n^{\text{dim}} - 2\,\ln(J)\,]\right] \tag{4.5.1}$$

Again, $\lambda_0$ and $\mu_0$ denote the classical Lamé constants and $n$ is an additional exponent usually allowed to vary between $1 \leq n \leq 3.5$. The derivatives of the free energy $\psi$ with respect to the material density $\rho_0$ and the deformation gradient $\boldsymbol{F}$ thus take the following format,

$$\begin{aligned} \mathrm{D}_{\rho_0}\psi &= [n-1]\left[\frac{\rho_0}{\rho_0^*}\right]^{[n-2]}\left[\frac{1}{\rho_0^*}\right]^2\left[\frac{1}{2}\,\lambda_0\,\ln^2(J) + \frac{1}{2}\,\mu_0\,[\,\boldsymbol{F}:\boldsymbol{F}^t - n^{\text{dim}} - 2\,\ln(J)\,]\right] \\ \mathrm{D}_{\boldsymbol{F}}\,\psi &= \left[\frac{\rho_0}{\rho_0^*}\right]^{[n-1]}\left[\frac{1}{\rho_0^*}\right]\;\left[[\lambda_0\,\ln(J) - \mu_0]\,\boldsymbol{F}^{-t} + \mu_0\boldsymbol{F}\right] \end{aligned} \tag{4.5.2}$$

whereby the first derivative can alternatively be expressed as $\mathrm{D}_{\rho_0}\psi = [n-1]\psi/\rho_0$. According to equation (4.2.5), the momentum flux, i.e. the reduced first Piola–Kirchhoff stress tensor

$$\bar{\boldsymbol{\Pi}}^t = \left[\frac{\rho_0}{\rho_0^*}\right]^n \left[[\lambda_0\,\ln(J) - \mu_0]\,\boldsymbol{F}^{-t} + \mu_0\,\boldsymbol{F}\right] \tag{4.5.3}$$

can be understood as the classical Neo–Hookean stress tensor $\boldsymbol{\Pi}^{\text{neo}t}$ introduced in equation (4.3.2)$_1$ weighted by the actual relative density $[\,\rho_0/\rho_0^*\,]^n$. Similar to the context of chemomechanics, the mass flux $\boldsymbol{r}$ or $\boldsymbol{R}$ is usually related to the spatial or material gradient of the density $\nabla_x\rho_0$ or $\nabla_X\rho_0$ as

$$\boldsymbol{r} = R_0\,\boldsymbol{b}\cdot\nabla_x\,\rho_0 \qquad \boldsymbol{R} = r_t\,\boldsymbol{B}\cdot\nabla_X\,\rho_0 \tag{4.5.4}$$

in analogy to Fick's law for concentrations. Herein, $R_0$ and $r_t$ denote the mass conduction coefficient, introducing either a materially or a spatially isotropic response. In the context of biomechanics, we typically find variations of the following constitutive equation for the mass source $\mathcal{R}_0$,

$$\mathcal{R}_0 = \left[\frac{\rho_0}{\rho_0^*}\right]^{-m} \psi_0 - \psi_0^* \tag{4.5.5}$$

whereby $\rho_0^*$ and $\psi_0^*$ denote the reference density and the reference free energy, respectively, while $m$ is an additional exponent that is commonly chosen to $m > n$, see Harrigan & Hamilton [87]. The reduced dissipation inequality (4.2.6)

$$-[n-1]\,\psi\,[\,\mathrm{Div}\,\boldsymbol{R} + \mathcal{R}_0\,] + \theta\,[\,\mathrm{Div}\,\boldsymbol{S} - \mathcal{S}_0\,] \geq 0 \tag{4.5.6}$$

places implicit restrictions on the dissipation generated by the density evolution $\mathrm{D}_t\,\rho_0$ through the mass flux $\boldsymbol{R}$ and the mass source $\mathcal{R}_0$. This possible amount of 'negative entropy' has at least to be compensated by an appropriate constitutive assumption for the extra external entropy input $\mathsf{s}_0$ through the extra entropy flux $\boldsymbol{S}$ and the extra entropy source $\mathcal{S}_0$.

$$\boldsymbol{S} \geq [\,n-1\,]\,\psi\,\frac{1}{\theta}\,\boldsymbol{R} \qquad \mathcal{S}_0 \geq -[\,n-1\,]\,\psi\,\frac{1}{\theta}\,\mathcal{R}_0 \tag{4.5.7}$$

For this particular specification of the constitutive equations, the partial derivatives of the mass source $\mathcal{R}_0$, the materially isotropic mass flux $\boldsymbol{R} = R_0\,\boldsymbol{G}\cdot\nabla_X\,\rho_0$ according to equation $(4.5.4)_1$ and the reduced momentum flux $\bar{\boldsymbol{\Pi}}^t$ with respect to the primary unknowns $\rho_0$, $\nabla_X\rho_0$ and $\boldsymbol{\varphi}$ which will be needed for the linearization carried out in section 7.6 take the following format.

$$\begin{aligned}
&\mathrm{D}_{\rho_0} \quad \mathcal{R}_0 = [n-m]\left[\frac{\rho_0}{\rho_0^*}\right]^{-m}\frac{1}{\rho_0}\,\psi_0\\
&\mathrm{D}_{\boldsymbol{F}} \quad \mathcal{R}_0 = \left[\frac{\rho_0}{\rho_0^*}\right]^{-m}\bar{\boldsymbol{\Pi}}^t\\
&\mathrm{D}_{\nabla_X\rho_0}\boldsymbol{R} = R_0\\
&\mathrm{D}_{\rho_0} \quad \bar{\boldsymbol{\Pi}}^t = n\,\frac{1}{\rho_0}\,\bar{\boldsymbol{\Pi}}^t\\
&\mathrm{D}_{\boldsymbol{F}} \quad \bar{\boldsymbol{\Pi}}^t = \left[\frac{\rho_0}{\rho_0^*}\right]^{n}[\,\mu_0\boldsymbol{I}\overline{\otimes}\boldsymbol{I} + \lambda_0\boldsymbol{F}^{-t}\otimes\boldsymbol{F}^{-t} - [\lambda_0\ln(J)-\mu_0]\,\boldsymbol{F}^{-t}\underline{\otimes}\boldsymbol{F}^{-1}\,]
\end{aligned} \tag{4.5.8}$$

The component representation of the non–standard dyadic products $\overline{\otimes}$ and $\underline{\otimes}$ defined in the above equations is introduced as $\{\bullet\overline{\otimes}\circ\}_{ijkl} = \{\bullet\}_{ik}\otimes\{\circ\}_{jl}$ and $\{\bullet\underline{\otimes}\circ\}_{ijkl} = \{\bullet\}_{il}\otimes\{\circ\}_{jk}$.

**Remark 4.5.1 (Materially vs. spatially isotropic mass flux)** *Observe that in the present contribution, we assume the mass flux to be isotropic in the reference configuration as* $\boldsymbol{R} = R_0\,\boldsymbol{G}\cdot\nabla_X\rho_0$ *or alternatively* $\boldsymbol{r} = j\,R_0\,\boldsymbol{b}\cdot\nabla_x\rho_0$. *Alternatively, one could introduce a spatially isotropic behavior as* $\boldsymbol{r} = r_t\,\boldsymbol{g}\cdot\nabla_x\rho_0$ *which corresponds to an anisotropic behavior in the reference configuration as* $\boldsymbol{R} = J\,r_t\,\boldsymbol{B}\cdot\nabla_X\rho_0$.

**Remark 4.5.2 (Constitutive equations for the mass flux and source)** *Unlike the reduced momentum fluxes $\bar{\boldsymbol{\Pi}}^t$ and $\bar{\boldsymbol{\pi}}^t$ which follow directly from the evaluation of the Clausius–Duhem inequality, the mass flux and source can be defined without any further restrictions. At this stage, the constitutive equations for the mass flux $\boldsymbol{R}$ and the mass source $\mathcal{R}_0$ are introduced by mere reasoning. However, it will turn out later, that the proposed constitutive equations coincide with the conclusions that can be drawn from the analysis of the material force method. Once $\boldsymbol{R}$ and $\mathcal{R}_0$ have been introduced constitutively, however, we have to ensure the satisfaction of the dissipation inequality upon approximate choices for the extra external entropy flux and source $\boldsymbol{S}$ and $\mathcal{S}_0$.*

**Remark 4.5.3 (Mechanics of hard tissues)** *In the context of hard tissue biomechanics, the influence of the mass source $\mathcal{R}_0$ is typically more relevant than the one of the mass flux, such that $\boldsymbol{R} = \boldsymbol{0}$ and $\boldsymbol{r} = \boldsymbol{0}$. In these cases, the driving force of the evolution of mass is typically referred to as 'biological stimulus'. Herein, we have suggested a free–energy based stimulus of the form $[\rho_0/\rho_0^*]^{-m}\psi_0$. Correspondingly, the reference free energy $\psi_0^*$ can be understood as 'attractor stimulus'. However, alternative stress– or strain based stimuli can be introduced as discussed e.g. by Weinans & Prendergast [216]. Even energy–dissipation based stimuli can be found in the recent literature, see e.g. Levenston & Carter [139]. Note that the choice of the exponent $m$ in the constitutive equation for the mass source $\mathcal{R}_0 = [\rho_0/\rho_0^*]^{-m}\psi_0 - \psi_0^*$ essentially determines the stability of the model. With $m = 1$ we obtain the classical model of Beaupré et al. [12]. Nevertheless, Harrigan & Hamilton [86, 87] choose $m > n$ to guarantee uniqueness and stability of the solution.*

**Remark 4.5.4 (Mechanics of soft tissues)** *In contrast to the mechanics of hard tissues, the migration of cells which is essentially accounted for through the mass flux $\boldsymbol{R}$ or $\boldsymbol{r}$ plays a major role in soft tissue mechanics. After injury of soft tissues, for instance in epidermal wound healing, there is no immediate increase in the rate of cell generation and thus no instantaneous change of the mass source, thus $\mathcal{R}_0 = 0$. Rather, right after injury, epidermal migration based on the spreading of existing cells can be observed. This effect is accounted for phenomenologically through the incorporation of a mass flux $\boldsymbol{R}$ or $\boldsymbol{r}$ as defined through equation (4.5.4). A similar constitutive assumption has been introduced by Murray [166] in the context of dermal wound healing, whereby the cell migration $\boldsymbol{R}$ is related to the cell density gradient multiplied by the cell motility coefficient $R_0$ as $\boldsymbol{R} = R_0\, \boldsymbol{G} \cdot \nabla_X \rho_0$.*

### 4.5.2 Chemomechanics

In the previous section, we have presented the constitutive equations for biomechanical problems. Another class of examples of open system thermodynamics is provided by a number of chemomechanical applications. In chemomechanics, the chemical reactant can be considered as an open system which is allowed to constantly gain or lose mass due to moisture transport in combination with chemical reactions. In the present section, we will illustrate how the framework of open system thermodynamics can be applied to chemomechanical damage. Thereby, the fundamental idea is to replace the density $\rho_0$ as primary unknown by the damaged reference density as $\rho_0 = [\,1 - d\,]\,\rho_0^*$ or rather introduce a scalar valued damaged variable $d$ as $d = 1 - \rho_0 \,/\, \rho_0^*$. The Helmholtz

free energy density $\psi_0 = [\,\rho_0 \,/\, \rho_0^*\,]\,\psi_0^{\text{neo}}$ can then be recast into the following familiar format,

$$\psi = [\,1-d\,]\,\psi^{\text{neo}} \qquad \psi^{\text{neo}} = \frac{1}{\rho_0}[\,\frac{1}{2}\lambda_0\,\ln^2(J) + \frac{1}{2}\mu_0\,[\,\boldsymbol{F}:\boldsymbol{F}^t - n^{\dim} - 2\,\ln(J)\,]\,] \quad (4.5.9)$$

whereby, in contrast to the previous example, the exponent $n$ has simply been set equal to one. Again, the momentum flux $\bar{\boldsymbol{\Pi}}^t$ or rather the reduced first Piola–Kirchhoff stress tensor follows from equation (4.2.5) as $\bar{\boldsymbol{\Pi}}^t = \rho_0\,\mathrm{D}_F\psi$.

$$\bar{\boldsymbol{\Pi}}^t = [\,1-d\,]\,[\,[\,\lambda_0\,\ln(J) - \mu_0\,]\,\boldsymbol{F}^{-t} + \mu_0\,\boldsymbol{F}\,] \quad (4.5.10)$$

It can thus be understood as the classical Neo–Hookean stress tensor $\boldsymbol{\Pi}^{\text{neo}t}$ introduced in equation $(4.3.2)_1$ weighted by the current amount of damage $[\,1-d\,]$ as $\bar{\boldsymbol{\Pi}}^t = [\,1-d\,]\,\boldsymbol{\Pi}^{\text{neo}t}$. According to Fick's law, the mass flux $\boldsymbol{r}$ or $\boldsymbol{R}$ is related to the spatial or material gradient of the density $\nabla_x\rho_0$ or $\nabla_X\rho_0$ or rather to the gradient of the damage variable $d$ as $\nabla_x\rho_0 = -\rho_0^*\,\nabla_x d$ or $\nabla_X\rho_0 = -\rho_0^*\,\nabla_X d$.

$$\boldsymbol{r} = R_0\,\boldsymbol{b}\cdot\rho_0 \qquad \boldsymbol{R} = r_t\,\boldsymbol{B}\cdot\rho_0 \quad (4.5.11)$$

Again, $R_0$ and $r_t$ denote the materially and spatially isotropic mass conduction coefficient, respectively. Note that in the case of progressive damage, it might seem reasonable to relate the mass conduction coefficient to the reduced cross section area as $\boldsymbol{r} = R_0\,/\,[\,1-d\,]\,\boldsymbol{b}\cdot\nabla_X\rho_0$ or $\boldsymbol{R} = r_t\,/\,[\,1-d\,]\,\boldsymbol{b}\cdot\nabla_X\rho_0$, respectively. In the case of chemically reacting concrete, the mass flux $\boldsymbol{r}$ or $\boldsymbol{R}$ can be related to the transport of solved cations and anions see e.g. Ulm et al. [211, 212], Torrenti et al. [208], Carmeliet [23] or Kuhl [123] for detailed studies of moisture transport in the context of calcium leaching. Finally, we introduce a mass source $\mathcal{R}_0$ of the following format.

$$\mathcal{R}_0 = -\rho_0^*\,\exp\,[\,-\alpha\,\frac{\psi_0^*}{\psi_0}\,] \quad (4.5.12)$$

In the context of chemomechanical damage of cementitious materials, the dissolution of portlandite or ettringite and the progressive decalcification of calcium silicate hydrates represent typical examples of changes in mass of the cementitious skeleton, see e.g. Coussy [35], Kuhl et al. [124] or Stark & Wicht [195] for detailed overviews. Recall that in the absence of transport phenomena as $\boldsymbol{r} = \boldsymbol{0}$ and $\boldsymbol{R} = \boldsymbol{0}$, the particular choice of $\mathcal{R}_0$ of equation (4.5.12) can be interpreted as an exponential damage evolution law as $\mathrm{D}_t\,d = \exp\,[\,-\alpha\,\psi_0^*\,/\,\psi_0\,]$. Finally, we shall a priori exclude the possibility of stiffness recovery by assuming a vanishing extra entropy supply $\mathsf{s}_0 = 0$ such that the extra entropy flux and source vanish identically.

$$\boldsymbol{S} = \boldsymbol{0} \qquad \mathcal{S}_0 = 0 \quad (4.5.13)$$

For this particular choice of constitutive equations, the partial derivatives of the mass source $\mathcal{R}_0$, the materially isotropic mass flux $\boldsymbol{R}$ and the reduced momentum flux $\bar{\boldsymbol{\Pi}}^t$ with respect to the primary unknowns $\rho_0$ and $\boldsymbol{\varphi}$ which will essentially be needed for

the linearization carried out in section 7.6 can be expressed in the following form.

$$\begin{aligned}
\mathrm{D}_{\rho_0} \quad \mathcal{R}_0 &= \frac{1}{[\,1-d\,]}\,\frac{\psi_0^*}{\psi_0}\;\alpha\,\mathcal{R}_0 \\
\mathrm{D}_{\boldsymbol{F}} \quad \mathcal{R}_0 &= \frac{1}{\psi_0}\,\frac{\psi_0^*}{\psi_0}\;\alpha\,\mathcal{R}_0\;\bar{\boldsymbol{\Pi}}^t \\
\mathrm{D}_{\nabla_X \rho_0}\boldsymbol{R} &= R_0 \\
\mathrm{D}_{\rho_0} \quad \bar{\boldsymbol{\Pi}}^t &= \frac{1}{[\,1-d\,]}\,\frac{1}{\rho_0^*}\;\bar{\boldsymbol{\Pi}}^t \\
\mathrm{D}_{\boldsymbol{F}} \quad \bar{\boldsymbol{\Pi}}^t &= [\,1-d\,]\;[\,\mu_0 \boldsymbol{I}\overline{\otimes}\boldsymbol{I} + \lambda_0 \boldsymbol{F}^{-t}\otimes\boldsymbol{F}^{-t} - [\lambda_0 \ln(J) - \mu_0]\,\boldsymbol{F}^{-t}\underline{\otimes}\boldsymbol{F}^{-1}\,]
\end{aligned} \tag{4.5.14}$$

Note the striking similarity of the resulting set of equations for open system thermodynamics compared to the equations for hygromechanical unsaturated porous media as presented by Carmeliet [23].

**Remark 4.5.5 (Biomechanics vs. chemomechanics)** *Although the proposed chemomechanical damage formulation seems closely related to biomechanics of growth and adaption, there are several severe differences between both formulations. While the biomechanical formulation introduces the reference density $\rho_0 = [\,1-d\,]\,\rho_0^*$ as primary unknown, chemomechanical damage is typically formulated in terms of the damage variable $d = 1 - \rho_0 \,/\, \rho_0^*$. In the biomechanical context, stiffness degradation is caused by an 'underloading' of the structure in response to which the reference density $\rho_0$ decreases as $0 \leq \rho_0 \leq \rho_0^*$. In chemomechanical damage, on the contrary, stiffness degradation takes place in response to 'overloading' such that the damage increases as $0 \leq d < 1$. A remarkable difference between both models can be observed in the opposite case. In the biomechanical model, 'overloading' classically causes a local stiffening, e.g. through functional adaption, growth or self–healing. If the biological structure is unable to carry the applied load, it responds with an increase in density as $\rho_0^* \leq \rho_0 \leq \infty$ through the deposition of additional biomaterial. Since this newly added biological ground substance is typically generated from other species, an external entropy supply has to be taken into account which manifests itself in the extra entropy flux $\boldsymbol{S}_0 \geq \boldsymbol{0}$ and the extra entropy source $\mathcal{S}_0 \geq 0$. In damage mechanics, stiffness recovery is a priori excluded, i.e. the decrease in damage is impossible as $\mathrm{D}_t\, d \geq 0$. The exclusion of stiffness recovery follows in a straightforward way from the dissipation inequality, since, in the case of chemomechanical damage, the external entropy supply has to vanish identically as $\boldsymbol{S}_0 = \boldsymbol{0}$ and $\mathcal{S}_0 = 0$.*

# 5 Adiabatic closed systems

To treat each thought as a realization is to trifle with your spirit.

Mumon's cautions,
The Mumon Koan, 13th century

## 5.1 Introduction

The deformation of a body is essentially characterized through the balance of linear momentum. Typically, this balance of momentum is formulated in terms of the spatial deformation map mapping the material placements of particles in the material configuration to their spatial placements in the spatial configuration. Alternatively, we could formulate the balance of momentum in terms of the material motion map, see Shield [189], Maugin [149, 150], Gurtin [82, 83], Kienzler & Herrmann [119], Steinmann [198–200] or Kuhl & Steinmann [132]. Being the inverse of the spatial motion map, the material motion map characterizes the mapping of particles from the spatial configuration to their material motion counterparts. While the former approach relates to the equilibration of the classical spatial forces in the sense of Newton, the latter lends itself to the equilibration of material forces in the sense of Eshelby. Thereby, spatial forces typically perform work over positional changes relative to their ambient space, whereas material forces perform work over positional changes relative to the ambient material. In the continuous case, the statement of spatial force equilibrium and material forces equilibrium are completely equivalent for homogeneous problems, i.e. they can be related to one another via a complete pull back onto the material manifold.
The finite element discretization renders the discrete residual statement of the balance of momentum. In the classical sense, the solution of the finite element method corresponds to the vanishing residual of the spatial force balance. It is typically parameterized in terms of the discrete spatial motion map or rather in terms of the discrete spatial placements of the node point positions. Within the finite element context, this solution is related to the minimum of the potential energy. This minimum, however, is only a minimum with respect to fixed material placements.
The discrete solution of the spatial motion problem does not necessarily have to coincide with the discrete solution of the material motion problem, i.e. a vanishing residual of discrete spatial forces does not necessarily imply that the discrete material forces vanish equivalently, see Braun [20], Müller & Maugin [158], Askes et al. [6], Kuhl et al. [125], Thoutireddy & Ortiz [207] and Thoutireddy [206]. Non–vanishing discrete material forces indicate that the underlying discretization is not yet optimal. An additional release of energy can take place when finite element nodes are moved in the

direction opposite to the resulting discrete material node point forces. In this respect, the proposed strategy can be interpreted as a particular version of an Arbitrary Lagrangian Eulerian formulation. It has long been recognized that purely Lagrangian and Eulerian descriptions of the continuum behavior have their limitations in case numerical solution strategies are taken. For instance, in Lagrangian finite element meshes the nodes are attached one–to–one to the material particles. Therefore, excessive deformation of the material invariably leads to excessive deformation of the mesh, which may result in element entanglement and singularities in the isoparametric mapping of the elements. On the other hand, Eulerian grids are attached one–to–one to space, so that a large boundary motion of the material cannot be accounted for accurately. Furthermore, a difficulty arises when fluid–structure–interaction is considered. When the fluid is described by a Eulerian method and the structure by a Lagrangian method, an ambiguity pertains for the interface zone.
To combine the advantages and to avoid the limitations of either approach, Arbitrary Lagrangian Eulerian approaches have been proposed in the literature, see e.g. the early approaches by Belytschko & Kennedy [13], Donéa et al. [48–51], Hughes et al. [103] or Liu [144] or the more recent work of Huerta & Casadei [100], Belytschko et al. [14], Wall [213], Braess & Wriggers [19], Rodriguez-Ferran et al. [183], Donéa & Huerta [52] and Kuhl et al. [128]. For more sophisticated applications in the context of mesh adaptivity, we refer to the recent works of Yadama & Kikuchi [224], Askes et al. [5–9], Armero & Love [3] and Kuhl et al. [125, 126], whereby the latter focusses on a related convexity analysis. As is implied by this denotation, an ALE approach is neither purely Lagrangian, i.e. nodes of a grid are not attached to the material, nor is it purely Eulerian, i.e. nodes of a grid are not fixed in space. In contrast, nodes are free to move in space independently of the material. Whereas the motion of the material is set by the applicable equations of mechanics, the motion of the nodes has to be prescribed by the user. As such, the motion of the nodes has become an additional unknown. In contrast to the existing ALE formulations, the selection of the mesh is no longer user–defined in the ALE formulation suggested in the sequel. Rather, the optimal mesh follows straightforwardly from a variational principle. Unlike classical ALE formulations, the formulation derived herein is thus inherently symmetric. In this contribution, we suggest to solve the spatial and the material motion problem simultaneously. We thus introduce both, the spatial and the material motion map as primary unknowns. The solution renders the spatial and the corresponding material configuration that are optimal in the sense of potential energy. In this sense, optimal meshes are defined through vanishing discrete material node point forces.
The present work is motivated by a one–dimensional model problem introduced in section 5.2. We then illustrate an alternative derivation of the governing equations within a variational framework based on the ALE Dirichlet principle in section 5.3 and introduce the corresponding weak forms in section 5.4. Section 5.5 finally treats the corresponding spatial discretization parameterized in terms of the material and the spatial reference mapping. The consistent linearization which is essentially needed for the solution within an incremental iterative Newton–Raphson solution strategy is carried out in section 5.6. Related algorithmic aspects are pointed out in section 5.7 before we finally discuss a number of illustrative examples in sections 5.8 and 5.9.

## 5.2 Motivation

Let us motivate our work by considering a simple one–dimensional bar, clamped on both sides and loaded by a constant line load $b = \text{const}$. The resulting displacement field can be determined analytically through the classical Dirichlet principle as the minimum of the potential energy $\mathcal{I}(\varphi)$. Hereby, the potential energy can be understood as the total potential energy density $U$ integrated over the entire bar length as $\mathcal{I} = \int_{\mathcal{B}} U \; dV$ whereby $U = W + V$ typically consists of an internal contribution, e.g. characterized through the free energy function of Neo–Hookean type $W = \frac{1}{4} E \left[ F^2 - 1 - 2 \ln(F) \right]$, and an external contribution, e.g. $V = -b\,\varphi$ for the particular example considered herein. The potential energy is thus a function of the spatial placement $\varphi$, its gradient $F = \nabla_X \varphi$, Young's modulus $E$ and of the amount of loading $b$. Its minimum is characterized through its vanishing variation with respect to the independent variables, in this case, the spatial placement $\varphi$.

$$\mathcal{I}(\varphi) = \int_{\mathcal{B}} U \; dV \rightarrow \inf_{\varphi} \qquad \delta\mathcal{I}(\varphi) = \int_{\mathcal{B}} \delta U \; dV \doteq 0 \tag{5.2.1}$$

The above equations define the spatial placement $\varphi$ or rather the deformation $u$ as the difference between the material placement $X$ and spatial placement $\varphi$, thus $u = \varphi - X$. The analytical solution for $b = 10$ and $b = 100$ for $EA = 1$ is indicated through the curves in figures 5.1, left, and 5.1, right, respectively. Note that due to the influence of the non–linearity, the maximum value for the displacement is not obtained right in the middle of the bar, but rather on its lefthand side. This non–symmetry, which is inherently introduced through the tension compression unsymmetry of the Neo–Hookean strain energy function, is of course more pronounced if the amount of loading increases. Recall that typically, the analytical solution is not easily computable such that a numerical approximation has to be carried out instead. In the simplest case, we could discretize the clamped bar with two linear finite elements as illustrated in figures 5.1, top. We thus introduce one single degree of freedom for the midpoint node which is located right in the middle of the bar at $X = 0.5\,L$. The discrete potential energy $\mathcal{I}(\varphi^h)$ can then be expressed as follows.

$$\mathcal{I}(\varphi^h) = X\,U_1^h + [\,L - X\,]\,U_2^h \rightarrow \inf_{\varphi^h} \tag{5.2.2}$$

The lines in figures 5.1 illustrate the corresponding discrete solution for the displacement $u^h = \varphi^h - X$ of this classical Lagrangian analysis with $b = 10$ and $b = 100$. The area between the curves of the analytical solution and the lines of the discrete solution represents a measure for the discretization error. A significant reduction of this area, and thus an improved approximation to the solution, can obviously be obtained by shifting the midnode to the left. Strictly speaking, we introduce the node point position or rather the material placement $\Phi^h$ as an additional nodal degree of freedom next to the spatial placement $\varphi^h$. The corresponding discrete potential energy $\mathcal{I}(\varphi^h, \Phi^h)$ can then be expressed in the following form.

$$\mathcal{I}(\Phi^h, \varphi^h) = \Phi^h\,U_1^h + [\,L - \Phi^h\,]U_2^h \rightarrow \inf_{\Phi^h, \varphi^h} \tag{5.2.3}$$

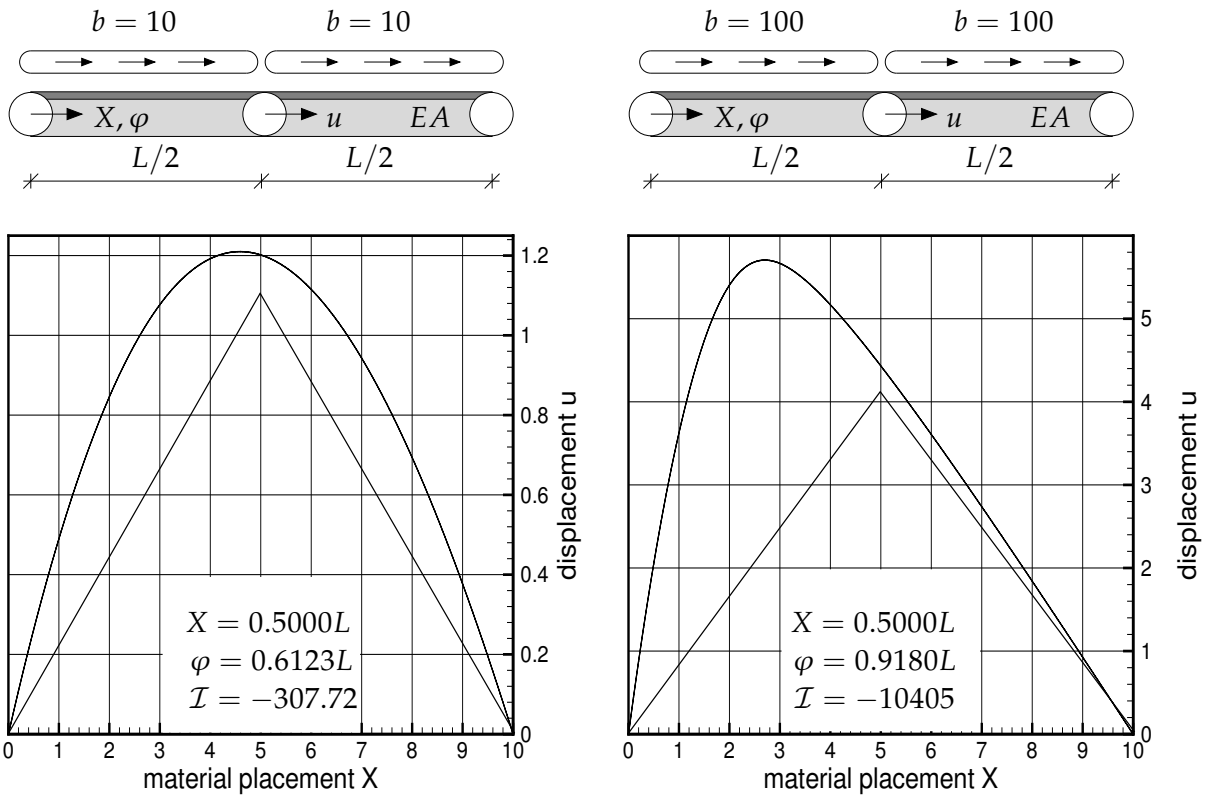


**Figure 5.1:** One-dimensional model problem - Continuous vs. discrete Lagrangian solution

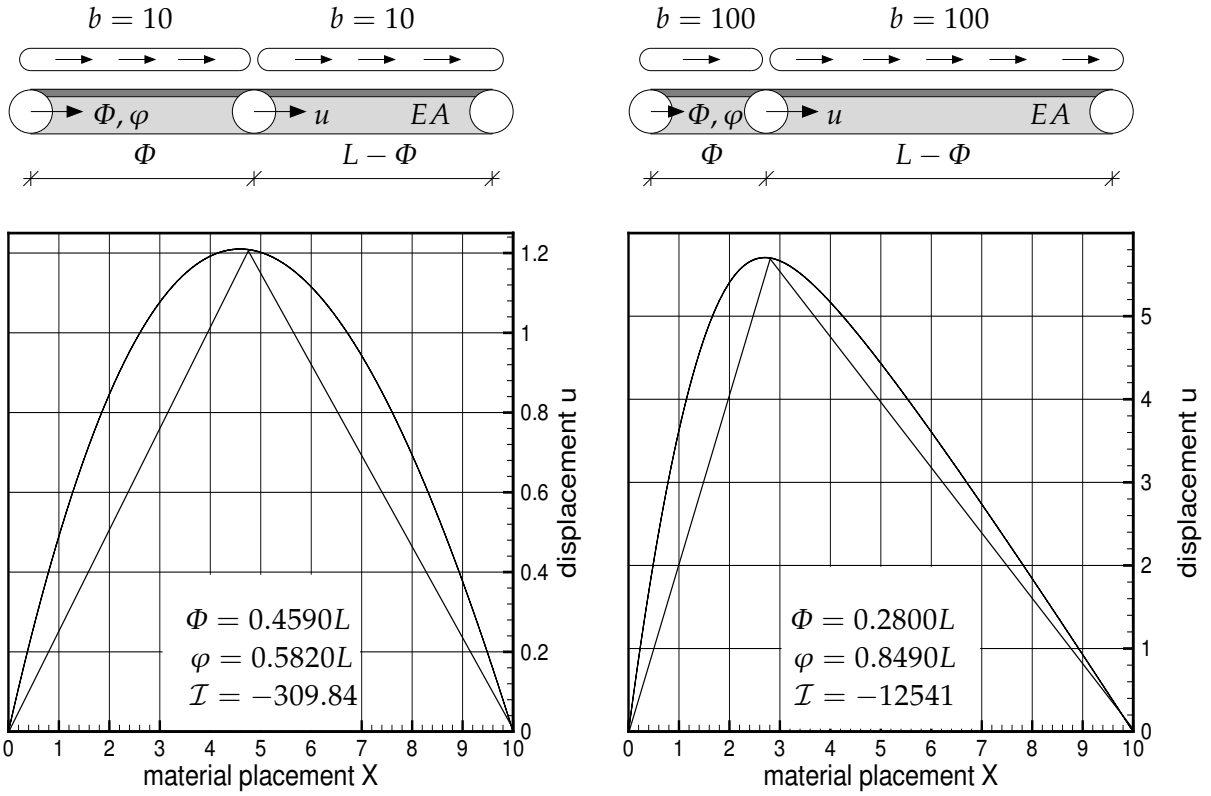


**Figure 5.2:** One-dimensional model problem - Continuous vs. discrete ALE solution

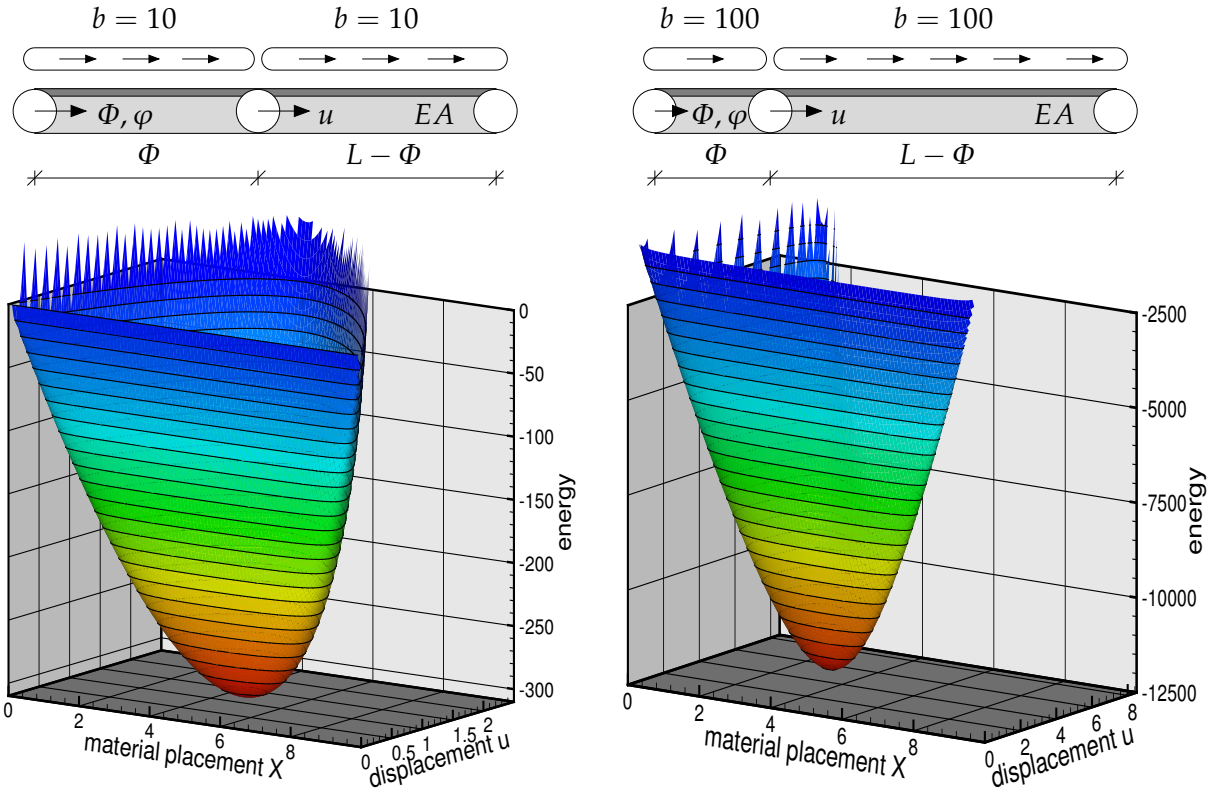


**Figure 5.3:** One-dimensional model problem - Potential energy $\mathcal{I}$

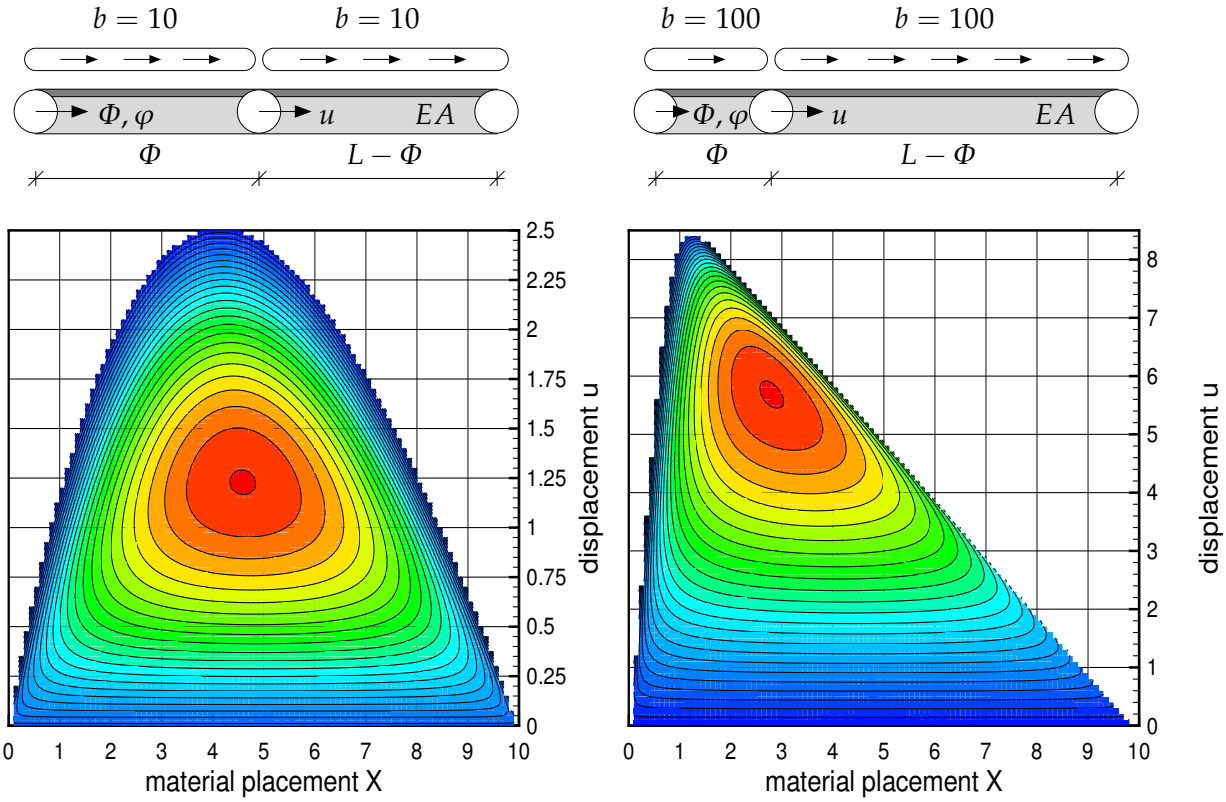


**Figure 5.4:** One-dimensional model problem - Isolines of potential energy $\mathcal{I}$

Figures 5.2, shows the discrete solution for the material placement $\Phi^h$ and the displacement $u^h = \varphi^h - \Phi^h$ for this so–called Arbitrary Lagrangian Eulerian analysis. The optimal node point positions are found at $\Phi = 0.4590L$ for a constant line load of $b = 10$ and at $\Phi = 0.2800L$ for a line load of $b = 100$, respectively. Again, the influence of the non–symmetry of the Neo–Hookean strain energy function becomes more pronounced for the case of higher loading. In particular, the potential energy of $\mathcal{I} = -12541$ for the load case of $b = 100$ indicates, that the potential energy $\mathcal{I} = -10405$ of the classical Lagrangian analysis has been reduced by more than 20 % through the relaxation of the node point position.
Figures 5.3 and 5.4, which show the potential energy $\mathcal{I}$ as a function of the material placements $X$ and the displacements $u$ support these observations. For the classical Lagrangian analysis, we look for the minimum of the potential energy at a fixed material position $X = 0.5$. It is obvious, that the potential energy can be reduced considerably upon relaxation of this node point position, as can be concluded also from the isolines given in figures 5.4. By introducing both, the spatial and the material placement as primary unknowns, we look for the absolute minimum of the potential energy, which takes the form of a parabola as illustrated in figures 5.3. In what follows, we will present a general theoretical and numerical strategy which allows to determine not only the spatial but also the material placements within a consistent variational framework.

## 5.3 Governing equations

Within the present section, we will present an alternative variational derivation of the spatial and the material version of the balance of momentum. The results will, of course, be identical to the ones derived earlier in section 3.5, compare equations (3.5.11) or (3.5.50) for the spatial and equations (3.5.32) or (3.5.59) for the material motion problem. In what follows, we shall restrict ourselves to the hyperelastostatic case for conservative systems for which the Dirichlet principle defines the appropriate variational setting. In this context, we introduce the internal potential energy density $W_\square$ per unit volume in $\mathcal{B}_\square$, which is typically referred to as strain energy density. Conservative loading is characterized through the external potential energy density for conservative systems $V_\square$ per unit volume in $\mathcal{B}_\square$.

$$\begin{aligned} W_\square\,(\ \bar{\boldsymbol{F}}, \tilde{\boldsymbol{f}}; \boldsymbol{\xi}\ ) &= \tilde{j}\, W_0\,(\ \boldsymbol{F}; \boldsymbol{X}\ ) = \bar{J}\, W_t\,(\ \boldsymbol{f}, \boldsymbol{\Phi}\ ) \\ V_\square\,(\ \bar{\boldsymbol{\varphi}}, \tilde{\boldsymbol{\Phi}}; \boldsymbol{\xi}\ ) &= \tilde{j}\, V_0\,(\ \boldsymbol{\varphi}; \boldsymbol{X}\ ) = \bar{J}\, V_t\,(\ \boldsymbol{x}; \boldsymbol{\Phi}\ ) \end{aligned} \tag{5.3.1}$$

The total potential energy density $U_\square$ per unit volume in $\mathcal{B}_\square$ can thus be expressed as the sum of the corresponding internal and external contribution $W_\square$ and $V_\square$ as $U_\square = W_\square + V_\square$.

$$U_\square\,(\ \bar{\boldsymbol{F}}, \tilde{\boldsymbol{f}}, \bar{\boldsymbol{\varphi}}, \tilde{\boldsymbol{\Phi}}; \boldsymbol{\xi}\ ) = \tilde{j}\, U_0\,(\ \boldsymbol{F}, \boldsymbol{\varphi}; \boldsymbol{X}\ ) = \bar{J}\, U_t\,(\ \boldsymbol{f}, \boldsymbol{\Phi}; \boldsymbol{x}\ ) \tag{5.3.2}$$

Then, the conservative mechanical system is essentially characterized through the total energy $\mathcal{I}$ defined through the integration of $U_\square$ over the reference domain $\mathcal{B}_\square$.

$$\mathcal{I}\,(\ \bar{\boldsymbol{\varphi}}, \tilde{\boldsymbol{\Phi}}\ ) = \int_{\mathcal{B}_\square} U_\square \,\mathrm{d}V_\square \to \inf \tag{5.3.3}$$

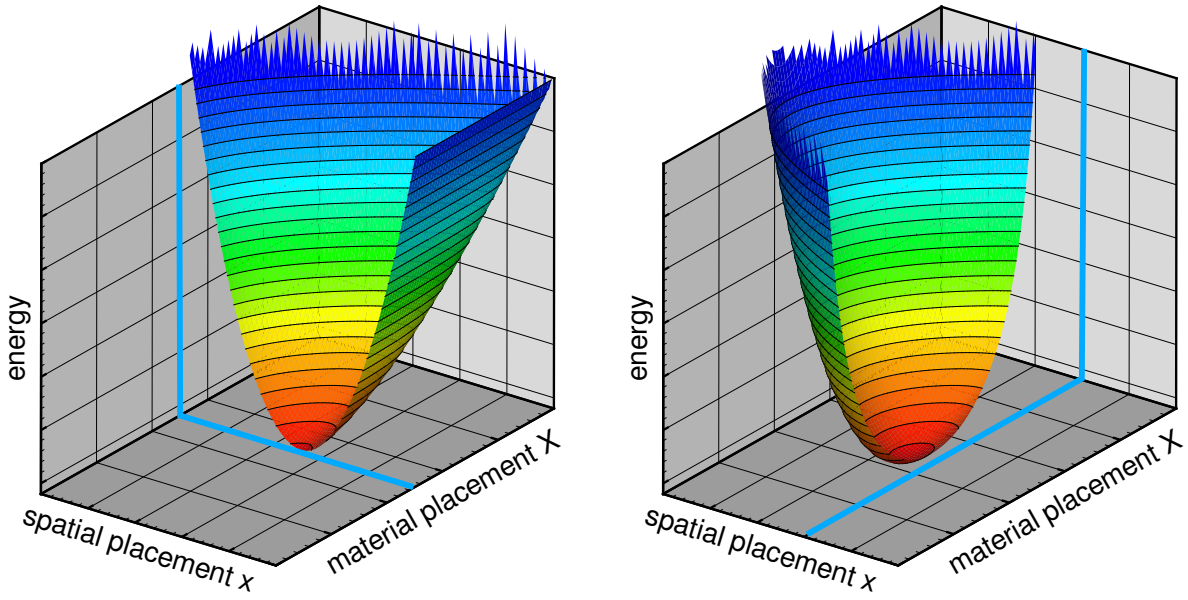


**Figure 5.5:** Variation of potential energy $\mathcal{I}$ at fixed material and spatial position

The infimum of the total potential energy $\mathcal{I}$ corresponds to a vanishing total variation, i.e. the variation at fixed referential coordinates $\boldsymbol{\xi}$.

$$\delta\mathcal{I} = \delta_x\mathcal{I} + \delta_X\mathcal{I} = 0 \tag{5.3.4}$$

According to equation (2.3.2), this total variation consists of a variation with respect to the spatial coordinates $\boldsymbol{x}$ at fixed material coordinates $\boldsymbol{X}$, as illustrated figure 5.5, left, plus variation with respect to the material coordinates $\boldsymbol{X}$ at fixed spatial coordinates $\boldsymbol{x}$, compare figure 5.5, right. These variations will be elaborated in detail in the sequel. Thereby, we will particularly emphasize the striking duality of both formulations.

### 5.3.1 Spatial motion problem

The variation of the total energy $\mathcal{I}$ with respect to the spatial coordinates $\boldsymbol{x}$ at fixed material coordinates $\boldsymbol{X}$ can be expressed in the following form.

$$\begin{aligned}
\delta_x\mathcal{I} &= \int_{\mathcal{B}_0} \nabla_X\, \delta\bar{\boldsymbol{\varphi}} : \qquad \mathrm{D}_F U_0 \qquad + \delta\bar{\boldsymbol{\varphi}} \cdot \partial_x U_0 \;\mathrm{d}V_0 \\
\delta_x\mathcal{I} &= \int_{\mathcal{B}_t} \nabla_x\; \delta\bar{\boldsymbol{\varphi}} : [U_t\, \boldsymbol{I} - \boldsymbol{f}^t \cdot \mathrm{d}_f U_t] + \delta\bar{\boldsymbol{\varphi}} \cdot \partial_x U_t \;\mathrm{d}V_t
\end{aligned} \tag{5.3.5}$$

Hereby, we have made use of equation (2.3.5) for the variation of scalar–valued functions. Note that the push forward to the spatial domain given in the second line will be needed later on for the linearization at fixed spatial coordinates. Thereby, the push forward of the first contribution is essentially based on the kinematic relation (2.2.11). The above format motivates the introduction of the spatial motion momentum fluxes $\boldsymbol{\Pi}^t$ and $\boldsymbol{\sigma}^t = j\,\boldsymbol{\Pi}^t \cdot \boldsymbol{F}^t$, whereby the former denotes the first Piola–Kirchhoff stress tensor while the latter is typically referred to as Cauchy stress. Moreover, we introduce the corresponding momentum sources $\boldsymbol{b}_0$ and $\boldsymbol{b}_t$, i.e. the spatial volume force densities

per unit volume in $\mathcal{B}_0$ and $\mathcal{B}_t$, respectively.

$$\begin{aligned} \boldsymbol{\Pi}^t &= \mathrm{D}_{\boldsymbol{F}} U_0 & \boldsymbol{b}_0 &= -\,\partial_{\boldsymbol{x}} U_0 \\ \boldsymbol{\sigma}^t &= U_t\,\boldsymbol{I} - \boldsymbol{f}^t \cdot \mathrm{d}_f U_t & \boldsymbol{b}_t &= -\,\partial_{\boldsymbol{x}} U_t \end{aligned} \tag{5.3.6}$$

According to the specific parametrization of the internal and external potential energy density $W_0$ and $V_0$ introduced in equation (5.3.1), we obtain the following explicit representations for the spatial motion momentum fluxes and sources,

$$\begin{aligned} \boldsymbol{\Pi}^t &= \mathrm{D}_{\boldsymbol{F}} W_0 & \boldsymbol{b}_0 &= -\,\partial_{\boldsymbol{x}} V_0 \\ \boldsymbol{\sigma}^t &= W_t\,\boldsymbol{I} - \boldsymbol{f}^t \cdot \mathrm{d}_f W_t & \boldsymbol{b}_t &= -\,\partial_{\boldsymbol{x}} V_t \end{aligned} \tag{5.3.7}$$

by making use of the fact that $\mathrm{D}_{\boldsymbol{F}} V_0 \equiv \boldsymbol{0}$, $\partial_{\boldsymbol{x}} W_0 \equiv \boldsymbol{0}$ and $\partial_{\boldsymbol{x}} W_t \equiv \boldsymbol{0}$. With the above definitions, the variation of the total energy (5.3.5) with respect to the spatial coordinates $\boldsymbol{x}$ takes the following more familiar format,

$$\begin{aligned} \text{mr} \qquad \delta_{\boldsymbol{x}}\mathcal{I} &= \int_{\mathcal{B}_0} \nabla_{\boldsymbol{X}}\, \delta\bar{\boldsymbol{\varphi}} : \boldsymbol{\Pi}^t \,\mathrm{d}V_0 - \int_{\mathcal{B}_0} \delta\bar{\boldsymbol{\varphi}} \cdot \boldsymbol{b}_0 \,\mathrm{d}V_0 \\ \text{sr} \qquad \delta_{\boldsymbol{x}}\mathcal{I} &= \int_{\mathcal{B}_t} \nabla_{\boldsymbol{x}}\, \delta\bar{\boldsymbol{\varphi}} : \boldsymbol{\sigma}^t \,\mathrm{d}V_t - \int_{\mathcal{B}_t} \delta\bar{\boldsymbol{\varphi}} \cdot \boldsymbol{b}_t \,\mathrm{d}V_t \end{aligned} \tag{5.3.8}$$

compare (3.5.11) or (3.5.50). The specification of the internal potential energy density $W_0$ and the corresponding spatial motion momentum fluxes $\boldsymbol{\Pi}^t$ and $\boldsymbol{\sigma}^t$ for the particular case of a classical compressible Neo–Hooke material is given in section 4.3.

### 5.3.2 Material motion problem

With the help of equation (2.3.8), the variation of total energy $\mathcal{I}$ with respect to the material coordinates $\boldsymbol{X}$ at fixed spatial coordinates $\boldsymbol{x}$ takes the following format.

$$\begin{aligned} \delta_{\boldsymbol{X}}\mathcal{I} &= \int_{\mathcal{B}_t} \nabla_{\boldsymbol{x}}\, \delta\tilde{\boldsymbol{\Phi}} : \qquad \mathrm{d}_f U_t \qquad + \delta\tilde{\boldsymbol{\Phi}} \cdot \partial_{\boldsymbol{X}} U_t \;\mathrm{d}V_t \\ \delta_{\boldsymbol{X}}\mathcal{I} &= \int_{\mathcal{B}_0} \nabla_{\boldsymbol{X}}\, \delta\tilde{\boldsymbol{\Phi}} : [U_0\,\boldsymbol{I} - \boldsymbol{F}^t \cdot \mathrm{D}_{\boldsymbol{F}} U_0] + \delta\tilde{\boldsymbol{\Phi}} \cdot \partial_{\boldsymbol{X}} U_0 \;\mathrm{d}V_0 \end{aligned} \tag{5.3.9}$$

The pull back to the material domain expressed in the second line of the above equation will be needed later on for the linearization at fixed material coordinates $\boldsymbol{X}$. In complete analogy to the spatial motion case, we can introduce the material motion momentum fluxes $\boldsymbol{\pi}^t$ and $\boldsymbol{\Sigma}^t$, a two–point stress tensor of Piola–Kirchhoff type and the classical Eshelby stress, respectively. Accordingly, the corresponding momentum sources, the material volume force densities per unit volume in $\mathcal{B}_t$ and $\mathcal{B}_0$, are introduced as $\boldsymbol{B}_t$ and $\boldsymbol{B}_0$.

$$\begin{aligned} \boldsymbol{\pi}^t &= \mathrm{d}_f U_t & \boldsymbol{B}_t &= -\,\partial_{\boldsymbol{X}} U_t \\ \boldsymbol{\Sigma}^t &= U_0\,\boldsymbol{I} - \boldsymbol{F}^t \cdot \mathrm{D}_{\boldsymbol{F}} U_0 & \boldsymbol{B}_0 &= -\,\partial_{\boldsymbol{X}} U_0 \end{aligned} \tag{5.3.10}$$

By making use of the specific parametrization of the internal and external potential energy introduced in equation (5.3.1), we can reformulate the momentum fluxes and sources.

$$\begin{aligned} \boldsymbol{\pi}^t &= \mathrm{d}_f W_t + V_t\, \boldsymbol{F}^t & \boldsymbol{B}_t &= -\,\partial_{\boldsymbol{X}} W_t - \partial_{\boldsymbol{X}} V_t \\ \boldsymbol{\Sigma}^t &= U_0\, \boldsymbol{I} - \boldsymbol{F}^t \cdot \mathrm{D}_{\boldsymbol{F}} W_0 & \boldsymbol{B}_0 &= -\,\partial_{\boldsymbol{X}} W_0 - \partial_{\boldsymbol{X}} V_0 \end{aligned} \tag{5.3.11}$$

Note that for the material motion problem, neither $\mathrm{d}_f V_t \neq \boldsymbol{0}$ nor $\partial_{\boldsymbol{X}} W_t \neq \boldsymbol{0}$ and $\partial_{\boldsymbol{X}} W_0 \neq \boldsymbol{0}$ vanish identically. In the above expressions, we have made use of the identities $\mathrm{d}_f V_t = V_t\, \boldsymbol{F}^t$ and $\mathrm{D}_{\boldsymbol{F}} V_t \equiv \boldsymbol{0}$, whereby the former accounts for contributions of possible volume forces. Consequently, the spatial variation of the total energy (5.3.9) can be reformulated in the following form,

$$\begin{aligned} \text{mr} \qquad \delta_{\boldsymbol{X}} \mathcal{I} &= \int_{\mathcal{B}_t} \nabla_{\boldsymbol{x}}\, \delta\tilde{\boldsymbol{\Phi}} : \boldsymbol{\pi}^t \, \mathrm{d}V_t - \int_{\mathcal{B}_t} \delta\tilde{\boldsymbol{\Phi}} \cdot \boldsymbol{B}_t \, \mathrm{d}V_t \\ \text{sr} \qquad \delta_{\boldsymbol{X}} \mathcal{I} &= \int_{\mathcal{B}_0} \nabla_{\boldsymbol{X}}\, \delta\tilde{\boldsymbol{\Phi}} : \boldsymbol{\Sigma}^t \, \mathrm{d}V_0 - \int_{\mathcal{B}_0} \delta\tilde{\boldsymbol{\Phi}} \cdot \boldsymbol{B}_0 \, \mathrm{d}V_0 \end{aligned} \tag{5.3.12}$$

compare also (3.5.32) and (3.5.59). For the particular case of a classical compressible Neo–Hooke material, the internal potential energy density $W_t$ and the corresponding material motion momentum fluxes $\boldsymbol{\pi}^t$ and $\boldsymbol{\Sigma}^t$ are given in section 4.3.

**Remark 5.3.1 (Spatial vs. material quantities)** *In the continuous case, we can define the following relations between the spatial and material momentum fluxes.*

$$\begin{aligned} \boldsymbol{\Pi}^t &= U_0\, \boldsymbol{f}^t - J\, \boldsymbol{f}^t \cdot \boldsymbol{\pi}^t \cdot \boldsymbol{f}^t & \boldsymbol{\sigma}^t &= U_t\, \boldsymbol{I} - \boldsymbol{f}^t \cdot \boldsymbol{\pi}^t \\ \boldsymbol{\pi}^t &= U_t\, \boldsymbol{F}^t - j\, \boldsymbol{F}^t \cdot \boldsymbol{\Pi}^t \cdot \boldsymbol{F}^t & \boldsymbol{\Sigma}^t &= U_0\, \boldsymbol{I} - \boldsymbol{F}^t \cdot \boldsymbol{\Pi}^t \end{aligned} \tag{5.3.13}$$

**Remark 5.3.2 (Spatial vs. material Euler–Lagrange equations)** *The material and spatial variation of the total potential energy density (5.3.5) and (5.3.9) suggest the spatial and the material version of the Euler–Lagrange field equations*

$$\mathrm{div}_{\boldsymbol{X}}(\mathrm{D}_{\boldsymbol{F}} U_0) - \partial_{\boldsymbol{x}} U_0 = \boldsymbol{0} \qquad \mathrm{div}_{\boldsymbol{x}}(\mathrm{d}_f U_t) - \partial_{\boldsymbol{X}} U_t = \boldsymbol{0}$$

*which can be recast into the following more familiar statements*

$$\mathrm{div}_{\boldsymbol{X}} \boldsymbol{\Pi}^t + \boldsymbol{b}_0 = \boldsymbol{0} \qquad \mathrm{div}_{\boldsymbol{x}} \boldsymbol{\pi}^t + \boldsymbol{B}_t = \boldsymbol{0}$$

*with the help of the definitions for the momentum fluxes and sources introduced in equations (5.3.6) and (5.3.10). The former is typically referred to as the classical or spatial motion momentum balance or balance of physical momentum while the latter corresponds to the material motion momentum balance also referred to as the balance of pseudomomentum. Recall that the former represents the balance of spatial forces, i.e. forces in the sense of Newton, while the latter corresponds to the balance of material forces, i.e. forces in the sense of Eshelby which are typically applied in defect mechanics.*

## 5.4 Weak form

The weak form of the ALE Dirichlet principle is based on the spatial and the material variation of the total potential energy (5.3.8) and (5.3.12), which can be reformulated in the following more familiar format,

$$\begin{aligned} \mathbf{r}^{\bar{\varphi}}(\bar{\boldsymbol{\varphi}}, \tilde{\boldsymbol{\Phi}}) &= -\mathbf{f}^{\bar{\varphi}}_{\text{sur}} - \mathbf{f}^{\bar{\varphi}}_{\text{vol}} = \mathbf{0} \\ \mathbf{R}^{\tilde{\Phi}}(\bar{\boldsymbol{\varphi}}, \tilde{\boldsymbol{\Phi}}) &= -\mathbf{F}^{\tilde{\Phi}}_{\text{sur}} - \mathbf{F}^{\tilde{\Phi}}_{\text{vol}} = \mathbf{0} \end{aligned} \tag{5.4.1}$$

whereby the surface and the volume contribution of the spatial and the material motion problem can be expressed in the following form.

$$\begin{aligned} \mathbf{f}^{\bar{\varphi}}_{\text{sur}} &= \int_{\partial\mathcal{B}_t} \boldsymbol{\sigma}^t \cdot \boldsymbol{n} \, \mathrm{d}A_t & \mathbf{f}^{\bar{\varphi}}_{\text{vol}} &= \int_{\mathcal{B}_t} \boldsymbol{b}_t \, \mathrm{d}V_t \\ \mathbf{F}^{\tilde{\Phi}}_{\text{sur}} &= \int_{\partial\mathcal{B}_0} \boldsymbol{\Sigma}^t \cdot \boldsymbol{N} \, \mathrm{d}A_0 & \mathbf{F}^{\tilde{\Phi}}_{\text{vol}} &= \int_{\mathcal{B}_0} \boldsymbol{B}_0 \, \mathrm{d}V_0 \end{aligned} \tag{5.4.2}$$

The residual statements (5.4.1) are supplemented by appropriate boundary conditions for the spatial and the material motion field. For the spatial motion problem $(5.4.1)_1$, the boundary $\partial\mathcal{B}_t$ is decomposed into disjoint parts as $\partial\mathcal{B}_t^{\bar{\varphi}} \cup \partial\mathcal{B}_t^t = \partial\mathcal{B}_t$ and $\partial\mathcal{B}_t^{\bar{\varphi}} \cap \partial\mathcal{B}_t^t = \emptyset$. Correspondingly, for the material motion problem $(5.4.1)_2$, the equivalent decomposition renders the disjoint boundary contributions $\partial\mathcal{B}_0^{\tilde{\Phi}} \cup \partial\mathcal{B}_0^T = \partial\mathcal{B}_0$ and $\partial\mathcal{B}_0^{\tilde{\Phi}} \cap \partial\mathcal{B}_0^T = \emptyset$. Dirichlet boundary conditions are prescribed for the mappings $\bar{\boldsymbol{\varphi}}$ and $\tilde{\boldsymbol{\Phi}}$ on $\mathcal{B}_t^{\bar{\varphi}}$ and $\mathcal{B}_0^{\tilde{\Phi}}$, whereas Neumann boundary can be introduced for the spatial and the material motion momentum fluxes $\boldsymbol{\sigma}^t$ and $\boldsymbol{\Sigma}^t$ on $\partial\mathcal{B}_t^t$ and $\partial\mathcal{B}_0^T$ in terms of the outward normals $\boldsymbol{n}$ and $\boldsymbol{N}$.

$$\begin{aligned} \bar{\boldsymbol{\varphi}} &= \bar{\bar{\boldsymbol{\varphi}}} \quad \text{on} \quad \partial\mathcal{B}_t^{\bar{\varphi}} & \boldsymbol{\sigma}^t \cdot \boldsymbol{n} &= \bar{\boldsymbol{t}} \quad \text{on} \quad \partial\mathcal{B}_t^t \\ \tilde{\boldsymbol{\Phi}} &= \bar{\tilde{\boldsymbol{\Phi}}} \quad \text{on} \quad \partial\mathcal{B}_0^{\tilde{\Phi}} & \boldsymbol{\Sigma}^t \cdot \boldsymbol{N} &= \bar{\boldsymbol{T}} \quad \text{on} \quad \partial\mathcal{B}_0^T \end{aligned} \tag{5.4.3}$$

By testing the local residual statements corresponding to $(5.4.1)_1$ and $(5.4.1)_2$ and the related Neumann boundary conditions $(5.4.3)_2$ and $(5.4.3)_4$ with the vector–valued test functions $\bar{\boldsymbol{w}}$ and $\tilde{\boldsymbol{W}}$, respectively, we can derive the corresponding weak forms

$$\begin{aligned} \mathsf{g}^{\bar{\varphi}}(\bar{\boldsymbol{w}}; \bar{\boldsymbol{\varphi}}, \tilde{\boldsymbol{\Phi}}) &= \mathsf{w}^{\bar{\varphi}}_{\text{int}} - \mathsf{w}^{\bar{\varphi}}_{\text{sur}} - \mathsf{w}^{\bar{\varphi}}_{\text{vol}} = 0 \quad \forall\, \bar{\boldsymbol{w}} \;\text{ in }\; H_1^0(\mathcal{B}_0) \\ \mathsf{G}^{\tilde{\Phi}}(\tilde{\boldsymbol{W}}; \bar{\boldsymbol{\varphi}}, \tilde{\boldsymbol{\Phi}}) &= \mathsf{W}^{\tilde{\Phi}}_{\text{int}} - \mathsf{W}^{\tilde{\Phi}}_{\text{sur}} - \mathsf{W}^{\tilde{\Phi}}_{\text{vol}} = 0 \quad \forall\, \tilde{\boldsymbol{W}} \;\text{ in }\; H_1^0(\mathcal{B}_0) \end{aligned} \tag{5.4.4}$$

provided that the related fields fulfill the necessary smoothness and boundary assumptions. By interpreting the test functions $\bar{\boldsymbol{w}}$ and $\tilde{\boldsymbol{W}}$ as the spatial and material virtual displacements $\bar{\boldsymbol{w}} = \delta\bar{\boldsymbol{\varphi}}$ and $\tilde{\boldsymbol{W}} = \delta\tilde{\boldsymbol{\varphi}}$, equations (5.4.4) can be identified as the virtual work expressions of the spatial and the material motion problem with the internal, the surface and the volume parts of the virtual work given in the familiar form.

$$\begin{aligned} \mathsf{w}^{\bar{\varphi}}_{\text{int}} &= \int_{\mathcal{B}_t} \nabla_x \bar{\boldsymbol{w}} : \boldsymbol{\sigma}^t \, \mathrm{d}V_t & \mathsf{w}^{\bar{\varphi}}_{\text{sur}} &= \int_{\partial\mathcal{B}_t^t} \bar{\boldsymbol{w}} \cdot \boldsymbol{\sigma}^t \cdot \boldsymbol{n} \, \mathrm{d}A_t & \mathsf{w}^{\bar{\varphi}}_{\text{vol}} &= \int_{\mathcal{B}_t} \bar{\boldsymbol{w}} \cdot \boldsymbol{b}_t \, \mathrm{d}V_t \\ \mathsf{W}^{\tilde{\Phi}}_{\text{int}} &= \int_{\mathcal{B}_0} \nabla_X \tilde{\boldsymbol{W}} : \boldsymbol{\Sigma}^t \, \mathrm{d}V_0 & \mathsf{W}^{\tilde{\Phi}}_{\text{sur}} &= \int_{\partial\mathcal{B}_0^T} \tilde{\boldsymbol{W}} \cdot \boldsymbol{\Sigma}^t \cdot \boldsymbol{N} \, \mathrm{d}A_0 & \mathsf{W}^{\tilde{\Phi}}_{\text{vol}} &= \int_{\mathcal{B}_0} \tilde{\boldsymbol{W}} \cdot \boldsymbol{B}_0 \, \mathrm{d}V_0 \end{aligned} \tag{5.4.5}$$

Thereby, the individual terms basically correspond to the terms of the spatial and the material variation of the total potential energy (5.3.8) and (5.3.12) derived in the previous section.

## 5.5 Discretization

In what follows, we will illustrate the spatial discretization of the governing equations derived in the previous section. Thereby, we shall make use of the finite element method, which has been introduced in the late 60s by Argyris [2], Clough [31], Zienkiewicz [225] and Oden [171]. For modern literature on the finite element method we refer to the classical textbooks of Crisfield [44, 45], Cook [33, 34], Bathe [11], Bonet & Wood [16], Belytschko et al. [14], Hughes [102], Reddy [176], Donéa & Huerta [52], Wriggers [221, 222] and Zienkiewicz & Taylor [226–228]. In contrast to the engineering approaches cited above, a rigorous mathematical description of the finite element method can be found in the famous textbooks by Strang & Fix [202] Szabó & Babuska [203], Brenner & Scott [21], Braess [18] or Ciarlet [30].

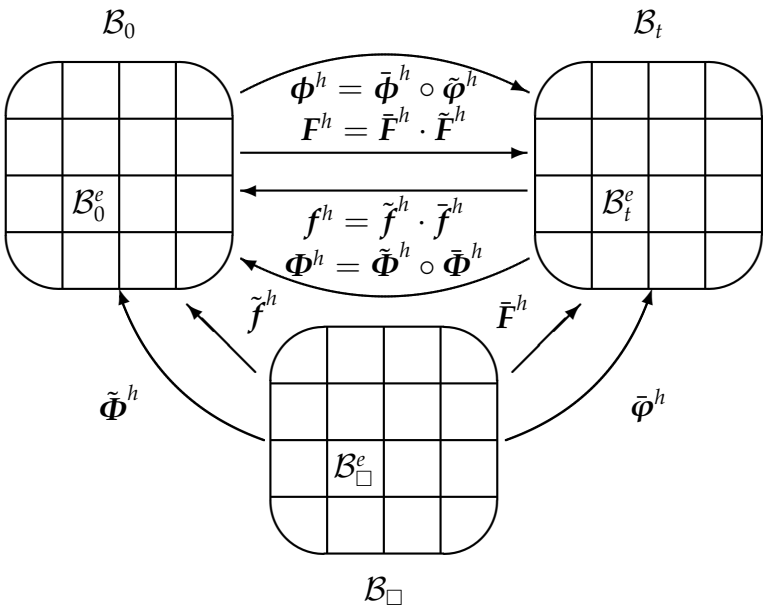


**Figure 5.6:** Spatial discretization

In the spirit of the finite element method, the reference domain $\mathcal{B}_\square$ is discretized in $e = 1, \dots, n_{\text{el}}$ elements which are characterized through the corresponding element domain $\mathcal{B}_\square^e$, compare figure 5.6. The underlying geometry $\boldsymbol{\xi}$ is interpolated elementwise by the shape functions $N_\xi^i$ in terms of the discrete node point positions $\boldsymbol{\xi}_i$ of the $i = 1, \dots, n_{\text{en}}$ element nodes.

$$\mathcal{B}_\square = \bigcup_{e=1}^{n_{\text{el}}} \mathcal{B}_\square^e \qquad \boldsymbol{\xi}^h|_{\mathcal{B}_\square^e} = \sum_{i=1}^{n_{\text{en}}} N_\xi^i \, \boldsymbol{\xi}_i \tag{5.5.1}$$

Following the isoparametric concept, the unknowns $\bar{\boldsymbol{\varphi}}$ and $\tilde{\boldsymbol{\Phi}}$ are interpolated on the element level with the same shape functions $N_{\bar{\varphi}}^i$ and $N_{\tilde{\Phi}}^j$ as the element geometry $\boldsymbol{\xi}$. Similar shape functions are applied to interpolate the test functions $\bar{\boldsymbol{w}}$ and $\tilde{\boldsymbol{W}}$ according

to the classical Bubnov–Galerkin technique.

$$\begin{aligned} \bar{\boldsymbol{w}}^h|_{\mathcal{B}^e_\square} &= \sum_{i=1}^{n_{\text{en}}} N^i_{\bar{\varphi}}\, \bar{\boldsymbol{w}}_i \;\in\; H^0_1(\mathcal{B}_\square) & \bar{\boldsymbol{\varphi}}^h|_{\mathcal{B}^e_\square} &= \sum_{k=1}^{n_{\text{en}}} N^k_{\bar{\varphi}}\, \bar{\boldsymbol{\varphi}}_k \;\in\; H_1(\mathcal{B}_\square) \\ \tilde{\boldsymbol{W}}^h|_{\mathcal{B}^e_\square} &= \sum_{j=1}^{n_{\text{en}}} N^j_{\tilde{\Phi}}\, \tilde{\boldsymbol{W}}_j \;\in\; H^0_1(\mathcal{B}_\square) & \tilde{\boldsymbol{\Phi}}^h|_{\mathcal{B}^e_\square} &= \sum_{l=1}^{n_{\text{en}}} N^l_{\tilde{\Phi}}\, \tilde{\boldsymbol{\Phi}}_l \;\in\; H_1(\mathcal{B}_\square) \end{aligned} \tag{5.5.2}$$

Consequently, the related gradients of the test functions $\nabla_\xi \bar{\boldsymbol{w}}^h$ and $\nabla_\xi \tilde{\boldsymbol{W}}^h$ and the gradients of the primary unknowns $\nabla_\xi \bar{\boldsymbol{\varphi}}^h$ and $\nabla_\xi \tilde{\boldsymbol{\Phi}}^h$ take the following elementwise interpolation.

$$\begin{aligned} \nabla_\xi\, \bar{\boldsymbol{w}}^h|_{\mathcal{B}^e_\square} &= \sum_{i=1}^{n_{\text{en}}} \bar{\boldsymbol{w}}_i \otimes \nabla_\xi N^i_{\bar{\varphi}} & \nabla_\xi\, \bar{\boldsymbol{\varphi}}^h|_{\mathcal{B}^e_\square} &= \sum_{k=1}^{n_{\text{en}}} \bar{\boldsymbol{\varphi}}_k \otimes \nabla_\xi N^k_{\bar{\varphi}} \\ \nabla_\xi\, \tilde{\boldsymbol{W}}^h|_{\mathcal{B}^e_\square} &= \sum_{j=1}^{n_{\text{en}}} \tilde{\boldsymbol{W}}_j \otimes \nabla_\xi N^j_{\tilde{\Phi}} & \nabla_\xi\, \tilde{\boldsymbol{\Phi}}^h|_{\mathcal{B}^e_\square} &= \sum_{l=1}^{n_{\text{en}}} \tilde{\boldsymbol{\Phi}}_l \otimes \nabla_\xi N^l_{\tilde{\Phi}} \end{aligned} \tag{5.5.3}$$

In particular, $\nabla_\xi \bar{\boldsymbol{\varphi}}^h$ and $\nabla_\xi \tilde{\boldsymbol{\Phi}}^h$ denote the discrete deformation gradients $\bar{\boldsymbol{F}}^h = \nabla_\xi \bar{\boldsymbol{\varphi}}^h$ and $\tilde{\boldsymbol{f}}^h = \nabla_\xi \tilde{\boldsymbol{\Phi}}^h$, which define the discrete spatial and material deformation gradient as $\boldsymbol{F}^h = \bar{\boldsymbol{F}}^h \cdot \tilde{\boldsymbol{F}}^h$ and $\boldsymbol{f}^h = \tilde{\boldsymbol{f}}^h \cdot \bar{\boldsymbol{f}}^h$. With the above suggested discretizations at hand, the discrete residual of the balance of momentum of the spatial motion problem $\mathbf{r}^{\bar{\varphi}h}_I$ and of the material motion problem $\mathbf{R}^{\tilde{\Phi}h}_J$ take the following format.

$$\begin{aligned} \mathbf{r}^{\bar{\varphi}h}_I(\bar{\boldsymbol{\varphi}}^h, \tilde{\boldsymbol{\Phi}}^h) &= \mathbf{f}^{\bar{\varphi}\,h}_{\text{int}I} - \mathbf{f}^{\bar{\varphi}\,h}_{\text{sur}I} - \mathbf{f}^{\bar{\varphi}\,h}_{\text{vol}I} = \mathbf{0} \qquad \forall \quad I = 1, \dots, n_{\text{np}} \\ \mathbf{R}^{\tilde{\Phi}h}_J(\bar{\boldsymbol{\varphi}}^h, \tilde{\boldsymbol{\Phi}}^h) &= \mathbf{F}^{\tilde{\Phi}\,h}_{\text{int}J} - \mathbf{F}^{\tilde{\Phi}\,h}_{\text{sur}J} - \mathbf{F}^{\tilde{\Phi}\,h}_{\text{vol}J} = \mathbf{0} \qquad \forall \quad J = 1, \dots, n_{\text{np}} \end{aligned} \tag{5.5.4}$$

Herein, the discrete internal forces, the surface forces and the volume forces of the spatial motion problem can be expressed as

$$\mathbf{f}^{\bar{\varphi}\,h}_{\text{int}I} = \mathop{\mathbf{A}}_{e=1}^{n_{\text{el}}} \int_{\mathcal{B}^e_t} \nabla_x N^i_{\bar{\varphi}} \cdot \boldsymbol{\sigma}\, \mathrm{d}V_t \quad \mathbf{f}^{\bar{\varphi}\,h}_{\text{sur}I} = \mathop{\mathbf{A}}_{e=1}^{n_{\text{el}}} \int_{\partial\mathcal{B}^{te}_t} N^i_{\bar{\varphi}}\, \boldsymbol{t}_t\, \mathrm{d}A_t \quad \mathbf{f}^{\bar{\varphi}\,h}_{\text{vol}I} = \mathop{\mathbf{A}}_{e=1}^{n_{\text{el}}} \int_{\mathcal{B}^e_t} N^i_{\bar{\varphi}}\, \boldsymbol{b}_t\, \mathrm{d}V_t \tag{5.5.5}$$

while the discrete internal, surface and volume forces of the material motion problem are given as follows.

$$\mathbf{F}^{\tilde{\Phi}\,h}_{\text{int}J} = \mathop{\mathbf{A}}_{e=1}^{n_{\text{el}}} \int_{\mathcal{B}^e_0} \nabla_X N^j_{\tilde{\Phi}} \cdot \boldsymbol{\Sigma}\, \mathrm{d}V_0 \quad \mathbf{F}^{\tilde{\Phi}\,h}_{\text{sur}J} = \mathop{\mathbf{A}}_{e=1}^{n_{\text{el}}} \int_{\partial\mathcal{B}^{te}_0} N^j_{\tilde{\Phi}}\, \boldsymbol{T}_0\, \mathrm{d}A_0 \quad \mathbf{F}^{\tilde{\Phi}\,h}_{\text{vol}J} = \mathop{\mathbf{A}}_{e=1}^{n_{\text{el}}} \int_{\mathcal{B}^e_0} N^j_{\tilde{\Phi}}\, \boldsymbol{B}_0\, \mathrm{d}V_0 \tag{5.5.6}$$

Herein, the operator $\mathop{\mathbf{A}}_{e=1}^{n_{\text{el}}}$ denotes the assembly over all $e = 1, \dots, n_{\text{el}}$ element contributions at the $i, j = 1, \dots, n_{\text{en}}$ element nodes to the global node point residuals at all $I, J = 1, \dots, n_{\text{enp}}$ global node points. The discrete residuals $\mathbf{r}^{\bar{\varphi}}_I$ and $\mathbf{R}^{\tilde{\Phi}}_J$ introduced in equation (5.5.4) define the discrete spatial and material surface forces $\mathbf{f}^{\bar{\varphi}\,h}_{\text{sur}I}$ and $\mathbf{F}^{\tilde{\Phi}\,h}_{\text{sur}J}$,

$$\begin{aligned} \mathbf{f}^{\bar{\varphi}\,h}_{\text{sur}I} &= \mathop{\mathbf{A}}_{e=1}^{n_{\text{el}}} \int_{\mathcal{B}^e_t} \nabla_{\boldsymbol{x}}\; N^i_{\bar{\varphi}} \cdot \boldsymbol{\sigma} - N^i_{\bar{\varphi}}\; \boldsymbol{b}_t\; \mathrm{d}V_t \\ \mathbf{F}^{\tilde{\Phi}\,h}_{\text{sur}J} &= \mathop{\mathbf{A}}_{e=1}^{n_{\text{el}}} \int_{\mathcal{B}^e_0} \nabla_{\boldsymbol{X}}\; N^j_{\tilde{\Phi}} \cdot \boldsymbol{\Sigma} - N^j_{\tilde{\Phi}}\; \boldsymbol{B}_0\; \mathrm{d}V_0 \end{aligned} \tag{5.5.7}$$

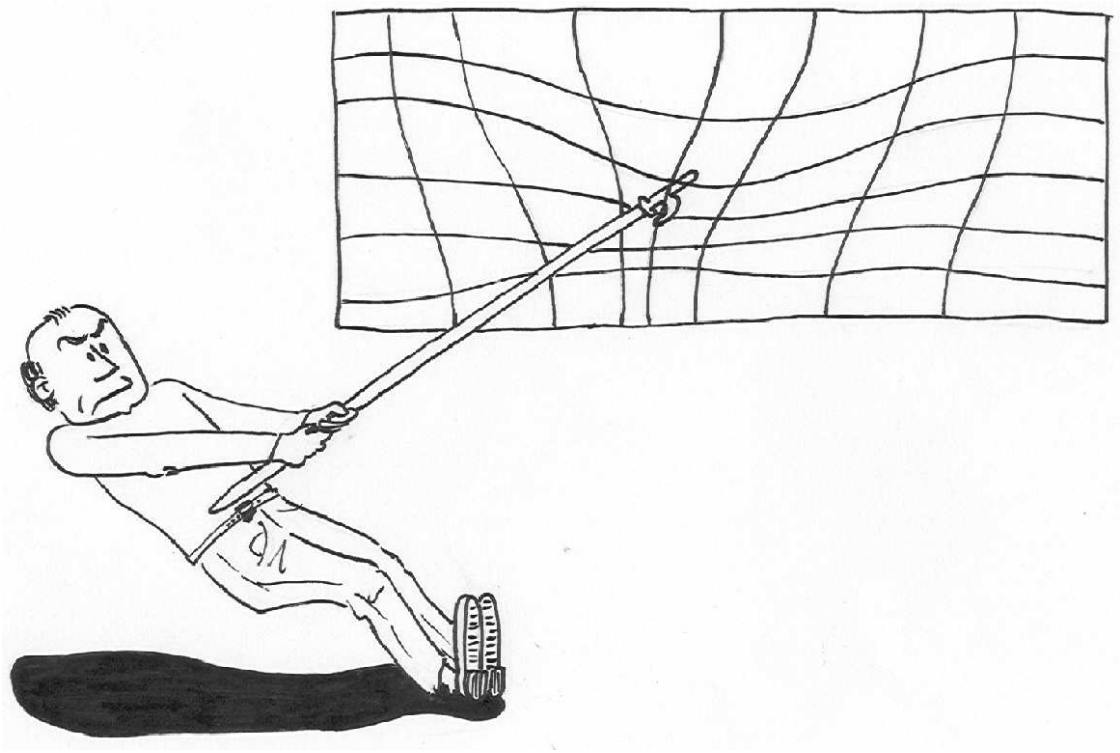

**Figure 5.7:** Discrete material forces acting on the Finite Element nodes

which are energetically conjugate to the spatial variations $\delta\bar{\boldsymbol{\varphi}}_I = \bar{\boldsymbol{w}}_I$ and to the material variations $\delta\tilde{\boldsymbol{\Phi}}_J = \tilde{\boldsymbol{W}}_J$ of the node point positions. Recall that material forces $\mathbf{F}^{J\,h}_{\Phi\mathrm{sur}}$ are typically associated with positional changes of defects, e.g. the motion of dislocations or the opening of a crack. In the context considered herein, the finite element discretization can thus be interpreted as a source of inhomogeneity introducing discrete defects. Figure 5.7 illustrates the discrete material forces acting on the node point positions.

**Remark 5.5.1 (Spatial vs. material quantities)** *It is important to recognize that the relations between spatial and material quantities derived in the previous sections are valid only for the continuous case. Upon discretization, we introduce the spatial and the material motion problem as independent statements. In particular, a vanishing residual* $\mathbf{r}^{\bar{\varphi}}_I$ *of the spatial motion problem does not necessarily have to correspond to a vanishing residual* $\mathbf{R}^{\tilde{\Phi}}_J$ *of the material motion problem and vice versa, see e.g. Kuhl et al. [125] and Askes et al. [6].*

**Remark 5.5.2 (Convection)** *The above–suggested algorithmic realization of the Arbitrary Lagrangian Eulerian formulation is particularly appealing in the context of inelasticity since it is parameterized in terms of the spatial and the material node point positions* $\bar{\boldsymbol{\varphi}}_I$ *and* $\tilde{\boldsymbol{\Phi}}_J$*. The integration can thus be carried out on the fixed reference domain* $\mathcal{B}_\square$*. In contrast to most existing ALE formulations in the literature, the algorithm suggested herein would not require the mapping of internal variables since these would typically be attached to fixed integration points on the reference domain* $\mathcal{B}_\square$*. The equations governing the evolution of these internal variables might, however, become more cumbersome.*

## 5.6 Linearization

The above derived discrete residual statements represent a highly nonlinear coupled system of equations which can be solved efficiently within the framework of a monolithic incremental iterative Newton–Raphson solution strategy. To this end, we perform a consistent linearization of the governing equations

$$\begin{aligned} \mathbf{r}\,{}^{\bar{\varphi}}_{I}{}^{k+1}_{n+1} &= \mathbf{r}\,{}^{\bar{\varphi}}_{I}{}^{k}_{n+1} + \mathrm{d}\mathbf{r}\,{}^{\bar{\varphi}}_{I} \doteq \mathbf{0} \qquad \forall \quad I = 1,\dots,n_{\mathrm{np}} \\ \mathbf{R}^{\tilde{\Phi}}_{J}{}^{k+1}_{n+1} &= \mathbf{R}^{\tilde{\Phi}}_{J}{}^{k}_{n+1} + \mathrm{d}\mathbf{R}^{\tilde{\Phi}}_{J} \doteq 0 \qquad \forall \quad J = 1,\dots,n_{\mathrm{np}} \end{aligned} \tag{5.6.1}$$

with $\mathrm{d}\mathbf{r}\,{}^{\bar{\varphi}}_{I}$ and $\mathrm{d}\mathbf{R}^{\tilde{\Phi}}_{J}$

$$\begin{aligned} \mathrm{d}\mathbf{r}\,{}^{\bar{\varphi}}_{I} &= \sum_{K=1}^{n_{\mathrm{np}}} \mathbf{K}^{\bar{\varphi}\bar{\varphi}}_{IK}\,\mathrm{d}\bar{\boldsymbol{\varphi}}_K + \sum_{L=1}^{n_{\mathrm{np}}} \mathbf{K}^{\bar{\varphi}\tilde{\Phi}}_{IL}\cdot\mathrm{d}\tilde{\boldsymbol{\Phi}}_L \qquad \forall\, I = 1,\dots,n_{\mathrm{np}} \\ \mathrm{d}\mathbf{R}^{\tilde{\Phi}}_{J} &= \sum_{K=1}^{n_{\mathrm{np}}} \mathbf{K}^{\tilde{\Phi}\bar{\varphi}}_{JK}\,\mathrm{d}\bar{\boldsymbol{\varphi}}_K + \sum_{L=1}^{n_{\mathrm{np}}} \mathbf{K}^{\tilde{\Phi}\tilde{\Phi}}_{JL}\cdot\mathrm{d}\tilde{\boldsymbol{\Phi}}_L \qquad \forall\, J = 1,\dots,n_{\mathrm{np}} \end{aligned} \tag{5.6.2}$$

denoting the iterative residua of the iteration $k+1$. The iteration matrices $\mathbf{K}^{\bar{\varphi}\bar{\varphi}}_{IK}$, $\mathbf{K}^{\bar{\varphi}\tilde{\Phi}}_{IL}$, $\mathbf{K}^{\tilde{\Phi}\bar{\varphi}}_{JK}$ and $\mathbf{K}^{\tilde{\Phi}\tilde{\Phi}}_{JL}$ can finally be expressed as

$$\begin{aligned} \mathbf{K}^{\bar{\varphi}\bar{\varphi}}_{IK} &= \frac{\partial \mathbf{r}\,{}^{\bar{\varphi}}_{I}}{\partial \bar{\boldsymbol{\varphi}}_K} = \mathop{\mathbf{A}}_{e=1}^{n_{\mathrm{el}}} \int_{\mathcal{B}^e_0} \nabla_{\boldsymbol{x}} N^i_{\bar{\varphi}} \cdot \mathbf{c} \cdot \nabla_{\boldsymbol{x}} N^k_{\bar{\varphi}} \,\mathrm{d}V_0 \\ \mathbf{K}^{\bar{\varphi}\tilde{\Phi}}_{IL} &= \frac{\partial \mathbf{r}\,{}^{\bar{\varphi}}_{I}}{\partial \tilde{\boldsymbol{\Phi}}_L} = \mathop{\mathbf{A}}_{e=1}^{n_{\mathrm{el}}} \int_{\mathcal{B}^e_t} \nabla_{\boldsymbol{x}} N^i_{\bar{\varphi}} \cdot \mathrm{d}_f\boldsymbol{\sigma}^t \cdot \nabla_{\boldsymbol{x}} N^l_{\tilde{\Phi}} - N^i_{\bar{\varphi}}\, \boldsymbol{b}_t \cdot \nabla_{\boldsymbol{X}} N^l_{\tilde{\Phi}} \,\mathrm{d}V_t \\ \mathbf{K}^{\tilde{\Phi}\bar{\varphi}}_{JK} &= \frac{\partial \mathbf{R}^{\tilde{\Phi}}_{J}}{\partial \bar{\boldsymbol{\varphi}}_K} = \mathop{\mathbf{A}}_{e=1}^{n_{\mathrm{el}}} \int_{\mathcal{B}^e_0} \nabla_{\boldsymbol{X}} N^j_{\tilde{\Phi}} \cdot \mathrm{D}_{\boldsymbol{F}}\boldsymbol{\Sigma}^t \cdot \nabla_{\boldsymbol{X}} N^k_{\bar{\varphi}} - \nabla_{\boldsymbol{X}} N^j_{\tilde{\Phi}} \cdot \boldsymbol{b}_0\, N^k_{\bar{\varphi}} \,\mathrm{d}V_0 \\ \mathbf{K}^{\tilde{\Phi}\tilde{\Phi}}_{JL} &= \frac{\partial \mathbf{R}^{\tilde{\Phi}}_{J}}{\partial \tilde{\boldsymbol{\Phi}}_L} = \mathop{\mathbf{A}}_{e=1}^{n_{\mathrm{el}}} \int_{\mathcal{B}^e_t} \nabla_{\boldsymbol{X}} N^j_{\tilde{\Phi}} \cdot \mathbf{C} \cdot \nabla_{\boldsymbol{X}} N^l_{\tilde{\Phi}} \,\mathrm{d}V_t \end{aligned} \tag{5.6.3}$$

in terms of the fourth order tensors $\mathbf{c}$, $\mathrm{d}_f\boldsymbol{\sigma}^t$, $\mathrm{D}_{\boldsymbol{F}}\boldsymbol{\Sigma}^t$ and $\mathbf{C}$ according to the definitions (4.3.4) and (4.3.8) which were specified for a particular choice of the free energies $W_0$ and $W_t$ in section 4.3. The solution of the system of equations (5.6.1) renders the iterative update for the global unknowns $\bar{\boldsymbol{\varphi}}_I$ and $\tilde{\boldsymbol{\Phi}}_J$.

$$\begin{aligned} \bar{\boldsymbol{\varphi}}_I &= \bar{\boldsymbol{\varphi}}_I + \mathrm{d}\,\bar{\boldsymbol{\varphi}}_I \qquad \forall \quad I = 1,\dots,n_{\mathrm{np}} \\ \tilde{\boldsymbol{\Phi}}_J &= \tilde{\boldsymbol{\Phi}}_J + \mathrm{d}\,\tilde{\boldsymbol{\Phi}}_J \qquad \forall \quad J = 1,\dots,n_{\mathrm{np}} \end{aligned} \tag{5.6.4}$$

**Remark 5.6.1 (Lagrangian vs. Eulerian viewpoint)** *The classical Lagrangian and Eulerian viewpoint can be derived as special cases with keeping either $\tilde{\boldsymbol{\Phi}}$ or $\bar{\boldsymbol{\varphi}}$ fixed such that either $\boldsymbol{\varphi} = \bar{\boldsymbol{\varphi}}$ or $\boldsymbol{\Phi} = \tilde{\boldsymbol{\Phi}}$. In the first case corresponding the Lagrangian viewpoint, the $\tilde{\boldsymbol{\Phi}}$ terms in equations (5.5.4) and (5.6.3) would vanish identically as $\mathbf{R}^{\tilde{\Phi}}_{J} = \mathbf{0}$, $\mathbf{K}^{\bar{\varphi}\tilde{\Phi}}_{IL} = \mathbf{0}$, $\mathbf{K}^{\tilde{\Phi}\bar{\varphi}}_{JK} = \mathbf{0}$ and $\mathbf{K}^{\tilde{\Phi}\tilde{\Phi}}_{JL} = \mathbf{0}$ while for the second case corresponding to the Eulerian viewpoint the $\bar{\boldsymbol{\varphi}}$ terms would vanish such that $\mathbf{r}\,{}^{\bar{\varphi}}_{I} = \mathbf{0}$, $\mathbf{K}^{\bar{\varphi}\bar{\varphi}}_{IK} = \mathbf{0}$, $\mathbf{K}^{\bar{\varphi}\tilde{\Phi}}_{IL} = \mathbf{0}$ and $\mathbf{K}^{\tilde{\Phi}\bar{\varphi}}_{JK} = \mathbf{0}$.*

## 5.7 Algorithmic aspects

A typical finite element solution algorithm for the suggested variational ALE method is sketched in the flowchart in table 5.1. Obviously, the referential mappings $\bar{\boldsymbol{\varphi}}$ and $\tilde{\boldsymbol{\Phi}}$ are introduced as global unknowns on the nodal level. They are determined by the simultaneous solution of the spatial and the material balance of momentum.

| |
|---|
| global Newton iteration |
| loop over all elements |
| loop over all integration points |
| evaluate spatial & material momentum balance |
| determine $\mathbf{r}^{\bar{\varphi}e}$, $\mathbf{R}^{\tilde{\Phi}e}$, $\partial_{\bar{\boldsymbol{\varphi}}}\mathbf{r}^{\bar{\varphi}e}$, $\partial_{\tilde{\boldsymbol{\Phi}}}\mathbf{r}^{\bar{\varphi}e}$, $\partial_{\bar{\boldsymbol{\varphi}}}\mathbf{R}^{\tilde{\Phi}e}$, $\partial_{\tilde{\boldsymbol{\Phi}}}\mathbf{R}^{\tilde{\Phi}e}$ |
| element residuals and their partial derivatives |
| determine $\mathbf{r}^{\bar{\varphi}}$, $\mathbf{R}^{\tilde{\Phi}}$, $\mathbf{K}^{\bar{\varphi}\bar{\varphi}}$, $\mathbf{K}^{\bar{\varphi}\tilde{\Phi}}$, $\mathbf{K}^{\tilde{\Phi}\bar{\varphi}}$, $\mathbf{K}^{\tilde{\Phi}\tilde{\Phi}}$ |
| global residuals and iteration matrices |
| determine $\bar{\boldsymbol{\varphi}}$ and $\tilde{\boldsymbol{\Phi}}$ and thus $\boldsymbol{\varphi}$ and $\boldsymbol{\Phi}$ |

**Table 5.1:** Algorithm of variational ALE method

**Remark 5.7.1 (Material force method)** *Within the variational ALE strategy suggested in the present approach, discrete material node point forces can be understood as driving forces for the material node point positions. Consequently, upon iteration towards the equilibrium state, these material forces vanish identically for those nodes which are allowed to move freely. By performing a classical Lagrangian analysis, however, we can determine the discrete material node point forces that would act on those nodes if they were fixed in the material domain according to the Lagrangian viewpoint. Thereby, first, a classical Lagrangian analysis is carried out to determine the spatial motion map $\boldsymbol{\varphi}$. In a post–processing step, we can then calculate the spatial motion stresses, e.g. the Cauchy stresses $\boldsymbol{\sigma}^t$, from which we determine the Eshelby stress $\boldsymbol{\Sigma}^t$ according to the following formula.*

$$\boldsymbol{\Sigma}^t = \psi_0 \, \boldsymbol{I} - J \, \boldsymbol{F}^t \cdot \boldsymbol{\sigma} \cdot \boldsymbol{F}^{-t} \tag{5.7.1}$$

*For homogeneous, volume force free cases considered in the sequel, the discrete material surface forces follow straightforwardly from equation (5.5.7)$_2$ with $\boldsymbol{B}_0 \equiv \boldsymbol{0}$. Table 5.2 depicts a typical flowchart of the material force method as advocated by Steinmann [197], Steinmann et al. [201] and Denzer et al. [46] in the context of linear and nonlinear elastic fracture mechanics.*

**Remark 5.7.2 (Monolithic vs. staggered solution)** *Note that the formulation derived herein suggests a monolithic solution for the spatial and the material node point positions. However, a staggered solution scheme can be derived from the proposed algorithm in a straightforward way. It essentially follows from the above–derived equations by neglecting the coupling matrices $\mathbf{K}_{IL}^{\bar{\varphi}\tilde{\Phi}} = \mathbf{0}$ and $\mathbf{K}_{JK}^{\tilde{\Phi}\bar{\varphi}} = \mathbf{0}$ such that the spatial and the material motion problem can be solved individually. A detailed comparison between monolithic and staggered schemes is given by Askes et al. [6].*

| |
|---|
| global Newton iteration |
| loop over all elements |
| loop over all integration points |
| evaluate spatial balance of momentum |
| determine $\mathbf{r}^{\varphi e}$, $\partial_\varphi \mathbf{r}^{\varphi e}$ |
| element residual and its partial derivative |
| determine $\mathbf{r}^{\varphi}$, $\mathbf{K}^{\varphi\varphi}$ |
| global residual and iteration matrix |
| determine $\boldsymbol{\varphi}$ |
| determine $\boldsymbol{\sigma}^t$, $\boldsymbol{\Sigma}^t$, $\mathbf{F}^{\Phi}_{\mathrm{sur}}$ |
| momentum fluxes and material forces |

**Table 5.2:** Algorithm of material force method

## 5.8 Example: Homogeneous block under tension

The first example concerns a homogeneous block under tension. The geometry and loading conditions are adopted from Müller & Maugin [158]. The elasticity constants are given as $\lambda_0 = 115385$ and $\mu_0 = 76923$. The finite element discretization consists of $4\times4$ bilinear Q1Q1 elements. For the spatial motion problem, the horizontal displacement of upper and lower edge, which are subjected to tension, are constrained. The specimen is loaded by displacement increments 0.0025 h, up to a final displacement of 0.5 h. Different boundary conditions have been taken for the material motion problem, in correspondence with the cases studied by Müller & Maugin [158]. Firstly, keeping all nodes fixed a Lagrangian description is obtained that serves to calculate material forces, as is depicted in figure 5.8, left. The total energy for this configuration is given as $\mathcal{I}^{\mathrm{lag}} = 11.6724$.

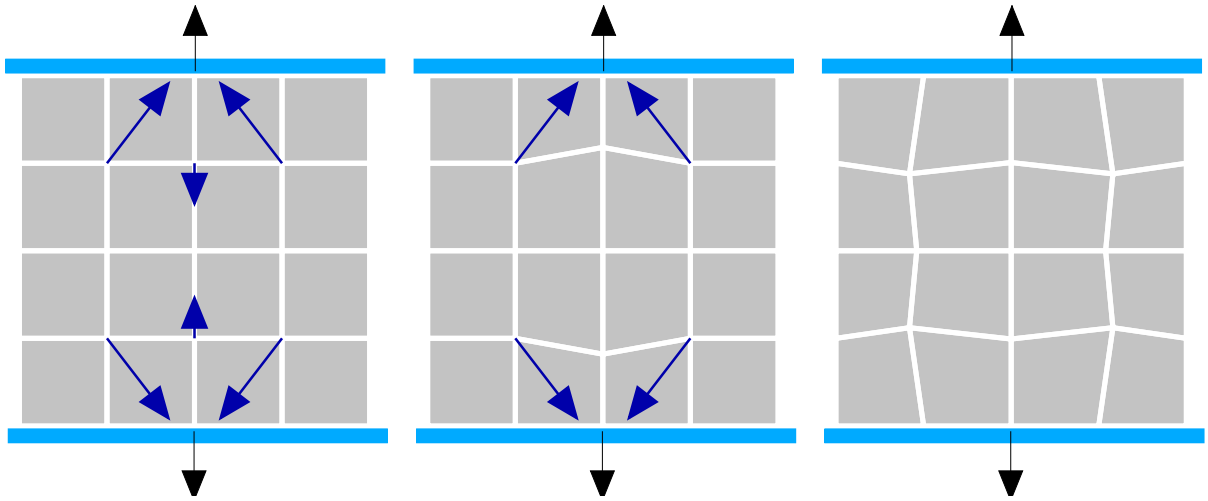

**Figure 5.8:** Homogeneous block under tension – 0, 2 and 12 material degrees of freedom

Secondly, only the second and fourth midnode on the vertical axis of symmetry are allowed to move, and only in the vertical direction, which corresponds to 2 degrees of freedom in the material motion problem. The resulting material configuration $\mathcal{B}_0$ is shown in figure 5.8, middle. The material displacement $\tilde{\Phi}$ of the considered second and fourth midnode is found as 0.0301h, thus new vertical coordinates 0.2199h and 0.7801h are obtained, which agree perfectly with the results given by Müller & Maugin [158]. For this set of boundary conditions, the total energy is $\mathcal{I}^{\text{ale02}} = 11.6717$, which is somewhat below the value obtained with the purely Lagrangian analysis. Finally, all internal nodes are allowed to move, we thus have 12 degrees of freedom

| iteration | norm of residual | total energy $\mathcal{I}^{\text{ale12}}$ |
|---|---|---|
| 0 | 1.58114E-02 | 0.0000000000E+00 |
| 1 | 3.92275E+00 | 1.1672534150E+01 |
| 2 | 1.24279E+01 | 1.1669273828E+01 |
| 3 | 1.27318E+00 | 1.1668864896E+01 |
| 4 | 1.85232E-02 | 1.1668859084E+01 |
| 5 | 5.75864E-06 | 1.1668859082E+01 |
| 6 | 6.31087E-11 | 1.1668859082E+01 |

**Table 5.3:** Homogeneous block under tension – Quadratic convergence of Newton iteration

in the material motion problem. The resulting mesh is shown in figure 5.8, right. For this case, the total energy is $\mathcal{I}^{\text{ale12}} = 11.6688$, which is again lower than in the previous analysis. In short, $\mathcal{I}^{\text{ale12}} < \mathcal{I}^{\text{ale02}} < \mathcal{I}^{\text{lag}}$; that is, the more degrees of freedom are included in the material motion problem or the more nodes are allowed to move the more the total energy decreases. For a representative load step, the convergence of the Newton-Raphson iteration is illustrated in table 5.8. As can be verified, a quadratic convergence towards an optimal mesh is obtained, which is an important improvement compared to the 500 iterations reported by Müller & Maugin [158] needed to obtain the optimal mesh.

## 5.9 Example: Homogeneous block under bending

Next, the same square, homogeneous block is subjected to bending. The material parameters are the same as in the previous section. For the discretization, $8 \times 8$ bilinear Q1Q1 elements are used. The boundary conditions of the spatial motion problem consist of prescribed displacements at vertical edges, whereas the left and right midhight node of each vertical edge are held fixed completely. For the material motion problem, nodes of all edges are constrained horizontally and vertically for the ALE analysis, and all nodes are fixed for the comparative Lagrangian analysis. The specimen is loaded by applying horizontal displacements of 0.16 mm in 80 equal steps at the vertices of the specimen. In this example, inhomogeneities arise due to the nonlinearity, where it is noted that the structural behavior differs in tension and compression, thus elements will tend to concentrate in the compressive regions.

mesh I – material and spatial configuration $\mathcal{B}_0$ and $\mathcal{B}_t$ of Lagrangian analysis

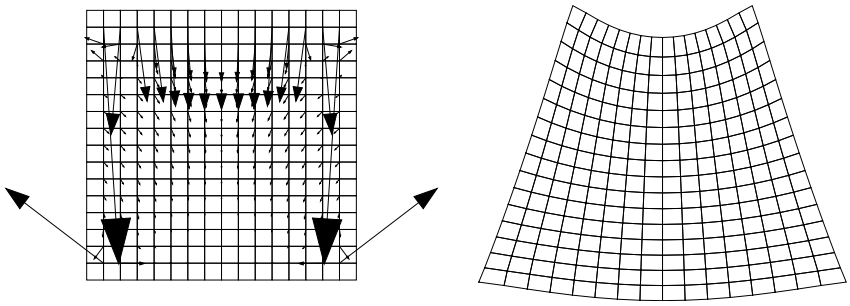

$\mathcal{I}^{\text{lag}} = 3657.3$

mesh I – material and spatial configuration $\mathcal{B}_0$ and $\mathcal{B}_t$ of ALE analysis

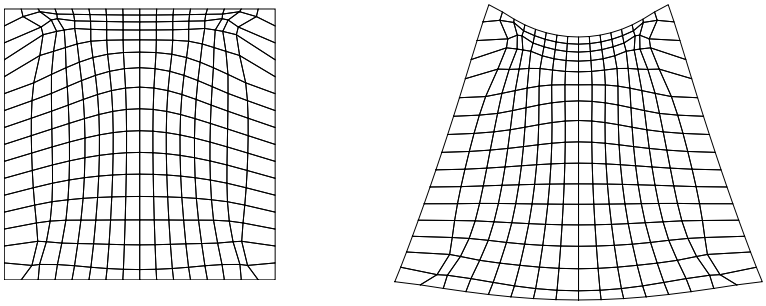

$\mathcal{I}^{\text{ale}} = 3650.7$

**Figure 5.9:** Homogeneous block under bending – Material and spatial configuration

mesh II – material and spatial configuration $\mathcal{B}_0$ and $\mathcal{B}_t$ of Lagrangian analysis

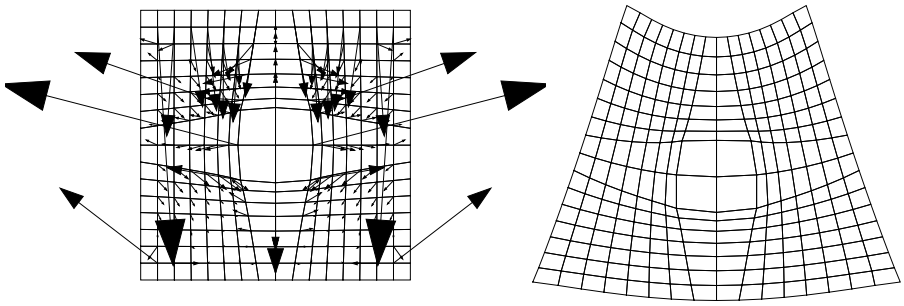

$\mathcal{I}^{\text{lag}} = 3660.6$

mesh II – material and spatial configuration $\mathcal{B}_0$ and $\mathcal{B}_t$ of ALE analysis

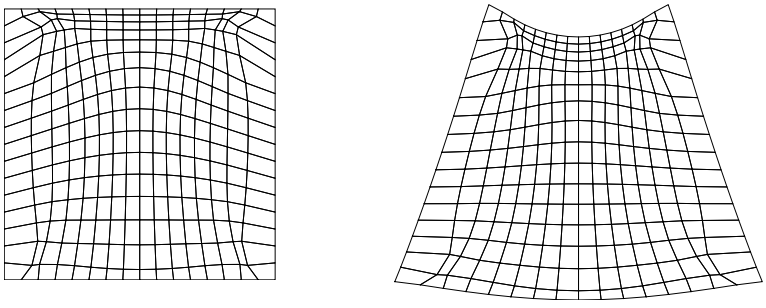

$\mathcal{I}^{\text{ale}} = 3650.7$

**Figure 5.10:** Homogeneous block under bending – Material and spatial configuration

mesh III – material and spatial configuration $\mathcal{B}_0$ and $\mathcal{B}_t$ of Lagrangian analysis

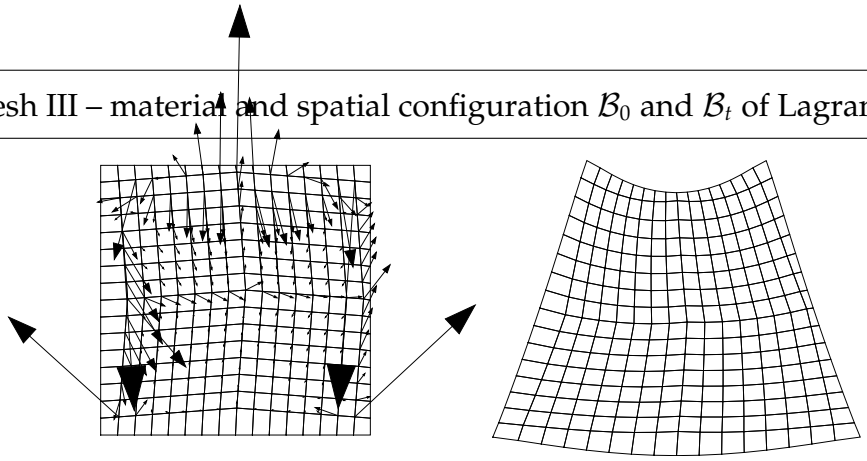

$\mathcal{I}^{\text{lag}} = 3655.8$

mesh III – material and spatial configuration $\mathcal{B}_0$ and $\mathcal{B}_t$ of ALE analysis

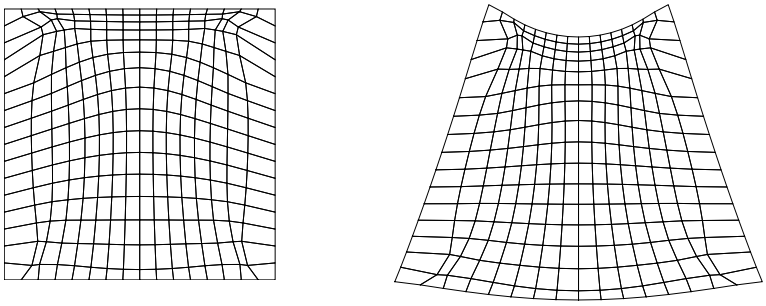

$\mathcal{I}^{\text{ale}} = 3650.7$

**Figure 5.11:** Homogeneous block under bending – Material and spatial configuration

mesh I – evolution of material configuration $\mathcal{B}_0$ of ALE analysis

$t = 0$ $t = 20$ $t = 40$ $t = 80$

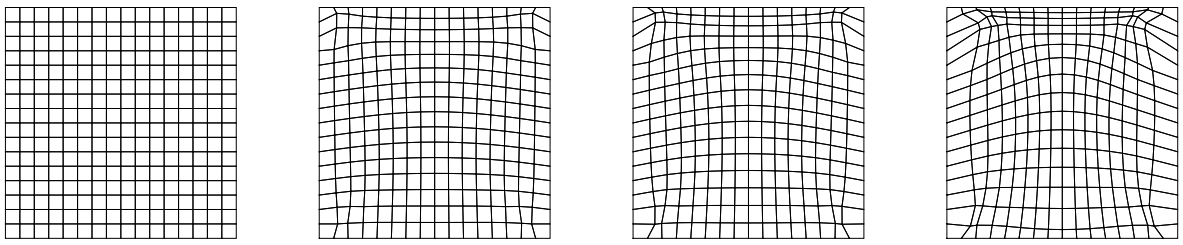

mesh I – evolution of spatial configuration $\mathcal{B}_t$ of ALE analysis

$t = 0$ $t = 20$ $t = 40$ $t = 80$

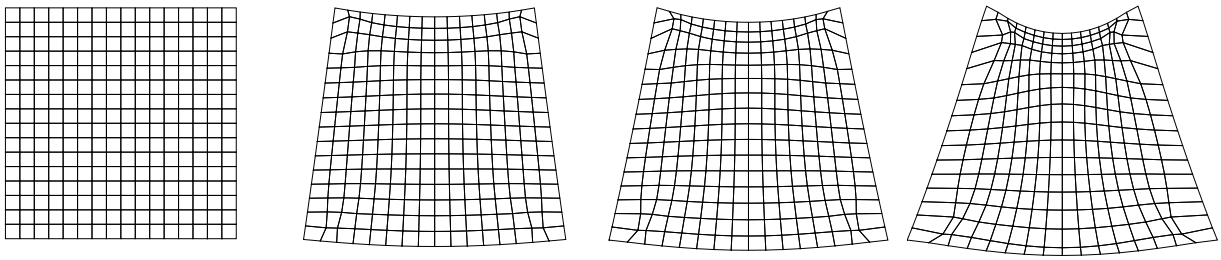

**Figure 5.12:** Homogeneous block under bending – Material and spatial configuration

Three different finite element discretizations have been used, one of which is regular. The other two are distorted versions of the regular mesh. Figures 5.9 to 5.11, top, show the results of the Lagrangian analyses for the three meshes, obtained by keeping $\tilde{\boldsymbol{\Phi}}$ fixed and thus $\boldsymbol{\varphi} \equiv \bar{\boldsymbol{\varphi}}$. On the left of figures 5.9 to 5.11, the material domains $\mathcal{B}_0$ with corresponding discrete material forces are shown, while on the right the corresponding spatial domains $\mathcal{B}_t$ are plotted. It is obvious, that different meshes lead to different discrete material force residuals. The total energy associated with these Lagrangian solutions is $\mathcal{I}^{\text{lag}}_{\text{meshI}} = 3657.3$, $\mathcal{I}^{\text{lag}}_{\text{meshII}} = 3660.6$ and $\mathcal{I}^{\text{lag}}_{\text{meshIII}} = 3655.8$, respectively. Clearly, the potential energies differ for the three meshes. The bottom row of figures 5.9 to 5.11 illustrates the results of the ALE approach with $\tilde{\boldsymbol{\Phi}}$ free, thus nodes of $\mathcal{B}_0$ are allowed to move freely in space. Remarkable, identical results are obtained with all three starting meshes. Furthermore, all ALE analyses lead to a total potential energy $\mathcal{I}^{\text{ale}}_{\text{meshI}} = \mathcal{I}^{\text{ale}}_{\text{meshII}} = \mathcal{I}^{\text{ale}}_{\text{meshIII}} = 3650.7$, which is independent of the initial discretization, and lower than the values obtained with either of the Lagrangian meshes. On the bottom, left of figures 5.9 to 5.11, the material domain $\mathcal{B}_0$ is shown. It is emphasized that here vanishing discrete material are found, since material node point positions are determined such that discrete material forces vanish identically. To illustrate the temporal evolution of the material and the spatial configuration for the simulation with the first starting mesh, figure 5.12 contrasts the different configurations at four different time steps for $t = 0$, $t = 20$, $t = 40$ and $t = 80$.

# 6 Closed systems

La chaleur pénètre, comme la gravité, toutes les substances de l'univers,ses rayons occupent toutes les parties de l'espace. Le but de notre ouvrage est d'exposer les lois mathématiques que suit cet élément. Cette théorie formera désormais une des branches importantes de la physique générale.

Joseph Fourier
Théorie Analytique de la Chaleur, 1807

## 6.1 Introduction

The present chapter deals with closed systems, i.e. thermodynamic systems which are allowed to exchange not only mechanical work but also heat with their surroundings. Closed systems typically introduce thermomechanical problems which are of particular importance for a number of industrial applications in civil, mechanical or aerospace engineering. Thereby, the coupling between the mechanical and the thermal response is twofold. On the one hand, we typically encounter thermally induced stresses, i.e. the deformation of the structure strongly depends on the temperature field it is subjected to. On the other hand, large deformations induce structural heating, a phenomenon which is classically referred to as Gough–Joule effect. Traditionally, thermodynamic effects are characterized in the spatial motion context within the framework of rational thermodynamics, see e.g. Truesdell & Toupin [210], Coleman & Noll [32], Truesdell & Noll [209] or the recent textbooks of Silhavý [191], Maugin [151], Haupt [91] or Liu [143]. Conceptually speaking, the underlying spatial setting of continuum thermodynamics considers the response to variations of spatial placements of particles with respect to the ambient space.
In a computational context, the basic concern is the evaluation of the spatial motion balance of momentum and energy, whereby the former essentially represents the equilibrium of spatial forces in the sense of Newton. The resulting coupled system of equations defines the evolution of the spatial deformation map and the temperature field. In a finite element context, first attempts towards a numerical solution of finite thermoelasticity date back to the early work of Oden [171]. A detailed analysis of different staggered solution techniques based on an isothermal or an adiabatic split can be found in Armero & Simo [4], compare also Miehe [157] or Holzapfel & Simo [99]. A comparison with a fully monolithic solution technique has been carried out by Miehe [154–156] and Simo [192]. In the present work, we shall focus on the simultaneous solution of the balance of momentum and energy, which has also been documented by Simo &

Miehe [193], Wriggers et al. [223], Holzapfel & Reiter [98], Reese & Govindjee [178], Reese & Wriggers [179], Reese [177] or Ibrahimbegovic et al. [112]. However, in contrast to most of the above mentioned references, we shall restrict ourselves to the thermohyperelastic case in the sequel.
The evolution of the deformation field and the temperature field is typically accompanied with the local rearrangement of material inhomogeneities which can be characterized elegantly within the material motion context, see e.g. the comprehensive overviews by Maugin [149, 150], Gurtin [83] or Kienzler & Herrmann [119] or the recent contributions by Steinmann [198, 200] and Kuhl & Steinmann [132]. In contrast to the spatial motion setting, the material motion setting of continuum thermodynamics is concerned with the response to variations of material placements of particles with respect to the ambient material. The material motion point of view is thus extremely prominent when dealing with defect mechanics to which it has originally been introduced by Eshelby [60, 61] more than half a century ago. In the context of closed system mechanics, its primary unknowns, the material deformation map and the temperature field are governed by the material motion balance of momentum, i.e. the balance of material forces on the material manifold in the sense of Eshelby, and the balance of energy.
From a computational point of view, the material version of the balance of momentum is particularly attractive since it renders additional information without requiring the solution of a completely new system of equations. Rather, it can be understood as a mere post–processing step once the spatial motion problem has been solved. Since the first numerical evaluation of the material force balance by Braun [20], the computational analysis of the material motion problem within the finite element framework has become a branch of active research. Herein, we shall adopt the so–called material force method as advocated by Steinmann et al. [197, 201] and Denzer et al. [46] in the context of linear and nonlinear elastic fracture mechanics. Due to its computational efficiency, the material force method has been applied to a number of different problem classes such as thermomechanics by Shih et al. [190] and Kuhl et al. [127], tire mechanics by Govindjee [76], classical fracture mechanics by Müller et al. [163] and Müller & Maugin [158], biomechanics by Kuhl & Steinmann [130, 135] or damage mechanics by Liebe et al. [141]. Since the resulting discrete material forces typically indicate a potential energy increase upon replacement of the material node point positions, spurious material forces can be utilized to improve the finite element mesh. To this end, Askes et al. [6] and Kuhl et al. [125] analyzed the staggered and the fully coupled solution of the spatial and the material motion balance of momentum introducing both, the spatial and the material motion map as primary unknowns. Within the present contribution, however, we shall restrict ourselves to a purely post–processing–based analysis of the material motion problem.
In hyperelastic applications, the discrete material node point forces can essentially be computed as a function of the material motion momentum flux, i.e. the static or dynamic Eshelby stress tensor. Nevertheless, for the class of thermoelastic problems considered herein, an additional contribution in the material motion momentum source has to be taken into account. In the context of thermodynamics, this additional term can basically be expressed as a function of the temperature gradient and the entropy

density. The elaboration of the influence of the temperature field on the material forces thus constitutes the main objective of the present chapter.
We will begin by briefly illustrating the thermomechanical coupling phenomena with the help of a one–dimensional model problem in section 6.2. Then, we shall summarize the governing equations of closed system thermomechanics in section 6.3. The residual statements of the balance of momentum and energy are then cast into their weak formats in section 6.4 before their temporal and spatial discretization is carried out in section 6.5. To illustrate the formal duality of the spatial and the material motion framework, we introduce both settings independently in each of the above–mentioned sections. Only at the end of each section, relations between the spatial and material motion quantities are pointed out. The consistent linearization of the governing equations and related algorithmic aspect are sketched in sections 6.6 and 6.7. Finally, the features of the presented model are illustrated with the help of some classical examples in sections 6.8 and 6.9.

## 6.2 Motivation

To motivate our closed system formulation for thermomechanical problems, let us have a closer look at the relevant thermomechanical interaction phenomena. Thereby, the coupling between the mechanical and the thermal field is typically twofold. On the one hand, we encounter a thermally induced deformation, on the other hand, deformations induce a structural heating which is commonly known as Gough–Joule effect. To study both phenomena independently, we consider a one–dimensional bi–material bar and elaborate first the case of temperature induced deformation and next the case of deformation induced temperature. To confine attention to thermal rather than elastic effects, the parameters of both materials are identical except for the thermal expansion coefficient $\alpha$. In the second half of the bar, the thermal expansion coefficient is chosen to be 10000 times smaller than in the first half, thus $\alpha_2 = \alpha_1 \,/\, 10000$.

**Temperature induced deformation** First, we consider the classical case of temperature induced deformation. To this end, the bar is clamped on both sides and a homogeneous temperature field $\theta$ is prescribed for the entire bar. During the first 20 time steps, the temperature is reduced to $-2^oC$ with respect to the reference temperature $\theta_0^*$, while during the next 120 time steps, it is increased again from $-2^oC$ to $+10^oC$. After the first 20 time steps, at a temperature of $\theta = \theta_0^* - 2^oC$, the displacement of the interface between the two materials reaches a value of $u_{\min} = -0.02998$, compare figure 6.1, left. According to the different thermal expansion coefficients, the first half of the bar exhibits a remarkable contraction which has to be compensated by the second half of the bar such that the interface is displaced in the direction of the material with the higher thermal expansion coefficient. During the cooling phase, the bar exhibits a uniform tensile stress which results in a spatial surface force of $\mathsf{f}^{\varphi}_{\text{sur}} = 0.15704$ at both ends of the bar. The corresponding material surface force which is identical to the material internal force takes the value of $\mathsf{F}^{\Phi}_{\text{sur}} = \mathsf{F}^{\Phi}_{\text{int}} = 0.166691$. Note, that the material volume force vanishes identically as $\mathsf{F}^{\Phi}_{\text{vol}} = 0$ due to the homogeneous temperature

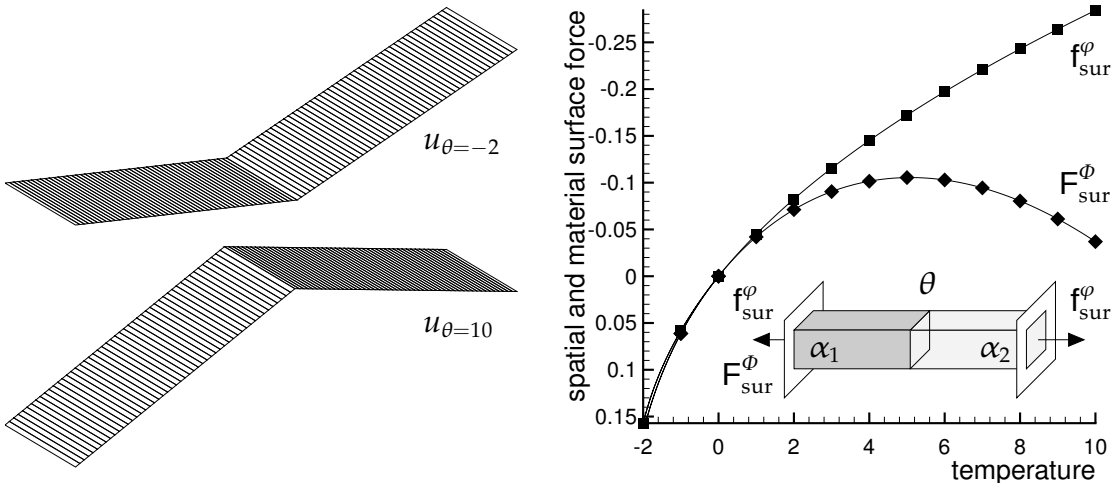


**Figure 6.1:** Temperature induced deformation – Spatial and material surface forces $f^{\varphi}_{sur}$ & $F^{\Phi}_{sur}$

distribution. Next, we increase the prescribed temperature over another 120 time steps to end up with a final temperature of $\theta = \theta_0^* + 10^oC$. The corresponding displacement of the interface thus takes the maximum value of $u_{max} = 0.01222$, compare figure 6.1, left. Under a homogeneous heating, the first half of the bar with the larger thermal expansion coefficient expands to a greater extend than the second half. The interface is thus displaced in the direction of the material with the lower thermal expansion coefficient. The spatial surface force thus takes values of $f^{\varphi}_{sur} = -0.28416$ at both ends of the bar while the material surface force only reaches a value of $F^{\Phi}_{sur} = F^{\Phi}_{int} = -.0369639$, compare figure 6.1, right. Recall that the material volume force vanishes identically as $F^{\Phi}_{vol} = 0$ due to the homogeneous temperature distribution.

**Deformation induced temperature** Next, the bi–material bar is loaded by a prescribed deformation at both ends. During the first 10 time steps, the bar is stretched under displacement control up to 120 % of its original length, then the prescribed deformation is held constant for another 90 time steps. After 10 time steps, at the end of the loading phase, the first half of the bar has cooled down to $\theta_1 = \theta_0^* - 4.14^oC$ while the temperature of the second half of the bar has not changed considerably as $\theta_2 = \theta_0^* - 0.000414^oC$. Figure 6.2, left visualizes the corresponding temperature distribution caused by the Gough–Joule effect. This effect is obviously more pronounced for larger thermal expansion coefficients $\alpha$. Due to the inhomogeneous temperature distribution, material volume forces arise at the interface. Since the material internal force at the interface is identical to zero as $F^{\Phi}_{int} = 0$, the material surface force corresponds identically to the material volume force $F^{\Phi}_{sur} = F^{\Phi}_{vol} = 7.23101$ which is essentially proportional to the temperature gradient. After another 90 time steps at constant deformation, the temperature has finally gone back to its reference value as $\theta_1 = \theta_2 = \theta_0^*$, compare figure 6.2, left. Due to thermal conductivity, inhomogeneous temperature distributions tend to equilibrate as time evolves. Correspondingly, the material volume force at the interface is reduced to $F^{\Phi}_{sur} = F^{\Phi}_{vol} = 0.16463$ indicating a nearly homogeneous temperature distribution.

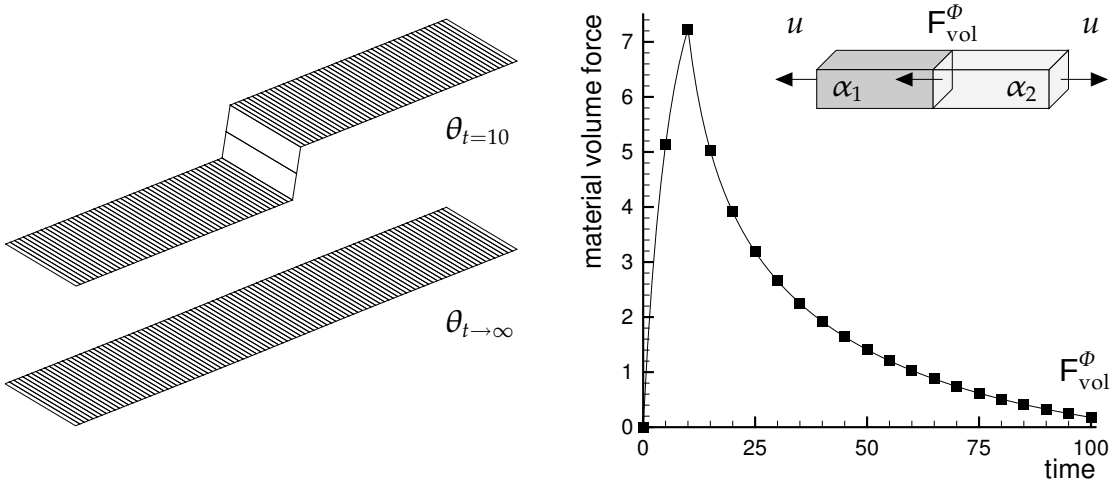


**Figure 6.2:** Deformation induced temperature – Material volume forces $F^{\Phi}_{vol}$

## 6.3 Governing equations

The following section is devoted to the derivation of the governing equations of closed system mechanics in the context of thermohyperelasticity. While the deformation problem is primarily governed by the balance of momentum, the temperature problem is characterized through the balance of energy. The latter can either be formulated in an energy or entropy based format or in the more familiar temperature based format. The latter is typically preferred since the temperature is readily available from related experiments while the energy or entropy cannot be accessed directly. After illustrating the derivation of the governing set of equations for the spatial and the material motion problem, relations between the individual spatial and material quantities will be given.

### 6.3.1 Spatial motion problem

For the spatial motion problem, the balance of momentum $(3.5.11)_1$ balances the rate of change of the spatial momentum density $\boldsymbol{p}_0$ with the momentum flux $\boldsymbol{\Pi}^t_D$, i.e. the first Piola–Kirchhoff stress tensor, and the momentum source $\boldsymbol{b}_0$.

$$\mathrm{D}_t\, \boldsymbol{p}_0 = \mathrm{Div}\, \boldsymbol{\Pi}^t_D + \boldsymbol{b}_0 \tag{6.3.1}$$

Recall that in general, the momentum source $\boldsymbol{b}_0$ consists of an external and an internal contribution as $\boldsymbol{b}_0 = \boldsymbol{b}_0^{\mathrm{ext}} + \boldsymbol{b}_0^{\mathrm{int}}$. The second fundamental balance equation in closed system thermodynamics is the balance of energy $(3.6.4)_1$, or to be more precise, the balance of internal energy $(3.6.7)_1$.

$$\mathrm{D}_t\, I_0 = -\mathrm{Div}\, \boldsymbol{Q}_D + \mathcal{Q}_0 + \boldsymbol{\Pi}^t : \mathrm{D_t}\boldsymbol{F} - \boldsymbol{v} \cdot \boldsymbol{b}_0^{\mathrm{int}} \tag{6.3.2}$$

Herein, $I_0$ denotes the internal energy density while $\boldsymbol{Q}_D$ and $\mathcal{Q}_0$ are the material heat flux vector and the material heat source, respectively. By making use of the Legendre–Fenchel transform as $\psi_0 = I_0 - \theta\, S_0$, we can express the internal energy $I_0$ in terms of

the Helmholtz free energy density $\psi_0$, the temperature $\theta$ and the entropy density $S_0$. The balance of energy can thus be expressed in the following entropy based format,

$$\theta \, \mathrm{D}_t \, S_0 = -\mathrm{Div} \, \boldsymbol{Q}_D + \mathcal{Q}_0 + \boldsymbol{\Pi}^t : \mathrm{D}_t \boldsymbol{F} - \boldsymbol{v} \cdot \boldsymbol{b}_0^{\mathrm{int}} - \mathrm{D}_t \psi_0 - S_0 \, \mathrm{D}_t \theta \tag{6.3.3}$$

or rather in short form as $\theta \, \mathrm{D}_t \, S_0 = -\mathrm{Div} \, \boldsymbol{Q}_D + \mathcal{Q}_0 + \mathsf{d}_0^{\mathrm{loc}}$ with $\mathsf{d}_0^{\mathrm{loc}}$ denoting the local dissipation rate for closed systems. With the free energy for closed systems $\psi_0 = \psi_0 \left( \boldsymbol{F}, \theta; \boldsymbol{X} \right)$ we readily obtain the corresponding definitions of the first Piola–Kirchhoff stress $\boldsymbol{\Pi}^t = \mathrm{D}_F \psi_0$, the specific entropy density $S_0 = -\mathrm{D}_\theta \psi_0$ and the internal volume forces $\boldsymbol{b}_0^{\mathrm{int}} = \boldsymbol{0}$ according to equations (4.2.12). Consequently, the last four terms in equation (6.3.3), or rather the local dissipation rate $\mathsf{d}_0^{\mathrm{loc}}$, vanish identically.

$$\theta \, \mathrm{D}_t \, S_0 = -\mathrm{Div} \, \boldsymbol{Q}_D + \mathcal{Q}_0 \tag{6.3.4}$$

In most practical applications, however, it proves more convenient to work with the temperature based format rather then with the entropy based format (6.3.4) since the temperature can be measured directly in the experiment. To this end, the material time derivative of the entropy density $S_0 = -\mathrm{D}_\theta \psi_0 \left( \boldsymbol{F}, \theta; \boldsymbol{X} \right)$ is expressed in the following form, $\mathrm{D}_t \, S_0 = -\mathrm{D}_{\theta \boldsymbol{F}} \, \psi_0 : \mathrm{D}_t \boldsymbol{F} - \mathrm{D}_{\theta\theta} \, \psi_0 \, \mathrm{D}_t \, \theta$ or rather as $\mathrm{D}_t \, S_0 = -\mathrm{D}_\theta \, \boldsymbol{\Pi}^t : \mathrm{D}_t \boldsymbol{F} + \mathrm{D}_\theta \, S_0 \, \mathrm{D}_t \, \theta$. With these results at hand, we can recast the entropy based balance of energy (6.3.4) in its more familiar temperature based format,

$$c_0 \, \mathrm{D}_t \, \theta = -\mathrm{Div} \, \boldsymbol{Q}_D + \mathcal{Q}_0 + \mathcal{Q}_0^{\mathrm{mech}} \tag{6.3.5}$$

by introducing the specific material heat capacity at constant deformation $c_0 = \theta \, \mathrm{D}_\theta \, S_0$ and the thermomechanical coupling term $\mathcal{Q}_0^{\mathrm{mech}} = \theta \, \mathrm{D}_\theta \boldsymbol{\Pi}^t : \mathrm{D}_t \boldsymbol{F}$ which is typically responsible for the so–called Gough–Joule effect.

### 6.3.2 Material motion problem

Conceptually speaking, the balance of momentum of the material motion problem follows from a complete projection of the classical momentum balance (6.3.1) onto the material manifold. As such, it balances the time rate of change of the material momentum density $\boldsymbol{P}_0$ with the material momentum flux $\boldsymbol{\pi}_D^t$, i.e. a two–field version of the energy momentum tensor, and momentum source $\boldsymbol{B}_t$, compare equation $(3.5.32)_2$.

$$j \, \mathrm{D}_t \, \boldsymbol{P}_0 = \mathrm{div} \, \boldsymbol{\pi}_D^t + \boldsymbol{B}_t \tag{6.3.6}$$

Note that in the transient case, the classical static material momentum flux $\boldsymbol{\pi}^t$ has to be modified by the correction term $K_t \, \boldsymbol{F}^t$ in terms of the kinetic energy density $K_t = \rho_t \boldsymbol{V} \cdot \boldsymbol{C} \cdot \boldsymbol{V}/2$ such that $\boldsymbol{\pi}_D^t = \boldsymbol{\pi}^t - K_t \, \boldsymbol{F}^t$. Likewise, the material volume force $\boldsymbol{B}_t = \boldsymbol{B}_t^{ext} + \boldsymbol{B}_t^{\mathrm{int}} + \partial_{\boldsymbol{\Phi}} K_t$ which typically consists of an external and an internal contribution alone contains an additional transient term $\partial_{\boldsymbol{\Phi}} K_t$. The balance of internal energy of the material motion problem can be stated in the following form,

$$j \, \mathrm{D}_t \, I_0 = -\mathrm{div} \, \boldsymbol{q}_D + \mathcal{Q}_t + j \, \boldsymbol{\Pi}^t : \mathrm{D}_t \boldsymbol{F} - \boldsymbol{v} \cdot \boldsymbol{b}_t^{\mathrm{int}} \tag{6.3.7}$$

with $I_0$ being the internal energy density and $\boldsymbol{q}_D$ and $\mathcal{Q}_t$ denoting the spatial heat flux vector and the heat source, compare equation $(3.6.7)_2$. Similar to the spatial motion

problem, we then make use of the Legendre–Fenchel transform $\psi_0 = I_0 - \theta\, S_0$ to replace the internal energy density $I_0$ and obtain the following entropy based format of the energy equation.

$$j\,\theta\,\mathrm{D}_t\,S_0 = -\mathrm{div}\,\boldsymbol{q}_D + \mathcal{Q}_t + j\,\boldsymbol{\Pi}^t : \mathrm{D}_t\boldsymbol{F} - \boldsymbol{v}\cdot\boldsymbol{b}_t^{\mathrm{int}} - j\,\mathrm{D}_t\psi_0 - S_t\,\mathrm{D}_t\theta \tag{6.3.8}$$

The above statement can equivalently be expressed as $j\,\theta\,\mathrm{D}_t\,S_0 = -\mathrm{div}\,\boldsymbol{q}_D + \mathcal{Q}_t + \mathsf{d}_t^{\mathrm{loc}}$ with $\mathsf{d}_t^{\mathrm{loc}} = 0$ vanishing identically, such that the dissipation inequality $\mathsf{d}_t \geq 0$ is a priori guaranteed for the class of thermohyperelastic materials considered in the sequel. Next, we introduce the free energy density for closed thermodynamic systems $\psi_t = \psi_t\,(\boldsymbol{f}, \theta, \boldsymbol{\Phi})$ as a function of the material motion deformation gradient $\boldsymbol{f}$, the absolute temperature $\theta$ and the material placement $\boldsymbol{\Phi}$. The evaluation of the material motion version of the Clausius–Planck inequality renders the definition of the material motion momentum flux $\boldsymbol{\pi}^t = \mathrm{d}_f\psi_t$ as thermodynamically conjugate variable to the material motion deformation gradient $\boldsymbol{f}$, the entropy density $S_0 = -\mathrm{D}_\theta\psi_0$ as conjugate variable to the temperature $\theta$ and the definition of the internal forces $\boldsymbol{B}_t^{\mathrm{int}} = S_t\,\nabla_X\theta - \partial_{\boldsymbol{\Phi}}\psi_t$ which are generally different from zero in the material setting, compare (4.2.23). Similar to the spatial motion problem, the entropy based version of the balance of energy can thus be expressed in the following form.

$$j\,\theta\,\mathrm{D}_t\,S_0 = -\mathrm{div}\,\boldsymbol{q}_D + \mathcal{Q}_t \tag{6.3.9}$$

With the material time derivative of the of the entropy density $\mathrm{D}_t\,S_0 = -\mathrm{D}_\theta\,\boldsymbol{\Pi}^t : \mathrm{D}_t\boldsymbol{F} + \mathrm{D}_\theta\,S_0\,\mathrm{D}_t\,\theta$ equation (6.3.9) can then be cast into its more familiar temperature based format.

$$c_t\,\mathrm{D}_t\,\theta = -\mathrm{div}\,\boldsymbol{q}_D + \mathcal{Q}_t + \mathcal{Q}_t^{\mathrm{mech}} \tag{6.3.10}$$

**Remark 6.3.1 (Spatial vs. material motion problem)** *While the material motion version of the balance of momentum follows from a complete projection of its spatial motion counterpart onto the material manifold, the material motion version of the balance of energy is simply related to its spatial version through a multiplication with the related Jacobian. We can thus set up the following relations between the spatial and material motion momentum densities and the corresponding flux and source terms.*

$$\begin{aligned}
\boldsymbol{P}_0 &= -\ \ \boldsymbol{F}^t\cdot\boldsymbol{p}_0 \\
\boldsymbol{\pi}_D^t &= -j\ \boldsymbol{F}^t\cdot\boldsymbol{\Pi}_D^t\cdot\boldsymbol{F}^t + j\,\psi_0\,\boldsymbol{F}^t \\
\boldsymbol{B}_t &= -j\ \boldsymbol{F}^t\cdot\boldsymbol{b}_0 + j\,S_0\,\nabla_X\theta + j\,\partial_{\boldsymbol{\Phi}}[\,K_0 - \psi_0\,]
\end{aligned} \tag{6.3.11}$$

*The related transformation formulae for the scalar– and vector–valued quantities of the balance of energy simply follow from the appropriate weighting with the Jacobian $c_t = j\,c_0$, $\mathcal{Q}_t = j\,\mathcal{Q}_0$, $\mathcal{Q}_t^{\mathrm{mech}} = j\,\mathcal{Q}_0^{\mathrm{mech}}$, $\mathsf{d}_t^{\mathrm{loc}} = j\,\mathsf{d}_0^{\mathrm{loc}}$ and from the corresponding Piola transform as $\boldsymbol{q}_D = j\,\boldsymbol{Q}_D\cdot\boldsymbol{f}^{-t}$.*

## 6.4 Weak form

As a prerequisite for the finite element formulation that will be derived in chapter 6.5, we shall reformulate the balance of momentum and energy in their weak format.

### 6.4.1 Spatial motion problem

The weak form of the spatial motion problem is based on the global residual statements of the balance of momentum and the temperature based version of the balance of energy

$$\begin{aligned} \mathbf{r}^{\varphi}\,(\boldsymbol{\varphi},\theta) &= \mathbf{f}^{\varphi}_{\mathrm{dyn}} - \mathbf{f}^{\varphi}_{\mathrm{sur}} - \mathbf{f}^{\varphi}_{\mathrm{vol}} = \mathbf{0} \\ \mathsf{r}^{\theta}\,(\boldsymbol{\varphi},\theta) &= \mathsf{f}^{\theta}_{\mathrm{dyn}} - \mathsf{f}^{\theta}_{\mathrm{sur}} - \mathsf{f}^{\theta}_{\mathrm{vol}} = 0 \end{aligned} \tag{6.4.1}$$

whereby the dynamic, the surface and the volume contribution expand in the following expressions.

$$\begin{aligned} \mathbf{f}^{\varphi}_{\mathrm{dyn}} &= \int_{\mathcal{B}_0} \mathrm{D}_t\,\boldsymbol{p}_0\,\mathrm{d}V_0 & \mathbf{f}^{\varphi}_{\mathrm{sur}} &= \int_{\partial\mathcal{B}_0} \boldsymbol{\Pi}^t_D\cdot\boldsymbol{N}\,\mathrm{d}A_0 & \mathbf{f}^{\varphi}_{\mathrm{vol}} &= \int_{\mathcal{B}_0} \boldsymbol{b}_0\,\mathrm{d}V_0 \\ \mathsf{f}^{\theta}_{\mathrm{dyn}} &= \int_{\mathcal{B}_0} c_0\,\mathrm{D}_t\,\theta\,\mathrm{d}V_0 & \mathsf{f}^{\theta}_{\mathrm{sur}} &= \int_{\partial\mathcal{B}_0} -\boldsymbol{Q}_D\cdot\boldsymbol{N}\,\mathrm{d}A_0 & \mathsf{f}^{\theta}_{\mathrm{vol}} &= \int_{\mathcal{B}_0} \mathcal{Q}_0 + \mathcal{Q}_0^{\mathrm{mech}}\,\mathrm{d}V_0 \end{aligned} \tag{6.4.2}$$

The residual statements (6.4.1) are supplemented by appropriate boundary conditions for the mechanical and the thermal fields. For the deformation problem $(6.4.1)_1$, the boundary $\partial\mathcal{B}_0$ is decomposed into disjoint parts as $\partial\mathcal{B}_0^{\varphi}\cup\partial\mathcal{B}_0^{t}=\partial\mathcal{B}_0$ and $\partial\mathcal{B}_0^{\varphi}\cap\partial\mathcal{B}_0^{t}=\emptyset$. Correspondingly, for the temperature problem $(6.4.1)_2$, the equivalent decomposition renders the disjoint boundary contributions $\partial\mathcal{B}_0^{\theta}\cup\partial\mathcal{B}_0^{q}=\partial\mathcal{B}_0$ and $\partial\mathcal{B}_0^{\theta}\cap\partial\mathcal{B}_0^{q}=\emptyset$. Dirichlet boundary conditions are prescribed for the deformation $\boldsymbol{\varphi}$ and the temperature $\theta$ on $\mathcal{B}_0^{\varphi}$ and $\mathcal{B}_0^{\theta}$, whereas Neumann boundary can be introduced for the momentum flux $\boldsymbol{\Pi}^t$ and the heat flux $\boldsymbol{Q}$ on $\partial\mathcal{B}_0^{t}$ and $\partial\mathcal{B}_0^{q}$ in terms of the outward normal $\boldsymbol{N}$.

$$\begin{aligned} \boldsymbol{\varphi} &= \bar{\boldsymbol{\varphi}} \quad \text{on} \quad \partial\mathcal{B}_0^{\varphi} & \boldsymbol{\Pi}^t_D\cdot\boldsymbol{N} &= \bar{\boldsymbol{t}} \quad \text{on} \quad \partial\mathcal{B}_0^{t} \\ \theta &= \bar{\theta} \quad \text{on} \quad \partial\mathcal{B}_0^{\theta} & \boldsymbol{Q}_D\cdot\boldsymbol{N} &= \bar{q} \quad \text{on} \quad \partial\mathcal{B}_0^{q} \end{aligned} \tag{6.4.3}$$

By testing the local residual statements corresponding to $(6.4.1)_1$ and $(6.4.1)_2$ and the related Neumann boundary conditions $(6.4.3)_2$ and $(6.4.3)_4$ with the vector– and scalar–valued test functions $\boldsymbol{w}$ and $\vartheta$, respectively, we can derive the corresponding weak forms

$$\begin{aligned} \mathsf{g}^{\varphi}\,(\,\boldsymbol{w};\boldsymbol{\varphi},\theta\,) &= \mathsf{w}^{\varphi}_{\mathrm{dyn}} + \mathsf{w}^{\varphi}_{\mathrm{int}} - \mathsf{w}^{\varphi}_{\mathrm{sur}} - \mathsf{w}^{\varphi}_{\mathrm{vol}} = 0 \quad \forall\,\boldsymbol{w} \;\text{ in }\; H^1_0(\mathcal{B}_0) \\ \mathsf{g}^{\theta}\,(\;\vartheta;\boldsymbol{\varphi},\theta\,) &= \mathsf{w}^{\theta}_{\mathrm{dyn}} + \mathsf{w}^{\theta}_{\mathrm{int}} - \mathsf{w}^{\theta}_{\mathrm{sur}} - \mathsf{w}^{\theta}_{\mathrm{vol}} = 0 \quad \forall\,\vartheta \;\text{ in }\; H^1_0(\mathcal{B}_0) \end{aligned} \tag{6.4.4}$$

provided that the related fields fulfill the necessary smoothness and boundary assumptions. By interpreting the vector–valued test function $\boldsymbol{w}$ as the spatial virtual displacement $\boldsymbol{w}=\delta\boldsymbol{\varphi}$, equation $(6.4.4)_1$ can be identified as the virtual work expression of the spatial motion problem with the dynamic, the internal, the surface and the volume parts of the virtual work given in the familiar form.

$$\begin{aligned} \mathsf{w}^{\varphi}_{\mathrm{dyn}} &= \int_{\mathcal{B}_0} \boldsymbol{w}\cdot\mathrm{D}_t\,\boldsymbol{p}_0\,\mathrm{d}V_0 & \mathsf{w}^{\varphi}_{\mathrm{int}} &= \int_{\mathcal{B}_0} \nabla_X\boldsymbol{w} : \boldsymbol{\Pi}^t_D\,\mathrm{d}V_0 \\ \mathsf{w}^{\varphi}_{\mathrm{sur}} &= \int_{\partial\mathcal{B}_0^t} \boldsymbol{w}\cdot\boldsymbol{\Pi}^t_D\cdot\boldsymbol{N}\,\mathrm{d}A_0 & \mathsf{w}^{\varphi}_{\mathrm{vol}} &= \int_{\mathcal{B}_0} \boldsymbol{w}\cdot\boldsymbol{b}_0\,\mathrm{d}V_0 \end{aligned} \tag{6.4.5}$$

Accordingly, the scalar–valued test function $\vartheta$ can be interpreted as the virtual temperature $\delta\theta$. The dynamic, the internal, the surface and the volume contribution to the virtual temperature problem thus expand into the following expressions.

$$\begin{aligned} \mathsf{w}^{\theta}_{\text{dyn}} &= \int_{\mathcal{B}_0} \vartheta\, c_0\, \mathrm{D}_t\,\theta \;\; \mathrm{d}V_0 & \mathsf{w}^{\theta}_{\text{int}} &= \int_{\mathcal{B}_0} -\nabla_X \vartheta \cdot \boldsymbol{Q}_D \;\; \mathrm{d}V_0 \\ \mathsf{w}^{\theta}_{\text{sur}} &= \int_{\partial\mathcal{B}^q_0} -\vartheta\, \boldsymbol{Q}_D \cdot \boldsymbol{N}\, \mathrm{d}A_0 & \mathsf{w}^{\theta}_{\text{vol}} &= \int_{\mathcal{B}_0} \vartheta\, [\mathcal{Q}_0 + \mathcal{Q}^{\text{mech}}_0]\, \mathrm{d}V_0 \end{aligned} \tag{6.4.6}$$

### 6.4.2 Material motion problem

Guided by arguments of duality, the global residual statements of the balance of momentum and energy of the material motion problem can be introduced in complete analogy to their spatial motion counterparts.

$$\begin{aligned} \mathbf{R}^{\Phi} &= \mathbf{F}^{\Phi}_{\text{dyn}} - \mathbf{F}^{\Phi}_{\text{sur}} - \mathbf{F}^{\Phi}_{\text{vol}} = \mathbf{0} \\ \mathsf{R}^{\theta} &= \mathsf{F}^{\theta}_{\text{dyn}} - \mathsf{F}^{\theta}_{\text{sur}} - \mathsf{F}^{\theta}_{\text{vol}} = 0 \end{aligned} \tag{6.4.7}$$

The dynamic, the surface and the internal contribution to both equations can be expressed in the following form.

$$\begin{aligned} \mathbf{F}^{\Phi}_{\text{dyn}} &= \int_{\mathcal{B}_t} j\, \mathrm{D}_t\, \boldsymbol{P}_0\, \mathrm{d}V_t & \mathbf{F}^{\Phi}_{\text{sur}} &= \int_{\partial\mathcal{B}_t} \boldsymbol{\pi}^t_D \cdot \boldsymbol{n}\, \mathrm{d}A_t & \mathbf{F}^{\Phi}_{\text{vol}} &= \int_{\mathcal{B}_t} \boldsymbol{B}_t \;\; \mathrm{d}V_t \\ \mathsf{F}^{\theta}_{\text{dyn}} &= \int_{\mathcal{B}_t} c_t\, \mathrm{D}_t\, \theta \;\; \mathrm{d}V_t & \mathsf{F}^{\theta}_{\text{sur}} &= \int_{\partial\mathcal{B}_t} -\boldsymbol{q}_D \cdot \boldsymbol{n}\, \mathrm{d}A_t & \mathsf{F}^{\theta}_{\text{vol}} &= \int_{\mathcal{B}_t} \mathcal{Q}_t + \mathcal{Q}^{\text{mech}}_t\, \mathrm{d}V_t \end{aligned} \tag{6.4.8}$$

Next, Dirichlet and Neumann boundary conditions can be defined for the material motion problem to illustrate the formal duality with the spatial motion problem. For the balance of momentum $(6.4.7)_1$, the corresponding parts of the boundary will be introduced as $\partial\mathcal{B}^{\Phi}_t \cup \partial\mathcal{B}^{T}_t = \partial\mathcal{B}_t$ and $\partial\mathcal{B}^{\Phi}_t \cap \partial\mathcal{B}^{T}_t = \emptyset$ while for the balance of energy $(6.4.7)_2$, they read $\partial\mathcal{B}^{\theta}_t \cup \partial\mathcal{B}^{Q}_t = \partial\mathcal{B}_t$ and $\partial\mathcal{B}^{\theta}_t \cap \partial\mathcal{B}^{Q}_t = \emptyset$. Accordingly, the corresponding boundary conditions can be expressed in the following form.

$$\begin{aligned} \boldsymbol{\Phi} &= \bar{\boldsymbol{\Phi}} \quad \text{on} \quad \partial\mathcal{B}^{\Phi}_t & \boldsymbol{\pi}^t_D \cdot \boldsymbol{n} &= \bar{\boldsymbol{T}} \quad \text{on} \quad \partial\mathcal{B}^{T}_t \\ \theta &= \bar{\theta} \quad \text{on} \quad \partial\mathcal{B}^{\theta}_t & \boldsymbol{q}_D \cdot \boldsymbol{n} &= \bar{Q} \quad \text{on} \quad \partial\mathcal{B}^{Q}_t \end{aligned} \tag{6.4.9}$$

By testing the pointwise statements of the material momentum and energy balance $(6.4.7)_1$ and $(6.4.7)_2$ and the related Neumann boundary conditions $(6.4.9)_2$ and $(6.4.9)_4$ with the vector– and scalar–valued test functions $\boldsymbol{W}$ and $\vartheta$, we obtain the weak forms of the material motion problem.

$$\begin{aligned} \mathsf{G}^{\Phi}(\boldsymbol{W}; \theta, \boldsymbol{\Phi}) &= \mathsf{W}^{\Phi}_{\text{dyn}} + \mathsf{W}^{\Phi}_{\text{int}} - \mathsf{W}^{\Phi}_{\text{sur}} - \mathsf{W}^{\Phi}_{\text{vol}} = 0 \qquad \forall\, \boldsymbol{W} \;\; \text{in} \;\; H^1_0(\mathcal{B}_t) \\ \mathsf{G}^{\theta}(\;\vartheta; \theta, \boldsymbol{\Phi}) &= \mathsf{W}^{\theta}_{\text{dyn}} + \mathsf{W}^{\theta}_{\text{int}} - \mathsf{W}^{\theta}_{\text{sur}} - \mathsf{W}^{\theta}_{\text{vol}} = 0 \qquad \forall\, \vartheta \;\; \text{in} \;\; H^1_0(\mathcal{B}_t) \end{aligned} \tag{6.4.10}$$

Note that by interpreting the test function $\boldsymbol{W}$ as the material virtual displacement $\boldsymbol{W} = \delta\boldsymbol{\Phi}$, equation $(6.4.10)_1$ can be interpreted as the material counterpart of the classical virtual work expression $(6.4.4)_1$. Accordingly, $\mathsf{W}^{\Phi}_{\text{dyn}}$ and $\mathsf{W}^{\Phi}_{\text{int}}$ denote the dynamic

and the internal virtual work, while $\mathsf{W}^{\Phi}_{\text{sur}}$ and $\mathsf{W}^{\Phi}_{\text{vol}}$ are the corresponding surface and volume contributions.

$$\begin{aligned} \mathsf{W}^{\Phi}_{\text{dyn}} &= \int_{\mathcal{B}_t} \boldsymbol{W} \cdot \, j \, \mathrm{D}_t \boldsymbol{P}_0 \, \mathrm{d}V_t \qquad \mathsf{W}^{\Phi}_{\text{int}} = \int_{\mathcal{B}_t} \nabla_x \boldsymbol{W} : \boldsymbol{\pi}^t_D \, \mathrm{d}V_t \\ \mathsf{W}^{\Phi}_{\text{sur}} &= \int_{\partial\mathcal{B}^T_t} \boldsymbol{W} \cdot \, \boldsymbol{\pi}^t_D \cdot \boldsymbol{n} \, \mathrm{d}A_t \qquad \mathsf{W}^{\Phi}_{\text{vol}} = \int_{\mathcal{B}_t} \boldsymbol{W} \cdot \boldsymbol{B}_t \, \mathrm{d}V_t \end{aligned} \tag{6.4.11}$$

Furthermore, the dynamic, the internal, the surface and the volume contribution to the weak form of the energy balance $(6.4.10)_2$ expand into the following formats.

$$\begin{aligned} \mathsf{W}^{\theta}_{\text{dyn}} &= \int_{\mathcal{B}_t} \vartheta \, c_t \, \mathrm{D}_t \theta \, \mathrm{d}V_t \qquad \mathsf{W}^{\theta}_{\text{int}} = \int_{\mathcal{B}_t} -\nabla_x \vartheta \cdot \boldsymbol{q}_D \quad \mathrm{d}V_t \\ \mathsf{W}^{\theta}_{\text{sur}} &= \int_{\partial\mathcal{B}^Q_t} - \vartheta \, \boldsymbol{q}_D \cdot \boldsymbol{n} \, \mathrm{d}A_t \qquad \mathsf{W}^{\theta}_{\text{vol}} = \int_{\mathcal{B}_t} \vartheta \, [\mathcal{Q}_t + \mathcal{Q}^{\text{mech}}_t] \, \mathrm{d}V_t \end{aligned} \tag{6.4.12}$$

**Remark 6.4.1 (Spatial vs. material test functions)** *While the scalar–valued test function $\vartheta$ testing the balance of energy is identical for the spatial and the material motion problem, the vector–valued test functions $\boldsymbol{w}$ and $\boldsymbol{W}$ are related by the fundamental relations $\boldsymbol{w} = -\boldsymbol{W} \cdot \boldsymbol{F}^t$ and $\boldsymbol{W} = -\boldsymbol{w} \cdot \boldsymbol{f}^t$ which can be verified easily by transforming the virtual work statements of the spatial and the material motion problem $(6.4.4)_2$ and $(6.4.10)_2$ into one another.*

**Remark 6.4.2 (Spatial vs. material forces)** *Note that equations $(6.4.2)_1$ define the different contributions to the spatial forces $\mathbf{f}^{\,\varphi}$ representing the traditional forces in the sense of Newton. These are generated by variations relative to the ambient space at fixed material position $\boldsymbol{X}$. On the contrary, equations $(6.4.8)_1$ define material forces $\mathbf{F}^{\Phi}$ in the sense of Eshelby which are generated by variations relative to the ambient material at fixed spatial position $\boldsymbol{x}$. These material forces represent important measures in the mechanics of material inhomogeneities.*

**Remark 6.4.3 (Material force method)** *Recall that for the spatial motion problem, the surface and the volume contributions to the weak forms (6.4.4), namely $\mathsf{w}^{\varphi}_{\text{sur}}$ and $\mathsf{w}^{\varphi}_{\text{vol}}$ for the deformation problem and $\mathsf{w}^{\theta}_{\text{sur}}$ and $\mathsf{w}^{\theta}_{\text{vol}}$ for the temperature problem typically represent given quantities which define the primary unknowns $\boldsymbol{\varphi}$ and $\theta$. Once the spatial motion problem is solved, the dynamic term $\mathsf{W}^{\Phi}_{\text{dyn}}$, the internal virtual work $\mathsf{W}^{\Phi}_{\text{int}}$ and the volume contribution $\mathsf{W}^{\Phi}_{\text{vol}}$ to the material momentum balance can be computed directly. Correspondingly, the material surface forces $\mathbf{F}^{\Phi}_{\text{sur}}$ furnish the primary unknown of the material motion problem. Their numerical evaluation has been advocated as material force method by Steinmann et al. [201], see also Denzer et al. [46], Kuhl et al. [127,135] or Liebe et al. [141].*

## 6.5 Discretization

Equations (6.4.4) and (6.4.10) define the weak forms of the initial boundary value problem of thermohyperelasticity for the spatial and the material motion problem. Traditionally, these equations are first discretized in time, typically with finite difference schemes, before a spatial discretization with the finite element method can be carried out. To this end, consider a partition of the time interval of interest $\mathcal{T}$

$$\mathcal{T} = \bigcup_{n=0}^{n_{\text{step}}-1} [\, t_n, t_{n+1} \,] \tag{6.5.1}$$

and focus on the typical subinterval $[\,t_n, t_{n+1}\,]$ whereby $\Delta t = t_{n+1} - t_n$ denotes the corresponding actual time increment. Assume that the primary unknowns, either the spatial or the material deformation $\boldsymbol{\varphi}_n$ or $\boldsymbol{\Phi}_n$ and the temperature $\theta_n$ and all derivable quantities are known at time $t_n$. In what follows, we shall make use of the classical Euler backward integration scheme to advance the solution in time from the known time step $t_n$ to the actual time step $t_{n+1}$. Consequently, the first order material time derivatives of the spatial and the material momentum $\boldsymbol{p}_0$ and $\boldsymbol{P}_0$ and the temperature $\theta$ can be approximated in the following way.

$$\begin{aligned} \mathrm{D}_t\,\boldsymbol{p}_0 &= \frac{1}{\Delta t}\,[\;\boldsymbol{p}_{0\,n+1} - \boldsymbol{p}_{0\,n}\;] \\ \mathrm{D}_t\,\boldsymbol{P}_0 &= \frac{1}{\Delta t}\,[\;\boldsymbol{P}_{0\,n+1} - \boldsymbol{P}_{0\,n}\;] \\ \mathrm{D}_t\,\theta\;\; &= \frac{1}{\Delta t}\,[\;\;\theta_{n+1} - \theta_n\;\;] \end{aligned} \tag{6.5.2}$$

Moreover, the governing equations can now be reformulated in terms of the unknown spatial deformation $\boldsymbol{\varphi}_{n+1}$ and the temperature $\theta_{n+1}$ at time $t_{n+1}$ for the spatial motion problem

$$\begin{aligned} \mathsf{g}^{\varphi}_{n+1}\,(\;\boldsymbol{w};\boldsymbol{\varphi}_{n+1},\theta_{n+1}\;) &= \mathsf{w}^{\varphi}_{\mathrm{dyn}} + \mathsf{w}^{\varphi}_{\mathrm{int}} - \mathsf{w}^{\varphi}_{\mathrm{sur}} - \mathsf{w}^{\varphi}_{\mathrm{vol}} = 0 \qquad \forall\,\boldsymbol{w} \;\text{ in}\, H^0_1(\mathcal{B}_0) \\ \mathsf{g}^{\theta}_{n+1}\,(\;\;\vartheta;\boldsymbol{\varphi}_{n+1},\theta_{n+1}\;) &= \mathsf{w}^{\theta}_{\mathrm{dyn}} + \mathsf{w}^{\theta}_{\mathrm{int}} - \mathsf{w}^{\theta}_{\mathrm{sur}} - \mathsf{w}^{\theta}_{\mathrm{vol}} = 0 \qquad \forall\,\vartheta \;\text{ in}\, H^0_1(\mathcal{B}_0) \end{aligned} \tag{6.5.3}$$

and in terms of the material deformation $\boldsymbol{\Phi}_{n+1}$ and the temperature $\theta_{n+1}$ for the material motion problem.

$$\begin{aligned} \mathsf{G}^{\theta}_{n+1}(\;\;\vartheta;\theta_{n+1},\boldsymbol{\Phi}_{n+1}\;) &= \mathsf{W}^{\theta}_{\mathrm{dyn}} + \mathsf{W}^{\theta}_{\mathrm{int}} - \mathsf{W}^{\theta}_{\mathrm{sur}} - \mathsf{W}^{\theta}_{\mathrm{vol}} = 0 \qquad \forall\,\vartheta \;\text{ in}\, H^0_1(\mathcal{B}_t) \\ \mathsf{G}^{\Phi}_{n+1}(\boldsymbol{W};\theta_{n+1},\boldsymbol{\Phi}_{n+1}\;) &= \mathsf{W}^{\Phi}_{\mathrm{dyn}} + \mathsf{W}^{\Phi}_{\mathrm{int}} - \mathsf{W}^{\Phi}_{\mathrm{sur}} - \mathsf{W}^{\Phi}_{\mathrm{vol}} = 0 \qquad \forall\,\boldsymbol{W} \;\text{ in}\, H^0_1(\mathcal{B}_t) \end{aligned} \tag{6.5.4}$$

The semi–discrete weak forms (6.5.3) and (6.5.4) lend themselves readily to the spatial discretization within the finite element framework which will be illustrated in the following sections. For additional reading on general nonlinear finite element technologies we refer to the excellent textbooks by Crisfield [44, 45], Cook [33, 34], Bathe [11], Bonet & Wood [16], Belytschko et al. [14], Hughes [102], Wriggers [221,222] and Zienkiewicz & Taylor [226–228]. Additional details on thermomechanically coupled problems can be found e.g. in the textbook by Lewis et al. [140].

### 6.5.1 Spatial motion problem

Let $\mathcal{B}_0$ denote the region occupied by the reference configuration of a solid continuum body at time $t = t_0$. In the spirit of the finite element method, this reference domain is discretized in $e = 1,\ldots,n_{\mathrm{el}}$ elements $\mathcal{B}^e_0$. The underlying geometry $\boldsymbol{X}$ is interpolated elementwise by the shape functions $N^i_X$ in terms of the discrete node point positions $\boldsymbol{X}_i$ of the $i = 1,\ldots,n_{\mathrm{en}}$ element nodes.

$$\mathcal{B}_0 = \bigcup_{e=1}^{n_{\mathrm{el}}} \mathcal{B}^e_0 \qquad \boldsymbol{X}^h|_{\mathcal{B}^e_0} = \sum_{i=1}^{n_{\mathrm{en}}} N^i_X\,\boldsymbol{X}_i \tag{6.5.5}$$

According to the isoparametric concept, we shall interpolate the unknowns $\boldsymbol{\varphi}$ and $\theta$ on the element level with the same shape functions $N^i_\varphi$ and $N^j_\theta$ as the element geometry $\boldsymbol{X}$. In the spirit of the classical Bubnov–Galerkin technique, the same shape functions are applied to interpolate the test functions $\boldsymbol{w}$ and $\vartheta$.

$$\begin{aligned} \boldsymbol{w}^h|_{\mathcal{B}_0^e} &= \sum_{i=1}^{n_{\text{en}}} N^i_\varphi\, \boldsymbol{w}_i \;\in\; H_1^0(\mathcal{B}_0) & \boldsymbol{\varphi}^h|_{\mathcal{B}_0^e} &= \sum_{k=1}^{n_{\text{en}}} N^k_\varphi\, \boldsymbol{\varphi}_k \;\in\; H_1(\mathcal{B}_0) \\ \vartheta^h|_{\mathcal{B}_0^e} &= \sum_{j=1}^{n_{\text{en}}} N^j_\theta\, \vartheta_j \;\in\; H_1^0(\mathcal{B}_0) & \theta^h|_{\mathcal{B}_0^e} &= \sum_{l=1}^{n_{\text{en}}} N^l_\theta\, \theta_l \;\in\; H_1(\mathcal{B}_0) \end{aligned} \tag{6.5.6}$$

The related gradients of the test functions $\nabla_X \boldsymbol{w}^h$ and $\nabla_X \vartheta^h$ and the gradients of the primary unknowns $\nabla_X \boldsymbol{\varphi}^h$ and $\nabla_X \theta^h$ thus take the following elementwise interpolation.

$$\begin{aligned} \nabla_X\, \boldsymbol{w}^h|_{\mathcal{B}_0^e} &= \sum_{i=1}^{n_{\text{en}}} \boldsymbol{w}_i \otimes \nabla_X N^i_\varphi & \nabla_X\, \boldsymbol{\varphi}^h|_{\mathcal{B}_0^e} &= \sum_{k=1}^{n_{\text{en}}} \boldsymbol{\varphi}_k \otimes \nabla_X N^k_\varphi \\ \nabla_X\, \vartheta^h|_{\mathcal{B}_0^e} &= \sum_{j=1}^{n_{\text{en}}} \vartheta_j \quad \nabla_X N^j_\theta & \nabla_X\, \theta^h|_{\mathcal{B}_0^e} &= \sum_{l=1}^{n_{\text{en}}} \theta_l \quad \nabla_X N^l_\theta \end{aligned} \tag{6.5.7}$$

Recall that herein, $\nabla_X \boldsymbol{\varphi}^h|_{\mathcal{B}_0^e}$ denotes the discrete spatial deformation gradient as $\boldsymbol{F}^h|_{\mathcal{B}_0^e} = \nabla_X \boldsymbol{\varphi}^h|_{\mathcal{B}_0^e}$. With the above–suggested discretizations in time and space, the fully discrete algorithmic balance of momentum and energy of the spatial motion problem take the following format.

$$\begin{aligned} \mathbf{r}^{\varphi h}_I(\boldsymbol{\varphi}^h_{n+1}, \theta^h_{n+1}) &= \mathbf{f}^{\varphi\ h}_{\text{dyn}\,I} + \mathbf{f}^{\varphi\ h}_{\text{int}\,I} - \mathbf{f}^{\varphi\ h}_{\text{sur}\,I} - \mathbf{f}^{\varphi\ h}_{\text{vol}\,I} = \mathbf{0} \qquad \forall \quad I = 1, \dots, n_{\text{np}} \\ \mathrm{r}^{\theta h}_J(\boldsymbol{\varphi}^h_{n+1}, \theta^h_{n+1}) &= \mathrm{f}^{\theta\ h}_{\text{dyn}\,J} + \mathrm{f}^{\theta\ h}_{\text{int}\,J} - \mathrm{f}^{\theta\ h}_{\text{sur}\,J} - \mathrm{f}^{\theta\ h}_{\text{vol}\,J} = 0 \qquad \forall \quad J = 1, \dots, n_{\text{np}} \end{aligned} \tag{6.5.8}$$

Herein, the discrete inertia forces, the internal forces, the surface forces and the volume forces can be expressed as

$$\begin{aligned} \mathbf{f}^{\varphi\ h}_{\text{dyn}\,I} &= \mathop{\mathbf{A}}_{e=1}^{n_{\text{el}}} \int_{\mathcal{B}_0^e} N^i_\varphi\, \frac{\boldsymbol{p}_{0n+1} - \boldsymbol{p}_{0n}}{\Delta t}\, \mathrm{d}V_0 & \mathbf{f}^{\varphi\ h}_{\text{int}\,I} &= \mathop{\mathbf{A}}_{e=1}^{n_{\text{el}}} \int_{\mathcal{B}_0^e} \nabla_X N^i_\varphi \cdot \boldsymbol{\Pi}_{D\,n+1}\, \mathrm{d}V_0 \\ \mathbf{f}^{\varphi\ h}_{\text{sur}\,I} &= \mathop{\mathbf{A}}_{e=1}^{n_{\text{el}}} \int_{\partial\mathcal{B}_0^{te}} N^i_\varphi \quad \bar{\boldsymbol{t}}_{n+1} \quad \mathrm{d}A_0 & \mathbf{f}^{\varphi\ h}_{\text{vol}\,I} &= \mathop{\mathbf{A}}_{e=1}^{n_{\text{el}}} \int_{\mathcal{B}_0^e} N^i_\varphi \quad \boldsymbol{b}_{0\,n+1}\, \mathrm{d}V_0 \end{aligned} \tag{6.5.9}$$

while the dynamic, the internal, the surface and the volume contribution of the balance of energy expand into the following expressions.

$$\begin{aligned} \mathrm{f}^{\theta\ h}_{\text{dyn}\,J} &= \mathop{\mathbf{A}}_{e=1}^{n_{\text{el}}} \int_{\mathcal{B}_0^e} N^j_\theta\, c_0 \frac{\theta_{n+1} - \theta_n}{\Delta t}\, \mathrm{d}V_0 & \mathrm{f}^{\theta\ h}_{\text{int}\,J} &= \mathop{\mathbf{A}}_{e=1}^{n_{\text{el}}} \int_{\mathcal{B}_0^e} \nabla_X N^j_\theta \cdot \boldsymbol{Q}_{D\,n+1} \quad \mathrm{d}V_0 \\ \mathrm{f}^{\theta\ h}_{\text{sur}\,J} &= \mathop{\mathbf{A}}_{e=1}^{n_{\text{el}}} \int_{\partial\mathcal{B}_0^{qe}} -N^j_\theta \quad \bar{q}_{n+1} \quad \mathrm{d}A_0 & \mathrm{f}^{\theta\ h}_{\text{vol}\,J} &= \mathop{\mathbf{A}}_{e=1}^{n_{\text{el}}} \int_{\mathcal{B}_0^e} N^j_\theta [\mathcal{Q}_{0n+1} + \mathcal{Q}^{\text{mech}}_{0n+1}]\, \mathrm{d}V_0 \end{aligned} \tag{6.5.10}$$

In the above definitions, the operator $\mathbf{A}$ denotes the assembly over all $e = 1, \dots, n_{\text{el}}$ element contributions at the $i, j = 1, \dots, n_{\text{en}}$ element nodes to the global node point vectors at all $I, J = 1, \dots, n_{\text{np}}$ global node points. Equations (6.5.8) thus represent the coupled nonlinear set of governing equations which is suggested to be solved in

a monolithic sense. The corresponding solution procedure in terms of the incremental iterative Newton Raphson scheme is illustrated in the section 6.6. Recall that the discrete spatial surface forces acting on the global node points can be calculated as

$$\mathbf{f}^{\varphi\,h}_{\mathrm{sur}\,I} = \mathop{\mathbf{A}}_{e=1}^{n_{\mathrm{el}}} \int_{\mathcal{B}_0^e} N^i_\varphi \, \frac{\boldsymbol{p}_{0\,n+1} - \boldsymbol{p}_{0n}}{\Delta t} + \nabla_X N^i_\varphi \cdot \boldsymbol{\Pi}_{D\,n+1} - N^i_\varphi \, \boldsymbol{b}_{0\,n+1} \, \mathrm{d}V_0 \tag{6.5.11}$$

and are thus energetically conjugate to spatial variations of the node point positions.

### 6.5.2 Material motion problem

In complete analogy, we can discretize the domain of interest $\mathcal{B}_t$ in $e = 1, \ldots, n_{\mathrm{el}}$ elements $\mathcal{B}_t^e$ for the material motion problem. Correspondingly, the geometry $\boldsymbol{x}$ of each element is interpolated from the $i = 1, \ldots, n_{\mathrm{en}}$ node point positions $\boldsymbol{x}_i$ by the shape functions $N^i_x$.

$$\mathcal{B}_t = \bigcup_{e=1}^{n_{\mathrm{el}}} \mathcal{B}_t^e \qquad \boldsymbol{x}^h|_{\mathcal{B}_t^e} = \sum_{i=1}^{n_{\mathrm{en}}} N^i_x \, \boldsymbol{x}_i \tag{6.5.12}$$

By making use of the isoparametric concept, we shall interpolate the primary unknowns $\boldsymbol{\Phi}$ and $\theta$ with the same shape functions $N^i_\Phi$ and $N^j_\theta$ as the element geometry $\boldsymbol{x}$. Moreover, according to the classical Bubnov–Galerkin technique, the test functions $\boldsymbol{W}$ and $\vartheta$ are discretized with the same shape functions $N^i_\Phi$ and $N^j_\theta$.

$$\begin{aligned}
\boldsymbol{W}^h|_{\mathcal{B}_t^e} &= \sum_{i=1}^{n_{\mathrm{en}}} N^i_\Phi \, \boldsymbol{W}_i \;\in\; H^0_1(\mathcal{B}_t) & \boldsymbol{\Phi}^h|_{\mathcal{B}_t^e} &= \sum_{k=1}^{n_{\mathrm{en}}} N^k_\Phi \, \boldsymbol{\Phi}_k \;\in\; H_1(\mathcal{B}_t) \\
\vartheta^h\;|_{\mathcal{B}_t^e} &= \sum_{j=1}^{n_{\mathrm{en}}} N^j_\theta \, \vartheta_j \;\in\; H^0_1(\mathcal{B}_t) & \theta^h\;|_{\mathcal{B}_t^e} &= \sum_{l=1}^{n_{\mathrm{en}}} N^l_\theta \, \theta_l \;\in\; H_1(\mathcal{B}_t)
\end{aligned} \tag{6.5.13}$$

Accordingly, the discretization of the gradients of the test functions $\nabla_x \boldsymbol{W}^h$ and $\nabla_x \vartheta^h$ and the gradients of the primary unknowns $\nabla_x \boldsymbol{\Phi}^h$ and $\nabla_x \theta^h$ takes the following representation.

$$\begin{aligned}
\nabla_x \, \boldsymbol{W}^h|_{\mathcal{B}_t^e} &= \sum_{i=1}^{n_{\mathrm{en}}} \boldsymbol{W}_i \otimes \nabla_x N^i_\Phi & \nabla_x \, \boldsymbol{\Phi}^h|_{\mathcal{B}_t^e} &= \sum_{k=1}^{n_{\mathrm{en}}} \boldsymbol{\Phi}_k \otimes \nabla_x N^k_\Phi \\
\nabla_x \, \vartheta^h\;|_{\mathcal{B}_t^e} &= \sum_{j=1}^{n_{\mathrm{en}}} \vartheta_j \quad \nabla_x N^j_\theta & \nabla_x \, \theta^h\;|_{\mathcal{B}_t^e} &= \sum_{l=1}^{n_{\mathrm{en}}} \theta_l \quad \nabla_x N^l_\theta
\end{aligned} \tag{6.5.14}$$

Herein, $\nabla_x \boldsymbol{\Phi}^h$ denotes the discrete material deformation gradient $\boldsymbol{f}^h|_{\mathcal{B}_t^e} = \nabla_x \boldsymbol{\Phi}^h|_{\mathcal{B}_t^e}$. Consequently, the discrete algorithmic balance of momentum and energy, the material motion counterparts of equations (6.5.8), take the following representations.

$$\begin{aligned}
\mathbf{R}^{\Phi h}_{\;I}\,(\boldsymbol{\Phi}^h_{n+1}, \theta^h_{n+1}) &= \mathbf{F}^{\Phi\;\;h}_{\mathrm{dyn}\,I} + \mathbf{F}^{\Phi\;\;h}_{\mathrm{int}\,I} - \mathbf{F}^{\Phi\;\;h}_{\mathrm{sur}\,I} - \mathbf{F}^{\Phi\;\;h}_{\mathrm{vol}\,I} = \mathbf{0} \quad \forall\; I = 1, \ldots, n_{\mathrm{np}} \\
\mathsf{R}^{\theta h}_{\;J}\,(\boldsymbol{\Phi}^h_{n+1}, \theta^h_{n+1}) &= \mathsf{F}^{\theta\;\;h}_{\mathrm{dyn}\,J} + \mathsf{F}^{\theta\;\;h}_{\mathrm{int}\,J} - \mathsf{F}^{\theta\;\;h}_{\mathrm{sur}\,J} - \mathsf{F}^{\theta\;\;h}_{\mathrm{vol}\,J} = 0 \quad \forall\; J = 1, \ldots, n_{\mathrm{np}}
\end{aligned} \tag{6.5.15}$$

The discrete material inertia forces, the internal forces, the surface forces and the volume forces can be expressed as

$$\begin{aligned} \mathsf{F}^{\varphi\ h}_{\mathrm{dyn}\,I} &= \mathop{\mathsf{A}}_{e=1}^{n_{\mathrm{el}}} \int_{\mathcal{B}_t^e} N^i_\Phi \, j \frac{\boldsymbol{P}_{0n+1} - \boldsymbol{P}_{0n}}{\Delta t} \, \mathrm{d}V_t \qquad \mathsf{F}^{\varphi\ h}_{\mathrm{int}\,I} = \mathop{\mathsf{A}}_{e=1}^{n_{\mathrm{el}}} \int_{\mathcal{B}_t^e} \nabla_x N^i_\Phi \cdot \boldsymbol{\pi}_{D\,n+1} \, \mathrm{d}V_t \\ \mathsf{F}^{\varphi\ h}_{\mathrm{sur}\,I} &= \mathop{\mathsf{A}}_{e=1}^{n_{\mathrm{el}}} \int_{\partial\mathcal{B}_t^{Te}} N^i_\Phi \qquad \bar{\boldsymbol{T}}_{n+1} \qquad \mathrm{d}A_t \qquad \mathsf{F}^{\varphi\ h}_{\mathrm{vol}\,I} = \mathop{\mathsf{A}}_{e=1}^{n_{\mathrm{el}}} \int_{\mathcal{B}_t^e} N^i_\Phi \qquad \boldsymbol{B}_{t\,n+1} \, \mathrm{d}V_t \end{aligned} \tag{6.5.16}$$

while the dynamic, the internal, the surface and the volume contribution of the energy balance take the following format.

$$\begin{aligned} \mathsf{F}^{\theta\ h}_{\mathrm{dyn}\,J} &= \mathop{\mathsf{A}}_{e=1}^{n_{\mathrm{el}}} \int_{\mathcal{B}_t^e} N^j_\theta \, c_t \, \frac{\theta_{n+1} - \theta_n}{\Delta t} \, \mathrm{d}V_t \qquad \mathsf{F}^{\theta\ h}_{\mathrm{int}\,J} = \mathop{\mathsf{A}}_{e=1}^{n_{\mathrm{el}}} \int_{\mathcal{B}_t^e} \nabla_x N^j_\theta \cdot \boldsymbol{q}_{D\,n+1} \qquad \mathrm{d}V_t \\ \mathsf{F}^{\theta\ h}_{\mathrm{sur}\,J} &= \mathop{\mathsf{A}}_{e=1}^{n_{\mathrm{el}}} \int_{\partial\mathcal{B}_t^{Qe}} N^j_\theta \qquad \bar{Q}_{tn+1} \qquad \mathrm{d}A_t \qquad \mathsf{F}^{\theta\ h}_{\mathrm{vol}\,J} = \mathop{\mathsf{A}}_{e=1}^{n_{\mathrm{el}}} \int_{\mathcal{B}_t^e} N^j_\theta [\mathcal{Q}_{tn+1} + \mathcal{Q}^{\mathrm{mech}}_{tn+1}] \, \mathrm{d}V_t \end{aligned} \tag{6.5.17}$$

As a fundamental difference to the spatial motion problem, the Neumann boundary conditions of the material motion problem cannot be considered as given input data. Correspondingly, the discrete material forces acting on the global node points can only be computed in a post–processing calculation once the spatial motion problem has been solved. Their definition parallels the definition of the discrete surface forces of the spatial motion problem given in equation (6.5.11). The discrete material surface forces

$$\mathsf{F}^{\Phi\ h}_{\mathrm{sur}\,I} = \mathop{\mathsf{A}}_{e=1}^{n_{\mathrm{el}}} \int_{\mathcal{B}_t^e} N^i_\Phi \, j \, \frac{\boldsymbol{P}_{0n+1} - \boldsymbol{P}_{0n}}{\Delta t} + \nabla_x N^i_\Phi \cdot \boldsymbol{\pi}_{D\,n+1} - N^i_\Phi \, \boldsymbol{B}_{t\,n+1} \mathrm{d}V_t \tag{6.5.18}$$

are thus energetically conjugate to material variations of the node point positions. They are readily computable once the solution to the spatial motion problem has been determined.

**Remark 6.5.1 (Transient terms in the residuals)** *Coupled thermomechanical problems tend to involve time scales which typically differ by several orders of magnitude. Rather than circumventing the problem of potentially ill–conditioned system matrices by making use of staggered solution techniques, we shall consider the balance of momentum (6.5.8)$_1$ or (6.5.15)$_1$ in a quasi–static sense in the sequel. In other words, the dynamic contributions which manifest themselves in the $N^j_\varphi[\boldsymbol{p}_{0n+1} - \boldsymbol{p}_{0n}]/\Delta t$ term of equation (6.5.9)$_1$ and in the $N^j_\Phi j[\boldsymbol{P}_{0n+1} - \boldsymbol{P}_{0n}]/\Delta t$ term of equation (6.5.16)$_1$ are assumed to be negligible. Moreover, the dynamic correction to the material motion momentum flux indicated through the index $D$ as $\{\,\square\,\}_D$ and $\{\,\Diamond\,\}_D$ vanish identically in the quasi–static case such that $\{\,\square\,\} = \{\,\square\,\}_D$ and $\{\,\Diamond\,\} = \{\,\Diamond\,\}_d$.*

**Remark 6.5.2 (Spatial vs. material quantities)** *For the class of quasi–static problems considered in the sequel, the discrete momentum flux $\boldsymbol{\pi}^t_{n+1}$, and the corresponding momentum source $\boldsymbol{B}_{t\,n+1}$ that are essentially needed to compute the discrete material node point forces defined in equation (6.5.18) are related to their spatial motion counterparts $\boldsymbol{\Pi}^t_{n+1}$ and $\boldsymbol{b}_{0\,n+1}$ through the following transformation formulae.*

$$\begin{aligned} \boldsymbol{\pi}^t_{n+1} &= -j \, \boldsymbol{F}^t_{n+1} \cdot \boldsymbol{\Pi}^t_{n+1} \cdot \boldsymbol{F}^t_{n+1} + j \, \psi_{0\,n+1} \, \boldsymbol{F}^t_{n+1} \\ \boldsymbol{B}_{t\,n+1} &= -j \, \boldsymbol{F}^t_{n+1} \cdot \boldsymbol{b}_{0\,n+1} + j \, S_0 \, \nabla_X \theta_{n+1} - j \, \partial_{\boldsymbol{\Phi}} \psi_{0\,n+1} \end{aligned} \tag{6.5.19}$$

**Remark 6.5.3 (Adiabatic thermohyperelasticity)** *Recall that in general, the computational analysis of adiabatic problems within the spatial setting does not require a $C^0$–continuous interpolation of the temperature field. Since the heat flux $\boldsymbol{Q}$ and with it a possible explicit dependence on the temperature gradient vanish in the adiabatic case, there is no obvious need to introduce the temperature as a nodal degree of freedom. For the material motion problem, however, the calculation of the material volume forces $\boldsymbol{B}_{t\,n+1}$ according to equation (6.5.19) essentially relies on the temperature gradient $\nabla_X \theta_{n+1}$, irrespective of the incorporation of a heat flux. The above–suggested $C^0$–continuous interpolation of the temperature field is thus mandatory in the context of the material force method.*

## 6.6 Linearization

The discrete coupled nonlinear system of equations of the spatial motion problem is solved in a monolithic sense with the help of an incremental iterative Newton–Raphson solution strategy. The discrete balance of momentum $(6.5.8)_1$ and the discrete balance of energy $(6.5.8)_2$ are thus solved simultaneously at time $t_{n+1}$. Consequently, the $k+1$–th iterate of the Newton iteration can be expressed as

$$\begin{aligned} \mathbf{r}_{I\ n+1}^{\varphi\ k+1} &= \mathbf{r}_{I\ n+1}^{\varphi\ k} + \mathrm{d}\mathbf{r}_I^{\varphi} \doteq \mathbf{0} \qquad \forall \quad I = 1, \dots, n_{\mathrm{np}} \\ \mathrm{r}_{J\ n+1}^{\theta\ k+1} &= \mathrm{r}_{J\ n+1}^{\theta\ k} + \mathrm{d}\mathrm{r}_J^{\theta} \doteq 0 \qquad \forall \quad J = 1, \dots, n_{\mathrm{np}} \end{aligned} \tag{6.6.1}$$

whereby $\mathrm{d}\mathbf{r}_{\ I}^{\varphi}$ and $\mathrm{dr}_J^{\theta}$ denote the iterative residua which are based on the consistent linearization of the governing equations.

$$\begin{aligned} \mathrm{d}\mathbf{r}_{\ I}^{\varphi} &= \sum_{K=1}^{n_{\mathrm{np}}} \mathbf{K}_{IK}^{\varphi\varphi} \cdot \mathrm{d}\boldsymbol{\varphi}_K + \sum_{L=1}^{n_{\mathrm{np}}} \mathbf{K}_{IL}^{\varphi\theta}\, \mathrm{d}\theta_L \qquad \forall \quad I = 1, \dots, n_{\mathrm{np}} \\ \mathrm{dr}_J^{\theta} &= \sum_{K=1}^{n_{\mathrm{np}}} \mathbf{K}_{JK}^{\theta\varphi} \cdot \mathrm{d}\boldsymbol{\varphi}_K + \sum_{L=1}^{n_{\mathrm{np}}} \mathrm{K}_{JL}^{\theta\theta}\, \mathrm{d}\theta_L \qquad \forall \quad J = 1, \dots, n_{\mathrm{np}} \end{aligned} \tag{6.6.2}$$

They can be expressed in terms of the iteration matrices $\mathbf{K}_{IK}^{\varphi\varphi}$, $\mathbf{K}_{IL}^{\varphi\theta}$, $\mathbf{K}_{JK}^{\theta\varphi}$, $\mathrm{K}_{JL}^{\theta\theta}$, and the incremental changes of the global vector of unknowns $\mathrm{d}\boldsymbol{\varphi}_K$ and $\mathrm{d}\theta_L$. For the problem at hand, these iteration matrices which can be interpreted as submatrices of the global tangential stiffness matrix take the following format.

$$\begin{aligned} \mathbf{K}_{IK}^{\varphi\varphi} &= \frac{\partial \mathbf{r}_{\ I}^{\varphi}}{\partial \boldsymbol{\varphi}_K} = \mathop{\mathsf{A}}_{e=1}^{n_{\mathrm{el}}} \int_{\mathcal{B}_0^e} N^i \rho_0 \, \frac{1}{\Delta t^2} \boldsymbol{I} N^k + \nabla_X N^i \cdot \mathrm{D}_{\boldsymbol{F}} \boldsymbol{\Pi}^t \cdot \nabla_X N^k \, \mathrm{d}V_0 \\ \mathbf{K}_{IL}^{\varphi\theta} &= \frac{\partial \mathbf{r}_{\ I}^{\varphi}}{\partial \theta_L} = \mathop{\mathsf{A}}_{e=1}^{n_{\mathrm{el}}} \int_{\mathcal{B}_0^e} \nabla_X N^i \cdot \mathrm{D}_{\theta} \boldsymbol{\Pi}^t N^l \, \mathrm{d}V_0 \\ \mathbf{K}_{JK}^{\theta\varphi} &= \frac{\partial \mathrm{r}_J^{\theta}}{\partial \boldsymbol{\varphi}_K} = \mathop{\mathsf{A}}_{e=1}^{n_{\mathrm{el}}} \int_{\mathcal{B}_0^e} -N^j \, \mathrm{D}_{\boldsymbol{F}} \mathcal{Q}_0^{\mathrm{mech}} \cdot \nabla_X N^k \, \mathrm{d}V_0 \\ \mathrm{K}_{JL}^{\theta\theta} &= \frac{\partial \mathrm{r}_J^{\theta}}{\partial \theta_L} = \mathop{\mathsf{A}}_{e=1}^{n_{\mathrm{el}}} \int_{\mathcal{B}_0^e} N^j c_0 \frac{1}{\Delta t} N^l - N^j \mathrm{D}_{\theta} \mathcal{Q}_0^{\mathrm{mech}} N^l + \nabla_X N^j \cdot \mathrm{D}_{\nabla_X \theta} \boldsymbol{Q} \cdot \nabla_X N^l \mathrm{d}V_0 \end{aligned} \tag{6.6.3}$$

Therein, the first terms of equations $(6.6.3)_1$ and $(6.6.3)_4$ illustrate the time–dependent nature of the problem. They represent the consistent mass and capacity matrix, respectively. The second term of $(6.6.3)_1$ corresponds to the classical structural stiffness,

which is typically introduced as sum of the geometric and the material part. Equation $(6.6.3)_2$ reflects the thermal influence in the constitutive equation. The indirect influence of the changes in temperature on the deformation field and on the temperature field introduced through the Gough–Joule effect is reflected through equation $(6.6.3)_3$ and the second term in $(6.6.3)_4$. The last term in equation $(6.6.3)_4$ accounts for heat convection. The above introduced derivatives of the momentum flux $\boldsymbol{\Pi}^t$, the thermo-mechanical coupling term $\mathcal{Q}_0^{\text{mech}}$ and the heat flux $\boldsymbol{Q}$ with respect to the deformation gradient $\boldsymbol{F}$, the temperature $\theta$ and the temperature gradient $\nabla_X \theta$ depend on the choice of the individual constitutive equations. A particular exemplification was given earlier in chapter 4.4. The solution of the linearized system of equations (6.6.1) finally defines the iterative update for the global unknowns $\boldsymbol{\varphi}_I$ and $\theta_J$.

$$\begin{aligned} \boldsymbol{\varphi}_I &= \boldsymbol{\varphi}_I + \mathrm{d}\,\boldsymbol{\varphi}_I \qquad \forall \quad I = 1, \dots, n_{\text{np}} \\ \theta_J &= \theta_J + \mathrm{d}\,\theta_J \qquad \forall \quad J = 1, \dots, n_{\text{np}} \end{aligned} \tag{6.6.4}$$

**Remark 6.6.1 (Transient terms in the linearized residuals)** *Recall that when considering the balance of momentum in the quasi–static sense, the term $N^I \rho_0 / \Delta t^2 \, \boldsymbol{I} \, N^K$ of equation $(6.6.3)_1$ vanishes identically.*

## 6.7 Algorithmic aspects

A typical finite element solution algorithm resulting from the above suggested solution strategy is sketched in the flowchart in table 6.1. It demonstrates that the balance

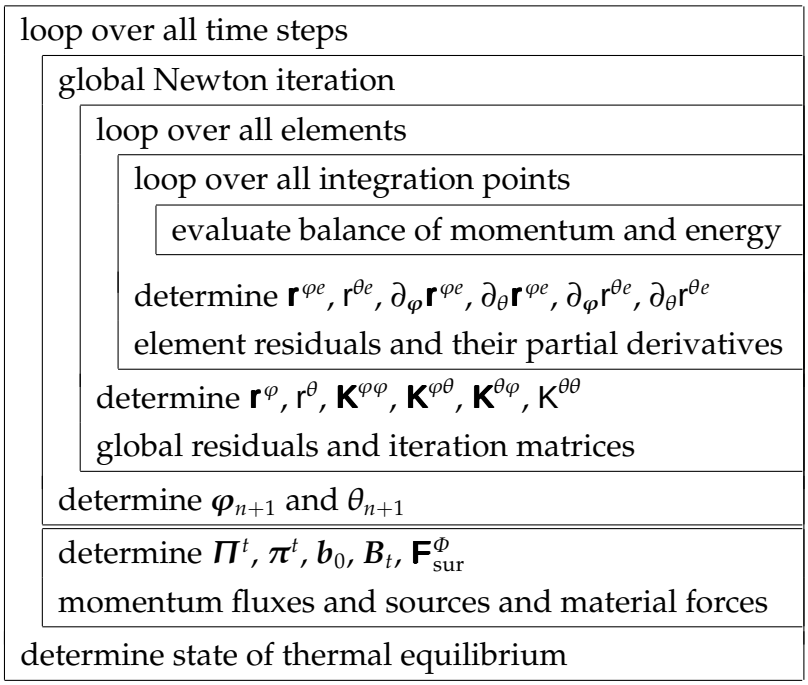


**Table 6.1:** Algorithm of node point based approach

of momentum and the balance of energy are solved simultaneously on the global level. Consequently, both, the deformation and the temperature are introduced as global unknowns and determined within a global Newton iteration procedure.

**Remark 6.7.1 (Material force method)** *Note that in the present non–adiabatic approach, the temperature $\theta$ has been interpolated in a $\mathcal{C}^0$–continuous way. The evaluation of the material temperature gradient $\nabla_X \theta$ that is essentially needed to evaluate the discrete material node point forces $\mathbf{F}^{\Phi}_{\text{sur}}$ in equation (6.5.18) is thus computationally straightforward. The calculation of the discrete material node point forces can thus be carried out in a simple post–processing step as illustrated in table 6.1.*

**Remark 6.7.2 (Integration point based approach)** *In particular for adiabatic problems which include a heat source but no heat flux, a $\mathcal{C}^{-1}$ continuous interpolation of the temperature field might yield sufficiently accurate results. Such a formulation typically lends itself to an*

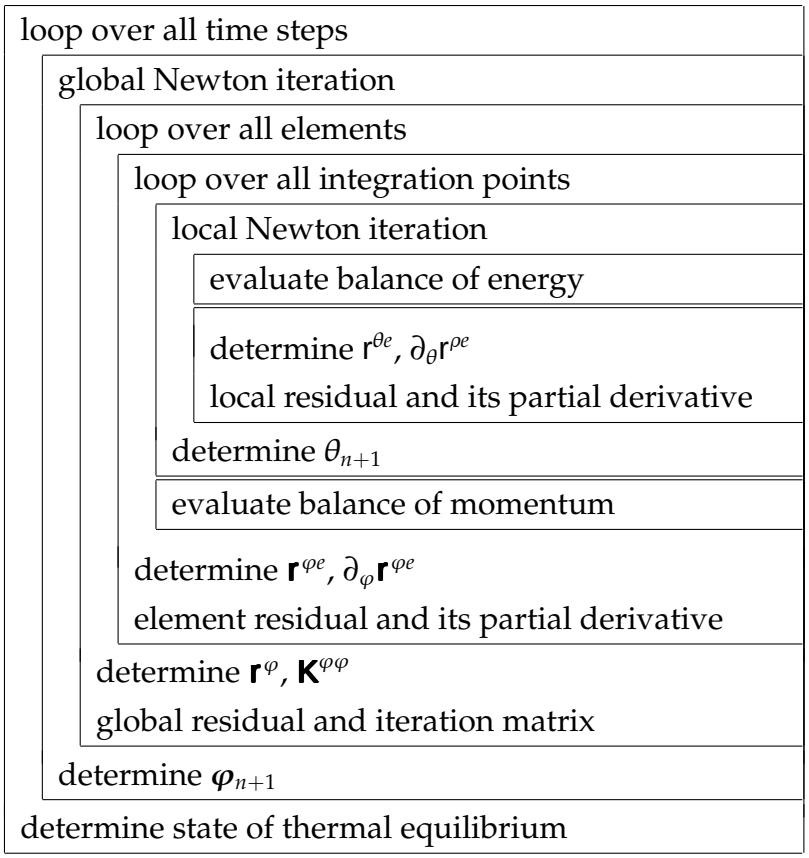


**Table 6.2:** Algorithm of integration point based approach

*integration point based introduction of the temperature and might thus be remarkably cheaper than the node point based approach from a computational point of view. Table 6.2 illustrates a typical flowchart resulting from the integration point based approach. Observe that in contrast to the node point based approach, the balance of momentum and energy are now solved in a staggered sense. The algorithm is thus characterized through a local Newton iteration for the actual temperature embedded in the global Newton iteration for the deformation field. A systematic comparison of the node point based approach and the integration point based approach for a flux–free formulation will be carried out in the following chapter in the context of open system thermodynamics.*

## 6.8 Example: Strip under tension

In the first example, we analyze a homogeneous two–dimensional plane strain strip subjected to a tensile loading. The specimen is discretized by 1200 Q1Q1 elements with a linear interpolation of the deformation $\boldsymbol{\varphi}$ and the temperature $\theta$. A geometric imperfection is introduced by reducing the cross section area of the strip to 50 % in the middle of the specimen. Figure 6.3 illustrates the geometry and the loading conditions.

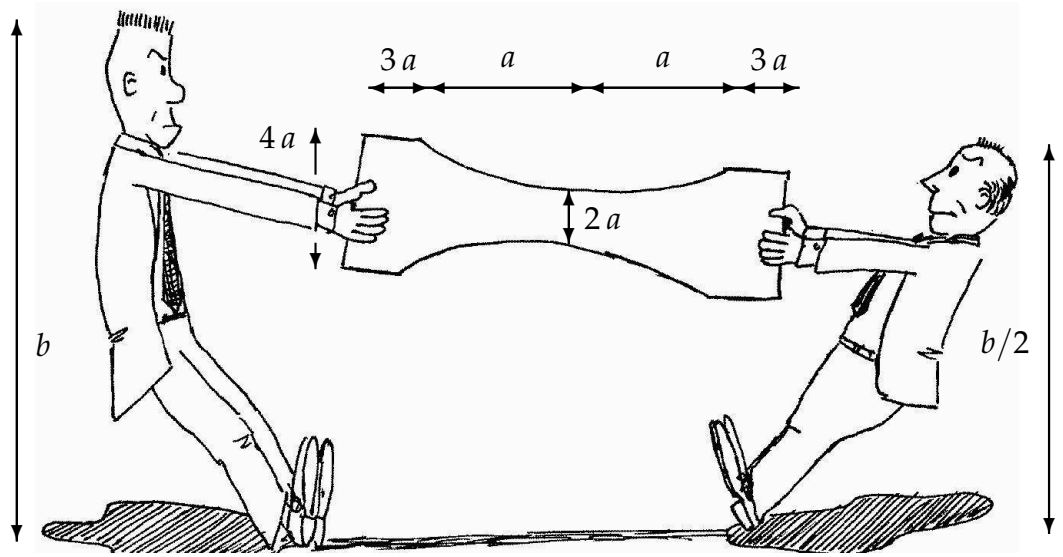


**Figure 6.3:** Strip under tension – Geometry and loading conditions

The two edges of the specimen are loaded under displacement control during 20 load steps of $\Delta t = 0.01$ whereby each load step is characterized through a prescribed edge displacement of $0.1\,a$. The final load thus corresponds to $2.0\,a$ representing a total stretch of 50 %. The material behavior is characterized through a thermohyperelastic free energy function of Neo–Hooke type as indicated in equation (4.4.1) of chapter 4. It introduces six material parameters, the two Lamé constants $\lambda = 115384.62$ and $\mu = 76923.08$ corresponding to Young's modulus of $E = 200000$ and Poisson's ratio of $\nu = 0.30$ in the linear regime, the thermal expansion coefficient $\alpha = 0.00001$, the specific heat capacity $c_0 = 460$, the reference temperature $\theta_0^* = 293$ and the reference entropy $S_0^* = 38.374$. Moreover, the definition of the heat flux (4.4.4) according to Fourier's law introduces the materially isotropic heat conduction coefficient, which has been chosen to $K_0 = 45$.

Figure 6.4 depicts the temperature distributions in the undeformed stage at $t = 0$, at $t = 0.10$ corresponding to $u = 1.0\,a$, at $t = 0.15$ corresponding to $u = 1.5\,a$ and at the final load step at $t = 0.20$ for which $u = 2.0\,a$. Due to the reduction of the cross section area, the stress takes highest values in the middle of the specimen. According to the Gough–Joule effect, the temperature decreases with increasing stress as indicated through the blue colors in figure 6.4. As the prescribed loading is increased, this effect becomes more and more pronounced and the middle of the specimen cools down considerably. Recall that herein, a thermohyperelastic material behavior has been assumed for the sake of simplicity. To capture the physical behavior of realistic metallic

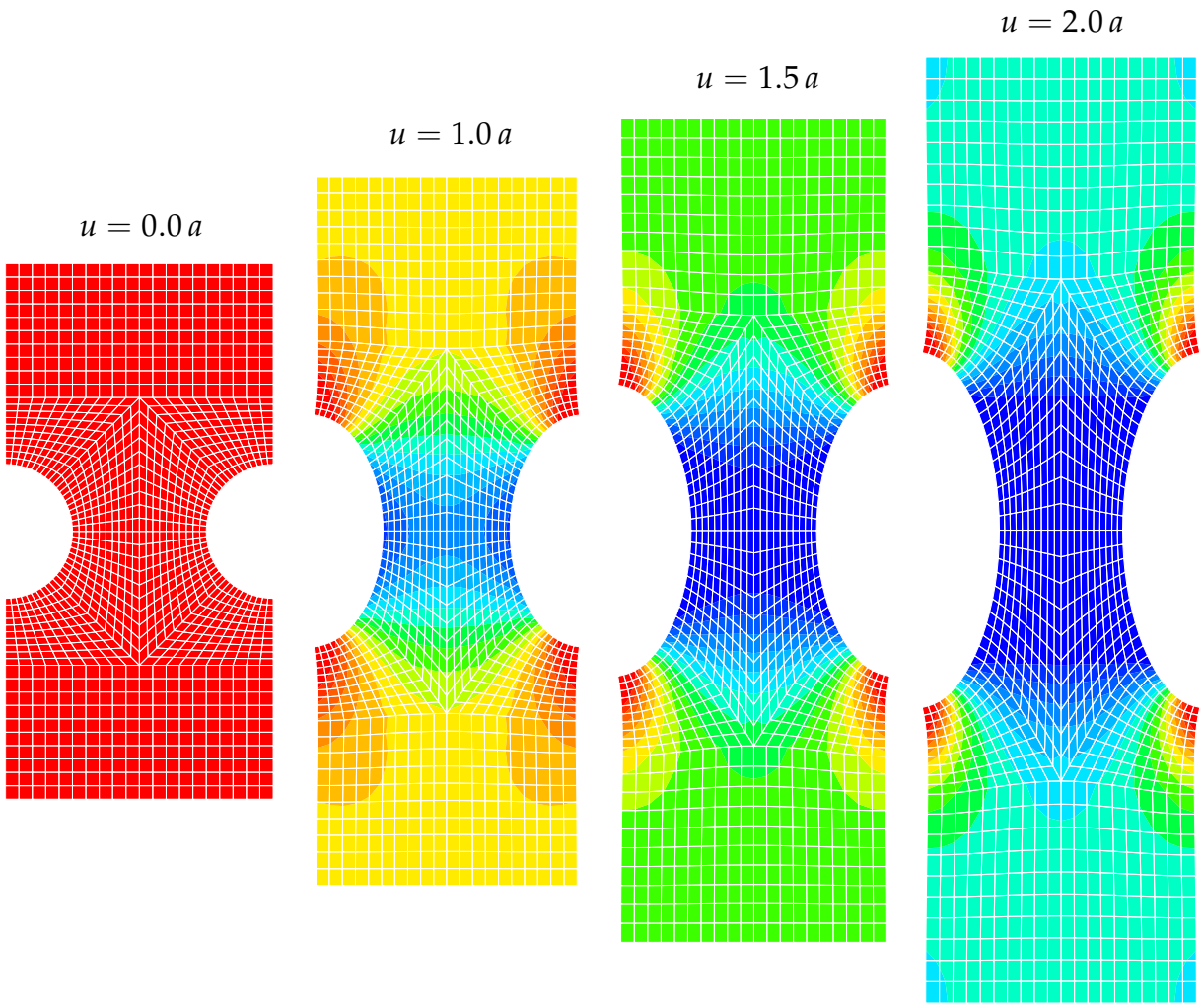


**Figure 6.4:** Strip under tension – Temperature $\theta$ for different loading stages

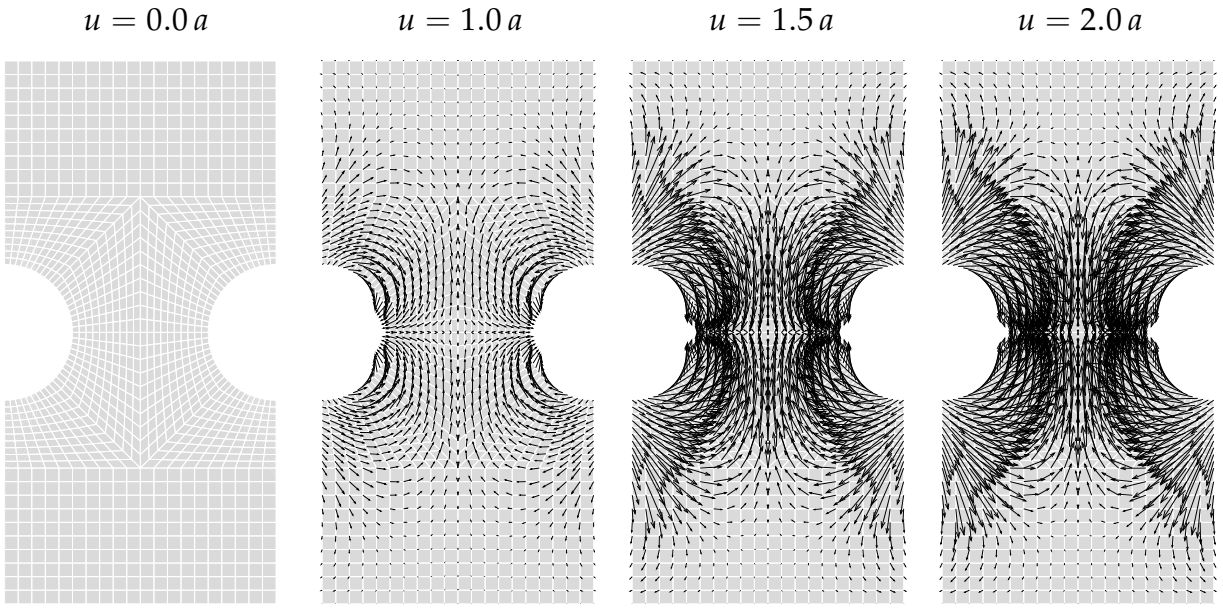


**Figure 6.5:** Strip under tension – Material volume forces $F_{\mathrm{vol}}^{\Phi}$ for different loading stages

materials, however, thermoelastoplastic constitutive equations as proposed by Simo & Miehe [193] or Miehe [155,156] seem to be appropriate. Figure 6.5 illustrates the corresponding material volume forces $\mathsf{F}^{\Phi}_{\text{vol}}$ which are essentially proportional to the temperature gradient $\nabla_X \theta$. The material volume forces are thus orthogonal to the temperature isolines of figure 6.4 pointing from zones of higher to zones of lower temperature. Material volume forces can thus be understood as an indicator for the equilibration of concentrations. In the context of thermohyperelasticity of closed systems, they motivate the incorporation of a temperature flux with the aim of rendering the overall temperature distribution more homogeneous. In the following example, the discrete material volume forces $\mathsf{F}^{\Phi}_{\text{vol}}$ will be compared to the corresponding internal forces $\mathsf{F}^{\Phi}_{\text{int}}$ as the sums of both constitute the overall material surface forces $\mathsf{F}^{\Phi}_{\text{sur}}$.

## 6.9 Example: Inclusion problem

We will now analyze the inclusion problem which represents a classical benchmark problem for composite materials. A circular inclusion with a radius $a$ is embedded in a matrix material arranged in rectangular shape of a width of $4\,a$ and a height of $8\,a$. The specimen has been discretized with 2400 Q1Q1 elements, whereby 1200 elements have been applied for the discretization of the inclusion and another 1200 elements have been used for the discretization of the surrounding matrix material. The matrix is loaded under displacement control at the upper and lower edge during 20 time steps of $\Delta t = 0.01$ each, whereby in each load step, a deformation of $u = 0.1\,a$ is applied such that the final load corresponds to a total axial stretch of 50 %. Similar to the previous example, the material parameters have been chosen to $\lambda = 115384.62$ and $\mu = 76923.08$, $c_0 = 460$, $\theta_0^* = 293$, $S_0^* = 38.374$ and $K_0 = 45$. While the thermal expansion coefficient $\alpha$ of the inclusion is kept constant to $\alpha_{\text{incl}} = 0.00001$ like in the previous example, the thermal expansion coefficient of the matrix material is varied systematically. For the first two analyses, it is chosen to $\alpha_{\text{matr}} = 0.0000001$ and $\alpha_{\text{matr}} = 0.000001$ thus being 100 and 10 times smaller than the corresponding modulus of the inclusion. Accordingly, for the third and fourth analysis $\alpha_{\text{matr}}$ is chosen to $\alpha_{\text{matr}} = 0.0001$ and $\alpha_{\text{matr}} = 0.001$ being 10 and 100 times larger than the thermal expansion coefficient of the circular inclusion. Correspondingly, we expect an inhomogeneous distribution of the deformation and the overall temperature. Note that in physically relevant composite materials, variations of the thermal expansion coefficients are typically less pronounced than variations in the elastic moduli. Nevertheless, in order to concentrate on thermal effects rather than on elastic ones, we will apply similar elastic moduli for both, the inclusion and the matrix keeping in mind that this example is therefore rather of academic nature.

Figure 6.6 depicts the four different stress distributions for the different $\alpha_{\text{incl}} : \alpha_{\text{matr}}$ ratios. Obviously, in the first two analyses, for which the thermal expansion coefficient of the inclusion is smaller than the one of the matrix, stresses tend to be larger in the matrix material than in the inclusion. Thereby, red colors represent higher stress values while blue colors obviously indicate lower stress levels. The overall stress, however, is of course positive throughout the entire bar. As a natural result of the inhomoge-

neous stress distribution, the matrix temperature becomes smaller than the temperature of the inclusion as indicated by the first two temperature distributions of figure 6.7. Thereby, blue colors represent lower temperature values than red ones. However, the changes in temperature are negative throughout the specimen due to the Gough–Joule effect since the structure as a whole has been subjected to a tensile loading. On the righthand side of figures 6.6 and 6.7, we see the stress and temperature distribution for the analyses in which the thermal expansion coefficient of the matrix has been chosen considerably lower than the one of the inclusion. In contrast to the previous two simulations, stress concentrations can now be observed in the inclusion. Accordingly, the temperature of the inclusion drops below the temperature of the matrix material. As expected the effect of inhomogeneity becomes more pronounced for larger $\alpha_{\text{incl}} : \alpha_{\text{matr}}$ ratios.

The corresponding solution of the material motion problem is illustrated in figures 6.8 and 6.9. While the first set of figures illustrates the internal forces $\mathsf{F}^{\Phi}_{\text{int}}$, the second set shows the material volume forces $\mathsf{F}^{\Phi}_{\text{vol}}$, which are characteristic for the temperature problem considered herein. The overall material surface forces $\mathsf{F}^{\Phi}_{\text{sur}}$ follow straightforwardly from summing up the corresponding internal and volume contributions. Recall that the internal forces $\mathsf{F}^{\Phi}_{\text{int}}$ illustrated in figure 6.8 are basically governed by the stress field. Their distribution is thus strongly related to the stress distribution given in figure 6.6. Thereby internal forces typically point from areas of high to areas of low stress. On the contrary, the material volume forces $\mathsf{F}^{\Phi}_{\text{vol}}$ which are depicted in figure 6.9 are essentially proportional to the temperature gradient and are thus strongly related to the temperature distribution of figure 6.7. They typically point from areas of high to areas of low temperature and thus indicate the tendency to equilibrate inhomogeneous temperature distributions.

Note that for visualizational purposes, the material force vectors given in figures 6.8 and 6.9 had to be scaled by different scaling factors as indicated on top of each individual figure. Typically, both contributions differ significantly in their order of magnitude. For this particular example, the material volume forces are larger than the corresponding internal forces according to the specific choice of material parameters. Since the structure is loaded in an extremely short period of time, changes in the temperature remain local and do not have the time to spread over the specimen. Consequently, relatively large temperature gradients can be observed and the material volume forces are significantly higher than their internal counterparts. Recall that herein, we have analyzed a purely academic example since physically realistic materials not only show a difference in the thermal expansion coefficient but also in Young's modulus. As the latter is typically more pronounced, the internal contribution to the material forces is often orders of magnitude larger than the corresponding volume contribution. Nevertheless, this example has demonstrated nicely, how the two contributions to the material surface force interact. Typically, material volume forces show the tendency to compensate the corresponding internal forces to a certain extend. In classical fracture mechanics, this effect is known as stress shielding.

In summary, this chapter has illustrated the physical relevance of material forces in multifield physics. To this end, the classical material force method which had originally introduced for linear and nonlinear elastic fracture mechanics has been extended

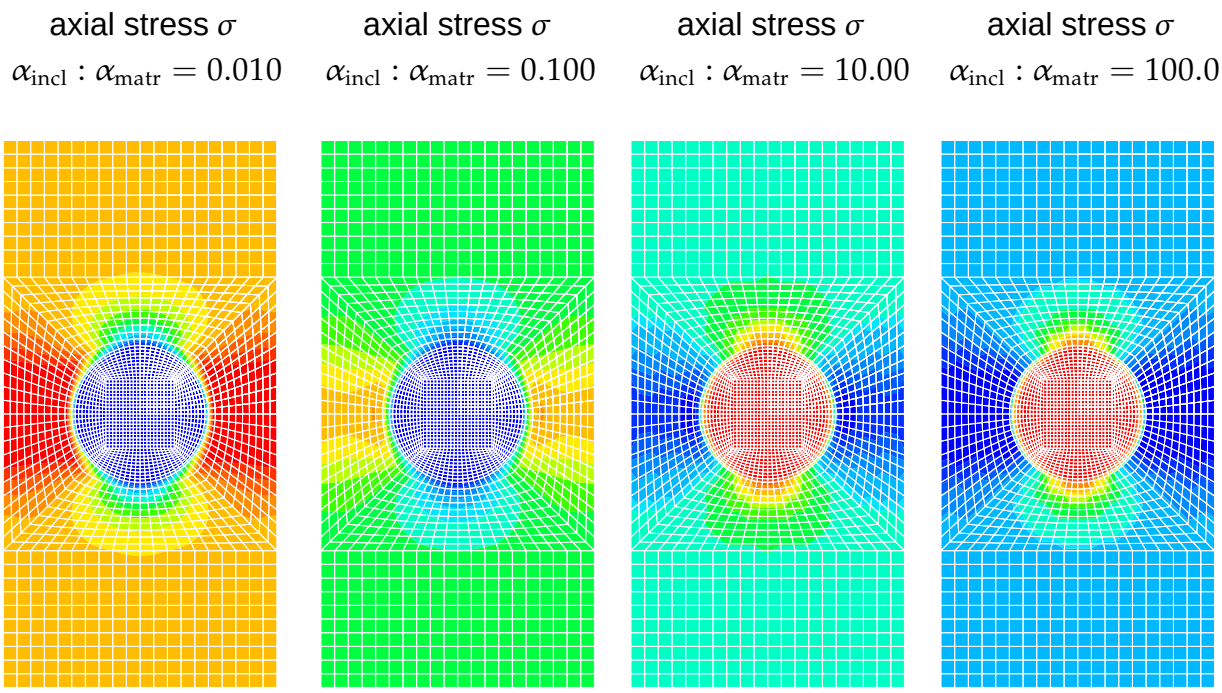


**Figure 6.6:** Inclusion problem – Axial stress $\sigma$ for different $\alpha_{\text{incl}} : \alpha_{\text{matr}}$ ratios

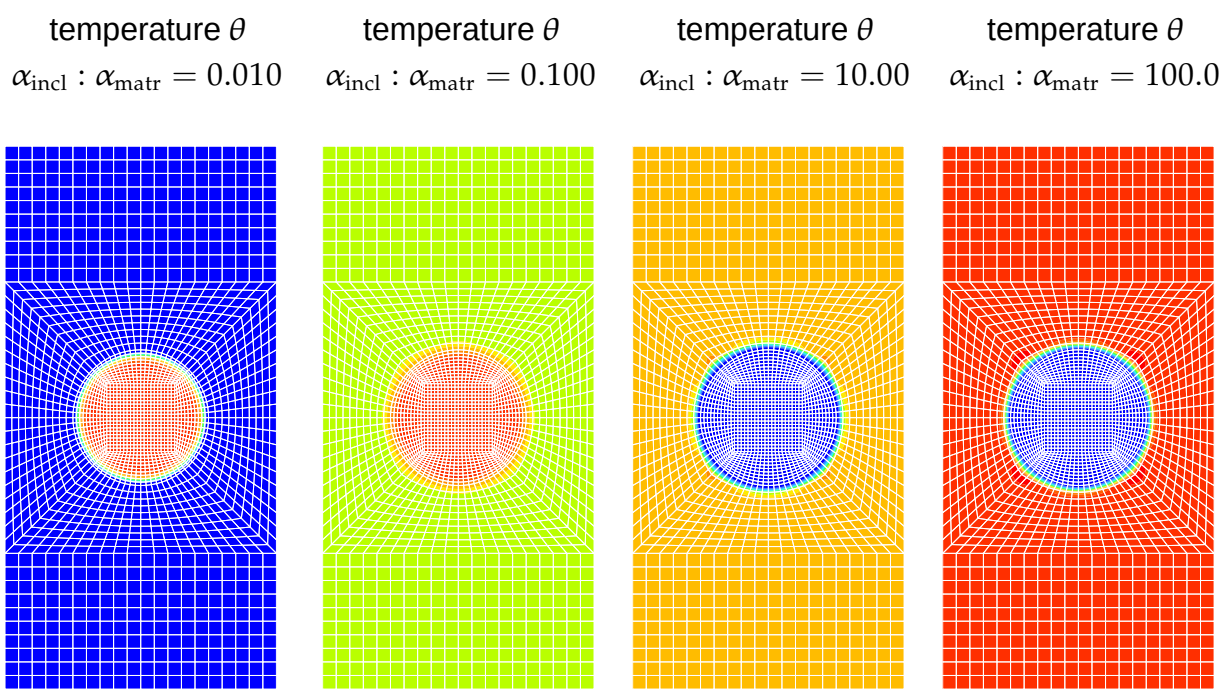


**Figure 6.7:** Inclusion problem – Temperature $\theta$ for different $\alpha_{\text{incl}} : \alpha_{\text{matr}}$ ratios

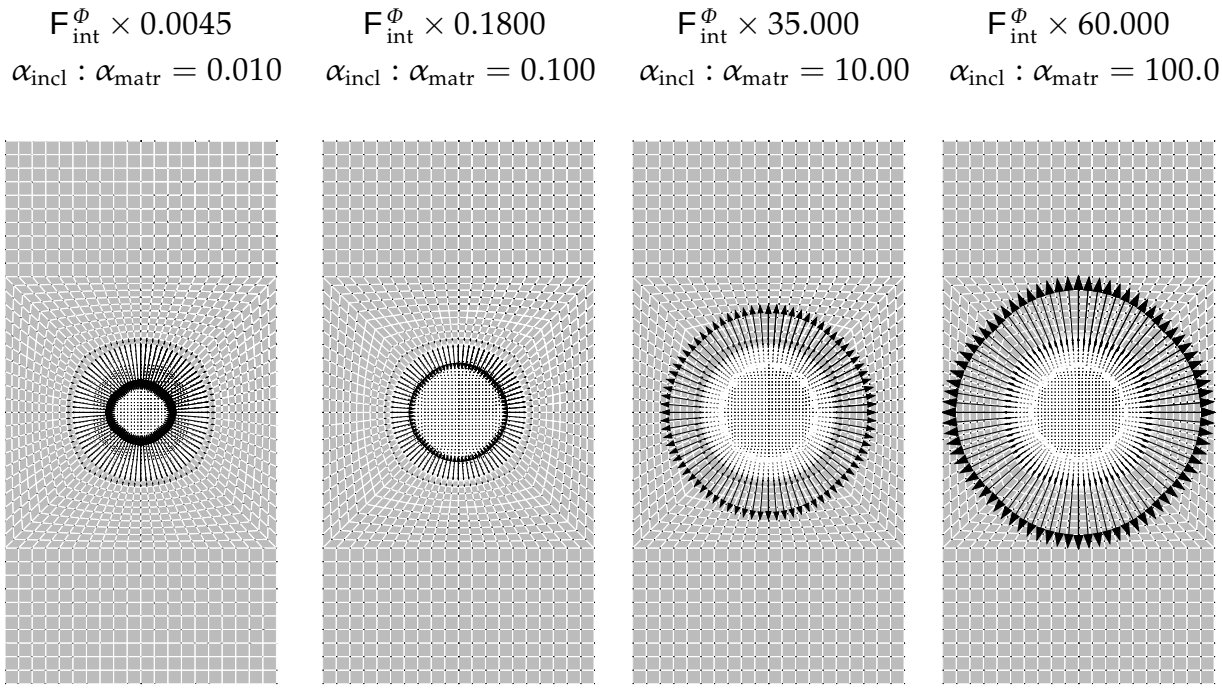


**Figure 6.8:** Inclusion problem – Material internal forces $F^{\Phi}_{int}$ for different $\alpha_{incl} : \alpha_{matr}$ ratios

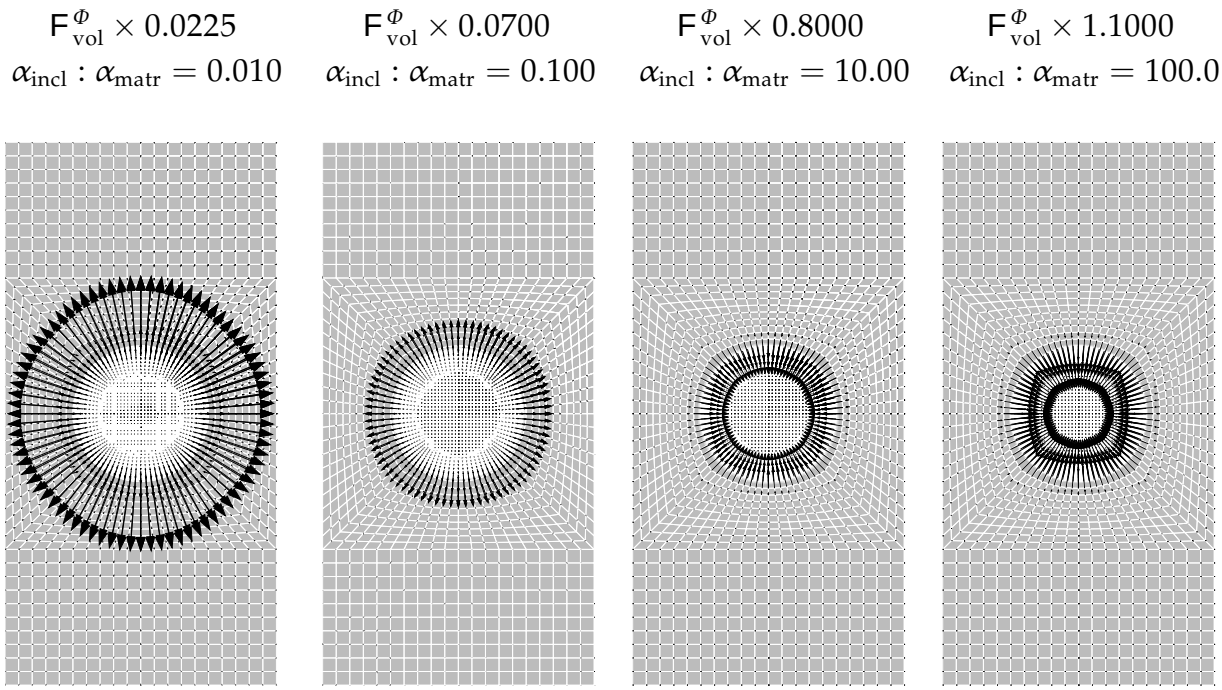


**Figure 6.9:** Inclusion problem – Material volume forces $F^{\Phi}_{vol}$ for different $\alpha_{incl} : \alpha_{matr}$ ratios

to the framework of thermohyperelastic closed systems. The algorithmic evaluation of the material surface forces turns out to be computationally cheap if the additional fields are discretized as global degrees of freedom within a node point based approach. Material surface forces can then be calculated in a mere post–processing procedure as the sum of the internal and volume contribution whereby the latter show the tendency to compensate the classical internal forces to a remarkable extend.

# 7 Open systems

The dream is to find the open channel. What, then, is the meaning of it all? What can we say today to dispel the mystery of existence? If we take everything into account, not only what the ancients knew, but also all those things that we have found out up to today that they didn't know, then I think that we must frankly admit that we do not know. But I think that in admitting this we have probably found the open channel.

Richard P. Feynman,
The Meaning of it All, 1963

## 7.1 Introduction

Since the formulation of the first continuum model of growth which was presented more than a quarter of a century ago by Cowin & Hegedus [41], the modeling and simulation of biomechanical processes has experienced an enormously growing interest. In contrast to traditional engineering materials, biomaterials, in particular hard and soft tissues, show the ability to adapt not only their external shape but also their internal microstructure to environmental changes. The functional adaption of hard tissues to changes in the mechanical loading situation has been known for more than a century and is often referred to as Wolff's law of bone remodeling. [220],

'Es ist demnach unter dem Gesetze der Transformation der Knochen dasjenige Gesetz zu verstehen, nach welchem im gefolge primärer Abänderungen der Form und Inanspruchnahme bestimmte, nach mathematischen Regeln eintretende Umwandlungen der inneren Architectur und ebenso bestimmte, denselben mathematischen Regeln folgende secundäre Umwandlungen der äusseren Form der betreffenden Knochen sich vollziehen.'

Comprehensive overviews on the experimental findings of growth phenomena can be found e.g. in the monographs by Roux [185], Thompson [205], Pauwels [173], Fung [66–69], Taber [204], Cowin [36, 38], Carter & Beaupré [24], Humphrey [108] and Murray [165, 166] or in the recent collections of Cowin & Humphrey [42], Cowin [39], Fung [69] and Holzapfel & Ogden [97]. Within the faculty of mechanical engineering of the Technical University of Kaiserslautern, the behavior of bones under cyclic loading has been studied intensively in a series of experiments by Fleck [64] and Fleck & Eifler [65].
The first continuum theory of growth for hard tissues has been presented under the name of 'theory of adaptive elasticity' by Cowin & Hegedus [41], Hegedus & Cowin

[92] and Cowin & Nachlinger [43]. Within their theory, the biological structure is considered as an open system which is allowed to constantly exchange mass, momentum, energy and entropy with its environment. While this exchange is accounted for exclusively in terms of volume source terms in the original model, the more enhanced 'theory of volumetric growth' by Epstein & Maugin [57] allows for an additional exchange in the form of surface fluxes, see also Kuhl & Steinmann [131]. Thereby, the flux of mass is typically attributed to the migration of cells while mass sources stem from cell growth and shrinkage, cell death, cell division or cell enlargement. A fundamentally different approach to hard and soft tissue mechanics falls within the framework of the 'theory of porous media', see e.g. Coussy [35], Ehlers & Markert [55], Nield & Bejan [170], de Boer [15], Kühn & Hauger [136], Humphrey & Rajagopal [109,110], Capriz et al. [22] or Steeb & Diebels [196]. Thereby, the exchange of mass, momentum, energy and entropy takes place between the individual constituents of the mixture, while the mass, momentum, energy and entropy of the overall mixture remain constant. Nevertheless, since the mechanical behavior of hard tissues is primarily governed by the response of the calcified bone matrix, we shall confine attention to the solid phase alone and make use of the open system framework in the sequel.

Driven by the development of modern computer technologies, the newly derived theories of growth were soon supplemented by finite element based numerical simulations. Although the initial class of models suffered from numerical instabilities, the first results in the area of bone remodeling were quite encouraging, see e.g. Huiskes et al. [105, 107], Carter et al. [26], Beaupré et al. [12], Weinans et al. [214, 215] or Harrigan & Hamilton [86, 87], Jacobs et al. [113, 114], Pettermann et al. [174], Reiter [180] or the recent overview by Hart [90]. However, these first models were basically restricted to the mechanics of hard tissues such as bones. In contrast to hard tissues, which are typically not subjected to large strains, the modeling of soft tissues requires a geometrically nonlinear kinematic description, see e.g. the first publication by Rodriguez et al. [182], the recent works of Cowin [37], Holzapfel et al. [94–96], Chen & Hoger [29], Gasser & Holzapfel [72], Lubarda & Hoger [146], Ambrosi & Mollica [1] or the recent enhanced version by Garikipati et al. [71]. For the particular application to wound healing, we refer to the work of Sherrat et al. [188] and Murray et al. [167] which is summarized in the comprehensive overview by Murray [166].

The first attempts of our own group to simulate biological growth processes within the geometrically exact framework are documented in Kuhl et al. [129–133, 135], see also Schwarz [187]. In the present chapter, we shall focus on the comparison of different finite element techniques for biomechanical growth processes. In particular, two alternative classes of models will be derived and elaborated: a node point based and an integration point based approach. While the former is based on the monolithic solution of the balance of mass and momentum for open systems and offers the potential to incorporate a mass flux, the latter is based on a staggered solution strategy by introducing the density as internal variable on the quadrature point level. In view of modern finite element technologies, both approaches will be combined with a fully implicit Euler backward time integration scheme and are embedded in an incremental iterative Newton–Raphson solution technique supplemented by a consistent linearization of the governing equations. Both, the node point and the integration point based

approach, will be compared in a systematic study of one–dimensional model problems and in the analysis of the classical two–dimensional benchmark problem of the proxima femur.
We begin our study with a review of the existing literature on the computational modeling of biological tissues which dates back to the mid eighties. Surprisingly, an enormous body of literature is related to the analysis of stability and uniqueness of the suggested models. Often, these properties are attributed to the final finite element solution although they typically originate from the ill–posedness of the underlying continuous problem. To clarify the notions of stability and uniqueness, we shall make a clear distinction between the continuous problem, the time–discrete problem and the fully discrete finite element problem.

**Stability and uniqueness of continuous model** The modeling of growth is basically characterized through two fundamental equations: the balance of mass and the balance of momentum. While the computational treatment of the balance of momentum, i.e. the deformation problem, is rather standard in modern finite element technologies, the numerical solution of the balance of mass, i.e. the density problem, can be carried out in various different ways. Conceptually speaking, the evolution of the material density has to be calculated according to some driving force, the so–called biological stimulus. After analyzing different mechanically induced stimuli, e.g. based on the current strain, see e.g. Cowin & Hegedus [41], the actual stress state, see e.g. Carter et al. [26] or the dissipated energy in the form of damage, see e.g. Levenston & Carter [139], it was agreed upon, that the free energy density of the calcified tissue represented the most reasonable candidate, compare also Krstin et al. [121, 122] or Weinans et al. [214, 215]. However, it soon turned out, that the use of the free energy density alone resulted in instabilities due to the positive feedback effect it had on the remodeling process. As documented by Carter et al. [26], Harrigan & Hamilton [85–88], Harrigan et al. [89] and Weinans et al. [214] it produced unstable 0–1–type solutions of either no bone or fully dense calcified bone which were physically meaningless. Several different remedies were suggested, e.g. the introduction of a so–called dead zone or lazy zone , compare e.g. Beaupré et al. [12], Carter & Beaupré [24] and Weinans et al. [215], the nonlocal averaging based on spatial influence functions, see Mullender et al. [159,160], the a posteriori smoothing of either the mechanical stimulus or the solution itself, see Fischer et al. [63], Jacobs et al. [113] or Nackenhorst [168,169], or the use of more sophisticated micromechanically motivated models, see Huiskes et al. [104, 106]. Nevertheless, the simplest and maybe also most efficient modification was motivated by pure mathematical reasoning. In a rigorous analysis on stability and uniqueness, Harrigan & Hamilton [86, 87] derived a modified remodeling rate equation which a priori guaranteed stable, unique and path–independent solutions for a particular choice of parameters. We shall thus apply a biomechanical stimulus in the sense of Harrigan & Hamilton in the sequel.

**Stability and uniqueness of semi–discrete model** The resulting set of equations defines the continuous initial boundary value problem which has to be discretized in time and space. Traditionally, finite difference schemes are applied for the temporal

discretization. Motivated by the computational efficiency of explicit time integration schemes, the first models were based on the classical explicit Euler forward method, see e.g. Carter et al. [26], Beaupré et al. [12], Huiskes et al. [107] or Weinans et al. [214, 215]. In contrast to the unconditionally stable implicit Euler backward scheme, the Euler forward method is only conditionally stable and poses restrictions on the time step size. These were discussed in detail by Levenston [137, 138] and Cowin et al. [40]. However, we do not believe, that the use of an explicit time marching scheme is the source, at least not the only one, for the particular instabilities reported in the literature. Nevertheless, to avoid this potential drawback of explicit schemes, Harrigan & Hamilton [86] suggested the use of the Euler backward method which was also applied by Nackenhorst [168, 169] and will be the method of choice for our further deviations.

**Stability and uniqueness of fully discrete model** The temporal discretization renders a highly nonlinear semi–discrete coupled system of equations. Its spatial discretization is usually embedded in the finite element framework. Upon all the existing finite element solution strategies, we can basically distinguish three different approaches to evaluate the balance of mass and momentum: a partitioned sequential solution, the partitioned staggered solution and the monolithic simultaneous solution. Most of the pioneering work falls within the first category, see e.g. Huiskes et al. [105, 107], Carter et al. [26], Beaupré et al. [12] or Weinans et al. [214, 215]. Driven by the need for computational efficiency that was a relevant issue in the mid eighties, the solution was traditionally carried out in a two–step–strategy. First, the balance of momentum was solved in the classical way. Only then, the density was determined in a mere post–processing step. The constitutive properties were adjusted according to the current density and a new set of material parameters was assigned to each element before the next iteration step was carried out. The structure of the applied commercial finite element codes basically prescribed the algorithmic setup. Since the density was assumed to be elementwise constant within this algorithm, this first strategy has been termed element based approach in the literature.
Unfortunately, most of the simulations of the element based approach produced unphysical checkerboard type solutions which were attributed to the fact that the density was interpolated in a $\mathcal{C}^{-1}$–continuous fashion. This deficiency of the original models led to the reconsideration of the finite element realization in the mid nineties. In a systematic case study, Jacobs et al. [113] compared the early element based approach with an integration point based approach and a node point based approach. For the integration point based approach, the balance of mass and momentum are still elaborated in a partitioned way, however, their evaluation is carried out in a staggered sense, see also Weng [217]. In the integration point based approach, which originates back to the computational modeling of inelasticity, the density is introduced as an internal variable on the integration point level. Nevertheless, since the integration point based approach is still based on a discrete pointwise representation of the density field, it did not yield remarkable improvements.
If the density field is assumed to be at least $\mathcal{C}^0$–continuous within the entire domain of consideration, the density has to be introduced as nodal degree of freedom on the

global level. According to Jacobs et al. [113] and Fischer et al. [63], only this node point based approach could guarantee a physically meaningful solution. In complete analogy to the temperature field in thermoelastic problems, the density is treated as an independent field which can be determined simultaneously with the deformation field, compare chapter 6. The monolithic solution of the balance of mass and momentum is computationally more expensive. It is thus not surprising that this solution strategy only became prominent after sufficient computational facilities had become available. Within the present work, we shall derive a class of node point and integration point based finite element formulations, which are based on a monolithic simultaneous and on a partitioned staggered solution strategy, respectively. However, it will turn out, that the approach that had been termed element based in the literature can be understood as a special case of either of the two categories. We will illustrate, that, provided that the spatial discretization is carried out in a consistent way, neither of the three approaches leads to unstable solutions if the underlying continuous problem is stable and unique in the sense of Harrigan & Hamilton [85–87].
This chapter is organized as follows. After a brief motivation in section 7.2, section 7.3 summarizes the basic equations of growth within the framework of finite strain kinematics. The corresponding weak form and its temporal and spatial discretization are derived in sections 7.4 and 7.5. Thereby, we shall essentially focus on the node point based approach while the integration point based treatment is sketched in the form of remarks. Next, we discuss the corresponding consistent linearization in section 7.6. Characteristic flowcharts and representative elements of the node point based approach and the integration point based approach are illustrated in section 7.7. The functionality of the suggested model is analyzed with a number of different examples. We begin with a brief parameter study in section 7.8. Next, the node point based approach and the integration point based approach are compared systematically with the help of two academic model problems in section 7.9. The applicability of the node point based approach to simulate topology optimization and size effects is elaborated in sections 7.10 and 7.11. We then turn to some biomechanical applications and discuss the computational modeling of growth in hard tissues in section 7.12 and the computational modeling of healing in soft tissues in section 7.13. Last, we shall illustrate that the suggested algorithm is not restricted to biomechanical problems alone and discuss its application to simulate chemomechanical damage in engineering materials in section 7.14.

## 7.2 Motivation

Let us motivate the open system formulation to be derived in the present chapter by the Galilei problem introduced in the famous monograph by Galilei [70] which dates back more than three centuries.

'Dal chè manifeſto, che chi voleſſe mantener in un vaſtiſſimo gigante le proporzioni che hanno le membra di un uomo ordinario, biſognerebbe o trovar materia molto più dura e reſiſtente, per formarne l'oſſa, o vero ammettere che la robuſtezza ſua fuſſe a proporzione aſſai più fiacca che ne gli uomini di ſtatura mediocre; altrimente, creſcendogli a ſmiſurata altezza, ſi vedrebbono dal proprio peſo opprimere e cadere.'

In this work, Galilei states that in geometrically similar or isometric structures, larger structures are weaker relative to their mass than smaller structures. Consequently, in the extreme case, a giant of enormous size would not be able to sustain the gravity load acting on his own body, if his bones were of the same strength as those of normal size people. Galilei thus concluded that bones of larger animals should be stronger relative to their size than those of small animals in order to maintain the same level of bone tissue loading. Since the strength of a structure increases with its density, the Galilei problem can be considered an illustrative motivation for open system thermodynamics.

**Closed system – homogeneous density** Let us first consider the classical case of closed systems for which the one–dimensional balance of momentum can be expressed in the following form.

$$\rho_0 \, \mathrm{D}_t \, p \; = \; \mathrm{Div} \; \Pi \; + \; b_0 \tag{7.2.1}$$

We shall further assume a free energy function $\psi_0$ of Neo–Hookean type $\psi_0 = \frac{1}{4} E_0 \, [\, F^2 - 1 - 2 \, \ln(F) \,]$, a function of one single material parameter, Young's modulus $E_0 = 1.0$. Then, the first Piola–Kirchhoff stress can be determined as energetically conjugate quantity to the deformation gradient $F = \nabla_X \varphi$ as $\Pi = \mathrm{D}_F \, \psi_0$, and thus $\Pi = \frac{1}{4} E_0 \, [\, 2 \, F - 2 \frac{1}{F} \,]$. We consider the quasi–static case as $\rho_0 \, \mathrm{D}_t \, p = 0$ and assume a constant gravity load, $b_0 = \mathrm{const}$, acting over the specimen height $h$. From equation (7.2.1), we conclude that the stress $\Pi$ is linear in the height $0 \leq X \leq h$ such that $\Pi = [\, X - h \,] \, b_0$. Figure 7.1 illustrates the relative change in density $[\, \rho - \rho_0^* \,] / \rho_0^*$ which is zero throughout the specimen height, indicating a constant density $\rho_0 = \rho_0^* = 1.0$. Moreover, figure

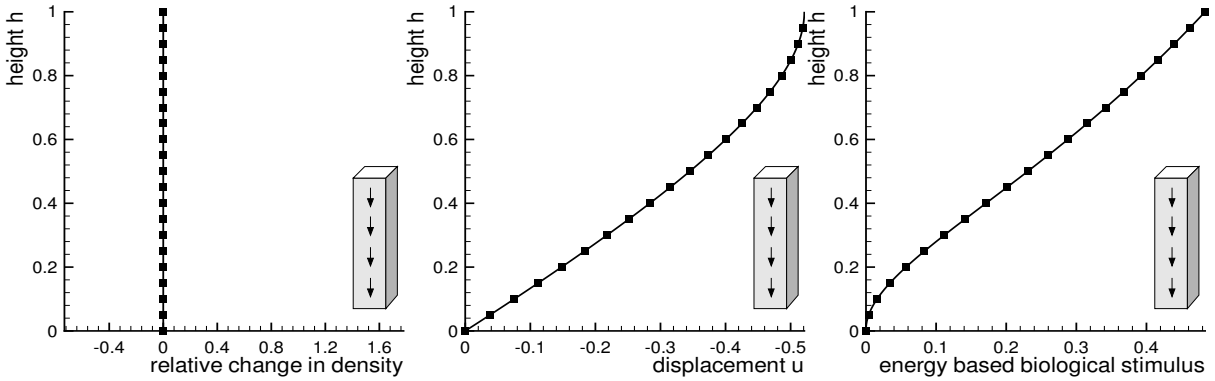


**Figure 7.1:** One–dimensional model problem - Closed system - Homogeneous density

7.1 depicts the displacement $u = \varphi - X$ resulting from equation (7.2.1) with a constant gravity load of $b_0 = 10$. It is quite obvious, that the top displacement increases with an increasing size of the giant. Due to the geometrically exact formulation in combination with the non–linear Neo–Hookean constitutive law, the increase in deformation is a nonlinear function of the specimen height. In figure 7.1, right, we see the corresponding energy based biological stimulus $[\, \rho_0 / \rho_0^* \,]^{-m} \, \psi_0 = \psi_0$ for a value of $m = 3$ which is apparently identical to the free energy density $\psi_0$ for the closed system case since

$\rho_0 = \rho_0^*$. In the spirit of Galilei, this biological stimulus can be interpreted as a measure of strength required to sustain the gravity load acting on the bones of the giant. For the homogeneous density distribution considered herein, the measure of required strength $[\,\rho_0/\rho_0^*\,]^{-m}\,\psi_0 = \psi_0$ increases considerably with increasing height, or in the sense of Galilei increasing size of the giant. This analysis thus supports the observation by Galilei stating that bones of larger animals have to be stronger than those of smaller animals in order to maintain the same level of bone tissue loading.

**Open system – homogeneous stimulus** Recall that bones can typically be classified as cellular materials, the strength of which increases with increasing density. In order to predict the correct density distribution, let us now consider the one–dimensional balance of mass and momentum of open system thermodynamics.

$$\begin{aligned} \mathrm{D}_t\,\rho_0 &= \mathrm{Div}\; R \;\; + \;\mathcal{R}_0 \\ \rho_0\,\mathrm{D}_t\,p &= \mathrm{Div}\;\bar{\Pi}_D \; + \;\bar{b}_0 \end{aligned} \tag{7.2.2}$$

The free energy density $\psi_0$ of open–pored cellular materials can be expressed in terms of the Neo–Hookean free energy $\psi_0^{\mathrm{neo}}$ weighted by the relative density $[\,\rho_0/\rho_0^*\,]^n$ as $\psi_0 = [\,\rho_0/\rho_0^*\,]^n \psi_0^{\mathrm{neo}}$. Again, the Neo–Hookean free energy is given as $\psi_0^{\mathrm{neo}} = \frac{1}{4}E_0\,[\,F^2 - 1 - 2\,\ln(F)\,]$ in terms of the deformation gradient $F = \nabla_X \varphi$. For the sake of simplicity, we shall restrict ourselves to the flux–free case as $R = 0$. The state of biological equilibrium is characterized through vanishing changes in the density as $\mathrm{D}_t\,\rho_0 = \mathcal{R}_0 = 0$. Consequently, the mass source has to vanish identically as $\mathcal{R}_0 = 0$. For the case considered herein, we assume an energy driven mass source as $\mathcal{R}_0 = [\,\rho_0/\rho_0^*\,]^{-m}\,\psi_0 - \psi_0^*$, which is given as the difference between the biological stimulus $[\,\rho_0/\rho_0^*\,]^{-m}\,\psi_0$ and the

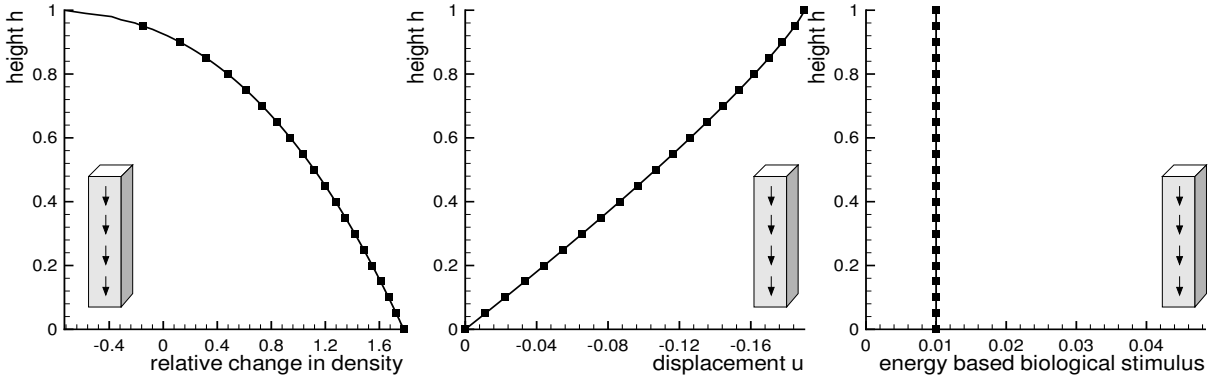


**Figure 7.2:** One–dimensional model problem - Open system - Homogeneous stimulus

attractor stimulus $\psi_0^*$. Accordingly, in the case of biological equilibrium, the density can be expressed as a function of the deformation gradient $F$ through the Neo–Hookean free energy $\psi_0^{\mathrm{neo}}(F)$ as $\rho_0 = [\,\psi_0^{\mathrm{neo}}/\psi_0^*\,]^{[m-n]}\,\rho_0^*$. Furthermore, for the quasi–static case considered herein, changes in the mechanical momentum vanish identically as $\rho_0\,\mathrm{D}_t\,p = 0$ and thus $\bar{\Pi}_D = \bar{\Pi}$. Similar to the previous case, the reduced first Piola–Kirchhoff stress is introduced as energetically conjugate quantity to the deformation gradient as $\bar{\Pi} = \rho_0\,\mathrm{D}_F\,\psi$ whereby $\psi = \psi_0/\rho_0$ and thus $\bar{\Pi} = \frac{1}{4}E_0\,[\,2\,F - 2\frac{1}{F}\,]$. Again, we

shall assume a constant gravity load $\bar{b}_0 = \text{const}$, such that the reduced stress is linear in the height $0 \leq X \leq h$ as $\bar{\Pi} = [\, X - h \,]\, \bar{b}_0$. Figure 7.2 shows the results of the Galileo problem (7.2.2) for the open system case. Thereby, the attractor stimulus has been chosen to $\psi_0^* = 0.01$ while the two exponents are chosen to $n = 2$ and $m = 3$. On the left of figure 7.2, we see the relative change in density $[\, \rho - \rho_0^* \,]/\rho_0^*$ which is obviously non–constant over the specimen height. Up to a height of approximately $0.925\, h$, the density increases in order to sustain the gravity load. Remarkably, above $0.925\, h$, the original material has been too strong to carry the load. Consequently, matter could even be taken away without violating the attractor stimulus. The non–constant density distribution results in an almost homogeneous deformation for which the displacement $u = \varphi - X$ is nearly linear in the height $X$, compare figure 7.2, middle. The generated density distribution is optimal in the sense of the energy based biological stimulus $[\, \rho_0/\rho_0^* \,]^{-m}\, \psi_0$, which obviously takes constant values throughout the specimen height. We shall now turn to the numerical solution of the governing equations of open system thermodynamics for the general multi–dimensional case.

## 7.3 Governing equations

We begin by briefly summarizing the relevant equations of open system thermodynamics whereby we shall restrict ourselves to the isothermal case. Consequently, the density problem is characterized through the balance of mass whereas the deformation problem is primarily defined in terms of the balance of momentum. Recall that the balance of mass plays a central role in the mechanics of open systems since it can be applied to transform the volume specific balance of momentum into its mass specific format. The direct impact of changes in mass is only visible in the volume specific balance equations whereas the mass specific format is typically free from all the explicit mass–dependent extra terms. The mass specific balance of momentum thus takes a similar structure as the balance of momentum of classical closed system thermodynamics and will therefore be the format of choice for further considerations.

### 7.3.1 Spatial motion problem

The balance of mass of the spatial motion problem essentially follows from equation $(3.3.9)_1$ or rather $(3.3.13)_1$.

$$\mathrm{D}_t\, \rho_0 = \mathrm{Div}\ \boldsymbol{R} + \mathcal{R}_0 \tag{7.3.1}$$

It balances the rate of change of the material density $\rho_0$ with the corresponding mass flux $\boldsymbol{R}$ and source $\mathcal{R}_0$. The spatial motion version of the balance of momentum formulated in material representation and material parametrization follows straightforwardly from equation $(3.5.11)_1$ as $\mathrm{D}_t\, \boldsymbol{p}_0 = \mathrm{Div}\, \boldsymbol{\Pi}_D^t + \boldsymbol{b}_0$. By expressing the total momentum flux and source $\boldsymbol{\Pi}_D^t$ and $\boldsymbol{b}_0$ in terms of their reduced counterparts $\bar{\boldsymbol{\Pi}}_D^t$ and $\bar{\boldsymbol{b}}_0$, we obtain the following spatial motion version of the volume specific balance of momentum.

$$\mathrm{D}_t\, \boldsymbol{p}_0 = \mathrm{Div}\, (\bar{\boldsymbol{\Pi}}_D^t - \boldsymbol{p} \otimes \boldsymbol{R}) + \bar{\boldsymbol{b}}_0 + \boldsymbol{p}\, \mathcal{R}_0 - \nabla_X \boldsymbol{p} \cdot \boldsymbol{R} \tag{7.3.2}$$

The subtraction of a weighted version of the balance of mass (7.3.1) finally renders its mass specific counterpart

$$\rho_0 \, \mathrm{D}_t \, \boldsymbol{p} = \mathrm{Div} \; \bar{\boldsymbol{\Pi}}^t_D + \bar{\boldsymbol{b}}_0 \tag{7.3.3}$$

which represents one of the fundamental equations in open system thermodynamics. It essentially corresponds to the mass specific version of the spatial balance of momentum derived in equation $(3.5.50)_1$, which is characterized through its material representation and material parametrization.

### 7.3.2 Material motion problem

The balance of mass of the material motion problem has been derived in equation $(3.3.9)_2$ or rather $(3.3.13)_2$.

$$j \, \mathrm{D}_t \, \rho_0 = \mathrm{div} \; \boldsymbol{r} + \mathcal{R}_t \tag{7.3.4}$$

It essentially balances the weighted rate of change of the material density $\rho_0$ with the corresponding mass flux $\boldsymbol{r}$ and source $\mathcal{R}_t$. The spatial representation and material parametrization of the volume specific balance of momentum is given by equation $(3.5.32)_2$ and can be stated as follows $j \, \mathrm{D}_t \, \boldsymbol{P}_0 = \mathrm{div} \, \boldsymbol{\pi}^t_D + \boldsymbol{B}_t$. Again, by replacing the total material motion momentum flux and source $\boldsymbol{\pi}^t_D$ and $\boldsymbol{B}_t$ by their reduced counterparts, we obtain the following statement.

$$j \, \mathrm{D}_t \, \boldsymbol{P}_0 = \mathrm{div} \, (\bar{\boldsymbol{\pi}}^t_D - \boldsymbol{P} \otimes \boldsymbol{r}) + \bar{\boldsymbol{B}}_t + \boldsymbol{P} \, \mathcal{R}_t - \nabla_X \boldsymbol{P} \cdot \boldsymbol{r} \tag{7.3.5}$$

By subtracting a weighted version of the balance of mass (7.3.4), we can transform this volume specific format into its more familiar mass specific counterpart

$$\rho_t \, \mathrm{D}_t \, \boldsymbol{P} = \mathrm{div} \; \bar{\boldsymbol{\pi}}^t_D + \bar{\boldsymbol{B}}_t \tag{7.3.6}$$

which essentially represents the mass specific version of the material motion balance of momentum in spatial representation and material parametrization given earlier in equation $(3.5.59)_2$.

**Remark 7.3.1 (Spatial vs. material motion problem)** *Recall that the spatial and the material motion version of a scalar–valued balance equation like the balance of mass (7.3.1) and (7.3.4) are simply related via the corresponding Jacobians. Consequently, the mass fluxes $\boldsymbol{R}$ and $\boldsymbol{r}$ simply transform into one another via the corresponding Piola transform as $\boldsymbol{r} = j \, \boldsymbol{R} \cdot \boldsymbol{f}^{-t}$ while the mass sources $\mathcal{R}_0$ and $\mathcal{R}_t$ are related via $\mathcal{R}_t = j \, \mathcal{R}_0$. The vector–valued material motion momentum balance (7.3.6), however, follows from a complete pull back of its spatial motion counterpart (7.3.3) onto the material manifold. The mass specific momentum densities $\boldsymbol{p}$ and $\boldsymbol{P}$ are thus related via $\boldsymbol{P} = -\boldsymbol{F}^t \cdot \boldsymbol{p}$ while the densities $\rho_0$ and $\rho_t$ simply transform as $\rho_t = j \, \rho_0$. Note, however, that relations between the corresponding flux and source terms $\bar{\boldsymbol{\Pi}}^t$ and $\bar{\boldsymbol{\pi}}^t$ and equivalently $\bar{\boldsymbol{b}}_0$ and $\bar{\boldsymbol{B}}_t$ strongly depend on the choice of the constitutive equations.*

**Remark 7.3.2 (Biological and mechanical equilibrium)** *In biomechanical applications, the balance of mass is typically referred to as 'biological equilibrium equation' whereas the balance of momentum corresponds to the 'mechanical equilibrium equation'.*

## 7.4 Weak form

In the present chapter, we shall highlight the formal duality of the notions of spatial and material forces by comparing the reduced momentum balance in its spatial and material format. For further considerations, it proves convenient to recast both, the mass and the momentum balance, in their weak or rather variational form. Later on, these weak forms will serve as fundamental basis for the finite element discretization.

### 7.4.1 Spatial motion problem

First, we shall recast the balance of mass and momentum into their residual format and evaluate those over an arbitrary subdomain $\mathcal{B}_0$,

$$\begin{aligned} \mathsf{r}^{\rho}\ (\rho_0, \boldsymbol{\varphi}) &= \mathsf{f}^{\rho}_{\text{dyn}} - \mathsf{f}^{\rho}_{\text{sur}} - \mathsf{f}^{\rho}_{\text{vol}} = 0 \\ \mathbf{r}^{\varphi}\ (\rho_0, \boldsymbol{\varphi}) &= \mathbf{f}^{\varphi}_{\text{dyn}} - \mathbf{f}^{\varphi}_{\text{sur}} - \mathbf{f}^{\varphi}_{\text{vol}} = \mathbf{0} \end{aligned} \tag{7.4.1}$$

whereby the dynamic, the surface and the volume contributions can be expressed in the following form.

$$\begin{aligned} \mathsf{f}^{\rho}_{\text{dyn}} &= \int_{\mathcal{B}_0} \mathrm{D}_t\, \rho_0 \,\mathrm{d}V_0 & \mathsf{f}^{\rho}_{\text{sur}} &= \int_{\partial\mathcal{B}_0} \boldsymbol{R}\cdot\boldsymbol{N}\,\mathrm{d}A_0 & \mathsf{f}^{\rho}_{\text{vol}} &= \int_{\mathcal{B}_0} \mathcal{R}_0\,\mathrm{d}V_0 \\ \mathbf{f}^{\varphi}_{\text{dyn}} &= \int_{\mathcal{B}_0} \rho_0\,\mathrm{D}_t\,\boldsymbol{p}\ \mathrm{d}V_0 & \mathbf{f}^{\varphi}_{\text{sur}} &= \int_{\partial\mathcal{B}_0} \bar{\boldsymbol{\Pi}}^{t}_{D}\cdot\boldsymbol{N}\,\mathrm{d}A_0 & \mathbf{f}^{\varphi}_{\text{vol}} &= \int_{\mathcal{B}_0} \bar{\boldsymbol{b}}_0\,\mathrm{d}V_0 \end{aligned} \tag{7.4.2}$$

For the density problem $(7.4.1)_1$, the boundary $\partial\mathcal{B}_0$ is decomposed into disjoint parts $\partial\mathcal{B}^{\rho}_0$ and $\partial\mathcal{B}^{r}_0$ as $\partial\mathcal{B}^{\rho}_0 \cup \partial\mathcal{B}^{r}_0 = \partial\mathcal{B}_0$ and $\partial\mathcal{B}^{\rho}_0 \cap \partial\mathcal{B}^{r}_0 = \emptyset$. For the deformation problem, the equivalent decomposition renders the disjoint boundary contributions $\partial\mathcal{B}^{\varphi}_0$ and $\partial\mathcal{B}^{t}_0$ as $\partial\mathcal{B}^{\varphi}_0 \cup \partial\mathcal{B}^{t}_0 = \partial\mathcal{B}_0$ and $\partial\mathcal{B}^{\varphi}_0 \cap \partial\mathcal{B}^{t}_0 = \emptyset$. Standard Dirichlet boundary conditions for the density $\rho_0$ and the deformation $\boldsymbol{\varphi}$ can be prescribed on $\partial\mathcal{B}^{\rho}_0$ and $\partial\mathcal{B}^{\varphi}_0$. On the Neumann boundary $\partial\mathcal{B}^{r}_0$ and $\partial\mathcal{B}^{t}_0$, the normal projection of the mass flux $\boldsymbol{R}$ and the reduced momentum source $\bar{\boldsymbol{\Pi}}^{t}_{D}$ are typically expressed in terms of the classical closed system terms $r^{\text{closed}}$ and $\boldsymbol{t}^{\text{closed}}$ and the possible non–standard open system contributions $\bar{r}^{\text{open}}$ and $\bar{\boldsymbol{t}}^{\text{open}}$.

$$\begin{aligned} \rho_0 &= \bar{\rho}_0 \quad \text{on} \quad \partial\mathcal{B}^{\rho}_0 & \boldsymbol{R}\ \cdot\boldsymbol{N} &= r^{\text{closed}} + \bar{r}^{\text{open}} \quad \text{on} \quad \partial\mathcal{B}^{r}_0 \\ \boldsymbol{\varphi} &= \bar{\boldsymbol{\varphi}} \quad \text{on} \quad \partial\mathcal{B}^{\varphi}_0 & \bar{\boldsymbol{\Pi}}^{t}_{D}\cdot\boldsymbol{N} &= \boldsymbol{t}^{\text{closed}} + \bar{\boldsymbol{t}}^{\text{open}} \quad \text{on} \quad \partial\mathcal{B}^{t}_0 \end{aligned} \tag{7.4.3}$$

The weak forms corresponding to equation $(7.4.1)_1$ and $(7.4.1)_2$ can be derived by testing the set of equations together with the related Neumann boundary conditions $(7.4.3)_2$ and $(7.4.3)_4$ with the scalar–valued test function $\vartheta$ and the vector–valued test function $\boldsymbol{w}$, respectively. Under the necessary smoothness and boundary assumptions, we straightly obtain the familiar weak forms of the spatial balance of mass and momentum.

$$\begin{aligned} \mathsf{g}^{\rho}\ (\ \vartheta; \rho_0, \boldsymbol{\varphi}\ ) &= \mathsf{w}^{\rho}_{\text{dyn}} + \mathsf{w}^{\rho}_{\text{int}} - \mathsf{w}^{\rho}_{\text{sur}} - \mathsf{w}^{\rho}_{\text{vol}} = 0 \qquad \forall\ \vartheta \quad \text{in}\ H^0_1(\mathcal{B}_0) \\ \mathsf{g}^{\varphi}\ (\ \boldsymbol{w}; \rho_0, \boldsymbol{\varphi}\ ) &= \mathsf{w}^{\varphi}_{\text{dyn}} + \mathsf{w}^{\varphi}_{\text{int}} - \mathsf{w}^{\varphi}_{\text{sur}} - \mathsf{w}^{\varphi}_{\text{vol}} = 0 \qquad \forall\ \boldsymbol{w} \quad \text{in}\ H^0_1(\mathcal{B}_0) \end{aligned} \tag{7.4.4}$$

The dynamic, the internal, the surface and the volume term related to the balance of mass $(7.4.4)_1$ are given in the following form.

$$\begin{aligned} \mathsf{w}^{\rho}_{\text{dyn}} &= \int_{\mathcal{B}_0} \vartheta \, \mathrm{D}_t \, \rho_0 \; \mathrm{d}V_0 \qquad & \mathsf{w}^{\rho}_{\text{int}} &= \int_{\mathcal{B}_0} \nabla_X \vartheta \cdot \boldsymbol{R} \, \mathrm{d}V_0 \\ \mathsf{w}^{\rho}_{\text{sur}} &= \int_{\partial\mathcal{B}_0} \vartheta \, \boldsymbol{R} \cdot \boldsymbol{N} \, \mathrm{d}A_0 \qquad & \mathsf{w}^{\rho}_{\text{vol}} &= \int_{\mathcal{B}_0} \vartheta \, \mathcal{R}_0 \quad \mathrm{d}V_0 \end{aligned} \tag{7.4.5}$$

By interpreting the test function $\boldsymbol{w}$ as the spatial virtual displacement $\boldsymbol{w} = \delta\boldsymbol{\varphi}$, equation $(7.4.4)_2$ can be identified as the virtual work expression of the spatial motion problem. The dynamic and the internal virtual work $\mathsf{w}^{\varphi}_{\text{dyn}}$ and $\mathsf{w}^{\varphi}_{\text{int}}$ and the corresponding surface and volume contributions $\mathsf{w}^{\varphi}_{\text{sur}}$ and $\mathsf{w}^{\varphi}_{\text{vol}}$ thus take the familiar form known from classical closed system mechanics.

$$\begin{aligned} \mathsf{w}^{\varphi}_{\text{dyn}} &= \int_{\mathcal{B}_0} \boldsymbol{w} \cdot \rho_0 \, \mathrm{D}_t \, \boldsymbol{p} \; \mathrm{d}V_0 \qquad & \mathsf{w}^{\varphi}_{\text{int}} &= \int_{\mathcal{B}_0} \nabla_X \boldsymbol{w} : \bar{\boldsymbol{\Pi}}^t_D \, \mathrm{d}V_0 \\ \mathsf{w}^{\varphi}_{\text{sur}} &= \int_{\partial\mathcal{B}_0} \boldsymbol{w} \cdot \bar{\boldsymbol{\Pi}}^t_D \cdot \boldsymbol{N} \, \mathrm{d}A_0 \qquad & \mathsf{w}^{\varphi}_{\text{vol}} &= \int_{\mathcal{B}_0} \boldsymbol{w} \cdot \bar{\boldsymbol{b}}_0 \quad \mathrm{d}V_0 \end{aligned} \tag{7.4.6}$$

### 7.4.2 Material motion problem

In complete duality to the spatial motion case, we can introduce the residual format of the balance of mass and momentum for the material motion problem,

$$\begin{aligned} \mathsf{R}^{\rho} &= \mathsf{F}^{\rho}_{\text{dyn}} - \mathsf{F}^{\rho}_{\text{sur}} - \mathsf{F}^{\rho}_{\text{vol}} = 0 \\ \mathbf{R}^{\Phi} &= \mathbf{F}^{\Phi}_{\text{dyn}} - \mathbf{F}^{\Phi}_{\text{sur}} - \mathbf{F}^{\Phi}_{\text{vol}} = \mathbf{0} \end{aligned} \tag{7.4.7}$$

with the dynamic, surface and volume contributions defined on the arbitrary spatial subdomain $\mathcal{B}_t$.

$$\begin{aligned} \mathsf{F}^{\rho}_{\text{dyn}} &= \int_{\mathcal{B}_t} j \;\; \mathrm{D}_t \, \rho_0 \, \mathrm{d}V_t \qquad & \mathsf{F}^{\rho}_{\text{sur}} &= \int_{\partial\mathcal{B}_t} \boldsymbol{r} \cdot \boldsymbol{n} \, \mathrm{d}A_t \qquad & \mathsf{F}^{\rho}_{\text{vol}} &= \int_{\mathcal{B}_t} \mathcal{R}_t \, \mathrm{d}V_t \\ \mathbf{F}^{\Phi}_{\text{dyn}} &= \int_{\mathcal{B}_t} \rho_t \, \mathrm{D}_t \, \boldsymbol{P} \; \mathrm{d}V_t \qquad & \mathbf{F}^{\Phi}_{\text{sur}} &= \int_{\partial\mathcal{B}_t} \bar{\boldsymbol{\pi}}^t_D \cdot \boldsymbol{n} \, \mathrm{d}A_t \qquad & \mathbf{F}^{\Phi}_{\text{vol}} &= \int_{\mathcal{B}_t} \bar{\boldsymbol{B}}_t \, \mathrm{d}V_t \end{aligned} \tag{7.4.8}$$

To illustrate the duality with the spatial motion problem, we can formally introduce Dirichlet and Neumann boundary conditions on $\partial\mathcal{B}^{\rho}_t$ and $\partial\mathcal{B}^{R}_t$ with $\partial\mathcal{B}^{\rho}_t \cup \partial\mathcal{B}^{R}_t = \partial\mathcal{B}_t$ and $\partial\mathcal{B}^{\rho}_t \cap \partial\mathcal{B}^{R}_t = \emptyset$ for the density problem and on $\partial\mathcal{B}^{\Phi}_t$ and $\partial\mathcal{B}^{T}_t$ with $\partial\mathcal{B}^{\Phi}_t \cup \partial\mathcal{B}^{T}_t = \partial\mathcal{B}_t$ and $\partial\mathcal{B}^{\Phi}_t \cap \partial\mathcal{B}^{T}_t = \emptyset$ for the deformation problem.

$$\begin{aligned} \rho_0 &= \bar{\rho}_0 \quad \text{on} \quad \partial\mathcal{B}^{\rho}_t \qquad & \boldsymbol{r} \quad \cdot \boldsymbol{n} &= R^{\text{closed}} + \bar{R}^{\text{open}} \quad \text{on} \quad \partial\mathcal{B}^{R}_t \\ \boldsymbol{\Phi} &= \bar{\boldsymbol{\Phi}} \quad \text{on} \quad \partial\mathcal{B}^{\Phi}_t \qquad & \bar{\boldsymbol{\pi}}^t_D \cdot \boldsymbol{n} &= \boldsymbol{T}^{\text{closed}} + \bar{\boldsymbol{T}}^{\text{open}} \quad \text{on} \quad \partial\mathcal{B}^{T}_t \end{aligned} \tag{7.4.9}$$

By testing the pointwise statements of the material mass and momentum balance $(7.4.7)_1$ and $(7.4.7)_2$ and the related Neumann boundary conditions $(7.4.9)_2$ and $(7.4.9)_4$ with the scalar– and vector–valued test functions $\vartheta$ and $\boldsymbol{W}$, we obtain the related weak forms.

$$\begin{aligned} \mathsf{G}^{\rho}(\;\vartheta; \rho_0, \boldsymbol{\Phi}\;) &= \mathsf{W}^{\rho}_{\text{dyn}} + \mathsf{W}^{\rho}_{\text{int}} - \mathsf{W}^{\rho}_{\text{sur}} - \mathsf{W}^{\rho}_{\text{vol}} = 0 \qquad \forall\, \vartheta \quad \text{in } H^0_1(\mathcal{B}_t) \\ \mathsf{G}^{\Phi}(\boldsymbol{W}; \rho_0, \boldsymbol{\Phi}\;) &= \mathsf{W}^{\Phi}_{\text{dyn}} + \mathsf{W}^{\Phi}_{\text{int}} - \mathsf{W}^{\Phi}_{\text{sur}} - \mathsf{W}^{\Phi}_{\text{vol}} = 0 \qquad \forall\, \boldsymbol{W} \quad \text{in } H^0_1(\mathcal{B}_t) \end{aligned} \tag{7.4.10}$$

Thereby, the dynamic, the internal, the surface and the volume contribution to the weak form of the mass balance $(7.4.10)_1$ can be expressed in the following form.

$$\begin{aligned} \mathsf{W}^{\rho}_{\text{dyn}} &= \int_{\mathcal{B}_t} \vartheta \, j \, \mathrm{D}_t \, \rho_0 \, \mathrm{d}V_t \qquad & \mathsf{W}^{\rho}_{\text{int}} &= \int_{\mathcal{B}_t} \nabla_x \vartheta \cdot \boldsymbol{r} \, \mathrm{d}V_t \\ \mathsf{W}^{\rho}_{\text{sur}} &= \int_{\partial\mathcal{B}_t} \vartheta \, \boldsymbol{r} \cdot \boldsymbol{n} \quad \mathrm{d}A_t \qquad & \mathsf{W}^{\rho}_{\text{vol}} &= \int_{\mathcal{B}_t} \vartheta \, \mathcal{R}_t \quad \mathrm{d}V_t \end{aligned} \tag{7.4.11}$$

Note that by interpreting the test function $\boldsymbol{W}$ as the material virtual displacement $\boldsymbol{W} = \delta\boldsymbol{\Phi}$, equation $(7.4.10)_2$ can be interpreted as the material counterpart of the classical virtual work expression $(7.4.4)_2$. Accordingly, $\mathsf{W}^{\Phi}_{\text{dyn}}$ and $\mathsf{W}^{\Phi}_{\text{int}}$ denote the dynamic and the internal virtual work, while $\mathsf{W}^{\Phi}_{\text{sur}}$ and $\mathsf{W}^{\Phi}_{\text{vol}}$ are the corresponding surface and volume contributions.

$$\begin{aligned} \mathsf{W}^{\Phi}_{\text{dyn}} &= \int_{\mathcal{B}_t} \boldsymbol{W} \cdot \rho_t \, \mathrm{D}_t \, \boldsymbol{P} \, \mathrm{d}V_t \qquad & \mathsf{W}^{\Phi}_{\text{int}} &= \int_{\mathcal{B}_t} \nabla_x \boldsymbol{W} : \bar{\boldsymbol{\pi}}^t_D \, \mathrm{d}V_t \\ \mathsf{W}^{\Phi}_{\text{sur}} &= \int_{\partial\mathcal{B}_t} \boldsymbol{W} \cdot \bar{\boldsymbol{\pi}}^t_D \cdot \boldsymbol{n} \; \mathrm{d}A_t \qquad & \mathsf{W}^{\Phi}_{\text{vol}} &= \int_{\mathcal{B}_t} \boldsymbol{W} \cdot \bar{\boldsymbol{B}}_t \quad \mathrm{d}V_t \end{aligned} \tag{7.4.12}$$

**Remark 7.4.1 (Spatial vs. material test functions)** *Note that the scalar–valued test function $\vartheta$ testing the balance of mass is identical for the spatial and the material motion problem. The weak forms of the reduced momentum balance, i.e. the virtual work expressions of the spatial and the material motion problem $(7.4.4)_2$ and $(7.4.10)_2$ can be transformed into one another in a straightforward way by making use of the fundamental relations $\boldsymbol{w} = -\boldsymbol{W} \cdot \boldsymbol{F}^t$ and $\boldsymbol{W} = -\boldsymbol{w} \cdot \boldsymbol{f}^t$ between the spatial and the material virtual displacements $\boldsymbol{w} = \delta\boldsymbol{\varphi}$ and $\boldsymbol{W} = \delta\boldsymbol{\Phi}$.*

**Remark 7.4.2 (Spatial vs. material forces)** *Note that equations $(7.4.2)_2$ define the different contributions to the spatial forces $\mathbf{f}^{\varphi}$ representing the traditional forces in the sense of Newton. They are generated by variations relative to the ambient space at fixed material position $\boldsymbol{X}$. On the contrary, equations $(7.4.8)_2$ define material forces $\mathbf{F}^{\Phi}$ in the sense of Eshelby. Material forces are generated by variations relative to the ambient material at fixed spatial position $\boldsymbol{x}$ and thus represent important measures in the mechanics of material inhomogeneities.*

**Remark 7.4.3 (Material force method)** *Recall that for the spatial motion case, the surface and the volume terms of the weak forms (7.4.4), namely $\mathsf{w}^{\rho}_{\text{sur}}$ and $\mathsf{w}^{\rho}_{\text{vol}}$ for the density problem and $\mathsf{w}^{\varphi}_{\text{sur}}$ and $\mathsf{w}^{\varphi}_{\text{vol}}$ for the deformation problem are usually given while the density $\rho_0$ and the spatial motion $\boldsymbol{\varphi}$ furnish the primary unknowns. Once the spatial motion problem is solved, the dynamic term $\mathsf{W}^{\Phi}_{\text{dyn}}$, the internal virtual work $\mathsf{W}^{\Phi}_{\text{int}}$ and the volume contribution $\mathsf{W}^{\Phi}_{\text{vol}}$ to the material momentum balance can be computed directly. Correspondingly, the material surface forces $\mathbf{F}^{\Phi}_{\text{sur}}$ furnish the unknown of the computational analysis, which has been advocated as 'material force method' by Steinmann et al. [201].*

## 7.5 Discretization

Equations (7.4.4) and (7.4.10) represent the continuous version of the spatial and the material initial boundary value problem of open system mechanics. Following the classical approach, we shall first perform a temporal discretization followed by a discretization in space to obtain the fully discrete spatial and material set of governing equations. For the temporal discretization, consider a partition of the time interval of interest $\mathcal{T}$

$$\mathcal{T} = \bigcup_{n=0}^{n_{\text{step}}-1} [\, t_n, t_{n+1} \,] \tag{7.5.1}$$

and focus on the typical subinterval $[\, t_n, t_{n+1} \,]$ whereby $\Delta t = t_{n+1} - t_n$ denotes the corresponding actual time increment. The primary unknowns $\rho_{0\,n}$ and $\boldsymbol{\varphi}_n$ for the spatial motion problem and $\rho_{0\,n}$ and $\boldsymbol{\Phi}_n$ for the material motion problem and all derivable quantities are assumed to be known at $t_n$. Without loss of generality, we shall apply the classical implicit Euler backward time integration scheme to advance the solution in time from the known time step $t_n$ to the actual time step $t_{n+1}$. Thereby, the first order material time derivatives of the density $\rho_0$ and the mass specific momentum densities $\boldsymbol{p}$ and $\boldsymbol{P}$ are approximated as

$$\begin{aligned} \mathrm{D}_t\, \rho_0 &= \frac{1}{\Delta t} \left[\, \rho_{0\,n+1} - \rho_{0\,n} \,\right] \\ \mathrm{D}_t\, \boldsymbol{p} &= \frac{1}{\Delta t} \left[\, \boldsymbol{p}_{n+1} - \boldsymbol{p}_n \,\right] \\ \mathrm{D}_t\, \boldsymbol{P} &= \frac{1}{\Delta t} \left[\, \boldsymbol{P}_{n+1} - \boldsymbol{P}_n \,\right] \end{aligned} \tag{7.5.2}$$

for the spatial and the material motion problem, respectively. We can now reformulate the governing equations for the spatial motion problem (7.4.4) in terms of the unknowns $\rho_{0\,n+1}$ and $\boldsymbol{\varphi}_{n+1}$.

$$\begin{aligned} \mathsf{g}^{\rho}_{n+1}\,(\ \vartheta; \rho_{0\,n+1}, \boldsymbol{\varphi}_{n+1}\,) &= \mathsf{w}^{\rho}_{\text{dyn}} + \mathsf{w}^{\rho}_{\text{int}} - \mathsf{w}^{\rho}_{\text{sur}} - \mathsf{w}^{\rho}_{\text{vol}} = 0 \qquad \forall\, \vartheta \ \text{ in } H^0_1(\mathcal{B}_0) \\ \mathsf{g}^{\varphi}_{n+1}\,(\ \boldsymbol{w}; \rho_{0\,n+1}, \boldsymbol{\varphi}_{n+1}\,) &= \mathsf{w}^{\varphi}_{\text{dyn}} + \mathsf{w}^{\varphi}_{\text{int}} - \mathsf{w}^{\varphi}_{\text{sur}} - \mathsf{w}^{\varphi}_{\text{vol}} = 0 \qquad \forall\, \boldsymbol{w} \ \text{ in } H^0_1(\mathcal{B}_0) \end{aligned} \tag{7.5.3}$$

Accordingly, the governing equations for the material motion problem (7.4.10) can be expressed in terms of $\rho_{0\,n+1}$ and $\boldsymbol{\Phi}_{n+1}$.

$$\begin{aligned} \mathsf{G}^{\rho}_{n+1}(\ \vartheta; \rho_{0\,n+1}, \boldsymbol{\Phi}_{n+1}\,) &= \mathsf{W}^{\rho}_{\text{dyn}} + \mathsf{W}^{\rho}_{\text{int}} - \mathsf{W}^{\rho}_{\text{sur}} - \mathsf{W}^{\rho}_{\text{vol}} = 0 \qquad \forall\, \vartheta \ \text{ in } H^0_1(\mathcal{B}_t) \\ \mathsf{G}^{\Phi}_{n+1}(\boldsymbol{W}; \rho_{0\,n+1}, \boldsymbol{\Phi}_{n+1}\,) &= \mathsf{W}^{\Phi}_{\text{dyn}} + \mathsf{W}^{\Phi}_{\text{int}} - \mathsf{W}^{\Phi}_{\text{sur}} - \mathsf{W}^{\Phi}_{\text{vol}} = 0 \qquad \forall\, \boldsymbol{W} \ \text{ in } H^0_1(\mathcal{B}_t) \end{aligned} \tag{7.5.4}$$

Next, the semi–discrete sets of governing equations (7.5.3) and (7.5.4) will be discretized in space with the finite element method. For addition information on nonlinear finite element technologies, we advise the classical finite element literature by Crisfield [44, 45], Cook [33, 34], Bathe [11], Bonet & Wood [16], Belytschko et al. [14], Hughes [102], Wriggers [221, 222] and Zienkiewicz & Taylor [226–228].

### 7.5.1 Spatial motion problem

Let $\mathcal{B}_0$ denote the region occupied by the reference configuration of a solid continuum body at time $t = t_0$. In the spirit of the finite element method, this reference domain is discretized in $e = 1, \dots, n_{\text{el}}$ elements $\mathcal{B}_0^e$. The underlying geometry $\boldsymbol{X}$ is interpolated elementwise by the shape functions $N_X^i$ in terms of the discrete node point positions $\boldsymbol{X}_i$ of the $i = 1, \dots, n_{\text{en}}$ element nodes.

$$\mathcal{B}_0 = \bigcup_{e=1}^{n_{\text{el}}} \mathcal{B}_0^e \qquad \boldsymbol{X}^h|_{\mathcal{B}_0^e} = \sum_{I=1}^{n_{\text{en}}} N_X^i \, \boldsymbol{X}_i \tag{7.5.5}$$

Following the isoparametric concept, the unknowns $\rho_0$ and $\boldsymbol{\varphi}$ are interpolated on the element level with the same shape functions $N_\rho^i$ and $N_\varphi^j$ as the element geometry $\boldsymbol{X}$. The same shape functions are applied to interpolate the test functions $\vartheta$ and $\boldsymbol{w}$ according to the classical Bubnov–Galerkin technique.

$$\begin{aligned} \vartheta^h|_{\mathcal{B}_0^e} &= \sum_{i=1}^{n_{\text{en}}} N_\rho^i \, \vartheta_i \in H_1^0(\mathcal{B}_0) & \rho_0^h|_{\mathcal{B}_0^e} &= \sum_{k=1}^{n_{\text{en}}} N_\rho^k \, \rho_k \in H_1(\mathcal{B}_0) \\ \boldsymbol{w}^h|_{\mathcal{B}_0^e} &= \sum_{j=1}^{n_{\text{en}}} N_\varphi^j \, \boldsymbol{w}_j \in H_1^0(\mathcal{B}_0) & \boldsymbol{\varphi}^h|_{\mathcal{B}_0^e} &= \sum_{l=1}^{n_{\text{en}}} N_\varphi^l \, \boldsymbol{\varphi}_l \in H_1(\mathcal{B}_0) \end{aligned} \tag{7.5.6}$$

The related gradients of the test functions $\nabla_X \vartheta^h$ and $\nabla_X \boldsymbol{w}^h$ and the gradients of the primary unknowns $\nabla_X \rho_0^h$ and $\nabla_X \boldsymbol{\varphi}^h$ thus take the following elementwise interpolation,

$$\begin{aligned} \nabla_X \vartheta^h|_{\mathcal{B}_0^e} &= \sum_{i=1}^{n_{\text{en}}} \vartheta_i \quad \nabla_X N_\rho^i & \nabla_X \rho_0^h|_{\mathcal{B}_0^e} &= \sum_{k=1}^{n_{\text{en}}} \rho_k \quad \nabla_X N_\rho^k \\ \nabla_X \boldsymbol{w}^h|_{\mathcal{B}_0^e} &= \sum_{j=1}^{n_{\text{en}}} \boldsymbol{w}_j \otimes \nabla_X N_\varphi^j & \nabla_X \boldsymbol{\varphi}^h|_{\mathcal{B}_0^e} &= \sum_{l=1}^{n_{\text{en}}} \boldsymbol{\varphi}_l \otimes \nabla_X N_\varphi^l \end{aligned} \tag{7.5.7}$$

whereby $\nabla_X \boldsymbol{\varphi}^h|_{\mathcal{B}_0^e}$ in particular denotes the discrete spatial deformation gradient as $\boldsymbol{F}^h|_{\mathcal{B}_0^e} = \nabla_X \boldsymbol{\varphi}^h|_{\mathcal{B}_0^e}$. With the above suggested discretizations in time and space, the discrete algorithmic balance of mass and momentum of the spatial motion problem can be expressed as

$$\begin{aligned} \mathsf{r}^{\rho h}_I(\rho_{0\,n+1}^h, \boldsymbol{\varphi}_{n+1}^h) &= \mathsf{f}^{\rho\ h}_{\text{dyn}\,I} + \mathsf{f}^{\rho\ h}_{\text{int}\,I} - \mathsf{f}^{\rho\ h}_{\text{sur}\,I} - \mathsf{f}^{\rho\ h}_{\text{vol}\,I} = 0 \qquad \forall \quad I = 1, \dots, n_{\text{np}} \\ \mathbf{r}^{\varphi h}_J(\rho_{0\,n+1}^h, \boldsymbol{\varphi}_{n+1}^h) &= \mathbf{f}^{\varphi\ h}_{\text{dyn}\,J} + \mathbf{f}^{\varphi\ h}_{\text{int}\,J} - \mathbf{f}^{\varphi\ h}_{\text{sur}\,J} - \mathbf{f}^{\varphi\ h}_{\text{vol}\,J} = \mathbf{0} \qquad \forall \quad J = 1, \dots, n_{\text{np}} \end{aligned} \tag{7.5.8}$$

with the dynamic, the internal, the surface and the volume contribution of the balance of mass expanding to the following expressions.

$$\begin{aligned} \mathsf{f}^{\rho\ h}_{\text{dyn}\,I} &= \mathop{\mathsf{A}}_{e=1}^{n_{\text{el}}} \int_{\mathcal{B}_0^e} N_\rho^i \, \frac{\rho_{0\,n+1} - \rho_{0n}}{\Delta t} \, \mathrm{d}V_0 & \mathsf{f}^{\rho\ h}_{\text{int}\,I} &= \mathop{\mathsf{A}}_{e=1}^{n_{\text{el}}} \int_{\mathcal{B}_0^e} \nabla_X N_\rho^i \cdot \boldsymbol{R}_{n+1} \, \mathrm{d}V_0 \\ \mathsf{f}^{\rho\ h}_{\text{sur}\,I} &= \mathop{\mathsf{A}}_{e=1}^{n_{\text{el}}} \int_{\partial \mathcal{B}_0^{re}} N_\rho^i \, [r_{n+1}^{\text{closed}} + \bar{r}_{n+1}^{\text{open}}] \, \mathrm{d}A_0 & \mathsf{f}^{\rho\ h}_{\text{vol}\,I} &= \mathop{\mathsf{A}}_{e=1}^{n_{\text{el}}} \int_{\mathcal{B}_0^e} N_\rho^i \, \mathcal{R}_{0\,n+1} \, \mathrm{d}V_0 \end{aligned} \tag{7.5.9}$$

The corresponding discrete inertia forces, the internal forces, the surface forces and the volume forces take the following format,

$$\begin{aligned}
\mathbf{f}^{\varphi\ h}_{\mathrm{dyn}J} &= \mathop{\mathbf{A}}_{e=1}^{n_{\mathrm{el}}} \int_{\mathcal{B}_0^e} N_\varphi^j \ \rho_0 \, \frac{\boldsymbol{p}_{n+1} - \boldsymbol{p}_n}{\Delta t} \ \mathrm{d}V_0 \qquad \mathbf{f}^{\varphi\ h}_{\mathrm{int}J} = \mathop{\mathbf{A}}_{e=1}^{n_{\mathrm{el}}} \int_{\mathcal{B}_0^e} \nabla_X N_\varphi^j \cdot \bar{\boldsymbol{\Pi}}_{Dn+1} \, \mathrm{d}V_0 \\
\mathbf{f}^{\varphi\ h}_{\mathrm{sur}J} &= \mathop{\mathbf{A}}_{e=1}^{n_{\mathrm{el}}} \int_{\partial\mathcal{B}_0^{te}} N_\varphi^j \, [\boldsymbol{t}^{\mathrm{closed}}_{n+1} + \bar{\boldsymbol{t}}^{\mathrm{open}}_{n+1}] \, \mathrm{d}A_0 \qquad \mathbf{f}^{\varphi\ h}_{\mathrm{vol}J} = \mathop{\mathbf{A}}_{e=1}^{n_{\mathrm{el}}} \int_{\mathcal{B}_0^e} N_\varphi^j \quad \bar{\boldsymbol{b}}_{0\,n+1} \, \mathrm{d}V_0
\end{aligned} \tag{7.5.10}$$

with the understanding that the operator $\mathbf{A}$ denotes the assembly over all $e = 1, \dots, n_{\mathrm{el}}$ element forces at the $i, j = 1, \dots, n_{\mathrm{en}}$ element nodes to the global node point forces at all $I, J = 1, \dots, n_{\mathrm{np}}$ global node points. Equations (7.5.8) represent the coupled nonlinear set of governing equations which is suggested to be solved in a monolithic sense. The corresponding solution procedure in terms of the incremental iterative Newton Raphson scheme is illustrated in section 7.6, see also Kuhl & Steinmann [133]. It is worth noting, that the discrete spatial surface forces acting on the global node points can be calculated as

$$\mathbf{f}^{\varphi\ h}_{\mathrm{sur}J} = \mathop{\mathbf{A}}_{e=1}^{n_{\mathrm{el}}} \int_{\mathcal{B}_0^e} N_\varphi^j \, \rho_0 \, \frac{\boldsymbol{p}_{n+1} - \boldsymbol{p}_n}{\Delta t} + \nabla_X N_\varphi^j \cdot \bar{\boldsymbol{\Pi}}_{Dn+1} - N_\varphi^j \, \bar{\boldsymbol{b}}_{0\,n+1} \, \mathrm{d}V_0 \tag{7.5.11}$$

and are thus energetically conjugate to spatial variations of the node point positions.

### 7.5.2 Material motion problem

For the material motion problem, we discretize the domain of interest $\mathcal{B}_t$ in $e = 1, \dots, n_{\mathrm{el}}$ elements $\mathcal{B}_t^e$. The geometry $\boldsymbol{x}$ of each element is interpolated from the $i = 1, \dots, n_{\mathrm{en}}$ node point positions $\boldsymbol{x}_i$ by the shape functions $N_x^i$.

$$\mathcal{B}_t = \bigcup_{e=1}^{n_{\mathrm{el}}} \mathcal{B}_t^e \qquad \boldsymbol{x}^h|_{\mathcal{B}_t^e} = \sum_{I=1}^{n_{\mathrm{en}}} N_x^i \, \boldsymbol{x}_i \tag{7.5.12}$$

Again, we shall interpolate the primary unknowns $\rho_0$ and $\boldsymbol{\Phi}$ with the same shape functions $N_\rho^i$ and $N_\Phi^j$ as the element geometry $\boldsymbol{x}$ by making use of the isoparametric concept. Following the classical Bubnov–Galerkin technique, the test functions $\vartheta$ and $\boldsymbol{W}$ are discretized with the same shape functions $N_\rho^i$ and $N_\Phi^j$.

$$\begin{aligned}
\vartheta^h \ |_{\mathcal{B}_t^e} &= \sum_{i=1}^{n_{\mathrm{en}}} N_\rho^i \ \vartheta_i \quad \in \ H_1^0(\mathcal{B}_t) \qquad \rho_0^h \ |_{\mathcal{B}_t^e} = \sum_{k=1}^{n_{\mathrm{en}}} N_\rho^k \ \rho_k \quad \in \ H_1(\mathcal{B}_t) \\
\boldsymbol{W}^h|_{\mathcal{B}_t^e} &= \sum_{j=1}^{n_{\mathrm{en}}} N_\varphi^j \ \boldsymbol{W}_j \ \in \ H_1^0(\mathcal{B}_t) \qquad \boldsymbol{\Phi}^h|_{\mathcal{B}_t^e} = \sum_{l=1}^{n_{\mathrm{en}}} N_\Phi^l \ \boldsymbol{\Phi}_l \ \in \ H_1(\mathcal{B}_t)
\end{aligned} \tag{7.5.13}$$

The discretization of the corresponding gradients of the test functions $\nabla_x \vartheta^h$ and $\nabla_x \boldsymbol{W}^h$ and the gradients of the primary unknowns $\nabla_x \rho_0^h$ and $\nabla_x \boldsymbol{\Phi}^h$ thus takes the following representation.

$$\begin{aligned}
\nabla_x \, \vartheta^h \ |_{\mathcal{B}_t^e} &= \sum_{i=1}^{n_{\mathrm{en}}} \vartheta_i \qquad \nabla_x N_\rho^i \qquad \nabla_x \, \rho_0^h \ |_{\mathcal{B}_t^e} = \sum_{k=1}^{n_{\mathrm{en}}} \rho_k \qquad \nabla_x N_\rho^k \\
\nabla_x \, \boldsymbol{W}^h|_{\mathcal{B}_t^e} &= \sum_{j=1}^{n_{\mathrm{en}}} \boldsymbol{W}_j \otimes \nabla_x N_\Phi^j \qquad \nabla_x \, \boldsymbol{\Phi}^h|_{\mathcal{B}_t^e} = \sum_{l=1}^{n_{\mathrm{en}}} \boldsymbol{\Phi}_l \otimes \nabla_x N_\Phi^l
\end{aligned} \tag{7.5.14}$$

Note that $\nabla_x \boldsymbol{\Phi}^h$ denotes the discrete material deformation gradient $\boldsymbol{f}^h|_{\mathcal{B}_t^e} = \nabla_x \boldsymbol{\Phi}^h|_{\mathcal{B}_t^e}$. Finally, the discrete algorithmic balance of mass and momentum of the material motion problem can be expressed as follows,

$$\begin{aligned} \mathsf{R}^{\rho h}_{\ I}\ (\rho_{0\,n+1}^{\ h}, \boldsymbol{\Phi}^h_{n+1}) &= \mathsf{F}^{\rho\ h}_{\mathrm{dyn}\,I} + \mathsf{F}^{\rho\ h}_{\mathrm{int}\,I} - \mathsf{F}^{\rho\ h}_{\mathrm{sur}\,I} - \mathsf{F}^{\rho\ h}_{\mathrm{vol}\,I} = 0 \qquad \forall \quad I = 1, \dots, n_{\mathrm{np}} \\ \mathbf{R}^{\Phi h}_{\ J}\ (\rho_{0\,n+1}^{\ h}, \boldsymbol{\Phi}^h_{n+1}) &= \mathbf{F}^{\Phi\ h}_{\mathrm{dyn}\,J} + \mathbf{F}^{\Phi\ h}_{\mathrm{int}\,J} - \mathbf{F}^{\Phi\ h}_{\mathrm{sur}\,J} - \mathbf{F}^{\Phi\ h}_{\mathrm{vol}\,J} = \mathbf{0} \qquad \forall \quad J = 1, \dots, n_{\mathrm{np}} \end{aligned} \tag{7.5.15}$$

whereby the dynamic, the internal, the surface and the volume contribution of the balance of mass are given in the following form.

$$\begin{aligned} \mathsf{F}^{\rho\ h}_{\mathrm{dyn}\,I} &= \mathop{\mathsf{A}}_{e=1}^{n_{\mathrm{el}}} \int_{\mathcal{B}_t^e} N_\rho^i \ j \frac{\rho_{0\,n+1} - \rho_{0n}}{\Delta t} \, \mathrm{d}V_t \qquad \mathsf{F}^{\rho\ h}_{\mathrm{int}\,I} = \mathop{\mathsf{A}}_{e=1}^{n_{\mathrm{el}}} \int_{\mathcal{B}_t^e} \nabla_x N_\rho^i \ \cdot \boldsymbol{r}_{n+1} \, \mathrm{d}V_t \\ \mathsf{F}^{\rho\ h}_{\mathrm{sur}\,I} &= \mathop{\mathsf{A}}_{e=1}^{n_{\mathrm{el}}} \int_{\partial\mathcal{B}_t^{Re}} N_\rho^i \, [R^{\mathrm{closed}}_{n+1} + \bar{R}^{\mathrm{open}}_{n+1}] \, \mathrm{d}A_t \qquad \mathsf{F}^{\rho\ h}_{\mathrm{vol}\,I} = \mathop{\mathsf{A}}_{e=1}^{n_{\mathrm{el}}} \int_{\mathcal{B}_t^e} N_\rho^i \, \mathcal{R}_{t\,n+1} \, \mathrm{d}V_t \end{aligned} \tag{7.5.16}$$

Moreover, the discrete material inertia forces, the internal forces, the surface forces and the volume forces take the following format.

$$\begin{aligned} \mathbf{F}^{\Phi\ h}_{\mathrm{dyn}\,J} &= \mathop{\mathsf{A}}_{e=1}^{n_{\mathrm{el}}} \int_{\mathcal{B}_t^e} N_\Phi^j \ \rho_t \frac{\boldsymbol{P}_{n+1} - \boldsymbol{P}_n}{\Delta t} \, \mathrm{d}V_t \qquad \mathbf{F}^{\Phi\ h}_{\mathrm{int}\,J} = \mathop{\mathsf{A}}_{e=1}^{n_{\mathrm{el}}} \int_{\mathcal{B}_t^e} \nabla_x N_\Phi^j \cdot \bar{\boldsymbol{\pi}}_{D\,n+1} \, \mathrm{d}V_t \\ \mathbf{F}^{\Phi\ h}_{\mathrm{sur}\,J} &= \mathop{\mathsf{A}}_{e=1}^{n_{\mathrm{el}}} \int_{\partial\mathcal{B}_t^{Te}} N_\Phi^j \, [\boldsymbol{T}^{\mathrm{closed}}_{n+1} + \bar{\boldsymbol{T}}^{\mathrm{open}}_{n+1}] \, \mathrm{d}A_t \qquad \mathbf{F}^{\Phi\ h}_{\mathrm{vol}\,J} = \mathop{\mathsf{A}}_{e=1}^{n_{\mathrm{el}}} \int_{\mathcal{B}_t^e} N_\Phi^j \ \bar{\boldsymbol{B}}_{t\,n+1} \, \mathrm{d}V_t \end{aligned} \tag{7.5.17}$$

As a fundamental difference to the spatial motion problem, the Neumann boundary conditions of the material motion problem cannot be considered as given input data. Correspondingly, the discrete material forces acting on the global node points can only be computed in a post processing calculation once the spatial motion problem has been solved. Their definition parallels the definition of the discrete surface forces of the spatial motion problem. The discrete material surface forces

$$\mathbf{F}^{\Phi\ h}_{\mathrm{sur}\,J} = \mathop{\mathsf{A}}_{e=1}^{n_{\mathrm{el}}} \int_{\mathcal{B}_t^e} N_\Phi^j \, \rho_t \frac{\boldsymbol{P}_{n+1} - \boldsymbol{P}_n}{\Delta t} + \nabla_x N_\Phi^j \cdot \bar{\boldsymbol{\pi}}_{D\,n+1} - N_\Phi^j \, \bar{\boldsymbol{B}}_{t\,n+1} \, \mathrm{d}V_t \tag{7.5.18}$$

are thus energetically conjugate to material variations of the node point positions.

**Remark 7.5.1 (Integration point based approach)** *In contrast to the previous approach, we shall now relax the assumption of $C^0$–continuity for the density field $\rho_0$ and allow for a discrete pointwise density representation while the deformation field $\boldsymbol{\varphi}$ is, of course, still required to be $C^0$–continuous. Consequently, the balance of mass can be evaluated locally on the integration point level, whereas the global system of equations is expressed in terms of the deformation only. By introducing the density as internal variable on the integration point level, we solve the balance of mass and momentum in a staggered sense. Recall that by relaxing the continuity requirement for the density, we a priori exclude the possibility of incorporating a mass flux. In complete analogy to the node point based approach, the spatial discretization is based on the*

*partition of the domain of interest $\mathcal{B}_0$ into $n_{\text{el}}$ elements $\mathcal{B}_0^e$ on which the element geometry $\boldsymbol{X}^h$ is interpolated according to the following formulae.*

$$\mathcal{B}_0 = \bigcup_{e=1}^{n_{\text{el}}} \mathcal{B}_0^e \qquad \boldsymbol{X}^h|_{\mathcal{B}_0^e} = \sum_{I=1}^{n_{\text{en}}} N_X^i \, \boldsymbol{X}_i \tag{7.5.19}$$

*Following the isoparametric concept in combination with the Bubnov–Galerkin technique, the same basis functions $N$ are applied for the interpolation of the test and trial functions $\boldsymbol{w}^h$ and $\boldsymbol{\varphi}^h$.*

$$\boldsymbol{w}^h|_{\mathcal{B}_0^e} = \sum_{j=1}^{n_{\text{en}}} N_\varphi^j \, \boldsymbol{w}_j \;\in\; H_1^0(\mathcal{B}_0) \qquad \boldsymbol{\varphi}^h|_{\mathcal{B}_0^e} = \sum_{l=1}^{n_{\text{en}}} N_\varphi^l \, \boldsymbol{\varphi}_l \;\in\; H_1(\mathcal{B}_0) \tag{7.5.20}$$

*Consequently, the spatial gradients of the test and trial functions $\nabla \boldsymbol{w}^h$ and $\nabla \boldsymbol{\varphi}^h$ can be expressed in the following format.*

$$\nabla_X \, \boldsymbol{w}^h|_{\mathcal{B}_0^e} \;=\; \sum_{j=1}^{n_{\text{en}}} \boldsymbol{w}_j \otimes \nabla_X N_\varphi^j \qquad \nabla_X \, \boldsymbol{\varphi}^h|_{\mathcal{B}_0^e} \;=\; \sum_{l=1}^{n_{\text{en}}} \boldsymbol{\varphi}_l \otimes \nabla_X N_\varphi^l \tag{7.5.21}$$

*The algorithmic balance of momentum can thus be stated as*

$$\mathbf{r}^{\varphi h}_J(\rho_{0\,n+1}^h, \boldsymbol{\varphi}_{n+1}^h) = \mathbf{f}^{\varphi\ h}_{\text{dyn}\,J} + \mathbf{f}^{\varphi\ h}_{\text{int}\,J} - \mathbf{f}^{\varphi\ h}_{\text{sur}\,J} - \mathbf{f}^{\varphi\ h}_{\text{vol}\,J} = \mathbf{0} \qquad \forall \quad J = 1, \ldots, n_{\text{np}} \tag{7.5.22}$$

*with the discrete inertia forces, the internal forces, the surface forces and the volume forces given as follows.*

$$\begin{aligned}
\mathbf{f}^{\varphi\ h}_{\text{dyn}\,J} &= \mathop{\mathbf{A}}_{e=1}^{n_{\text{el}}} \int_{\mathcal{B}_0^e} N_\varphi^j \;\; \rho_0 \, \frac{\boldsymbol{p}_{n+1} - \boldsymbol{p}_n}{\Delta t} \;\; \mathrm{d}V_0 \qquad \mathbf{f}^{\varphi\ h}_{\text{int}\,J} = \mathop{\mathbf{A}}_{e=1}^{n_{\text{el}}} \int_{\mathcal{B}_0^e} \nabla_X N_\varphi^j \cdot \bar{\boldsymbol{\Pi}}_{D\,n+1} \, \mathrm{d}V_0 \\
\mathbf{f}^{\varphi\ h}_{\text{sur}\,J} &= \mathop{\mathbf{A}}_{e=1}^{n_{\text{el}}} \int_{\partial\mathcal{B}_0^{te}} N_\varphi^j \, [\boldsymbol{t}_{n+1}^{\text{closed}} + \bar{\boldsymbol{t}}_{n+1}^{\text{open}}] \, \mathrm{d}A_0 \qquad \mathbf{f}^{\varphi\ h}_{\text{vol}\,J} = \mathop{\mathbf{A}}_{e=1}^{n_{\text{el}}} \int_{\mathcal{B}_0^e} N_\varphi^j \quad \bar{\boldsymbol{b}}_{0\,n+1} \, \mathrm{d}V_0
\end{aligned} \tag{7.5.23}$$

**Remark 7.5.2 (Transient terms in the residuals)** *In most practical applications, the time rate of change of the mass and momentum typically differ by several orders of magnitude. For biological problems, for example, the momentum balance is therefore considered in a quasi–static sense in order to avoid numerical problems. Consequently, the dynamic contributions which manifest themselves in the $N_\varphi^j \rho_0 \, [\boldsymbol{p}_{n+1} - \boldsymbol{p}_n]/\Delta t$ term of equation (7.5.10)$_1$ and in the $N_\Phi^j \rho_t \, [\boldsymbol{P}_{n+1} - \boldsymbol{P}_n]/\Delta t$ term of equation (7.5.17)$_1$ are typically neglected. Since the distinction of the different momentum fluxes is then no longer necessary, the additional subscripts $d$ and $D$ will be neglected in the sequel, as $\bar{\boldsymbol{\Pi}} = \bar{\boldsymbol{\Pi}}_D = \bar{\boldsymbol{\Pi}}_d$ and $\bar{\boldsymbol{\pi}} = \bar{\boldsymbol{\pi}}_D = \bar{\boldsymbol{\pi}}_d$.*

**Remark 7.5.3 (Spatial vs. material quantities)** *For the quasi–static case, the discrete reduced momentum flux $\bar{\boldsymbol{\pi}}_{n+1}^t$, and the corresponding momentum source $\bar{\boldsymbol{B}}_{t\,n+1}$ that are essentially needed to compute the discrete material node point forces defined in equation (7.5.18) are related to their spatial motion counterparts through the following transformation formulae.*

$$\begin{aligned}
\bar{\boldsymbol{\pi}}_{n+1}^t &= -j \, \boldsymbol{F}_{n+1}^t \cdot \bar{\boldsymbol{\Pi}}_{n+1}^t \cdot \boldsymbol{F}_{n+1}^t + \rho_{t\,n+1} \psi_{n+1} \, \boldsymbol{F}_{n+1}^t \\
\bar{\boldsymbol{B}}_{t\,n+1} &= j \, \boldsymbol{F}_{n+1}^t \cdot \bar{\boldsymbol{b}}_{0\,n+1} - \rho_{t\,n+1} \, \partial_{\rho_0} \psi_{n+1} \, \nabla_X \rho_{0\,n+1} - \partial_{\boldsymbol{\Phi}} [\, \rho_{t\,n+1} \psi_{n+1} \,]
\end{aligned} \tag{7.5.24}$$

**Remark 7.5.4 (Material forces in biomechanics)** *In many biomechanical applications, in particular in functional adaption and wound healing, material forces play an important role, since they essentially pinpoint locations where changes in mass are about to take place. In section 7.12, we will illustrate the information provided by the discrete material node point forces in the context of growth in hard tissues such as bones, compare also Kuhl & Steinmann [135]. In the qualitative study carried out in section 7.13, material forces will be applied as a pure indicator for healing processes, compare also Kuhl & Steinmann [130]. However, one could think of interpreting them as driving force for growth or healing in the future and develop a material force based mechanical stimulus. The effects of wound shape on the healing process, e.g. the slower healing of circular wounds in comparison to flat wounds as illustrated by Murray [166] would then be incorporated in the healing model in a natural way.*

## 7.6 Linearization

To solve the discrete coupled nonlinear system of equations of the spatial motion problem, we suggest a monolithic solution strategy based on the consistent linearization of the governing equations. The discrete balance of mass $(7.5.8)_1$ and the discrete mass specific balance of momentum $(7.5.8)_2$ thus have to be solved simultaneously. To this end, we apply an incremental iterative Newton–Raphson solution procedure supplemented by the consistent linearization of the governing equations at time $t_{n+1}$.

$$\begin{aligned} \mathsf{r}_{I\ n+1}^{\rho\ k+1} &= \mathsf{r}_{I\ n+1}^{\rho\ k} + \mathrm{d}\mathsf{r}_I^{\rho} \doteq 0 \qquad \forall \quad I = 1, \dots, n_{\mathrm{np}} \\ \mathbf{r}_{J\ n+1}^{\varphi\ k+1} &= \mathbf{r}_{J\ n+1}^{\varphi\ k} + \mathrm{d}\mathbf{r}_J^{\varphi} \doteq \mathbf{0} \qquad \forall \quad J = 1, \dots, n_{\mathrm{np}} \end{aligned} \tag{7.6.1}$$

The iterative residua $\mathrm{d}\mathsf{r}_I^{\rho}$ and $\mathrm{d}\mathbf{r}_J^{\varphi}$

$$\begin{aligned} \mathrm{d}\mathsf{r}_I^{\rho} &= \sum_{K=1}^{n_{\mathrm{np}}} \mathsf{K}_{IK}^{\rho\rho}\ \mathrm{d}\rho_K + \sum_{L=1}^{n_{\mathrm{np}}} \mathbf{K}_{IL}^{\rho\varphi} \cdot \mathrm{d}\boldsymbol{\varphi}_L \qquad \forall \quad I = 1, \dots, n_{\mathrm{np}} \\ \mathrm{d}\mathbf{r}_J^{\varphi} &= \sum_{K=1}^{n_{\mathrm{np}}} \mathbf{K}_{JK}^{\varphi\rho}\ \mathrm{d}\rho_K + \sum_{L=1}^{n_{\mathrm{np}}} \mathbf{K}_{JL}^{\varphi\varphi} \cdot \mathrm{d}\boldsymbol{\varphi}_L \qquad \forall \quad J = 1, \dots, n_{\mathrm{np}} \end{aligned} \tag{7.6.2}$$

can be expressed in terms of the iteration matrices $\mathsf{K}_{IK}^{\rho\rho}$, $\mathbf{K}_{IL}^{\rho\varphi}$, $\mathbf{K}_{JK}^{\varphi\rho}$ and $\mathbf{K}_{JL}^{\varphi\varphi}$ and the incremental changes of the global vector of unknowns $\mathrm{d}\rho_K$ and $\mathrm{d}\boldsymbol{\varphi}_L$. For the problem at hand, these iteration matrices which can be interpreted as submatrices of the global tangential stiffness matrix take the following format.

$$\begin{aligned} \mathsf{K}_{IK}^{\rho\rho} &= \frac{\partial \mathsf{r}_I^{\rho}}{\partial \rho_K} = \mathop{\mathsf{A}}_{e=1}^{n_{\mathrm{el}}} \int_{\mathcal{B}_0^e} N^i \frac{1}{\Delta t} N^k - N^i \mathrm{D}_{\rho_0} \mathcal{R}_0 N^k + \nabla_X N^i \cdot \mathrm{D}_{\nabla_X \rho_0} \boldsymbol{R} \cdot \nabla_X N^k \mathrm{d}V_0 \\ \mathbf{K}_{IL}^{\rho\varphi} &= \frac{\partial \mathsf{r}_I^{\rho}}{\partial \boldsymbol{\varphi}_L} = \mathop{\mathsf{A}}_{e=1}^{n_{\mathrm{el}}} \int_{\mathcal{B}_0^e} -N^i\ \mathrm{D}_{\boldsymbol{F}} \mathcal{R}_0 \cdot \nabla_X N^l \ \mathrm{d}V_0 \\ \mathbf{K}_{JK}^{\varphi\rho} &= \frac{\partial \mathbf{r}_J^{\varphi}}{\partial \rho_K} = \mathop{\mathsf{A}}_{e=1}^{n_{\mathrm{el}}} \int_{\mathcal{B}_0^e} \nabla_X N^j \cdot \mathrm{D}_{\rho_0} \bar{\boldsymbol{\Pi}}^t N^k \ \mathrm{d}V_0 \\ \mathbf{K}_{JL}^{\varphi\varphi} &= \frac{\partial \mathbf{r}_J^{\varphi}}{\partial \boldsymbol{\varphi}_L} = \mathop{\mathsf{A}}_{e=1}^{n_{\mathrm{el}}} \int_{\mathcal{B}_0^e} N^j \rho_0\ \frac{1}{\Delta t}\, \boldsymbol{I} N^l + \nabla_X N^j \cdot \mathrm{D}_{\boldsymbol{F}} \bar{\boldsymbol{\Pi}}^t \cdot \nabla_X N^l \ \mathrm{d}V_0 \end{aligned} \tag{7.6.3}$$

Herein, $\mathbf{K}^{\varphi\varphi}$ represents the classical tangential stiffness matrix of the standard deformation problem, whereby its second term collects both, the geometric and the material contribution. The partial derivatives of the mass source $\mathcal{R}_0$, the mass flux $\boldsymbol{R}$ and the reduced momentum flux $\bar{\boldsymbol{\Pi}}^t$ with respect to the primary unknowns $\rho_0$ and $\boldsymbol{\varphi}$ obviously depend on the choice of the constitutive equations which was exemplified earlier in section 4.5. Finally, the solution of the linearized system of equations (7.6.1) defines the iterative update for the global unknowns $\rho_I$ and $\boldsymbol{\varphi}_J$.

$$\begin{aligned} \rho_I &= \rho_I + \mathrm{d}\,\boldsymbol{\rho}_I \qquad \forall \quad I = 1, \dots, n_{\mathrm{np}} \\ \boldsymbol{\varphi}_J &= \boldsymbol{\varphi}_J + \mathrm{d}\,\boldsymbol{\varphi}_J \qquad \forall \quad J = 1, \dots, n_{\mathrm{np}} \end{aligned} \tag{7.6.4}$$

**Remark 7.6.1 (Integration point based approach)** *Similar to the node point based approach, the nonlinear equilibrium equation (7.5.22) is solved within the incremental iterative Newton–Raphson iteration scheme requiring a consistent linearization at time $t_{n+1}$.*

$$\mathbf{r}\,{}^{\varphi\ k+1}_{J\ n+1} = \mathbf{r}\,{}^{\varphi\ k}_{J\ n+1} + \mathrm{d}\mathbf{r}\,{}^{\varphi}_{J} \doteq \mathbf{0} \qquad \forall\ J = 1, \dots, n_{n\varphi} \tag{7.6.5}$$

*The iterative residual* $\mathrm{d}\mathbf{r}\,{}^{\varphi}_{J}$

$$\mathrm{d}\mathbf{r}^{\varphi}_{J} = \sum_{L=1}^{n_{\mathrm{np}}} \mathbf{K}^{\varphi\varphi}_{JL} \cdot \mathrm{d}\boldsymbol{\varphi}_L \qquad \forall \quad J = 1, \dots, n_{\mathrm{np}} \tag{7.6.6}$$

*can be expressed in terms of the iteration matrix*

$$\mathbf{K}^{\varphi\varphi}_{JL} = \frac{\partial \mathbf{r}^{\varphi}_{J}}{\partial \boldsymbol{\varphi}_L} = \overset{n_{\mathrm{el}}}{\underset{e=1}{\boldsymbol{A}}} \int_{\mathcal{B}^e_0} N^j \rho_0 \, \frac{1}{\Delta t} \boldsymbol{I} N^l + \nabla_X N^j \cdot \mathrm{D}_{\boldsymbol{F}} \bar{\boldsymbol{\Pi}}^t \cdot \nabla_X N^l \mathrm{d}V_0 \tag{7.6.7}$$

*which takes the interpretation of the global tangential stiffness matrix. Therein,* $\mathrm{D}_F \bar{\boldsymbol{\Pi}}^t$ *denotes the consistent tangent operator,*

$$\mathrm{D}_F \bar{\boldsymbol{\Pi}}^t = \partial_F \bar{\boldsymbol{\Pi}}^t - \partial_{\rho_0} \bar{\boldsymbol{\Pi}}^t \left[ \overline{\partial_{\rho_0} \mathcal{R}_0} \right]^{-1} \partial_F \mathcal{R}_0 \tag{7.6.8}$$

*whereby the partial derivatives of the mass source $\mathcal{R}_0$ and of the reduced momentum flux $\bar{\boldsymbol{\Pi}}^t$ with respect to $\rho_0$ and $\boldsymbol{F}$, $\partial_F \bar{\boldsymbol{\Pi}}^t$, $\partial_{\rho_0} \bar{\boldsymbol{\Pi}}^t$ and $\partial_F \mathcal{R}_0$, again depend on the particular constitutive equations which were exemplified earlier in section 4.5. The remaining partial derivative $\overline{\partial_{\rho_0} \mathcal{R}_0}$ can be expressed in the following form.*

$$\overline{\partial_{\rho_0} \mathcal{R}_0} = [n - m] \frac{1}{\rho_0} \left[ \frac{\rho_0}{\rho_0^*} \right]^{-m} \psi_0 \, \Delta t - 1 \tag{7.6.9}$$

*The iterative update for the global unknowns* $\boldsymbol{\varphi}_J$

$$\boldsymbol{\varphi}_J = \boldsymbol{\varphi}_J + \mathrm{d}\,\boldsymbol{\varphi}_J \qquad \forall \quad J = 1, \dots, n_{n\varphi} \tag{7.6.10}$$

*can finally be determined in terms of the solution* $\mathrm{d}\boldsymbol{\varphi}_J$ *of the linearized system of equations (7.6.5).*

**Remark 7.6.2 (Transient terms in the linearized residuals)** *Recall that when considering the reduced balance of momentum in the quasi–static sense, the term* $N^J \rho_0 / \Delta t \, \boldsymbol{I} \, N^L$ *of equation* $(7.6.3)_4$ *vanishes identically.*

**Remark 7.6.3 (Consistent vs. lumped dynamic matrices)** *When consistent dynamic matrices are applied to interpolate the time–dependent contributions, i.e. the* $N^i_\rho \, [\rho_{0\,n+1} - \rho_{0\,n}] \, \Delta t$ *and the* $N^i_\rho \, 1/\Delta t \, N^k_\rho$ *terms in equations* $(7.5.16)_1$ *and* $(7.6.3)_1$*, the numerical solution might tend to develop spurious oscillations near sharp fronts. The use of lumped dynamic matrices typically reduces these numerical artifacts.*

## 7.7 Algorithmic aspects

Figure 7.3 depicts the four applied finite element formulations as typical representatives of the node point based approach, whereby the white circles characterize the density nodes whereas the dark circles mark the deformation nodes. While the classical Q1Q1 and Q2Q2 element are based on an equal order interpolation of the density and the deformation field, the Q1P0 element and the S2Q1 element interpolate the density one order lower than the deformation. All elements except for the Q2Q2 element which

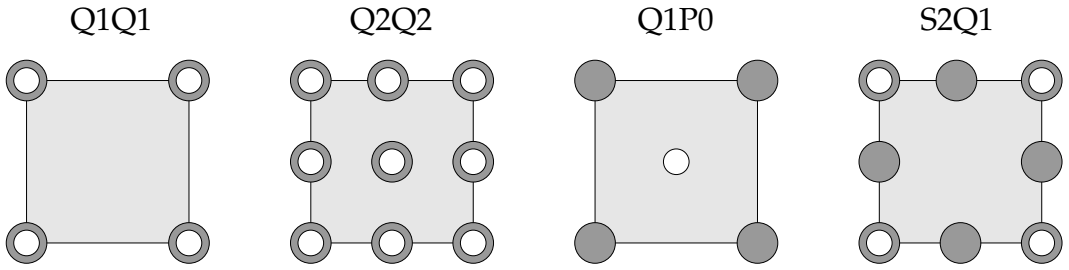


**Figure 7.3:** Different element formulations – Node point based approach

is evaluated numerically at $3 \times 3$ integration points make use of a Gauss–Legendre quadrature based on $2 \times 2$ integration points. A typical finite element solution algorithm resulting from the node point based approach is sketched in the flowchart in table 7.1. It illustrates that the balance of mass and momentum are solved simultaneously on the global level. Both, the density and the deformation are introduced as global unknowns and determined within a global Newton iteration procedure.

**Remark 7.7.1 (Material force method)** *Observe that in the node point based approach, the density* $\rho_0$ *has been interpolated in a* $\mathcal{C}^0$*–continuous way. The evaluation of the material density gradient* $\nabla_X \rho_0$ *required to determine the discrete material node point forces* $\mathbf{F}^{\Phi}_{\text{sur}}$ *in equation (7.5.18) does not demand any additional computational effort. Rather, their calculation can be carried out as a mere post–processing procedure as sketched in table 7.1.*

**Remark 7.7.2 (Integration point based approach)** *Within the integration point based approach, we will analyze four different element formulations which are depicted in figure 7.4. While the Q1 and the Q2 element are classically integrated with* $2 \times 2$ *and* $3 \times 3$ *quadrature points, respectively, the* $Q1^{\text{sri}}$ *element is based on a selectively reduced one–point–integration*

| |
|---|
| loop over all time steps |
| global Newton iteration |
| loop over all elements |
| loop over all integration points |
| evaluate balance of mass and momentum |
| determine $\mathsf{r}^{\rho e}$, $\mathbf{r}^{\varphi e}$, $\partial_\rho \mathsf{r}^{\rho e}$, $\partial_{\boldsymbol{\varphi}} \mathsf{r}^{\rho e}$, $\partial_\rho \mathbf{r}^{\varphi e}$, $\partial_{\boldsymbol{\varphi}} \mathbf{r}^{\varphi e}$ |
| element residuals and their partial derivatives |
| determine $\mathsf{r}^{\rho}$, $\mathbf{r}^{\varphi}$, $\mathsf{K}^{\rho\rho}$, $\mathbf{K}^{\rho\varphi}$, $\mathbf{K}^{\varphi\rho}$, $\mathbf{K}^{\varphi\varphi}$ |
| global residuals and iteration matrices |
| determine $\rho_{n+1}$ and $\boldsymbol{\varphi}_{n+1}$ |
| determine $\bar{\boldsymbol{\Pi}}^t$, $\bar{\boldsymbol{\pi}}^t$, $\bar{b}_0$, $\bar{\boldsymbol{B}}_t$, $\mathbf{F}^{\Phi}_{\text{sur}}$ |
| red. momentum fluxes and sources and material forces |
| determine state of biological equilibrium |

**Table 7.1:** Algorithm of node point based approach

*of the density part in combination with a 2 × 2 integration of the deformation part. The S2*$^{\text{fri}}$ *element, however, applies a fully reduced 2 × 2 integration of both contributions. Table 7.2 illustrates a typical flowchart resulting from the integration point based approach. The balance*

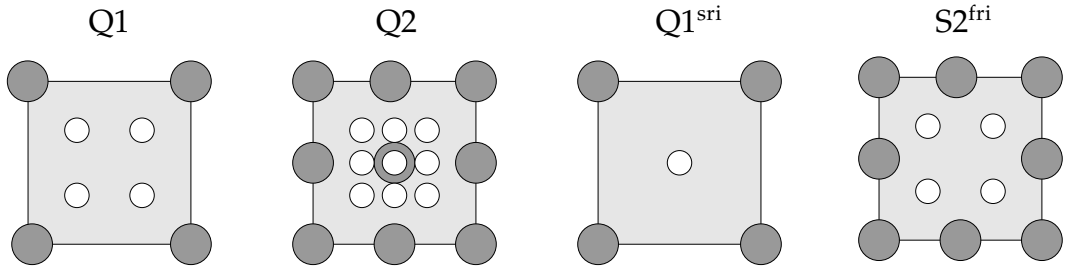


**Figure 7.4:** Different element formulations – Integration point based approach

*equations are solved in a staggered way, characterized through a local Newton iteration for the actual integration point density embedded in the global Newton iteration for the deformation field.*

**Remark 7.7.3 (Q1P0 element)** *Within the node point based approach, we typically solve the balance of mass and momentum simultaneously on the global level assuming a* $\mathcal{C}^0$*–continuous interpolation of the density* $\rho_0$ *and the deformation* $\boldsymbol{\varphi}$*. The only node point based finite element formulation that relaxes this continuity requirement is the Q1P0 element, which is based on an elementwise constant and thus* $\mathcal{C}^{-1}$*–continuous density interpolation. Recall that for this element, which is classically applied for constrained problems arising in computational fluid dynamics or in incompressible elastodynamics, the constantly interpolated degree of freedom, in our case the density, can be eliminated locally on the element level. This procedure, which*

loop over all time steps
- global Newton iteration
  - loop over all elements
    - loop over all integration points
      - local Newton iteration
        - evaluate balance of mass
        - determine $\mathsf{r}^{\rho e}$, $\partial_\rho \mathsf{r}^{\rho e}$
          local residual and its partial derivative
      - determine $\rho_{n+1}$
      - evaluate balance of momentum
    - determine $\mathbf{r}^{\varphi e}$, $\partial_\varphi \mathbf{r}^{\varphi e}$
      element residual and its partial derivative
  - determine $\mathbf{r}^{\varphi}$, $\mathbf{K}^{\varphi\varphi}$
    global residual and iteration matrix
  - determine $\boldsymbol{\varphi}_{n+1}$

determine state of biological equilibrium

**Table 7.2:** Algorithm of integration point based approach

*bares strong resemblance to the classical static condensation, results in the modified residual* $\tilde{\mathbf{r}}^{\,\varphi}_{J}$ *and the modified stiffness matrix* $\tilde{\mathbf{K}}^{\varphi\varphi}_{JL}$.

$$\begin{aligned} \tilde{\mathbf{r}}^{\,\varphi}_{J} &= \mathbf{r}^{\,\varphi}_{J} - \mathbf{K}^{\varphi\rho}_{JK} \left[\mathsf{K}^{\rho\rho}_{IK}\right]^{-1} \mathsf{r}^{\rho}_{I} \\ \tilde{\mathbf{K}}^{\varphi\varphi}_{JL} &= \mathbf{K}^{\varphi\varphi}_{JL} - \mathbf{K}^{\varphi\rho}_{JK} \left[\mathsf{K}^{\rho\rho}_{IK}\right]^{-1} \mathbf{K}^{\rho\varphi}_{IL} \end{aligned} \tag{7.7.1}$$

*In the biomechanical literature, the algorithm resulting from an elementwise constant density distribution has been termed element based approach. It is worth noting that the numerical computation of the Q1P0 element with an elementwise constant density distribution requires some modifications in the algorithmic realization. In this particular case, the balance of mass and momentum are evaluated sequentially. First the midpoint density is advanced in time by performing a local Newton iteration on the element level. Only then, the balance of momentum is evaluated at each integration point with the element density given. Since the deformation* $\boldsymbol{\varphi}_{n+1}$ *is now the only unknown on the global level, the related residual and the tangential stiffness have to be modified according to equations (7.7.1). Note that within the Q1P0 approach the evolution of the element density is driven by the average element mass source.*

$$\frac{\rho_{0n+1} - \rho_{0n}}{\Delta t} = \frac{1}{V} \int_{\mathcal{B}^e_0} \mathcal{R}_0 \left(\rho_{0n+1}, \boldsymbol{\varphi}_{n+1}\right) \mathrm{d}V \tag{7.7.2}$$

*Since the driving force* $\mathcal{R}_0$ *is a nonlinear function of the deformation* $\boldsymbol{\varphi}_{n+1}$*, it has to be evaluated numerically by an appropriate numerical integration before the element density can be determined through the suggested local Newton iteration.*

**Remark 7.7.4 (Q1$^{\text{sri}}$ element)** *Similar to the node point based approach, the realization of an elementwise constant density distribution based on a selectively reduced integration of the scalar field requires some algorithmic modifications. In this case, the balance of mass and momentum are solved sequentially. Just like for the Q1P0 element, the actual midpoint density has to be determined in a local Newton iteration before the balance of momentum is evaluated on the integration point level. In contrast to the Q1P0 element, however, the density evolution is now driven by the midpoint mass source.*

$$\frac{\rho_{0\,n+1} - \rho_{0\,n}}{\Delta t} = \mathcal{R}_0\left(\rho_{0\,n+1}, \boldsymbol{\varphi}_{n+1}\right)\Big|_{\text{midpoint}} \tag{7.7.3}$$

*As the mass source $\mathcal{R}_0$ is a nonlinear function of the deformation $\boldsymbol{\varphi}_{n+1}$, its midpoint value generally differs from its element average. Consequently, the Q1P0 element and the Q1$^{\text{sri}}$ element generally render different results. The significance of this difference strongly depends on the inhomogeneity of the discrete deformation field $\boldsymbol{\varphi}_{n+1}$ and vanishes identically for a homogeneous deformation.*

**Remark 7.7.5 (Tangent operators)** *Note that the structure of the consistent tangent operator for the integration point based approach introduced in equation (7.6.8) resembles the structure of the modified element stiffness matrix after static condensation for the Q1P0 element defined in equation (7.7.1).*

$$\begin{aligned} \mathrm{D}_F \bar{\boldsymbol{\Pi}}^t &= \partial_F \bar{\boldsymbol{\Pi}}^t - \partial_{\rho_0} \bar{\boldsymbol{\Pi}}^t \left[\, \overline{\partial_{\rho_0} \mathcal{R}_0} \,\right]^{-1} \partial_F \mathcal{R}_0 \\ \tilde{\mathbf{K}}^{\varphi\varphi}_{JL} &= \mathbf{K}^{\varphi\varphi}_{JL} - \mathbf{K}^{\varphi\rho}_{JK} \left[\, \mathsf{K}^{\rho\rho}_{IK} \,\right]^{-1} \mathbf{K}^{\rho\varphi}_{IL} \end{aligned} \tag{7.7.4}$$

*The difference between the terms $\overline{\partial_{\rho_0} \mathcal{R}_0}$ and $\partial_{\rho_0} \mathcal{R}_0$ somehow reflects the influence of the algorithmic treatment. By replacing the continuous term $\partial_{\rho_0} \mathcal{R}_0$ with its algorithmic counterpart $\overline{\partial_{\rho_0} \mathcal{R}_0}$ we ensure the consistent linearization of the discrete constitutive equations.*

## 7.8 Example: Parameter sensitivity

In order to gain a better understanding of the constitutive equations introduced in section 4.5.1, we shall first carry out a number of systematic parameter studies for the one–dimensional case.

### 7.8.1 Spatial motion problem

**Influence of mass source** In the first example, we shall illustrate the sensitivity of the density evolution with respect to the parameters characterizing the mass source $\mathcal{R}_0$. To this end, we shall assume the mass flux to vanish identically as $\boldsymbol{R} = \mathbf{0}$ such that the balance of mass takes the following simple format.

$$\mathrm{D}_t\, \rho_0 = \mathcal{R}_0 \qquad \text{with} \qquad \mathcal{R}_0 = \left[\frac{\rho_0}{\rho_0^*}\right]^{-m} \psi_0 - \psi_0^*$$

We consider a one–dimensional homogeneous specimen of unit size with an elasticity modulus of $E = 1$ and a Poisson's ratio of $\nu = 0$ for which the Lamé constants take

values of $\lambda = 0$ and $\mu = 0.5$. Unless otherwise stated, the reference density is chosen to $\rho_0^* = 1$, the value of the reference free energy is $\psi_0^* = 1$ and the two exponents are chosen as $n = 2$ and $m = 3$ while no mass flux is assumed to take place as $R_0 = 0$. The time integration is performed with time increments of $\Delta t = 0.1$ if not stated otherwise. The specimen is loaded by a multiple step loading function with f = 0.5 N for $0.0 \leq t \leq 2.0$, f = 1.0 N for $2.0 < t \leq 4.0$, f = 1.5 N for $4.0 < t \leq 6.0$ and finally f = 2.0 N for $6.0 < t \leq 8.0$, compare figure 7.6, left. The corresponding deformation illustrated in figure 7.5 clearly reflects the nonlinearity of the problem introduced on the one hand through the coupling of density and deformation and on the other hand through the geometric nonlinearity itself.

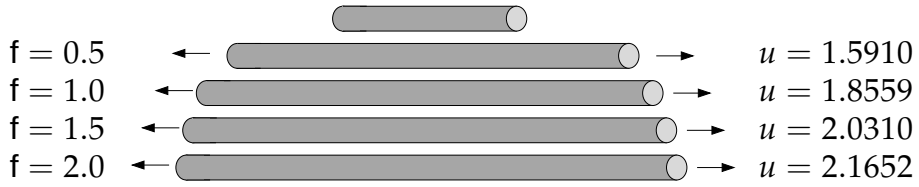


**Figure 7.5:** One–dimensional model problem

The time–dependent nature of the balance of mass is visualized in figures 7.6, left, and 7.6, right. The former depicts the evolution of the primary unknowns, the relative changes in material density $[\rho_0 - \rho_0^*]/\rho_0^*$ and the displacements $u$ for the prescribed loading history f while the latter shows the resulting evolution of the free energy $\psi_0$ and the 'biological stimulus' $[\rho_0/\rho_0^*]^{-m}\psi_0$. All curves obviously demonstrate the relaxation of the corresponding quantities towards 'biological equilibrium', the state at which the density distribution has converged to a final equilibrium value. Each increase of the loading f is followed by changes in the primary unknowns converging towards a new equilibrium state. Figures 7.7, left, and 7.7, right, illustrate the sensitivity of the evolution of relative changes in density $[\rho_0 - \rho_0^*]/\rho_0^*$ with respect to changes in the exponents $n$ and $m$ and the reference value of the free energy $\psi_0^*$. It is clearly visible, that the amount of change in density increases with increasing exponents $n$ and $m$. For $n = 2$ and $m = 3$ the relative change in density is inversely proportional to the reference free energy $\psi_0^*$ as $[\rho_0 - \rho_0^*]/\rho_0^* = \psi_0^{\text{neo}}/\psi_0^* - 1$. Its value thus increases for decreasing values of $\psi_0^*$ as illustrated in figure 7.7, right.
Figures 7.8, left, and 7.8, right, demonstrate the remarkable fact, that for the chosen exponents of $n = 2$ and $m = 3$, the equilibrium value of the relative change in density $[\rho_0 - \rho_0^*]/\rho_0^*$ is not only insensitive to changes in the reference density $\rho_0^*$ as $[\rho_0 - \rho_0^*]/\rho_0^* = \psi_0^{\text{neo}}/\psi_0^* - 1$ but also insensitive to the choice of the time step $\Delta t$. Nevertheless, both, $\psi_0^*$ and $\Delta t$ influence the rate of convergence towards this value of equilibrium. Convergence is thus faster for smaller initial densities $\rho_0^*$ and smaller time steps $\Delta t$.

**Influence of mass flux** The second example demonstrates the sensitivity of the solution with respect to the mass flux. Consequently, we neglect the mass source as $\mathcal{R}_0 = 0$. The balance of mass

$$\mathrm{D}_t\, \rho_0 = \mathrm{Div}\, \boldsymbol{R} \qquad \text{with} \qquad \boldsymbol{R} = R_0\, \nabla \rho_0$$

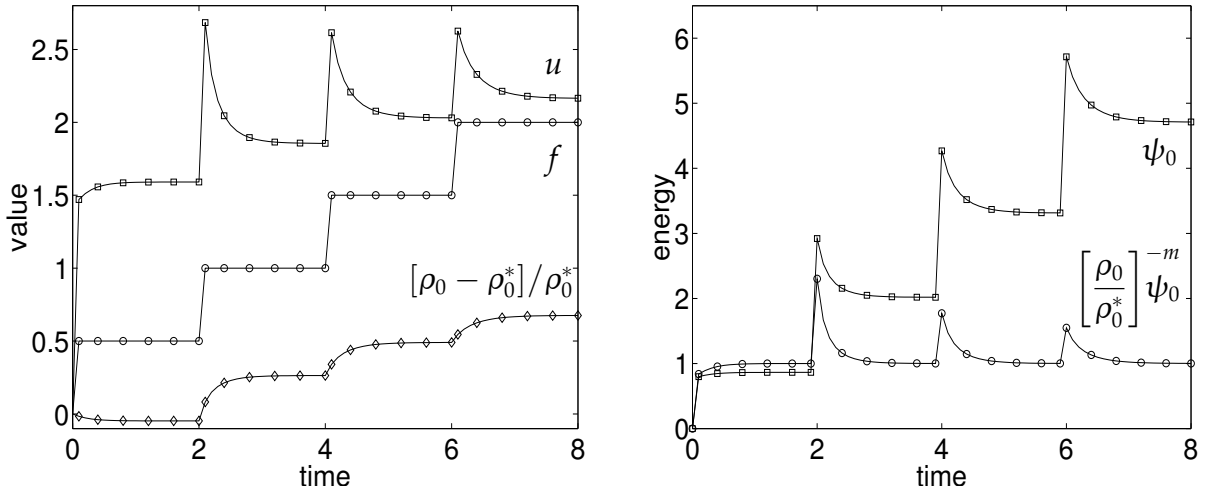


**Figure 7.6:** Temporal evolution of density $[\rho_0 - \rho_0^*]/\rho_0^*$, displacements $u$ and energy $\psi_0$

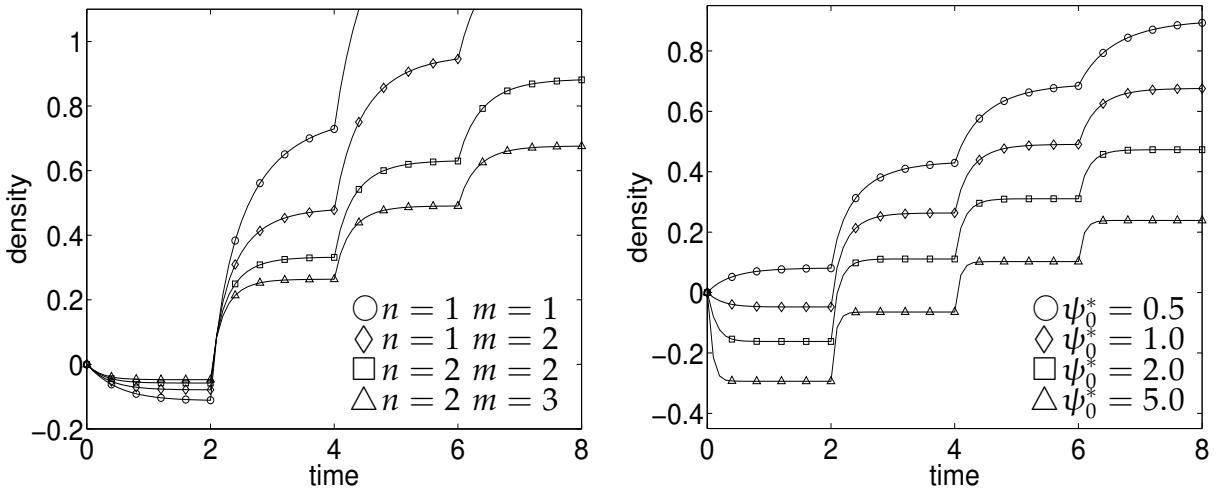


**Figure 7.7:** Parameter sensitivity with respect to $n$, $m$ and $\psi_0^*$

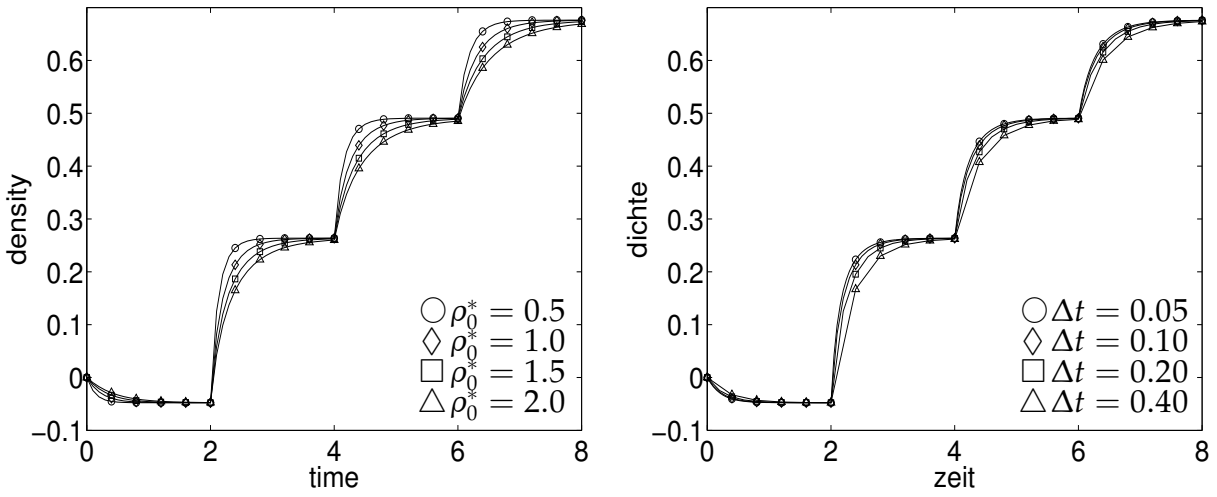


**Figure 7.8:** Parameter sensitivity with respect to $\rho_0^*$ and $\Delta t$

thus fully decouples from the balance of momentum and we consider the pure diffusion problem. We assume an initial hat–type distribution of the density with initial values of $\rho_0 = 1$ and $\rho_0 = 2$ introducing a density jump of $\Delta\rho_0 = 1$. Thereby, the high initial density is prescribed in an $l/2$ wide area of half of the specimen length which is situated right in the middle of the bar as depicted in figure 7.9.

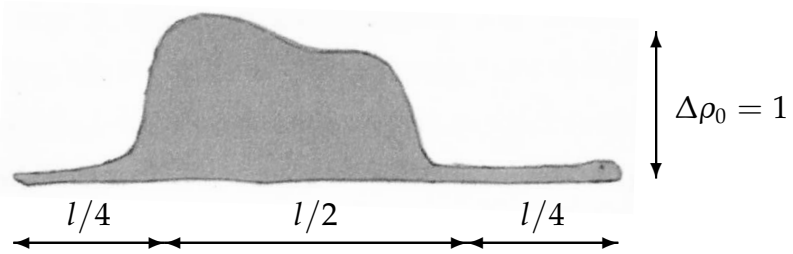


**Figure 7.9:** Initial hat–type density distribution

The corresponding density evolution characterized through the outflux of mass driven by a mass conduction coefficient of $R_0 = 1.0$ is illustrated in figure 7.10. As time proceeds, mass flows out of the areas of high initial mass concentration. After $t = 500$, a state of equilibrium is reached, for which the mass is distributed uniformly at $\rho_0 = 1.5$ in the entire domain. An increase of either the mass conduction coefficient $R_0$ or the time step $\Delta t$ tends to speed up this process of equalization of the mass concentration.

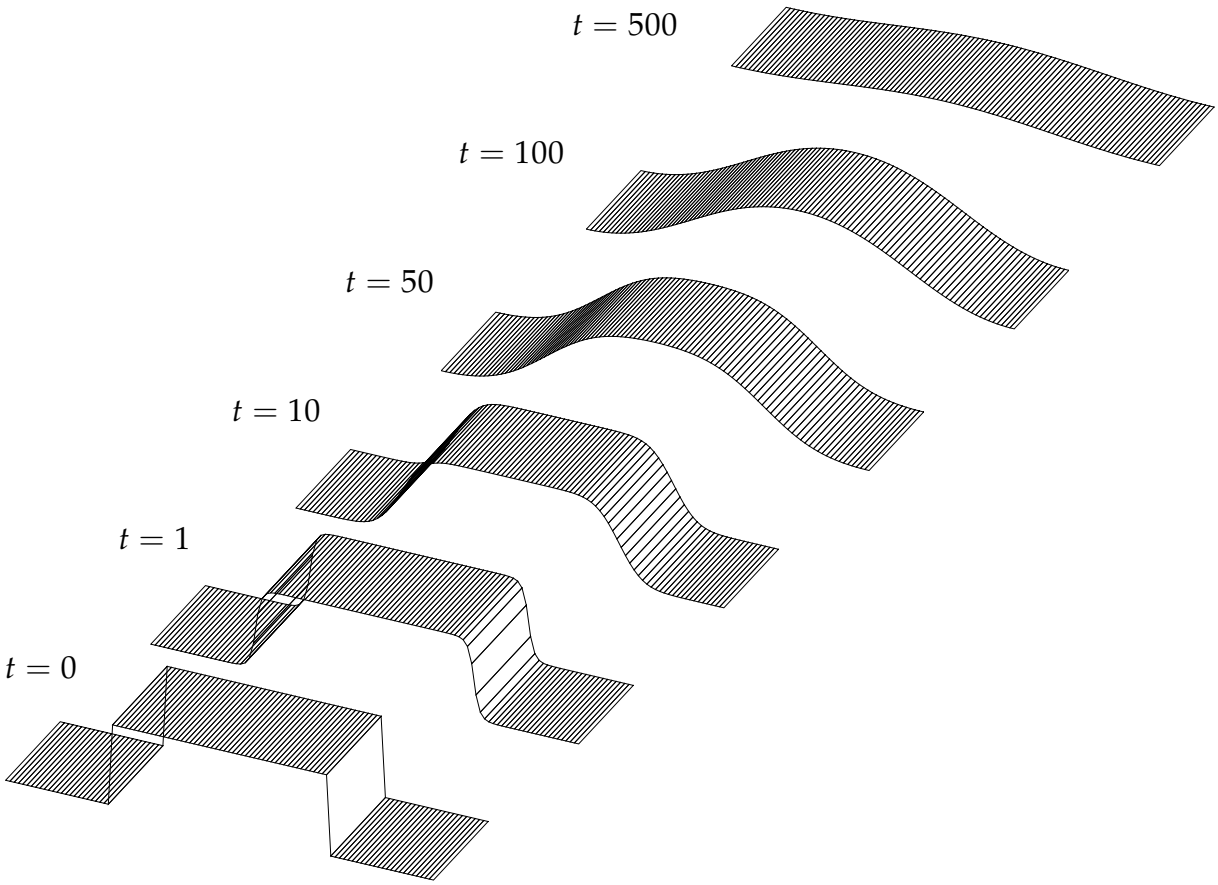


**Figure 7.10:** Time evolution of density due to outflux of mass

**Remark 7.8.1 (Initial hat–type density distribution)** *Mon dessin 7.9 ne représentait pas un chapeau. Il représentait un serpent boa qui digérait un éléphant. J'ai alors dessiné*

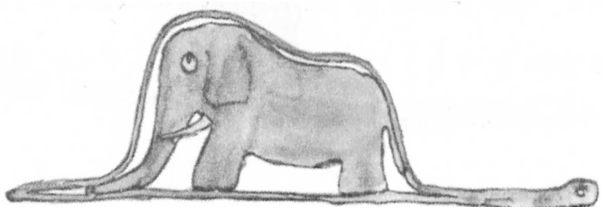

**Figure 7.11:** Initial hat–type density distribution

*l'intérieur du serpent boa, afin que les grandes personnes puissent comprendre. Elles ont toujours besoin d'explications. Antoine de Saint–Exupéry, Le Petit Prince, 1943*

**Influence of mass source and mass flux** Finally, we consider a one–dimensional specimen whereby both, a mass source and a mass flux are present.

$$\mathrm{D}_t\,\rho_0 = \mathrm{Div}\,\boldsymbol{R} + \mathcal{R}_0 \qquad \text{with} \qquad \mathcal{R}_0 = \left[\frac{\rho_0}{\rho_0^*}\right]^{-m} \psi_0 - \psi_0^* \qquad \text{and} \qquad \boldsymbol{R} = R_0\,\nabla\,\rho_0$$

In order to perturb the homogeneous solution, the reference value of the free energy, the attractor stimulus $\psi_0^*$ has been reduced to $\psi_0^* = 1$ in an area of 20% of the total specimen length in the middle of the bar, while it takes values of $\psi_0^* = 2$ outside this area. The other material parameters take homogeneous values throughout the specimen with $E$=1, $\nu = 0$, and thus $\lambda = 0$ and $\mu = 0.5$, $\rho_0^* = 1$, $n = 2$ and $m = 3$.
Figures 7.12 document the influence of the mass conduction coefficient $R_0$ which is gradually increased from $R_0 = 0$ to $R_0 = 1$. The depicted density distributions of the different simulations correspond to the converged equilibrium states after 50 time steps of $\Delta t = 0.1$ each. The discontinuity in the reference free energy $\psi_0^*$ induces a non–homogeneous density distribution with maximum values in the middle of the specimen. For $R_0 = 0$, the analytical solution corresponds to a discontinuous hat–type density distribution which typically cannot be captured by the $C^0$–continuous finite element simulation. The simulation with $R_0 = 0$ and thus without mass flux produces density oscillations close to the density jump. Recall that the discontinuous distribution of material parameters analyzed herein represents an extreme test case from an algorithmic point of view. Basically all existing bone remodeling algorithms in biomechanics a priori neglect the flux of mass with $R_0$ being identical to zero throughout. In most practical applications, however, the material parameters do not vary discontinuously in space. Thus the potential drawback of a non–diffusive formulation is typically not visible in the examples studied in the literature.
Figures 7.12 illustrate how the inclusion of the mass flux through the increase of the mass conduction coefficient smoothes the density profile. The area affected by the disturbed material parameter increases considerably with increasing mass conduction coefficients while the gradients of the density decrease. Since the mass conduction coefficient $R_0$ operates on a Laplacian term, it automatically introduces an additional length scale into the formulation with $R_0$ having the unit of a microstructural length

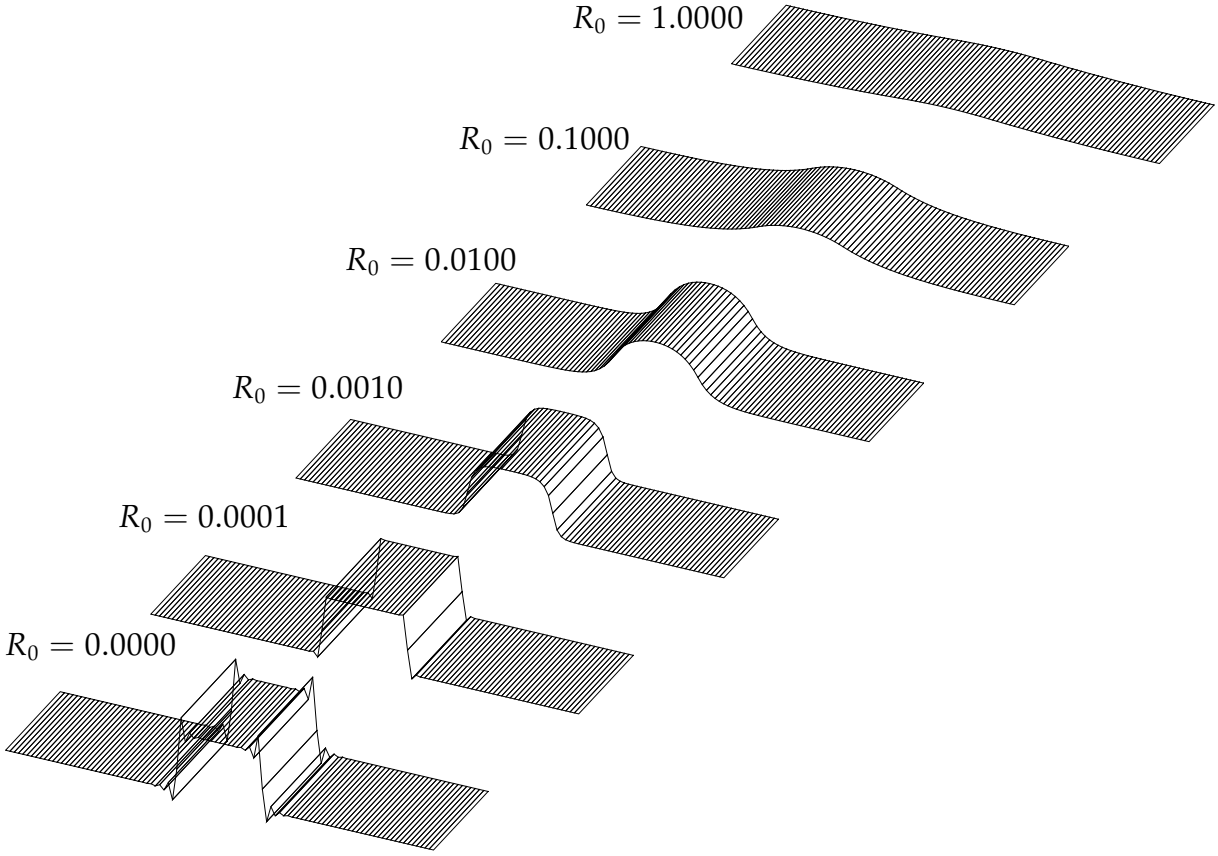


**Figure 7.12:** Density distributions for varying $R_0$

squared divided by the time. In this respect, the mass conduction coefficient takes an analogous interpretation as the gradient parameter in gradient enhanced continuum mechanics. The effect of smoothing of the density distribution and the characteristic size effect of microstructural materials like hard tissues are thus incorporated in the proposed model in a natural and physically justified way.

### 7.8.2 Material motion problem

Let us again consider the academic example of a one–dimensional bar of unit size with Lamé constants of $\lambda = 0$ and $\mu = 0.5$ with

$$\mathrm{D}_t \, \rho_0 = \mathrm{Div} \, \boldsymbol{R} + \mathcal{R}_0 \qquad \text{with} \qquad \mathcal{R}_0 = \left[ \frac{\rho_0}{\rho_0^*} \right]^{-m} \psi_0 - \psi_0^* \qquad \text{and} \qquad \boldsymbol{R} = R_0 \, \nabla \, \rho_0$$

as introduced in the previous section. Again, the specimen has a reference density of $\rho_0^* = 1$ and a reference free energy of $\psi_0^* = 2$, while the two exponents are chosen to $n = 2$ and $m = 3$. In order to trigger an imperfection, the reference free energy $\psi_0^*$ has been reduced to $\psi_0^* = 1$ in an area of 20 % of the total specimen length right in the middle of the bar. We apply a constant load of $\mathsf{f} = 1$ and simulate 50 time steps of $\Delta t = 0.1$ each, until the density has converged to its final equilibrium distribution. Since most existing models for open systems a priori exclude the influence of mass

diffusion, we shall first analyze the model response of a bar for which the mass flux is suppressed as $R_0 = 0$. The resulting density distribution is depicted in figure 7.13, bottom. To illustrate the tendency of the material to form a homogeneous distribution of matter, we have included the volume contribution to the material forces $\mathsf{F}^{\Phi}_{\text{vol}}$. Obviously, the material tends to smooth sharp density contours by flowing in the direction of negative density gradients to achieve an equal concentration throughout the entire bar. This observation coincides with the numerical findings of Müller & Maugin [158], who observed that material forces always try to render the total body more homogeneous.

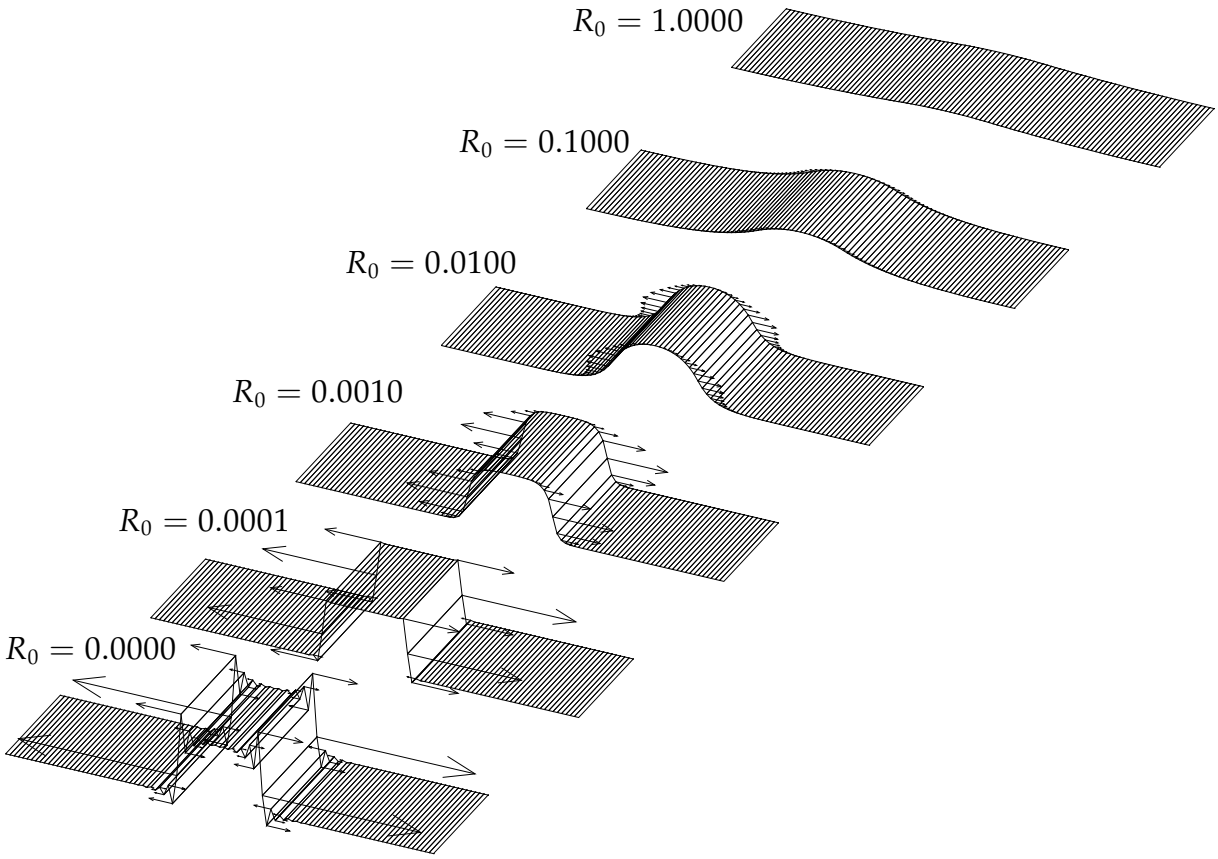


**Figure 7.13:** Material volume forces for varying $R_0$

Next, we shall therefore allow for the outflux of mass in the direction of the material volume forces $\mathsf{F}^{\Phi}_{\text{vol}}$, whereby the amount of outflux is primarily governed by the mass conduction coefficient $R_0$ through the constitutive equation for the mass flux (4.5.4). Figures 7.13 illustrate the resulting density distributions for gradually increasing values of $R_0$. The increase of the mass conduction coefficient clearly smoothes the density profile and widens the area that is affected by the initial imperfection. The smoother the density distribution, the smaller the related density gradients. The resulting material forces thus decrease with an increasing mass flux. For values of $R_0$ larger than a critical value, a homogeneous density distribution can be found, for which the material volume forces vanish identically, compare figure 7.13, top.

In summary, the volume contribution to the material forces $\mathsf{F}^{\Phi}_{\mathrm{vol}}$ can be interpreted as a driving force for the movement of material inhomogeneities in the interior of the considered domain. The material force method provides a motivation for the incorporation of the flow of matter along the direction of descending density gradients. The considered matter thus tends to flow through the material with the aim of equilibrating initially unequal density distributions.

## 7.9 Example: One–dimensional model problem

To compare the essential features of the node point based and the integration point based approach, we shall now elaborate their behavior with respect to two academic model problems upon which the first relates to a discontinuous solution whereas the solution of the second is supposed to be continuous. These two examples somehow represent the extreme cases we assume to encounter in realistic biomechanical applications. In both cases, we analyze a similar tension specimen of unit length with a length to width ratio of one percent. The elastic material parameters are chosen to $\mathrm{E} = 1$ and $\nu = 0.2$, which correspond to $\lambda = 0.2778$ and $\mu = 0.4167$. The growth–related parameters take values of $\rho_0^* = 1$, $\psi_0^* = 2$, $n = 2$ and $m = 3$, whereby stability is guaranteed as $m > n$. A unit tensile load is applied to both ends of the specimen. In combination with the chosen set of parameters, this load generates stretches of about 250 %. To guarantee convergence within the global Newton iteration, the load has to be applied incrementally in ten steps of $\Delta t = 0.1$ each. After the loading phase, the load is held constant for another 50 time steps of $\Delta t = 0.1$ while the solution converges towards the biological equilibrium state. Both, the discontinuous and the continuous model problem will be analyzed systematically for the node point based and the integration point based approach. In total, the characteristic behavior of all the node point based elements introduced in figure 7.3 and all the integration point based elements sketched in figure 7.4 will be elaborated.

### 7.9.1 Node point based approach

Let us begin by analyzing the characteristic features of the node point based approach. The resulting number of degrees of freedom and the number of integration points as a characteristic measures of computational efficiency are given in table 7.3. Thereby, the individual columns are related to a discretization with 10, 40 and 100 elements, thus representing a typical h–refinement. The rows which correspond to the different element formulations as introduced in figure 7.3 can be interpreted as a sort of p–refinement.

**Discontinuous model problem** First, we trigger a discontinuous solution by varying the value of the attractor stimulus $\psi_0^*$ from $\psi_0^* = 2.0$ at both ends in discrete steps of $\Delta\psi_0^* = -0.25$ towards $\psi_0^* = 1.0$ in the middle of the specimen. Obviously, the local reduction of the attractor stimulus has a direct influence on the creation of new material. The decrease of its value is compensated by a considerable local increase in density, as

| | number of degrees of freedom | | | number of integration points | | |
|---|---|---|---|---|---|---|
| | $n_{el} = 10$ | $n_{el} = 40$ | $n_{el} = 100$ | $n_{el} = 10$ | $n_{el} = 40$ | $n_{el} = 100$ |
| Q1Q1 | 66 | 246 | 606 | 40 | 160 | 400 |
| Q2Q2 | 189 | 729 | 1809 | 90 | 360 | 900 |
| Q1P0 | 44 | 164 | 404 | 40 | 160 | 400 |
| S2Q1 | 128 | 488 | 1208 | 40 | 160 | 400 |

**Table 7.3:** Number of degrees of freedom and integration points

illustrated in figure 7.14. The quantitative results of the discontinuous model problem are summarized in table 7.4, which show the relative change in density $[\rho_0 - \rho_0^*]/\rho_0^*$ in the center of the specimen where it takes its maximum value and the maximum displacement $u$ at the endpoint, respectively. The depicted density distributions illus-

| | maximum density $[\rho_0 - \rho_0^*]/\rho_0^*$ | | | maximum displacement $u$ | | |
|---|---|---|---|---|---|---|
| | $n_{el} = 10$ | $n_{el} = 40$ | $n_{el} = 100$ | $n_{el} = 10$ | $n_{el} = 40$ | $n_{el} = 100$ |
| Q1Q1 | 0.321502 | 0.297437 | 0.305828 | 2.32251 | 2.37135 | 2.36629 |
| Q2Q2 | 0.256541 | 0.302062 | 0.306116 | 2.37124 | 2.37151 | 2.37156 |
| Q1P0 | 0.300028 | 0.306185 | 0.306171 | 2.32239 | 2.37122 | 2.36624 |
| S2Q1 | 0.318560 | 0.305875 | 0.306171 | 2.37221 | 2.37181 | 2.37166 |

**Table 7.4:** Discontinuous problem – Maximum density $[\rho_0 - \rho_0^*]/\rho_0^*$ and displacement $u$

trate that the Q1Q1 element produces spurious oscillations close to sharp fronts. It converges to the discontinuous solution upon mesh refinement, however, the artificial overshoots in the solution remain. The element of highest order, the Q2Q2 element, performs worst upon all elements analyzed, compare also table 7.4. The corresponding density distribution is by far too smooth and the results are only valuable upon a considerable mesh refinement. Since the Q2Q2 element is the most expensive element from a computational point of view, it can be classified as non–reasonable for practical use. For this particular discontinuous type of solution, the Q1P0 element with a $\mathcal{C}^{-1}$–continuous density interpolation performs best upon all elements tested. With an elementwise constant density distribution, it is able to capture sharp fronts by construction. The S2Q1 element shows a less oscillatory behavior than the Q1Q1 element. Unlike the Q2Q2 element, it is able to capture discontinuities in a reasonable way. It converges fast upon refinement and is also not too expensive from a computational point of view.

**Continuous model problem** The second example is based upon a continuous solution which is generated by smoothly varying the width of the specimen from 1 % of the specimen length at both ends towards 0.5 % in the middle of the bar. Thereby, the material parameters are kept constant throughout the specimen. The characteristics of

the different elements for a continuous solution can be concluded from figure 7.15 and table 7.5.

| | maximum density $[\rho_0 - \rho_0^*]/\rho_0^*$ | | | maximum displacement $u$ | | |
|---|---|---|---|---|---|---|
| | $n_{\text{el}} = 10$ | $n_{\text{el}} = 40$ | $n_{\text{el}} = 100$ | $n_{\text{el}} = 10$ | $n_{\text{el}} = 40$ | $n_{\text{el}} = 100$ |
| Q1Q1 | 0.509938 | 0.525144 | 0.527496 | 2.92605 | 2.92755 | 2.92780 |
| Q2Q2 | 0.527441 | 0.527699 | 0.534161 | 2.92732 | 2.92785 | 2.92793 |
| Q1P0 | 0.470753 | 0.513734 | 0.522864 | 2.92554 | 2.92752 | 2.92780 |
| S2Q1 | 0.526425 | 0.528890 | 0.529023 | 2.92792 | 2.92794 | 2.92794 |

**Table 7.5:** Continuous problem – Maximum density $[\rho_0 - \rho_0^*]/\rho_0^*$ and displacement $u$

Obviously, the local reduction of the cross section is directly compensated by the creation of material in the center of the specimen. Remarkably, all node point based formulations of a $\mathcal{C}^0$–continuous density interpolation perform equally well for this sufficiently smooth problem. Already for the discretization with 40 elements, the results of the Q1Q1 element, the Q2Q2 element and the S2Q1 element have converged to a reasonable extend, since their continuous density interpolations are typically designed to capture continuous solutions. While the Q1P0 element yields useless results for the coarsest mesh, it converges rapidly upon mesh refinement even though it applies only a $\mathcal{C}^{-1}$–continuous density interpolation, see also table 7.5.

### 7.9.2 Integration point based approach

We now turn to the illustration of the integration point based approach in terms of the discontinuous and the continuous model problem defined in the previous subsection. The number of degrees of freedom and integration points, which is considerably

| | number of degrees of freedom | | | number of integration points | | |
|---|---|---|---|---|---|---|
| | $n_{\text{el}} = 10$ | $n_{\text{el}} = 40$ | $n_{\text{el}} = 100$ | $n_{\text{el}} = 10$ | $n_{\text{el}} = 40$ | $n_{\text{el}} = 100$ |
| Q1 | 44 | 164 | 404 | 40 | 160 | 400 |
| Q2 | 126 | 486 | 1206 | 90 | 360 | 900 |
| $\text{Q1}^{\text{sri}}$ | 44 | 164 | 404 | 10/40 | 40/160 | 100/400 |
| $\text{S2}^{\text{fri}}$ | 106 | 406 | 1006 | 40 | 160 | 400 |

**Table 7.6:** Number of degrees of freedom and integration points

lower than in the previous node point based approach, is depicted in table 7.6. The corresponding four different elements are summarized in figure 7.4.

**Discontinuous model problem** The resulting density distribution, the relative change in density $[\rho_0 - \rho_0^*]/\rho_0^*$ in the middle of the specimen and the endpoint displacement $u$ are given in figure 7.16 and table 7.7, respectively. Note that in order to illustrate

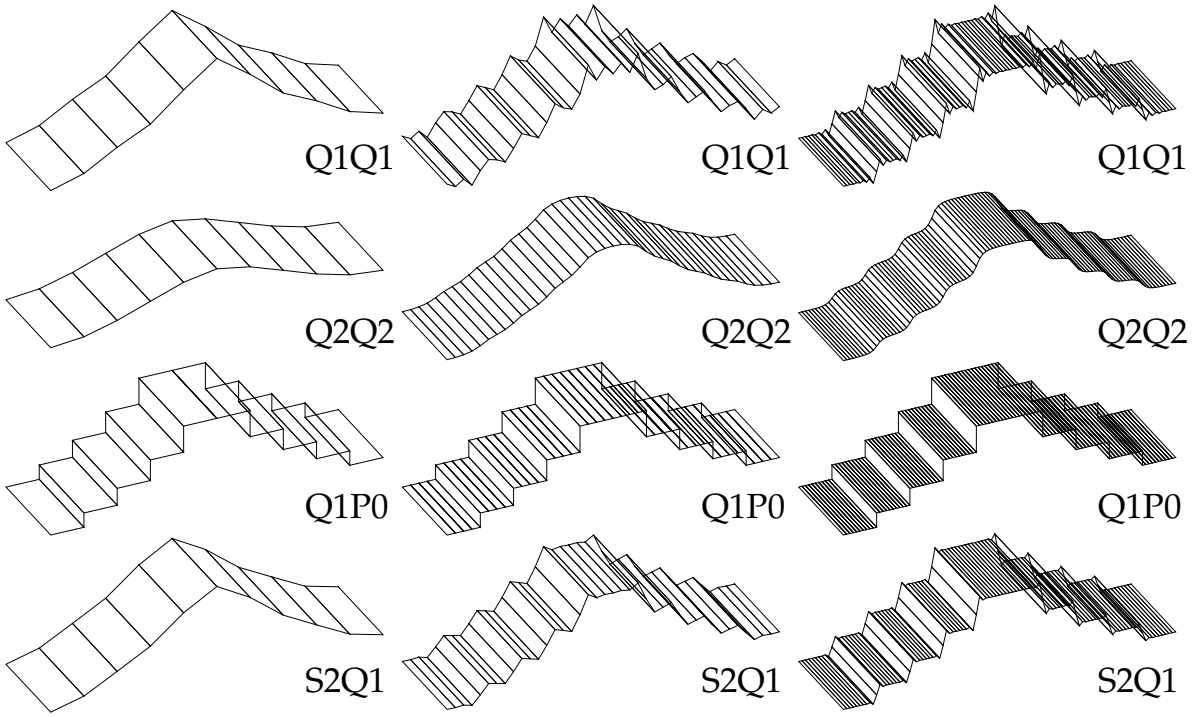


**Figure 7.14:** Discontinuous problem – Density distribution node point based approach

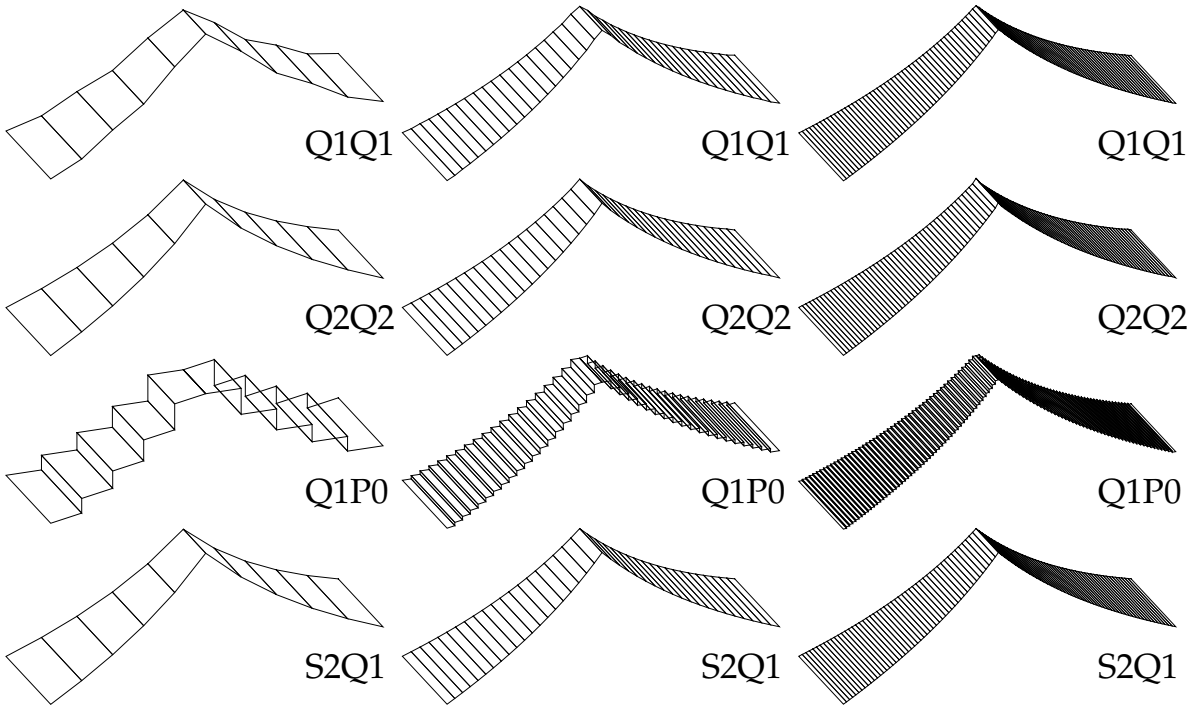


**Figure 7.15:** Continuous problem – Density distribution node point based approach

the typical features of the integration point based approach, the integration point values are plotted in a non–smoothed discontinuous fashion. Unlike in classical finite

| | maximum density $[\rho_0 - \rho_0^*]/\rho_0^*$ | | | maximum displacement $u$ | | |
|---|---|---|---|---|---|---|
| | $n_{\text{el}} = 10$ | $n_{\text{el}} = 40$ | $n_{\text{el}} = 100$ | $n_{\text{el}} = 10$ | $n_{\text{el}} = 40$ | $n_{\text{el}} = 100$ |
| Q1 | 0.300028 | 0.306185 | 0.306418 | 2.32239 | 2.37122 | 2.36624 |
| Q2 | 0.306443 | 0.306186 | 0.306188 | 2.37095 | 2.37146 | 2.37154 |
| $Q1^{\text{sri}}$ | 0.300028 | 0.306168 | 0.306171 | 2.32239 | 2.37135 | 2.36630 |
| $S2^{\text{fri}}$ | 0.306504 | 0.306282 | 0.306171 | 2.37156 | 2.37155 | 2.37155 |

**Table 7.7:** Discontinuous problem – Maximum density $[\rho_0 - \rho_0^*]/\rho_0^*$ and displacement $u$

element post–processing, where the integration point values are typically extrapolated to the nodes and then averaged, we plot the actual constant integration point value in the entire area that is assigned to the particular quadrature point. As expected, all elements with the density as internal variable perform excellent for this particular discontinuous problem. By construction, the integration point based approach is ideally suited for discontinuous solutions with sharp fronts.

**Continuous model problem** Even for the continuous problem, the integration point based elements perform remarkably well. Not only the classical Q1 element and the Q2 element but also the $Q1^{\text{sri}}$ element and the $S2^{\text{fri}}$ element converge fast upon mesh refinement, compare also figure 7.17 and table 7.8. Thereby, the computationally cheap-

| | maximum density $[\rho_0 - \rho_0^*]/\rho_0^*$ | | | maximum displacement $u$ | | |
|---|---|---|---|---|---|---|
| | $n_{\text{el}} = 10$ | $n_{\text{el}} = 40$ | $n_{\text{el}} = 100$ | $n_{\text{el}} = 10$ | $n_{\text{el}} = 40$ | $n_{\text{el}} = 100$ |
| Q1 | 0.470754 | 0.513734 | 0.522864 | 2.92548 | 2.92751 | 2.92780 |
| Q2 | 0.514584 | 0.526201 | 0.529164 | 2.92732 | 2.92785 | 2.92793 |
| $Q1^{\text{sri}}$ | 0.470753 | 0.513734 | 0.522864 | 2.92599 | 2.92765 | 2.92786 |
| $S2^{\text{fri}}$ | 0.503670 | 0.522526 | 0.526427 | 2.92789 | 2.92794 | 2.92794 |

**Table 7.8:** Continuous problem – Maximum density $[\rho_0 - \rho_0^*]/\rho_0^*$ and displacement $u$

est approaches, namely the Q1 element and the selectively reduced integrated $Q1^{\text{sri}}$ element show only minor differences. Both of them can thus be classified as extremely fast and efficient for practical use. Nevertheless, due to the standard computational structure of the related numerical algorithm, we would prefer the classical Q1 element over the $Q1^{\text{sri}}$ element for practical applications.

**Remark 7.9.1 (Element based approach)** *In the literature, the constant density element is typically said to produce spatial instabilities in the form of checkerboard type density distributions. However, from the systematic case studies carried out within this work, we would*

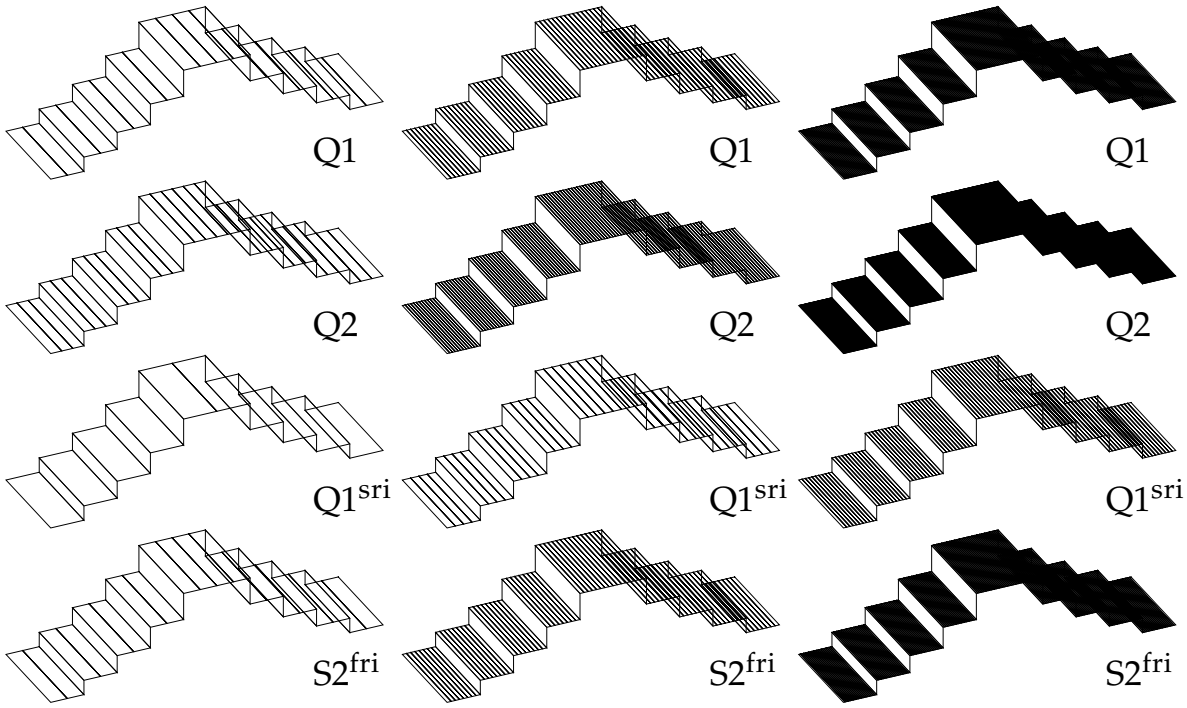


**Figure 7.16:** Discontinuous problem- Density distribution integration point based approach

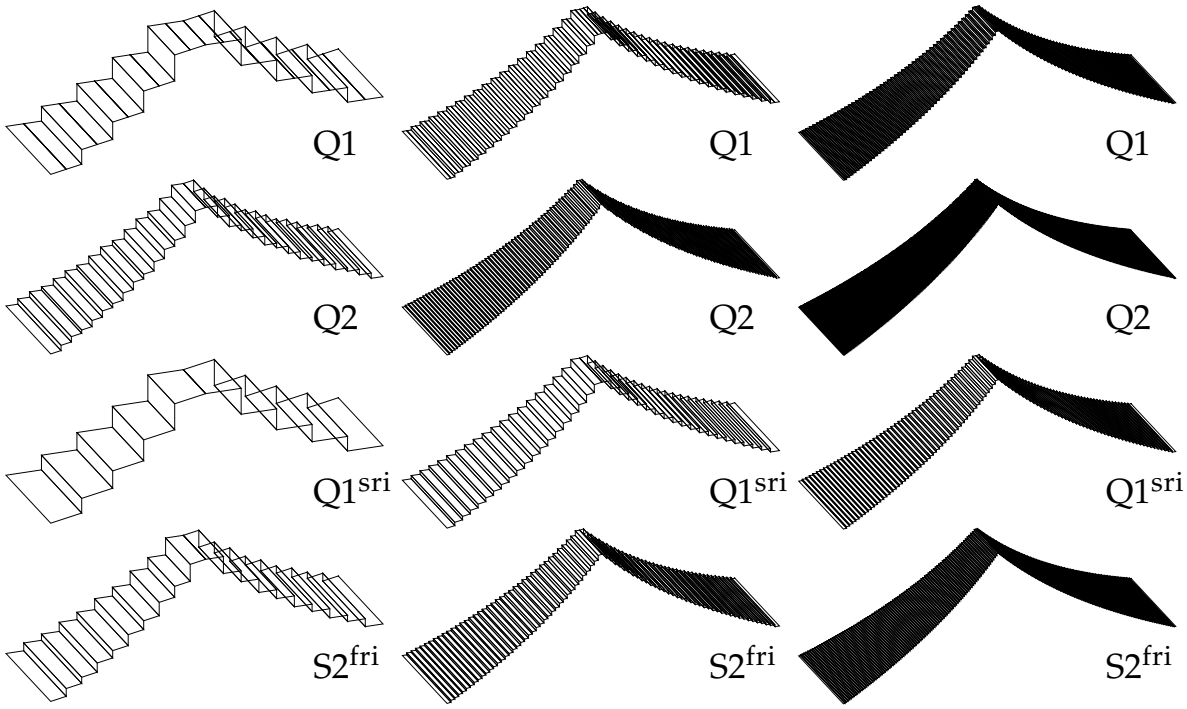


**Figure 7.17:** Continuous problem – Density distribution integration point based approach

*rather attribute these instabilities to the unstable continuum formulation than to the underlying spatial discretization. With the well–posed continuum problem analyzed herein, which is integrated implicitly in time and discretized consistently in space, we do neither observe the spatial instabilities nor the problems of convergence that were reported in the literature.*

**Remark 7.9.2 (Q1P0 element vs. Q1$^{\text{sri}}$ element)** *This particular model problem still shows a rather homogeneous deformation in each element. Thus, the difference between the Q1P0 element and the Q1$^{\text{sri}}$ element is only of minor nature. However, by comparing the resulting maximum density and the endpoint displacements, slight deviations of both approaches can be observed.*

## 7.10 Example: Computational modeling of topology optimization

The following example is motivated by the work of Weng [218], who applied an algorithm for the functional adaption of hard tissues to find the optimal arrangement of material in a rectangular panel under prescribed loads, see figures 7.18, left, and 7.18, right. A similar example has been analyzed by Maute [153] in the context of the topology optimization aiming to find the optimal structure of a bicycle frame, see 7.18, middle. The Lamé parameters of the simulation are chosen to $\lambda = 576.92$ and

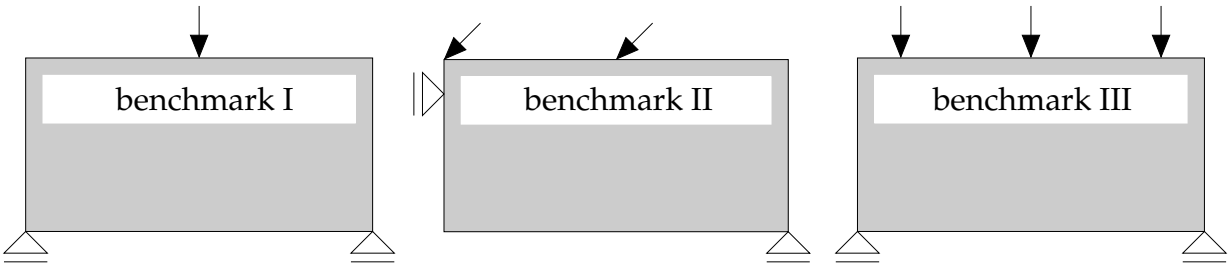


**Figure 7.18:** Topology optimization – Geometry and loading conditions

$\mu = 384.62$ corresponding to Young's modulus of $E = 1000$ and Poisson's ratio of $\nu = 0.30$. Changes in the density are caused by a density source defined through $\rho_0^* = 0.1$ and $\psi_0^* = 0.5$ in combination with the two exponents $n = 2$ and $m = 3$. In the first part of the example, the flux of matter is assumed to be suppressed as $R_0 = 0$. The design spaces of the panel of 1m length and 0.5m height as well as the three different types of loading and boundary conditions are depicted in figures 7.18. The load is applied as a single step load in the first time step and then held constant throughout the analysis. The simulation is carried out until the density distribution has completely adapted to the applied loading scenario. In the cases considered herein, this state of convergence is achieved after 20 time steps of $\Delta t = 0.01$ each.
The resulting density distributions for the three different loading situations are depicted in figures 7.19. Thereby, the blue areas indicate a decrease in local density caused by a resorption of material up to -80 %, while the red areas indicate an increase in local density and thus the absorption of new material up to +20 %. The algorithm clearly tends to generate strut–like structures by resorbing material in regions that do not contribute to the load transfer while absorbing material in load carrying areas. Mass is

added locally in regions where the driving force $[\,\rho_0^*\,/\,\rho_0\,]^m\,\psi_0$ exceeds the given attractor stimulus $\psi_0^*$ while mass is removed locally where the driving force takes values below this attractor stimulus.
The results of the simulations are in good qualitative agreement with the results of Weng [218] and Maute [153]. However, since the density $\rho_0$ is not introduced as primary unknown on the nodal level but rather determined in a post–processing step, the algorithm for topology optimization introduced by Maute [153] tends to form sharper contours of struts. In the context of topology optimization, the intensity of these contours strongly depends on the type of smoothing function that is typically included in the optimization algorithm.
A physically motivated smoothing effect can be incorporated in the present theory through the incorporation of the mass flux $\boldsymbol{R}$. Figures 7.20 and 7.21 contrast six different simulations of the frame depicted in figure 7.18, left, whereby the mass conduction coefficient $R_0$ has been gradually increased from $R_0 = 0.00$ to $R_0 = 5.00$. The smoothing effect of the mass flux is clearly visible. The larger the mass conduction coefficient, the wider the affected zone and the smoother the contours of the density distribution. In the limit case, which is achieved if the value of $R_0$ is chosen large enough, even a homogeneous density distribution can be found.

## 7.11 Example: Computational modeling of size effect

The next example shows the qualitative influence of the incorporation of the mass flux, which has so far been neglected in biomechanical analyses of hard tissues. The study is motivated by the famous monograph by Galilei [70] who observed already more than three centuries ago, that bone is a microstructural material. Bone thus shows the classical size effect with smaller structures being relatively stronger than larger ones, see figure 7.22. Figure 7.23, middle, shows the result of the simulation of the Galilei bone subjected to a hypothetical loading situation. To study the formation of microstructures, both, the geometry and the amount of loading have been scaled by a factor 0.5 and 2.0 in comparison to the medium sized bone depicted in the middle of figure 7.23. Thereby, the material parameters, in particular the mass conduction coefficient $R_0 = 0.1$, have been held constant. The resulting density distributions illustrated in figure 7.23, top, and 7.23, bottom, clearly demonstrate the fact, that the proposed model is able to capture the characteristic size effect of microstructural materials in a natural way. The larger structure is characterized through the formation of sharp microstructures while the small bone shows a diffuse almost homogeneous density distribution. Note that upon neglection of the mass flux as $R_0 = 0$ the predicted density distribution is completely identical for the different bone sizes. The additional incorporation of the mass flux can thus be interpreted as a natural extension of the existing flux–free models that enables the simulation of microstructural effects in a physically motivated way.

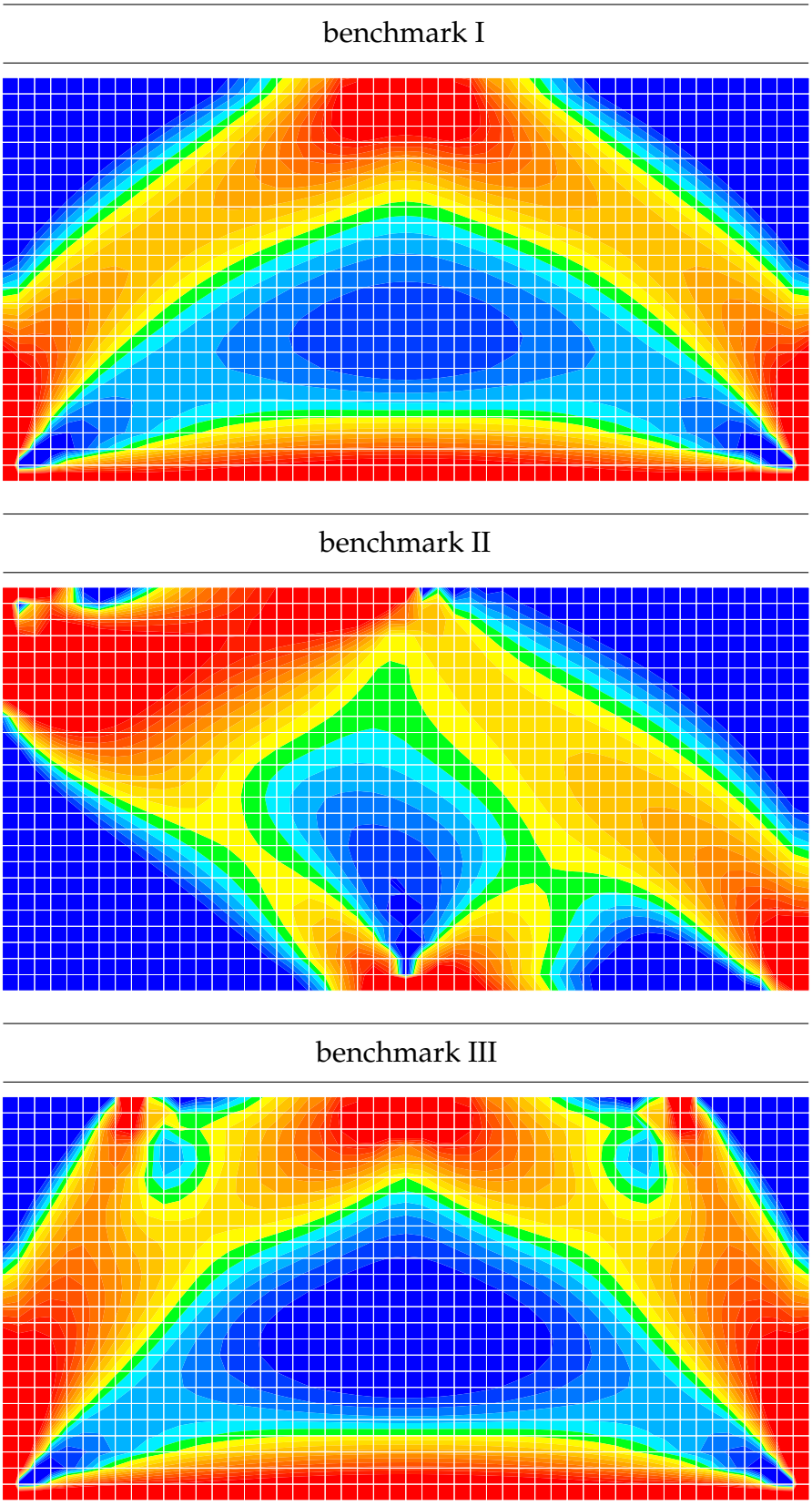


**Figure 7.19:** Topology optimization – Density distribution benchmark I, II, III

$R_0 = 0.00$

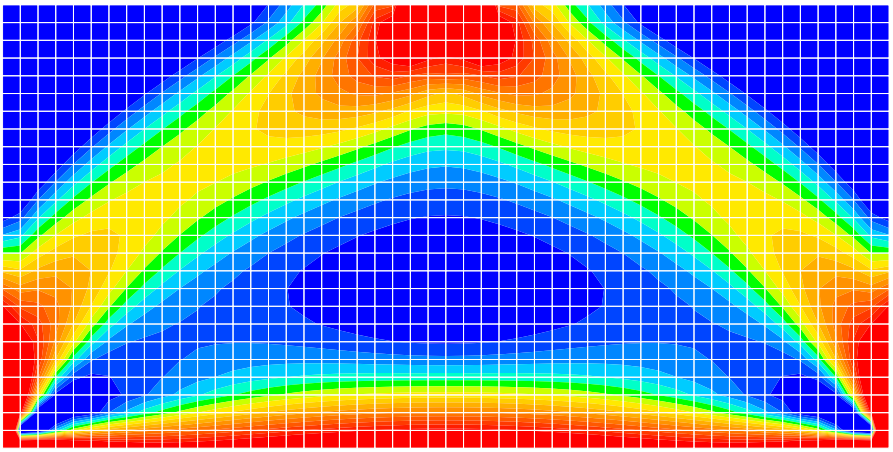

$R_0 = 0.05$

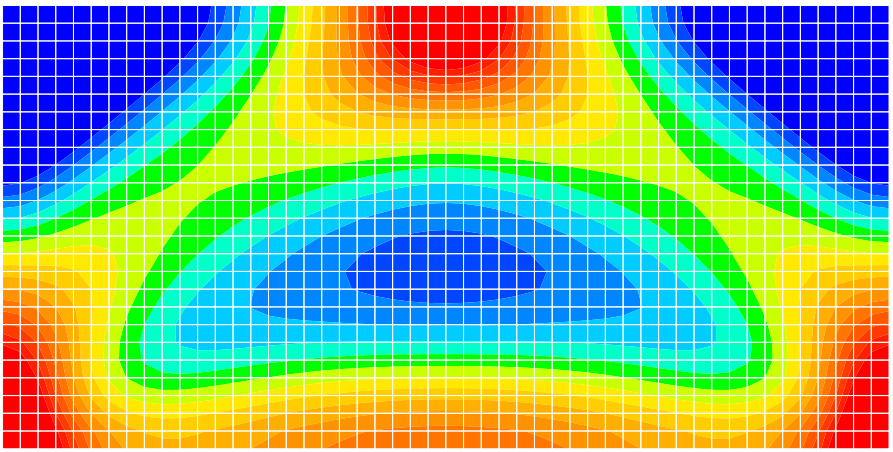

$R_0 = 0.10$

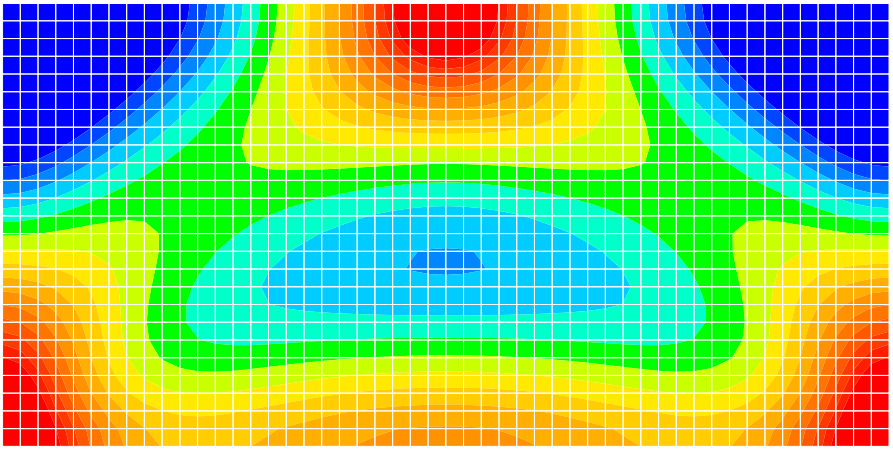

**Figure 7.20:** Topology optimization – Density distribution for varying $R_0$

$R_0 = 0.20$

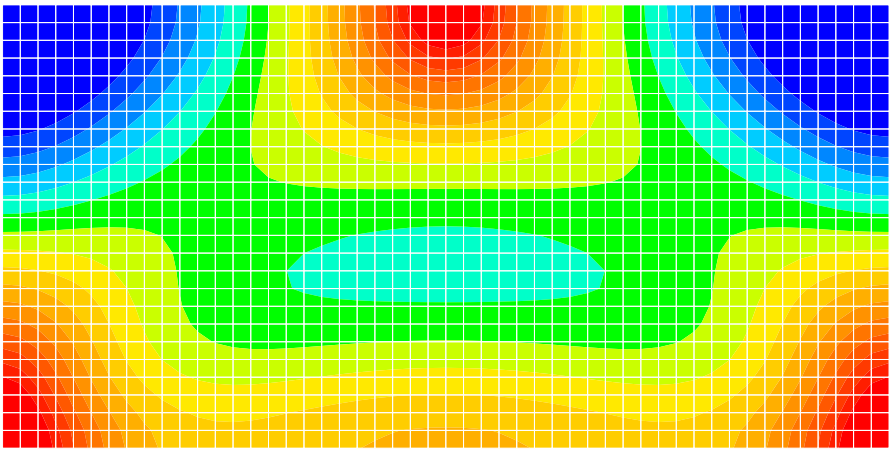

$R_0 = 0.50$

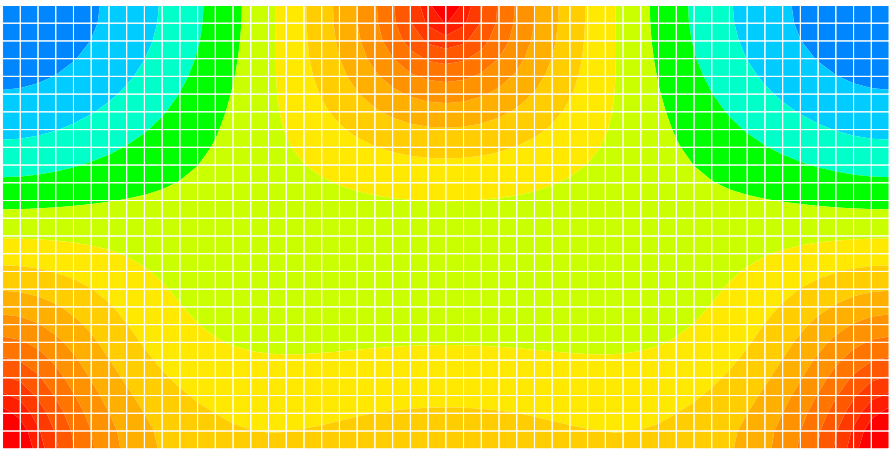

$R_0 = 1.00$

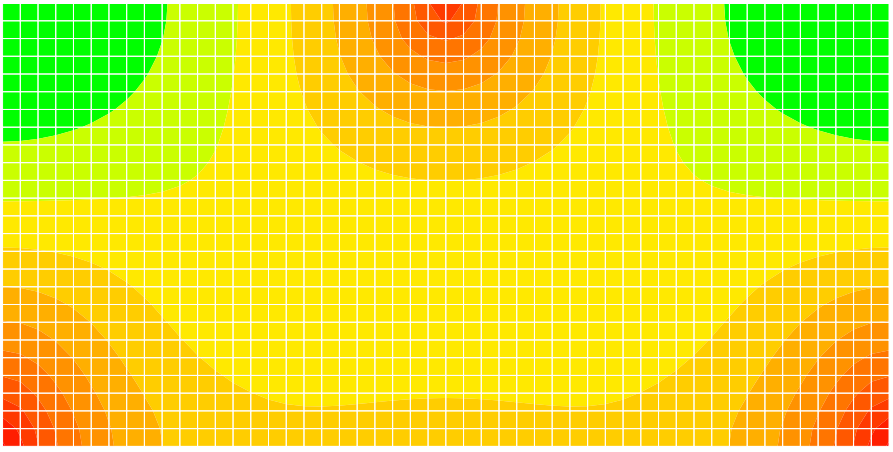

**Figure 7.21:** Topology optimization – Density distribution for varying $R_0$

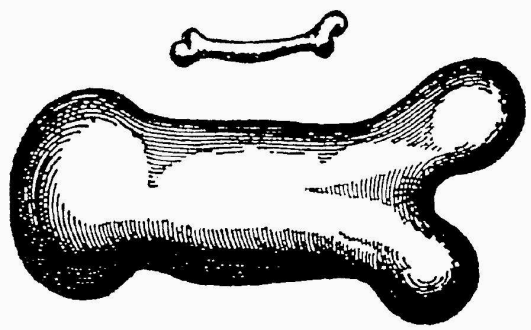

**Figure 7.22:** Functional adaption – Size effect in bones as predicted by Galilei

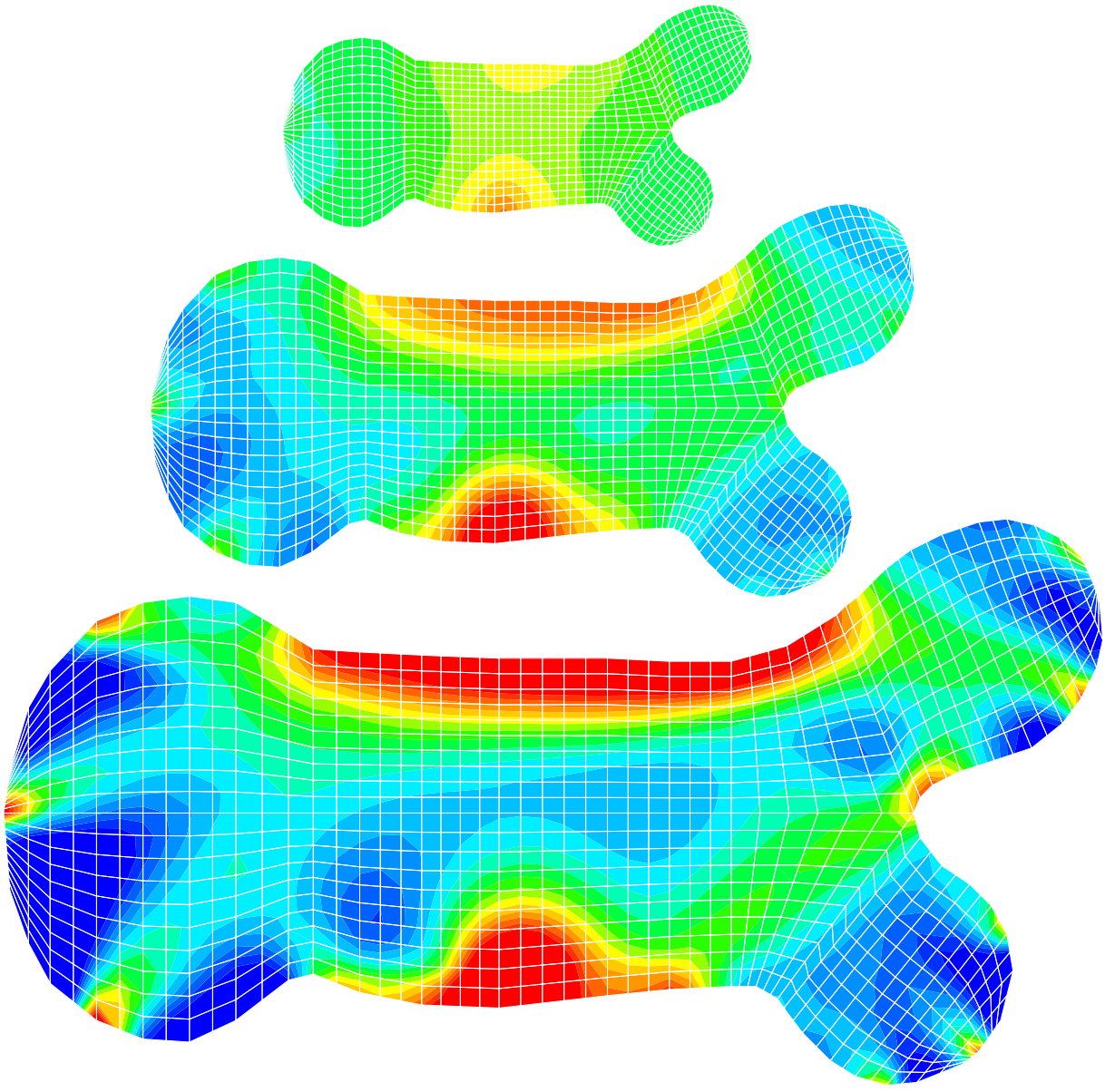

**Figure 7.23:** Functional adaption – Size effect in bones as predicted computationally

## 7.12 Example: Computational modeling of growth

### 7.12.1 Spatial motion problem

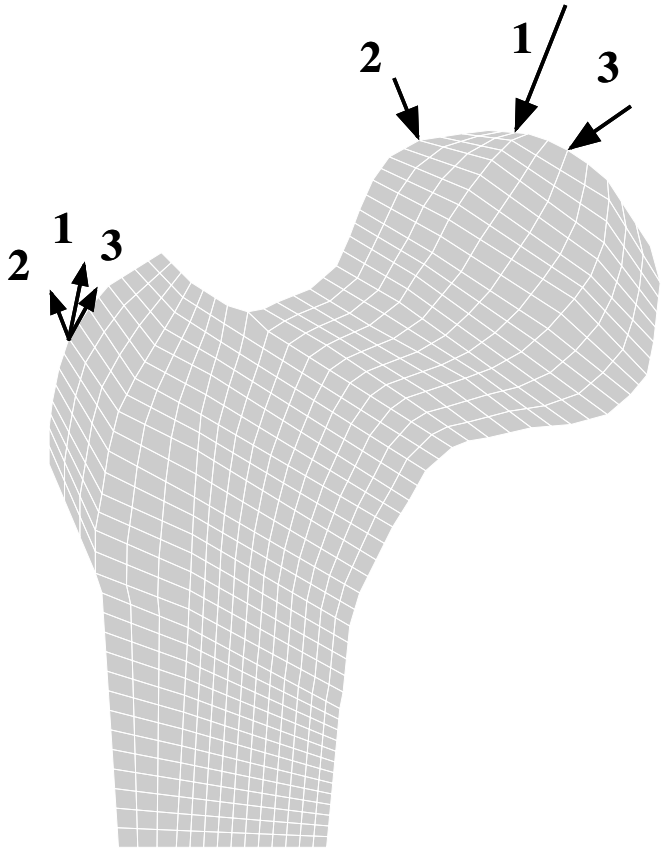


**Figure 7.24:** Femur – Loading conditions

Finally, the derived classes of algorithms shall be compared in terms of a representative example from biomechanics. To this end, we study the classical benchmark problem of bone remodeling of the proxima femur subjected to an average daily loading situation. A detailed specification of the problem is given by Carter & Beaupré [24]. For the model suggested herein, we chose the elastic parameters to E $=$ 500 and $\nu = 0.2$ corresponding to the Lamé constants $\lambda = 138.89$ and $\mu = 208.33$, while the additional growth related parameters are chosen to $\rho_0^* = 1.2$, $\psi_0^* = 0.01$, $n = 2$ and $m = 3$. The geometry and the loading conditions are depicted in figure 7.24. Typically, three different loading situations can be identified. Load case 1 corresponds to the load condition for the midstance phase of gait, while load cases 2 and 3 represent the extreme cases of abduction and adduction as defined in table 7.9.

| load case | type of loading | value | direction | value | direction |
|---|---|---|---|---|---|
| 1 | midstance phase of gait | 2317 N | $24^0$ | 703 N | $28^0$ |
| 2 | extreme range of abduction | 1158 N | $-15^0$ | 351 N | $-8^0$ |
| 3 | extreme range of adduction | 1548 N | $56^0$ | 468 N | $35^0$ |

**Table 7.9:** Femur – Loading conditions

Figure 7.25 shows the spatial distribution of the density concentration $[\rho_0 - \rho_0^*]/\rho_0^*$ for each of the three different loading cases defined in table 7.9. The resulting density distribution of each individual load case clearly visualizes the load carrying mechanism of the proxima femur. However, none of the three loading scenarios alone is able to generate the biologically observed density pattern. In the context of living tissues, the exact determination of the mechanical forces acting on the biological structure is extremely difficult, particularly in in vivo experiments. In the early literature, the application of strain gauges has been suggested to measure the exact amount of loading.

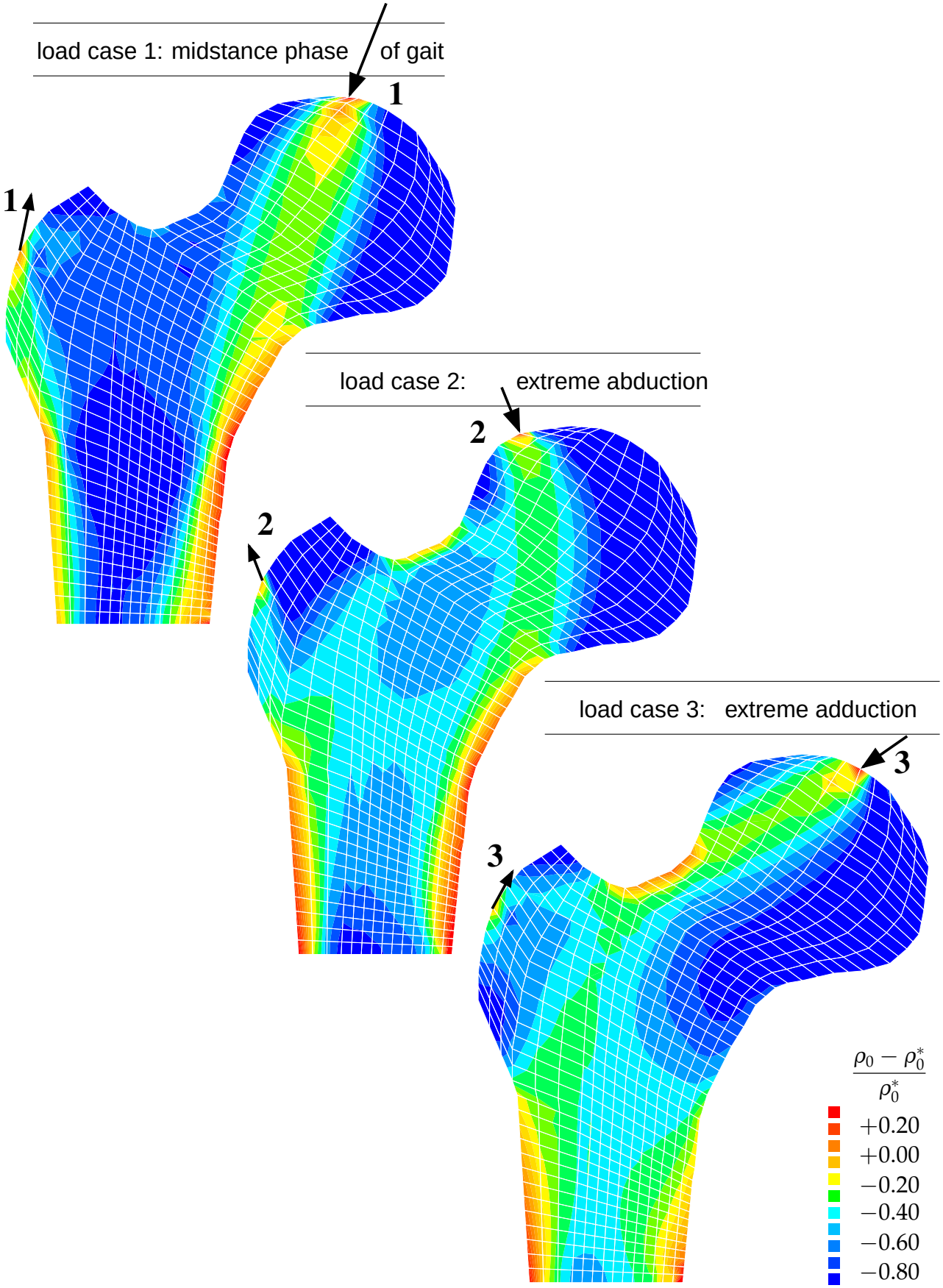


**Figure 7.25:** Density distribution – Three different loading cases

In contrast, the result of the mechanical forces, namely the response in terms of the density distribution, is relatively easy to measure, even in in vivo experiments. It could, for instance, be determined with the help of computer tomography. Once the exact density distribution is known, the responsible forces could be determined in an inverse analysis. Figure 7.25 motivates the application of such an inverse strategy for which the loads are usually varied systematically until the computationally obtained density distribution finally corresponds to the experimentally observed density pattern. Note that in addition to the classical load cases, i.e. the midstance phase of gait, extreme abduction and extreme adduction, some long bones could even be subjected to the less frequent load case of captain caveman type as illustrated in figure 7.26.

**Figure 7.26:** Load case of captain caveman type

Figure 7.27 shows the mechanically predicted and experimentally observed density distribution by Wolff [220] in comparison with the numerically simulated density distribution. Thereby, all three load cases have been applied simultaneously. Remarkably, the finite element simulation is able to capture all the typical biomechanical characteristics of the solution: the development of a dense system of compressive trabeculae carrying the stress from the superior contact surface to the calcar region of the medial cortex, a secondary arc system of trabeculae through the infero–medial joint surface into the lateral metaphyseal region, the formation of Ward's triangle and the development of a dense cortical shaft around the medullary core.

Figures 7.28 to 7.31 illustrate the distribution of the relative changes in density $[\,\rho_0 - \rho_0^*\,]/\rho_0^*$ as a result of the different spatial discretization techniques. The first set of figures 7.28 illustrates the behavior of the Q1Q1 element with respect to h–refinement. Surprisingly, the results do not differ considerably upon refinement of the mesh. Already the coarsest mesh with 658 Q1Q1 elements seems to be sufficient to represent the characteristic features of the density distribution, such that we can restrict ourselves to the coarsest 658 element mesh in the sequel.
Figure 7.29 contrasts the results of the different node point based finite element formulations. Remarkably, the Q1Q1 element, the Q2Q2 element, the Q1P0 element and the S2Q1 element render nearly identical results. Unlike reported in the related literature, the Q1P0 formulation with an elementwise constant density interpolation does not show any spatial instabilities. Due to the choice of a well–posed continuum formulation in combination with an implicit time integration scheme, all finite element formulations, even the one based on an elementwise constant density interpolation, render stable and unique results.
Figures 7.30 and 7.31 show the integration point based counterparts of the solution which result from the classical Q1 element, the Q2 element, the selectively reduced integrated $Q1^{sri}$ element and the fully reduced integrated $S2^{fri}$ element. While figure 7.30 depicts the discrete values of the internal variables for each area assigned to the corresponding quadrature point, figure 7.31 illustrates the classical post–processing result that is obtained by an extrapolation of the integration point values to the nodes in combination with an averaging of these nodal values. The Q1 element and the $S2^{fri}$ element apply the same number of integration points per element. However, the solution of the classical Q1 element seems to be slightly oscillatory while the $S2^{fri}$ solution is rather smooth due to its quadratic interpolation of the deformation field. Since the solution is rather homogeneous within each element, the integration point based $Q1^{sri}$ element renders nearly identical results as the node point based Q1P0 element. The differences of the individual integration point based elements vanish upon smoothing as illustrated in figure 7.31. By making use of the traditional post–processing step which is typically applied for the graphic representation of internal variables, all results of the integration point based approach are nearly alike. Moreover, they all roughly correspond to the results of the node point based approach depicted in figure 7.29.

mechanically predicted density distribution

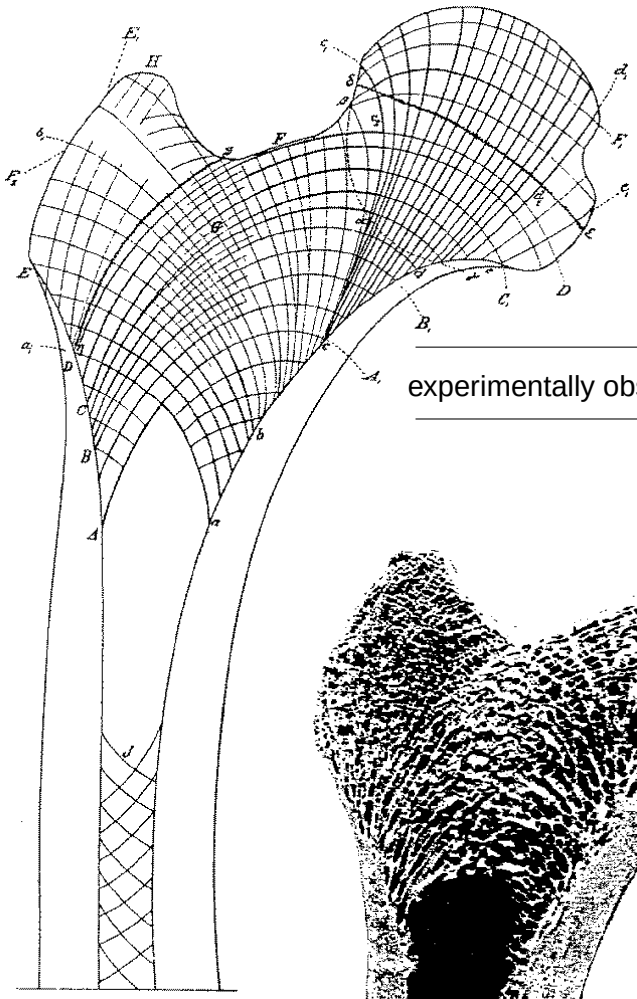

experimentally observed density distribution

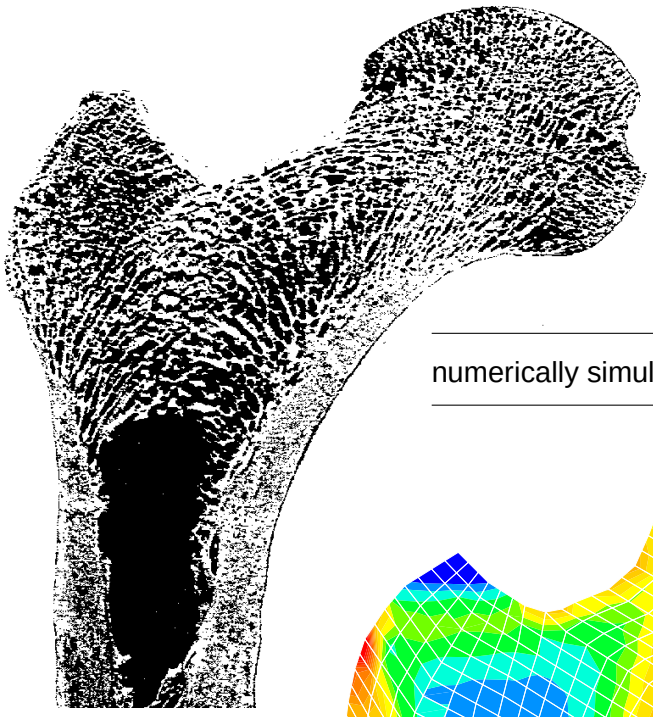

numerically simulated density distribution

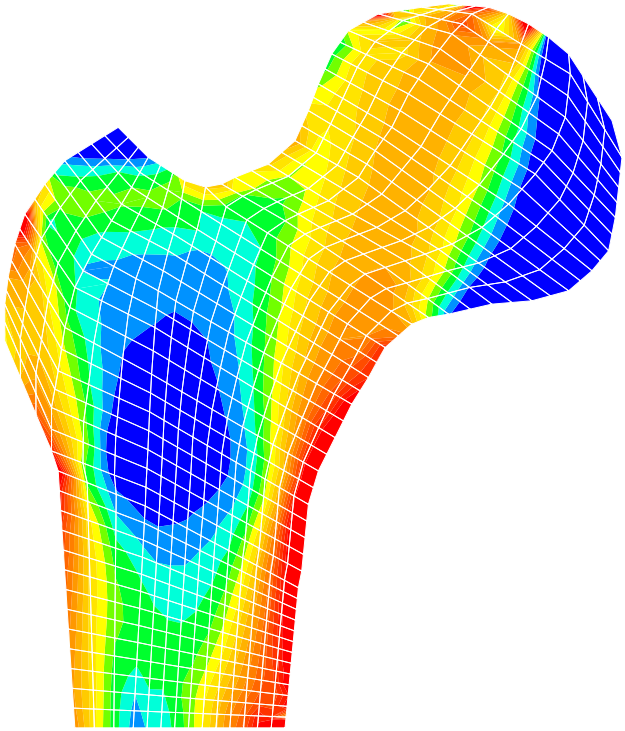

**Figure 7.27:** Femur – Density distribution as predicted and determined by Wolff

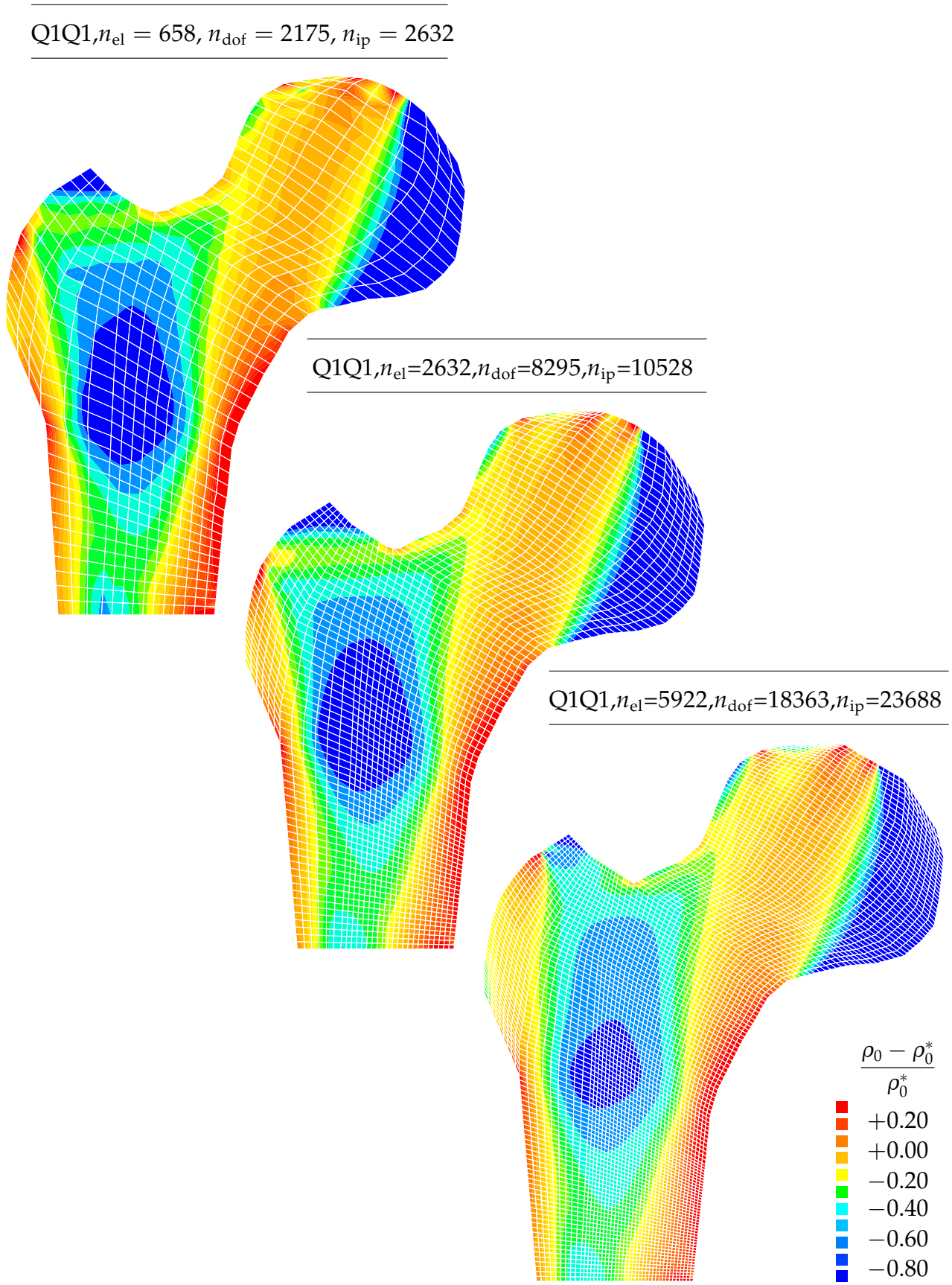


**Figure 7.28:** Density distribution – Node point based approach

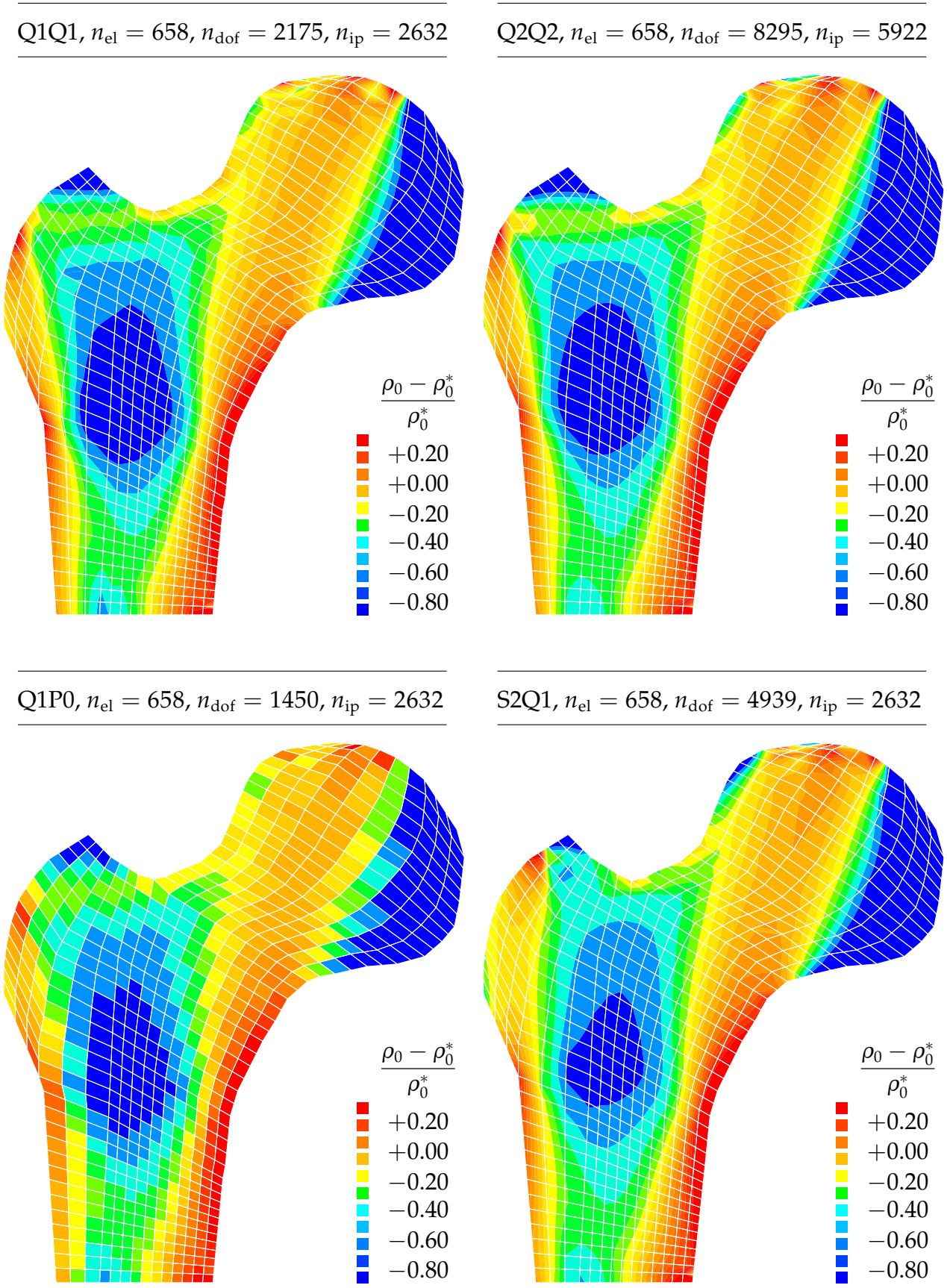


**Figure 7.29:** Density distribution – Node point based approach

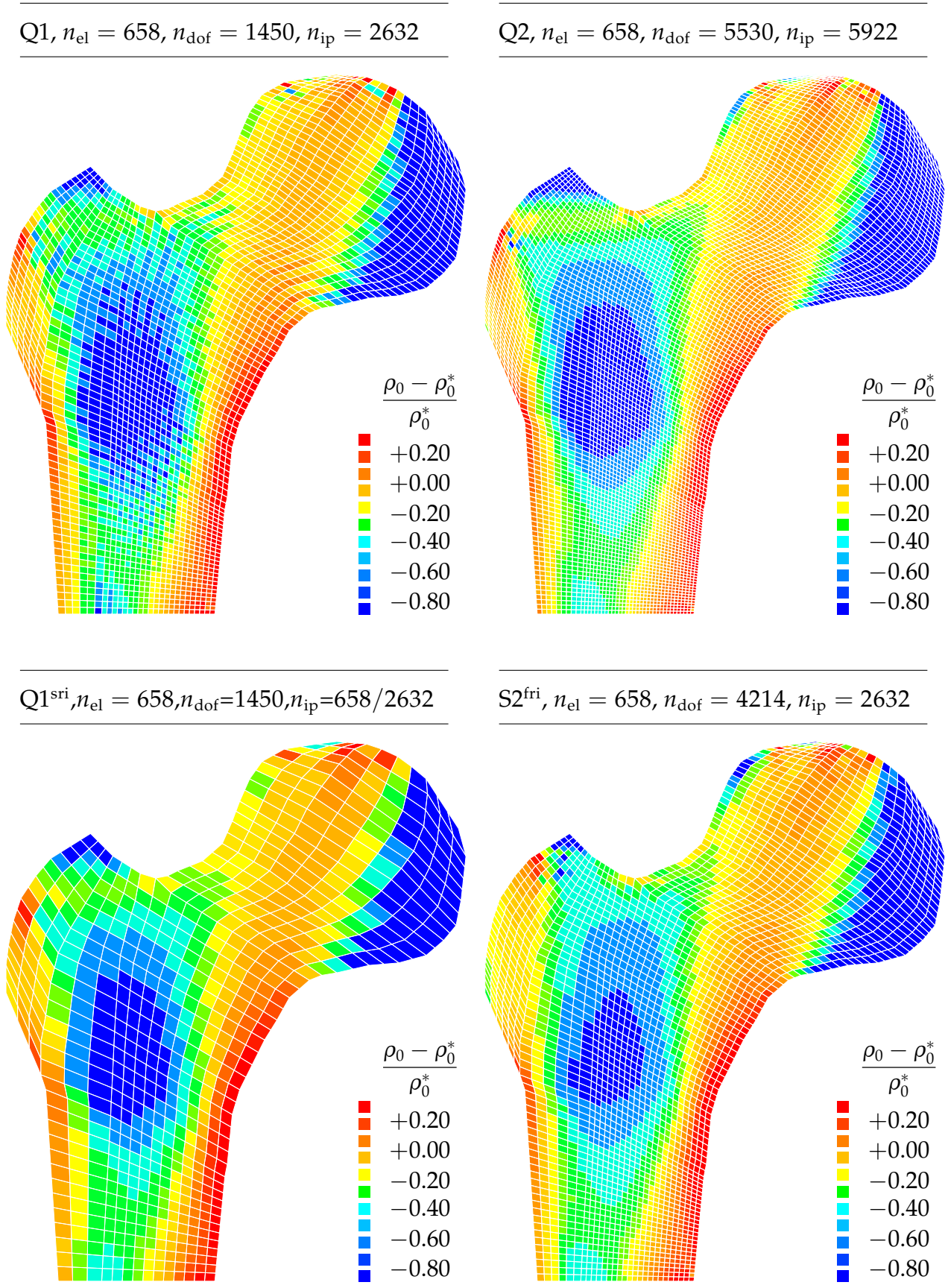


**Figure 7.30:** Density distribution – Integration point based approach

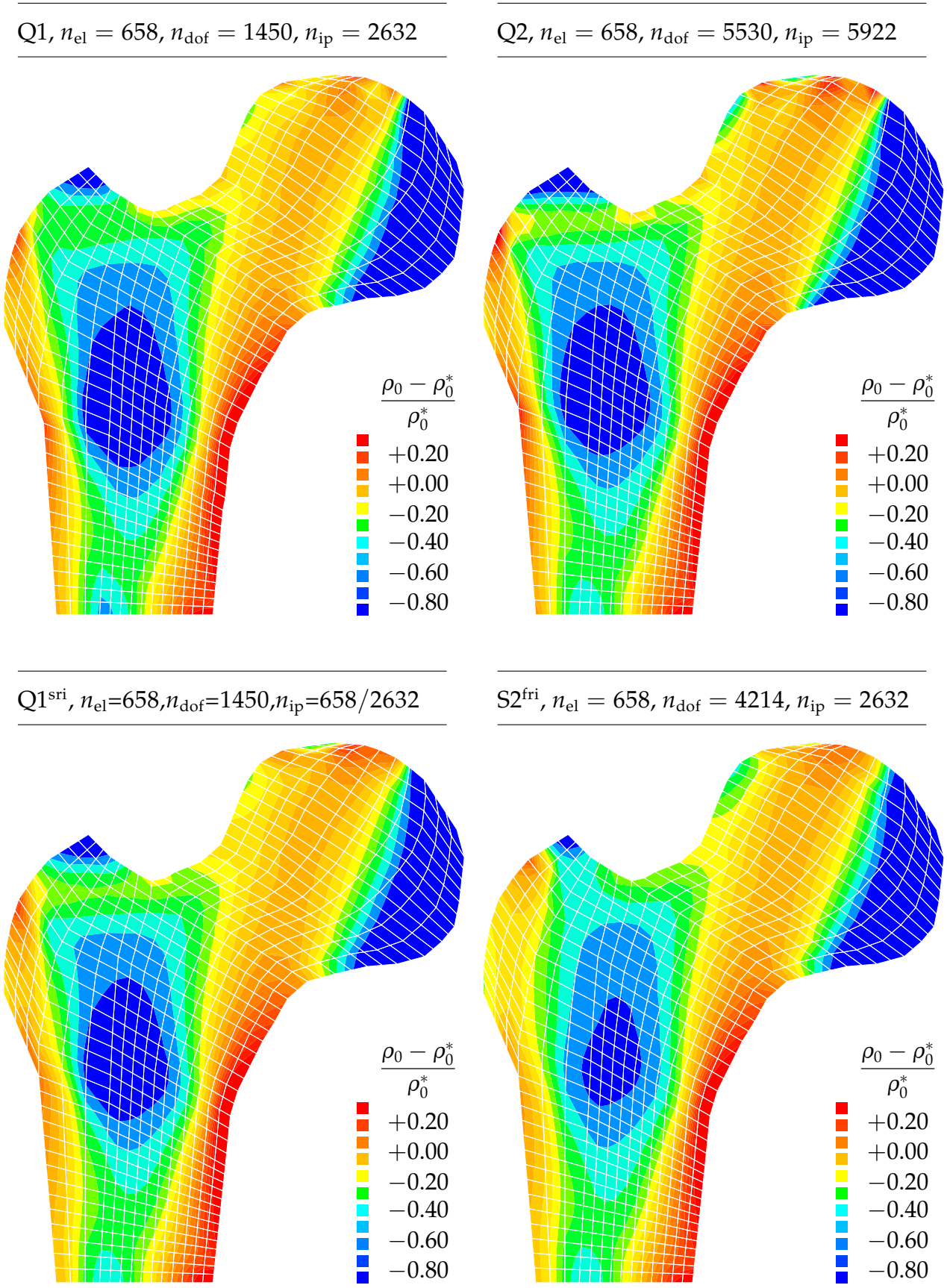


**Figure 7.31:** Density distribution – Integration point based approach (smoothed)

$Q1^{sri}$, $n_{el} = 658$, $n = 2$, $m = 3$ (unstable)

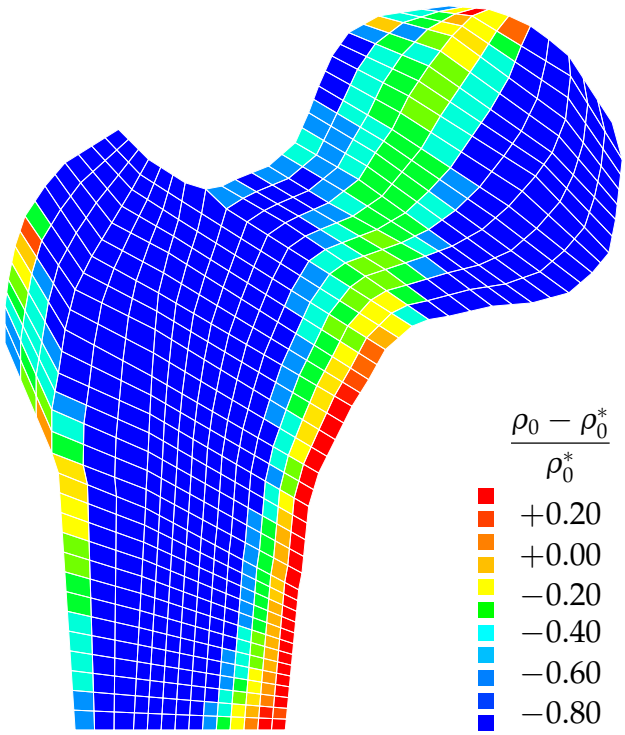


**Figure 7.32:** Unstable density distribution

Within the present approach, neither the node point based Q1P0 element nor the integration point based $Q1^{sri}$ element tend to develop the spatial instabilities reported in the literature. To document the fact, that these spatial instabilities are already introduced on the continuum level and then carry over to the temporally and spatially discrete problem, we analyzed the similar problem described above, only now with the parameters $n = 2$ and $m = 0$. According to Harrigan & Hamilton [86,88], this set of parameters is supposed to produce a non–unique and unstable solution. The numerical result depicted in figure 7.32 shows the typical discontinuous 0–1 type of solution with the classical tendency towards checkerboarding. The given density distribution corresponds to the last converged state of the simulation. The calculation stopped after half of the prescribed time period because of the loss of convergence within the global Newton iteration caused by ill-conditioned system matrices.

### 7.12.2 Material motion problem

We now turn to the evaluation of the material forces for the femur problem introduced in the previous section by looking at the analysis with 658 node point based Q1Q1 elements. Recall that a $\mathcal{C}^0$–continuous density interpolation is mandatory to calculate the material node point forces if algorithmically complex smoothing procedures should be avoided. Figure 7.33 depicts the resulting material surface forces $\mathsf{F}^{\Phi}_{sur}$ and the corresponding material volume forces $\mathsf{F}^{\Phi}_{vol}$. Note that for the sake of visualization, the latter have been magnified by a factor four in comparison to the former. Again, the volume contribution depicted on the right indicates the tendency of the material to flow out of areas of high density concentration. When comparing the intensity of the material volume forces with the density distribution of figure 7.28, top, one typically finds largest forces in areas of highest density gradients, e.g. pointing form the dense media and lateral cortices towards the low density mellulary core in the shaft region. The material surface forces depicted on the lefthand side are about four times larger in their absolute value. On the boundary, material surface forces can be interpreted as a measure of shape sensitivity of the specimen geometry. They thus take larger values at non–smooth surfaces, e.g. close to the medial shaft. In biomechanical applications, the material surface forces on the domain boundary could thus be understood as indica-

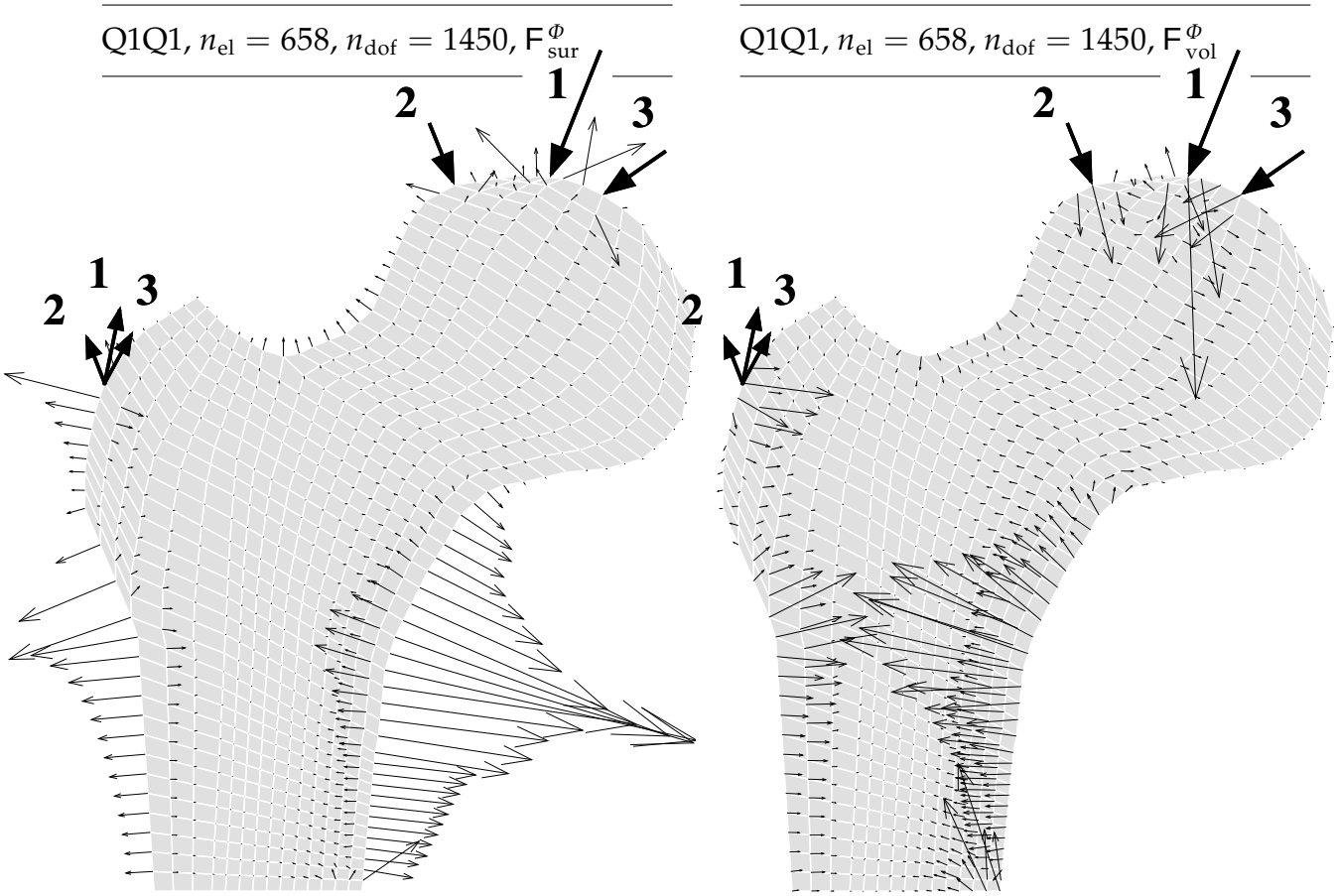


**Figure 7.33:** Material surface and volume forces $F^{\Phi}_{sur}$ and $F^{\Phi}_{vol}$

tors for external or surface remodeling. Note that for reasons of visualization, material surface forces on the fixed boundary that appear as a natural reaction to the constraint placed by fixing material node point positions in the reference configuration are not included in the plot of figure 7.33.
In summary, this example has convincingly demonstrated the application of the material force method to bone remodeling. The knowledge of material forces provides additional insight into the biologically induced rearrangement of material inhomogeneities inside the specimen and the reorganization of structural surfaces.

## 7.13 Example: Computational modeling of healing

Another highly interesting example of open system thermodynamics in the context of biomechanics is provided by the class of healing phenomena. Typical applications of healing can be found in reconstructive or cosmetic surgery or in surgical operation planning in the context of burned wounds, skin cancers or birth defects. The process of wound healing is strongly affected by the stress after suture, by the shape and size of the excision and by the biomechanical properties of skin. The following examples can be understood as a first step towards the understanding of the complex phenomena encountered in wound healing.

### 7.13.1 Two–dimensional simulation

The following example is originally borrowed from nonlinear elastic fracture mechanics. It represents the qualitative study of healing in a single edge notched specimen subjected to tensile loading. The specimen is of rectangular shape with a length of $l = 225$ and a width of $w = 75$ units. The corresponding finite element discretization consisting of 3565 node points and 1140 finite elements is depicted in figure 7.35, top. Eight–noded serendipity elements are applied throughout except for the crack tip close to which we apply quadratic triangles. A close–up of the heavily defined mesh at the crack tip is given in figure 7.35, bottom. The Lamé constants are chosen as similar to the previous example as $\lambda = 138.89$ and $\mu = 208.33$. Again, the two exponents are taken as $n = 2$ and $m = 3$, the reference density is chosen to $\rho_0^* = 1.00$ and the mass flux is neglected as $R_0 = 0$. Since we aim at subjecting the specimen to large strains, the value of the reference free energy has been enlarged by a factor 50 in comparison to the previous example, thus $\psi_0^* = 0.50$. Moreover, the analysis of large strains requires a stepwise application of the total load. The specimen is thus loaded by a ramp

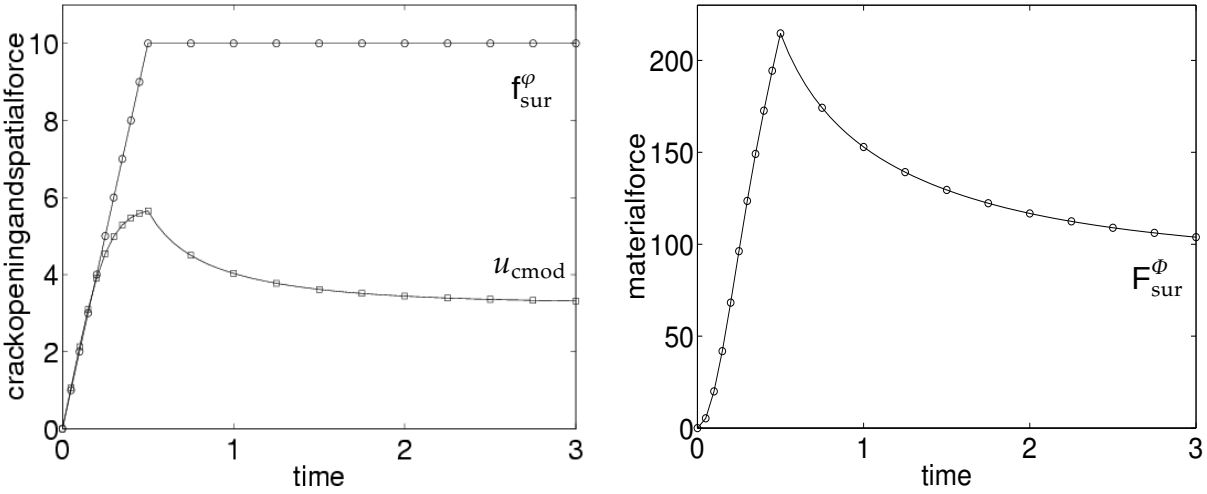


**Figure 7.34:** Tension – Evolution of crack mouth opening displacement & material forces

load over 10 time steps of $\Delta t = 0.05$ each, by an incrementally increasing spatial force of $\Delta f^{\varphi}_{sur} = 250$ applied on the upper and lower boundary. The 10 load steps are depicted in figure 7.34, left. Once the final load level of $f^{\varphi}_{sur} = 2500$ is reached, the load is held constant for another 50 time steps of $\Delta t = 0.05$ while the density distribution converges towards the biological equilibrium state. Figure 7.34, left, shows the prescribed spatial force $f^{\varphi}_{sur}$ scaled by a factor 250 and the corresponding evolution of the crack mouth opening displacement $u_{cmod}$ on the left boundary as a result of the spatial motion problem. As the load is increased, the crack opening $u_{cmod}$ increases correspondingly up to approximately 5 % of the total specimen length. However, during the phase of constant loading from $t = 0.5$ to $t = 3.0$, a clear tendency towards self–healing can be observed. The healing process manifests itself in a considerable closure of the crack to about two third of its maximum size. Figure 7.35, top, supports this observation. It shows the deformed configurations corresponding to $t = 0.25$ right in

the middle of the loading phase, $t = 0.50$ at the end of the loading phase and $t = 3.0$ close to biological equilibrium.
The total deformation increases during the loading phase but then decreases again during the phase of constant loading. The decrease in deformation and the corresponding closure of the crack illustrate the biomechanical coupling. They can be explained by the apposition of new material close to the crack tip which can be interpreted as a biomechanically induced self–healing process. The density contours depicted in figure 7.35 indicate an enormous increase in density close to the crack tip while material is resorbed locally near the stress free crack faces.
Let us now turn to the solution of the material motion problem and analyze the evolution of the material forces. Figure 7.34, right, depicts the material force $\mathsf{F}^{\Phi}_{\text{sur}}$ at the crack tip which increases during the loading phase but then relaxes towards a remarkably lower value at biological equilibrium. Apparently, due to the apposition of new material close to the crack tip, the absolute value of the material force at the crack tip could be reduced considerably up to about 60 % of its maximum value. The spatial distribution of the discrete material surface forces $\mathsf{F}^{\Phi}_{\text{sur}}$ and the corresponding discrete volume forces $\mathsf{F}^{\Phi}_{\text{vol}}$ is depicted in figure 7.35, bottom. Note that for the sake of visualization, the nodal volume forces have been magnified by a factor 50 in comparison to the corresponding surface terms. Obviously, the discrete material volume forces are essentially orthogonal to the isolines of the density contour plot. Both, the surface and volume forces increase upon loading but show a relaxation at constant applied load.
Discrete material surface forces typically point in the direction of a potential energy increase upon replacement of the material node point positions. They thus indicate, that the apposition of new material opposite to this direction would reduce the potential energy. Exactly this property is reflected by the balance of mass for open systems in combination with an appropriate constitutive assumption for the source term $\mathcal{R}_0$. For the free energy based approach considered herein, the balance of mass at biological equilibrium with $\mathrm{D}_t \rho_0 = 0$ can be rewritten as $[\,\rho_0^*/\rho_0\,]^{m-n}\psi_0 = \psi_0^*$. If the value of the reference free energy $\psi_0^*$ is locally exceeded, the apposition of new material with $\rho_0 > \rho_0^*$ essentially helps to decrease the value of the free energy based biological stimulus $[\,\rho_0^*/\rho_0\,]^{m-n}\psi_0$, since $m > n$. As the biological stimulus approaches the attractor stimulus $\psi_0^*$, the absolute value of the corresponding material surface force decreases indicating that enough material has been created to support the applied load.
Especially the present example has shown the relevance of material forces in biomechanical applications. Unlike engineering materials, biomaterials show the remarkable ability to react to changes in the environmental situation in the form of self–healing. In this context, material forces can be utilized to locate areas of potential material apposition and to improve the understanding of biomechanically induced self–healing phenomena.

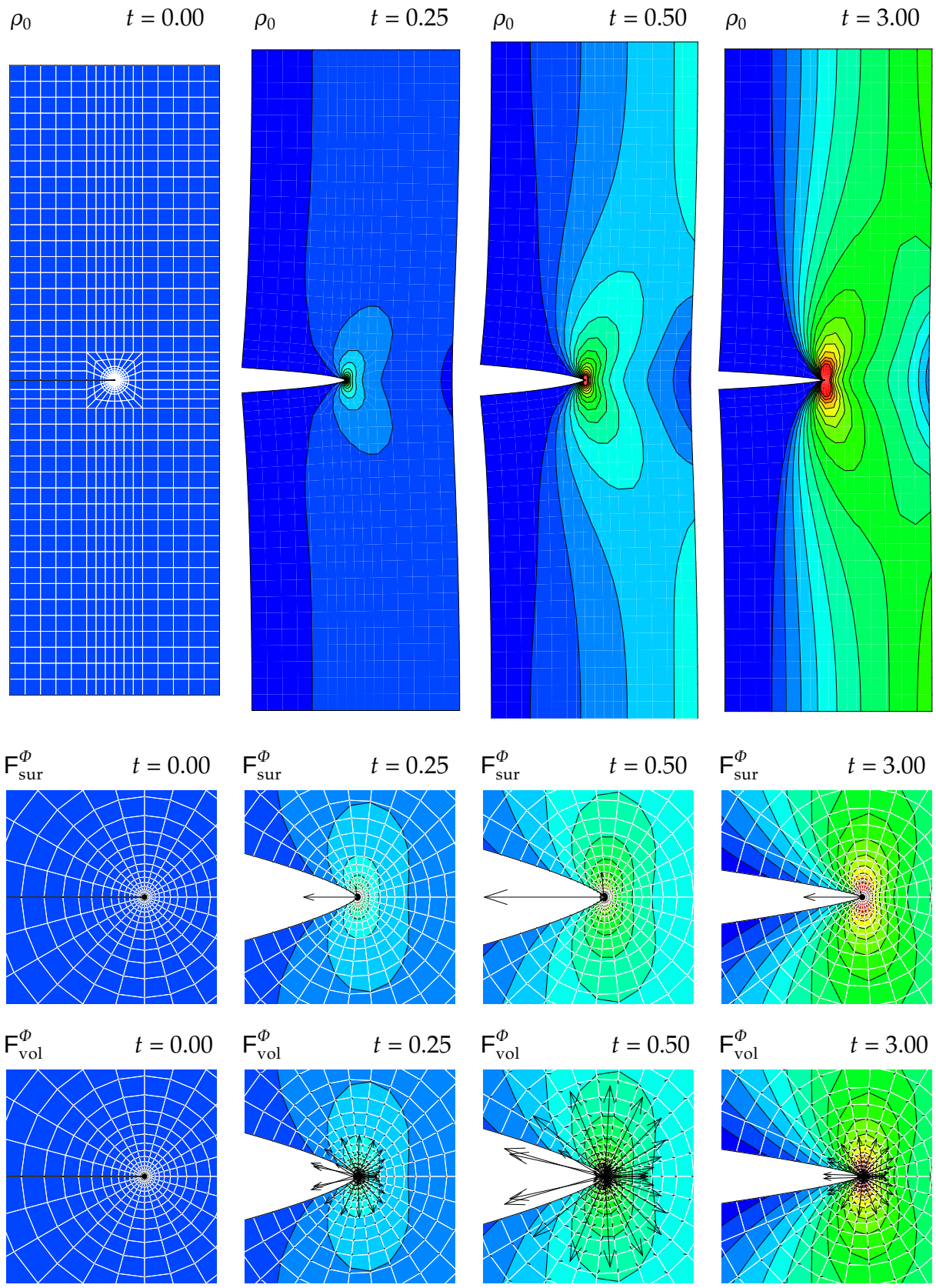


**Figure 7.35:** Tension – Evolution of density, material surface and volume forces

### 7.13.2 Three–dimensional simulation

Finally, the full potential of the developed framework will be elaborated in terms of several three–dimensional examples. Rather than analyzing the response of entire biological structures which is primarily predefined by the complex geometry of the structures themselves, we shall now focus on the systematic elaboration of a simple model geometry subjected to different loading conditions. The selected prototype specimen has a height to width to depth ratio of 2 : 1 : 0.5 and is discretized with 24 : 12 : 6 tri–linear Q1Q1 elements with one density degree of freedom and three deformation degrees of freedom at each node thus introducing a total of approximately 10 000 degrees of freedom. We shall analyze two representative topologies, one being cut horizontally on the entire side facet the second being cut horizontally in the middle of the front surface only. Both, the edge cut and the surface cut specimen are subjected to the three characteristic loading scenarios as defined by Carter & Beaupré [24], tension, torsion and bending. The three different loading cases are illustrated in figure 7.36. The elastic

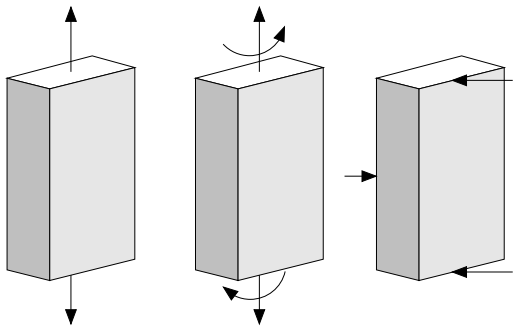

**Figure 7.36:** Different load cases – Tension, torsion, bending

parameters are again chosen as $\lambda = 138.89$ and $\mu = 208.33$. It should be emphasized that real soft tissues often show a quasi–incompressible material behavior. Nevertheless, to avoid potential numerical difficulties caused by volumetric locking, we choose a set of model parameters $\lambda$ and $\mu$ which does not fall within this quasi–incompressible range and refer to Gasser & Holzapfel [72] for the appropriate algorithmic treatment of quasi–incompressible biomaterials. The growth–related parameters are assumed to take values of $\rho_0^* = 1.0$, $\psi_0^* = 0.1$, $n = 2$ and $m = 3$, the influence of the mass flux is assumed to be negligible as $R_0 = 0$. Since we aim at subjecting the specimen to large strains, the load is increased incrementally during the first 10 time steps of $\Delta t = 0.01$ just like in the previous example. In each of the analyzed problems, the applied load is then held constant for another 50 time steps of $\Delta t = 0.01$ corresponding to the regeneration phase during which the solution is supposed to converge towards a biological equilibrium state.

To illustrate the evolution of the primary unknowns of the spatial motion problem, we plot the contours of the actual material density projected onto the current configuration at five different stages of the loading history, i.e. at time step 2 right at the beginning of the loading phase, at time step 10 corresponding to the end of the load increase, at time steps 20 and 40 during the convergence towards biological equilibrium at constant loading and at time step 60 which basically corresponds to the biological equilibrium state for the particular loading situation. Note that under the given loading condi-

tions, the specimen is subjected to large strains such that the depicted deformation is not magnified. The legend to the density contours is common to all the analyses and varies from blue to red as the relative density increases from $0 \leq [\,\rho_0 - \rho_0^*\,] \,/\, \rho_0^* \leq 1$. Blue colors thus correspond to a non–increasing value of the relative density while red colors indicate an increase in local density due to the apposition of new material. In a second series of figures, we illustrate the solution of the material motion problem, i.e. the evolution of the discrete material node point forces in the horizonal precracked layer of the specimen. Furthermore, to quantify wound closure during the regeneration process, we shall include diagrams illustrating the temporal evolution of the crack mouth opening or sliding displacement $u_{\text{cmod}}$ or $u_{\text{cmsd}}$ in combination with the discrete material force $\mathsf{F}^{\Phi}_{\text{sur}}$ at the crack tip.

**Load case tension** In the first case study, both prototype geometries are subjected to a uniform tensile loading applied consistently at the upper and lower facet. The first load case thus represents a typical benchmark problem from fracture mechanics inducing a classical mode I type failure. It can thus be understood as a three–dimensional generalization of the example presented in section 7.13.1. Figures 7.37 and 7.38 illustrate the corresponding density distributions projected onto the deformed configuration. The first figures on the left of each series show the beginning of the loading phase at which the prescribed density is right about to adapt to the prescribed environmental changes. The second set of figures corresponds to the end of the load increase which is obviously associated with the maximum opening of the crack. At this stage, the beginning of the healing phase is already indicated through a slight increase in density at the crack tips. As time evolves, more and more biological substance is deposited locally at the crack tips at which the free energy based stimulus obviously takes largest values. The influence of the healing mechanism manifests itself in a local redistribution of matter indicated through the local increase and decrease in density which in turn affects the deformation of the specimen: the cracks clearly show a tendency to close, moreover, the magnitude of the overall deformation decreases considerably. The local rearrangement of matter can be visualized most elegantly through the evolution of the discrete material node point forces in the precracked layer which are illustrated in the bottom row of figures 7.37 and 7.38. In figure 7.37, we see the evolution of the material forces in the edge cut specimen which takes the characteristic finger nail type distribution corresponding to three–dimensional fracture mechanics analyses of mode I failure. Figure 7.38 demonstrates the material forces in the surface cut specimen. Discrete material forces typically point in the direction of a potential energy increase upon replacement of the node point position. In the context of healing, they sense the direction of a potential deposition of new biomaterial. Material forces generally sense a geometric imperfection, i.e. they point in the direction of the cracked edge in the first analysis whereas they are clearly oriented towards the surface cut in the second example. Experimentally observed effects of wound geometry on the healing process are thus inherently incorporated in the additional information provided by the material force method. The diagrams in figure 7.43 illustrate the progression of healing in terms of the temporal evolution of the crack mouth opening displacement $u_{\text{cmod}}$ and the resulting material surface force $\mathsf{F}^{\Phi}_{\text{sur}}$ at the crack tip. The temporal evolution of the latter

indicates the changes in magnitude of the driving force for the healing mechanism. At the beginning of the loading history corresponding to a small crack opening, the material forces still have a very low magnitude which increases considerably upon further loading. Maximum values are obtained at the end of the load increase phase. As time evolves, the deposition of new material at the crack tip reduces the stress concentration at the crack tip, the material forces reduce significantly. At the end of the healing phase, both, the edge and the surface crack have nearly closed and the material forces have almost vanished.

**Load case torsion** In the second example, the edge cut specimen and the surface cut specimen are subjected to a torsional loading along the longitudinal axis. To avoid potential contact problems, a tensile load is superposed to the applied torsion whereby both are applied consistently at the nodes of the upper and lower facet. The change of loading conditions towards mode III failure has a strong impact not only on the deformation field but also on the density distribution, compare figures 7.39 and 7.40. For both prototype geometries, the axis of maximum density rotates towards the axis of maximum principle strain. The torsion–induced out of plane deformation is clearly visible, in particular in the second figure from the left of each series, which corresponds to the end of the load increase phase. During the healing phase, however, more and more biomaterial is deposited at the areas where the biological stimulus takes maximum values to locally strengthen the structural setup. As a natural consequence of healing, both, the edge crack and the surface crack tend to close. Crack closure is accompanied by a decrease of the overall deformation, in particular a decrease of the twist. The second series of plots of figures 7.39 and 7.40 shows the corresponding evolution of the material forces projected onto the precut layer. Note that due to the applied torsional load, the material forces on the lefthand side of the edge cut specimen actually point upwards while those on the right edge point downwards sensing the area of potential material deposition. For the surface cut specimen, threedimensionality leads to a downward orientation of the material forces at the rear side while the material forces at the leading edge point in the upward direction. The temporal evolution of both, the crack mouth sliding displacement $u_{\mathrm{cmsd}}$ and the material force at the crack tip $\mathsf{F}^{\Phi}_{\mathrm{sur}}$ is depicted in figures 7.44. Again, a considerable decrease in magnitude of both quantities can be observed during the healing phase.

**Load case bending** The final example treats the load case of bending which is most probably typical for hard rather than soft tissues. Nevertheless, we analyze the response of both prototype geometries with respect to a three–dimensional generalization of the classical three point bending test represented through a line load on the upper and lower front edge and on the horizontal symmetry axis of the backside. While the surface cut specimen shown in figure 7.42 clearly undergoes a symmetric deformation, the edge cut specimen illustrated in the figure 7.41 shows a non–symmetric response due to the precut edge. To avoid penetration, nodes of its crack facet that are located in the compressive zone have been identified in the first load step and were then glued together for the remaining simulation. In principle, the bending simulation supports the results of the tension and torsion test. Nevertheless, the results differ

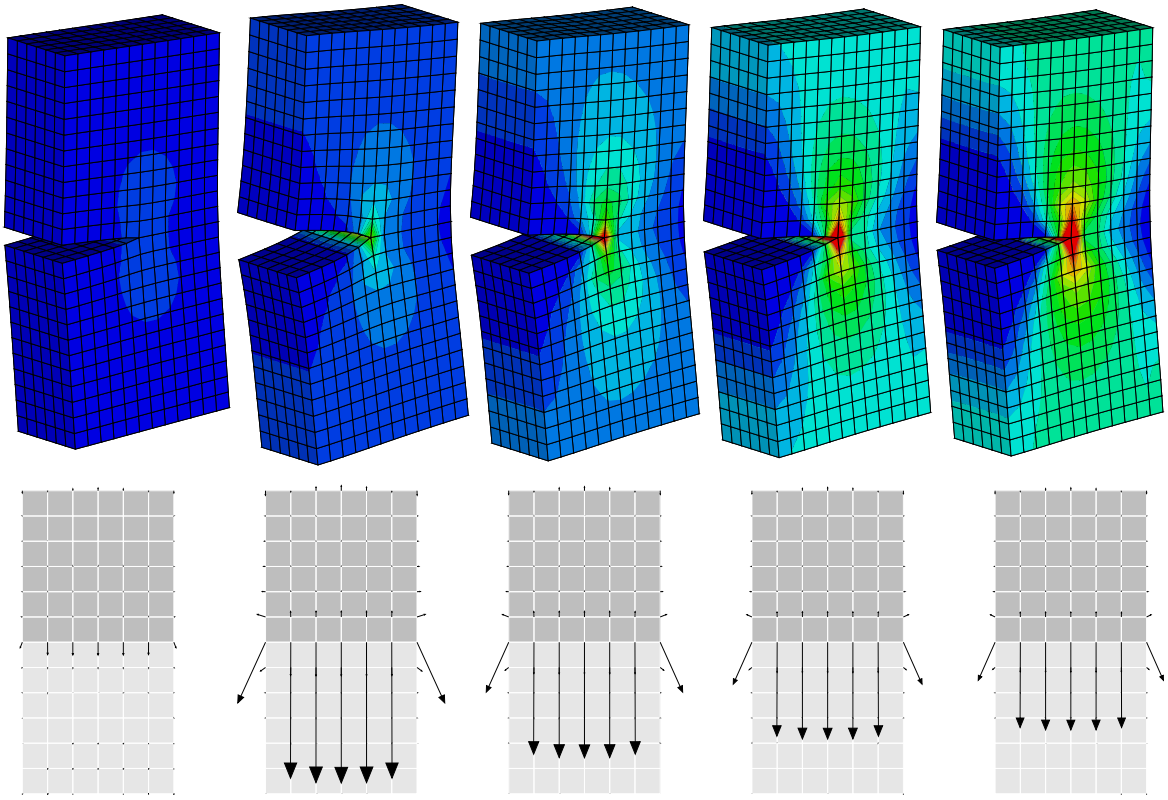

**Figure 7.37:** Tension – Evolution of density and material forces in edge cut specimen

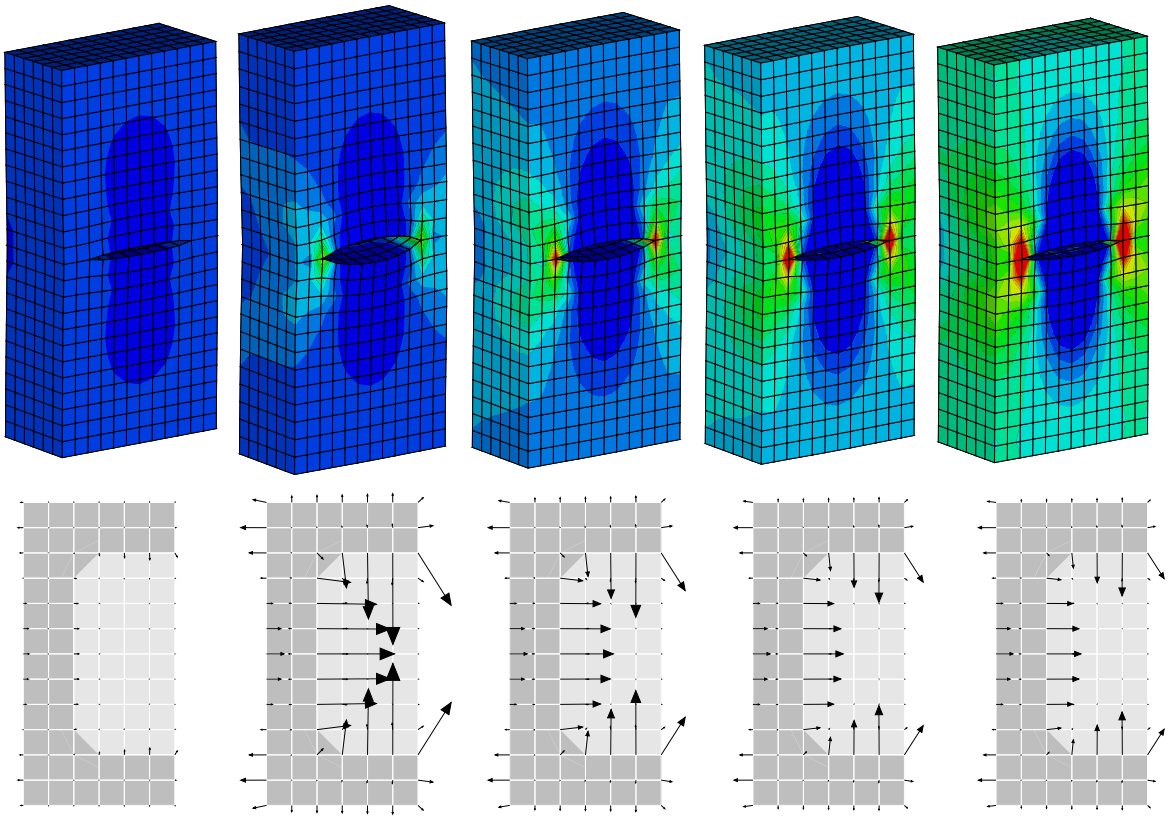

**Figure 7.38:** Tension – Evolution of density and material forces in surface cut specimen

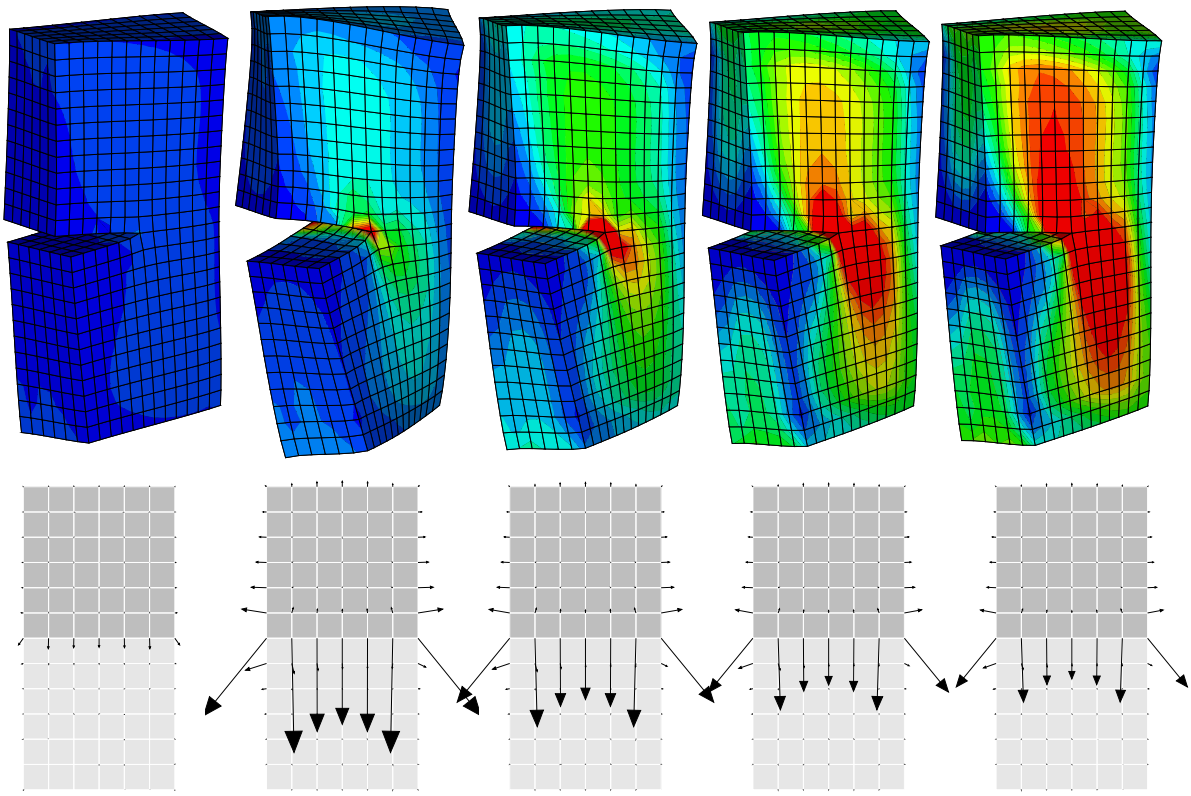

**Figure 7.39:** Torsion – Evolution of density and material forces in edge cut specimen

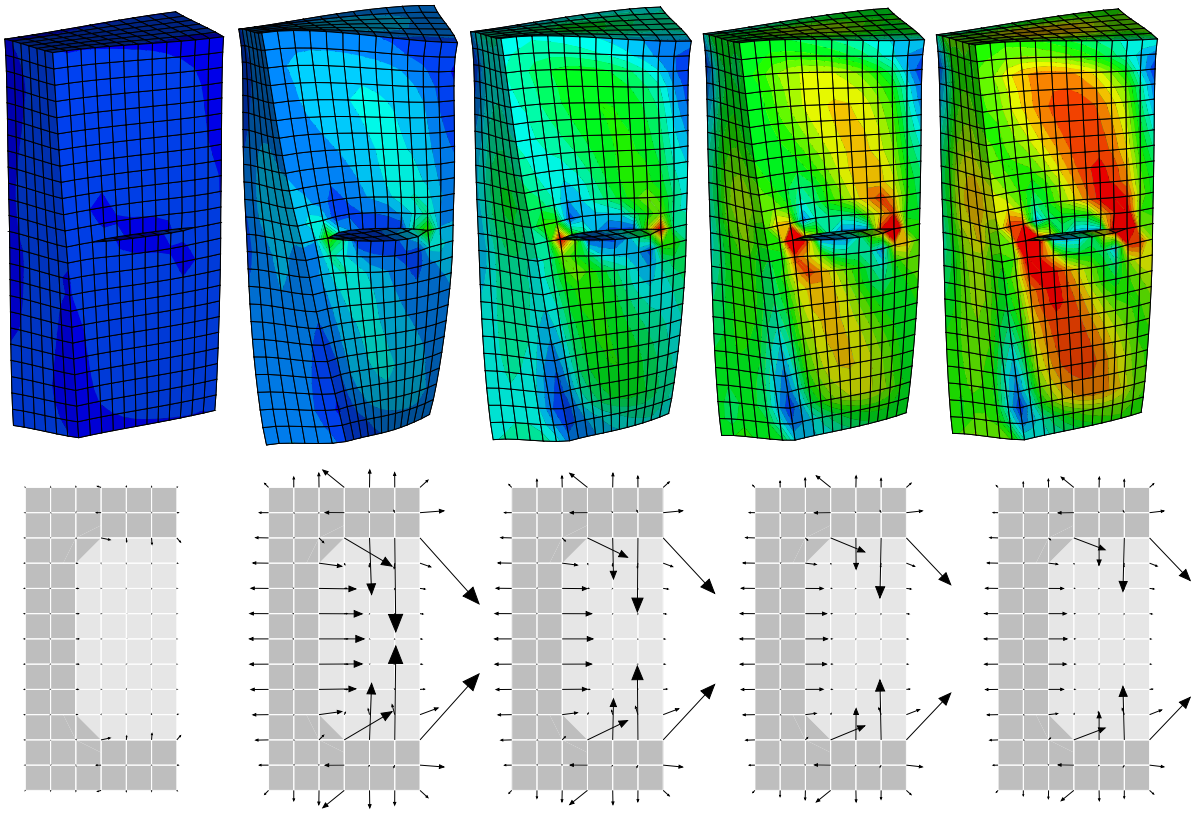

**Figure 7.40:** Torsion – Evolution of density and material forces in surface cut specimen

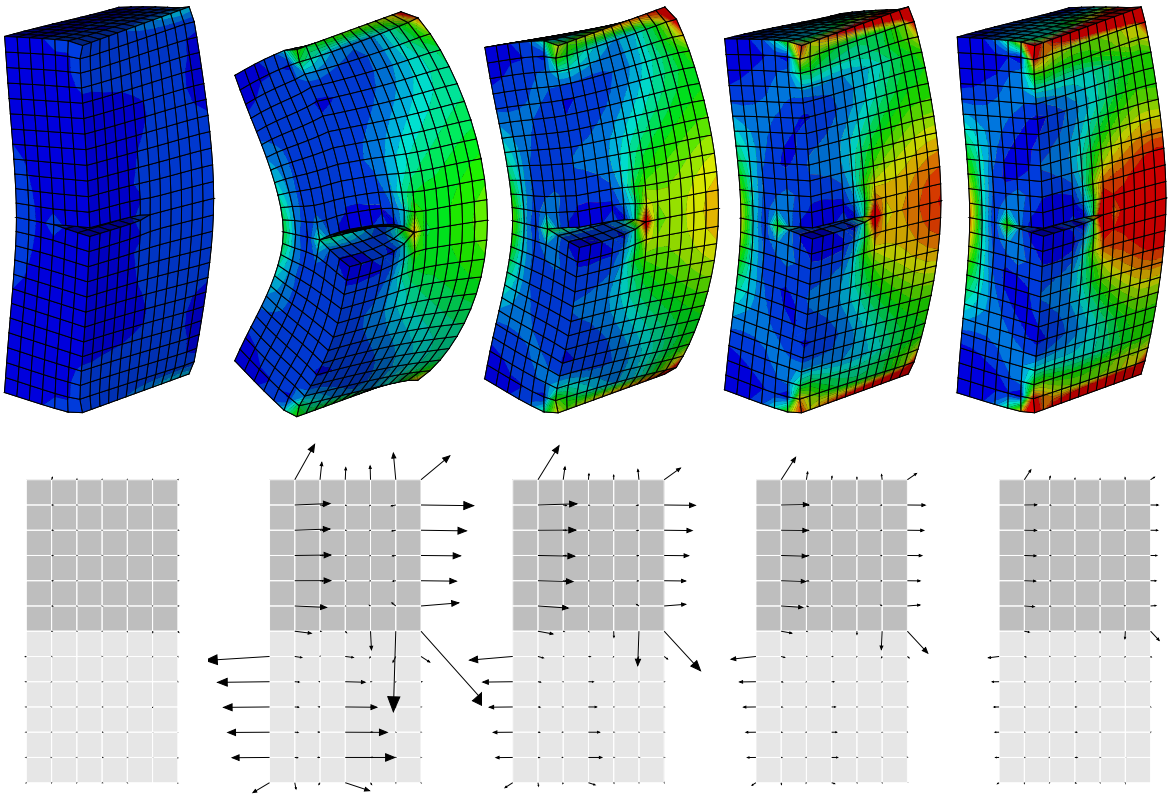

**Figure 7.41:** Bending – Evolution of density and material forces in edge cut specimen

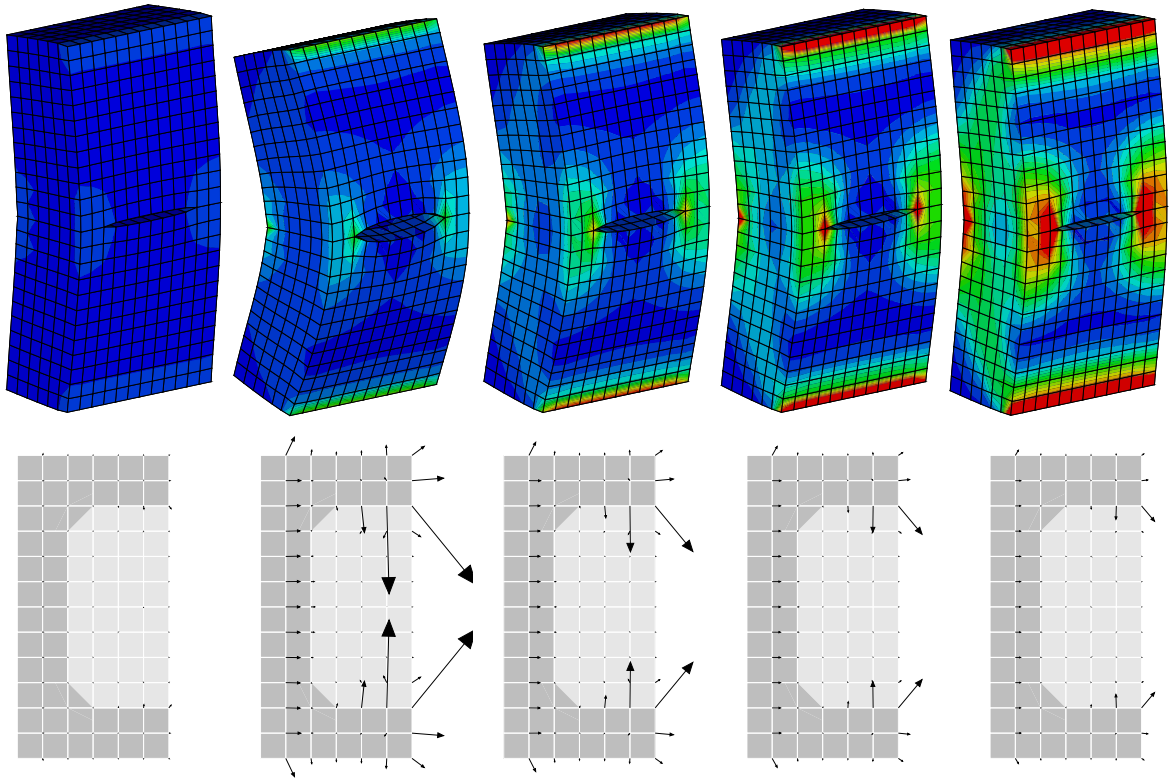

**Figure 7.42:** Bending – Evolution of density and material forces in surface cut specimen

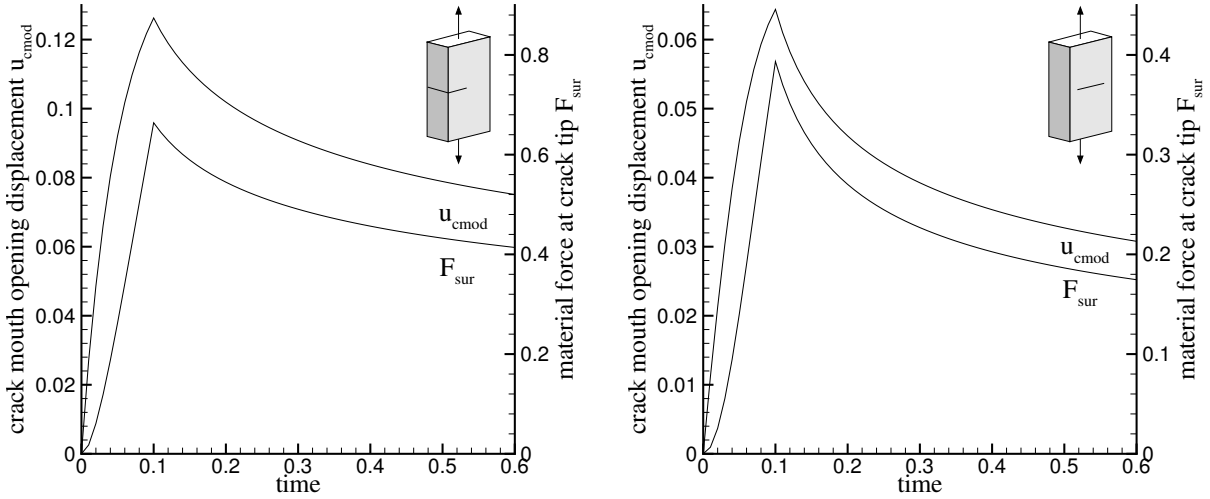


**Figure 7.43:** Tension – Evolution of crack mouth opening displacement & material forces

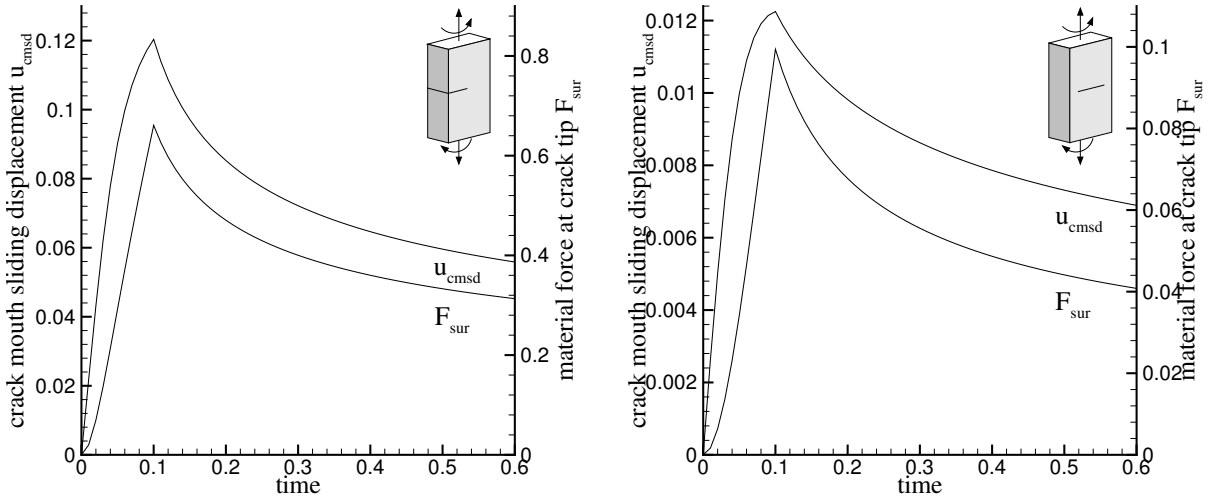


**Figure 7.44:** Torsion – Evolution of crack mouth sliding displacement & material forces

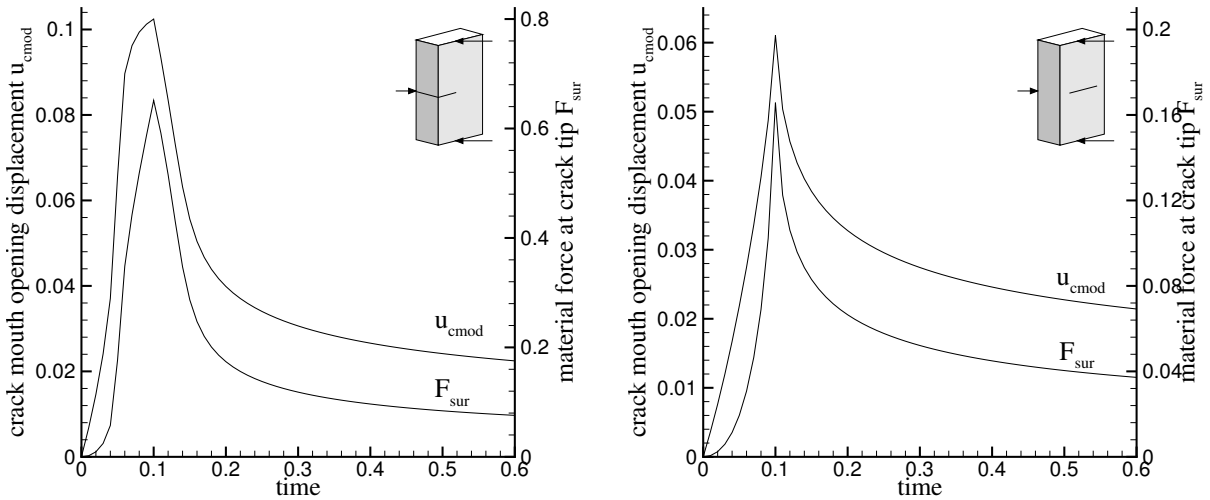


**Figure 7.45:** Bending – Evolution of crack mouth opening displacement & material forces

slightly due to the fact that the last load case rather represents a global deformation whereas the first examples were dominated by zones of highly localized straining. First, the overall deformation increases with increasing load and the cracks open considerably. Accordingly, the material forces take maximum values, see also figures 7.45. During the healing phase of constant loading, the tissue adapts to its environment, biomaterial is deposited at areas of maximum stimulus, particularly at the crack tips. The local rearrangement of matter which is visualized elegantly in terms of the material forces causes a considerable closure of cracks, thereupon the overall deformation tends to decrease.

**Remark 7.13.1 (Quantitative validation of results)** *The suggested algorithm has proven to yield qualitatively reasonable results as it predicts the closure of cracks and cuts due to local changes in density. It should be mentioned, however, that a closer study of the mass source and flux is needed to quantify on the one hand the amount of matter to be deposited and on the other hand the exact location of its deposition. In this respect, in particular the bending simulation might have predicted a too global deposition of material. To elaborate the degree of locality, i.e. the area that should be affected by the healing process, quantitative comparisons with experimental results have to be carried out in the future.*

## 7.14 Example: Computational modeling of chemomechanical damage

Last, we shall elaborate the applicability of the proposed open system framework to problems characterized through chemomechanical damage.

### 7.14.1 One–dimensional model problem

To illustrate the physical nature of the chemomechanical damage model introduced in section 4.5.2, figure 7.46 shows the material response in a one–dimensional tension test. For the sake of transparency, we shall neglect transport effects as $\boldsymbol{R} = \boldsymbol{0}$ such that the density evolution is governed by the mass source $\mathcal{R}_0 = -\rho_0^* \exp\left[-\alpha\, \psi_0^* / \psi_0\right]$ as introduced in equation (4.5.12). Thereby, the reference density and the reference free energy are chosen to $\rho_0^* = 1.0$ and $\psi_0^* = 0.1$ while the exponent $\alpha$ takes the value of $\alpha = 0.25$. The Lamé constants of the hyperelastic free energy function introduced in equation (4.5.9) are chosen to $\lambda = 0.5769$ and $\mu = 0.3846$. In particular, the curves on the left of figure 7.46 show the evolution of damage $d = 1 - \rho_0 \,/\, \rho_0^*$ versus the stretch $\lambda$ for different time step sizes $t$. The value of the damage variable starts at zero and increases exponentially with increasing stretches until it finally converges to one. Thereby, the onset of damage is, of course, more pronounced for larger time scales. The curves on the right, on the contrary, depict the evolution of damage versus time for different stretches $\lambda$. For larger stretches, the evolution of damage obviously proceeds faster than for moderate stretches. In contrast to commonly applied time–independent damage models, the model suggested herein is not determined by the amount of loading alone. Rather, the specimen damages further upon constant loading as time evolves.

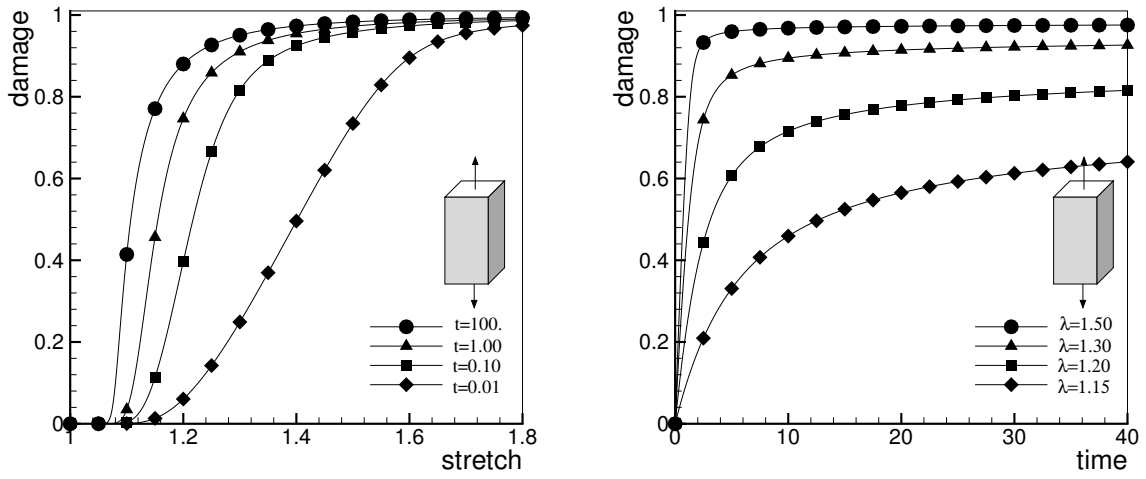


**Figure 7.46:** Evolution of damage with increased stretch and time

From a physical point of view, this property of the model captures the effect of ageing in a natural and straightforward way. Moreover, from a continuum point of view, the inclusion of rate effects essentially stabilizes the formulation, in particular in the post–critical regime.

### 7.14.2 Three–dimensional simulation

Finally, we elaborate the behavior of the derived chemomechanical damage model in response to the three different three–dimensional loading scenarios defined in section 7.13. With a size of $2 : 1 : 0.5$ and a discretization with $24 : 12 : 6$ trilinear Q1Q1 elements, the geometry and the discretization of the specimen are identical to the one of section 7.13.2. The material parameters are chosen to $\lambda = 288.46$, $\mu = 192.31$, $\rho_0^* = 1.0$, $\psi_0^* = 1.0$ and $\alpha = 2.5$, whereas the mass conduction coefficient is set equal to

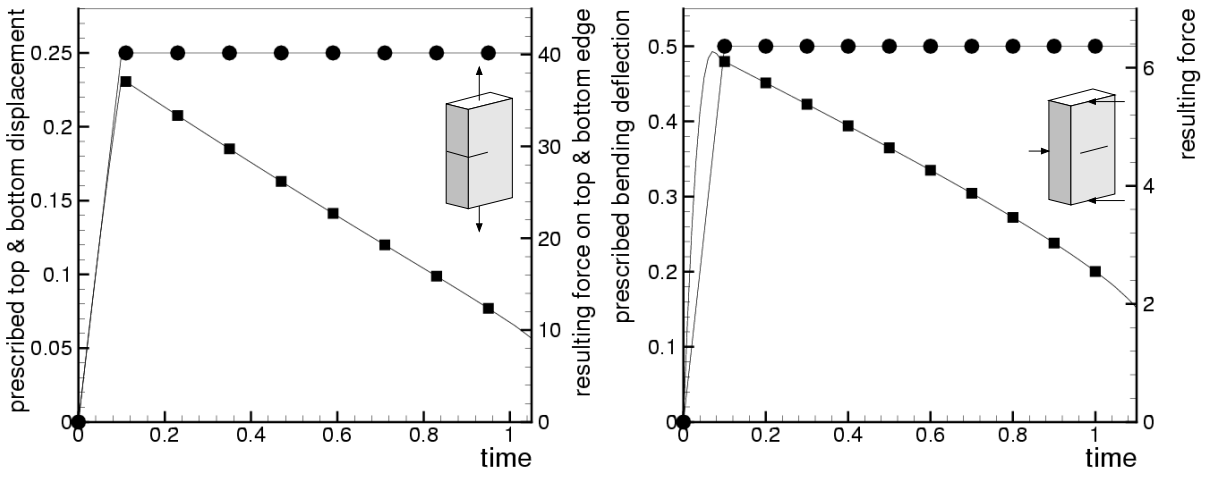


**Figure 7.47:** Tension and bending – Prescribed displacement and resulting force

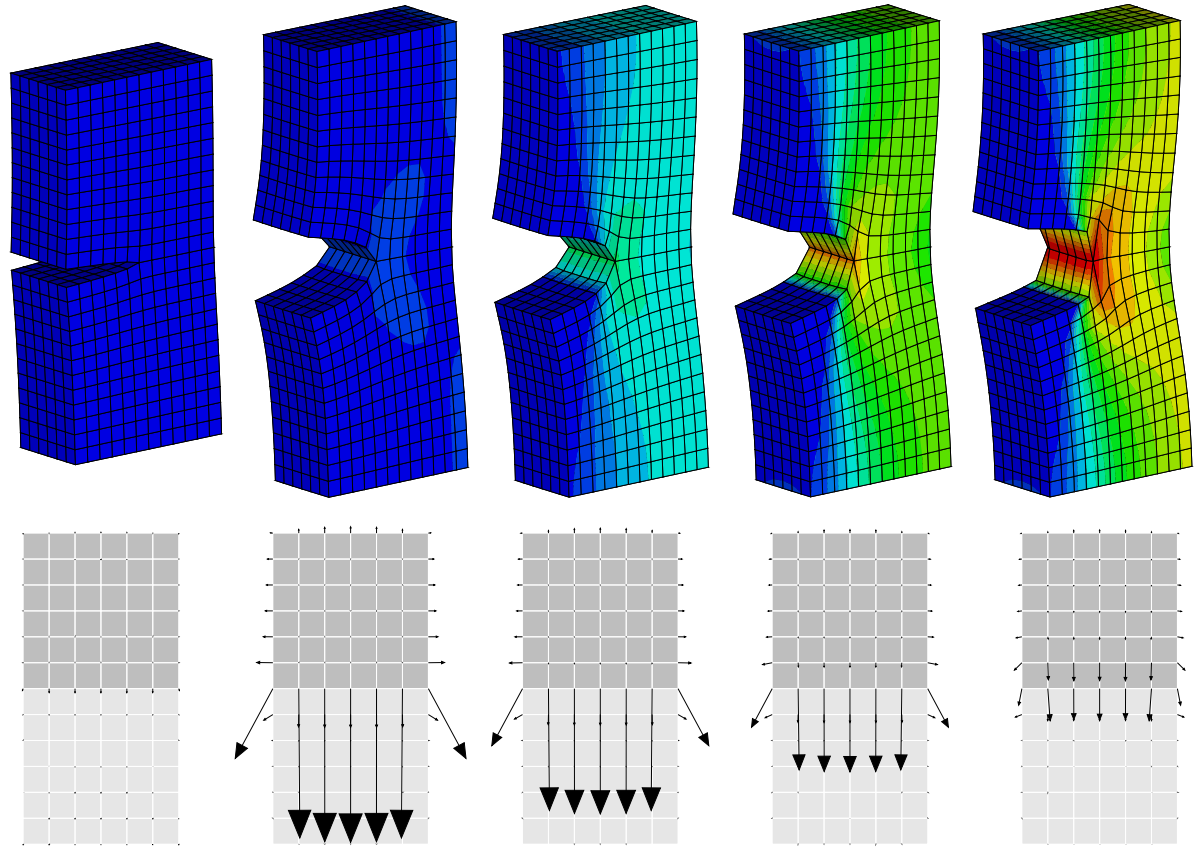

**Figure 7.48:** Tension – Evolution of density and material forces in edge cut specimen

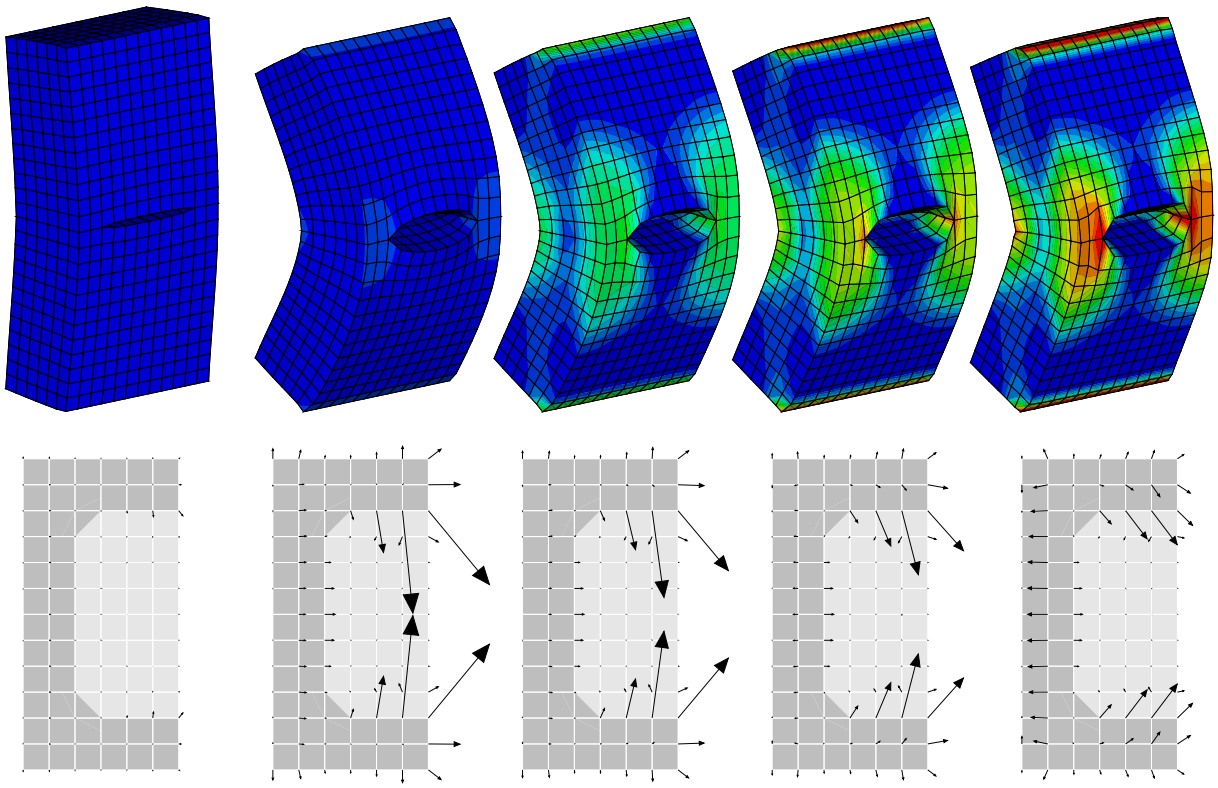

**Figure 7.49:** Bending – Evolution of density and material forces in surface cut specimen

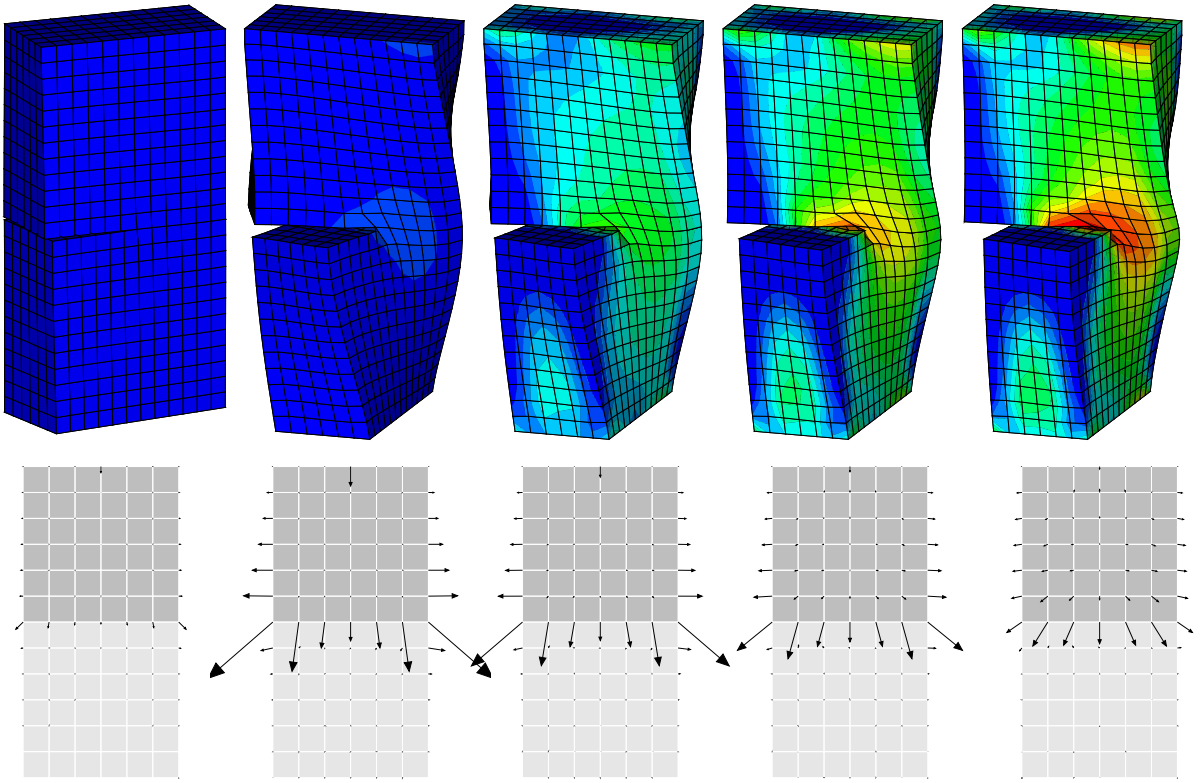

**Figure 7.50:** Torsion – Evolution of density and material forces in edge cut specimen

zero as $R_0 = 0$. Since we aim at predicting the post–peak response of the specimen, the load is applied by displacement control as opposed to the biomechanical examples of section 7.13.2. Figure 7.47 shows the prescribed top and bottom displacement and the prescribed bending deflection which both are increased during the first ten time steps of $\Delta t = 0.01$ and then held constant for another 90 time steps. Figure 7.47 nicely reflects the fact that the overall load carrying capacity drops down considerably at the onset of damage. For both, the tension and the bending problem, the resulting spatial force reduces to about a third of its maximum value due to the damage induced stiffness degradation.
Figures 7.48 to 7.50 depict the corresponding evolutions of the density, the deformation and the discrete material surface forces for the tension, the bending and the torsion problem. Thereby, the five different stages depicted in the figures correspond to time step 2 right at the beginning of the loading phase, to time step 10 at the end of the load increase and to time step 40, time step 60 and time step 100 which illustrate the onset of damage upon constant prescribed deformation. In contrast to the biomechanical examples, mechanical loading induces a reduction of the load carrying capacity in the context of damage mechanics. Consequently, the deformation tends to localize in narrow bands which was not the case for the biomechanical problems simulated in section 7.13. As damage evolves, the localization of deformation in small bands becomes more and more pronounced while the remaining parts of the structure tend to unload almost completely. Especially for the torsion problem, the effects of localization

and unloading are clearly visible in figure 7.50. At the end of the simulation, we can observe two nearly undeformed sub–blocks which have slided upon one another and have rotated by an angle of about $\Pi / 2$.
The tension, bending and torsion example have nicely demonstrated the potential of the suggested open system framework which is obviously not restricted to biomechanical applications alone but can equally well be applied to chemomechanical problems. The particularly appealing feature of the proposed chemomechanical damage formulation is based on the fact that we no longer deal with an 'artificial' internal damage variable which we cannot determine explicitly in experiments but that we rather introduce $d$ as a function of the current reference density $\rho_0$ which can obviously be accessed directly through appropriate experimental setups.
It should be pointed out, that in contrast to classical time–independent damage simulations, we did not encounter any algorithmic problems throughout all the analyses, even when we calculated far into the softening branch. The incorporation of time–dependent effects apparently regularizes the underlying damage formulation. Stability might also have been enhanced due to the fact that damage was interpolated continuously on the node point level in contrast to most classical damage formulations which typically suggest an integration point based approach.

# 8 Discussion

Die Lösung des Problems des Lebens
merkt man am Verschwinden des Problems.

Ludwig Wittgenstein,
Tractatus Logico–Philosophicus, §6.521, 1921

## 8.1 Basic results of the present work

**Continuum model for open system thermodynamics** First, to set the basis for the computational models that were derived in the second part of the work, a general framework for the thermodynamics of open systems has been set up. The provided set of equations is believed to be particularly useful for problems typically encountered in the fields of biomechanics or chemomechanics. In contrast to most existing formulations for open systems in which an interaction with the environment takes part exclusively via the exchange of source terms, we have allowed for an additional in– or outflux of matter keeping the underlying theory as general as possible. Consequently, not only the balance of mass, but also all the other balance equations had to be reconsidered since changes in mass might have a direct impact on all the other balance equations as well. To clarify the influence of the non–constant amount of matter, we have introduced the notions of volume specific and mass specific format. Thereby, the latter is believed to be of particular interest, since the mass specific balance equations typically take the well–known format of classical closed system thermodynamics.
Throughout the entire derivation, we have followed a three–step strategy. First, we have summarized the classical balance equations for the spatial motion problem. Next, the balance equations for the material motion problem have formally been introduced in complete analogy to their well–known spatial motion counterparts. Thereby, the quantities introduced in the material motion context, the related fluxes and sources, have initially been introduced through mere definitions guided by duality arguments in comparison to the spatial motion setting. In a final step, we tried to bridge the gap between the spatial and the material motion problem. For this purpose, the first and second law of thermodynamics have been further elaborated to yield additional useful relations between the individual spatial and material quantities. These relations give rise to further physical interpretation of the material motion problem which is particularly well–suited to characterize the nature of open systems, especially in the presence of material inhomogeneities.
Having introduced the fundamental kinematic relations, the relevant balance equations and the appropriate constitutive restrictions, we specified three different classes of two–field problems which we elaborated computationally within the finite element

framework. According to the degree of interaction with the environment, we classified adiabatic closed systems, closed systems and open systems. All of them were, of course, characterized in terms of the spatial deformation map. For adiabatic closed systems the material deformation map was introduced as second vector–valued field. Closed systems and open systems were characterized through a second field of scalar–valued nature, namely the temperature and the density. In all three cases, the second field was interpolated in a $\mathcal{C}^0$–continuous way and introduced as nodal degree of freedom similar to the first field of the spatial deformation map. Monolithic solution strategies have been suggested throughout. In all three cases, not only the spatial but also the material motion problem has been solved numerically. For adiabatic closed systems, the discrete material force residual was enforced to vanish in a weak sense to render optimal node point positions. For closed and open systems, however, discrete material node point forces were calculated in a mere post–processing step to provide further information about a possible internal rearrangement of material inhomogeneities.

**Discrete model for adiabatic closed systems** The main idea of the first class of multifield problems, i.e. the one of adiabatic closed systems, was the derivation of an Arbitrary Lagrangian Eulerian formulation which was embedded in a consistent variational framework. Being essentially characterized through a spatial and a material mapping, the formulation is inherently related to the mechanics on the spatial and the material manifold. The governing equations follow in a straightforward way from the evaluation of the corresponding ALE Dirichlet principle based on the total variation of the overall potential energy. By reformulating this total variation with respect to fixed reference coordinates as the sum of the variation with respect to the spatial coordinates at fixed material positions plus the variation with respect to the material coordinates at fixed spatial position, we obtained the Euler–Lagrange equations of the ALE formulation. These are the spatial and the material motion version of the balance of linear momentum, which, of course, correspond identically to the balance equations derived by arguments of duality. The solution of the former renders the spatial configuration while the latter defines the related material configuration and thus the optimal node point positions of the underlying mesh which minimizes the overall potential energy.
The Euler–Lagrange equations can be interpreted as spatial and material force balance, respectively. In the continuous hyperelastic case, both statements are entirely equivalent for homogeneous problems. However, this equivalence is no longer valid upon discretization, i.e. a vanishing discrete spatial forces residual does not necessarily have to coincide with a vanishing discrete material forces residual and vice versa. Paralleling the traditional application, where continuous material forces are used to investigate material inhomogeneities, discrete material forces can be used to detect numerical inhomogeneities induced by the underlying finite element discretization. An additional release of energy can be observed when moving nodes of the finite element mesh in the direction opposite to the material force acting on it. An optimal mesh thus corresponds to vanishing discrete material node point forces. In this sense, the ALE remeshing strategy is no longer user–defined but objective with respect to energy minimization.
Based on arguments of duality, our formulation is essentially characterized through

the discretization and simultaneous solution of both, the spatial and the material motion problem. In this sense, the variational ALE framework is particularly appealing since it renders symmetric system matrices upon discretization. The presented generic framework is therefore considered as an elegant and powerful strategy to derive optimal meshes on a consistent variational basis.

**Discrete model for closed systems** The main objective of the second category of two–field problems was the theoretical and numerical exploitation of the notion of material forces in closed system mechanics. To this end, we have highlighted the fundamental duality between the classical spatial and the material point of view. Both, the spatial and the material version of the governing equations have been reformulated in their weak form and discretized in space to set the stage for a Galerkin type finite element analysis. While the spatial motion problem typically renders the discrete node point values of the deformation and the temperature in response to given spatial forces, the material force method requires the solution of the coupled deformation temperature problem to determine the discrete material surface forces. As such, the material force method can be considered as a mere post–processing step. The determination of the discrete material node point forces is thus computationally cheap and extremely straightforward once the spatial motion problem has been solved.
In contrast to linear or nonlinear elastic fracture mechanics where the discrete material node point forces are characterized through the deformation alone, we might have an additional contribution from the discrete material volume forces in the context of thermoelasticity. These discrete material volume forces are directly related to the temperature gradient which is readily available if a node point based approach with a $\mathcal{C}^0$–continuous temperature interpolation is applied. The individual contributions to the discrete material surface forces have been elaborated systematically by means of selected model problems.

**Discrete model for open systems** Within the context of open system thermodynamics, we basically focused on the analysis of different spatial discretization techniques for the spatial motion problem while the material motion problem was again solved in a purely post–processing sense. Thereby, the deformation field was treated in the classical way. For the density field, however, we suggested two alternative discretization strategies, a node point based and an integration point based approach. For the former, the density has been introduced as a global unknown on the nodal level, whereas it was treated as an internal variable on the integration point level in the latter approach. The traditional element based approach reported in the related literature can then be classified as a special case of either the node point based or the integration point based approach. For the geometrically exact formulation analyzed herein, the corresponding finite element formulations, namely the Q1P0 element and the $\text{Q1}^{\text{sri}}$ element, showed a slightly different behavior, while for the linear elastic model applied in the literature, both formulations should be absolutely identical to the element based approach. In the context of modern finite element technologies, the discretized equations were linearized consistently and their solution was embedded in an incremental iterative Newton–Raphson procedure.

Both alternative discretization strategies were finally compared numerically in terms of a discontinuous and a continuous model problem. As expected, the node point based elements performed better for continuous smooth solutions whereas the integration point based elements proved advantageous for discontinuous problems with sharp fronts. Despite of this difference, both strategies yielded remarkably similar results upon mesh refinement. In most cases, the analyzed lower order elements, i.e. the Q1P0 element, the classical Q1 element and the $Q1^{sri}$ element, were superior over the higher order elements. They proved computationally cheap, i.e. cheap in memory, storage and computer time, and thus turned out to be extremely fast. Especially the computationally most expensive Q2Q2 element performed poor close to sharp fronts and is thus not recommended for further practical use.
Another remarkable difference between the two alternative discretization techniques is the size of the overall problem, which is directly related to the computer time required for the solution. For small scale problems, both strategies needed approximately the same calculation time. While the node point based approach basically suffers from larger system matrices, the integration point based approach requires a local Newton iteration at the integration point level. Nevertheless, the influence of the former becomes more and more pronounced upon mesh refinement. Provided that both strategies give similar results, this lack of computational efficiency of the node point based approach might be an important drawback for realistic large scale simulations. However, one has to keep in mind, that the node point based approach becomes unavoidable, if higher order gradients of the density are to be incorporated, e.g. by the incorporation of a mass flux or by the need to reproduce the classical size effect.
Finally, we would like to point out, that the results of the present study are not necessarily restricted to the modeling of growth but rather hold in a more general sense. Any multifield problem in continuum mechanics, e.g. convection–diffusion in chemomechanical applications, the classical thermoelasticity or problems arising in computational inelasticity such as damage or plasticity, can be treated in an analogous way. As long as no gradients of the additional field, e.g. the concentration, the temperature, the damage variable or the plastic multiplier, are incorporated in the formulation, one is free to choose either a $C^0$–continuous node point based approach or a discrete pointwise representation within the integration point based approach. Upon mesh refinement, both strategies should converge to the same solution, provided that the different interpolation orders of the individual fields are chosen appropriately. As soon as higher order spatial gradients enter the formulation, e.g. through diffusion, heat conduction, gradient damage or gradient plasticity, the node point based $C^0$–continuous approach becomes mandatory. In this sense, the comparative study of the present work is believed not only to yield a contribution to the computational modeling of open systems in particular but also to the numerical simulation of multifield problems in general.
Moreover, we have considered not only the classical spatial motion problem of open system mechanics but also its material motion counterpart. A computational framework has been outlined to evaluate both, the spatial and the material motion problem in the context of the finite element method. To this end, the sets of governing equations for the spatial and the material motion have been reformulated in a weak sense

and discretized in space with the classical Galerkin based finite element technique. The spatial motion problem renders the discrete node point values of the density and deformation, whereas the material force method renders the discrete material surface forces. Their determination can be carried out in a simple post–processing step similar to the closed system case. Once the spatial motion problem has been evaluated, the calculation of the discrete material node point forces is thus extremely cheap from a computational point of view.
The computed discrete material node point forces are energetically conjugate to variations of material node point positions. In the context of biomechanics, they can be computed effectively to provide on the one hand an indicator for the biomechanically induced rearrangement of material inhomogeneities responsible for internal remodeling processes. On the other hand, material forces on the specimen boundary can be interpreted as a measure of shape sensitivity indicating the tendency towards surface changes in the form of external remodeling. Pointing from high to low density concentrations, discrete material volume forces motivate the incorporation of a mass flux being essentially proportional to the density gradient. This additional mass flux tends to equilibrate concentrations and also smoothes spurious oscillations of the density field close to spatial discontinuities. Discrete material surface forces typically point into the direction of a potential energy increase upon replacement of material node point positions. Consequently, they can be applied to locate areas of potential material apposition, whereby material will be deposited locally in the direction opposite to the material force. These findings have been underlined computationally by a systematic study of selected model examples, in particular the simulation of mechanically induced growth and healing phenomena.

**Computational modeling of growth** Finally, the potential of the derived algorithmic framework for open system thermodynamics has been elaborated for classical biomechanical benchmark problems. The basic concern of the first study was the comparison of different computational strategies to model growth processes typically encountered in modern biomechanical applications. Motivated by the huge body of literature on this highly active branch of research, we began by comparing the existing formulations in terms of appropriated classifications. It turned out, that the notions of stability and uniqueness were often attributed to the temporal or to the spatial discretization although the cause of instability actually originated back to the ill–posedness of the underlying continuous problem. The formulation suggested in the present work, however, is based on a well–posed continuous model embedded in the framework of finite deformations. Unlike the existing small strain formulations, the derived geometrically exact model is not a priori restricted to hard tissue mechanics but is potentially able to simulate the behavior of soft tissues as well. In contrast to most existing formulations in the literature, we suggested the use of an implicit time stepping scheme which is unconditionally stable and thus poses no additional restrictions on the choice of the time step size.
Consequently, both classes of derived algorithms, the node point based and the integration point based approach yielded stable and physically meaningful results when applied to the classical benchmark problem of the proxima femur. Starting from an

initially homogeneous density distribution, we were able to simulate the formation of the characteristic structure of the proxima femur with a dense system of compressive trabeculae carrying stresses form the superior contact surface to the calcar region, a secondary arc system through the infero medial joint surface, Ward's triangle and a dense cortical shaft around the medullary core. These results were in excellent agreement with experimental findings and computational simulations reported in the literature. Remarkably, the difference between the node point based approach and the integration point based approach was almost negligible, in particular when the traditional smoothing procedure of the graphic post–processor was included to determine smoothed density distributions.
The solution of the material force method in the context of growth provided additional information about the local reorganization of matter. Thereby, the material surface forces have been shown to sense geometric imperfections on the femur surface and can thus be interpreted as an indicator for external remodeling. Material volume forces, on the contrary, indicate the flow of matter to render the overall structure more homogeneous. As such, they essentially motivate the incorporation of the mass flux pointing in the direction of the density gradient. Material volume forces can thus be interpreted as an indicator for internal remodeling.
Motivated by the material volume forces being proportional to the gradient of concentrations, we have incorporated an additional mass flux into our formulation. The numerical results revealed nicely, that the incorporation of the mass flux enabled the simulation of size effects characteristic for microstructural materials such as bones. Moreover, due to the introduction of the mass flux, sharp fronts could be resolved smoothly and spurious oscillations close to discontinuous density distributions could be avoided. The additional incorporation of the flow of matter can thus be considered as a natural extension of the existing flux–free formulations that enables the simulation of microstructural effects and also enhances the computational stability in a physically motivated way.

**Computational modeling of healing** Last, we have applied the derived algorithm for open system thermodynamics to the qualitative simulation of healing mechanisms in biological tissues. To this end, the solution of the spatial and the material motion problem has been elaborated systematically by means of two prototype geometries subjected to three different representative loading scenarios. The present model for open system mechanics and its algorithmic realization have been shown capable of reproducing healing phenomena and regeneration processes in biological tissues. Due to the local deposition of matter, the structure was strengthened locally at areas of maximum deformation. The underlying healing mechanism manifested itself in the reorganization and densification of the biological ground substance particularly at the crack tips which in turn causes closure of cracks and healing of wounds accompanied by a considerable decrease of the overall deformation.
The particularly new aspect of this contribution is the application of the material force method as a qualitative measure for the driving force of healing. Material forces have been shown to sense geometrical and material inhomogeneities as they illustrate the tendency to render the material more homogeneous. In living tissues, which, in con-

trast to engineering materials, show the fascinating ability to adapt naturally to changes in their environment, material forces indicate the flow of matter during a healing process. It has been demonstrated, that material forces provide additional information on the experimentally observed dependence of the wound healing process on the shape of the wound. The complete range of application of the material force method is still far from being fully exploited. Nevertheless, we believe it has a far reaching potential especially in biomechanical applications. When a biological tissue is grown or healing takes place, be it inside or outside the living organism, material forces could be utilized to identify an optimal mechanical stimulation to essentially speed up the growth or healing process. This issue of mechanically stimulated healing might be relevant not only for damaged soft tissues, e.g. optimal wound healing of skin or healing of microdamaged skeletal muscles but also for healing of fracture in hard tissues such as bones. Moreover, stress–induced optimal growth could be of practical relevance in the context of tissue engineering which aims at the creation of living artificial tissue substitutes with human cells.

## 8.2 Future perspectives

The continuum model of open system thermodynamics provided in this work is of general nature and captures not only the spatial but also the material motion problem in a completely dual approach. Its entire range of application is not yet fully exploited especially in the context of biomechanics or chemomechanics. The derived theoretical framework can easily be extended to more sophisticated applications such as inelasticity in the form of viscosity, plasticity or damage or combinations thereof. In this context, the incorporation of an initial transversal isotropy, an initial orthotropy or a general initial anisotropy is also rather straightforward. On the continuous level, the above–suggested changes would only affect the constitutive equations while the presented kinematic relations and the balance equations would remain valid throughout. On the discrete level, inelasticity introduces a number of additional algorithmic challenges. Computational inelasticity is typically evaluated on the integration point level. It is realized with the help of a number of internal variables. Usually, their evolution equations are highly nonlinear and local iterations have to be carried out to determine the values of the internal variables of the current step. Another important aspect which is relevant in particular for soft tissues is their almost incompressible material behavior which necessitates sophisticated mathematical strategies to handle the additional incompressibility constraint. In contrast to the extension to inelasticity, which can mainly be carried out on the integration point level, algorithmic modifications due to incompressibility have to be introduced on the element level.
Until now, only isotropic changes of the material microstructure have been considered in our group. The microstructural alignment of individual trabeculae in hard tissues as well as the local strengthening and reorientation of fibers in soft tissues have thus been entirely neglected in the present work. To incorporate not only initial anisotropy but also the evolution of the principal directions in response to changes in mechanical loading, basically two alternative strategies can be followed. Anisotropy can either

be introduced via structural tensors and their invariants or via the concept of an incompatible intermediate configuration. The former approach provides a sound physical interpretation in particular if the material microstructure is of fibrous nature. In this context, e.g. in the mechanics of arteries where discrete fiber directions can be measured experimentally, the list of arguments of the free energy function can be enhanced by invariants of the structural tensors, which in turn, are functions of the fiber directions. Two distinct effects, namely the local strengthening of the fiber itself on the one hand and the reorientation of the fiber direction on the other hand can then be addressed individually. The appealing advantage of the structural tensors' approach is that it can be classified as a natural extension of the model of isotropic functional adaption within the framework of open system thermodynamics.
Surprisingly, in the biomechanical literature, the second approach based on the introduction of an incompatible intermediate configuration seems to be favored over the structural tensors' approach. Certainly, one of its most convincing advantages is, that residual stresses can be incorporated elegantly into the intermediate configuration framework. Moreover, its computational realization is closely related to multiplicative plasticity and existing algorithmic frameworks could maybe be applied with minor modifications. However, the definition of a physically meaningful evolution law for the incompatible growth configuration in this second approach is probably incomparably more difficult than the formulation of appropriate evolution laws for the fiber directions in the first approach. In any case, the concept of an intermediate configuration cannot be related to the framework of open systems thermodynamics in a straightforward way. The systematic comparison of both alternative strategies therefore represents a highly interesting brach of research that will be followed by our research group in the near future.
Next to the suggested biomechanical applications, chemomechanics certainly represents a highly attractive field of current interest to which the derived framework of open system thermodynamics could easily be applied. In particular the interpretation of the change in density as the evolution of chemically induced damage provides a subject of potential research. In the context of isotropic damage, changes in density give a clear physical interpretation to the damage variable, which can then be measured explicitly in related experiments. As a particularly promising side aspect, the time dependent nature of damage, or rather the change in density, essentially enhances the stability of the chemomechanical damage formulation.
Finally, the role of the material force method and the physical interpretation of the discrete material node point forces is still not fully understood and certainly requires further investigations. In particular, material forces could be applied as driving forces for mechanically induced biological processes such as growth and healing. The reformulation of the biological stimulus in a material force based fashion is therefore a highly interesting aspect that will be part of future research. In the discrete setting, further elaborations of the material motion problem will be carried out in the context of the variational Arbitrary Lagrangian Eulerian technique. The present work has shown that a vanishing discrete material force residual can basically be applied as a consistently derived remeshing criterion. Its full range of application is, however, not yet fully exploited.

Last, we would like to point out, that within the present work, the field of biomechanics has been approached from a rather theoretical point of view. We should not forget, however, that biomechanics is a highly interdisciplinary branch of science which essentially lives from interaction between scientists of different fields. The quantitative validation of our models which have, up to now, only been adjusted qualitatively to the related literature is still an open issue. In particular the improved understanding of the biomechanical stimuli and the identification of other potential influence factors of purely biological or maybe biochemical nature is planned to play a central role in future research. To this end, a closer cooperation with experts from the fields of biology and medicine is currently being set up.

ovon man nicht ſprechen kann, darüber muß man ſchweigen.

Ludwig Wittgenstein,
Tractatus Logico–Philosophicus, §7, 1921

# Bibliography


[1] Ambrosi, D. & F. Mollica [2002]. 'On the mechanics of a growing tumor.' *Int. J. Eng. Science*, **40**, pp. 1297–1316.

[2] Argyris, J. H. [1960]. *Energy Theorems and Structural Analysis*. Butterworth London.

[3] Armero, F. & E. Love [2003]. 'An arbitrary Lagrangian–Eulerian finite element method for finite strain plasticity.' *Int. J. Num. Meth. Eng.*, **35**, pp. 737–766.

[4] Armero, F. & J. C. Simo [1992]. 'A new unconditionally stable fractional step method for non–linear coupled thermo–mechanical problems.' *Int. J. Num. Meth. Eng.*, **35**, pp. 737–766.

[5] Askes, H. [2000]. *Advanced spatial discretisation strategies for localised failure. Mesh adaptivity and meshless methods*. Ph.D. thesis, Technische Universiteit Delft, Delft, Nederlands.

[6] Askes, H., E. Kuhl & P. Steinmann [2003]. 'An ALE formulation based on spatial and material settings of continuum mechanics. Part 2: Classification and applications.' *Comp. Meth. Appl. Mech. Eng., in press*.

[7] Askes, H. & A. Rodríguez-Ferran [2001]. 'A combined rh–adaptive scheme based on domain subdivision. Formulation and linear examples.' *Int. J. Num. Meth. Eng.*, **51**, pp. 253–273.

[8] Askes, H., A. Rodríguez-Ferran & A. Huerta [1999]. 'Adaptive analysis of yield line patterns in plates with the arbitrary Lagrangian–Eulerian method.' *Computers & Structures*, **70**, pp. 257–271.

[9] Askes, H. & L. J. Sluys [2000]. 'Remeshing strategies for adaptive ALE analysis of strain localisation.' *Eur. J. Mech. / A: Solids*, **51**, pp. 447–467.

[10] Atkins, P. W. [1978]. *Physical Chemistry*. W. H. Freeman and Company – San Francisco, first edition.

[11] Bathe, K. J. [1995]. *Finite Element Procedures*. Prentice Hall, Englewood Cliffs, New Jersey.

[12] Beaupré, G. S., T. E. Orr & D. R. Carter [1990]. 'An approach for time–dependent bone modelling and remodelling.' *J. Orthop. Res.*, **8**, pp. 651–670.

[13] Belytschko, T. & J. M. Kennedy [1978]. 'Computer models for subassembly simulation.' *Nuclear Engineering & Design*, **49**, pp. 17–38.

[14] Belytschko, T., W. K. Liu & B. Moran [2000]. *Nonlinear Finite Element Analysis for Continua and Structures*. John Wiley & Sons.

[15] de Boer, R. [2000]. *Theory of Porous Media – Highlights in the Historical Development and Current State*. Springer Verlag, Berlin – Heidelberg – New York.

[16] Bonet, J. & R. D. Wood [1997]. *Nonlinear Continuum Mechanics for Finite Element Analysis*. Cambridge University Press.

[17] Bowen, R. M. [1976]. 'Theory of mixtures.' In *Continuum Physics – Volume III – Mixtures and EM Field Theories*, edited by A. C. Eringen, pp. 1–127. Academic Press, New York – San Francisco – London.

[18] Braess, D. [1997]. *Finite Elemente*. Springer Verlag, Berlin – Heidelberg, 2. Auflage.

[19] Braess, H. & P. Wriggers [2000]. 'Arbitrary Lagrangian Eulerian finite element analysis for free surface flow.' *Comp. Meth. Appl. Mech. Eng.*, **190**, pp. 95–109.

[20] Braun, M. [1997]. 'Configurational forces induced by finite–element discretization.' *Proc. Estonian Acad. Sci. Phys. Math.*, **46**, pp. 24–31.

[21] Brenner, S. C. & L. R. Scott [1994]. *The Mathematical Theory of Finite Element Methods*. Springer Verlag, Berlin – Heidelberg – New York.

[22] Capriz, G., V. N. Ghionna & P. Giovine [2002]. *Modeling and Mechanics of Granular and Porous Materials*. Birkhäuser, Basel – Boston – Berlin.

[23] Carmeliet, J. [1998]. 'A poroviscoelastic damage model for hygromechanical damage processes in unsaturated porous media.' In *Computational Modelling of Concrete Structures*, edited by R. de Borst, N. Bićanić, H. Mang & G. Meschke, pp. 559–566. Balkema, Rotterdam.

[24] Carter, D. R. & G. S. Beaupré [2001]. *Skeletal Function and Form – Mechanobiology of Skeletal Development, Aging and Regeneration*. Cambridge University Press.

[25] Carter, D. R. & W. C. Hayes [1977]. 'The behavior of bone as a two–phase porous structure.' *J. Bone Jt. Surgery*, **59-A**, pp. 785–794.

[26] Carter, D. R., T. E. Orr & D. P. Fhyrie [1989]. 'Relationships between loading history and femoral cancellous bone architecture.' *J. Biomechanics*, **22**, pp. 231–244.

[27] Chadwick, P. [1975]. 'Applications of an energy–momentum tensor in non–linear elastostatics.' *J. Elasticity*, **5**, pp. 249–258.

[28] Chadwick, P. [1976]. *Continuum Mechanics – Concise Theory and Problems*. George Allen & Unwin Ltd – London.

[29] Chen, Y.-C. & A. Hoger [2000]. 'Constitutive functions of elastic materials in finite growth and deformation.' *J. Elasticity*, **59**, pp. 175–193.

[30] Ciarlet, P. G. [1998]. *The Finite Element Method for Elliptic Problems*, volume 40. SIAM classics in Applied Mathematics, republication edition.

[31] Clough, R. W. [1965]. 'The finite element method in structural mechanics.' In *Stress Analysis: Recent Developments in Numerical and Experimental Methods*, edited by O. C. Zienkiewicz & S. Holister. John Wiley & Sons.

[32] Coleman, B. D. & W. Noll [1963]. 'The thermodynamics of elastic materials with heat conduction and viscosity.' *Arch. Rat. Mech. Anal.*, **13**, pp. 167–178.

[33] Cook, R. D. [1995]. *Finite Element Modeling for Stress Analysis*. John Wiley & Sons.

[34] Cook, R. D., D. S. Malkus, M. E. Plesha & R. J. Witt [2002]. *Concepts and Applications of Finite Element Analysis*. John Wiley & Sons.

[35] Coussy, O. [1995]. *Mechanics of Porous Continua*. John Wiley & Sons.

[36] Cowin, S. C. [1986]. 'Wolff's law of trabecular architecture at remodeling equilibrium.' *J. Biomech. Eng.*, **108**, pp. 83–88.

[37] Cowin, S. C. [1996]. 'Strain or deformation rate dependent finite growth in soft tissues.' *J. Biomechanics*, **29**, pp. 647–649.

[38] Cowin, S. C. [2000]. 'How is a tissue build?' *J. Biomech. Eng.*, **122**, pp. 553–569.

[39] Cowin, S. C. [2001]. *Bone Mechanics Handbook*. CRC Press, Boca Raton – London – New York, second edition.

[40] Cowin, S. C., Y. P. Arramon, G. M. Luo & A. M. Sadegh [1998]. 'Remarks on the technical note entitled 'Temporal stability of node–based internal bone adaption'.' *J. Biomechanics*, **31**, pp. 103–104.

[41] Cowin, S. C. & D. H. Hegedus [1976]. 'Bone remodelling I: Theory of adaptive elasticity.' *J. Elasticity*, **6**, pp. 313–326.

[42] Cowin, S. C. & J. D. Humphrey [2001]. *Cariovascular Soft Tissue Mechanics*. John Wiley & Sons, Chichester – New York.

[43] Cowin, S. C. & R. R. Nachlinger [1978]. 'Bone remodelling III: Uniqueness and stability in adaptive elasticity theory.' *J. Elasticity*, **8**, pp. 285–295.

[44] Crisfield, M. A. [1991]. *Non–linear Finite Element Analysis of Solids and Structures – Essentials*, volume I. John Wiley & Sons, Chichester – New York.

[45] Crisfield, M. A. [1997]. *Non–linear Finite Element Analysis of Solids and Structures – Advanced Topics*, volume II. John Wiley & Sons, Chichester – New York.

[46] Denzer, R., F. J. Barth & P. Steinmann [2003]. 'Studies in elastic fracture mechanics based on the material force method.' *Int. J. Num. Meth. Eng.*, **58**, pp. 1817–1835.

[47] Diebels, S. [2000]. *Mikropolare Zweiphasenmodelle: Formulierung auf der Basis der Theorie Poröser Medien*. Habilitationsschrift, Bericht aus dem Institut für Mechanik (Bauwesen) Nr. II-4, Universität Stuttgart.

[48] Donéa, J. [1980]. 'Finite element analysis of transient dynamic fluid–structure interaction.' In *Advanced Structural Dynamics*, edited by J. Donéa, pp. 255–290. Applied Science Publishers, London.

[49] Donéa, J. [1983]. 'Arbitrary Lagrangian Eulerian finite element methods.' In *Computer Methods for Transient Analysis*, edited by T. Belytschko & T. J. R. Hughes, pp. 473–516. Elsevier Science Publishers.

[50] Donéa, J., P. Fasoli-Stella & S. Giuliani [1977]. 'Lagrangian and Eulerian finite element techniques for transient fluid–structure interaction problems.' In *Transactions of the 4th International Conference on Structural Mechanics in Reactor Technology – Volume B: Thermal and Fluid / Structure Dynamics Analysis*, edited by T. A. Jaeger & B. A. Boley, pp. B 1/2: 1–12. North–Holland Publishing Company.

[51] Donéa, J., S. Giuliani & J. P. Halleux [1982]. 'An arbitrary Lagrangian–Eulerian finite element method for transient dynamic fluid–structure interactions.' *Comp. Meth. Appl. Mech. Eng.*, **33**, pp. 689–723.

[52] Donéa, J. & A. Huerta [2003]. *Finite Element Methods for Flow Problems*. John Wiley & Sons, Chichester – New York.

[53] Duhem, P. [1898]. *Traité Élémentaire de Mécanique Chimique Fondée sur la Thermodynamique*, volume I–IV. Librairie Scientifique A. Hermann.

[54] Ehlers, W. [1996]. 'Grundlegende Konzepte in der Theorie poröser Medien.' *Technische Mechanik*, **16**, pp. 63–76.

[55] Ehlers, W. & B. Markert [1998]. 'Modellierung fluidgesättigter, viskoelastischer poröser Festkörper in der Biomechanik.' In *Die Methode der Finiten Elemente in der Biomechanik, Biomedizin und angrenzenden Gebieten*. Workshop 1998, Universität Ulm.

[56] Epstein, M. & G. A. Maugin [1990]. 'The energy–momentum tensor and material uniformity in finite elasticity.' *Acta Mechanica*, **83**, pp. 127–133.

[57] Epstein, M. & G. A. Maugin [2000]. 'Thermomechanics of volumetric growth in uniform bodies.' *Int. J. Plasticity*, **16**, pp. 951–978.

[58] Eringen, A. C. [1962]. *Nonlinear Theory of Continuous Media*. Mc Graw–Hill, New York – London.

[59] Eringen, A. C. [1967]. *Mechanics of Continua*. John Wiley & Sons, Chichester – New York, first edition.

[60] Eshelby, J. D. [1951]. 'The force on an elastic singularity.' *Philosophical Transactions of the Royal Society of London*, **244**, pp. 87–112.

[61] Eshelby, J. D. [1957]. 'The determination of the elastic field of an ellipsoidal inclusion and related problems.' *Proceedings of the Royal Society of London*, **A 241**, pp. 376–396.

[62] Eshelby, J. D. [1975]. 'The elastic energy–momentum tensor.' *J. Elasticity*, **5**, pp. 321–335.

[63] Fischer, K. J., C. R. Jacobs, M. E. Levenston & D. R. Carter [1997]. 'Observations of convergence and uniqueness of node–based bone remodeling simulations.' *Annals Biomed. Eng.*, **25**, pp. 261–268.

[64] Fleck, C. [1996]. *Struktur und mechanische Eigenschaften kortikalen Knochens unter quasistatischer und zyklischer Beanspruchung*. Dissertation, Lehrstuhl für Werkstoffkunde, Werkstoffkundliche Berichte, Band 1, Universität Kaiserslautern.

[65] Fleck, C. & D. Eifler [1997]. 'Verformungsverhalten und mikrostrukturelle Schädigung kortikalen Knochens unter zyklischer Kriechbeanspruchung.' In *Die Methode der Finiten Elemente in der Biomechanik, Biomedizin und angrenzenden Gebieten*. Workshop 1997, Universität Ulm.

[66] Fung, Y. C. [1990]. *Biomechanics – Motion, Flow, Stress, and Growth*. Springer Verlag, Berlin – Heidelberg – New York.

[67] Fung, Y. C. [1993]. *Biomechanics – Mechanical Properties of Living Tissues*. Springer Verlag, Berlin – Heidelberg – New York, second edition.

[68] Fung, Y. C. [1997]. *Biomechanics – Circulation*. Springer Verlag, Berlin – Heidelberg – New York, second edition.

[69] Fung, Y. C. [2001]. *Introduction to Bioengineering*. World Scientific Publishing Co., Singapore – New Jersey, London – Hong Kong.

[70] Galilei, G. [1638]. *Discorsi e Dimostrazioni Matematiche Intorno a Due Nuove Scienze*. Appresso gli Elsevirii, Leida.

[71] Garikipati, K., H. Narayanan, E. M. Arruda, K. Grosh & S. Calve [2003]. 'Material forces in the context of bio–tissue remodelling.' In *Mechanics of material forces*, edited by P. Steinmann & G. A. Maugin. Kluwer Academic Publishers.

[72] Gasser, T. C. & G. A. Holzapfel [2002]. 'A rate–independent elastoplastic constitutive model for biological fiber–reinforced composites at finite strains: Continuum basis, algorithmic formulation and finite element implementation.' *Comp. Mech.*, **29**, pp. 340–360.

[73] Gibson, L. J. & M. F. Ashby [1982]. 'The mechanics of three–dimensional cellular materials.' *Proceedings of the Royal Society of London*, **A 382**, pp. 43–59.

[74] Gibson, L. J. & M. F. Ashby [1997]. *Cellular Solids*. Cambridge University Press, second edition.

[75] Goldstein, H. [1950]. *Classical Mechanics*. Addison–Wesley Publishing Company.

[76] Govindjee, S. [2001]. 'Firestone tire analysis.' *Internal Report, Lafayette, CA*.

[77] Green, A. E. & P. M. Naghdi [1991]. 'A re–examination of the basic postulates of thermomechanics.' *Proceedings of the Royal Society of London A*, **432**, pp. 171–194.

[78] Green, A. E. & P. M. Naghdi [1995]. 'A unified procedure for construction of theories of deformable media. I. Classical continuum physics.' *Proceedings of the Royal Society of London A*, **448**, pp. 335–356.

[79] de Groot, S. R. [1951]. *Thermodynamics of Irreversible Processes*. North–Holland Publishing Company – Amsterdam.

[80] de Groot, S. R. & P. Mazur [1962]. *Non–Equilibrium Thermodynamics*. North–Holland Publishing Company – Amsterdam.

[81] Guggenheim, E. A. [1966]. *Elements of Chemical Thermodynamics*. Royal Institute of Chemistry – Monographs for Teachers.

[82] Gurtin, M. E. [1995]. 'On the nature of configurational forces.' *Arch. Rat. Mech. Anal.*, **131**, pp. 67–100.

[83] Gurtin, M. E. [2000]. *Configurational Forces as Basic Concepts of Continuum Physics*. Springer Verlag, New York – Berlin – Heidelberg.

[84] Haase, R. [1969]. *Thermodynamics of Irreversible Processes*. Addison–Wesley Publishing Company, Reading – Massachusetts.

[85] Harrigan, T. P. & J. J. Hamilton [1992]. 'An analytical and numerical study of the stability of bone remodelling theories: Dependence on microstructural stimulus.' *J. Biomechanics*, **25**, pp. 477–488. Corrigendum, 26:365–366 (1993).

[86] Harrigan, T. P. & J. J. Hamilton [1992]. 'Optimality condition for finite element simulation of adaptive bone remodeling.' *Int. J. Solids & Structures*, **29**, pp. 2897–2906.

[87] Harrigan, T. P. & J. J. Hamilton [1993]. 'Finite element simulation of adaptive bone remodelling: A stability criterion and a time stepping method.' *Int. J. Num. Meth. Eng.*, **36**, pp. 837–854.

[88] Harrigan, T. P. & J. J. Hamilton [1994]. 'Necessary and sufficient conditions for global stability and uniqueness in finite element siumlations of adaptive bone remodeling.' *Int. J. Solids & Structures*, **31**, pp. 97–107.

[89] Harrigan, T. P., J. J. Hamilton, J. D. Reuben, A. Tone & M. Viceconti [1996]. 'Bone remodelling adjcent to intromedullary stems: An optimal structures approach.' *Biomaterials*, **17**, pp. 223–232.

[90] Hart, R. T. [2001]. 'Bone modeling and remodeling: Theories and computation.' In *Bone Biomechanics Handbook*, edited by S. C. Cowin, chapter 31, pp. 1–42. CRC-Press, Boca Raton.

[91] Haupt, P. [2000]. *Continuum Mechanics and Theory of Materials*. Springer Verlag, Berlin – Heidelberg – New York.

[92] Hegedus, D. H. & S. C. Cowin [1976]. 'Bone remodelling II: Small strain adaptive elasticity.' *J. Elasticity*, **6**, pp. 337–352.

[93] Holzapfel, G. A. [2000]. *Nonlinear Solid Mechanics: A Continuum Approach for Engineering*. John Wiley & Sons.

[94] Holzapfel, G. A. [2001]. 'Biomechanics of soft tissues.' In *The Handbook of Materials Behavior Models, Volume III, Multiphysics Behaviors*, edited by J. Lemaitre, pp. 1049–1063. Academic Press, Boston.

[95] Holzapfel, G. A. & T. C. Gasser [2001]. 'A viscoelastic model for fiber–reinforced composites at finite strain: Continuum basis, computational aspects and applications.' *Comp. Meth. Appl. Mech. Eng.*, **190**, pp. 4379–4430.

[96] Holzapfel, G. A., T. C. Gasser & R. W. Ogden [2000]. 'A new constitutive framework for arterial wall mechanics and a comparative study of material models.' *J. Elasticity*, **61**, pp. 1–48.

[97] Holzapfel, G. A. & R. W. Ogden [2003]. *Biomechanics of Soft Tissue in Cardiovascular Systems*. CISM Courses and Lectures No. 441, Springer Verlag, Wien – New York.

[98] Holzapfel, G. A. & G. Reiter [1995]. 'Fully coupled thermomechanical behaviour of viscoelastic solids treated with finite elements.' *Int. J. Eng. Science*, **33**, pp. 1037–1058.

[99] Holzapfel, G. A. & J. C. Simo [1996]. 'Entropy elasticity of isotropic rubber-like solids at finite strains.' *Comp. Meth. Appl. Mech. Eng.*, **132**, pp. 17–44.

[100] Huerta, A. & F. Casadei [1994]. 'New ALE application in non–linear fast–transient solid dynamics.' *Eng. Comp.*, **11**, pp. 317–345.

[101] Huerta, A. & W. K. Liu [1988]. 'Viscous flow with large free surface motion.' *Comp. Meth. Appl. Mech. Eng.*, **69**, pp. 227–324.

[102] Hughes, T. J. R. [2000]. *The Finite Element Method – Linear Static and Dynamic Finite Element Analysis*. Prentice Hall, Englewood Cliffs, New Jersey.

[103] Hughes, T. J. R., W. K. Liu & T. K. Zimmermann [1981]. 'Lagrangian–Eulerian finite element formulation for viscous flows.' *Comp. Meth. Appl. Mech. Eng.*, **29**, pp. 329–349.

[104] Huiskes, R. [2000]. *Challenges in Bone Biomechanics*. Intreerede, Technische Universiteit Eindhoven.

[105] Huiskes, R. & E. Y. S. Chao [1983]. 'A survey of finite element analysis in orthopedic biomechanics: The first decade.' *J. Biomechanics*, **16**, pp. 385–409.

[106] Huiskes, R., R. Ruimerman, G. H. van Lenthe & J. D. Janssen [1990]. 'Effects of mechanical forces on maintenance and adaption of form in trabecular bone.' *Nature*, **405**, pp. 704–706.

[107] Huiskes, R., H. Weinans, H. J. Grootenboer, M. Dalstra, B. Fudala & T. J. Slooff [1987]. 'Adaptive bone–remodeling theory applied to prosthetic–design analysis.' *J. Biomechanics*, **20**, pp. 1135–1150.

[108] Humphrey, J. D. [2002]. *Cardiovasular Solid Mechanics*. Springer Verlag, Berlin – Heidelberg – New York.

[109] Humphrey, J. D. & K. R. Rajagopal [2002]. 'A constrained mixture model for growth and remodeling of soft tissues.' *Mathematical Models & Methods in Applied Sciences*, **12**, pp. 407–430.

[110] Humphrey, J. D. & K. R. Rajagopal [2003]. 'A constrained mixture model for arterial adaptions to a sustained step change in blood flow.' *Biomechanics and Modeling in Mechanobiology*, **2**, pp. 109–126.

[111] Hutter, K. [2003]. *Fluid– und Thermodynamik – Eine Einführung*. Springer Verlag, Berlin – Heidelberg – New York, second edition.

[112] Ibrahimbegovic, A., L. Chorfi & F. Gharzeddine [2001]. 'Thermomechanical coupling at finite elastic strain: covariant formulation and numerical implementation.' *Commun. Num. Meth. Eng.*, **17**, pp. 275–289.

[113] Jacobs, C. R., M. E. Levenston, G. S. Beaupré, J. C. Simo & D. R. Carter [1995]. 'Numerical instabilities in bone remodeling simulations: The advantages of a node–based finite element approach.' *J. Biomechanics*, **28**, pp. 449–459.

[114] Jacobs, C. R., J. C. Simo, G. S. Beaupré & D. R. Carter [1997]. 'Adaptive bone remodeling incorporating simultaneous density and anisotropy considerations.' *J. Biomechanics*, **30**, pp. 603–613.

[115] Kalpakides, V. K. & C. Dascalu [2002]. 'On the configurational force balance in thermomechanics.' *Proceedings of the Royal Society of London A, submitted for publication*.

[116] Katchalsky, A. & P. F. Curran [1965]. *Nonequilibrium Thermodynamics in Biophysics*. Harvard University Press – Cambridge, Massachusetts.

[117] Kestin, J. [1966]. *A Course in Thermodynamics – Volume I*. Blaisdell Publishing Company – Waltham, first edition.

[118] Kestin, J. [1968]. *A Course in Thermodynamics – Volume II*. Blaisdell Publishing Company – Waltham, first edition.

[119] Kienzler, R. & G. Herrmann [2000]. *Mechanics in Material Space with Applications to Defect and Fracture Mechanics*. Springer Verlag, Berlin – Heidelberg – New York.

[120] Kirkwood, J. G. & I. Oppenheim [1961]. *Chemical Thermodynamics*. Mc Graw–Hill, New York – London.

[121] Krstin, N., U. Nackenhorst & R. Lammering [1999]. 'Zur konstitutiven Beschreibung des anisotropen beanspruchungsadaptiven Knochenumbaus.' In *Die Methode der Finiten Elemente in der Biomechanik, Biomedizin und angrenzenden Gebieten*. Workshop 1999, Universität Ulm.

[122] Krstin, N., U. Nackenhorst & R. Lammering [2000]. 'Zur konstitutiven Beschreibung des anisotropen beanspruchungsadaptiven Knochenumbaus.' *Technische Mechanik*, **20**, pp. 31–40.

[123] Kuhl, D. [2003]. 'Ion diffusion models based on the Debye–Hückel–Onsager theory applied to calcium leaching of cementitious materials.' *J. Struct. Eng., ASCE, submitted for publication*.

[124] Kuhl, D., F. Bangert & G. Meschke [2000]. 'An extension of damage theory to coupled chemo–mechanical processes.' In *Proceedings of 'ECCOMAS 2000', Barcelona, Spain, 11-14. September 2000*. CIMNE, Barcelona, Spain.

[125] Kuhl, E., H. Askes & P. Steinmann [2003]. 'An ALE formulation based on spatial and material settings of continuum mechanics. Part 1: Generic hyperelastic formulation.' *Comp. Meth. Appl. Mech. Eng., in press*.

[126] Kuhl, E., H. Askes & P. Steinmann [2004]. 'Convexity conditions in hyperelasticity – Spatial and material settings.' *J. Elast., submitted for publication*.

[127] Kuhl, E., R. Denzer, F. J. Barth & P. Steinmann [2003]. 'Application of the material force method to thermo–hyperelasticity.' *Comp. Meth. Appl. Mech. Eng., in press*.

[128] Kuhl, E., S. Hulshoff & R. de Borst [2003]. 'An arbitrary Lagrangian Eulerian finite–element approach for fluid–structure interaction phenomena.' *Int. J. Num. Meth. Eng.*, **57**, pp. 117–142.

[129] Kuhl, E., A. Menzel & P. Steinmann [2003]. 'Computational modeling of growth: A critical review, a classification of concepts and two new consistent approaches.' *Comp. Mech.*, **32**, pp. 71–88.

[130] Kuhl, E. & P. Steinmann [2003]. 'Computational modeling of healing: An application of the material force method.' *Biomechanics and Modeling in Mechanobiology, available online first*, pp. DOI: 10.1007/s10237–003–0034–3.

[131] Kuhl, E. & P. Steinmann [2003]. 'Mass– and volume specific views on thermodynamics for open systems.' *Proceedings of the Royal Society of London*, **459**, pp. 2547–2568.

[132] Kuhl, E. & P. Steinmann [2003]. 'On spatial and material settings of thermo–hyperelastodynamics for open systems.' *Acta Mechanica*, **160**, pp. 179–217.

[133] Kuhl, E. & P. Steinmann [2003]. 'Theory and numerics of geometrically non–linear open system mechanics.' *Int. J. Num. Meth. Eng.*, **58**, pp. 1593–1615.

[134] Kuhl, E. & P. Steinmann [2003]. 'Thermodynamics of open systems with application to chemomechanical problems.' In *Computational Modelling of Concrete Structures*, edited by N. Bićanić, R. de Borst, H. Mang & G. Meschke, pp. 463–472. Balkema, Rotterdam.

[135] Kuhl, E. & P. Steinmann [2004]. 'Material forces in open system mechanics.' *Comp. Meth. Appl. Mech. Eng.*, **193**, pp. 2357–2381.

[136] Kühn, W. & W. Hauger [2000]. 'A theory of adaptive growth of biological materials.' *Arch. Appl. Mech.*, **70**, pp. 183–192.

[137] Levenston, M. E. [1997]. 'Temporal stability of node–based internal bone adaption simulations.' *J. Biomechanics*, **30**, pp. 403–407.

[138] Levenston, M. E. [1998]. 'Author's response to comments by cowin et al. regarding levenston (1997).' *J. Biomechanics*, **31**, pp. 105–106.

[139] Levenston, M. E. & D. R. Carter [1998]. 'An energy dissipation–based model for damage stimulated bone adaption.' *J. Biomechanics*, **31**, pp. 579–586.

[140] Lewis, R. W., K. Moran, H. R. Thomas & K. N. Seetharamu [1996]. *The Finite Element Method in Heat Transfer Analysis*. John Wiley & Sons, Chichester – New York.

[141] Liebe, T., R. Denzer & P. Steinmann [2003]. 'Application of the material force method to isotropic continuum damage.' *Computational Mechanics*, **30**, pp. 171–184.

[142] Liu, I. S. [1972]. 'Method of Lagrange multipliers for exploitation of the entropy principle.' *Arch. Rat. Mech. Anal.*, **46**, pp. 131–148.

[143] Liu, I. S. [2002]. *Continuum Mechanics*. Springer Verlag, Berlin – Heidelberg – New York.

[144] Liu, W. K. [1981]. 'Finite element procedures for fluid–structure interacions and application to liquid storage tanks.' *Nuclear Engineering & Design*, **65**, pp. 221–238.

[145] Liu, W. K. & J. Gvildys [1986]. 'Fluid–structure interaction of tanks with an eccentric core barrel.' *Comp. Meht. Appl. Mech. Eng.*, **58**, pp. 51–77.

[146] Lubarda, V. A. & A. Hoger [2002]. 'On the mechanics of solids with a growing mass.' *Int. J. Solids & Structures*, **39**, pp. 4627–4664.

[147] Malvern, L. E. [1969]. *Introduction to the Mechanics of a Continuous Medium*. Prentice Hall, Englewood Cliffs, New Jersey.

[148] Marsden, J. E. & T. J. R. Hughes [1983]. *Mathematical Foundations of Elasticity*. Prentice Hall, Englewood Cliffs, New Jersey.

[149] Maugin, G. A. [1993]. *Material Inhomogeneities in Elasticity*. Chapman & Hall, London.

[150] Maugin, G. A. [1995]. 'Material forces: Concepts and applications.' *Appl. Mech. Rev.*, **48**, pp. 213–245.

[151] Maugin, G. A. [1999]. *The Thermomechanics of Nonlinear Irreversible Behaviors*. World Scientific Publishing Co.

[152] Maugin, G. A. & C. Trimarco [1992]. 'Pseudomomentum and material forces in nonlinear elasticity: Variational formulations and application to brittle fracture.' *Acta Mechanica*, **94**, pp. 1–28.

[153] Maute, K. [1998]. *Topologie– und Formoptimierung von dünnwandigen Tragwerken*. Dissertation, Bericht des Instituts für Baustatik Nr. 25, Universität Stuttgart.

[154] Miehe, C. [1988]. *Zur numerischen Behandlung thermomechanischer Prozesse*. Dissertation, Universität Hannover, Institut für Baumechanik und Numerische Mechanik, Bericht-Nr. 88/6.

[155] Miehe, C. [1993]. *Kanonische Modelle multiplikativer Elasto–Plastizität – Thermodynamische Formulierung und Numerische Implementation*. Habilitationsschrift, Institut für Baumechanik und Numerische Mechanik, Universität Hannover, Bericht-Nr. 93/1.

[156] Miehe, C. [1995]. 'Entropic thermoelasticity at finite strains. Aspects of the formulation and numerical implementation.' *Comp. Meth. Appl. Mech. Eng.*, **120**, pp. 243–269.

[157] Miehe, C. [1995]. 'A theory of large–strain isotropic thermoplasticity based on metric transformation tensors.' *Arch. Appl. Mech.*, **66**, pp. 45–64.

[158] Mueller, R. & G. A. Maugin [2002]. 'On material forces and finite element discretizations.' *Comp. Mech.*, **29**, pp. 52–60.

[159] Mullender, M. G. & R. Huiskes [1995]. 'A proposal for the regulatory mechanisms of Wolff's law.' *J. Orthop. Res.*, **13**, pp. 503–512.

[160] Mullender, M. G., R. Huiskes & A. Weinans [1994]. 'A physiological approach to the simulation of bone remodeling as a self–organizational control process.' *J. Biomechanics*, **27**, pp. 1389–1394.

[161] Müller, I. [1973]. *Thermodynamik: die Grundlagen der Materialtheorie*. Bertelsmann Universitätsverlag, Düsseldorf.

[162] Müller, I. [1994]. *Grundzüge der Thermodynamik*. Springer Verlag, Berlin – Heidelberg – New York.

[163] Müller, R., S. Kolling & D. Gross [2002]. 'On configurational forces in the context of the finite element method.' *Int. J. Num. Meth. Eng.*, **53**, pp. 1557–1574.

[164] Murnaghan, F. D. [1951]. *Finite Deformation of an Elastic Solid*. John Wiley & Sons, New York – Chapman & Hall, London – limited, first edition.

[165] Murray, J. D. [2003]. *Mathematical Biology – Volume I: An Introduction*. Springer Verlag, Berlin – Heidelberg – New York, third edition.

[166] Murray, J. D. [2003]. *Mathematical Biology – Volume II: Spatial Models Biomedical Applications*. Springer Verlag, Berlin – Heidelberg – New York, third edition.

[167] Murray, J. D., J. Cook, R. Tyson & S. R. Lubkin [1998]. 'Spatial pattern formation in biology: I. Dermal wound healing. II. Bacterial patterns.' *J. Franklin Inst.*, **335B**, pp. 303–332.

[168] Nackenhorst, U. [1997]. 'Ein effizientes Finite Element Verfahren zur Simulation des beanspruchungsadaptiven Knochenwachstums.' In *Die Methode der Finiten Elemente in der Biomechanik, Biomedizin und angrenzenden Gebieten*. Workshop 1997, Universität Ulm.

[169] Nackenhorst, U. [1997]. 'Numerical simulations of stress stimulated bone remodeling.' *Technische Mechanik*, **17**, pp. 31–40.

[170] Nield, D. A. & A. Bejan [1999]. *Convection in Porous Media*. Springer Verlag, Berlin – Heidelberg – New York.

[171] Oden, J. T. [1972]. *Finite Elements of Nonlinear Continua*. Mc Graw–Hill Advanced Engineering Series.

[172] Ogden, R. W. [1997]. *Non–Linear Elastic Deformations*. Dover Publications, Mineola – New York.

[173] Pauwels [1965]. *Gesammelte Abhandlungen zur funktionellen Anatomie des Bewegungsapparates*. Springer Verlag, New York – Berlin – Heidelberg.

[174] Pettermann, H. E., T. J. Reiter & F. G. Rammerstorfer [1997]. 'Computational simulation of internal bone remodeling.' *Arch. Comp. Meth. Eng.*, **4**, pp. 295–323.

[175] Podio-Guidugli, P. [2000]. *A Primer in Elasticity*. Kluwer Academic Publishers, Dordrecht – Boston – London.

[176] Reddy, J. N. [2002]. *Energy Principles and Variational Methos in Applied Mechanics*. John Wiley & Sons, Chichester – New York, second edition.

[177] Reese, S. [2001]. *Thermomechanische Modellierung gummiartiger Polymerstrukturen*. Habilitationsschrift, Institut für Baumechanik und Numerische Mechanik, Universität Hannover, Bericht-Nr. F01/4.

[178] Reese, S. & S. Govindjee [1998]. 'Theoretical and numerical aspects in the thermo–viscoelastic mateiral behavior of rubber–like polymers.' *Mechanics of Time–Dependent Materials*, **1**, pp. 357–396.

[179] Reese, S. & P. Wriggers [1998]. 'Thermo–viscoelastic material behaviour at finite deformations with temperature–dependent material parameters.' *ZAMM*, **78**, pp. S157–S160.

[180] Reiter, T. J. [1996]. *Functional Adaption of Bone and Application in Optimal Structual Design*. VDI Berichte Reihe 17, Nr. 145, VDI–Verlag, Düsseldorf.

[181] Roberts, A. J. [1994]. *A One–Dimensional Introduction to Continuum Mechanics*. World Scientific Publishing Co., Singapore – New Jersey, London – Hong Kong.

[182] Rodriguez, E. K., A. Hoger & A. D. Mc Culloch [1994]. 'Stress–dependent finite growth in soft elastic tissues.' *J. Biomechanics*, **27**, pp. 455–467.

[183] Rodríguez-Ferran, A., A. Pérez-Foguet & A. Huerta [2002]. 'Arbitrary Lagrangian–Eulerian (ALE) formulation for hyperelastoplacitcity.' *Int. J. Num. Meth. Eng.*, **53**, pp. 1831–1851.

[184] Rogula, D. [1977]. 'Forces in material space.' *Arch. Mech.*, **29**, pp. 705–713.

[185] Roux, W. [1881]. *Der Kampf der Teile im Organismus*. Engelmann, Leipzig.

[186] Schrödinger, E. [1944]. *What is Life?*. reprinted by Cambridge University Press.

[187] Schwarz, V. [2002]. 'Optimale Formfindung von Ingenieurstrukturen im Rahmen der Thermodynamik offener Systeme.' *Diplomarbeit, LTM, University of Kaiserslautern*, **U02–02**.

[188] Sherrat, J. A., P. Martin, J. D. Murray & J. Lewis [1992]. 'Mathematical models of wound healing in embryonic and adult epidermis.' *IMA J. Math. Appl. Med. Biol.*, **9**, pp. 177–196.

[189] Shield, R. T. [1967]. 'Inverse deformation results in finite elasticity.' *ZAMP*, **18**, pp. 490–500.

[190] Shih, C. F., B. Moran & T. Nakamura [1986]. 'Energy release rate along a three–dimensional front in a thermally stressed body.' *Int. J. Fracture*, **30**, pp. 79–102.

[191] Silhavý, M. [1997]. *The Mechanics and Thermodynamics of Continuous Media*. Springer Verlag, New York – Berlin – Heidelberg.

[192] Simo, J. C. [1998]. 'Numerical analysis and simulation of plasticity.' In *Handbook of Numerical Analysis*, edited by P. G. Ciarlet & J. L. Lions, volume VI, pp. 183–499. North–Holland, Elsevier.

[193] Simo, J. C. & C. Miehe [1992]. 'Associative coupled thermo–plasticity at finite strains: Formulation, numerical analysis and implementation.' *Comp. Meth. Appl. Mech. Eng.*, **98**, pp. 41–104.

[194] Sommerfeld, A. [1942]. *Vorlesungen über Theoretische Physik, Band I: Mechanik*. Adademische Verlagsgesellschaft Geest & Portig, Leipzig.

[195] Stark, J. & B. Wicht [2002]. *Dauerhaftigkeit von Beton – Der Baustoff als Werkstoff*. Birkhäuser, Basel – Boston – Berlin.

[196] Steeb, H. & S. Diebels [2002]. 'A thermodynamic–consistent model describing growth and remodeling phenomena.' *Comp. Mat. Sc., submitted for publication*.

[197] Steinmann, P. [2000]. 'Application of material forces to hyperelastostatic fracture mechanics. I. Continuum mechanical setting.' *Int. J. Solids & Structures*, **37**, pp. 7371–7391.

[198] Steinmann, P. [2002]. 'On spatial and material settings of hyperelastodynamics.' *Acta Mechanica*, **156**, pp. 193–218.

[199] Steinmann, P. [2002]. 'On spatial and material settings of hyperelastostatic crystal defects.' *J. Mech. Phys. Solids*, **50**, pp. 1743–1766.

[200] Steinmann, P. [2002]. 'On spatial and material settings of thermo–hyperelastodynamics.' *J. Elasticity*, **66**, pp. 109–157.

[201] Steinmann, P., D. Ackermann & F. J. Barth [2001]. 'Application of material forces to hyperelastostatic fracture mechanics. II. Computational setting.' *Int. J. Solids & Structures*, **38**, pp. 5509–5526.

[202] Strang, G. & G. J. Fix [1973]. *An Analysis of the Finite Element Method*. Prentice Hall, Englewood Cliffs, New Jersey.

[203] Szabó, B. & I. Babuska [1991]. *Finite Element Analysis*. John Wiley & Sons, Chichester – New York, first edition.

[204] Taber, L. A. [1995]. 'Biomechanics of growth, remodeling, and morphogenesis.' *ASME Appl. Mech. Rev.*, **48**, pp. 487–545.

[205] Thompson, W. [1961]. *On Growth and Form*. Cambridge University Press, abridged edition of the 1917 version.

[206] Thoutireddy, P. [2003]. *Variational Arbitrary Lagrangian–Eulerian method*. Ph.D. thesis, California Institute of Technology, Passadena, California. available via `http://etd.caltech.edu`.

[207] Thoutireddy, P. & M. Ortiz [2003]. 'A variational Arbitrary Lagrangian–Eulerian (VALE) method of mesh adaption and optimization in static finite–element calculations.' *Int. J. Num. Meth. Eng.*, **53**, pp. 1337–1351.

[208] Torrenti, J.-M., M. Mainguy, F. Adenot & C. Tognazzi [1998]. 'Modelling of leaching in concrete.' In *Computational Modelling of Concrete Structures*, edited by R. de Borst, N. Bićanić, H. Mang & G. Meschke, pp. 531–538. Balkema, Rotterdam.

[209] Truesdell, C. & W. Noll [1965]. 'The non–linear field theories of mechanics.' In *Handbuch der Physik*, edited by S. Flügge, volume III/3. Springer Verlag, Berlin.

[210] Truesdell, C. & R. Toupin [1960]. 'The classical field theories.' In *Handbuch der Physik*, edited by S. Flügge, volume III/1. Springer Verlag, Berlin.

[211] Ulm, F.-J. & O. Coussy [1995]. 'Modelling of thermomechanical coupling of concrete at early ages.' *J. Eng. Mech.*, **121**, pp. 785–794.

[212] Ulm, F.-J., J.-M. Torrenti & F. Adenot [1999]. 'Chemoporoplasticity of calcium leaching in concrete.' *J. Eng. Mech.*, **125**, pp. 1200–1211.

[213] Wall, W. A. [1999]. *Fluid–Struktur–Interaktion mit stabilisierten Finiten Elementen*. Ph.D. thesis, Bericht des Instituts für Baustatik Nr. 31, Universität Stuttgart.

[214] Weinans, H., R. Huiskes & H. J. Grootenboer [1992]. 'The behavior of adaptive bone–remodeling simulation models.' *J. Biomechanics*, **25**, pp. 1425–1441.

[215] Weinans, H., R. Huiskes & H. J. Grootenboer [1994]. 'Effects of fit and bonding characteristics of femoral stems on adaptive bone remodeling.' *J. Biomech. Eng.*, **116**, pp. 393–400.

[216] Weinans, H. & P. J. Prendergast [1996]. 'Tissue adaption as a dynamic process far from equilibrium.' *Bone*, **19**, pp. 143–149.

[217] Weng, S. [1997]. *Ein Evolutionsmodell zur mechanischen Analyse biologischer Strukturen*. Dissertation, Mitteilungen aus dem Institut für Mechanik, Ruhr–Universität Bochum, Bochum.

[218] Weng, S. [1997]. *Ein Evolutionsmodell zur mechanischen Analyse biologischer Strukturen*. Dissertation, Mitteilungen aus dem Institut für Mechanik, Ruhr–Universität Bochum.

[219] Wilmański, K. [1998]. *Thermomechanics of Continua*. Springer Verlag, Berlin – Heidelberg – New York.

[220] Wolff, J. [1892]. *Das Gesetz der Knochentransformation*. Hirschwald, Berlin.

[221] Wriggers, P. [2001]. *Nichtlineare Finite–Element–Methoden*. Springer Verlag, Berlin.

[222] Wriggers, P. [2002]. *Computational Contact Mechanics*. John Wiley & Sons, Chichester – New York.

[223] Wriggers, P., C. Miehe, M. Kleiber & J. C. Simo [1992]. 'On the coupled thermomechanical treatment of necking problems via finite element methods.' *Int. J. Num. Meth. Eng.*, **22**, pp. 869–883.

[224] Yamada, T. & F. Kikuchi [1993]. 'An arbitrary Lagrangian–Eulerian finite element method for incompressible hyperelasticity.' *Comp. Meth. Appl. Mech. Eng.*, **102**, pp. 149–177.

[225] Zienkiewicz, O. C. [1967]. *The Finite Element Method in Structural and Continuum Mechanics*. Mc Graw–Hill, New York – London.

[226] Zienkiewicz, O. C. & R. L. Taylor [2000]. *The Finite Element Method, Volume I: The Basis*. Butterworth Heinemann, fifth edition.

[227] Zienkiewicz, O. C. & R. L. Taylor [2000]. *The Finite Element Method, Volume II: Solid Mechanics*. Butterworth Heinemann, fifth edition.

[228] Zienkiewicz, O. C. & R. L. Taylor [2000]. *The Finite Element Method, Volume III: Fluid Dynamics*. Butterworth Heinemann, fifth edition.

# Index